An Exploration of Molecular Electro- and Photocatalysts towards Carbon Dioxide Reduction and Hydrogen Evolution

This Thesis is Presented for the Degree of

Doctor of Philosophy

By

Liam Frayne, B. Sc.

Under the supervision of Dr. M. T. Pryce and Prof. J. G. Vos

School of Chemical Sciences

Dublin City University

September 2017

Declaration

I hereby certify that this material, which I now submit for assessment on the programme of study leading to the award of Doctor of Philosophy is entirely my own work, and that I have exercised reasonable care to ensure that the work is original, and does not to the best of my knowledge breach any law of copyright, and has not been taken from the work of others save and to the extent that such work has been cited and acknowledged within the text of my work.

Signed: _____ ID No.:_____ Date: _____

Dedicated to the memories of

Dr. Paraic James

Conor (Bosco) Hatton

Mairead Moran

Acknowledgements

I would like to thank my supervisor Dr. Mary Pryce, for her insight, support, patience and guidance over the course of this Ph.D. For forming what can be best described as a family within the group, for allowing me the freedom within my own project, for giving me the scope to try what I wanted, and for providing me with an introduction to some brilliant minds. Also, to my co-supervisor Prof. Han Vos, again for the same qualities. Particularly for your patience!

To my dad, Tom. I cannot begin to describe how much you've contributed to me getting to this point. You are the kindest and most honest man that I know, and would do anything that I asked to help. To my mother, Helen. Your love has been endless, and unconditional. To my sister, Edel. You've again been there any time I needed anything. Considering how similar we are, we get on too well! To my brother, John and sister-in-law, Deborah. Thank you for your support. We've all pulled together during the toughest times. To my nephews and niece, Luke, Jody, Lucy and Josh, you've been a constant source of motivation!

To all of my uncles and aunts (and cousins!) that have gone far above and beyond to help out. Particularly to Eamonn, Séan and Michael (and Tina) O'Gorman, Mary (and Michael) Mahony, Eileen Sheridan, Willie and Pat Frayne. You've always drilled home the value of education, been there for us in more ways than many could imagine. I am so grateful to have such a wonderful extended family, thank you all. I'd like to especially mention Carmel Hall under the heading of family also, thank you!

Before I go further with a friends section, I cannot say strongly enough how lucky I am to have you guys (I use the word friend as friend, not just meaning acquaintance). My Kilkenny friends, particularly Jamie and Arran. The many friends that I have made in DCU. The chem UG/PG friends, Chris, Monty, Aurélien, Disha, Nilesh, Diego, Cathal, Aisling, Darragh, Sam, Mohammad, Ahmed, Andy, Hannah, Claire and Laura. To my non-chem DCU friends, Heather, Davo, Mick, Kev, Callum, Leanne, Owen, Aisling, Dimitar, Eva, Joseph.

Mick and Callum, a special thank you, you know why! Dimi and Eva, thank you so much for being your awesome selves!! Heather, thank you for being there. Disha, thank you again! Everyone that I haven't mentioned, there isn't enough space unfortunately to write all the things that I want to say. I know that I'm forgetting some important people here. Make sure you guilt me enough after!

To the "brudder sahn" that may as well have carried me the past couple of weeks… and few years! Ru Chris bpy, AKA Christopher Burke. You have gone so unbelievably far to help me out on countless occasions. For many, the go-to guy for all things science-related and many things non-science-related. To an unbelievable mind, and a fantastic friend. Thank you. Thank you also, Aoife!

Mr. Colm Montgomery, Mr. Monty McColm! You've helped me more than you know, and more than I've been able to tell you. Also… Did you know that you're from Swords? Because I didn't!

To the MPRG lab group, past and present. You've all been incredibly supportive throughout this. I've never come across someone that didn't go out of their way to help me in any way possible. Jen, Suzanne, Laura, Finn, Nive, I don't know where to start. I think over the course of a Ph.D, it's hard not to see someone get into difficulty at least a few times. You've all picked me up so many times. Luckily, we have gotten to/will get to see each other on one of our happiest days. Suzie and Jen, again, cannot thank you enough for listening to science Liam, and non-science Liam. Yvonne and Jane, thank you very much for the help! To all others that I've had the pleasure of researching with, particularly Aoife, Tasha, Emma, Nicola, Diana, Tony, Aoibhin, Suraj.

Dr. Jamie Walsh, thank you very much for your expert advice! Prof. Wesley Browne, a sincere thank you for the masterclass/crash course in electrochemistry. Prof. Jonathan Rochford, thank you for your very highly valued input. A special thank you also to the very helpful Prof. Conor Long and Dr. David Collins.

To the DCU chem lab techs, particularly Maurice, Veronica, Vinny, John, Catherine, Ambrose, Damien, Mary. The place wouldn't run without you. I couldn't begin to count the amount of times that you went completely out of the way to help me. Aside from the amazing job that you do, the most important things that you gave me were your welcoming smiles and random laughs! Never a stupid question, and always checking in on us. Random treats, dropping in for a chat, many, many laughs, or a game of dots and dashes. You are the pillars that the chem building stands on.

Thank you also to the chemistry lecturers and staff within DCU. I have landed in unexpectedly on enough of you throughout, and you've always welcomed me.

To the many people that have helped me get to this point. Only here for the party (tag rugby team, not a statement!), everyone responsible for chemistry at IT Carlow for giving me a love for chemistry (special thanks to Ray Benson), Tom and Jenny, Mick McGrath, and a massive thank you to DCU Access.

Without a doubt, I will have missed important people. Pints on me for it.

Finally, a thank you to the Irish Research Council and the ESB.

Table of Contents

Title page i

Declaration ii

Dedication iii

Acknowledgements iv

Table of Contents vi

Abbreviations xi

Table of Tables xvii

Table of Figures xix

Abstract xxxi

1. Chapter 1. Introduction 1

1.1. The greenhouse effect and the rising levels of CO_2 1
1.1.1. Consequences of the rise in CO_2 concentration 2
1.2. Population growth, the demand for energy and energy policies 5
1.2.1. Depleting the reserves of fossil fuels 7
1.2.2. Alternatives to fossil fuels 7
1.3. CO_2 reduction and hydrogen generation 9
1.3.1. Molecular photocatalytic CO_2 reduction 11
1.3.1.1. Intramolecular approaches towards photocatalytic CO_2 reduction 14
1.3.1.1.1. Ru diimine-cyclam Ni and Ru diimine-diimine Co/Ni intramolecular approaches 16
1.3.1.1.2. Ru-Re intramolecular approaches 18
1.3.1.1.3. Ru – $Ru(CO)_2$ intramolecular systems 30
1.3.1.1.4. Os-Re intramolecular systems 35
1.3.1.1.5. Ir – Re systems 35
1.3.1.1.6. Bodipy – Re intramolecular systems 36
1.3.1.1.7. Re – Re systems 37
1.3.1.1.7.1.Re oligonuclear PSs of note 40
1.3.1.1.8. Porphyrin – Diimine and related complexes 41
1.3.1.1.9. Ir-Ir intramolecular complexes 45
1.3.2. Molecular electrocatalytic CO_2 reduction overview 47
1.3.2.1. Assessment of electrocatalytic activity 48
1.3.2.2. Recent advances in molecular CO_2 electrocatalysis 51
1.3.2.2.1. Homogeneous electrocatalysts towards CO_2 reduction 52
1.3.2.2.1.1. Diimine complexes of $Mn(CO)_3X$ and related complexes 52
1.3.2.2.1.2. Diimine $M(CO)_4$ and $M(CO)_6$ (M = Cr, Mo, W) complexes 62
1.3.2.2.1.3. Iron and cobalt porphyrins and related macrocycles 65
1.3.2.2.1.4. Nickel cyclams and related complexes containing Cu and Co 68

1.3.2.2.1.5. Schiff base complexes of Ni, Cu and Co 72
1.3.2.2.1.6. Bisterpyridyl complexes 73
1.3.2.2.1.7. Other Complexes containing first row transition metals 75
1.3.2.2.2. Heterogeneous electrocatalysts towards CO_2 reduction 81
1.3.2.2.2.1. Manganese diimine complexes 81
1.3.2.2.2.2. Iron, cobalt and copper porphyrins and related macrocycles 83
1.3.2.2.2.3. Nickel cyclams and related complexes containing Cu and Co 88
1.3.2.2.2.4. Cu, Ni and Co Schiff base complexes 89
1.3.2.2.2.5. Tetraruthenated pyridyl porphyrins 90
1.3.2.2.2.6. Surface-bound chelating ligand 91
1.3.3. Cobalt based metal complexes towards H_2 generation in organic media 91
1.3.3.1. Co-centred heteromacrocycles 92
1.3.3.1.1. Co porphyrins, corroles and phthalocyanines 95
1.3.3.2. Cobaloximes, Co diimine-dioximes and BF_2 analogues 99
1.3.3.3. Co polypyridyl complexes 100
1.3.3.4. Co phosphines and cyclopentadienyl complexes 109
1.3.3.5. Co dithiolate complexes 114
1.3.3.6. Other Co complexes 116
1.4. References 121

2. Chapter 2. The intramolecular photocatalytic activity of bis-2,2'-bipyridyl ruthenium 2,2':5',3'':6'',2'''-quaterpyridine rhenium tricarbonyl chloride bishexafluorophosphate (RuRe) towards CO_2 reduction 137

2.1. Introduction 137
2.2. Results and Discussion 140
2.2.1. Photocatalytic assessment of RuRe towards CO_2 reduction 140
2.2.1.1. Optimisation of the solvent/sacrificial electron donor system 140
2.2.1.2. Photocatalytic reduction of CO_2 using RuRe and intermolecular system of $[Ru(bpy)_3]^{2+}$ with $Re(bpy)(CO)_3Cl$ in DMF/TEOA (5:1 v/v) 142
2.2.2. Voltammetric assessment of the complexes 144
2.2.2.1. Reductive voltammetry of RuRe, $Re(qpy)(CO)_3Cl$, $[Ru(bpy)_3]^{2+}$ and $Re(bpy)(CO)_3Cl$ 144
2.2.2.2. Oxidative voltammetry of RuRe and $Re(qpy)(CO)_3Cl$ 146
2.2.2.3. Summary of electrochemical data 148
2.2.3. Oxidative UV-visible spectroelectrochemistry (SEC) 150
2.2.3.1. RuRe oxidative UV-visible spectroelectrochemistry 151
2.2.3.2. $Re(qpy)(CO)_3Cl$ oxidative UV-visible SEC 153
2.2.3.3. $[Ru(bpy)_3]^{2+}$ oxidative UV-visible SEC 154
2.2.3.4. Comparison of RuRe UV-visible SEC results with those of $Re(qpy)(CO)_3Cl$ and $[Ru(bpy)_3]^{2+}$ 156
2.2.4. Oxidative IR-SEC of $Re(bpy)(CO)_3Cl$, $Re(qpy)(CO)_3Cl$ and RuRe 156
2.2.4.1. Oxidative IR-SEC of $Re(bpy)(CO)_3Cl$ 157
2.2.4.2. Oxidative IR-SEC of $Re(qpy)(CO)_3Cl$ 158
2.2.4.3. Oxidative IR-SEC of RuRe 160
2.2.5. Energetic feasibility of the systems towards the generation of a Re(ligand) based one electron reduced species 162
2.2.5.1. Oxidative quenching scenario of the $[Ru(bpy)_3]^{2+}$, $Re(bpy)(CO)_3Cl$ and TEOA system 163

2.2.5.2. Reductive quenching scenario of the $[Ru(bpy)_3]^{2+}$, $Re(bpy)(CO)_3Cl$ and TEOA system 164
2.2.5.3. Oxidative quenching scenario of RuRe and TEOA system 164
2.2.5.4. Reductive quenching scenario of RuRe and TEOA system 165
2.2.6. Photocatalytic reduction of CO_2 using $Re(Brbpy)(CO)_3Cl$ with $[Ru(bpy)_3]^{2+}$ in DMF/TEOA (5:1 v/v) 166
2.3. Concluding remarks 167
2.4. References 169

3. Chapter 3. The electrocatalytic activity of a series of Cobalt salicylidene (Salen) complexes towards CO_2 reduction 172

3.1. Introduction 172
3.2. Results and Discussion 174
3.2.1. Electrocatalytic CO_2 reduction by Cobalt Salen complexes, cyclic voltammetry 174
3.2.1.1. Voltammetry of the complexes as reported within the literature 175
3.2.1.2. Voltammetry of the complexes under Ar in DMF/0.1 M $TBAPF_6$ 177
3.2.1.3. Voltammetric response of homogeneous Co salens towards CO_2 reduction in DMF/0.1 M $TBAPF_6$ 185
3.2.1.3.1. Voltammetric response of CoSal towards CO_2 reduction 186
3.2.1.3.2. Voltammetric response of CobdtChexSal towards CO_2 reduction 188
3.2.1.3.3. Voltammetric response of CodBrSal towards CO_2 reduction 193
3.2.1.3.4. Voltammetric response of CopdSal towards CO_2 reduction 196
3.2.1.4. Summary of the $Co^{2+/3+}$ and $Co^{2+/1+}$ redox potentials under Ar and under CO_2 with 5% water 198
3.2.2. Homogeneous controlled-potential electrolysis (CPE) under CO_2 in DMF with 5% water at a 0.071 cm^2 glassy carbon electrode 199
3.2.3. Optimisation of electrocatalytic conditions pertaining to CobdtChexSal 204
3.2.3.1. Homogeneous electrocatalytic CO_2 reduction utilising $Re(bpy)(CO)_3Cl$ with carbon paper working electrode 206
3.2.3.2. Electrode size optimisation for CobdtChexSal 208
3.2.3.3. Voltage optimisation for CobdtChexSal 213
3.2.3.4. SEM of electrode utilised within 3-hour electrolysis at -2.00 V 215
3.3. Concluding remarks 220
3.4. References 222

4. Chapter 4. Electrocatalytic proton reduction with Cobalt(II) bis[3-(salicylidenamino)propyl]methylamine (*(1)*) 226

4.1. Introduction 226
4.2. Results and Discussion 228
4.2.1. Electrochemical experiments at glassy carbon 229
4.2.1.1. Homogeneous electrolyses of ***(1)*** under Ar vs CO_2 at glassy carbon in the presence of water 229
4.2.1.2. Voltammetry of ***(1)*** under Ar and Ar with 5% water 230

4.2.1.3. Reusability of the ***(1)*** solution beyond one hour of electrolysis at glassy carbon 236
4.2.1.4. Electrosynthesised product of ***(1)*** as a heterogeneous proton reduction electrocatalyst, heterogeneous vs homogeneous electrolysis 238
4.2.1.5. Electrolysis of 1 mM ***(1)*** in the absence of water 241
4.2.2. Electrolyses at 3.13 cm^2 (apparent surface area) Toray carbon paper 242
4.2.2.1. Electrolysis results obtained following "Solution" hour 1 and hour 2, and "Surface-1" hours 1 and 2 at Toray carbon paper 242
4.2.2.2. Surface-2 electrolysis results at Toray carbon paper 244
4.2.2.3. Time dependence of H_2 evolution for solution hour 1, surface-1 and control experiments 245
4.2.3. SEM and EDX analysis of carbon paper following "solution" and "surface" experiments undertaken in section 4.2.2 251
4.2.3.1. SEM images of "Solution" hour 1 and control Toray carbon paper electrodes 251
4.2.3.2. SEM images and EDX spectra of "Solution" hour 2 Toray carbon paper electrodes 254
4.2.3.3. SEM images and EDX spectra of Toray carbon paper electrodes, "surface-1" hours 1+2 and "surface-1" 2 hours 261
4.2.3.4. SEM images of Toray carbon paper electrodes submerged in 1 mM ***(1)***, non-electrolysed and electrolysed sample 267
4.2.4. In-situ UV-visible spectroelectrochemistry (UV-visible monitored bulk electrolysis) of ***(1)*** in DMF/0.1 M $TBAPF_6$ 269
4.2.4.1. ***(1)*** at -2.48 V vs Fc/Fc^+ without water 270
4.2.4.2. Control experiments regarding UV-visible monitored bulk electrolysis of ***(1)*** 273
4.2.4.2.1. ***(1)*** with 15 μl water, without an applied potential 273
4.2.4.2.2. With 15 μl water, without ***(1)*** or applied potential 275
4.2.4.2.3. 15 μl water in DMF electrolysed at -2.71 V vs Fc/Fc^+ 276
4.2.4.3. ***(1)*** electrolysed at -2.42 V vs Fc/Fc^+ with 15 μl water 278
4.2.4.4. ***(1)*** electrolysed at -2.71 V vs Fc/Fc^+ without water 281
4.2.4.5. ***(1)*** electrolysed at -2.71 V vs Fc/Fc^+, with 15 μl water 285
4.2.5. UV-visible and electrochemical experiments of H_2pdSal ligand 289
4.2.5.1. UV-visible spectrum of the H_2pdSal ligand 289
4.2.5.2. Cyclic voltammetry of the H_2pdSal ligand 290
4.2.5.3. UV-visible monitored electrolysis of the H_2pdSal ligand at -2.71 V vs Fc/Fc^+, with 15 μl water 292
4.3. Concluding remarks 295
4.4. References 298

5. Chapter 5. Materials and methods 301

5.1. Synthesis 301
5.1.1. Synthesis of rhenium 2,2'-bipyridine tricarbonyl chloride ($Re(bpy)(CO)_3Cl$) 301
5.1.2. Synthesis of 5-bromo-2,2'-bipyridine (Brbpy) 302
5.1.3. Synthesis of rhenium 5-bromo-2,2'-bipyridine tricarbonyl chloride ($Re(Brbpy)(CO)_3Cl$) 303

5.1.4. Synthesis of bis(5-bromosalicylidene)ethylenediamine (H_2dBrSal) 304
5.1.5. Synthesis of cobalt bis(5-bromosalicylidene)ethylenediamine monohydrate (CodBrSal) 305
5.1.6. Synthesis of Bis[3-(salicylidenamino)propyl]methylamine (H_2pdSal) 306
5.2. Instrumentation and methods 307
5.2.1. Gas chromatography 307
5.2.1.1. Standards and sample injection 307
5.2.1.2. Calculation of gas generated, TON and Faradaic efficiency 308
5.2.2. Electrochemistry 309
5.2.2.1. Voltammetry and bulk electrolyses (controlled potential electrolyses/Coulometry) 309
5.2.2.1.1. Preparation of carbon paper electrodes 311
5.2.2.2. UV-visible spectrelectrochemistry (UV-vis monitored bulk electrolyses) (chapter four) 312
5.2.2.3. UV-visible-NIR spectroelectrochemistry (chapter two) 313
5.2.2.4. IR spectroelectrochemistry (chapter two) 313
5.2.3. Photocatalysis (chapter two) 313
5.2.4. SEM and EDX 315
5.2.5. Characterisation of synthesised complexes 315
5.3. Chemicals and materials 315
5.4. References 316

6. Conclusion and future work 317

Table of figures and tables within Appendix A A-i

Appendix A – Pertaining to Chapter Two A-1

Table of figures and tables within Appendix B B-i

Appendix B – Pertaining to Chapter Three B-1

Table of figures and tables within Appendix C C-i

Appendix C – Pertaining to Chapter Four C-1

Abbreviations:

ΔE_p	peak-to-peak separation
Φ	quantum yield
η	overpotential
λ	wavelength
ν	scan rate
$[Ru(bpy)_3]^{2+}$	trisbipyridine ruthenium dichloride
(1)	Bis(salicylideniminato-3-propyl)methylamino Cobalt (convention for chapter four)
^{3}MLCT	triplet metal to ligand charge transfer
AA	ascorbic acid
Ag/Ag^+	silver/silver ion reference electrode
Ag/AgCl	silver/silver chloride reference electrode
B	bridging ligand
BE	Bulk electrolysis, also referred to as controlled potential electrolysis
BIH	1,3-dimethyl-2-phenyl-2,3-dihydro-1H-benzoimidazole
$BI(CO_2H)H$	2-(1,3-dimethyl-2,3-dihydro-1H-benzimidazol-2-yl)benzoic acid
BI(OH)H	1,3-dimethyl-(o-hydroxyphenyl)-dihydrobenzoimidazole
BID	barrier ionisation detector
$BMIMBF_4$	1-butyl-3-methylimidazolium tetrafluoroborate
BNAH	1-benzyl-1,4-dihydronicotinamide
bpm	2,2'-bipyrimidine
bpy	2,2'-bipyridine
$bpy(NHAc)_2$	4,4'-diacetamide-2,2'-bipyridine
Brbpy	5-bromo-2,2'-bipyridine

Cat	catalyst
$CDCl_3$	deuterated chloroform
CNT	carbon nanotubes
CO	carbon monoxide
CO_2	carbon dioxide
COF	covalent organic framework
CoO_x	cobalt oxide
CobdtChexSal	Cobalt bisditertbutylcyclohexylenesalen
CodBrSal	Cobalt dibromosalen
CoSal	Cobalt salen
CopdSal	bis(salicylideniminato-3-propyl)methylamino Cobalt (convention for chapter three)
Cp	cyclopentadiene
CV	cyclic voltammetry/voltammogram
dacbpy	4,4’-bis(acetamidomethyl)-2,2’-bipyridine
dceb	4,4’-dicarboxyethyl-2,2’-bipyridine
DCM	dichloromethane
DFT	density functional theory
DMA	dimethylacetamide
dmb	dimethyl-2,2’-bipyridine
dmpb	4,4’-dimethylphosphonatebpy
DMF	dimethylformamide
DMSO	dimethylsulfoxide
dpb	diphosphonatebipyridine
DPV	differential pulsed voltammetry
e^-	electron
$E_{0\text{-}0}$	zero-zero excitation energy
$E_{1/2}$	$(E_{pa} + E_{pc}) / 2$
EDX	Energy-dispersive X-ray spectroscopy

EDTA	ethylenediaminetetraacetic acid
$E_{p/2}$	half-wave potential
E_{pa}	anodic peak potential
E_{pc}	cathodic peak potential
Et	ethyl
EtOH	ethanol
Fc/Fc^{+}	ferrocene/ferrocenium ion ($Fe^{2+/3+}$) redox couple
FE	Faradaic efficiency
FTO	fluorine-doped tin oxide
GC	gas chromatography
H^{+}	hydrogen ion
H_2	hydrogen gas
H_2bdtChexSal	bisditertbutylcyclohexylenesalen ligand
H_2pdSal	bis(salicylideniminato-3-propyl)methylamine ligand
HDME	hanging drop mercury electrode
HER	Hydrogen evolution reaction
HOMO	highest occupied molecular orbital
HPLC	high performance liquid chromatography
IR	infrared
ITO	indium tin oxide
IVCT	intervalence charge transfer band
L	ligand
LED	light emitting diode
LSV	linear sweep voltammetry/voltammogram
LUMO	lowest unoccupied molecular orbital
M	molar, moles per litre
mbpy	4-methylbipyridine
MeCN	acetonitrile

MeO-BNAH	1-(4-methoxybenzyl)-1,4-dihydronicotinamide
MeOH	methanol
mesbpy	dimesitylbipyridine
MOF	metal-organic framework
MS-ESI	Mass spectrometry, Electrospray ionisation
MWCNT	multi-walled carbon nanotubes
NCS^-	isothiocyanate
NHE	normal hydrogen electrode
NMP	n-methyl-2-pyrrolidone
NMR	nuclear magnetic resonance spectroscopy
OCP	open circuit potential
OER	one-electron reduced
OTTLE	optically-transparent thin-layer electrochemical
$P(OEt)_3$	triethylphosphite
P4VP	poly-4-vinylpyridine
phen	1,10-phenanthroline
PhOH	phenol
pic	3-picoline
piq	2-phenylisoquinoline
PMO	periodic mesoporous organosilica
PPh_3	triphenylphosphine
ppic	2-phenyl-(4-picoline)
ppm	parts per million
ppy	2-phenylpyridine
PS	photosensitiser
PTFE	polytetrafluoroethylene
py	pyridine
qpy	2,2’:5’,3’’:6’’,2’’’-quaterpyridine
	unless otherwise stated

RBF	round-bottom flask
$Re(bpy)(CO)_3Cl$	rhenium bipyridine tricarbonyl chloride
$Re(Brbpy)(CO)_3Cl$	rhenium 5-bromo-2,2'-bipyridine tricarbonyl chloride
$Re(qpy)(CO)_3Cl$	rhenium quaterpyridine tricarbonyl chloride
RHE	reversible hydrogen electrode
RuRe	bisbipyridyl ruthenium quaterpyridyl rhenium tricarbonyl chloride bishexafluorophosphate
SCE	saturated calomel electrode
SD	sacrificial electron donor
SEC	spectroelectrochemistry
SEM	(Field Emission) Scanning Electron Microscopy
Si-NW	silicon nanowires
Sol	solvent
$TBABF_4$	tetrabutylammonium tetrafluoroborate
TBAOAc	tetrabutylammonium acetate
TBAP	tetrabutylammonium perchlorate
$TBAPF_6$	tetrabutylammonium hexafluorophosphate
tbubpy	ditertbutylbipyridine
TCPP	tetracarboxyphenylporphyrin
TEA	triethylamine
TEAP	tetraethylammonium perchlorate
$TEAPF_6$	tetraethylammonium hexafluorophosphate
TEOA	triethanolamine
TFA	trifluoroacetic acid
TFE	trifluoroethanol
THF	tetrahydrofuran
TOF	turnover frequency
TON	turnover number
TPP	tetraphenylporphyrin

tptz	2,4,6-tris(2-pyridyl)-1,3,5-triazine
tpy	2,2’-6’,2’’-terpyridine
TR-IR	time-resolved infrared spectroscopy
UV-vis-NIR	ultraviolet-visible-near infrared
V	Volts
XPS	X-ray photoelectron spectroscopy

Table of Tables

Chapter 2.

Table 2.1: Summary of the first oxidation and reduction potentials vs Fc/Fc^+ of the assessed complexes at 100 mV s^{-1} in MeCN/0.1 M $TBAPF_6$

Table 2.2: UV-visible spectral features associated with ligand $\pi-\pi^*$ and MLCTs in MeCN with 0.1 M $TBAPF_6$

Chapter 3.

Table 3.1: Redox values within the literature related to the first reduction and first oxidation of cobalt salens appearing within chapter three

Table 3.2. Redox potentials associated with the first oxidation and first reduction of the cobalt salens assessed in DMF/0.1 M $TBAPF_6$

Table 3.3: Redox potentials of $Co^{2+/3+}$ and $Co^{2+/1+}$ couple under argon and E_{pc} of the Co^{2+} reduction process under Ar and CO_2 with 5% water (ν = 100mV s^{-1})

Table 3.4: Bulk electrolyses undertaken at a 0.071 cm^2 glassy carbon working electrode in DMF/0.1 M $TBAPF_6$ under CO_2 with 5% H_2O in the presence and absence of 1 mM CoSal, bdtChexSal and dBrSal

Table 3.5: Bulk electrolyses undertaken in DMF/0.1 M $TBAPF_6$ under CO_2 with varied water in the presence and absence of 1 mM CopdSal, results in triplicate for varied potential electrolyses, all other electrolyses in singlicate

Table 3.6. One hour bulk electrolyses of CO_2-purged 1 mM $Re(bpy)(CO)_3Cl$ in DMF/5% H_2O/0.1 M $TBAPF_6$ at -2.21 V vs Fc/Fc^+. Large = 1 cm x 2 cm x 370 μm carbon paper, of 4.2 cm^2 apparent submerged surface area), small = 0.071 cm^2 glassy carbon electrode. n = 3

Table 3.7: Varied working electrode size (with dimensions shown in Figure 3.16) for electrocatalytic CO_2 reduction with 1 mM CobdtChexSal at -2.00 V vs Fc/Fc^+ Electrolyte: 5% H_2O in DMF containing 0.1 M $TBAPF_6$. n = 3. The apparent electrode areas submerged are A = 6.2 cm^2, B = 3.1 cm^2, C = 2.1 cm^2

Table 3.8: Varied electrolysis potential (using Figure 3.16 "Electrode B", 3.1 cm^2) for electrocatalytic CO_2 reduction with 1 mM CobdtChexSal. Potentials: -1.83, -1.91, -2.00 and -2.10 V vs Fc/Fc^+. Electrolyte: 5% H_2O in DMF containing 0.1 M $TBAPF_6$. n = 3 with blanks n = 1

Chapter 4.

Table 4.1: Results obtained from one hour-long electrolyses in the presence and absence of ***(1)*** and in the presence and absence of CO_2. Electrolyses were carried out at -2.71 V in a DMF/5% H_2O/$TBAPF_6$ solution with a glassy carbon electrode
Table 4.2: Results of hour-long bulk electrolyses of 1 mM ***(1)*** at -2.71 V vs Fc/Fc^+ and 0.071 cm^2 glassy carbon electrode in DMF/0.1 M $TBAPF_6$/5% water under Ar. Solution hour 2 reused the solution but replaced the electrode and the cell was repurged

Table 4.3: Results obtained from single hour-long electrolyses obtained in the presence and absence of 1 mM ***(1)***. Electrolyses undertaken at -2.71 V in a DMF/5% H_2O/0.1 M $TBAPF_6$ solution with a 0.071 cm^2 glassy carbon electrode. Surface experiments were undertaken in the absence of ***(1)***. The experimental descriptions of "Solution" and "Surface" are as described at the beginning of section 4.2

Table 4.4: Results obtained during the second hour of electrolysis of 1 mM ***(1)***.and subsequent electrolysis of a DMF / 5% H_2O / 0.1 M $TBAPF_6$ solution with the same electrode (surface-2). Electrolyses were undertaken at -2.71 V with a glassy carbon electrode

Table 4.5: Results obtained from single hour-long "solution" electrolyses with 1 mM ***(1)*** in the absence of water, and subsequent "surface" experiments in the presence of 5% water. Electrolyses undertaken at -2.71 V in a DMF/0.1 M $TBAPF_6$ solution with a 0.071 cm^2 glassy carbon electrode

Table 4.6: 1 mM solutions of ***(1)*** or deposit as a result of the first hour of electrolysis in complex electrolysed at carbon paper. Electrolysis at -2.71 V in DMF, 0.1 M $TBAPF_6$ with 5% H_2O

Table 4.7: Surface-1, surface-2 and solution hour 2 electrolyses results at carbon paper. Electrolysis at -2.71 V in DMF, 0.1 M $TBAPF_6$ with 5% H_2O

Table 4.8: Time-monitored H_2 generation within solution hour 1, surface hour 1 and control electrolysis at -2.71 V vs Fc/Fc^+ and 3.13 cm^2 apparent area Toray carbon paper in DMF/0.1 M $TBAPF_6$/5% water

Table of Figures

Chapter 1.

Figure 1.1: Monthly (red) and mean (black) atmospheric CO_2 values recorded at Mauna Loa

Figure 1.2: The change in global surface temperature relative to 1951-1980 average, white = annual mean, black = 5 year mean. Reproduced from NASA/GISS

Figure 1.3: Global patterns of major and minor impacts in recent decades attributed to climate change. Reproduced from IPPC WG II

Figure 1.4: The presence of CO_2 in the atmosphere and the decrease in pH, as analysed at Mauna Loa and station Aloha, Hawaii respectively, and reproduced from the NOAA

Figure 1.5: World energy consumption from 2000-1015, reproduced from Enerdata. Mtoe = Million tonnes of oil equivalent, CIS = former Soviet Union countries. Total figures include coal, gas, oil, electricity, heat and biomass

Figure 1.6: Global energy consumption by type, expressed in Mtoe per year. Reproduced from British Petroleum

Figure 1.7: Growth of renewable source utilisation within Ireland from 1990-2015, reproduced from Sustainable Energy Authority of Ireland (SEAI)

Figure 1.8: Examples of chemical fixation of CO_2, reproduced from Maeda *et al*.

Figure 1.9: A proposed photocatalytic reaction mechanism of $Re(bpy)(CO)_3NCS$

Figure 1.10: The solar irradiation spectrum at sea level, modified from Hummelen

Figure 1.11: **(1)**, the most active intramolecular photocatalyst to date for CO_2 reduction

Figure 1.12: Common sacrificial donors utilised towards photocatalytic CO_2 reduction

Figure 1.13: Intramolecular Ru-Ni complexes **(2)**, **(3)**, **(4)** and **(5)**

Figure 1.14: Intramolecular Ru-Co and Ru-Ni complexes **(6)**, **(7)** and **(8)**

Figure 1.15: Structures of intramolecular Ru-Re complexes, **(9)**, **(10)**, **(11)**, **(13)**, **(14)** and $Ru\text{-}Re_3$ complex **(12)**

Figure 1.16: Trinuclear Ru_2Re and $RuRe_2$ complexes, **(15)** and **(16)**

Figure 1.17: Alkyl chain length variation within the bridge of Ru-Re complexes resulting in **(17)**, **(18)** and **(19)**, and the $Ru\text{-}Re_2$ complex **(20)**

Figure 1.18: Intramolecular complexes of Ru-Re, **(21)** and **(22)**

Figure 1.19: The intramolecular complex **(23)**

Figure 1.20: Ru-Re intramolecular complexes **(24)** as a conjugated comparison to **(17)** and **(25)**

Figure 1.21: **(26)** and **(27)**, cis-, trans- biscarbonyl bisphosphine/phosphite complexes of Ru-Re with respective monomers

Figure 1.22: **(28)** and **(29)**, unsaturated and saturated linkers between Ru_2 and Re metal centres

Figure 1.23: bisethylene-bridged Ru-Re complexes **(30)** and **(31)**

Figure 1.24: Ru-Re complexes **(32)**, **(33)** and **(34)** with varied bridge and O-bridged Ru-Re DMF complex **(35)**

Figure 1.25: Ru-Re complex **(36)**, bearing phosphonate groups

Figure 1.26: Ru-tpy-amide-bpy-Re type complexes **(37)**, **(38)** and **(39)** unsuccessful as CO_2 reduction photocatalysts

Figure 1.27: Ru-$Ru(CO)_2$ complexes **(40)**, **(41)**, **(42)** and **(43)**

Figure 1.28: Ru-$Ru(CO)_2Cl_2$ complexes **(44)** and **(45)** and mononuclear complexes

Figure 1.29: Os-Re intramolecular complexes **(46)** and **(47)** and associated monomolecular complexes

Figure 1.30: Ir-Re complex **(48)**

Figure 1.31: Bodipy tethered Re complexes **(49)** and **(50)** unsuccessful as photocatalyst towards CO_2 reduction, and Re homologue to **(49)**

Figure 1.32: Re-Re complexes of general structure $LReC_nReL$ (alkyl-linked methylbpy units) as assessed for photocatalytic CO_2 reduction

Figure 1.33: Re-Re dinuclear complex **(63)** for the photocatalytic reduction of CO_2

Figure 1.34: An example of oligonuclear Re-centred PSs utilised within intermolecular systems. This example was utilised by Morimoto *et al*.

Figure 1.35: Zn-Re and Pd-Re intramolecular approaches towards CO_2 reduction

Figure 1.36: Rigid porphyrin-diimine and chlorophyll-Re approaches to photocatalytic CO_2 reduction

Figure 1.37: Mono-, di- and trinuclear iridium complexes

Figure 1.38: The terms utilised for CO_2 electroreduction under the headings of robustness, selectivity and efficiency

Figure 1.39: Cyclic voltammetry (ν = 100 mV s^{-1}) of **(89)** (Figure 1.40), reproduced from Bourrez *et al*., in the presence of Ar (a), CO_2 (b), and CO_2 with 5% water (c) in MeCN, potentials quoted vs SCE and undertaken at glassy carbon

Figure 1.40: Manganese bipyridyl complexes appearing in the literature

Figure 1.41: Mn terpyridyl complexes, reproduced from Machan and Kubiak

Figure 1.42: Structures of **(102)**, **(103)**, **(104)**, **(105)** and **(106)** as appearing in the literature

Figure 1.43: Structures of 6-monosubstituted, and 4,6-disubstituted Mn bipyridines as appearing in the literature

Figure 1.44: Mn diaminobutadiene (DAB) complexes as appearing within the literature

Figure 1.45: Structures of Mn pyridyl/pyrimidyl imidazoliyidine-type complexes assessed for electrocatalytic CO_2 reduction

Figure 1.46: Various Mn carbonyl complexes assessed for electrocatalytic CO_2 reduction

Figure 1.47: Structures of Cr, Mo and W bipyridyl complexes assessed towards electrocatalytic CO_2 reduction

Figure 1.48: pyridine monoimine and dipyridylamine tetracarbonyl complexes and metal hexa- and decacarbonyls assessed for electrocatalytic CO_2 reduction

Figure 1.49: Structures of a variety of meso-substituted Fe, Co and Cu porphyrins as appearing within the literature

Figure 1.50: **(156)**, **(157)**, **(158)** and **(159)** as assessed for their electrocatalytic CO_2 reduction ability

Figure 1.51; Structures of various mono- and dinuclear Fe porphyrins assessed towards electrocatalytic CO_2 reduction

Figure 1.52: Structures of Ni and Cu cyclams within the literature

Figure 1.53: Cu, Ni and Co cyclam-related and Ni Schiff base complexes as studied for their CO_2 reducing ability

Figure 1.54: Schiff base and related complexes studied towards CO_2 reduction

Figure 1.55: Bisterpyridyl complexes as assessed for electrocatalytic CO_2 reduction

Figure 1.56: Co tetrapyridyl macrocycles studied towards electrocatalytic CO_2 reduction

Figure 1.57: Various Co complexes assessed towards electrocatalytic CO_2 reduction

Figure 1.58: Various iron-centred complexes of interest to CO_2 reduction

Figure 1.59: Various metal complexes assessed towards electrocatalytic CO_2 reduction

Figure 1.60: Ni complexes assessed towards electrocatalytic CO_2 reduction

Figure 1.61: Cyclopentadienyl complexes assessed towards electrocatalytic CO_2 reduction

Figure 1.62: Various Co and Cu macrocycles as assessed towards heterogeneous electrocatalytic CO_2 reduction

Figure 1.63: Tetraruthenated porphyrin complexes assessed for their electrocatalytic CO_2 reduction ability

Figure 1.64: Various Co macrocycles assessed towards electrocatalytic H_2 generation

Figure 1.65: Co Schiff base dinuclear complexes assessed towards electrocatalytic H_2 generation

Figure 1.66: Various Co porphyrins utilised in electrocatalytic H_2 generation

Figure 1.67: Co hangman porphyrin complexes assessed towards electrocatalytic H_2 generation

Figure 1.68: Co corroles and phthalocyanine assessed towards electrocatalytic H_2 generation

Figure 1.69: Cobalt imine-oxime complexes shown to deposit onto electrode surfaces

Figure 1.70: Various Co polypyridyl complexes reported for electrocatalytic H_2 generation

Figure 1.71: Various Co polypyridyl complexes utilised for electrocatalytic H_2 generation

Figure 1.72: Polypyridyl Co complexes assessed towards electrocatalytic H_2 generation

Figure 1.73: Co polypyridyl complexes assessed towards electro- and/or photocatalytic H_2 generation

Figure 1.74: Dinuclear Co complexes assessed for activity towards electrocatalytic H_2 generation

Figure 1.75: Co and Co-Fe complexes assessed as electrocatalyts towards H_2 generation

Figure 1.76: Co di-, tri- and tetraphos complexes studied towards electrocatalytic H^+ reduction

Figure 1.77: Co cyclopentadienyl triazolylidine complexes assessed towards electrocatalytic proton reduction

Figure 1.78: Co dithiolene complexes assessed towards electrocatalytic H_2 generation

Figure 1.79: Co salen-related complexes utilised towards electrocatalytic proton reduction

Figure 1.80: The similarly reported Co complexes of Zhan *et al*. towards electrocatalytic H^+ reduction

Chapter 2.

Figure 2.1: $[Ru(bpy)_3]^{2+}$, $Re(bpy)(CO)_3Cl$, $Re(Brbpy)(CO)_3Cl$, $Re(qpy)(CO)_3Cl$, RuRe complexes and TEA, TEOA and BNAH sacrificial electron donors studied within this chapter

Figure 2.2: A comparison of UV-visible spectra of $[Ru(bpy)_3]^{2+}$, $Re(bpy)(CO)_3Cl$, $Re(qpy)(CO)_3Cl$, $Re(Brbpy)(CO)_3Cl$ and RuRe, undertaken at room temperature in MeCN

Figure 2.3: The effect of different solvents and sacrificial donors on H_2 and CO production from CO_2 in 134 μM $[Ru(bpy)_3]^{2+}$ with 100 μM $Re(bpy)(CO)_3Cl$ (at λ = 355, 470 and > 400 nm), with an irradiation time of 21 hours

Figure 2.4: Intermolecular vs intramolecular photocatalytic CO_2 reductive performance of 100 μM RuRe, 134 μM $[Ru(bpy)_3]^{2+}$ + 100 μM $Re(bpy)(CO)_3Cl$, 134 μM $[Ru(bpy)_3]^{2+}$, and 100 μM $Re(bpy)(CO)_3Cl$ in DMF/TEOA (5:1 v/v)

Figure 2.5: Reductive electrochemistry of Ar-purged RuRe and $Re(qpy)(CO)_3Cl$ (0.75 mM) in MeCN with 0.1M $TBAPF_6$

Figure 2.6: Oxidative electrochemistry of RuRe dinuclear and $Re(qpy)(CO)_3Cl$ mononuclear complex (0.75mM) in MeCN with 0.1M $TBAPF_6$

Figure 2.7: Top: UV-vis SEC spectra of RuRe bulk-oxidised after the second oxidation feature (1.75 V vs Ag wire) in MeCN with 0.1M $TBAPF_6$. Bottom: Difference spectra from pre-electrolysis spectrum. Successive UV scans were recorded 3.5 minutes apart with the number in the parenthesis representing the scan number

Figure 2.8: Top: UV SEC spectra of $Re(qpy)(CO)_3Cl$ bulk-oxidised after E_{pa} (1.65 V vs Ag wire) in MeCN with 0.1 M $TBAPF_6$. Inset: Depletion of Re -> qpy MLCT. Bottom: Difference spectra from pre-electrolysis spectrum

Figure 2.9: Oxidative UV-visible SEC of $[Ru(bpy)_3]^{2+}$, oxidised with Pt mesh electrode at 1.6 V vs Ag wire and 0 V following oxidation at 1.6 V, in MeCN with 0.1 M $TBAPF_6$. BE = bulk electrolysis or controlled potential electrolysis

Figure 2.10: Oxidative IR-SEC of $Re(bpy)(CO)_3Cl$, cyclic voltammetric scans at Pt mesh to 1.6V vs Ag wire in MeCN, 0.1M $TBAPF_6$

Figure 2.11: Above: Oxidative IR-SEC of $Re(qpy)(CO)_3Cl$. at rest and 0 to 1.4 V vs Ag wire in MeCN, 0.1 M $TBAPF_6$. Below: Difference spectrum of changes occurring (0 to 1.4 V – rest)

Figure 2.12: IR-SEC difference spectra of $Re(qpy)(CO)_3Cl$ in MeCN with controlled potential electrolyses from 0.7 V to 1.2 V vs Ag wire. Spectra are baseline corrected to 1995 cm^{-1}

Figure 2.13: IR SEC of the first and second changes observed for RuRe, controlled potential electrolysis at Pt gauze electrode in MeCN with 0.1 M $TBAPF_6$, potentials vs Ag quasi-reference electrode

Figure 2.14: Oxidative and reductive quenching scenarios related to photocatalytic reduction, reproduced from Yamazaki *et al*.

Figure 2.15: Photocatalytic reduction of CO_2 with 134 μM $[Ru(bpy)_3]^{2+}$ and either 100 μM $Re(Brbpy)(CO)_3Cl$ or 100 μM $Re(bpy)(CO)_3Cl$ in DMF/TEOA (5:1). Samples were irradiated for 21 hours

Chapter 3.

Figure 3.1: Cobalt salen structures; CoSal, CobdtChexSal, CodBrSal and CopdSal assessed for electrocatalytic CO_2 reduction

Figure 3.2: Cyclic voltammetry of approximately 1 mM CoSal, 1 mM CobdtChexSal, CodBrSal and CopdSal in DMF with 0.1 M $TBAPF_6$ under Ar (ν = 100 mV sec^{-1}). The voltammograms are offset by 30 μA. The initial scanning direction was positive for CoSal and negative for CobdtChexSal, CodBrSal and CopdSal from an OCP of approximately -0.7 V

Figure 3.3: Cyclic voltammetry of 1 mM CobdtChexSal to -2.89 V and to -3.49 V under Ar in DMF/0.1 M $TBAPF_6$, including background DMF/0.1 M $TBAPF_6$ under Ar, (ν = 100 mV s^{-1}). CobdtChexSal to -2.89 V and background scans are offset by 25 and 40 μA respectively. Inset: no current offset and magnified, scans of regions containing the first reduction (left) and first oxidation (right)

Figure 3.4: Cyclic voltammetry of CodBrSal under Ar in DMF/0.1 M $TBAPF_6$, (ν = 100 mV s^{-1}). Scans to -2.84 V and -2.44 V are offset by 50 and 80 μA respectively

Figure 3.5: 1 mM CopdSal under Ar in DMF with 0.1 M $TBAPF_6$ (100 mV s^{-1}), switching potential of -2.71, -2.76, -3.06 and -3.21 V

Figure 3.6: Cyclic voltammetry of approximately 1mM CoSal in DMF with 0.1M $TBAPF_6$ under Ar, CO_2 and CO_2 with 5% H_2O (ν = 100 mV sec^{-1}). The initial scanning direction was positive from an OCP of approximately -0.7 V

Figure 3.7: Cyclic voltammetry of approximately 1mM CoSal in DMF with 0.1M $TBAPF_6$ under CO_2 with 5% H_2O (ν = 100 mV sec^{-1}), 0.06 to -0.86, -1.26, -1.66 and -2.06 V vs Fc/Fc^+. The initial scanning direction was positive from an OCP of approximately -0.5 V

Figure 3.8: 1 mM CobdtChexSal in DMF with 0.1 M $TBAPF_6$ under Ar, CO_2 and CO_2 with 5% H_2O. The initial scan direction is negative

Figure 3.9: Cyclic voltammetry of CO_2 purged 1 mM CobdtChexSal in DMF with 5% water (ν = 100 mV s^{-1}) with potential sweeps to -0.85 V and -2.45 V. The initial scanning direction is negative

Figure 3.10: Cyclic voltammetry of 1 mM CobdtChexSal featuring the second reduction, in DMF with 0.1 M $TBAPF_6$ under Ar and CO_2 (ν = 100 mV sec^{-1}). The insets include voltammograms halted before the second reduction

Figure 3.11: Cyclic voltammetry of approximately 1 mM CobdtChexSal under Ar with 10% H_2O, CO_2 with 10% H_2O. Initial scan direction from OCP (approximately -0.6 V) is positive for Ar purged, negative for CO_2 purged

Figure 3.12: Cyclic voltammetry of 1 mM CodBrSal in DMF with 0.1 M $TBAPF_6$ under Ar, CO_2 and CO_2 with 5% H_2O. The initial scanning direction is negative

Figure 3.13: 1 mM CodBrSal in DMF with 0.1 M $TBAPF_6$ under Ar, CO_2 and CO_2 with 5% water (ν = 100 mV s^{-1}), -0.04 to -3.24 V vs Fc/Fc^+. The initial scanning direction was negative. CVs under Ar and under CO_2 are offset by 110 and 50 μA respectively

Figure 3.14: Cyclic voltammetry of 1 mM CopdSal in DMF with 0.1 M $TBAPF_6$ under Ar, CO_2 and CO_2 with 5% H_2O, ν = 100 mV s^{-1}. The initial scanning direction is negative

Figure 3.15: Cyclic voltammetry of 1 mM CopdSal at slower scan rate of 10 mV s^{-1} in DMF with 0.1 M $TBAPF_6$ under Ar, CO_2 and CO_2 with 5% H_2O. Initial scanning direction is negative

Figure 3.16: Electrode sizes utilised within size optimisation for CobdtChexSal, the third dimension is 370 μm. The apparent electrode areas submerged are A = 6.2 cm^2, B = 3.1 cm^2, C = 2.1 cm^2

Figure 3.17: **i**. μmol of product , **ii**. FE (%) and **iii**. selectivity of CO/H_2 generated with conditions as specified in Table 3.7

Figure 3.18: UV-visible spectra of 1 mM CobdtChexSal in DMF with 0.1 M $TBAPF_6$ and 5% water (diluted to 0.14 mM with the same electrolyte), acquired in aerated samples following electrolysis one and two (two hours) and pre-electrolysis, experimental conditions as per Table 3.7 “A”

Figure 3.19: SEM images at 1000, 5000 and 110000x magnification (top, middle and bottom respectively) of carbon paper utilised in electrolysis at -2.00 V with CobdtChexSal (left) and without (right), 20 kV accelerating voltage, 19 μA probe current

Figure 3.20: Left: Carbon paper electrode used to electrolyse 1 mM CobdtChexSal at -2.20 V under CO_2 in DMF/5% H_2O. Right: Without compound present. Top to bottom: 1300, 5000, 10000, 20000, 50000 and 100000x magnification. 15 kV accelerating voltage, 4.7 μA probe current

Figure 3.21: EDX spectrum of electrode used in electrolysis at -2.2 V for three hours under CO_2 with 1 mM CobdtChexSal, DMF with 5% water and 0.1 M $TBAPF_6$, including image of region examined

Chapter 4.

Figure 4.1: ***(1)***, formerly referred to as CopdSal, as assessed towards proton reduction in chapter four

Figure 4.2: 1 mM ***(1)*** in DMF with 0.1 M $TBAPF_6$ under Ar (ν = 100 mV s^{-1}), switching potential of -2.62, -2.95 V vs Fc/Fc^+ showing the first and second reduction, including the $Co^{2+/3+}$ oxidation. Also included is the third reduction (offset and switching potential of -3.16 V)

Figure 4.3: First two reductions of 1 mM ***(1)*** in DMF with 0.1 M $TBAPF_6$ under Ar and under Ar with 5% water (ν = 100 mV s^{-1}). The voltammograms contain the $Co^{2+/3+}$ oxidation

Figure 4.4: Scan rate dependence of 1 mM ***(1)*** in DMF with 0.1 M $TBAPF_6$ and 5% H_2O under Ar, potential window encapsulating the first oxidation and first reduction only. Scan rate; **i.** 10, 100, 300 and 500 mV s^{-1} and **ii.** 1,000, 3,000, 5,000 and 10,000 mV s^{-1}. Voltammograms are separated in two plots for clarity

Figure 4.5: Linear sweep voltammograms of 1 mM ***(1)*** in DMF with 0.1 M $TBAPF_6$ under Ar and under Ar with 5% water (ν = 100 mV s^{-1}), scans to -2.95 V

Figure 4.6: Bulk electrolysis current-time plots for 1 mM ***(1)*** electrolysed for one hour and second subsequent hour with electrode change between. Electrolysis was undertaken at -2.71 V vs Fc/Fc^+ with a glassy carbon electrode in DMF/0.1 M $TBAPF_6$ with 5% water

Figure 4.7: Averaged bulk electrolysis current-time plots for solution hour 1 (1 mM ***(1)***) and surface-1 hours 1 and 2. Electrolyses were undertaken at -2.71 V vs Fc/Fc^+ with a glassy carbon electrode in DMF/0.1 M $TBAPF_6$ with 5% water

Figure 4.8: Bulk electrolysis current-time plots for **i.** solution hour one (containing 1 mM ***(1)***) and **ii.** surface-1 hours one and two at -2.71 V vs Fc/Fc^+ with carbon paper in DMF/0.1 M $TBAPF_6$ with 5% water

Figure 4.9: **i.** moles H_2 generated and **ii.** FE_{H2} with associated time points of 5, 10, 20, 40 and 60 minutes for solution hour 1, surface hour 1 and control 1 hour at -2.71 V vs Fc/Fc^+ and a carbon paper electrode in DMF/0.1 M $TBAPF_6$/5% water (data as per Table 4.8)

Figure 4.9 continued: **iii.** The charge passed plotted versus time points of 5, 10, 20, 40 and 60 minutes of time dependence H_2 monitoring experiment, **iv.** moles H_2 generated versus charge passed within experiment for 5, 10, 20, 40 and 60 minute time points. Curves include solution hour 1, surface hour 1 and control 1 hour. Electrolysis at -2.71 V vs Fc/Fc^+ and a carbon paper electrode in DMF/0.1 M $TBAPF_6$/5% water (data as per Table 4.8)

Figure 4.10: SEM images of "Soln hr 1 #1", the carbon paper used as working electrode in the first hour electrolysis of 1 mM ***(1)*** in DMF/5% H_2O/0.1 M $TBAPF_6$, 10 kV accelerating voltage, 19.6 – 20 μA probe current. Magnification left to right, top to bottom: 1300, 5000, 10000, 20000, 50000 and 100000 and 500000x

Figure 4.11: SEM images of "Control hrs 1 and 2", the carbon paper used as working electrode in the first hour electrolysis of DMF/5% H_2O/0.1 M $TBAPF_6$, 1 kV accelerating voltage, 21.6 μA probe current. Magnification left to right, top to bottom: 1300, 5000, 10000, 20000, 50000 and 100000x

Figure 4.12: SEM images of "Control 2 hrs", the carbon paper used as working electrode in the first hour electrolysis of DMF/5% H_2O/0.1 M $TBAPF_6$, 10 kV accelerating voltage, 21.6 μA probe current. Magnification left to right, top to bottom: 1300, 5000, 10000, 20000, 50000 and 100000x

Figure 4.13: SEM images of "Soln hr 2 #1", the carbon paper used as working electrode in the second hour electrolysis of 1 mM ***(1)*** in DMF/5% H_2O/0.1 M $TBAPF_6$, 10 kV accelerating voltage, 20.4 – 20.8 μA probe current. Magnification left to right, top to bottom: 1300, 5000, 10000, 20000, 50000 and 100000x

Figure 4.14: SEM images of "Soln hr 2 #1", the carbon paper used as working electrode in the second hour electrolysis of 1 mM ***(1)*** in DMF/5% H_2O/0.1 M $TBAPF_6$, 1 kV accelerating voltage, 19.6 μA probe current. Magnification left to right, top to bottom: 1300, 5000, 10000, 20000, 50000 and 100000x

Figure 4.15: SEM image (top) and the associated EDX spectrum (bottom) of the "Soln hr 2 #1" electrode. the carbon paper used as working electrode in the second hour electrolysis of 1 mM ***(1)*** in DMF/5% H_2O/0.1 M $TBAPF_6$. 15 kV accelerating voltage

Figure 4.16: SEM images of "Soln hr 2 #2", the carbon paper used as working electrode in the second hour electrolysis of 1 mM ***(1)*** in DMF/5% H_2O/0.1 M $TBAPF_6$, 1 kV accelerating voltage, 19.6 – 21.2 μA probe current. Magnification left to right, top to bottom: 1300, 5000, 10000, 20000, 50000 and 100000x

Figure 4.17: SEM images of select locations appearing on "Soln hr 2 #2", the carbon paper used as working electrode in the second hour electrolysis of 1 mM ***(1)*** in DMF/5% H_2O/0.1 M $TBAPF_6$, 1 kV accelerating voltage, 18.4 – 19.2 μA probe current. Magnification top to bottom: 70000, 70000 and 80000x

Figure 4.18: EDX spectrum of the "Soln hr 2 #2" electrode. the carbon paper used as working electrode in the second hour electrolysis of 1 mM ***(1)*** in DMF/5% H_2O/0.1 M $TBAPF_6$. 15 kV accelerating voltage

Figure 4.19: SEM images of "Surface-1 hrs 1+2 #1", the carbon paper used as working electrode following one hour electrolysis of 1 mM ***(1)*** in DMF/5% H_2O/0.1 M $TBAPF_6$ at -2.71 V vs Fc/Fc^+, and subsequent electrolysis for two interrupted hours in the absence of ***(1)***. 1 kV accelerating voltage, 17.6 – 18.8 μA probe current. Magnification left to right, top to bottom: 1300, 5000, 10000, 20000, 50000 and 100000x

Figure 4.20: SEM image (top) and the associated EDX spectrum (bottom) of the "Surface-1 hrs 1+2 #1" electrode, the carbon paper used as working electrode following one hour electrolysis of 1 mM ***(1)*** in DMF/5% H_2O/0.1 M $TBAPF_6$ at -2.71 V vs Fc/Fc^+, and subsequent electrolysis for two interrupted hours in the absence of ***(1)***. The image and spectrum were acquired at 15 kV accelerating voltage

Figure 4.21: SEM images of "Surface-1 2 hrs #1", the carbon paper used as working electrode following one hour electrolysis of 1 mM ***(1)*** in DMF/5% H_2O/0.1 M $TBAPF_6$ at -2.71 V vs Fc/Fc^+, and subsequent electrolysis for two continuous hours in the absence of ***(1)***. 1 kV accelerating voltage, 21.2 – 21.6 μA probe current. Magnification left to right, top to bottom: 1300, 5000, 10000, 20000, 50000 and 100000x

Figure 4.22: SEM images of a deeper region of "Surface-1 2 hrs #1", the carbon paper used as working electrode following one hour electrolysis of 1 mM ***(1)*** in DMF/5% H_2O/0.1 M $TBAPF_6$ at -2.71 V vs Fc/Fc^+, and subsequent electrolysis for two continuous hours in the absence of ***(1)***. 1 kV accelerating voltage, 20.8 – 21.2 μA probe current. Magnification left to right, top to bottom: 1300, 5000, 10000, 20000, 50000 and 100000x

Figure 4.23: SEM image (top) and the associated EDX spectrum (bottom) of a deeper fibre within the "Surface-1 2 hrs #1" electrode, acquired at 15 kV accelerating voltage

Figure 4.24: Elemental map of the inner region of a deeper fibre within the "Surface 2 hrs #1" electrode, acquired at 15 kV accelerating voltage (associated with the EDX spectrum shown in Figure 4.23)

Figure 4.25: SEM images of "Surface-1 2 hrs #2", the carbon paper used as working electrode following one hour electrolysis of 1 mM ***(1)*** in DMF/5% H_2O/0.1 M $TBAPF_6$ at -2.71 V vs Fc/Fc^+, and subsequent electrolysis for two continuous hours in the absence of ***(1)***. 1 kV accelerating voltage, 21.2 – 21.6 μA probe current. Magnification left to right, top to bottom: 1300, 5000, 10000, 20000, 50000 and 100000x

Figure 4.26: SEM images of carbon paper soaked in 1 mM ***(1)*** dissolved in DMF/5% H_2O/0.1 M $TBAPF_6$ with no electrolysis. 10 kV accelerating voltage, 18.8 – 19.2 μA probe current. Magnification left to right, top to bottom: 1300, 5000, 10000, 20000, 50000 and 100000x

Figure 4.27: SEM images of carbon paper soaked in 1 mM ***(1)*** dissolved in DMF/5% H_2O/0.1 M $TBAPF_6$ at -2.71 V vs Fc/Fc^+, and subsequent electrolysis for two interrupted hours in the absence of ***(1)***. 10 kV accelerating voltage, 18.4 – 18.8 μA probe current. Magnification left to right, top to bottom: 1300, 5000, 10000, 20000, 50000 and 100000x

Figure 4.28: UV-visible monitored bulk electrolysis of 60 μM ***(1)*** at -2.48 V vs Fc/Fc^+ in DMF/0.1 M $TBAPF_6$. Electrolysis was undertaken for two hours

Figure 4.29: Difference spectra associated with the spectra appearing in Figure 4.28 (UV-visible monitored bulk electrolysis of 60 μM ***(1)*** at -2.48 V vs Fc/Fc^+ in DMF/0.1 M $TBAPF_6$. Electrolysis was undertaken for two hours)

Figure 4.30: UV-visible spectra of 60 μM ***(1)*** in stirred Ar-purged DMF with 0.1 M $TBAPF_6$ and 15 μl water

Figure 4.31: UV-visible spectra up to 2.5 hours of Ar-purged and stirred electrolysis cell, containing 15 ml DMF with 0.1 M $TBAPF_6$ and 15 μl water. The solution was not electrolysed

Figure 4.32: UV-visible monitored electrolysis of 15 ml DMF with 0.1 M $TBAPF_6$ and 15μl water (in the absence of ***(1)***) at -2.71 V vs Fc/Fc^+ for 120 minutes

Figure 4.33: UV-visible spectra acquired during the electrolysis of 60 μM ***(1)*** in 15ml DMF/0.1 M $TBAPF_6$ with 15 μl water at -2.42 V vs Fc/Fc^+. The spectra are displayed up to 120 minutes of electrolysis

Figure 4.34: Difference spectra associated with the spectra appearing in Figure 4.33 (UV-visible monitored bulk electrolysis of 60 μM ***(1)*** at -2.42 V vs Fc/Fc^+ in 15 ml DMF/0.1 M $TBAPF_6$ with 15μl water. The spectra are displayed up to 120 minutes of electrolysis)

Figure 4.35: UV-visible spectra as per Figure 4.33 (electrolysis of 60 μM ***(1)*** in 15ml DMF/0.1 M $TBAPF_6$ with 15 μl water at -2.42 V vs Fc/Fc^+) up to 23 minutes of electrolysis

Figure 4.36: UV-visible spectra acquired during the electrolysis of 60 μM ***(1)*** in 15ml DMF/0.1 M $TBAPF_6$ at -2.71 V vs Fc/Fc^+. The spectra were undertaken up to 120 minutes of electrolysis

Figure 4.37: The difference UV-visible spectra associated with Figure 4.36 (as acquired during the electrolysis of 60 μM ***(1)*** in 15ml DMF/0.1 M $TBAPF_6$ at -2.71 V vs Fc/Fc^+). The spectra were undertaken up to 120 minutes of electrolysis

Figure 4.38: UV-visible spectra acquired during the electrolysis of approximately 60 μM ***(1)*** in 15ml DMF/0.1 M $TBAPF_6$ with 15 μl water at -2.71 V vs Fc/Fc^+. The spectra were undertaken up to 120 minutes of electrolysis

Figure 4.39: The difference UV-visible spectra associated with Figure 4.38 (as acquired during the electrolysis of 60 μM ***(1)*** in 15ml DMF/0.1 M $TBAPF_6$ with 15 μl water at -2.71 V vs Fc/Fc^+). The spectra were undertaken up to 120 minutes of electrolysis

Figure 4.40: UV-visible spectra of 77.4 μM Ar-purged ***(1)*** and H_2pdSal in DMF

Figure 4.41: Reductive cyclic voltammetry of H_2pdSal in DMF with 0.1 M $TBAPF_6$ in the absence and presence of 5% water. Scans were undertaken at a glassy carbon electrode (ν = 100 mV s^{-1}) with switching potential of -2.82 V vs Fc/Fc^+

Figure 4.42: UV-visible spectra acquired during the electrolysis of approximately 60 μM H_2pdSal in 15ml DMF/0.1 M $TBAPF_6$ with 15 μl water at -2.71 V vs Fc/Fc^+. The spectra were undertaken up to 120 minutes of electrolysis

Figure 4.43: UV-visible difference spectra acquired during the electrolysis of approximately 60 μM H_2pdSal in 15ml DMF/0.1 M $TBAPF_6$ with 15 μl water at -2.71 V vs Fc/Fc^+. The spectra were undertaken up to 120 minutes of electrolysis

Liam Frayne – An exploration of molecular electro- and photocatalysts towards carbon dioxide reduction and hydrogen evolution

Abstract

The research presented in this thesis focusses on photo- and electrocatalysts for CO_2 reduction and an electrocatalyst towards proton reduction to hydrogen.

Introduced in Chapter one is a brief overview of the issues surrounding rising CO_2 levels and energy consumption, in addition to a literature survey covering intramolecular photocatalytic systems towards CO_2 reduction, the recent advancements in the field of molecular electrocatalysts for CO_2 reduction and Co-centred molecular electrocatalysts active towards proton reduction in organic electrolyte.

Chapter two reports the assessment of a dinuclear ruthenium-quaterpyridine-rhenium complex towards photocatalytic CO_2 reduction. Communication between the metal centres was assessed through electrochemistry, UV- and IR-spectroelectrochemistry.

Within Chapter three, four cobalt salens are screened as potential homogeneous CO_2 electrocatalysts. Of these, the complex, bis(3,5-di-tert-butylsalicylidene)-1,2-cyclohexanediamino cobalt(II) (CobdtChexSal) demonstrated the highest activity in DMF/5% water, with CO observed. With a higher level of charge consumption, H_2 evolution became prevalent.

Chapter four explores the potential of bis(salicylideniminato-3-propyl)methylamino cobalt(II) (CopdSal), for the electrocatalytic generation of hydrogen. Homogeneous solutions or electro-deposited catalytically active electrodes led to the generation of hydrogen. Techniques including electrochemistry, FESEM with EDX and UV-vis monitored electrolyses were utilised in gaining information as to the identity of the active catalyst.

Chapter five contains details regarding materials used and methods undertaken within Chapters two to four.

Chapter six concludes and discusses future work regarding chapters two, three and four.

Chapter 1. Introduction

1.1. The greenhouse effect and the rising levels of CO_2

In recent times, the term "greenhouse effect" may have derived a negative connotation. The sun emits shortwave radiation, which passes through the atmosphere to the earth's surface. Reflectance occurs, with energy at longer wavelengths (IR radiation) returning from the surface [1]. The longer waves can interact with "greenhouse gases", including water vapour and carbon dioxide [2,3], which absorb the infra-red energy. The energy within the greenhouse gases then radiates in each direction, thereby increasing the Earth's temperature from -18 ^{o}C to 14 ^{o}C [4]. Without the natural greenhouse effect, the temperature of the earth would be too cold to sustain the current diversity of life [4].

Carbon dioxide (CO_2) is a low energy gas, derived from the complete combustion of carbonaceous materials. Its atmospheric lifetime is long [3], with rates of uptake varying between 5 and 200 years [5]. Prior to the dawn of the industrial revolution, CO_2 levels within the atmosphere were estimated at approximately 278 ppm [5]. In 1958, the Scripps Institution of Oceanography began monitoring CO_2 levels at Mauna Loa, Hawaii, whereby the first yearly mean figure of 316 ppm was recorded [6]. The U.S. National Oceanic and Atmospheric Administration (NOAA) have since reported far higher and continually rising values. For example, in May of 2013, the level of CO_2 surpassed 400 ppm. Following this, 2016 was the first year in which values greater than 400 ppm were continually detected. The trend from 1959 onward is available in Figure 1.1, providing strong evidence that the level of CO_2 is continually rising.

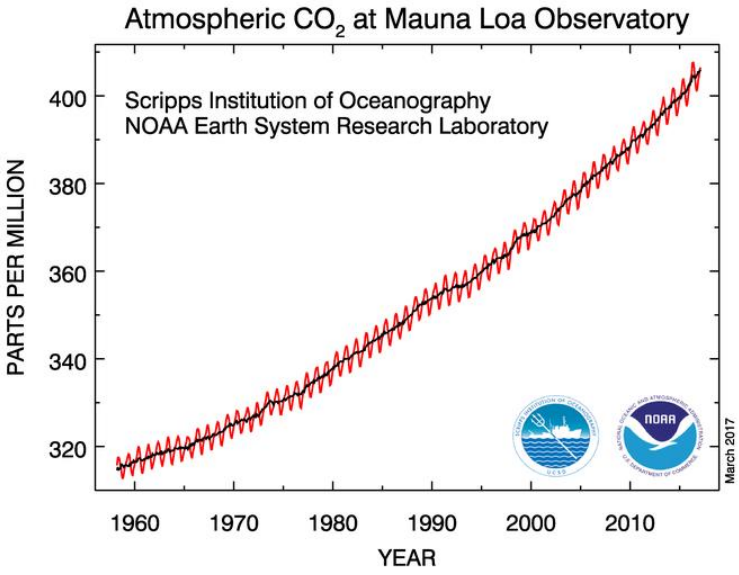

Figure 1.1: Monthly (red) and mean (black) atmospheric CO_2 values recorded at Mauna Loa [6].

1.1.1. Consequences of the rise in CO_2 concentration

The increased presence of CO_2 in the atmosphere brings with it, negative effects. Due to its central involvement, the Kyoto protocol's first commitment period prioritised a reduction in CO_2 emissions, in addition to methane, nitrous oxide, hydrofluorocarbons, perfluorocarbons and sulphur hexafluoride [7]. The preceding section briefly describes the greenhouse effect, caused in part by the presence of CO_2. Unsurprisingly, an increase of CO_2 can be correlated with an increase in the average temperature of the earth. The 2013-published IPCC (Intergovernmental Panel on Climate Change) fifth assessment report specified that 1983–2012 was likely to have been the warmest 30-year period within the previous 1400 years in the northern hemisphere [5]. As is shown in Figure 1.2, the global temperature has been steadily rising since publication of the IPCC report. In 136 years, NASA's Goddard Institute for Space Studies have noted that 2016 was the hottest year on record [8]. Furthermore, with the exception of 1998, the 10 hottest years on record have occurred since 2000.

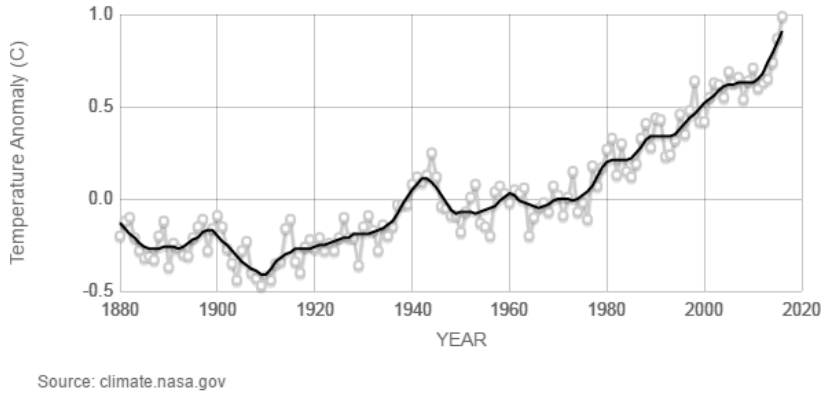

Figure 1.2: The change in global surface temperature relative to 1951-1980 average, white = annual mean, black = 5 year mean. Reproduced from NASA/GISS [8]

In brief, the observed impacts of climate change have been summarised in the IPPC working group II contribution to the fifth assessment report and are presented in Figure 1.3 [9]. These include extreme events such as heat waves, droughts, floods, tornadoes and wildfires leading to damaged ecosystems in addition to reductions in crop yields [10].

The effect of rising global temperatures on the sea levels across the world is two-fold. A higher temperature leads to a melting of glacial ice [10], in addition to thermal expansion of water body volumes [11]. This inevitably leads to an increased risk of flooding and also erosion of costal regions [12]. Though immediate effects (in terms of consumption of countries) will be less obvious, Clark *et al*. for example, project that over the course of the next 10 millennia, populous cities such as Hong Kong, Shanghai, Cairo, Mumbai, Calcutta, Tokyo, Hanoi, Ho Chi Minh and New York city may become at least partly submerged, with countries such as Bangladesh largely claimed by water [11].

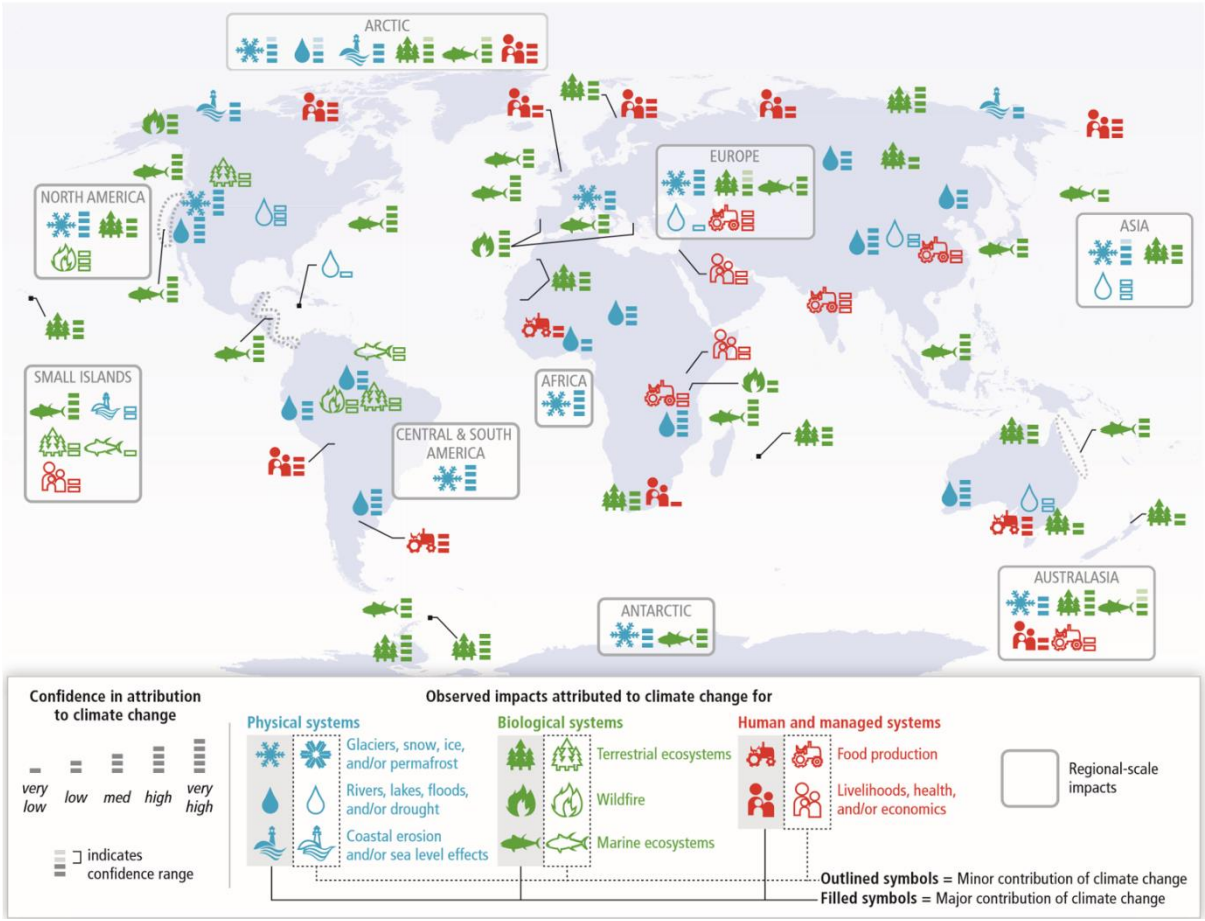

Figure 1.3: Global patterns of major and minor impacts in recent decades attributed to climate change. Reproduced from IPPC WG II [9].

The rise in CO_2 is further evident by its effect on ocean acidification. A decrease in pH of 0.1 unit is estimated from the beginning of the industrial era [5]. The trend acquired by the NOAA related to the acidification of the Pacific Ocean is shown in Figure 1.4. This acidification is believed to pose a threat to marine life [9,13]. Furthermore, the highly publicised bleaching of the Great Barrier Reef for example, is attributed to a 0.5 – 1 K rise in sea temperature over the past 30 years [14].

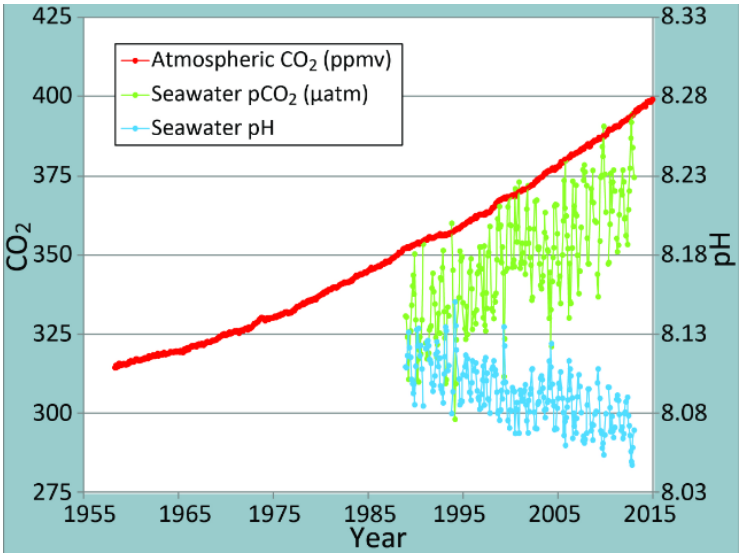

Figure 1.4: The presence of CO_2 in the atmosphere and the decrease in pH, as analysed at Mauna Loa and station ALOHA, Hawaii respectively, and reproduced from the NOAA [13]

1.2. Population growth, the demand for energy and energy policies

The UN estimates that the world population will increase from 7.35 billion in 2015, to 9.7 billion and 11.2 billion in 2050 and 2100 respectively [15]. To 2015, the world's population increased 1 billion since 2003 and 2 billion since 1990. Consequently, the world's demand of energy continues to rise and is further projected to increase [16]. However, though the world population rose 36 % between 1990 and 2013, energy use during the same period increased disproportionately by ~ 54% [17].

By 2020, the EU aims to reduce greenhouse gas emissions to 20% below those of 1990, with a further push to 80% that of 1990 by 2050 [18]. As of 2012, an 18% reduction had been noted, with the potential for the figure to reach 24% by 2020 [19]. The EU 2030 climate and energy framework has called for a minimum of 40% decrease on 1990 levels [20]. Though the EU is aiming to tackle the issue, the population of its 28 member states amounts to approximately 507 million (2014 value [21]), or approximately only 7% of the world's population. The 2016 US Energy Information Administration (EIA) international energy outlook report contains world energy consumption trends up to 2012, including projected energy use [16]. These figures have risen and are projected to continue rising. More recent world energy consumption data,

obtained from Enerdata, is available in Figure 1.5 [22]. This data continues to show a rise of energy use in more recent times.

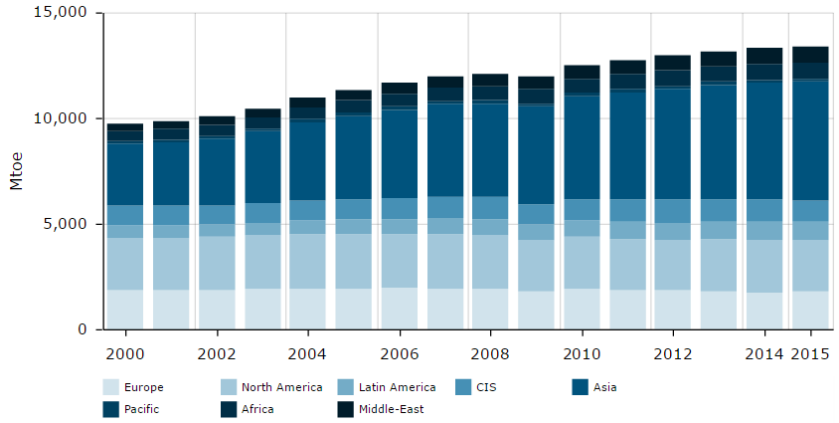

Figure 1.5: World energy consumption from 2000-1015, reproduced from Enerdata [22]. Mtoe = Million tonnes of oil equivalent, CIS = former Soviet Union countries. Total figures include coal, gas, oil, electricity, heat and biomass

The UN Paris climate conference took place in December 2015, whereby 195 countries agreed on a universal action plan, termed the Paris agreement [23]. Previous to this, the Kyoto Protocol has been deemed as unsuccessful, and the 2009 UN convention in Copenhagen failed to produce an international agreement [24,25]. The primary aim of the Paris agreement is to reduce emissions so that Earth's temperature increase due to climate change is kept to well below 2 K higher than that at pre-industrial times, and if possible, to limit it to 1.5 K [23]. The agreement required all participating countries to produce an "intended nationally determined contribution" (INDC) plan/target. The INDCs in their initial form are not anticipated as adequate to meet the 2 K upper limit. However, the agreement encapsulates a revision period of every 5 years, with the aim of each country setting more ambitious targets. Although the issue of climate change should be eased by social obligation, individual national monetary incentives are already in place. For example, the Irish 2010 budget included a carbon tax on liquid fossil fuels, at a rate of €15 per tonne of carbon [26], which rose to €20 per tonne in 2012 [27] with application to solid fuels (excluding wood and biofuels) in 2013 [28].

1.2.1. Depleting the reserves of fossil fuels

The main source of increased CO_2 within the atmosphere is attributable to anthropogenic energy consumption, which is currently sourced primarily via fossil fuels [5]. BP's 2016 review of world energy placed hydroelectricity, renewable, and nuclear energy at a combined 14 % of the source for the 13,147 Mtoe of global energy consumed [29]. As shown in Figure 1.6, a rise of renewable/nuclear energy is observed to continue from 1990, though a similar trend is shown with fossil fuels. Globally proven reserves for oil, gas and coal are expected to be sufficient to meet 50.7, 52.8 and 114 years respectively from the 2015 production levels [29].

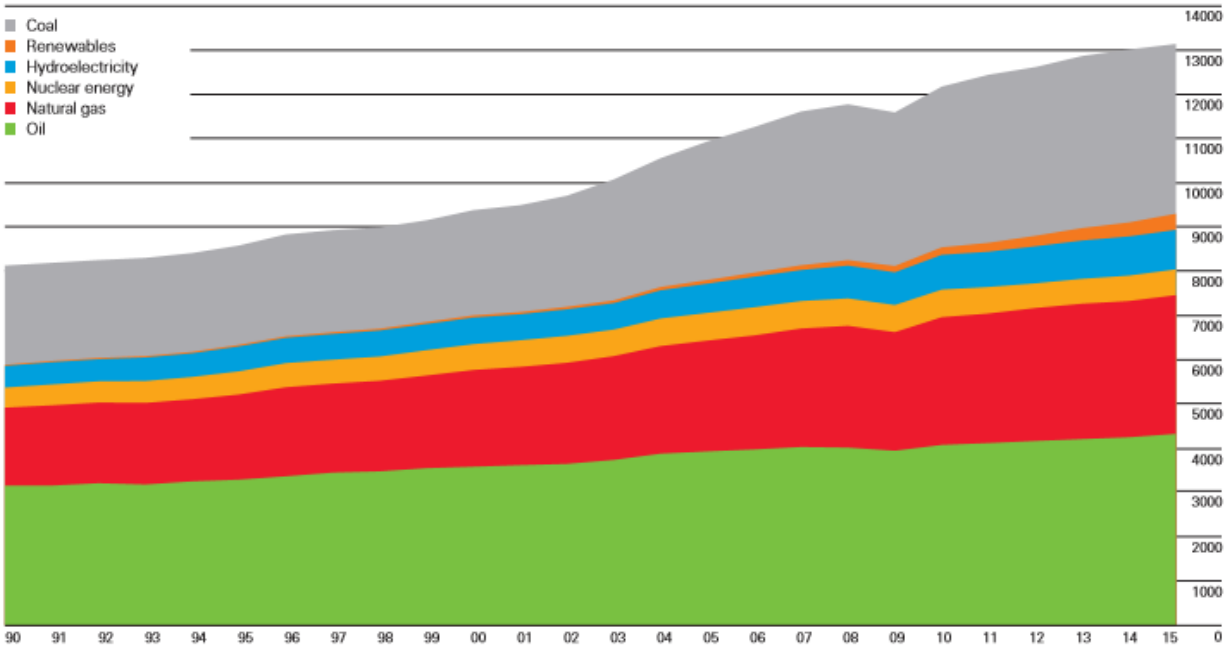

Figure 1.6: Global energy consumption by type, expressed in Mtoe per year. Reproduced from British Petroleum [29].

1.2.2. Alternatives to fossil fuels

Nuclear energy production has shown increasing potential as an energy source. Although it would significantly outlast fossil fuels, it is not a renewable form of energy. Public confidence has also been damaged by such incidents as those in Fukushima, Japan [30] and Chernobyl, Ukraine [31]. In general, there is a negative public perception and fear about nuclear power [32,33]. Such was the fear of a potential accident or terror attack on the Sellafield plant in England, that in 2002, the Irish

government issued potassium iodate tablets nationwide [34]. Though possibly misinformed, public perception must be addressed before nuclear energy could be seen to be a viable option in Ireland. Currently, production of energy by nuclear fission is prohibited within Ireland [35]. Recently, an assessment of a potential nuclear accident close to Ireland was undertaken by the Economic and Social Research Institute and for the Irish government. In such an event, financial losses to Ireland could stand at between approximately €4 and €161 billion [36]. In addition to public concerns, issues further arise regarding adequate treatment of waste water and spent rods along with the general decommission of plants.

Multiple forms of renewable energy exist, such as wind, solar, geothermal, biomass and hydroelectricity. The trend in renewable energy from 1990 to 2015 in Ireland is shown in Figure 1.7 [37]. The total energy produced from renewable sources was 8.3 % in 2015. This figure is below that of the 9.6 % global average (which excludes nuclear power) for 2015 [29]. Wind energy and biomass (including solid biomass, landfill gas, the renewable portion of waste and other biogas) account for a large amount of the renewable energy consumed in 2015. No one technology is likely to solve the world's dependence on fossil fuels alone. Therefore, a concerted effort between technologies is required.

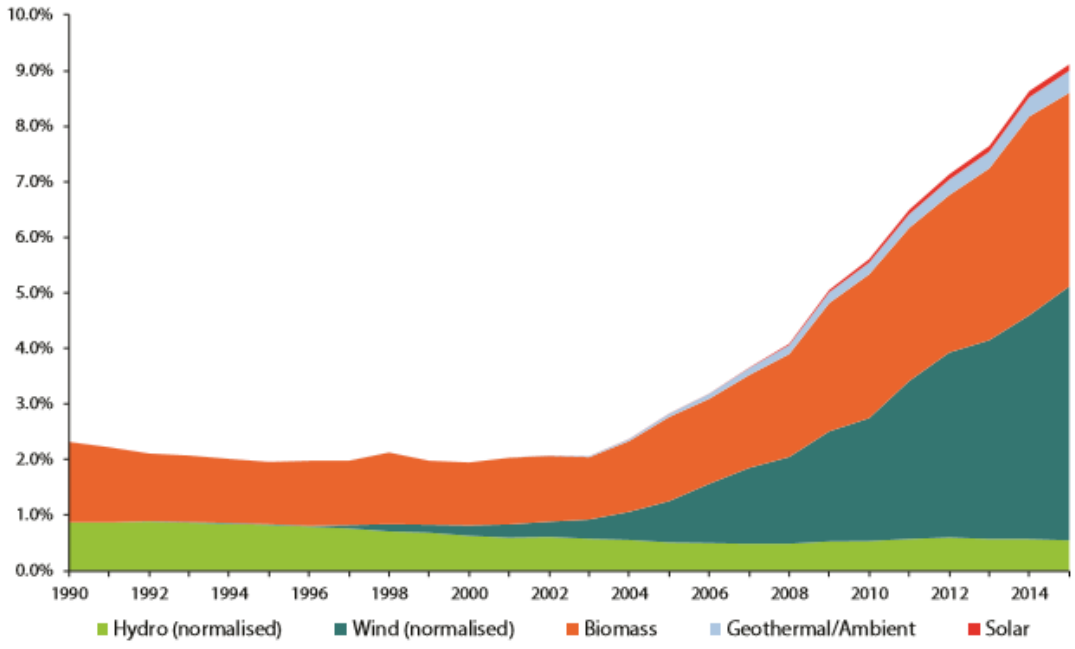

Figure 1.7: Growth of renewable source utilisation within Ireland from 1990-2015, reproduced from Sustainable Energy Authority of Ireland (SEAI) [37].

1.3. CO_2 reduction and hydrogen generation

The work within this thesis is focussed on photo- (chapter two) and electrocatalytic CO_2 reduction (chapter three) in addition to electrocatalytic hydrogen generation (chapter four). Prior to discussing the aforementioned areas, it is noted that other areas of CO_2 utilisation exist. Areas of CO_2 chemical conversion extends beyond that of the electro- and photocatalytic reduction approaches examined within this thesis. Examples of CO_2 as a synthetic starting material are shown in Figure 1.8, with recent developments summarised by Maeda *et al*. [38]. Although this appears to be a practical solution to CO_2 conversion, these synthetic routes employ the use of catalysts that may similarly degrade/deactivate over time and the reactions consume starting materials in addition to CO_2. Some reactions also require co-catalysts. In contrast, though a Brønsted acid is frequently employed for molecular electrocatalytic CO_2 reduction [39], water is often used in this capacity, and additionally, no substrates other than CO_2 and Brønsted acid are utilised. Regarding photocatalysis, a sacrificial electron donor is utilised which is itself converted to an oxidised species. As discussed previously, research into the substitution of sacrificial donors with water is of interest [40,41], and though a more recent area of research, regeneration of the donors may be of interest as an interim fix [42]. Another attractive area of CO_2 mitigation is the use of biological organisms such as cyanobacteria and genetic modifications of such that may be directed to convert CO_2 to higher energy products such as carbohydrates, alcohols and fatty acids [43].

The photocatalytic conversion of CO_2 has the potential to be implemented as part of exploiting solar energy. As can be observed within Figure 1.7, solar energy within Ireland accounts for a minor proportion of the energy utilised. Further efforts within the area is envisaged, with the noted reduction in the costs of solar photovoltaic technology [44,45]. A lower solar insolation in Ireland due to its higher latitude [46,47] may also play a role. In the context of molecular photocatalytic CO_2 reduction, this may result in an advantage as some systems have been shown to perform less efficiently with higher light intensity [48,49].

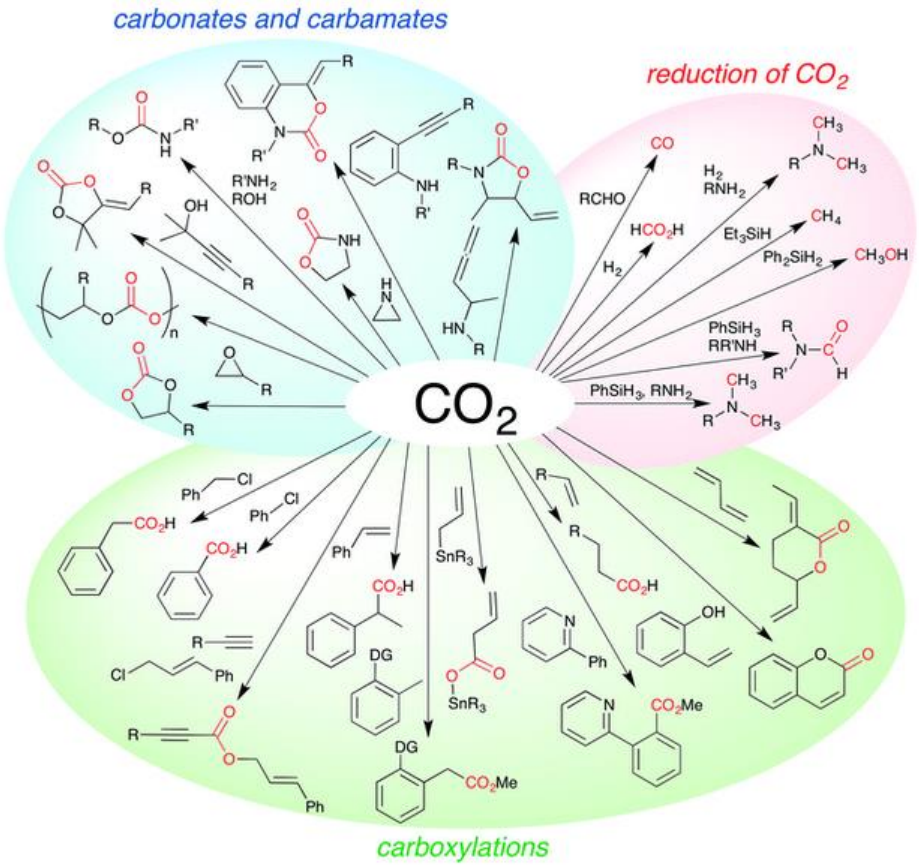

Figure 1.8: Examples of chemical fixation of CO_2, reproduced from Maeda *et al*. [38]

Electrocatalysed CO_2 reduction provides a means of energy storage within chemical bonds. In conjunction with renewable technologies, the process could also serve to remove CO_2 from the environment, surpassing carbon neutrality. Furthermore, molecular electrocatalysts may often be tuned to operate in photocatalytic systems under the right conditions.

Hydrogen is a very energy dense gas [50], with an energy density of 120 MJ kg^{-1} (as compared to 44.4 MJ kg^{-1} of petrol) [51]. When combusted with oxygen, H_2 produces water as its only by-product [51,52]. Hydrogen has been used primarily in the production of ammonia, hydrocracking and in terms of fuel, as a rocket propellant [51].

Commercially available hydrogen fuel cell vehicles exist, though teething issues are also present [53], including that of a lesser developed infrastructure [54][1].

1.3.1. Molecular photocatalytic CO_2 reduction

Three common approaches are utilised in the literature for molecular photocatalytic CO_2 reduction. All three systems contain a light absorber (known as a photosensitiser, PS), a catalytic species (Cat) and a sacrificial electron donor. Within the first type of system, the Cat also acts as the PS, i.e. the Cat is a true photocatalyst. Examples include 2,2'-bipyridyl (bpy) Re dicarbonyl and tricarbonyl complexes [13] and more recently, terpyridyl phenylpyridyl Ir complexes [55] and Fe tetrakistrimethylammoniotetraphenylporphyrin [56]. Complexes within this series often lack the ability to utilise lower energy visible light.

The second type is an intermolecular approach between a PS (commonly trisbipyridyl Ru complexes and more recently using Ir complexes) and Cat. The third approach is the use of intramolecular complexes whereby a PS is bound covalently to the Cat through a bridging ligand (B). The choice of B is not trivial. A π-conjugated system may allow for communication between metal centres (and result in a quicker rate of electron transfer from PS to catalyst [57]). As, or more important than this, often a conjugated system alters the reducing power of PS and Cat centres, and it is stated that the reducing power of the PS should be higher than that of Cat. Furthermore, trends are evident in that the greater the reducing power of Cat, the better its photocatalytic ability may be [58,59].

A proposed reaction scheme of $Re(bpy)(CO)_3SCN$ is shown in Figure 1.9 [60]. Excitation of the photocatalyst precursor leads to a triplet metal to ligand charge transfer (^{3}MLCT) from the Re centre to bpy. Reductive quenching of the excited state by a sacrificial electron donor, in this case triethanolamine (TEOA), produces a radical anion in which the charge resides on the ligand. Dissociation of the axial ligand (NCS^- here) opens a site for CO_2 binding. A second one-electron reduced (OER) species undergoes a bimolecular reaction with the CO_2 adduct, liberating CO and allowing the oxidised complex to become the precursor once again with free NCS^- in solution. It is worth

[1] For example, according to www.afdc.energy.gov/fuels/hydrogen_locations.html (accessed 21 Mar 2017), 34 hydrogen stations exist within the U.S., whereas 15,495 electric, 2,869 ethanol and 210 biodiesel stations exist (excludes private stations).

noting that the axial ligand of MeCN within $[Re(bpy)(CO)_3MeCN]^+$ exchanges quantitatively with DMF. Furthermore, upon the introduction of TEOA, a TEOA adduct was observed, which subsequently allowed insertion of CO_2, upon purging the solution with CO_2 [61]. Similar formation of the CO_2-inserted TEOA adduct was observed in the photocatalytic reaction of $Re(bpy)(CO)_3Br$. A further interesting point is that the CO released following the cycle varies, so that substitution of the three carbonyl groups may be observed [60].

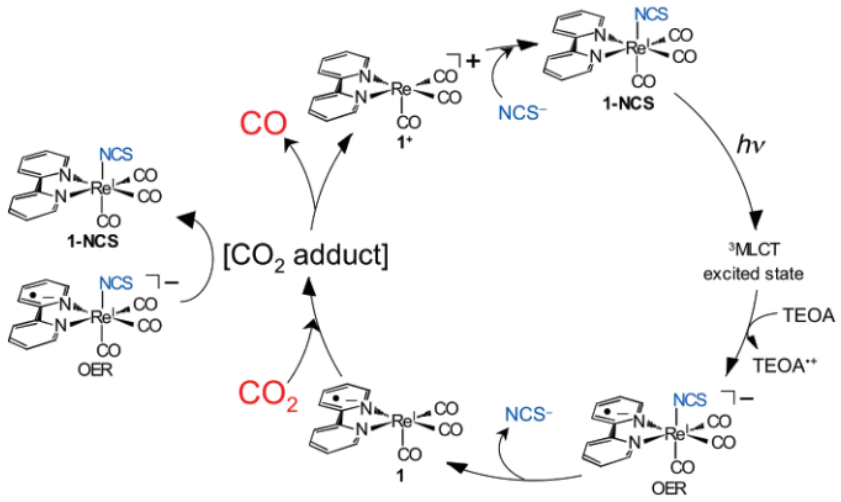

Figure 1.9: A proposed photocatalytic reaction mechanism of $Re(bpy)(CO)_3NCS$ [60]

The second type of reaction, i.e. the intermolecular approach, may occur under either a reductive or oxidative quenching scenario of the excited state PS (PS*) [62]. The reductive quenching scenario is described below [63].

$PS + h\nu \rightarrow PS^*$ Equation 1.1

$PS^* + SD \rightarrow PS^- + SD^{\bullet+}$ Equation 1.2

$PS^- + Cat \rightarrow PS + Cat^-$ Equation 1.3

$Cat^- + CO_2 \rightarrow Cat$ + products (eg. see Figure 1.9) Equation 1.4

The PS is excited typically by visible light, whereby an electron from the highest occupied molecular orbital (HOMO) enters the lowest unoccupied molecular orbital (LUMO) (Equation 1.1). From this, the sacrificial electron donor (SD) donates an

electron into the lowest available energy level (before excitation, the HOMO) of PS* (Equation 1.2). PS^- is now higher in energy than the LUMO of Cat, therefore the electron now in the PS^- LUMO is passed to the LUMO of Cat (Equation 1.3). From here, catalysis is expected to proceed via a mechanism dependent on the specific catalyst (Equation 1.4). This outline does not highlight the transfer of a second electron to the catalyst. For an explanation of the oxidative quenching scenario, the reader is directed to section 2.2.5.

The third approach, i.e. the intramolecular route involves tethering one or more PSs to one or more Cats via a bridging ligand. Within a bimetallic intramolecular complex, some electronic communication between the metal centres is anticipated, so that electron transfer can occur from the PS to the catalyst [64]. Over larger distances, a rigid complex of fixed geometry is stated as preferred for electron transfer [65], however, conjugation of diimines between Ru and Re metal centres may lower the reduction ability of the Re centre [66].

Typical products formed in molecular photo/electrocatalytic CO_2 reduction are CO and formate [67], and rare reports such as the formation of oxalate [68], methanol [69], methane [70], in addition to dimethylformamide from reaction with the sacrificial donor [71]. Approaches to photocatalytic reduction of CO_2 can include the incorporation of semiconductors, metal oxides, metal-organic frameworks (MOFs) [72,73], among others. Direct photochemical CO_2 reduction to CO is even achievable at wavelengths shorter than 200 nm, however, research in this area is not as prevalent due to high energy consumption [74–76]. In this respect, the solar irradiation spectrum at sea level is shown in Figure 1.10. The high energy UV light required for direct conversion is absent from the spectrum. The benefit of molecular photocatalysts is that these catalysts may be integrated into a system with the aforementioned approaches [77]; thereby allowing for CO_2 conversion as part of, for example, a photoelectrochemical cell, with renewable sacrificial donors [42], or with the use of common solvents [78], preferably water, as electron donor [41].

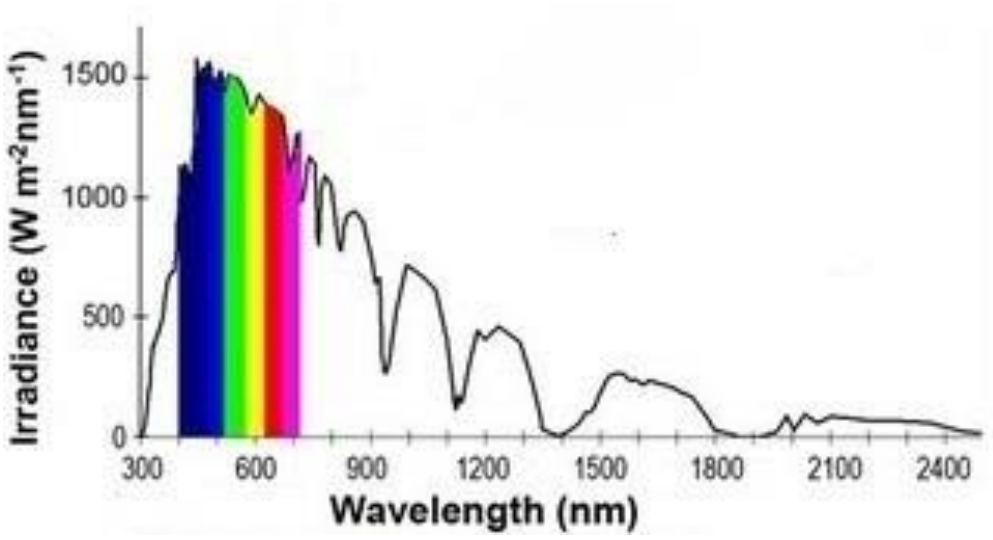

Figure 1.10: The solar irradiation spectrum at sea level, modified from Hummelen [79]

1.3.1.1. Intramolecular approaches towards photocatalytic CO_2 reduction

To provide a background for the work undertaken in chapter two, this section provides a review of intramolecular complexes utilised in the photocatalytic reduction of CO_2. Of the three approaches mentioned for molecular photocatalytic reduction, both proton and CO_2 reduction research to date has shown large interest in intramolecular complexes with the aim of increased speed of electron transfer from the PS to Cat, thus avoiding a potentially rate limiting step of collision of the one electron reduced (OER) PS and Cat in a two-component system. Furthermore, potential immobilisation of PS and catalyst pairings on materials such as semiconductor surfaces can become problematic in the intermolecular approach, since the probability of the PS and Cat being in close enough proximity to each other to pass electrons is less likely [58]. Ru-Ni, Ru-Co, Zn-Re, Ru-Ru, Ru-Re, Re-Re and Ir-Ir PS-Cat metal centres have been utilised regarding photocatalytic intramolecular systems towards CO_2 reduction, with **(1)** (Figure 1.11) [58] appearing as the most superior homogeneous photocatalyst regarding durability with a quoted turnover number (TON_{CO}) of 3029 and turnover frequency (TOF_{CO}) of 35.7 min^{-1} (quantum yield, Φ_{CO} of 0.45) for CO [80,81].

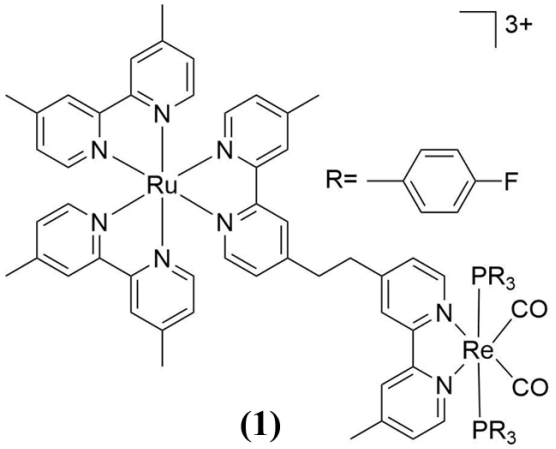

(1)

Figure 1.11: **(1)**, the most active intramolecular photocatalyst to date for CO_2 reduction [80,81]

A range of photosensitisers have appeared in the literature for two component systems, including trisdiimine complexes of ruthenium [71–73,82], cyanoanthracene [83], p-terphenyl [84], phenazine [85], osmium trisdiimines [86], mono- and multinuclear Re diimines [87], and the more recently favoured tris-phenylpyridine and/or diimine Ir-based complexes [83,88–91]. The benefit of Ir-based complexes is the added reducing power of the reduced PS within reductive quenching scenarios. Recently, copper complexes have also gained interest as PSs towards photocatalytic CO_2 reduction [92,93], in addition to iron tetrakistrimethylammoniotetraphenylporphyrin as a self-sensitising photocatalyst [56]. Many examples of well-performing catalysts are diimine rhenium derivatives, with the recent emergence of catalytically active first row transition metal complexes such as nickel [88], iron [83,94], cobalt [89] and manganese [73,95], and renewed interest in second row metals, such as Ru dicarbonyl complexes [82,96], along with rhodium [72]. Common sacrificial electron donors include triethylamine (TEA), triethanolamine (TEOA), 1-benzyl-1,4-dihydronicotinamide (BNAH) in addition to ascorbic acid. More recently, 1,3-dimethyl-2-phenyl-2,3-dihydro-1H-benzoimidazole (BIH) [80] and also derivatives of BNAH and BIH have been reported. The choice of sacrificial donors along with that of the photosensitiser, catalyst (including metal centre) and solvent is often of significant importance regarding the optimisation, and indeed the selectivity of a system [90].

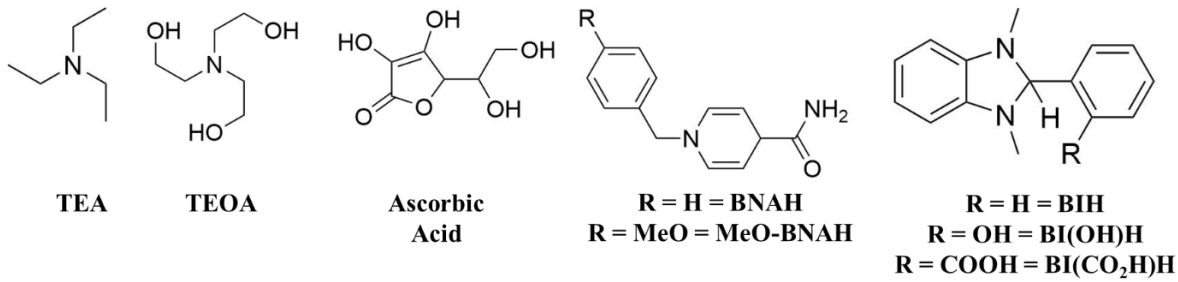

Figure 1.12: Common sacrificial donors utilised towards photocatalytic CO_2 reduction

1.3.1.1.1. Ru diimine-cyclam Ni and Ru diimine-diimine Co/Ni intramolecular approaches

Following the realisation of Ni(cyclam) as an active CO_2 reduction catalyst [97], Kimura *et al*. synthesised [98] and assessed the photocatalytic properties [99] of the Ru-Ni complexes **(2)** and **(3)** (Figure 1.13). An induction period was observed for **(3)** compared to the intermolecular system of $[Ru(bpy)_3]^{2+}$ and Ni(cyclam) (0.09 μl CO vs 0.24 μl CO generated after 1 hour respectively). However, an increased stability was evident within **(3)** relative to the reference system with 44 hr irradiation, producing 3.51 and 1.39 μl CO and H_2 respectively, compared to 1.29 and 2.26 μl CO and H_2 for the reference system. **(2)** showed poorer photocatalytic activity, possibly resulting from the steric hindrance of substitution at the 6 position of the bpy ligand (leading to reduced lifetimes of ^{3}MLCT [100]). Linking bpy and cyclam may be more beneficial on the carbon skeleton rather than at the nitrogens of the cyclam, as for example, a previous electrocatalytic CO_2 reduction study showed that alkylation of the nitrogens led to inhibited catalysis [101]. Irradiation was performed at $\lambda \geq 350$ nm in 1 M, ascorbate buffer (pH 4).

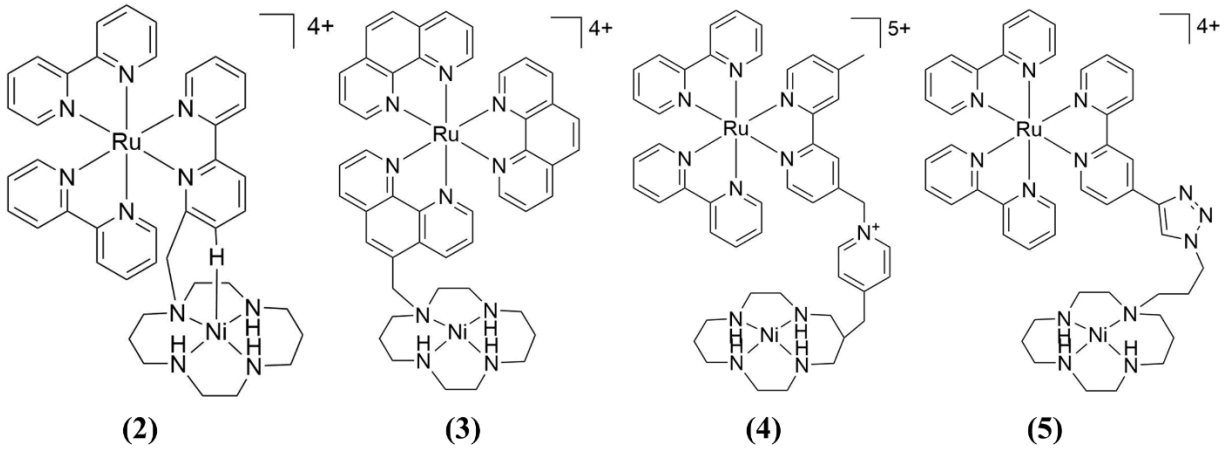

Figure 1.13: Intramolecular Ru-Ni complexes **(2)**, **(3)**, **(4)** and **(5)**

In further work, Kimura *et al*. [102] synthesised and assessed a pyridinium bridged Ru-Ni complex **(4)** (Figure 1.13) and irradiated solutions at $\lambda > 350$ nm for 2 hours. The efficiency of this photocatalytic assembly is modest. Based on data within the study, TONs of 0.55 for CO and 4.4 for H_2 can be calculated. The generation of CO and H_2 were greater and lower respectively than the unsubstituted $[Ru(bpy)_3]^{2+}$ and $[Ni(cyclam)]^{2+}$ in the same concentration as **(4)** (10 μM, 0.32 TON_{CO} and 15.3 TON_{H2}). Though selectivity was increased, the amount of gaseous products produced was less.

More recently, Herrero *et al*. assessed the Ru-Ni complex **(5)** (Figure 1.13), bearing a triazolyl bridge [103]. They reported that the PS unit was quenched by ascorbic acid, however, back-electron transfer to the donor was noted. In a MeCN/H_2O mixed solvent system containing 0.2 M ascorbate buffer (pH 6.4), 30 μM **(5)** generated 5.2 TON_{CO} with 2 TON_{H2} when irradiated with > 435 nm light (800 W halogen lamp) for 60 hours. It was postulated within the study that the relatively low rate/activity of CO generation may be due to the relatively low driving force from the $[Ru]^{1+}$ to the $[Ni]^{2+}$ moeity, whereby the back transfer of electrons from the $[Ru]^{1+}$ subunit to the oxidised ascorbate occurs. The corresponding mononuclear system was not assessed.

Komatsuzaki *et al*. [104] introduced phen-alkyl-phen bridges between Ru and Co (**(6)** and **(7)**) and also Ru and Ni (**(8)**) (Figure 1.14). Upon irradiation with a λ range of 400 - 750 nm, formate was the dominant product in all inter- and intramolecular systems in a 3:1:1 DMF/H_2O/TEOA solvent mix. However, increased selectivity of CO over H_2 was

achieved for the intra- over the intermolecular systems. Based on the electrochemical similarities of the redox potentials with the dinuclear and mononuclear complexes, it was assumed that there was little interaction between the two metal centres. In the case of Co, CO_2 binding was reported as the rate limiting step in both inter- and intramolecular studies, and therefore, electron transfer from the Ru centre to **(6)** and **(7)** did not hinder the reaction. Hence, similar numbers were obtained for both systems. The added electron donation from the pentylene bridge to the Co centre compared with that of the ethylene bridge likely allowed for a higher reduction power of the Co centre, which may explain the higher activity of Ru phen-5-phen Co over Ru phen-2-phen Co towards CO_2 reduction.

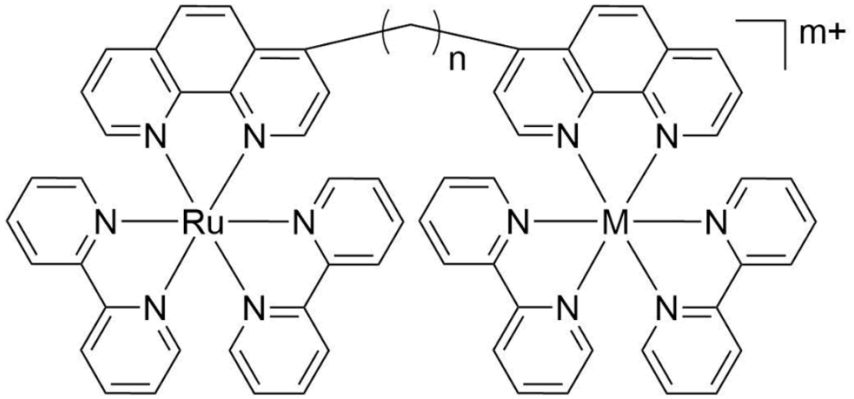

M = Co, n = 2, m = 5 : (6)

M = Co, n = 5, m = 5 : (7)

M = Ni, n = 2, m = 4 : (8)

Figure 1.14: Intramolecular Ru-Co and Ru-Ni complexes **(6)**, **(7)** and **(8)**

1.3.1.1.2. Ru-Re intramolecular approaches

The pairing of trisdiimine Ru and diimine Re complexes for CO_2 reduction has been a common approach to both inter- and intramolecular systems. Furthermore, remaining ligands on the Ru centre allow for selective tuning of the reduction potentials, and therefore, enhancement of catalysis. In this respect, Gholamkhass *et al*. [105] varied the electron density on the Ru subunit with **(9)**, **(10)**, **(11)**, in addition to increasing the number of catalytic centres in the form of **(12)** and a varied bridge in **(13)** and **(14)**, as shown in Figure 1.15. In DMF/TEOA (5:1) with 0.1 M BNAH, **(12)** and **(10)** performed most effectively when irradiated using a high pressure Hg lamp ($\lambda \geq 500$ nm) for 12.5, 16 or 18.5 hours. Quantum yields for CO were measured as 0.093 and 0.12 respectively, compared to 0.062 from a 1:1 ratio of $[Ru(dmb)_3]^{2+}$ to $Re(dmb)(CO)_3Cl$ (dmb =

dimethylbipyridine) with TON_{CO} of 240 and 170 reported versus 101 from the intermolecular system. It may be argued that per catalytic site, **(12)** underperformed compared to the 1:1 system and that the most efficient system was **(10)**. With the series of complexes **(9)**, **(10)**, and **(11)**, the efficiency followed the order of the best having electron-donating ligands with TON_{CO} for **(10)** of 170, 50 for **(9)** and 3 for **(11)**.

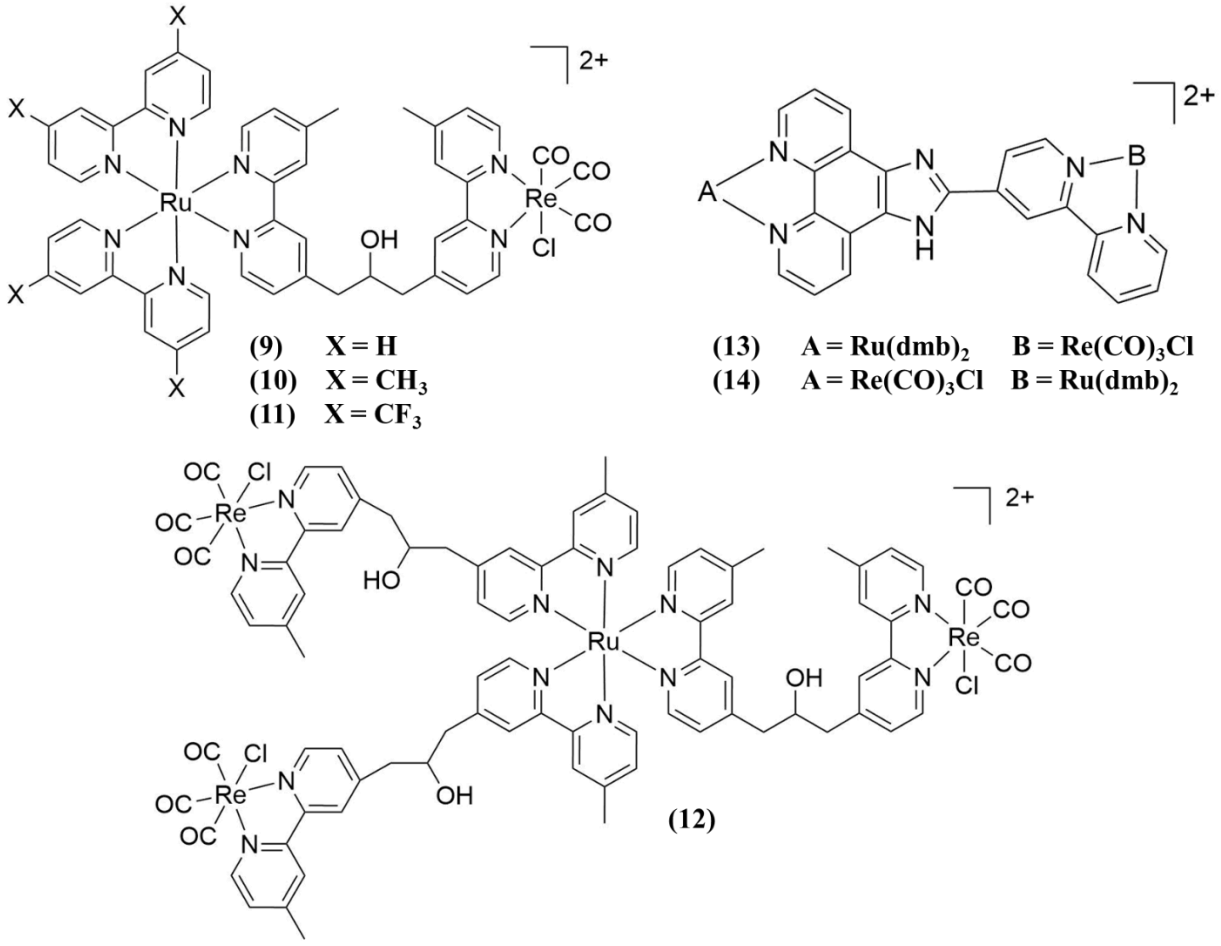

Figure 1.15: Structures of intramolecular Ru-Re complexes, **(9)**, **(10)**, **(11)**, **(13)**, **(14)** and $Ru\text{-}Re_3$ complex **(12)**

Both of the conjugated-bridged Ru-Re complexes (**(13)** and **(14)**) underperformed, with **(13)** generating TON_{CO} of 14 and **(14)** generating twice as much in 28. Both complexes were significantly less active than the intermolecular $[Ru(dmb)_3]^{2+}$ and $Re(dmb)(CO)_3Cl$ system, generating a TON_{CO} of 101. The ligand was stated to allow substantial electronic communication between the metal centres based on voltammetric values.

A closer assessment of the Ru to Re ratio in an intramolecular complex was undertaken by Bian *et al*. [106,107], with the assessment of trinuclear complexes (**(15)** and **(16)**, Figure 1.16). Both systems outperformed their 2-component equivalents with **(16)** producing 190 TON_{CO}, (89 for 2-component) and **(15)** again producing twice the TON_{CO} of the 2-component system (110 vs 55). The increase with the addition of more catalytic centres was evident (**(10)** and **(12)** amassing a TON_{CO} of 160 and 240 respectively), suggesting that both Re sites can be one-electron reduced and also that the OER catalytic sites could be bridged by a molecule of CO_2. **(15)**'s enhanced performance was assumed as the ability to pass two electrons to the Re centre, one from each of the PS subunits.

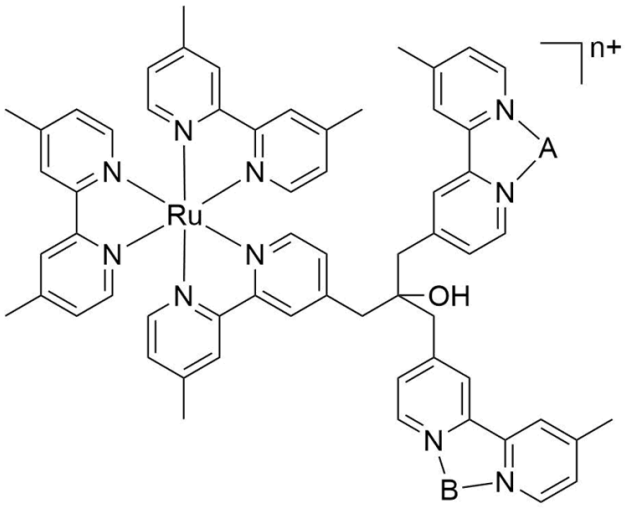

A	B	n +	
$Ru(dmb)_2$	$Re(CO)_3Cl$	4	**(15)**
$Re(CO)_3Cl$	$Re(CO)_3Cl$	2	**(16)**

Figure 1.16: Trinuclear Ru_2Re and $RuRe_2$ complexes, **(15)** and **(16)**

Meister *et al*. also probed the variation of Re units, but with a different ligand. Complexes **(17)** (as also assessed by Koike *et al*. [66]) and **(20)** (Figure 1.17) in addition to **(51)** (Figure 1.32), were irradiated under comparative scenarios [108]. The concentration of metal centres were kept constant at 90 μM in DMF with 1.7 M TEOA and 0.1 M BNAH. When irradiated at 520 ± 50 nm (LED source), the intermolecular approach of $Re(dmb)(CO)_3Cl$ and $[Ru(dmb)_3]^{2+}$ (2:1 ratio) produced 40 TON_{CO}. Covalent attachment of the Re units (**(51)**, Figure 1.32, + $[Ru(dmb)_3]^{2+}$, 1:1 ratio) allowed for a greater than threefold increase in TON_{CO} to 129. Further increases to 174 and then 199 TON_{CO} were obtained with respect to the systems employing **(17)** + $Re(dmb)(CO)_3Cl$ (1:1) and **(20)**. The benefit of covalent attachment of both the Re

centres and also PS to catalytic centres was clearly shown, in addition to the benefit of more than one catalytic centre. The latter point mainly stems from degradation of the PS over the course of the experiment, whereby the authors showed that further additions of $[Ru(dmb)_3]^{2+}$ regenerated catalytic activity. The concentration of **(20)** was increased to 50 μM (150 μM w.r.t. metal centres) to allow a more apt comparison with other groups' studies and a further experiment decreased the photon flux of the LED source to 2.5% that of the previous experiment. A more gradual activity was noted, with TON_{CO} amounting to 315 following 24 hours of irradiation. This behaviour was also previously noted for the mononuclear $Re(dmb)(CO)_3Cl$ [48,49]. It is worth noting that TON_{CO} with respect to the amount of catalytic centres is ~ 100 and 158 where **(20)** was utilised.

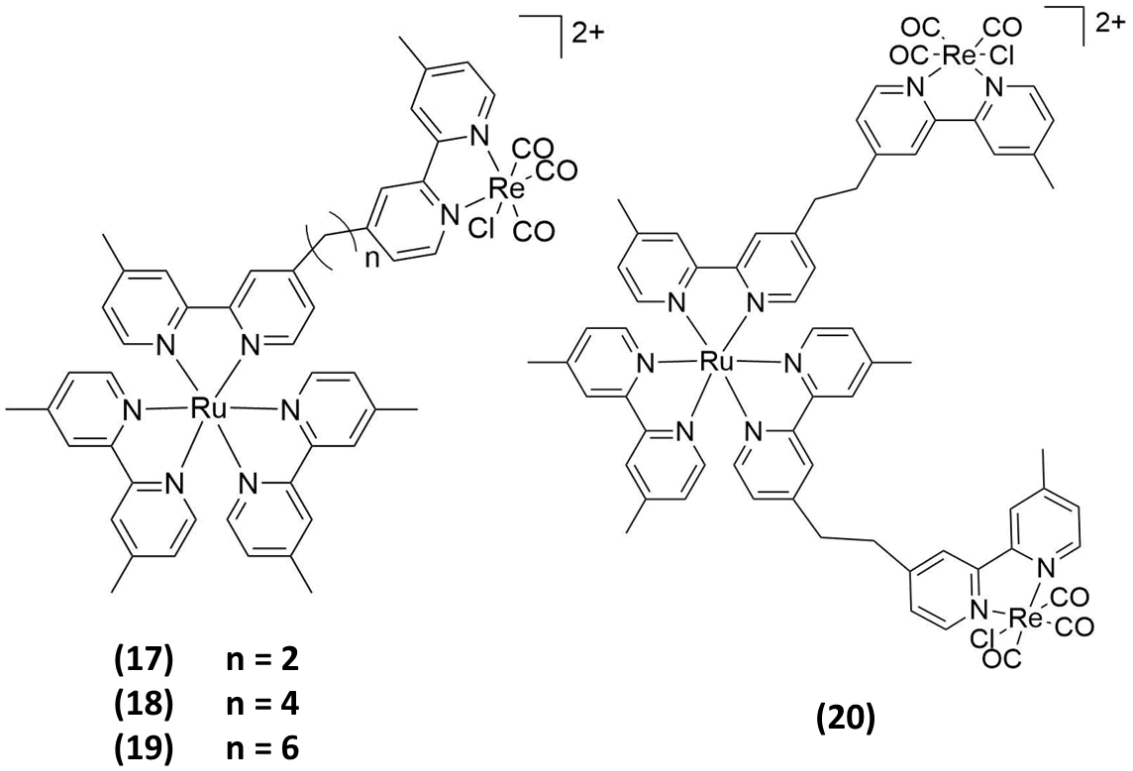

(17) **n = 2**
(18) **n = 4**
(19) **n = 6**

(20)

Figure 1.17: Alkyl chain length variation within the bridge of Ru-Re complexes resulting in **(17)**, **(18)** and **(19)**, and the Ru-Re_2 complex **(20)**.

Subsequent to the work of Bian *et al*., the group and others have shown that substitution of Cl^- with $P(OEt)_3$ was effective at increasing the catalytic activity of the one-component system [109–111]. Therefore, the idea to explore **(21)** and **(22)** (Figure 1.18) was developed [112]. These complexes varied only by the substitution of Cl^- on the Re

centre of **(10)** with either triethylphosphite or pyridine. **(21)** was stated to perform the most efficiently with TON_{CO} of up to 232 and Φ_{CO} of 0.21, as compared with **(10)** (TON_{CO} of 160) and **(22)** (TON_{CO} of 97). Therefore, substitution of Cl^- with $P(OEt)_3$ led to higher TONs and the addition of either free pyridine (TON_{CO} of 120 with 50 μM pyridine added to **(21)**) and the pyridine-bound complex underperformed. The reason for this was thought to be that **(21)** was rapidly converted into the solvento complex $[Ru\text{-}ReSol]^{3+}$, (Sol = DMF or TEOA), believed to be the active catalyst. Cl^- and pyridine binding led to decomposition of the complex, with the pyridine stated to lead to detachment of $Re(CO)_3L$(or Sol). As with the previous study, photocatalytic samples were introduced into DMF/TEOA 5:1 with 0.1M BNAH and irradiated using a high pressure mercury lamp ($\lambda \geq 500$ nm).

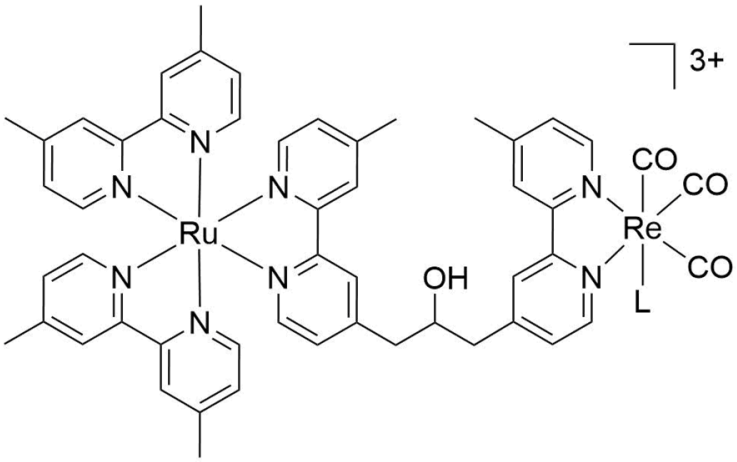

L	
$P(OEt)_3$	**(21)**
Pyridine	**(22)**

Figure 1.18: Intramolecular complexes of Ru-Re, **(21)** and **(22)**

A further study of the Ru-Re series concentrated on varying the alkyl length of the bridge between methyl bipyridines, with **(17)**, **(18)** and **(19)** (Figure 1.17) synthesised for this purpose [66]. The homologue for this study was again **(10)**. **(17)** performed the most efficiently of the series, producing TON_{CO} of 180 with Φ_{CO} of 0.13. **(10)** produced ~150 TONs for CO, whereas **(18)** and **(19)** produced almost identical behaviour with TON_{CO} of 115 and Φ_{CO} of 0.11. Through a slight anodic shift in the complex' potentials, very weak interaction between the subunits was stated in **(17)**, which was not observed in either **(18)** or **(19)**. The authors concluded that this behaviour led to a higher reductive quenching efficiency of ^{3}MLCT excited state of **(17)** by BNAH. Again, the

irradiation conditions and the solvent system were the same as that reported previously [105].

A very closely related complex to **(17)** was utilised by Nakada *et al*. [113], in which the two dmb ligands bound to the Ru centre were replaced with bpy ligands, producing **(23)** (Figure 1.19). The water-soluble complex was assessed for CO_2 photocatalysis in an aqueous solution of 200 mM ascorbate. The product selectivity shifted dramatically from CO observed in DMF with TEOA and BNAH with use of **(17)**, to formate (0.83 selectivity) in aqueous conditions with **(23)**. Irradiation ($\lambda \geq 500$ nm) for 24 hours produced TON_{HCOOH} of 25 as analysed by capillary electrophoresis, whereas TONs for CO and H_2 were 1.2 and 4.6 respectively. Φ_{HCOOH} was measured as 0.002 ($\lambda = 546$ nm). The "model" complexes utilised for comparison to **(23)** included $[Ru(bpy)_3]^{2+}$ and $Re(dmpb)(CO)_3Cl$ (dmpb = 4,4'-dimethylphosphonatebpy). Though it was likely required to include the phosphonate groups to achieve water solubility, the groups may have strongly altered the reducing power of the catalyst. Therefore, interpretation of the ineffective intermolecular system (TON_{HCOOH} of 1.9) should be treated with caution.

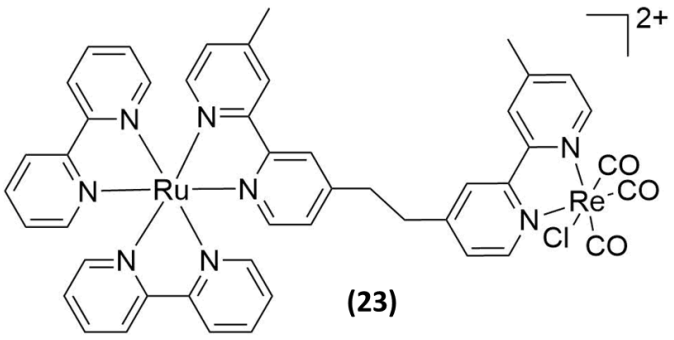

(23)

Figure 1.19: The intramolecular Ru-Re complex **(23)**

Later, **(17)** was also incorporated into an aqueous system [114]. The relative stability of the one electron oxidised product of ascorbate, and therefore, its ability to reoxidise the reduced photosensitiser led to the use of a new, water-soluble, sacrificial donor. 50 μM **(17)** was irradiated with a high pressure mercury lamp ($\lambda \geq 500$ nm) in aqueous solution containing 10 mM dimethyldihydrobenzimidazolylbenzoic acid ($BI(CO_2H)H$), whereby 130 TON_{CO} was achieved over 6 hours. Selectivity towards CO was reported as 0.81 following 3 hours, with the remaining H_2 and some formate attributed to deligation of

the Ru centre. Φ_{CO} was determined to be 13% with a 300 W Xe lamp and a 480 nm monochromatic filter. The mononuclear complexes $[Ru(dmb)_2(mbpy)]^{2+}$ (mbpy = 4-methylbipyridine) and $Re(dmpb)(CO)_3Cl$ together produced 9 times less CO than did the dinuclear complex following three hours irradiation under photocatalytic conditions. Though the complexes vary slightly, when compared to the study with **(23)** (*vide supra*), a shift in products is observed from formate to CO, potentially resulting from substitution of ascorbate for $BI(CO_2H)H$.

Further studies assessed conjugation within the bridge, whereby Bian *et al*. [115,116] produced **(24)** (Figure 1.20), creating a direct comparison to **(17)** (Figure 1.17). In DMF with TEOA and BNAH ($\lambda \geq 500$ nm), the conjugated bridge was found to have lower catalytic activity for CO production than the unconjugated **(17)**. Electrochemical studies showed that conjugation within the bridge resulted in an anodic shift of potential to the bridging ligand's reductions. As a result, the reducing power of the Re centre was decreased, manifesting in lower catalytic activity, with the saturated linker, i.e. **(17)** producing TON_{CO} of 100 and the unsaturated bridge of **(24)** producing half that of 50 TON, following 9 hours of irradiation.

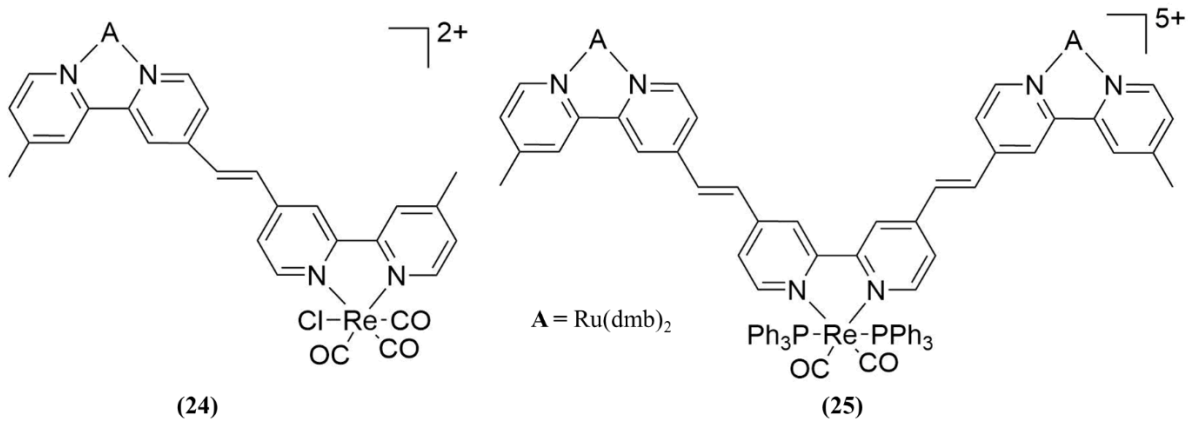

(24) (25)

Figure 1.20: Ru-Re intramolecular complexes **(24)** as a conjugated comparison to **(17)** [115,116] and **(25)**

In 2012, Tamaki *et al*. as stated previously [81], reported **(1),** the most photocatalytically active homogeneous intramolecular complex towards CO_2 reduction to date, along with **(26)** and **(27)** (Figure 1.21). The choice of the bridge stemmed from their previous intramolecular study [66] and the choice of bisphosphines/phosphites

arose from photophysical [117] and intermolecular studies [118] showing that of a series of ten R-substituted complexes (see Figure 1.21), Re(FPh) and Re(Ph) generated the highest TON_{CO} and Φ_{CO}. Regarding the intramolecular complexes (50 μM concentration, 0.1 M BNAH in DMF/TEOA (5:1)), the order of efficiency was **(1)** > **(26)** > **(27)** with TON_{CO}s of 207, 144 and 27 over the course of 20 hours (λ ≥ 500 nm, high pressure Hg)), with Φ_{CO} of 0.15, 0.1 and 0.1 respectively (λ = 480 nm, 500 W Xe short arc). The intermolecular systems with $[Ru(dmb)_3]^{2+}$ and Re(FPh), Re(Ph) and Re(OEt) (Figure 1.21) produced TON_{CO} of 48, 24 and 3 respectively, holding the same trend as the dinuclear complexes but with much lower activity. To draw a comparison to the most successful previous system, **(17)** was analysed under the same conditions (λ > 500 nm/λ = 480 nm, 0.1 M BNAH in DMF/TEOA 5:1) and provided a lower TON_{CO} = 180, and Φ_{CO} = 0.13 relative to **(1)**. Note: a further study within the group showed very similar values regarding the TON_{CO} and Φ_{CO} of **(1)** (212 vs 207 TON_{CO} and both at 0.15 Φ_{CO}, quantum yield undertaken with a 300 W Xe lamp in this case (λ = 480 nm), validating comparison between complexes developed by different researchers within the group [119]. In a later study [80] with **(1)**, substitution of BNAH in the system by BIH was met with great success and resulted in far greater efficiency with TON_{CO} = 3029, TOF = 35.7/min and Φ_{CO} = 0.45.

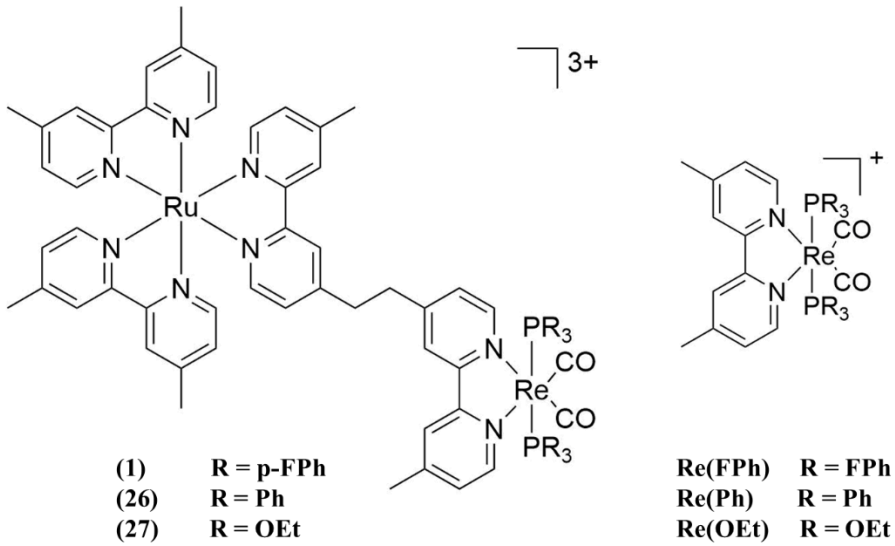

Figure 1.21: **(26)** and **(27)**, cis-, trans- biscarbonyl bisphosphine/phosphite complexes of Ru-Re with respective monomers

Yamazaki *et al*. concentrated their efforts on a more direct synthetic route of hetero- di- and trinuclear complexes, whereby a Re(4-bromo- or 4,4'-dibromo-bipyridine) dicarbonyl unit was reacted with a 4-ethenyl-4'-methylbipyridine ligand attached to $[Ru(bpy)_2]$, $[Ru(dmb)_2]$, $[Ir(ppy)_2]$ (ppy = 2-phenylpyridine) or $[Re(CO)_2(P(OEt)_3)_2]$ [120]. Within this study, **(25)** (Figure 1.20) was found to display catalytic activity when a 50 μM solution (DMF/TEOA, 5:1 with 0.1 M BIH) was irradiated at 600 nm for 22 hours, yielding TON_{CO} = 115.

A further publication from Yamazaki *et al*. showed that saturation of the double bond of various Ru, Ir and Re homo- or hetero- di or trinuclear bipyridyl chelated complexes proceeded with 600 or 510 nm irradiation (depending on the PS unit) in MeCN/pyridine/trifluoroacetic acid (3:1:0.1) with 10 – 50 mM BIH [121]. The presence of pyridine was thought to aid with deprotonation of the one-electron oxidised species of BIH, thereby generating a species capable of a stronger second reduction. Within the study, the photocatalytic ability of **(28)** was compared with the saturated linker of **(29)** (Figure 1.22). A 20 hour irradiation of 50 μM **(29)** and **(28)** (DMF/TEOA (5:1) containing 0.1 M BNAH) with λ > 500 nm (high pressure Hg) produced TON_{CO} of 313 and 283, TON_{HCOOH} of 85 and 100 and TON_{H2} of 26 and 26 respectively. However, **(28)** was observed to convert to the saturated complex. Bisdiimine bissolvento Ru centres and complex-$Re(CO)_3$ species were also observed over the course of both photocatalytic reactions.

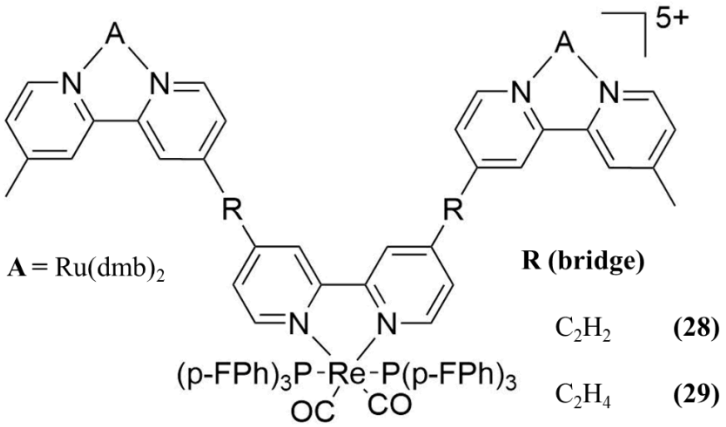

Figure 1.22: **(28)** and **(29)**, containing unsaturated and saturated linkers between Ru_2 and Re metal centres [121].

Ohkubo *et al*. compared the activity of **(17)** and **(1)** with two new photocatalysts in the form of **(30)** and **(31)** (Figure 1.23) [119]. In DMF/TEOA (5:1) with 0.1 M BNAH, 50 μM **(30)** produced a marginally elevated TON_{CO} with respect to **(17)** (TON_{CO} of 204 and 194 with Φ_{CO} of 0.16 and 0.13 respectively) when irradiated ($\lambda > 500$ nm) at a high pressure Hg lamp. Despite **(1)** producing TON_{CO} and Φ_{CO} of 212 and 0.15 respectively, **(31)** produced a significantly lower TON_{CO} and Φ_{CO} of 123 and 0.09 respectively. Akin to Kato *et al*.'s study of **(33)** [122] (Figure 1.24, *vide infra*), both **(1)** and **(31)** were observed to undergo substitution of both of the trisfluorophenylphosphine groups with a CO and a CO_2-TEOA adduct ligand, with the rate of formation being faster in the case of **(1)**. The Re tricarbonyl CO_2-TEOA adduct complex was believed to be the true active catalyst in the case of such complexes.

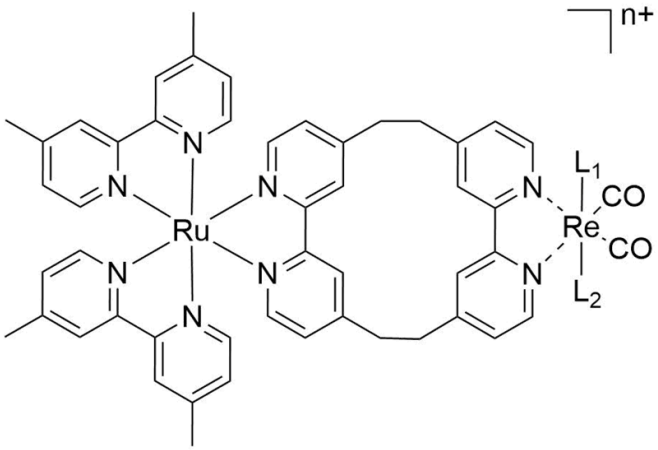

L_1	L_2	n +	
CO	Cl	2	**(30)**
$P(p\text{-}FPh)_3$	$P(p\text{-}FPh)_3$	3	**(31)**

Figure 1.23: bisethylene-bridged Ru-Re complexes **(30)** and **(31)**

Stemming from the work of Tamaki *et al*. [80], Kato *et al*. [122] assessed a saturated propyl bridge (**(32)**) akin to **(1)**, in addition to spacing both bridging carbons with an oxygen and sulphur, producing **(33)** and **(34)** respectively (Figure 1.24). Utilising the DMF with TEOA 5:1 ratio with 0.1 M BNAH solvent/donor system, TON_{CO} of 253, 178 and 73 were achieved for **(33)**, **(32)** and **(34)** respectively (with Φ_{CO} of 0.18, 0.1 and 0.09 respectively at $\lambda = 480$ nm), following 20 hour irradiation ($\lambda > 500$ nm). Upon probing the reason for higher efficiency with complex **(33)**, the authors found that the complex (as with **(34)**) was 10% more efficient at quenching the Ru MLCT state than **(32)** under photocatalytic conditions. Ligand-based reduction potentials attached to the Ru centre further suggest that an increased oxidising power was achieved for the Ru

centre (with respect to BNAH), with the introduction of an electron-withdrawing atom such as O and S. Electrochemical analyses concluded that the reversibility of the Re ligand based reduction was not observed in **(34)**, therefore the complex may be prone to cleavage of the sulphur-carbon bonds. Further electrochemical analysis compared the dinuclear complexes with their associated monomers. In the case of **(33)**, it was found that the introduction of the O bridge had a stronger effect on the reduction potential of Re ligand OER than that of Ru ligand OER, thus widening the potential difference between first and second reductions and therefore increasing the driving force from Ru to Re compared to that of **(32)**. The active catalyst, akin to the aforementioned study, was believed to be the tricarbonyl CO_2-TEOA adduct.

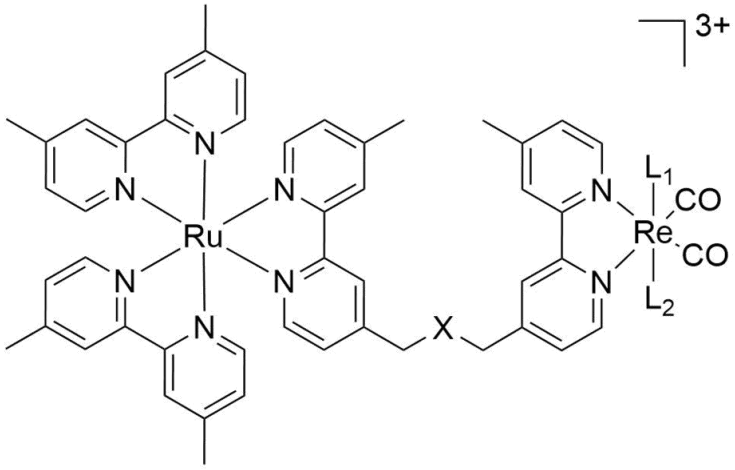

L_1	L_2	X	
$P(p\text{-}FPh)_3$	$P(p\text{-}FPh)_3$	CH_2	**(32)**
$P(p\text{-}FPh)_3$	$P(p\text{-}FPh)_3$	O	**(33)**
$P(p\text{-}FPh)_3$	$P(p\text{-}FPh)_3$	S	**(34)**
CO	DMF	O	**(35)**

Figure 1.24: Ru-Re complexes **(32)**, **(33)** and **(34)** with varied bridge and O-bridged Ru-Re DMF complex **(35)**

The O-bridged Ru-Re tricarbonyl DMF analogue, **(35)** (Figure 1.24) was assessed for activity where the concentration of CO_2 was varied [123]. In DMF/TEOA (5:1) with 0.1 M BIH and in the presence of 10%, 50% or pure CO_2, a mixed system of **(35)** and the tricarbonyl CO_2-TEOA adduct (substitution of the DMF ligand) analogue (6 and 44 μM respectively) generated 871, > 900 and ~1000 TON_{CO} respectively over the course of 19 hours irradiation with 480 nm light (300 W Xe). However, 1% and 0.5% CO_2 did not produce CO beyond approximately 200 TON_{CO}. Following 26 hours of irradiation, 10% CO_2 yielded 1020 TON_{CO} ($\Phi_{CO} > 0.4$) whereas under a pure CO_2 atmosphere, ~1200 TON_{CO} with $\Phi_{CO} = 0.5$ was measured. With pure CO_2, the system was also found to be active in the absence of TEOA, however, a three-fold decrease in activity was noted.

Periodic mesoporous organosilica (PMO) was utilised with the binding of **(36)**, containing phosphonate groups [124] (Figure 1.25). This system, bound to the acrylidone light absorbing unit in the walls of the PMO, produced 635 TON_{CO} with only TON_{H2} of 10 (based on molecular catalyst loading) after 24 hours at λ = 405 nm (in DMF/TEOA 5:1 with 0.1 M BIH). In a further study, **(36)** was adhered through hydrogen bonding to the NH_2- surface groups of carbon nitride (C_3N_4) [125]. A TON_{CO} of up to 29 was obtained in dimethylacetamide (DMA) with 20% V/V TEOA with irradiation from a 400 W mercury lamp with a $NaNO_2$ solution filter for 5 hours. Some formate was also detected. In the absence of CO_2, TEOA and catalyst, no CO was detected. Where the catalyst was bound to the insulating Al_2O_3, 9 times lower TON_{CO} was noted. The surface loading of C_3N_4 with the catalyst was determined to be limited at approximately 20-25 μmol g^{-1} and also appeared to limit the TON_{CO}. In an attempt to further increase surface coverage, the transparent SiO_2 was introduced to C_3N_4, prior to introduction of the photocatalyst. However, the efficiency of electron transfer from C_3N_4 to the Ru centre was believed to be hindered, as though the amount of CO increased, TON_{CO} decreased.

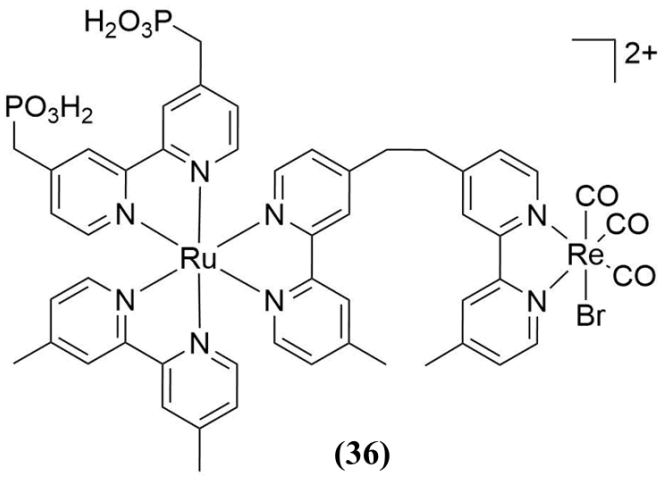

(36)

Figure 1.25: Ru-Re complex **(36)**, bearing phosphonate groups

In addition to the previous studies, **(36)** was bound to NiO-coated fluorine-doped tin oxide (FTO) [126,127]. In a CO_2-purged aqueous pH 6.6 $NaHCO_3$ buffer, 32 TON_{CO}s (~ 3 TON_{H2}) were achieved with 64% FE after 12 hours irradiation at λ > 460 nm (with a 300 W Xe lamp, and an applied potential at -0.7 V vs Ag/AgCl. The photocathode

was incorporated with a cobalt oxide/tantalum oxynitride (CoO_x/TaON) photoanode, and with irradiation at $\lambda > 400$ nm and an applied potential of -0.3 V vs CoO_x/TaON, the cathodic compartment produced 17 TON_{CO} (~ 1 TON_{H2}) with 37% FE following 1 hour.

Dietrich *et al.* explored the possibility of the Ru-tpy-amide-bpy-Re (tpy = 2,2'-6',2''-terpyridine) type complexes **(37)**, **(38)** and **(39)** (Figure 1.26) towards photocatalytic CO_2 reduction [128]. Through IR monitoring of the Re-CO bonds with addition of one and two equivalents of the chemical reductants, cobaltocene and decamethylcobaltocene respectively, the first reduction was believed in each case to occur on the tpy (Ru moiety), with the second occurring on the bpy attached to Re. With this in mind, a reductive quenching mechanism was unlikely to proceed, despite the complexes showing an ability to quench the Ru-based excited state. Irradiation of the complexes at 400 nm and 470 nm in MeCN/TEOA (5:1) produced no CO. Inactivity was attributed to the wrong site of electron localisation within the OER species.

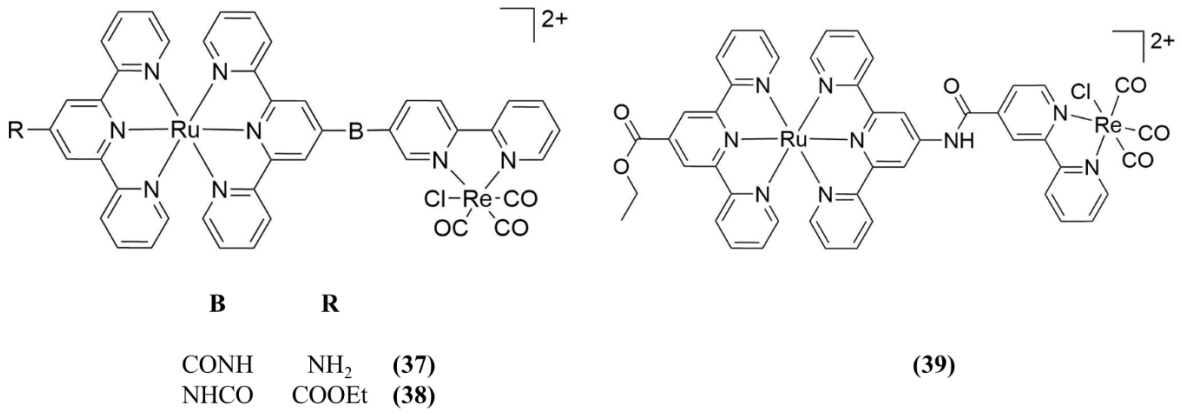

B	R	
CONH	NH_2	**(37)**
NHCO	COOEt	**(38)**

(39)

Figure 1.26: Ru-tpy-amide-bpy-Re type complexes **(37)**, **(38)** and **(39)** unsuccessful as CO_2 reduction photocatalysts

1.3.1.1.3. Ru – $Ru(CO)_2$ intramolecular systems:

Four complexes, **(40)**, **(41)**, **(42)** and **(43)** (Figure 1.27) containing the Ru PS subunit $[Ru(dmb)_3]^{2+}$ and the catalytic site $[Ru(dmb)_2(CO)_2]^{2+}$, were assessed by Tamaki *et al.* for their ability to reduce CO_2 to formate [129], following on from the investigation of the two-component system of $[Ru(bpy)_3]^{2+}$ and $[Ru(bpy)_2(CO)_2]^{2+}$ by Ishida *et al.* [130]. Interestingly the experiment (in DMF/TEOA (4:1) with 0.1 M BNAH irradiated at $\lambda \geq$

500 nm for 20 hours) mirrored observations by others in that more than one PS to Cat improved the catalytic TON (w.r.t. Cat). TON_{HCOOH} amounted to 562, 315, 353 and 234, with the quantum yield reported as 0.041, 0.038, 0.03 and 0.017 for the complexes **(42)**, **(40)**, **(41)** and **(43)** respectively. For equimolar concentrations of $[Ru(dmb)_3]^{2+}$ and $[Ru(dmb)_2(CO)_2]^{2+}$ for the intermolecular approach, TON_{HCOOH} amounted to 316. Therefore, both **(42)** and **(41)** surpassed the activity of the monomers.

A final photocatalytic experiment involved the addition of MeO-BNAH (1-(4-methoxybenzyl)-1,4-dihydronicotinamide) instead of BNAH to **(42)** and TONs exhibited a rise to 671 for formate (as analysed by capillary electrophoresis). Under λ = 480 nm irradiation, per catalytic site, the trend of formate production observed was **(42)** > **(40)** > $[Ru(dmb)_2(CO)_2]^{2+}$ + $[Ru(dmb)_3]^{2+}$ > **(41)** > **(43)**. It was believed that a higher PS-Cat ratio would lead to the greater possibility of 2 e^- reduction of the catalyst, whereas with more catalytic subunits, more OER species would be formed which could lead to oligomerisation of catalytic centres.

(42) was further probed with the use of 0.1 M of either BIH or a new electron donor, dimethyl-(o-hydroxyphenyl)-dihydrobenzoimidazole (BI(OH)H) in DMF/TEOA (4:1) [131]. Whereas BNAH produced a TON_{HCOOH}, TOF_{HCOOH} and Φ_{HCOOH} of 562, 7.8 min^{-1} and 0.04-0.06, BI(OH)H produced dramatic increases, of 2766 TON_{HCOOH}, TOF_{HCOOH} of 44.9 min^{-1} and Φ_{HCOOH} of 0.42-0.46. BIH also allowed for some increase in activity over BNAH, producing TON_{HCOOH}, TOF_{HCOOH} and Φ_{HCOOH} of 641, 10.2 min^{-1} and 0.17-0.18. Illumination of 25 μM of the complex was undertaken with a 500 W high pressure Hg lamp with λ > 500 nm for 25 hours for TON_{HCOOH} values, whereas > 420 nm for TOF_{HCOOH} and a 300 W Xe lamp with 480 nm filter was used to obtain Φ_{HCOOH} values (with 25-150 μM of the complex). The mixed monomer system of $[Ru(dmb)_3]^{2+}$ (50 μM) and $[Ru(dmb)_2(CO)_2]^{2+}$ (25 μM) produced 1969 TON_{HCOOH} w.r.t. catalytic centre following 20 hours irradiation, with the intramolecular complex generating approximately 2600 TON_{HCOOH} in the same time frame. Furthermore, omission of TEOA was found to decrease TONs by 27%. A twice oxidised product of BI(OH)H was detected by HPLC (UV detector), confirming its role as a $2e^-$ (and potentially 2 H^+) donor. The values obtained with the use of BI(OH)H remain the highest for formate production from CO_2 from a homogeneous intramolecular photocatalyst [132].

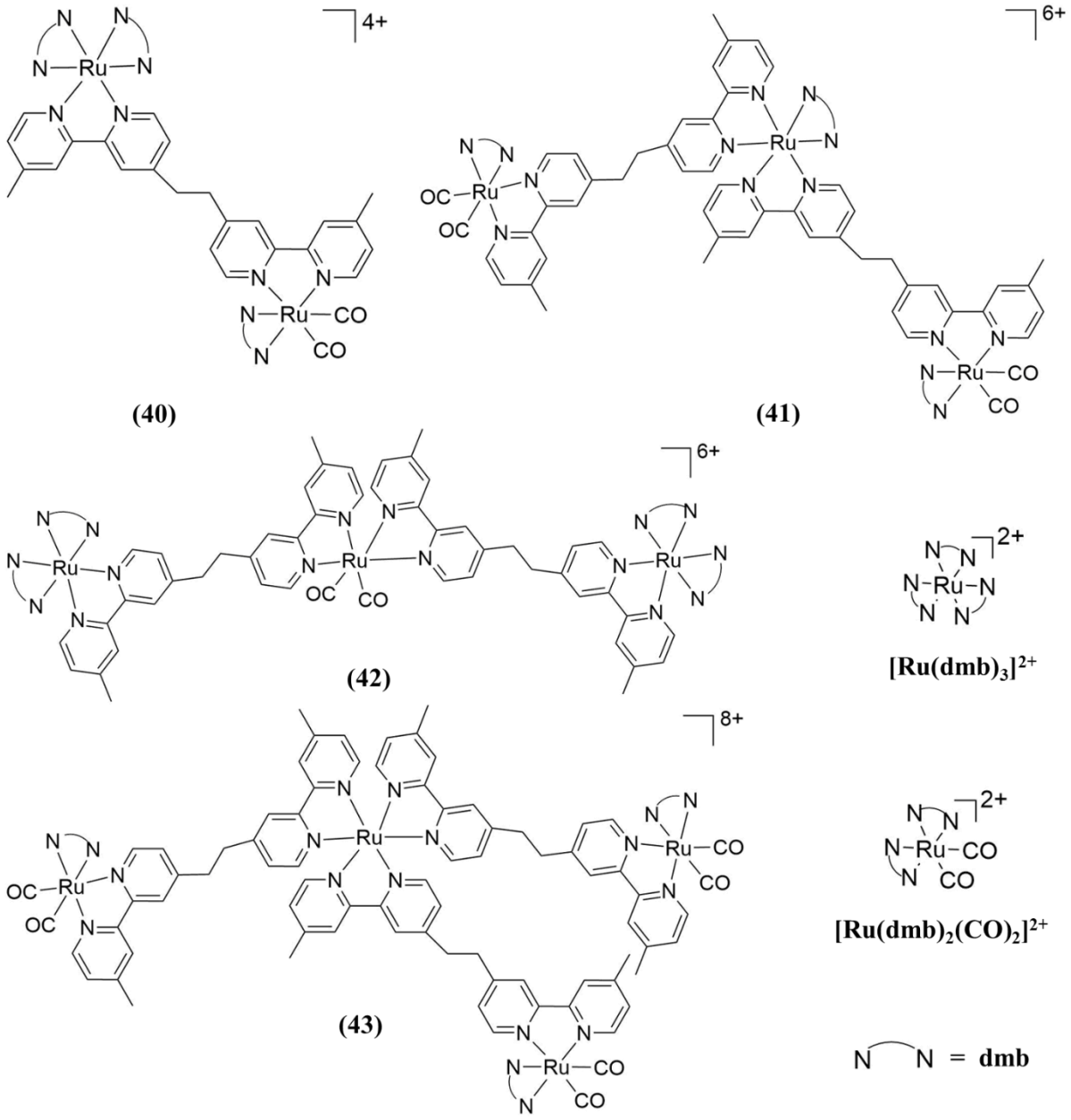

Figure 1.27: Ru-Ru(CO)$_2$ complexes **(40)**, **(41)**, **(42)** and **(43)**

A similar photocatalyst (**(44)**, Figure 1.28) was incorporated onto a Ag loaded tantalum oxinitride (Ag-TaON) particles through the use of a dmpb ligand incorporated on the PS unit (similar to approaches of Ru-Re heterodinuclear complex immobilisation [124–127]), creating an artificial "Z-scheme"[78]. In methanol, the **(44)** incorporated system generated 41 TON_{HCOOH} in 9 hours. It is of note that a partial source of formate may be the oxidation of MeOH [133]. **(44)**, bound to Ag-TaON, was further assessed in aqueous conditions [133]. With 10 mM Na_2EDTA and at a pH of 4.3, 750 TON_{HCOOH}

was obtained, with concomitant H_2 (TON_{H2} of 1240) over 24 hours irradiation with $\lambda >$ 400 nm (high pressure Hg lamp). The presence of 0.1 M Na_2CO_3 adjusted the pH of the solution to pH 7. Though selectivity towards formate increased (85% vs 37%) (TON_{H2} ~ 60 after 15 hours), the TON_{HCOOH} also decreased (far less dramatically than in the case of H_2) to 620. The TON_{HCOOH} was not increased beyond 750 under any conditions further assessed (varied pH/alkali metal cation of CO_3^{2-} and strength of phosphate buffer). This was attributed to a higher level of desorption of the photocatalyst with a higher salt content in solution. In relation to this, the unbound **(45)** was assessed in solution with Ag-TaON, whereby a heavily reduced 56 TON_{HCOOH} and 46 TON_{H2} were achieved following 15 hours irradiation.

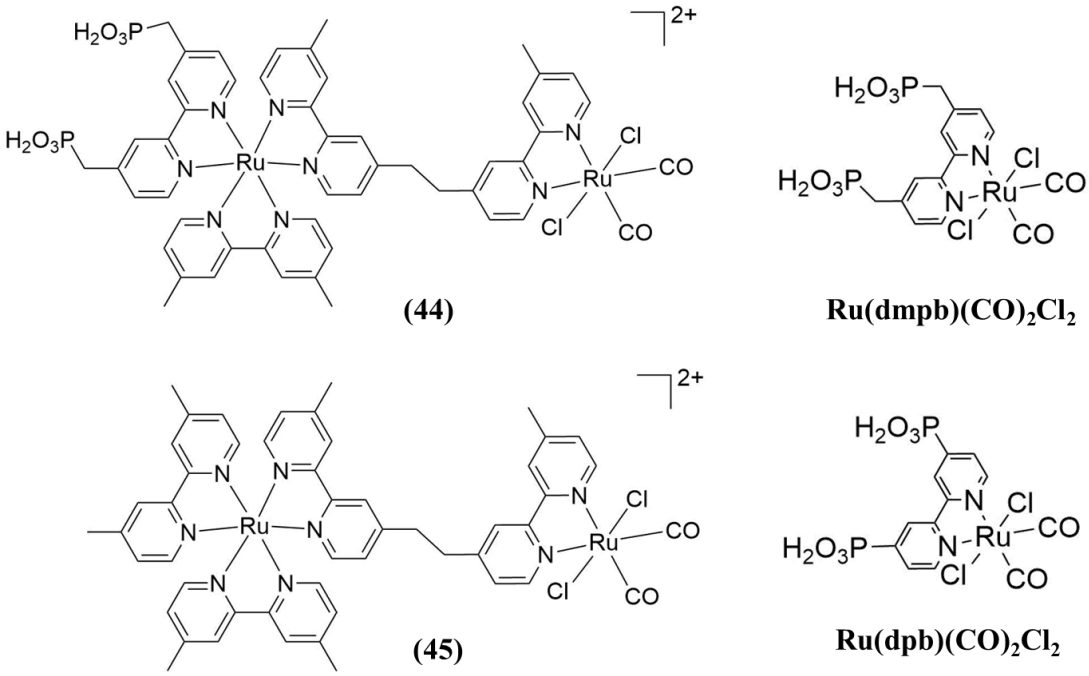

Figure 1.28: Ru-$Ru(CO)_2Cl_2$ complexes **(44)** and **(45)** and mononuclear complexes

The system, employing 1% Ag loaded calcium tantalum oxinitride with bound **(44)** (Figure 1.28) generated 320 TON_{HCOOH} with > 99% selectivity in DMA/TEOA (4:1) over the course of 15 hours of irradiation with a 400 W high pressure Hg lamp ($\lambda >$ 400 nm) [134]. The absence of either Ag or the PS unit (comparison with $Ru(dmpb)(CO)_2Cl_2$) produced approximately 3 times lower a level formate. Under the conditions specified, the homogeneous intramolecular complex did not generate formate, CO or H_2 either.

$Ru(dmpb)(CO)_2Cl_2$ and $Ru(dpb)(CO)_2Cl_2$ (Figure 1.28, dpb = diphosphonatebipyridine) were bound to C_3N_4 and the systems were reported towards photocatalytic production of formate from CO_2 [135,136]. $Ru(dpb)(CO)_2Cl_2$ was found (and shown via voltammetric response) to undergo a greater level of catalytic current at a more positive potential by voltammetry as compared to $Ru(dmpb)(CO)_2Cl_2$. This trait translated into higher TON_{HCOOH} for $Ru(dpb)(CO)_2Cl_2$ vs $Ru(dmpb)(CO)_2Cl_2$ attached to C_3N_4 (55 vs 20 for catalyst loading of 7.8 μmol g^{-1} in MeCN/TEOA, 4:1 ratio over 1 hour irradiated at a 400 W high pressure Hg lamp, $\lambda > 400$ nm). When DMA was used instead of MeCN, MeOH or H_2O (4:1 ratio to TEOA), TON_{HCOOH} was increased to 141 over the hour. Over 20 hours, this system accumulated over 1000 TON_{HCOOH} with approximately 250 TON_{CO} (~ 80% selectivity for formate).

Inspired by this, **(44)** (in addition to the mononuclear PS and catalyst) was attached to Ag-C_3N_4 and assessed for photocatalytic CO_2 reduction [137]. Where the photocatalyst was immobilised at 3.4 μmol g^{-1} to C_3N_4 (12 nm pore size, mesoporous) without Ag, **(44)** produced 10 times less formate over 5 hours than did $Ru(dpb)(CO)_2Cl_2$ (TON_{HCOOH} of 43 vs 429, selectivity of 52% vs 74%) in DMA/TEOA (4:1). However, when 5% w/w Ag (optimal amount) was introduced, TON_{HCOOH} and selectivity surpassed that of $Ru(dpb)(CO)_2Cl_2$ (TON_{HCOOH} and selectivity of 3110 and 99% vs 1428 and 98% respectively). Each component of C_3N_4 (as compared to Al_2O_3), Ag (relative to systems incorporating Cu, Au and Pt and the absence of Ag) and the photocatalyst (with respect to the mononuclear PS and catalyst units bound) were a requirement for significant levels of activity. Furthermore, with 5% w/w Ag, 0.5 μmol g^{-1} was found to be an optimal surface concentration, leading to > 33,000 TON_{HCOOH} after 48 hours. The effect of pore size of the C_3N_4 was also examined, whereby particularly non-porous and also 7 nm pore size C_3N_4 proved to be less active than the 12 nm size. The scheme was assessed in an aqueous solution of 10 mM Na_2EDTA, and though the system was less active than in DMA with TEOA, a TON_{HCOOH} of 200 was achieved.

The photocatalyst was also anchored to yttrium tantalum oxynitride (YTON) coupled with Ag [138]. In DMA with TEOA present, a 4.5 μmol g^{-1} **(44)** and 1.5% Ag loading on YTON produced 18 TON_{HCOOH} in comparison to 5 associated without Ag when irradiated with a high pressure Hg lamp ($\lambda > 400$ nm). The system was not further optimised.

1.3.1.1.4. Os-Re intramolecular systems:

Tamaki *et al*. [86] synthesised the intramolecular complexes **(46)** and **(47)** along with the Os and Re centred monomers (Figure 1.29) for the photoreduction of CO_2 and particularly for the use of $\lambda > 620$ nm. In a 5:1 ratio of DMF to TEOA with 0.1 M BIH, 20 hours irradiation produced TON_{CO} and Φ_{CO} of 1138 and 0.12 for **(47)**, 762 and 0.1 for **(46)** respectively and TON_{CO} of 363 and 240 for $[Os(dmb)_3]^{2+}$ with $[Re(dmb)(CO)_2(p\text{-}ClPh)_2]^+$ and $[Re(dmb)(CO)_2(p\text{-}FPh)_2]^+$ respectively. The intramolecular complexes surpassed the two component system in conversion of CO_2 to CO. For comparison to previous systems, **(1)** [80,81] (Figure 1.21) was irradiated at $\lambda > 620$ nm and a modest TON_{CO} of 3 was achieved, further accentuating the ability of these complexes (and the inability of more standard complexes) to utilise red light.

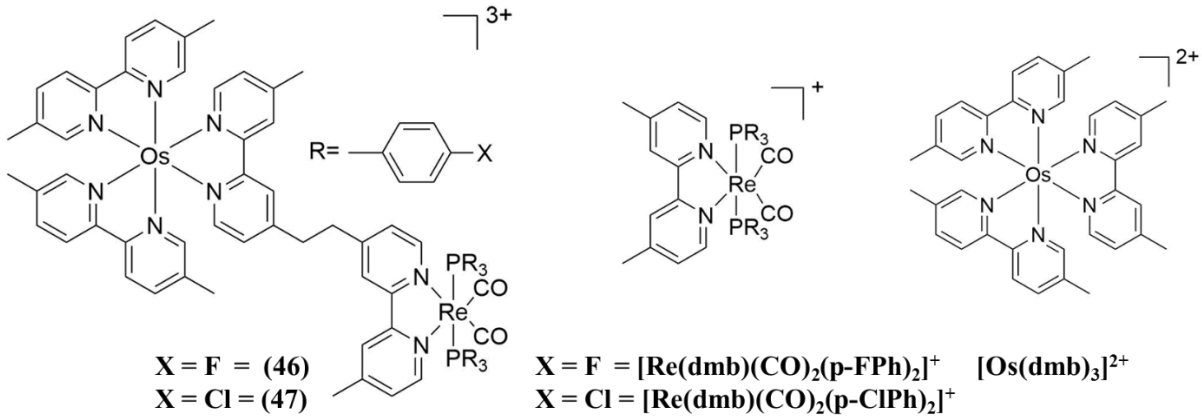

Figure 1.29: Os-Re intramolecular complexes **(46)** and **(47)** and associated monomolecular complexes

1.3.1.1.5. Ir – Re systems

Kuramochi and Ishitani explored the complex **(48)** (Figure 1.30) in DMA/TEOA (5:1) with 0.1 M of either BNAH or BIH present [139]. BIH was found to reductively quench the excited PS moiety 40 times more efficiently than did BNAH, potentially due to its greater reducing power, and also its capacity as a two electron donor. However, TEOA did not quench all of the Ir complexes assessed. The $E_{0\text{-}0}$ was determined and it was deduced that an oxidative quenching pathway was energetically unfavourable to proceed. Despite the first reduction potential of the Ir and Re moieties being of close

energy, the system employing either BNAH or BIH as an electron donor generated CO when irradiated with a high pressure Hg lamp ($\lambda > 500$ nm). Irradiation of the dinuclear complex for 15 hours produced 1700 and 130 TON_{CO} selectively within the systems employing BIH and BNAH as sacrificial donors respectively. The mononuclear comparison ($[Ir(piq)_2(dmb)]^+$ and $Re(dmb)(CO)_3Br$, piq = 2-phenylisoquinoline) produced very similar TON_{CO} as **(48)**, in the case of BIH as donor, whereas with BNAH, a TON_{CO} of 68 was approximately half that of the intramolecular approach. **(17)** was also compared to **(48)** in the presence of BNAH, and though 190 TON_{CO} was generated, **(17)** was less selective with the generation of 55 TON_{HCOOH}. The Φ_{CO} for **(48)** was determined to be 0.41 and 0.21 at λ = 480 nm with BIH and BNAH respectively.

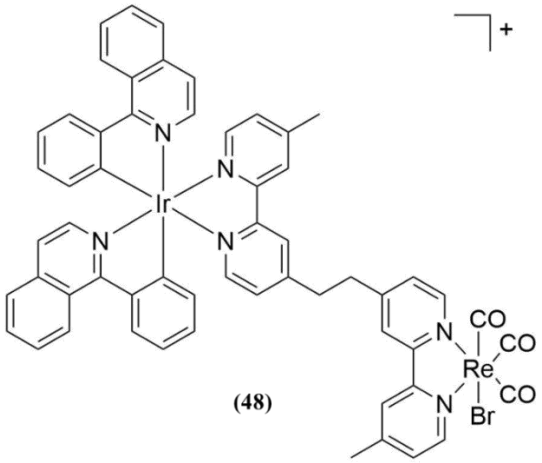

(48)

Figure 1.30: Ir-Re complex **(48)**

1.3.1.1.6. Bodipy – Re intramolecular systems

Andrade *et al*. [140] explored the possibility of utilising **(49)** (Figure 1.31). Bodipys are well known as highly absorbing species, particularly at $\lambda \approx 525$ nm, with extinction coefficients in the tens of thousands or above [141]. However, when attached to a Re catalytic centre in DMF/TEOA 5:1, effective intramolecular photosensitisation was not realised for CO_2 reduction. Samples irradiated at $\lambda \geq 400$ nm produced TON_{CO} of 20 with **(49)** as compared with the one-component $Re(tapmb)(CO)_3Cl$ (Figure 1.31) which produced TON_{CO} of 22. Irradiation with wavelengths of $\lambda \geq 495$ nm produced minimal CO in both systems, further supporting that the Bodipy moiety did not act as an efficient

photosensitiser. The Bodipy and [Re(CO)$_3$Cl] moieties of **(49)** were additionally stated to have poor communication.

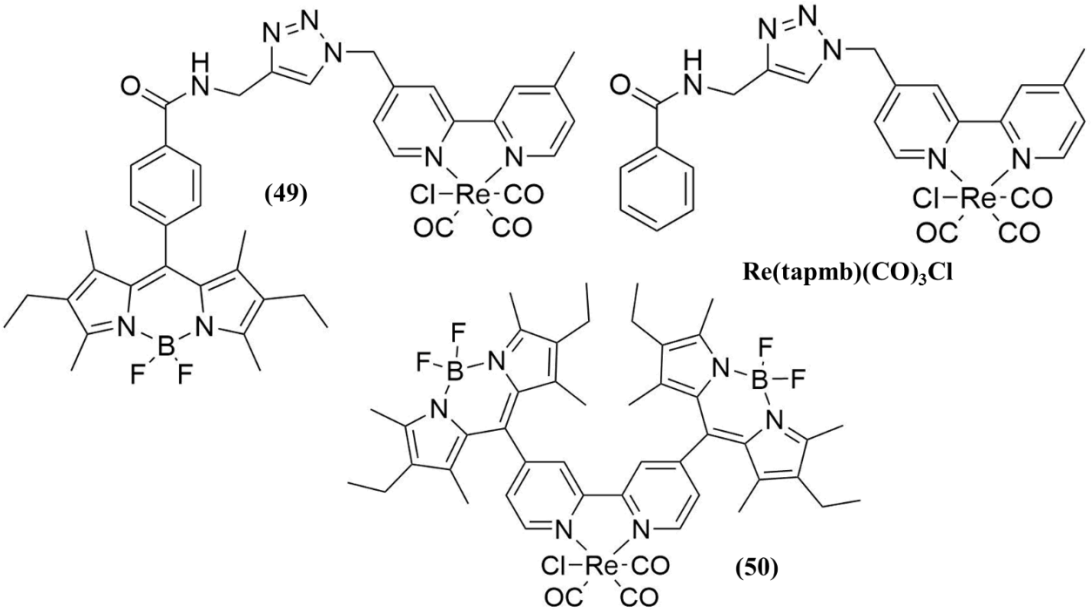

Figure 1.31: Bodipy tethered Re complexes **(49)** and **(50)** unsuccessful as photocatalysts towards CO_2 reduction, and Re(tapmb)(CO)$_3$Cl for comparison to **(49)**

Teesdale *et al*. assessed the capability of **(50)** (Figure 1.31), a [Re(bpy)(CO)$_3$Cl] bound directly to the meso position of two bodipys [142]. Negligible photocatalytic capabilities were reported with $\lambda \geq 500$ nm or ≥ 400 nm in DMF:TEOA 5:1 for the formation of CO. Though electrochemical processes associated with the [Re(bpy)(CO)$_3$Cl] moiety were shifted ~350 mV more positively (lowering reducing power of the metal), significant electrocatalytic activity was retained towards CO generation.

1.3.1.1.7. Re – Re systems

The ligands bismethylbisbipyridine with an ethylene or dodeclyene linker were utilised in the synthesis of **(52)**, **(53)**, **(54)**, **(55)**, **(60)** and **(61)** (Figure 1.32) [143]. These complexes along with the mononuclear equivalents containing the dmb ligand were assessed for CO_2 photocatalytic activity in 17:5 DMF/TEOA. The focus of their assessment was on TOF_{CO}, therefore experiments were undertaken for 25 minutes only

and TONs may be incomparable to studies of longer irradiation times (due to the relatively short irradiation time). Of the comprehensive study undertaken with λ = 450 nm, they observed that **(52)** performed approximately 1.5 times as efficiently (TOF_{CO} of 30 hr^{-1}) for CO generation as **(60)** or $Re(dmb)(CO)_3Br$ (doubly concentrated), suggesting that the dodecylene bridge did not allow for an intramolecular approach and that an intermolecular approach proceeded, with both metals acting independently. Both **(53)** and **(61)** showed an approximate 9-fold increase in CO generation compared to $Re(dmb)(CO)_3NCS$, however, the most active of the NCS complexes i.e. both **(53)** and **(61)** were only half as active (TOF_{CO}s of 15 each) as **(52)**. In both **(54)** and **(55)**, the dinuclear species outperformed mononuclear species. **(54)** displayed similar TOF_{CO} to **(52)** over the course of 25 minutes, however **(55)** displayed diminished results as compared to both.

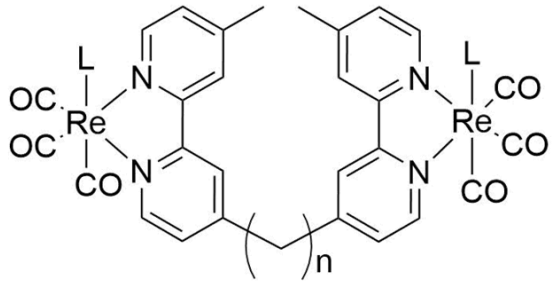

L	n	
Cl	2	**(51)**
Br	2	**(52)**
NCS	2	**(53)**
MeCN	2	**(54)**
$P(OEt)_3$	2	**(55)**
$OC(O)OC_2H_4N(C_2H_4OH)_2$	2	**(56)**
$OC(O)OC_2H_4N(C_2H_4OH)_2$	3	**(57)**
$OC(O)OC_2H_4N(C_2H_4OH)_2$	4	**(58)**
$OC(O)OC_2H_4N(C_2H_4OH)_2$	6	**(59)**
Br	12	**(60)**
NCS	12	**(61)**
$OC(O)OC_2H_4N(C_2H_4OH)_2$	14	**(62)**

Figure 1.32: Re-Re complexes of general structure $LReC_nReL$ (alkyl-linked methylbpy units) as assessed for photocatalytic CO_2 reduction [49,108,143]

As described within section 1.3.1.1.2, Meister *et al*. explored **(51)** with $[Ru(dmb)_3]^{2+}$ in DMF with TEOA and BNAH [108]. Later, **(51)** and **(52)** (Figure 1.32) were shown to be equally active without additional PS in DMF/TEOA (17:5) [49]. At 450 nm (9.1 x 10^{-6} Einsteins s^{-1}), **(51)** and **(52)** produced 11.8 and 11.4 TON_{CO} and when irradiated at 365 nm (4.3 x 10^{-7} Einsteins s^{-1}), both produced 19.6 TON_{CO} each. TON_{CO} is based on the amount of complex as opposed to catalytic centres. $Re(dmb)(CO)_3$(Cl or Br) displayed approximately half the activity of the dinuclear complexes. However,

$Re(bpy)(CO)_3$(Cl or Br) displayed superior activity per catalytic centre than did the dinuclear complexes.

Tamaki *et al*. studied the CO_2-TEOA bound complexes of **(56)**, **(57)**, **(58)**, **(59)** and **(62)** (Figure 1.32) in addition to the CO_2-TEOA bound monomer with the inclusion of $[Ru(dmb)_3]^{2+}$ as intermolecular PS [144]. In DMF/TEOA (5:1) with 0.1 M BNAH, 50 μM $[Ru(dmb)_3]^{2+}$ with either 50 μM $Re(dmb)(CO)_3CO_2TEOA$ or 25 μM of the dinuclear species were irradiated for 18 hours at $\lambda > 500$ nm (high pressure Hg). Remarkably, per catalytic centre, the dimers were superior to the monomer, whereby the order of activity was $C_2 > C_3 > C_4 > C_6 > C_{14} > Re(dmb)(CO)_3CO_2TEOA$ with TON_{CO}s of 192, 151, 143, 118, 103 and 72 respectively. The Φ_{CO} at two different light intensities (λ = 510 nm) ranged from 0.061 and 0.088 within the monomer to between 0.064 and 0.1 within the dinuclear complexes.

Degradation of the $[Ru(dmb)_3]^{2+}$ PS was found to account for loss of activity. Due to minimal decomposition of the PS in the absence of BNAH, it was assumed that reductive quenching of the PS* to PS^- led to ligand replacement with solvent molecules, and therefore, deactivation. Competition between back transfer of the PS^- to the oxidised product of BNAH and transfer to the catalyst was monitored at 510 nm with flash photolysis excitation at 532 nm. The presence of **(56)** resulted in a quicker decay of the ~510 nm absorption band as compared to the doubly concentrated $Re(dmb)(CO)_3CO_2TEOA$. Therefore, it was concluded that the greater rate of electron transfer to **(56)** preserved the life of the PS, and therefore the system, compared to $Re(dmb)(CO)_3CO_2TEOA$. Meister *et al*. have previously noticed that lower light intensity additionally increased the life of **(20)** where BNAH and TEOA was present [108], which may support these findings.

2,4,6-tris(2-pyridyl)-1,3,5-triazine (tptz) was utilised as a bridging ligand in the synthesis of **(63)** (Figure 1.33) [145]. The Re-Re dinuclear complex was assessed for its capability as a photocatalyst towards CO_2 reduction (λ = 365 nm. 4:1 ratio of DMF to TEA or TEOA). Further to this, a DMF/TEOA/NEt_4Cl (concentration of NEt_4Cl not specified, in excess) solution was assessed (possibly due to the observations of Hawecker *et al*. [146] in which excess chloride present with $Re(bpy)(CO)_3Cl$ led to increased production of CO). The activity of the complex was in the order of DMF/TEOA/NEt_4Cl > DMF/TEOA > DMF/TEA with TON_{CO} of 16, 13.5 and 9 with

no H_2 or formic acid detected. The dinuclear species was not assessed against a mononuclear equivalent.

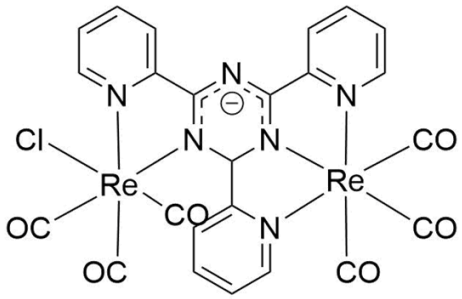

(63)

Figure 1.33: Re-Re dinuclear complex **(63)** for the photocatalytic reduction of CO_2

1.3.1.1.7.1. Re oligonuclear PSs of note

Although the Morimoto *et al*. trinuclear [Re(dmb)$(CO)_2$] PS (as shown in Figure 1.34) with [Re(bpy)$(CO)_3$MeCN]$^+$ [147] is not an intramolecular system, it is noteworthy due to the photosensitiser being a trinuclear species, and likely resulted from the efforts of synthesising and testing a multinuclear intramolecular system of linear Re oligomers attached to a Ru PS centre [148]. In addition to this, the system has a very high quantum yield for CO of 0.82 (of the most efficient to date) with TON_{CO} of up to 526 with [Re(bpy)$(CO)_3$MeCN]$^+$ as catalyst. It is worth noting that though efficiency is not as high in the mononuclear homologue with a catalyst (Φ_{CO} = 0.6), TON_{CO} was higher (563). Further development of this type of photosensitiser led to a phenylene bridge phosphine linker and variation of the bpy ligand [87]. The complexes were active as PSs towards CO_2 reduction in the presence of [Re(bpy)$(CO)_3$MeCN]$^+$ (producing 98 TON_{CO}), Ru(tbubpy)$(CO)_2Cl_2$ (tbubpy = ditert-butyl bipyridine) (producing 290 TON_{HCOOH}) and [Mn(tbubpy)$(CO)_3$MeCN]$^+$ (producing 85 TON_{HCOOH}). $\Phi_{CO/HCOOH}$ ranged between 0.37 and 0.74.

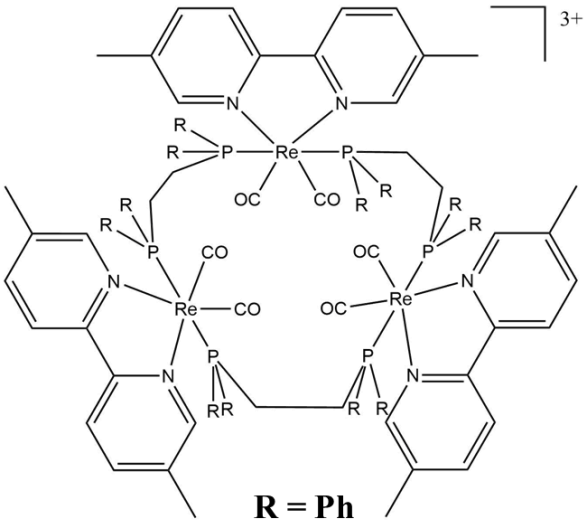

Figure 1.34: An example of oligonuclear Re-centred PSs utilised within intermolecular systems. This example was utilised by Morimoto *et al*. [147]

1.3.1.1.8. Porphyrin – Diimine and related complexes

Kiyosawa *et al*. explored **(64)**, a Zn trimesityl porphyrin as a PS with a Re tricarbonyl catalytic centre (Figure 1.35) [149,150]. When irradiated at 560 nm (500 W Xe arc) or 428 nm (corresponding to the S_1 and S_2 transitions respectively) in DMF/TEOA (5:1), TON_{CO}s of 60 and 21 were obtained respectively. Remarkably, when TEOA was substituted with TEA, 428 nm irradiation provided 70 TON_{CO}, whereby a lower TON_{CO} of 17 was noted when λ = 560 nm was employed. With either TEOA or TEA present, the monomers of Zn trimesitylmethoxycarbonylphenylporphyrin and $Re(bpy(NHAc)_2)(CO)_3Cl$ (bpy(NHAc)$_2$ = diacetamidebpy) together produced no CO. It was postulated from fluorescence quenching experiments that TEOA induced reductive quenching of the PS moiety when irradiated at 560 nm (associated with the S_1 transition). When TEA was irradiated at the S_2 transition (428 nm), charge separation, leading to oxidative quenching was stated to occur.

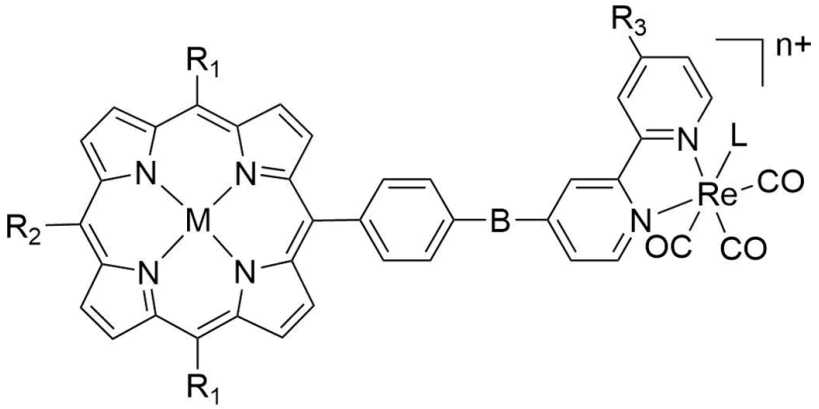

M	R_1	R_2	B (bridge)	R_3	L	n +	
Zn	mesityl	mesityl	CONH	$NHCOCH_3$	Cl	0	**(64)**
Zn	mesityl	COOH	CONH	$NHCOCH_3$	Cl	0	**(65)**
Zn	phenyl	phenyl	NHCO	CH_3	3-picoline	1	**(66)**
Zn	phenyl	phenyl	NHCO	CH_3	Br	0	**(67)**
Zn	phenyl	phenyl	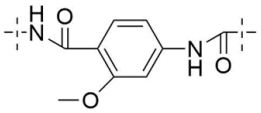	CH_3	3-picoline	1	**(68)**
Zn	phenyl	phenyl		CH_3	Br	0	**(69)**
Zn	phenyl	phenyl	$NHCOCH_2$	CH_3	3-picoline	1	**(70)**
Zn	phenyl	phenyl	$NHCOCH_2$	CH_3	Br	0	**(71)**
Pd	phenyl	phenyl	NHCO	CH_3	3-picoline	1	**(72)**

Figure 1.35: Zn-Re and Pd-Re intramolecular approaches towards photocatalytic CO_2 reduction

(65) (Figure 1.35) was assessed for CO_2 reduction in DMF/TEA 4:1 at λ = 430 nm [151]. The quantum yield for CO was stated to be 0.0012 at 4 hours, and a TON_{CO} of 14 was achieved following 30 hours irradiation. A comparative intermolecular system was not assessed for activity. The carboxyl functional group on the porphyrin was later used to anchor the complex onto NiO particle layers deposited on fluorine-doped tin oxide.

(66) and **(68)** (Figure 1.35) were explored by Windle *et al*. [152]. The TON_{CO} was approximately 30 and 10 for **(68)** and **(66)** respectively after 80 minutes in DMF/TEOA (5:1 ratio), (irradiation at λ > 520 nm). Under the same conditions, the two-component systems Zn tetraphenylporphyrin (TPP) with $[Re(bpy)(CO)_3pic]^+$ (pic = 3-picoline) together and Zn triphenylporphyrin with phenyl-amide-methoxyphenyl-amide-methylbpy and $[Re(bpy)(CO)_3pic]^+$ together produced just over and just under 50

TON_{CO} respectively. Therefore, in this case, bridging the PS and catalytic units did not result in success.

Later, **(70)** and **(71)** were synthesised and assessed for CO_2 reduction, with comparison to **(66)**, **(67)**, **(68)** and **(69)** [153]. Introduction of the additional methylene group of **(70)** as compared to **(66)** manifested a more cathodic first reduction (associated with the Re moiety) of -1.68 V vs Fc/Fc^+ than that of **(66)** (-1.44 V) and **(68)** (-1.42 V). Introduction of the bromine group resulted in the first reduction potentials shifting to -1.83, -1.63 and -1.6 V vs Fc/Fc^+ for **(71)**, **(66)** and **(68)** respectively. Of the complexes examined, **(70)** and **(71)** both showed less quenching and less of a decrease in the excited state lifetime with comparison to the Zn porphyrin-bpy monomer than did **(66)**, **(67)**, **(68)** and **(69)**. This suggests that oxidative quenching is less feasible with **(70)** and **(71)**. The first reduction potential associated with the Zn porphyrin moieties were not shown, therefore, the feasibility of TEOA or TEA as an adequate electron donor towards a reductive quenching pathway may not be calculated. However, ZnTPP and Zn tetraphenylchlorin were stated not to undergo fluorescence quenching in the presence of TEOA. Remarkably, when 50 μM of dyad in 5:1 DMF/TEOA was irradiated at 660 nm > λ > 520 nm (Xe arc), **(70)** and **(71)** produced superior TON_{CO}s (332 and 262 following 7 and 3 hours respectively) as compared to **(66)**, **(67)**, **(68)** and **(69)** (TON_{CO} of 27, 32, 30 and 23 after 6, 4, 8, and 4 hours respectively). The monomeric system of ZnTPP with $[Re(bpy)(CO)_3pic]^+$ was stated to produce ~100 TON_{CO} following 2 hours irradiation. Elongation of the bridge by a methylene group to bpy resulted in a remarkable improvement in activity.

In an additional approach by the groups of George and Perutz, **(72)** (Figure 1.35) was assessed for its capability towards CO_2 reduction [154]. In DMF/TEA (5:1), narrow bandwidth excitation at 520 nm was found to produce only trace amounts of CO following 8 hours irradiation. In contrast, excitation into the S_0-S_2 transition (> 420 nm) produced 2 TON_{CO} after 4 hours. An induction period (corresponding to chlorin formation from the porphyrin) was observed where CO was generated in mono- and dinuclear systems. As a result, it was found that PdTPP with $[Re(bpy)(CO)_3pic]^+$ produced approximately 3-4 TON_{CO}, whereas Pd tetraphenylchlorin with $[Re(bpy)(CO)_3pic]^+$ produced 9 TON_{CO}.

A rigid porphyrin diimine (TPP-DI) architecture (Figure 1.36) was availed of by Matlachowski and Schwalbe in the tethering of cobalt, copper, iron and palladium centres, **(73)**, **(74)**, **(75)** and **(76)** respectively, to a [Ru(tbubpy)$_2$] moiety for the reduction of CO_2 to CO [155].

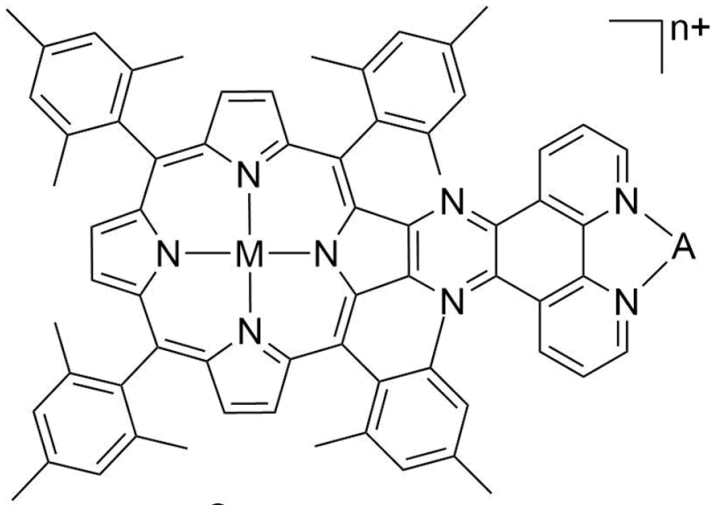

M	A	n +	
Co	$Ru(tbubpy)_2$	2	**(73)**
Cu	$Ru(tbubpy)_2$	2	**(74)**
FeCl	$Ru(tbubpy)_2$	2	**(75)**
Pd	$Ru(tbubpy)_2$	2	**(76)**
Co	$Re(CO)_3Cl$	0	**(77)**
Zn	$Re(CO)_3Cl$	0	**(78)**
FeCl	$Re(CO)_3Cl$	0	**(79)**
Cu	$Re(CO)_3Cl$	0	**(80)**
Pd	$Re(CO)_3Cl$	0	**(81)**
H_2	$Re(CO)_3Cl$	0	**(82)**

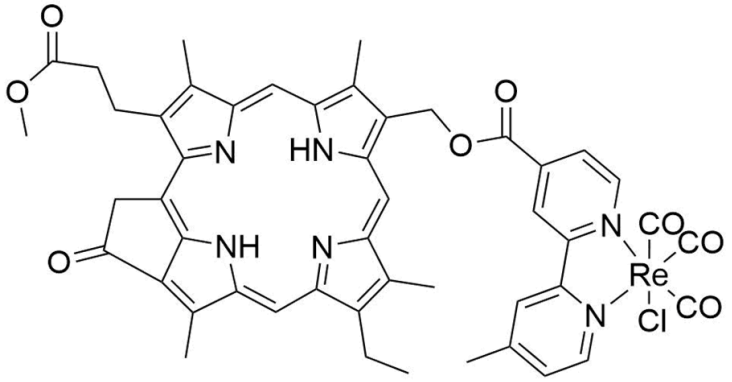

(83)

Figure 1.36: Rigid porphyrin-diimine and chlorophyll-Re approaches to photocatalytic CO_2 reduction

In DMF with 5% TEA, TON_{CO}s reached 11 for **(75)** at $\lambda > 305$ nm with **(73)**, **(74)** and **(76)** producing TON_{CO} of 5, 3 and 3 respectively. In each case, the intramolecular complexes produced more CO than when M-TPP-DI was present alone. A remarkable wavelength dependence was observed with Co and Fe TPPs (in addition to **(73)** and **(75)** in the absence of the Ru moiety), whereby the complexes were most active with UV light. For example, extending the cut-off wavelength from > 320 nm to > 305 nm resulted in over a 5-fold increase in the case of **(75)**. Substitution of different electron donors (TEA, TEOA and BNAH) was undertaken with the fixed use of **(73)** and similar

production of CO was observed with TEA and TEOA, but in the presence of 0.1 M BNAH, photocatalytic activity was not observed. The complexes, either containing or not containing the Ru moiety, could not however utilise light of $\lambda > 375$ nm, whereby the greatest TON_{CO} of 0.7 was achieved for **(75)** in DMF with 5% TEA without light of greater energy.

In a later approach, the same ligand was utilised to bridge Co, Zn, FeCl, Cu and Pd in addition to the free base porphyrin with a $[Re(CO)_3Cl]$ sub-unit, creating **(77)**, **(78)**, **(79)**, **(80)**, **(81)** and **(82)** respectively (Figure 1.36). The complexes were assessed for activity at $\lambda > 305$ and $\lambda > 375$ nm (high pressure 200 W Hg lamp) in DMF with 5% TEA [156]. **(78)** was the only active photocatalyst of the complexes assessed towards CO_2 reduction at $\lambda > 375$ nm, whereby 12.8 TON_{CO} was generated. At $\lambda > 305$ nm, both **(81)** and **(78)** were more active, with 12.1 and 12.5 TON_{CO} generated respectively. **(77)**, **(79)**, **(80)** and **(82)** each generated between 7.3 and 8 TON_{CO} at $\lambda > 305$ nm.

As a means to develop a system that absorbed and utilised red light, while in the process, developing an intramolecular complex containing an organic PS, Kitagawa *et al*. assessed **(83)** (Figure 1.36), a chlorophyll-Re complex, towards CO_2 reduction [157]. In DMF/TEOA (5:1) with 0.1 M BIH, **(83)** generated 18 TON_{CO} when irradiated at $\lambda >$ 540 nm for 13 hours. Individually, the methoxychlorophyll and Re(4-methyl-4'-methylesterbpy)$(CO)_3Cl$ components produced 0 and < 1 TON_{CO}, however, the two component system was not analysed. The group later studied complexes containing two chlorophyll units, deoxochlorophyll- [158] and Zn-metallated chlorophyll- [159] Re bipyridyl complexes for their ability to create a charge-separated state (oxidative quenching), however, photocatalytic experiments were not undertaken.

1.3.1.1.9. Ir-Ir intramolecular complexes

Re bipyridyl complexes have the ability to act as both PS and catalyst. Meister *et al*. showed that **(51)** allowed for a higher catalytic activity than twice the equivalents of mononuclear complexes in the presence of $[Ru(dmb)_3]^{2+}$ [108]. [Ir(tpy)(ppy)] type complexes share the same photocatalytic ability as that of the Re bipyridyl complexes. Reithmeier assessed dinuclear complexes of [Ir(tpy)X] (X = Cl or I) with phenylpyridinyl ligands separated by ethylene, octylene or tetradecylene chains (**(84)**

and **(85)**, **(86)** and **(87)** respectively) for photocatalytic CO_2 reduction, in addition to the mononuclear $[Ir(ppic)(tpy)Cl]^+$ and $[Ir(ppic)(tpy)I]^+$ (ppic = 2-phenyl-(4-picoline)) (Figure 1.37) [55]. At λ = 450 nm in 5:1 MeCN to TEOA, TON_{CO} was in the order of **(85)** with 135 TON_{CO} > **(86)** with 92 TON_{CO} > **(87)** with 83 TON_{CO} > **(84)** with 81 TON_{CO}. Under the same conditions, the mononuclear species $[Ir(ppic)(tpy)Cl]^+$ and $[Ir(ppic)(tpy)I]^+$ (in double the concentration) produced 33 and 54 TON_{CO} respectively. With consideration that TONs were calculated per molecule and not catalytic site, all of the dinuclear complexes still outperformed their associated monomers. Timescales of these experiments varied from less than 1 hour to 6.75 hours.

The quantum yield for CO formation was determined at λ = 450 nm and was in the order of $[Ir(ppic)(tpy)Cl]^+$ (0.18) > **(87)** (0.16) > **(86)** (0.14) > $[Ir(ppic)(tpy)I]^+$ (0.07) > **(84)** (0.06) > **(85)** (0.04). Quantum efficiency is lowered within the dinuclear species as compared to mononuclear species. A similar ethylene linker has previously shown weak electronic interaction between centres [66], which was thought in this case to lead to intramolecular quenching. The iodo species also had lower quantum yields through dissociation of iodide, hampering a bimetallic reaction. Though quantum efficiencies were lower, the dinuclear complexes were more stable and produced more CO than the monomers. Later, the group assessed **(88)** and compared activity to the monomer $[Ir(ppic)(tpy)Cl]^+$ and dinuclear **(84)** in MeCN/TEOA 5:1 [160]. Irradiation at 450 nm led to TON_{CO} (per catalytic site) of 60, 41 and 33 for the tri-, di- and mononuclear species respectively.

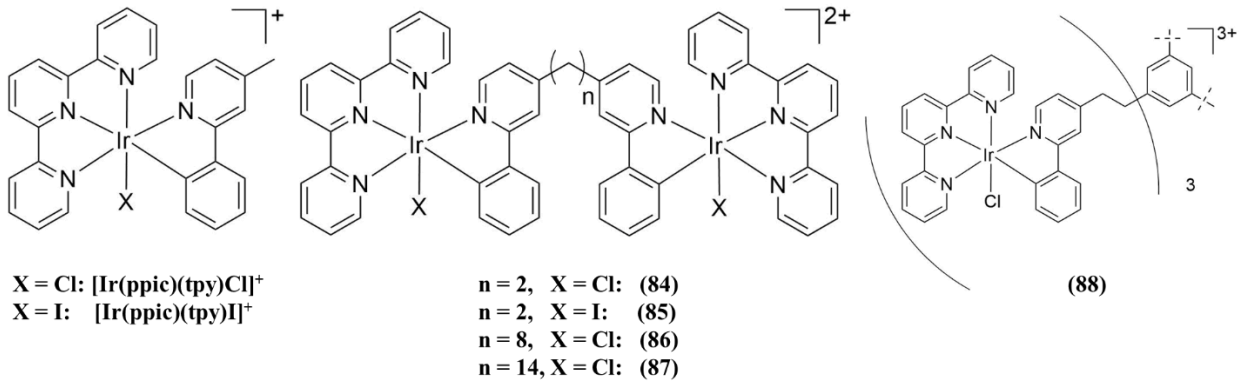

Figure 1.37: Mono-, di- and trinuclear iridium complexes

1.3.2. Molecular electrocatalytic CO_2 reduction overview

Electrocatalytic CO_2 reduction requires the use of an electroactive substance that catalyses the conversion of CO_2 to higher energy products. Electrocatalytic approaches include that of bare metal electrodes [161], surface-bound metal organic frameworks [162], homogeneous molecular electrocatalysts, heterogeneous bioelectrocatalysts [163], surface-modified electrodes such as polymer trapped molecular catalysts [164] or electropolymerised electrocatalysts [165,166]. For a relatively recent (2014) extensive review in the general area, the reader is directed to Qiao *et al*. [167]. A more recent review on the very active area of molecularly defined electrocatalytic CO_2 reduction is provided herein. This review details relevant recent papers to heterogeneous and homogeneous electrocatalytic CO_2 reduction, undertaken at atmospheric pressure and room temperature, with an emphasis on catalysts that contain a first-row transition metal centre.

Often, forms of renewable energy may be intermittent, and therefore, energy storage can be realised through electrosynthesis of single carbon-containing building blocks such as CO or formate. Particularly relevant to molecular electrocatalysts (as with photocatalysts), rare are examples of C_2 products yet [168]. With use of the Fischer Tropsch process, CO can be converted with the aid of H_2 (often a byproduct of electrochemical CO_2 reduction) to energy-dense liquid hydrocarbons [169]. Companies are already electrocatalytically reducing CO_2 with the production of formate, CO, formaldehyde and hydrocarbons [170], in addition to glycols and alcohols [171], strongly suggesting commercial viability. In the area of molecular electrocatalytic CO_2 reduction, the vast majority of publications focus on selective formation of a target CO_2 reduction product. Reports concerned with the generation of the syngas ratio (2:1 H_2 to CO) required for the Fischer Tropsch process have been less in number [172–175]. Alleviation of purification costs may also be achieved through the simultaneous formation of a gaseous and a liquid product [170,176].

1.3.2.1. Assessment of electrocatalytic activity

Various terms exist in benchmarking complexes for activity towards electrocatalytic CO_2 reduction. These include the following:

Turnover number (TON): Calculated as the number of moles of product generated divided by the number of moles of catalyst. This assesses the robustness of a catalyst only. TONs are often higher in surface-bound electrocatalytic experiments. One reason for this is that electrolysis is often not exhaustive with respect to the catalyst, i.e. that an arbitrary shorter timescale of catalysis is chosen. Due to the significantly larger amount of catalyst in usual homogeneous electrocatalytic experiments as compared to heterogeneous experiments, the time taken for each molecule in homogeneous conditions to undergo a catalytic cycle will likely be far greater.

A case also exists in solution electrocatalysis, whereby exclusion of the concentration of the bulk solution (and factoring in only the concentration of catalyst in the diffusion layer) has led to record homogeneous TON_{CO} values [177]. This alteration certainly has merit in attempting to allow for a fair comparison between surface and solution (hetero- and homogeneous respectively) TONs. However, the result of this approach may be interpreted as a direct result of homogeneous electrolysis [167,178] (considering the bulk solution concentration). For example, the group of Savéant calculated a TON_{CO} of 50,000,000 for **(145)** in DMF with 2 M H_2O [179] (Figure 1.49), whereas exhaustive electrolysis in DMF with 3 M PhOH was reported to produce 210 catalytic cycles [180].

Turnover frequency (TOF): Calculated as turnover number per unit time, i.e. the number of moles of product obtained divided by the number of moles of catalyst, divided by time. This is an important indicator of the speed at which a catalyst converts CO_2 to a particular product. Akin to TON calculations as an effort to benchmark catalysts, TOF calculations (potentially far in excess of what would be observed in an electrolysis experiment due to size of electrode, volume of the solution and catalyst robustness) may be derived from voltammograms and non-exhaustive controlled potential electrolysis [181].

Selectivity: Selectivity within CO_2 reduction can have different meanings but is often specified. This could include the ratio between a product formed during electrocatalysis and H_2 [182], the ratio in which a product forms and the sum of any detected products in

addition to H_2, or the ratio of total CO_2 products formed and H_2 generated. This is as suggested, a measure of how selective the system is in generating CO_2 reduction product(s) over that of competing reactions, particularly hydrogen evolution. However, this does not express how quickly or how much of a product is generated, or if any competing processes (not involving CO_2 or proton reduction) are occurring.

Faradaic efficiency (FE): Calculated based on the moles of a specific product obtained multiplied by the number of electrons required to convert CO_2 to the desired product, and divided by the moles of electrons utilised in electrolysis. This is a good indication of selectivity of catalysis for a specific product, but also, of the electrochemical system as a whole, i.e. limiting non-Faradaic current, re-reduction of oxidised species created at the anode or other competing Faradaic processes.

Overportential (η): The potential in excess of the thermodynamic reduction potential required to convert CO_2 to the intended product. The introduction of a catalyst is designed to bypass/stabilise the formation of the $CO_2^{\bullet -}$ radical ion, which undergoes a thermodynamically unfavourable bent conformation. The thermodynamic potential of $CO_2^{\bullet -}$ production has been stated as being approximately 1.3 - 1.4 V more negative to that at which conversion formic acid and CO occurs in aqueous solution [67].

The above terms are categorised under the headings of robustness, selectivity and efficiency for ease in Figure 1.38. Note that overpotential is included in efficiency in that an increase in driving force often affects reaction kinetics [179]. Further to the aforementioned indicators of performance, the cost of the complex is not considered in any common terminology, but is of high importance. If a synthesis is low-yielding, provided that the catalyst is efficient, selective and robust, research will likely concentrate on alternative methods to synthesise the product. However, if the complex involves the addition of a rare transition metal, the cost of synthesis cannot be decreased significantly. Therefore, the need arises for first-row transition metal centres.

From Figure 1.38, it is seen that there is no overlap in definitions and that each term can be quite exclusive to each other (TOF may be described as a measure of robustness, but only over the course of exhaustive electrolysis).

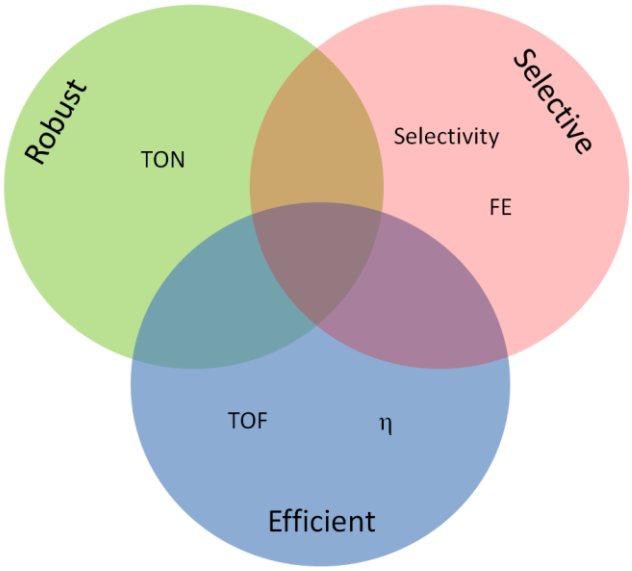

Figure 1.38: The terms utilised for CO_2 electroreduction under the headings of robustness, selectivity and efficiency.

A strong indicator of reductive electrocatalysis is the appearance of an enhanced cathodic current within the voltammetry obtained in the presence of the substrate, relative to the voltammetry obtained in the absence of the reacting substrate. In the case of homogeneous electrocatalysis, this is frequently supported by the loss of a reoxidation associated with a previously reversible reduction. For example, the cyclic voltammetry of **(89)** (Figure 1.40), acquired by Bourrez *et al*. [183] and in the presence of Ar, CO_2, and CO_2 with 5% water in MeCN is shown in Figure 1.39. The introduction of water (in the presence of CO_2) causes a strong cathodic current enhancement at approximately the potential of the complex' second reduction. It is worth noting that voltammetry alone is not adequate to suggest catalytic activity, and electrolyses should be undertaken to assess the identity and efficiency of the products associated with the enhancement.

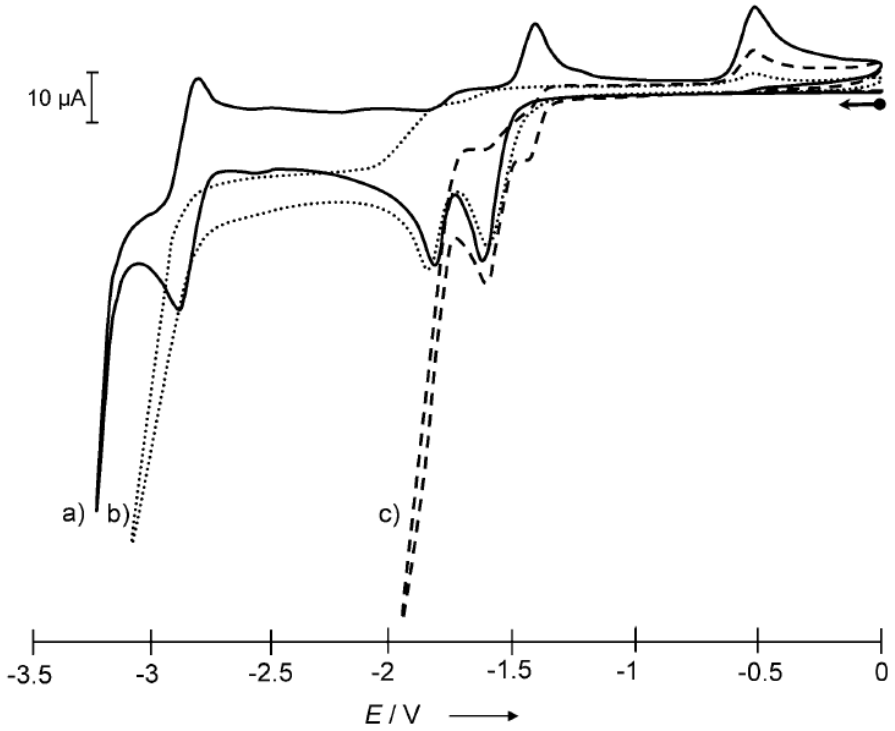

Figure 1.39: An example of voltammetric enhancement indicative of electrocatalytic CO_2 reduction, as undertaken by Bourrez *et al*. [183]. Cyclic voltammetry (ν = 100 mV s^{-1}) of **(89)** (Figure 1.40) was performed in the presence of Ar (a), CO_2 (b), and CO_2 with 5% water (c) in MeCN, potentials quoted vs SCE and undertaken at glassy carbon.

1.3.2.2. Recent advances in molecular CO_2 electrocatalysis

This introduction to the area of molecular electrocatalysed CO_2 reduction focuses on publications relating to first-row transition metal-centred complexes, published 2014 – present, though the area has existed since 1974 [184]. Both homogenous and heterogeneous molecular electrocatalysts are discussed and second and third row transition metal-centred catalysts, as relevant, are also considered. Homogeneous and heterogeneous approaches are separated within the text, as TONs for example (and therefore TOFs) are often higher in heterogeneous materials due to the lower amount of catalyst present and the often non-exhaustive trait of bulk electrolyses within homogeneous experiments. The term "homogeneous" specifically relates to the state of the catalyst precursor (as dissolved in solution), whereby the actual catalyst may be heterogeneous in nature [101,185–187]. In turn, "heterogeneous" refers to the precursor being confined to the surface of the electrode prior to electrolyses. One approach

existing between these terms is $Re(bpy)(CO)_3Cl$, as assessed in a "brush polymer" gel that exhibits diffusive behaviour of electroactive species [188]. Specific attention to first-row transition metal-centred electrocatalysts stems from the metal's abundance and low cost.

1.3.2.2.1. Homogeneous electrocatalysts towards CO_2 reduction

1.3.2.2.1.1. Diimine complexes of $Mn(CO)_3X$ and related complexes

Bipyridyl-based rhenium catalysts (i.e. **(106)**, Figure 1.42) have received considerable attention as both photo- and electrocatalytic CO_2 reductants since the pioneering work of Hawecker *et al*. [146]. Bipyridyl manganese complexes were previously discounted as feasible catalysts [189,190] as the substantial synergistic contribution of Brønsted acids to the family was not yet understood [191]. In 2011, Bourrez *et al*. [183] explored the use of **(89)** and **(92)** (Figure 1.40) as CO_2 electro-reduction catalysts. In the absence of water, the catalysts showed no activity towards CO_2 reduction in MeCN (0.1 M tetrabutylammonium perchlorate (TBAP)). However, upon the introduction of 5% water, a rapid CO_2 reduction current was observed. Bulk electrolyses were executed at -1.7 V vs Ag/Ag^+ with a carbon plate, whereby **(89)** produced CO with quantitative FE and a TON of 13 after 4 hours. At longer timescales (22 hours electrolysis, after 130 Coulombs (C) were passed), the catalyst became less selective, producing CO (FE of 85%) and H_2 (FE of 15%). **(92)** proved to be more selective and stable over longer periods, with quantitative FE_{CO} and TON_{CO} of 34 after 18 hours with 138 C passed. Intermediates have been studied via UV-visible spectroscopy, pulsed electron paramagnetic resonance experiments in conjunction with density functional theory calculations [192] and pulse radiolysis with TR-IR [193].

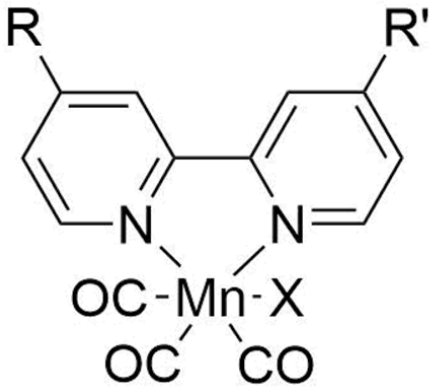

R	R'	X	
H	H	Br	**(89)**
H	H	MeCN (PF_6 salt)	**(90)**
H	H	CN	**(91)**
CH_3	CH_3	Br	**(92)**
CH_3	CH_3	MeCN (PF_6 salt)	**(93)**
t-bu	t-bu	Br	**(94)**
OH	OH	Br	**(95)**
COOH	COOH	Br	**(96)**
PO_3H_2	PO_3H_2	Br	**(97)**
CH_3	C_3H_6-Pyrrole	MeCN (PF_6 salt)	**(98)**
$CH_2NH(C=O)CH_3$	$CH_2NH(C=O)CH_3$	Br	**(99)**

Figure 1.40: Manganese bipyridyl complexes appearing in the literature

From the study of Bourrez *et al*., the group assessed the CO releasing ability of the terpyridyl Mn complexes [194]. Machan and Kubiak further studied **(100)** and **(101)** (Figure 1.41) for their ability as CO_2 reduction catalysts [195]. At negative potentials, evidence from IR-SEC experiments is present to show that both **(100)** and **(101)** form a Mn-Mn tetracarbonyl dimer. FE_{CO} of higher than 100% further corroborates this in the case of **(100)**, with Compain *et al*. [194] having also reported **(100)** as a CO releasing molecule. After approximately two hours, bulk electrolyses at -2.2 V vs Fc/Fc^+ with a graphite rod in the presence of 0.5 M phenol produced 4.1 TON_{CO} with 129 % FE_{CO} (1% FE_{H2}) for **(100)** and at 4.1 TON_{CO}, **(101)** achieved FE_{CO} of 93% with 6% FE_{H2}. Both complexes were observed to lose selectivity following TON_{CO} of approximately 4.

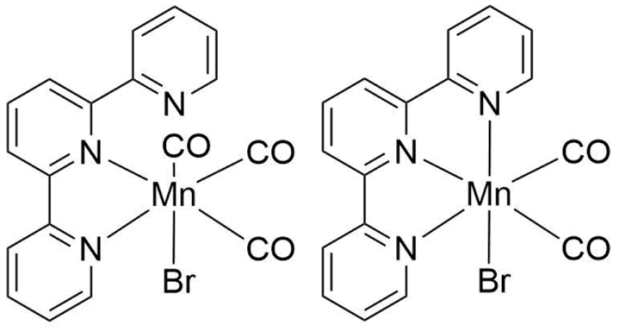

Figure 1.41: Mn terpyridyl complexes, reported by Machan and Kubiak [195].

Following the discovery of **(89)**'s activity, the area was expanded by Smieja *et al*. [196] using **(94)** (Figure 1.40) which was stable for more than 3 hours under electrocatalytic conditions in MeCN (0.1 M tetrabutylammonium hexafluorophosphate ($TBAPF_6$)). Bulk electrolyses were carried out utilising various concentrations of Brønsted acids (1.4 M and greater), such as trifluoroethanol (TFE), methanol (MeOH) and water. Despite a relatively negative applied potential -2.2 V vs SCE, over 800 mV beyond the second reduction peak of **(94)** (-1.57 V vs SCE), CO was observed with a quantitative Faradaic yield. TONs were not quoted. Electrolyses were likely not exhaustive as the glassy carbon electrode was a modest size regarding active area. Instead of exhaustive electrolyses, foot of the wave (FOTW) analyses, initially incorporated by Saveant *et al*. [177,179], towards CO_2 reduction were implemented to assess efficiency of the catalyst and it was stated that **(94)** was 300 times faster with 1.4 M TFE than 5% water as acid. This is approximately 7 times less active than **(106)** (Figure 1.42) in 2 M water in DMF and approximately in line with the activity of **(171)** (Figure 1.52) in 1:4 water to MeCN [196].

Sampson *et al*. further studied **(103)** and **(104)** (Figure 1.42) [197]. No evidence of dimerisation, reported for **(89)** and **(94)** was observed for these complexes. TOF calculations based on peak current and catalytic current indicate that **(104)** is an order of magnitude more active than **(94)** upon the addition of 1.4M TFE. A TON_{CO} of 4 and FE of 98% was achieved within the first 70 minutes of bulk electrolysis at -2.2V vs Fc/Fc^+ with 0.3 M TFE in MeCN. Interestingly, **(104)** produced no H_2 under the same conditions. In contrast, at -1.5 V vs Fc/Fc^+, high TOFs for H_2 were reported when electrolysis was performed in the presence of a strong acid, trifluoroacetic acid (TFA) [198]. The catalyst was believed to form a Mn(I)-COOH species upon its first reduction, which undergoes a further reduction at more negative potentials.

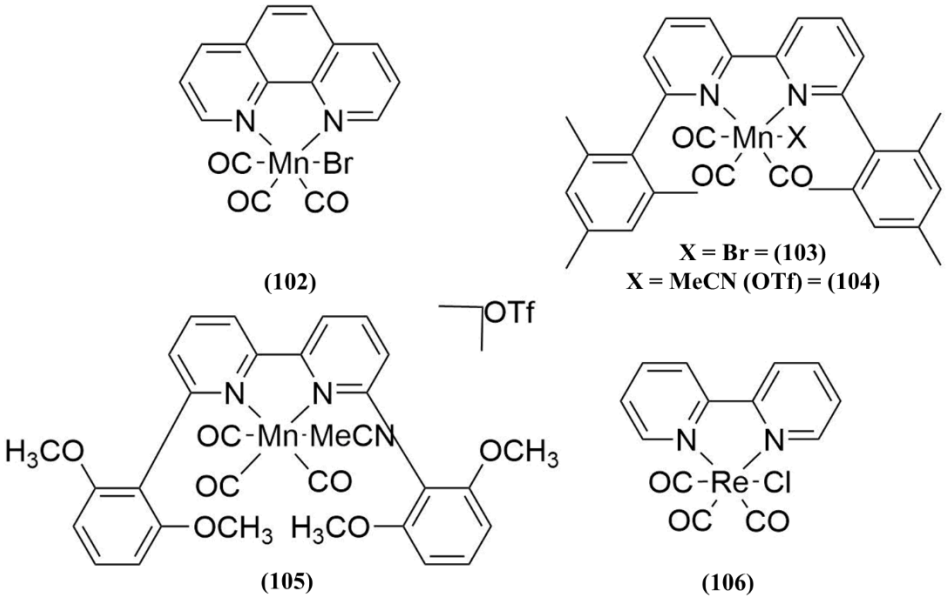

Figure 1.42: Structures of **(102)**, **(103)**, **(104)**, **(105)** and **(106)** as appearing in the literature

Both complexes were further probed with the use of Mg^{2+} as Lewis acid instead of TFE [199]. The use of alkaline earth metals as Lewis acids have been reported previously with **(143)** [200] (Figure 1.49), as have alkali metals for cobalt salens [201] (Figure 1.54). The purpose of Mg^{2+} addition was to aid a disproportionation reaction at the first reduction potential, resulting in the release of $MgCO_3$ and CO. In this system, a reduction in overpotential of 600 mV was obtained, as compared with electrolyses undertaken with TFE. When the use of Mg^{2+} and TFE were assessed with **(104)** at -1.6 V vs Fc/Fc^+, 36 TON_{CO}s were recorded after 6 hours with Mg^{2+} (98% FE) as compared to 14 with TFE. Due to the insolubility of $MgCO_3$ in MeCN, a sacrificial Mg anode along with the use of $Mg(OTf)_2$ was employed to allow the concentration of Mg^{2+} to remain at 0.2 M.

A particularly interesting study of bipyridyl manganese complexes (including Re homologues) was reported by Franco *et al*. with the electrocatalytic assessment of **(107)** and its dimethoxy equivalent, **(108)** (Figure 1.43) [202]. Of interest also is Agarwal *et al*.'s later study [203] of **(109)** and **(110)** respectively, (Figure 1.43). Regarding electrocatalysis of CO_2, two key effects of substitution of the bpy ligand can be considered. Introduction of the electron donating groups allows for a higher reducing

power of the metal, thus accelerating catalysis as observed with the higher activity of **(94)** > **(92)** > **(89)** [183,196]. Additionally, the ligand may stabilise intermediates, thereby aiding catalysis through local pendant amines or hydroxyl groups [179]. The addition of a phenolic group should serve to shift behaviour in the absence of CO_2, to more positive potentials due to increased stabilisation within the ligand. Therefore this would be counterproductive for the reducing power of the metal centre.

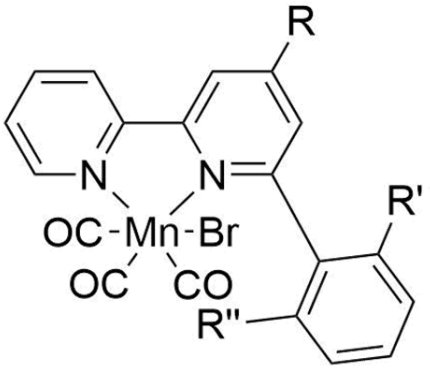

R	R'	R"	
C_6H_5	OH	OH	**(107)**
C_6H_5	OCH_3	OCH_3	**(108)**
H	OH	H	**(109)**
H	OCH_3	H	**(110)**

Figure 1.43: Structures of 6-monosubstituted, and 4,6-disubstituted Mn bipyridines as appearing in the literature

However, Agarwal observed that the inclusion of an ortho-phenolic group allowed for a 7-fold current enhancement compared to **(89)**, upon the introduction of CO_2. Faradaic efficiency of 76% was achieved for CO with **(109)** in MeCN with 5% water and 0.1 M tetrabutylammonium perchlorate (TBAP). Remarkably, Franco *et al*. did not require the addition of water to observe a catalytic wave upon CO_2 reduction. Following electrolysis for 4 hours at -1.8V vs saturated calomel electrode (SCE) in dry MeCN with 0.1 M $TBAPF_6$, a TON_{CO} of 19 corresponding to FE of 70% was observed. This is in line with **(89)** with 5% water present, though it is demonstrated that **(107)** undergoes deactivation more rapidly. A very interesting point is that TON_{HCOOH} of 6 was observed (22% FE), which has previously only been observed for Mn bipyridyl complexes in photocatalytic conditions [73] and had not been observed by Agarwal with very similar complexes. The source of H^+ for the generation of six equivalents of formate is uncertain. A maximum of 2 TON_{HCOO^-} (or 1 TON_{HCOOH}) equivalents may have derived from utilisation of the catalyst's phenolic protons. Dry solvents were evident through voltammetric behaviour of **(108)**. The lack of a catalytic wave in the dimethoxy

complex without a proton source present indicates that the peripheral hydroxyl groups played a vital role in catalysis.

These studies led to Ngo *et al.*'s recent assessment of **(105)** (Figure 1.42) with direct comparison to **(104)** [204]. The authors established that in MeCN and with the addition of either water, MeOH, TFE or PhOH, calculated TOF values were higher with **(105)** as compared to **(104)**. Further to this, substantially lower calculated TOFs were achieved for **(104)** than that reported by Sampson *et al*. [197]. Particularly in the presence of the stronger Brønsted acids PhOH and TFE, enhancement of voltammetric current was observed at the first ($2e^-$) reduction, corresponding to a proposed pathway involving protonation of the carboxylate species with the release of water prior to further reductions (in contrast to the more negatively occurring reduction first, protonation second pathway).

Ngo *et al*. further undertook electrolyses of **(104)** and **(105)** in MeCN with optimal concentrations of the four Brønsted acids [204]. A one hour electrolysis showed that water was the least compatible acid in both cases, leading to a FE % for $CO:H_2$ of 61:38 and 73:27 respectively. Within the hour, the highest FE_{CO} for **(105)** was at the reduction first process (-2.36 V vs Fc/Fc^+) with TFE, amounting to FE_{CO} of 100%. Over the course of 3 hours, the highest TON_{CO} achieved for **(105)** was 15-20 (in 2.09 M MeOH at -2.36 V vs Fc/Fc^+), whereas TON_{CO} of **(104)** was also highest in MeOH (2.09 M at -2.26 V vs Fc/Fc^+), generating over 30 TON_{CO}. The lack of stability of both complexes was acknowledged. In a benzoate-buffered system, the overpotentials for CO_2 reduction were calculated as 0.42 V and 0.45 V for the benzoate adducts of **(105)** and **(104)** respectively.

Following the revelation of $Re(dacbpy)(CO)_3Cl$ (dacbpy = 4,4'-bis(acetamidomethyl)bpy) forming a supramolecular assembly and allowing for higher TONs and FE_{CO} (at -1.6 V vs Ag/AgCl in MeCN with 0.5 M TFE) than $Re(dmb)(CO)_3Cl$ [205], Machan and Kubiak assessed whether the approach could be extended to Mn centres [206]. In MeCN with 0.5 M phenol, electrolysis of **(99)** (Figure 1.40) at -2.2 V vs Ag/AgCl produced 4.14 TON_{CO} with quantitative FE_{CO}. At the same potential, $Re(dacbpy)(CO)_3Cl$ also produced 4.14 TON_{CO} but at a reduced efficiency of 76 %. Voltammograms involving a mixture of 1 mM **(99)** and $Re(dacbpy)(CO)_3Cl$ showed approximately a 10% increase in catalytic current upon the introduction of CO_2

than did the sum of 1 mM of both complexes independently, and also different electrochemical behaviour of the mixture to the independent complexes under Ar. The voltammetric behaviour, along with IR-SEC experiments, alludes to the formation of Mn-Re metal to metal dimers upon reduction of the respective complexes. However, bulk electrolysis under identical conditions with 0.5 mM of each complex together showed no benefit, producing 4.15 TON_{CO} with FE_{CO} of 86% (the average FE_{CO} of the individual complexes is 88%). The time of electrolysis or criteria for halting electrolysis was not stated, so it is uncertain as to whether electrolyses were exhaustive.

A further four diimine complexes of [$MnCO_3Br$] utilising the bisphenyl diaminobutyldiene ligand i.e. **(111)**, **(112)**, **(113)** and **(114)** (Figure 1.44) were explored along with six similar rhenium-centred complexes [207]. Only modest activity was observed with the introduction of a proton source. Currents within electrolyses were observed to diminish rapidly and no Faradaic efficiencies were stated. Previous to this, Zeng *et al*. [208] studied **(112)** and found that catalysis was observed by voltammetry. However, the study did not include electrolysis.

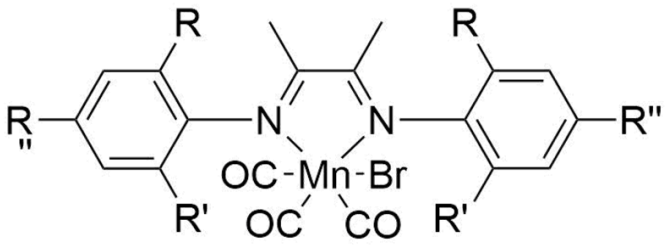

R	R'	R''	
CH_3	CH_3	CH_3	**(111)**
i-pr	i-pr	H	**(112)**
H	H	Br	**(113)**
CF_3	H	H	**(114)**

Figure 1.44: Mn diaminobutadiene (DAB) complexes as appearing within the literature

Agarwal *et al*. synthesised methylpyridylimidazoliyidine and methylpyridylbenzimidazoliyidine complexes of [$Mn(CO)_3Br$], **(115)** and **(116)** respectively (Figure 1.45) [209]. These complexes demonstrated a 2-fold catalytic current wave in 5% H_2O in MeCN compared to that under Ar without water, corresponding to calculated TOFs of 0.08 and 0.07 s^{-1} (**(89)** of 0.14 s^{-1} for comparison) respectively. Electrolysis of **(115)** at the first reduction potential (~ -1.3V vs SCE) led to the formation of CO with 35% efficiency and with the absence of H_2. Later, Agarwal *et al*. further reported **(117)**, **(118)**, **(119)** and **(120)** (Figure 1.45) [210]. Electrolysis of

these compounds was undertaken at the first reduction potential in MeCN with 5% H_2O, and at a 2.5 cm^2 glassy carbon electrode. The electrocatalytic ability of **(117)** was superior to the other complexes, whereby 67% FE_{CO} was generated without the detection of H_2. **(117)** also demonstrated the greater i/i_p response (2.1 x) of the four complexes assessed. In terms of stability under light and calculated TOF (0.86 s^{-1}) / efficiency, these complexes are not attractive as compared to bipyridyl manganese complexes.

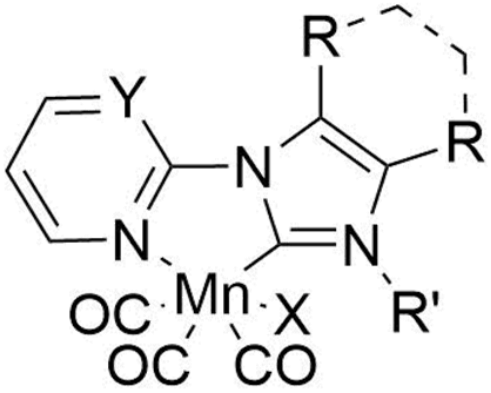

R	R'	X	Y	
H	CH_3	Br	CH	**(115)**
C_4H_4	CH_3	Br	CH	**(116)**
H	C_2H_5	Br	CH	**(117)**
H	C_2H_5	CN	CH	**(118)**
H	C_2H_5	SCN	CH	**(119)**
C_4H_4	C_2H_5	CN	CH	**(120)**
C_4H_4	C_2H_5	Br	CH	**(121)**
C_4H_4	C_2H_5	Br	N	**(122)**

Figure 1.45: Structures of Mn pyridyl/pyrimidyl imidazoliyidine-type complexes as assessed towards electrocatalytic CO_2 reduction

The group further assessed **(121)** and **(122)** (Figure 1.45) [211]. It was found that **(121)** and **(122)** showed a 1.7 and 5.2-fold current enhancement at approximately the potential of the first reduction under Ar. When electrolyses were undertaken at a glassy carbon rod, poised at -1.75 V vs Ag/AgCl under CO_2 and with 5% water (acidified to pH 3.7 with perchloric acid), **(121)** consumed 20 C with FE_{CO} of 48%. **(122)** on the other hand, produced an efficiency of 72% after the passage of 35 C (approximately 4 TON_{CO}). For comparison, **(89)** produced a 2.1-fold i/i_p enhancement, with electrolysis at -1.75 V vs Ag/AgCl leading to a 73% FE_{CO} after 35 C of charge consumed. In both cases of **(122)** and **(89)**, the rate of electron consumption was observed to diminish. Inspiration for the pyrimidyl modification may have stemmed from a computational study by Lam *et al.* [212], who predicted that $[Mn(bpm)(CO)_3]^-$ (bpm = bipyrimidine) would allow for electrocatalytic CO_2 reduction at more positive potentials than that of **(89)** (but at a cost of TOF_{CO}).

The complexes of **(90)** and **(93)** (Figure 1.40) were reported for their capacity as photoelectrocatalysts by Torralba-Peñalver *et al*. [213]. In these studies, the Mn complexes were utilised homogeneously in conjunction with silicon nanowires (Si-NW). When electrolysis was performed at -1.1 V vs SCE in MeCN with 5% H_2O, quantitative FE_{CO} was obtained. At -1 V, a photocurrent density of 1.14 mA cm^{-2} was obtained with **(90)** when irradiated with $\lambda > 600$ nm compared to ≈ 0 mA cm^{-2} without irradiation. A pyrole-containing bpy (**(98)**) was further synthesised for heterogeneous use, as described in section 1.3.2.2.2.

With the rising interest in Mn diimines and the large body of research in existence for Re diimine as both an electro- and photocatalyst, mechanistic limitations between these complexes may provide hints into tweaking conditions and/or ideal ligand substitution. With such purpose in mind, Riplinger *et al*. assessed the differences in mechanistic pathways with the use of computational chemistry [191]. The study alluded to a potential benefit of using a stronger accompanying acid (or stronger concentrations of weak acid) to assist with CO_2 protonation and binding stabilisation [39] with **(89)**. With stronger acids however, direct proton reduction at the electrode could disrupt selectivity.

The novel Mn tricarbonyl complexes **(123)** (*mer*-tricarbonyl) and **(124)** (*fac*-tricarbonyl) were assessed in MeCN with 0.1 M $TBAPF_6$, with and without 5% water (Figure 1.46) [214]. Remarkably, electrolysis of **(123)** at -2.3 V vs Fc/Fc^+ demonstrated that the addition of 5% water hindered catalysis, in stark contrast to the behaviour observed for Mn bipyridyl complexes [183,196]. In the absence of a proton source, CO was evolved selectively with a FE of 96% and a rate of 6 μmol hr^{-1} over approximately 5.5 hours. When a proton source was present, a 100 minute electrolysis led to an average FE_{CO} and FE_{H2} contribution of 48.5 and 32%, whereby the rate of CO production decreased markedly upon approaching 100 minutes. The average FE between CO and H_2 in the presence of the proton source was found to be 80.8% as opposed to the FE_{CO} of 96% without water present. **(124)**, contrary to **(123)**, did require the addition of a proton source to observe catalytic behaviour via voltammetry, akin to other bidentate diimine Mn complexes. Electrolysis of **(124)** at -2.5 V vs Fc/Fc^+ in MeCN with 5% water led initially to CO, however an approximate 3:2 ratio of CO:H_2 was generated (albeit with total FE of approximately 99%) following the initial 50 minutes of electrolysis.

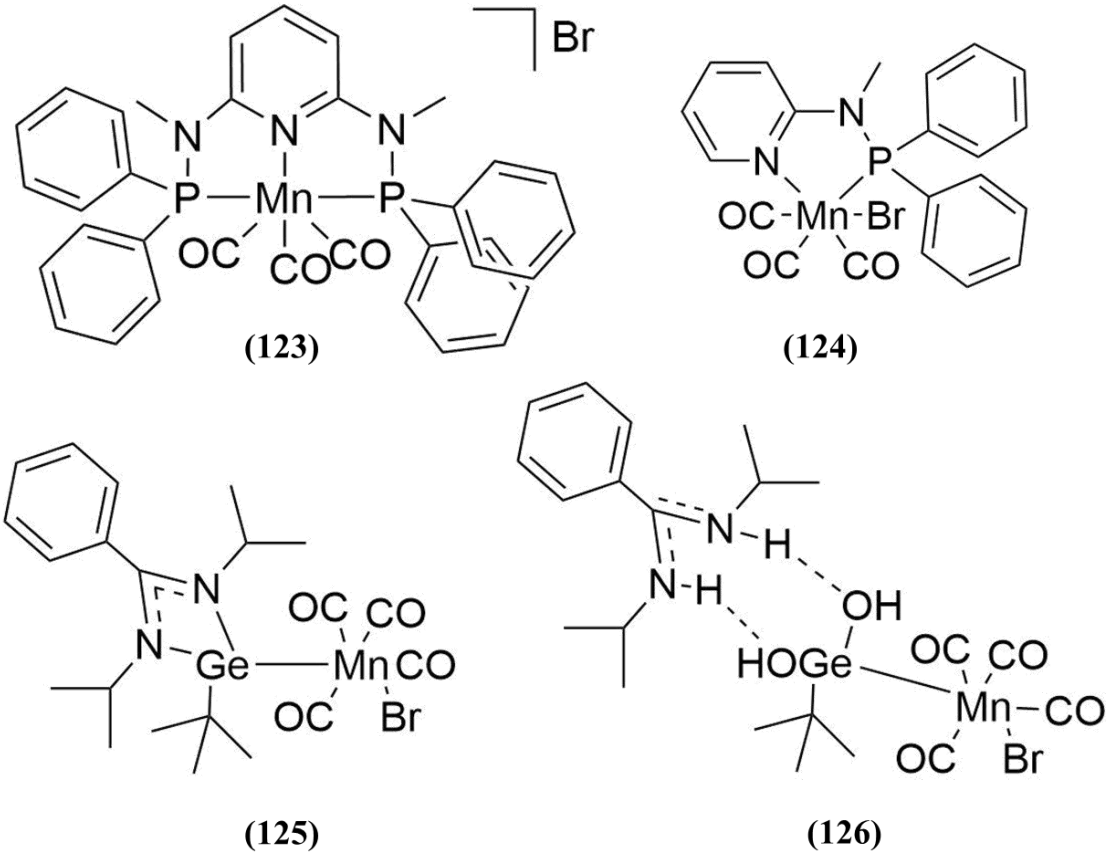

Figure 1.46: Various Mn carbonyl complexes assessed towards electrocatalytic CO_2 reduction

A worthy short note within this section is that $[Mn(CO)_4Br]$ complexes have been assessed homogeneously in the form of **(125)** and **(126)**, Figure 1.46) [215]. **(125)** and **(126)** were electrolysed at -1.9 and -2.33 V vs Fc/Fc^+ respectively in MeCN with 5% water and produced a TON_{CO} of 0.97 and 0.8 and TON_{H2} of 3.3 and 1.8 respectively (140 and 103 mins electrolysis time). The complexes were not competitive as catalysts in terms of selectivity or TON_{CO} reported.

Research into the use of bipyridyl manganese tricarbonyl catalysts has further extended into the areas of electrocatalytic H^+ reduction [198], surface-bound CO_2 electroreduction (as described in section 1.3.2.2.2), photoelectro- [73] (also described in section 1.3.2.2.2) and homogeneous photocatalytic CO_2 reduction [95,216]. **(89)** was successfully incorporated photocatalytically [95] through the inclusion of 1-benzyl-1,4-dihydronicotinamide (BNAH) as sacrificial electron donor, triethanolamine (TEOA)

likely to maintain pH [217], and $[Ru(dmb)_3]^{2+}$ as photosensitiser. Most interestingly, within this system, 149 TON_{HCOOH} with 12 TON_{CO} and 14 TON for H_2 was detected, as opposed to selective CO formation witnessed electrocatalytically [183,196]. Fei *et al*. [73] assessed the photocatalytic activity of **(96)** bound to a Zr-containing metalorganic framework with $[Ru(dmb)_3]^{2+}$ as photosensitiser, and 0.2 M BNAH in a 4:1 DMF to TEOA ratio. At 470 nm monochromatic light, 18 hour irradiations produced TON_{HCOOH} of 110, TON_{CO} of 4.5 and TON_{H2} of 1. Without the MOF present, **(89)** was found to produce TON_{HCOOH} of 70 and TON_{CO} of 5. The absence of MOF and **(89)** produced TON_{HCOOH} of 33.

(102) (Figure 1.42) was paired with Zn tetraphenylporphyrin as photosensitiser and triethylamine (TEA) as sacrificial electron donor, however containing 5% water in MeCN [216]. The system was more selective towards CO generation (with TON_{CO} of 64 and TON_{HCOOH} of 16) as compared to that of **(89)** [95]. Cheung *et al*. also incorporated **(91)** photocatalytically with $[Ru(dmb)_3]^{2+}$, BNAH and TEOA in an attempt to avoid dimerisation of the manganese centres [218]. Though it was speculated that a disproportionation reaction occurred in place of dimerisation, results did not vary significantly to that of Ishitani *et al*. [95]. The inspiration of this research was borne from electrocatalytic studies by Machan *et al*. whereby electrolysis at -2.2 V vs Fc/Fc^+ yielded efficiencies of 98% and 1% for CO and H_2 respectively ($TON_{CO} > 4$) in MeCN with 0.5 M phenol [219].

1.3.2.2.1.2. Diimine $M(CO)_4$ and $M(CO)_6$ (M = Cr, Mo, W) complexes

Within this subsection, though molybdenum and tungsten are second and third row transition metals, research into the utilisation of molecular complexes containing these metals have gained momentum in recent years. It is likely that any significant advances within Mo or W complexes may be extended to their Cr analogue as has been the case with Re and Mn bipyridyl complexes.

A study by Tory *et al*. [220] suggested that $M(bpy)(CO)_4$ type compounds (M = Cr, Mo or W, i.e. **(127)**, **(128)** and **(129)** respectively, Figure 1.47) are electrocatalytically active in tetrahydrofuran (THF) and n-methyl-2-pyrrolidone (NMP), particularly at a gold electrode. This was demonstrated with the use of voltammetry, UV and IR

spectroelectrochemistry. However, the potential of the first reduction of **(128)** is approximately 0.5 V more negative than the first reduction of **(89)** and -0.25 more than the formation of $[Mn(bpy)(CO)_3]^-$. No bulk electrolyses were undertaken to gauge stability, selectivity or efficiency. Clark *et al*. [221] previously studied **(130)** and **(131)** (Figure 1.47) and stated that electrocatalytic CO_2 reduction was observed in acetonitrile. TOFs were calculated based on i/i_p and were found to be 1 and 2.9 s^{-1} respectively. Faradaic efficiency was stated to be 109% for CO with 3% H_2. Reductively and oxidatively, these species have been reported to lose CO, which reasoned a FE > 100%.

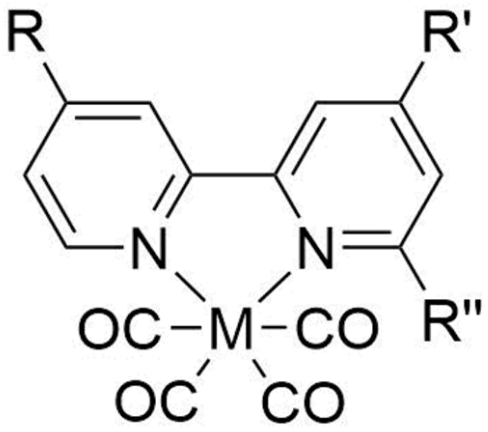

R	R'	R''	M	
H	H	H	Cr	**(127)**
H	H	H	Mo	**(128)**
H	H	H	W	**(129)**
t-bu	t-bu	H	Mo	**(130)**
t-bu	t-bu	H	W	**(131)**
H	C_6H_5	C_6H_5	W	**(132)**
H	C_6H_5	o,o'-$(CH_3O)_2$-C_6H_3	W	**(133)**

Figure 1.47: Structures of Cr, Mo and W bipyridyl complexes assessed towards electrocatalytic CO_2 reduction

Following on from Clark *et al.*'s work, Sieh *et al*. explored the use of pyridine monoimine complexes, **(134)** and **(135)** (Figure 1.48) [222] as a related 2-pyridinylmethylene phenylamine ligand allowed for approximately a 400 mV anodic potential shift to the ligand reduction of the associated $[Re(CO)_3Cl]$ complex as compared to **(106)** [223]. Though **(134)**'s first and second reductions were more positive than those of **(128)**, a one-hour electrolysis at -2.5 V vs Fc/Fc^+ in MeCN led to only 10% FE_{CO} with trace amounts of H_2 observed. Chemical reduction experiments monitored by NMR, in addition to DFT suggest that the carbon of CO_2 bonds to the imine carbon and an oxygen to the metal centre (vacant site as a CO ligand had previously been liberated), thus deactivating the complex. Further to this, the ligand of **(135)** was isolated with CO_2 bound to the carbon of the imine bond as a decomposition product, and was confirmed by crystallography.

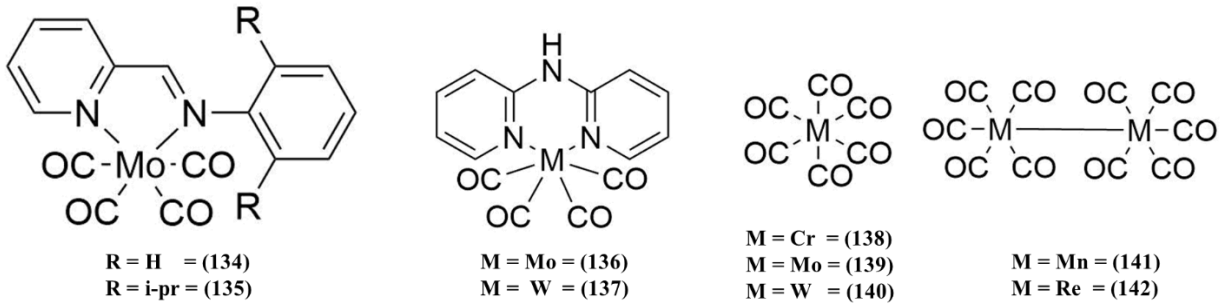

Figure 1.48: Pyridine monoimine and dipyridylamine tetracarbonyl complexes and metal hexa- and decacarbonyls assessed for electrocatalytic CO_2 reduction

(132) and **(133)** (Figure 1.47) and 2,2'-dipyridylamine complexes of Mo and W (**(136)** and **(137)**, Figure 1.48) were studied in MeCN [224]. **(137)** displayed reasonable activity at -2.2 V vs SCE, generating 8 TON_{CO} following the first hour of electrolysis, corresponding to FE_{CO} of 55%. However, rapid deactivation of the catalyst was observed following the second hour of electrolysis with TON_{CO} increasing by 2, but FE_{CO} approximately equating to half that of the first hour. Interestingly though, electrolysis of the complex under Ar showed no evidence of CO, confirming that the reduction observed for **(137)**, and indeed, the reason for deactivation was likely not that of CO release.

The precursor metal hexacarbonyls to the above complexes, **(138)**, **(139)** and **(140)** (Figure 1.48) were assessed homogeneously in DMF and with water present [225]. All three compounds showed voltammetric enhancement under CO_2, however with the catalytic current occurring beyond -2.5 V vs Fc/Fc^+. This is in contrast to the decacarbonyl dinuclear Mn and Re precursors **(141)** and **(142)** (Figure 1.48) also studied, which showed CO_2 binding but with a lack of enhancement to the reduction wave. **(139)** was electrolysed at -2.8 V vs Fc/Fc^+ without water present and it was found to produce 83-95% FE_{CO} over 30 minutes and two hour electrolyses led to 8.1 TON_{CO}. H_2 was detected at < 1% of the products. With 0.98 M water present, 35% and 47% Faradaic efficiencies for CO and H_2 were stated, with the average current density less than half that without water.

1.3.2.2.1.3. Iron and cobalt porphyrins and related macrocycles

Iron tetraphenylporphyrin complexes were revisited by Costentin *et al*. [179] with the introduction of hydroxy and methoxy groups on the ortho and ortho' positions on the porphyrin (**(145)** and **(146)** respectively, Figure 1.49). Both complexes were compared with **(143)**. **(145)** was the most active of the complexes assessed for CO_2 reducing ability. In DMF with 2 M H_2O, a two hour electrolysis at -1.16 V vs normal hydrogen electrode (NHE) produced Faradaic efficiencies for CO and H_2 of 94% and 6%. TONs based on the concentration of the catalyst in the reaction diffusion layer resulted in TON_{CO} in excess of 50,000,000, after which the authors stated that there was no observed degradation of the catalyst. It must again be noted that negating the bulk concentration of catalyst within homogeneous electrocatalysis increases the TONs (and TOFs) dramatically. This catalyst was later used by Bonin *et al*. [83,94] in the photocatalytic reduction of CO_2 to CO.

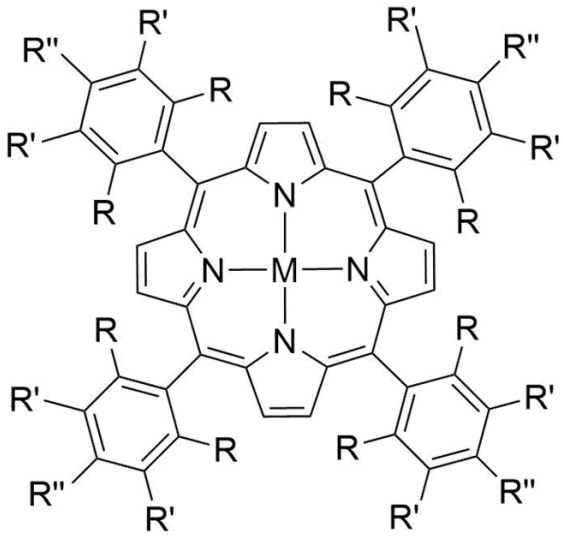

R =	R' =	R'' =	M =	#
H	H	H	Fe Cl	**(143)**
H	H	H	Co Cl	**(144)**
OH	H	H	Fe Cl	**(145)**
OCH_3	H	H	Fe Cl	**(146)**
OH	H	H	Cu	**(147)**
OCH_3	H	H	Cu	**(148)**
F	F	F	Fe Cl	**(149)**
H	H	$N(CH_3)_3$	Fe Cl	**(150)**
H	H	COOH	Fe Cl	**(151)**
H	H	COOH	Co	**(152)**
H	H	Carbazole	Fe Cl	**(153)**
H	H	NH_2	Co	**(154)**
H	H	NH_2	Fe Cl	**(155)**

Figure 1.49: Structures of a variety of meso-substituted Fe, Co and Cu porphyrins as appearing within the literature

Costentin *et al*. further modified **(145)** by introducing two perfluorophenyl groups with two phenyl groups remaining as o,o'-hydroxylated, leading to **(159)** (Figure 1.50) [180]. In DMF with 3 M phenol present, voltammograms yielded calculated TOF values of 240 and 170 s^{-1} for **(159)** and **(145)** respectively. Greater stability was observed with **(159)** than **(145)** with current densities remaining constant for the first 3 and 0.5 hours

respectively. In both cases, 100% CO efficiencies were observed (with < 1% H_2). Further assessment of stability was evident with exhaustion of the catalyst in solution. 600, 210, and 300 catalytic cycles were observed before complete degradation for **(159)**, **(145)** and **(143)** respectively.

The use of perfluorophenyl groups has not been confined to the aforementioned study. Alenezi attempted incorporation of **(149)** (Figure 1.49) with p-Si as a means to lower the potential required for reduction in MeCN with 5% DMF and 1.5 mM TFE [226]. However, at a saving of 500 mV, selectivity of CO over H_2 was greatly reduced. The same approach was applied to **(144)** (Figure 1.49), resulting in a lesser applied potential of 300 mV upon irradiation. A decrease in selectivity was observed compared with the utilisation of a carbon electrode [227].

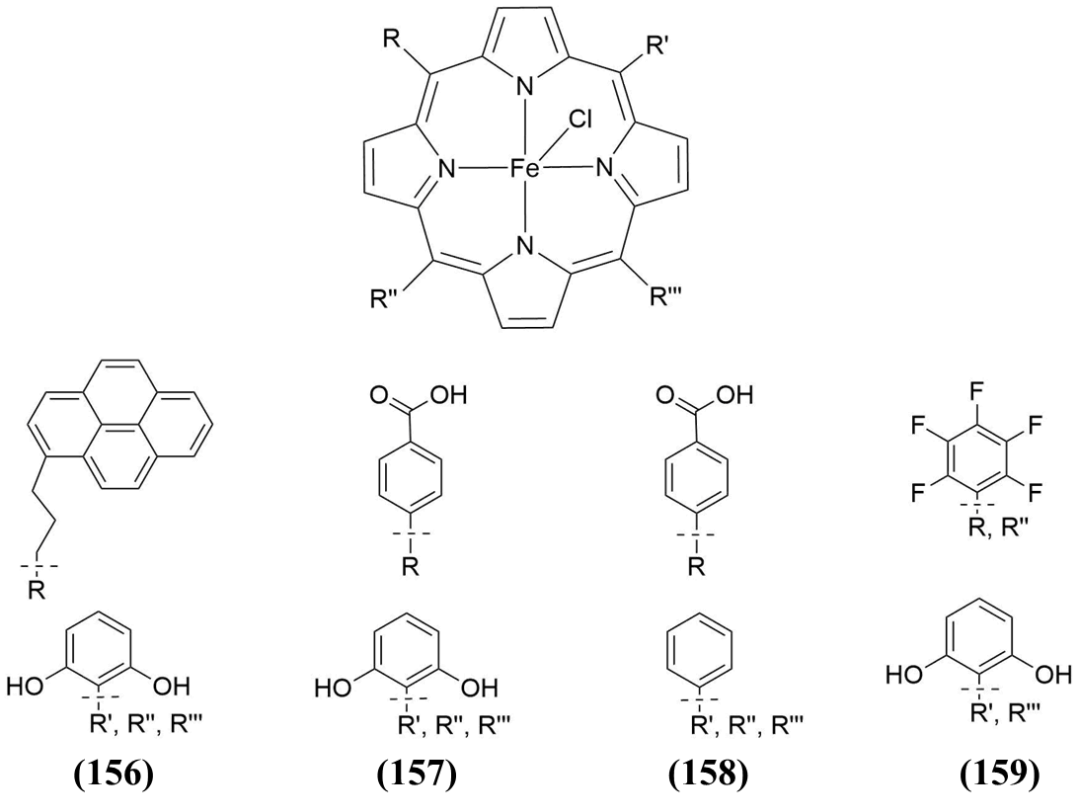

Figure 1.50: **(156)**, **(157)**, **(158)** and **(159)** as assessed for their ability as electrocatalysts towards CO_2 reduction

Even further modification of **(143)** produced the water soluble **(150)** (Figure 1.49) [228]. For this compound, an applied potential of -0.86 V vs NHE produced CO with

FEs of 98-100% in an aqueous solution of complex containing 0.1 M KCl (with KOH used to acquire a pH of 6.7). Following 3 days electrolysis, the charge lowered to approximately half of its initial value. However, CO efficiency remained quantitative. pH was found to play an important role in selectivity. At a pH of 3.7 (formic acid buffered), the system exclusively produced hydrogen while at pH 6.7, 0.1 M phosphate (adjusted), a 1:1 ratio of CO to H_2 was achieved. A preliminary calculated TOF was stated to be in the region of 10,000,000 s^{-1}. In this estimate, TOF is only concerned with molecules in the diffusion layer adjacent to the electrode and not the concentration of bulk solution. **(150)** was later incorporated as a heterogeneous CO_2 electrocatalyst, as discussed in section 1.3.2.2.2.

Dimeric Fe unsubstituted tetraphenylporphyrins, bound by an ortho or meta phenylene bridge (**(160)** and **(161)** respectively, Figure 1.51) were investigated in DMF with 10% H_2O [229]. Following the passage of 41.4 C over 10 hours, **(160)** demonstrated an 88% FE_{CO} with a selectivity over H_2 of 7.3 at -1.35 V vs NHE. Experimental TONs were not specified, however, voltammetric data in the presence of 10% H_2O showed i/i_p values with and without CO_2 present were 200 for **(160)**, 36 for **(161)** and 35 for **(143)**. Chemical reduction to the (simultaneously occurring) $(Fe^{2+})_2$ doubly reduced state followed by introduction of CO_2 showed a change in the Soret band of the porphyrin's UV, a change that was not observed in **(143)**. This suggests the benefit of two close metal centres to interact concurrently with CO_2. Further experiments on this series led to the comparison of 5 more dinuclear iron porphyrins [230], namely **(166)**, **(167)**, **(168)**, **(169)** and **(170)**, with **(160)**, in addition to the relevant mononuclear complexes of **(162)**, **(163)**, **(164)**, **(143)** and **(165)** (Figure 1.51). Perfluorination lowered the overpotential of **(166)** by 300 mV compared to that of the electron donated **(169)** as expected. However, this was at a cost of calculated TOF, as of the series, the most electron donated species had the greater calculated TOF. In DMF with 10% water, **(166)** produced FEs of 92 % and 8% for CO and H_2 respectively when electrolysed at -1.25 V vs NHE with a glassy carbon working electrode. As compared to the mononuclear species, each of the dinuclear complexes demonstrated a considerable increase in catalytic current (by voltammetry) at their respective $Fe^{1+/0}$ processes.

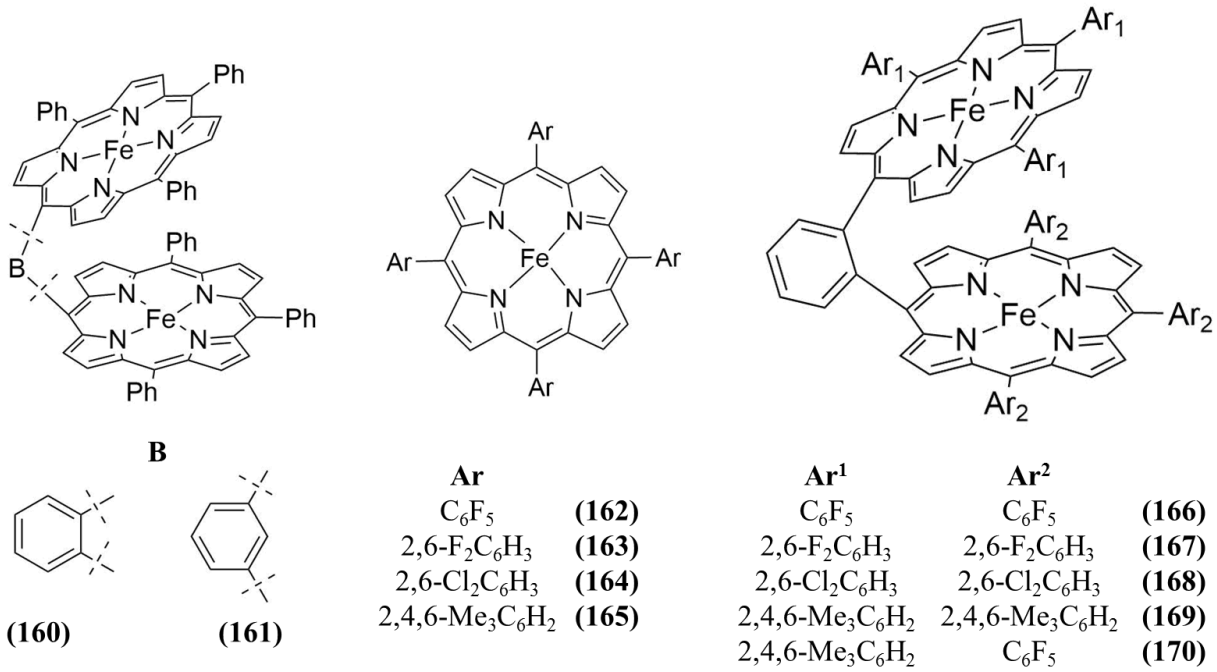

Figure 1.51; Structures of various mono- and dinuclear Fe porphyrins assessed towards electrocatalytic CO_2 reduction

(143) (Figure 1.49) has been studied by Choi *et al*. [231] in DMF with 0.1 M $TBAPF_6$ and 1 M TFE, but with the novel addition of 0.3 M the ionic liquid, 1-butyl-3-methylimidazolium tetrafluoroborate ($BMIMBF_4$). Addition of $BMIMBF_4$ was found to increase the rate of CO generation by 3.4 times that in its absence. FE_{CO} was approximately 90% in both cases.

1.3.2.2.1.4. Nickel cyclams and related complexes containing Cu and Co

Froehlich and Kubiak explored Ni cyclams **(171)**, **(173)** and **(174)** (Figure 1.52) in a 1:4 H_2O/MeCN solution at a glassy carbon electrode [174] in a similar study to Bujno *et al*. [101]. As with the work of Bujno *et al*., Froehlich reaffirmed that alkylation of the nitrogens of the cyclam weakened the effect of CO_2 electrocatalysis. DFT calculations suggested that a heterogeneous trans I conformational isomer of **(171)** was far more active for CO_2 reduction than the trans III isomer possibly due to a stabilisation of the oxygens of CO_2 with amine protons. The benefit of this research was that the behaviour was observed at glassy carbon as well as mercury working electrodes. A further

computational study on **(171)** pointed to the formation of Ni-CO_2 as opposed to Ni-OCO (the latter potentially undertaking a formate-producing route) with concerted proton-electron transfer followed by CO cleavage [232].

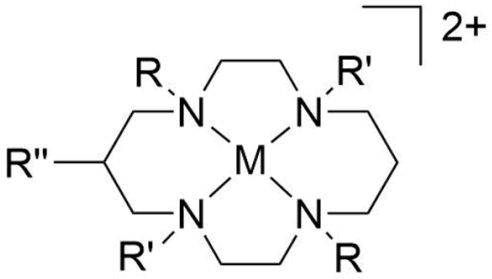

R	R'	R''	M	
H	H	H	Ni	**(171)**
H	H	H	Cu	**(172)**
CH_3	H	H	Ni	**(173)**
CH_3	CH_3	H	Ni	**(174)**
H	H	COOH	Ni	**(175)**

Figure 1.52: Structures of Ni and Cu cyclams within the literature

The truly novel nature of Froehlich and Kubiak's involvement with **(171)** was demonstrated in a following publication regarding the use of the tetramethylated **(174)**, (Figure 1.52) as a scavenger for CO [187], which had previously been found to poison mercury electrodes and deactivate the catalytic **(171)** species. The effect of the H_2O content on the activity of **(171)** was assessed and 4 M H_2O addition to MeCN appeared to be optimal. However, a 1:4 ratio H_2O/MeCN (11.1 M) was used for the follow-on studies. The formation of **(174)**-CO was shown spectroelectrochemically. Therefore, the voltammetry of 1 mM **(171)** in 1:4 H_2O/MeCN was assessed with between 1 mM and 20 mM **(174)**. With 20 mM **(174)** present, a 10-fold i/i_p increase was reported. Electrolyses have not been reported for the system with addition of the scavenger. The enhancement of current with the additions of **(174)** (in a voltammetric region that **(174)** does not demonstrate enhancement) suggests that a rate determining step of catalysis within **(171)** is the release of CO following binding and conversion of CO_2, and that **(174)** sequesters the CO from **(171)**-CO, thereby allowing for a further catalytic cycle of **(171)** to begin.

(171) was further incorporated into Zn- and Cu-containing azurin enzymes through binding to a free histidine site in wild-type (WT) azurin (Az), and forming a double mutant to allow **(171)** to be in a solvent-exposed environment (H83Q/Q107H Az) [233]. Incubation in basic pH allowed the binding of **(171)** and the unbound complex (~40% efficiency) was removed by size exclusion chromatography. Homogeneous

voltammetry at a glassy carbon electrode under CO_2 in a mixed phosphate/KCl buffer (pH 6.1) showed an earlier onset of current within WTCuAz-**(171)** and H83Q/Q107H CuAz-**(171)** than did **(171)** alone. No electrolyses were undertaken, but CO was produced photocatalytically with $[Ru(bpy)_3]^{2+}$ as photosensitiser within both enzymes incorporating **(171)**.

Neri *et al*. demonstrated the use of **(175)** (Figure 1.52) as an electrocatalytic CO_2 reduction catalyst in a 0.1 M $NaClO_4$ aqueous solution [234]. At 0.1 mM concentration with the use of a hanging drop mercury electrode (HDME), approximately the same large catalytic currents were observed for both **(171)** and **(175)**. With the aid of a Hg/Au amalgam working electrode, bulk electrolysis of **(175)** at -1.4 V vs Ag/AgCl produced a 100-fold selectivity of CO to H_2, with both products totalling 88% FE.

The pH became a focus of a further study on this catalyst [235]. **(175)** was electrolysed at -0.99 V vs NHE in pH 2 solution of 0.1 M $NaClO_4$ and good selectivity towards CO generation was maintained (66% and 15% for FE_{CO} and FE_{H2}, selectivity of 4.4). At this potential, the parent complex of **(171)** demonstrated only 13% and 73% FE_{CO} and FE_{H2}. Overall activity was greater also, with 5.2 vs 2 Coulombs passed within the hour equating to TON_{CO}s of 591 and 45 for **(175)** and **(171)** respectively. Increased activity at lower pH was shown to correlate with the protonation of the carboxyl group. An analogous complex with cobalt centre reports that binding of the metal centre to the COO^- group, lending credence to the feasible interaction between the Ni centre and the carboxyl proton [236]. This may also result in distortion of the ligand as it has previously noted that activity of Ni cyclams towards CO_2 reduction are sensitive to geometric orientation [101]. Importantly, when comparing these TONs to other homogeneous systems that in many cases, electrolysis concentrations are ~ 0.5 – 1 mM, but in this study, the catalyst is in 3 μM concentration. For example, assuming the same electrode area and activity, a 1 mM solution would likely require in the region of a two-week-long electrolysis to achieve such numbers. Nevertheless, this system very impressively holds selectivity towards CO_2 reduction in a very acidic and aqueous medium, with consideration that contribution of the bare electrode towards H_2 generation would likely be magnified with lower catalyst concentration.

The voltammetry of **(172)** (Figure 1.52 and cyclam-related complexes **(176)** and **(177)** (Figure 1.53) was briefly assessed under Ar and CO_2 in 50 mM pH 8.25 tris-HCl buffer

[237]. An irreversible oxidation was observed under either Ar or CO_2 at approximately 0.0 V vs Ag/AgCl following a reductive sweep, and was attributed to Cu^0 (liberated from the ligand) oxidation. **(176)** showed less demetallation of the complex (with **(177)** exhibiting very little demetallation) following the reductive scan. However, neither complex was found to show catalytic enhancement to voltammetry. No electrolyses were undertaken.

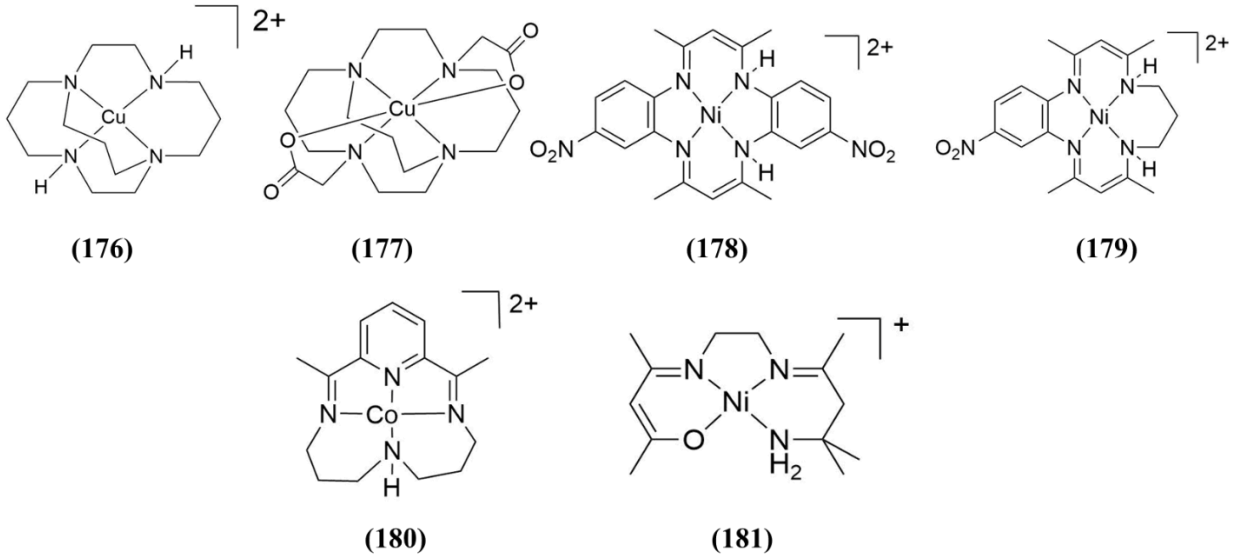

Figure 1.53: Cu, Ni and Co cyclam-related and Ni Schiff base complexes as studied for their CO_2 reducing ability

Khoshro *et al*. explored the concept of symmetry within unsaturated tetradentate cyclam-related ligands containing either two or one nitro group respectively [238]. The Ni-centred complexes **(178)** and **(179)** (Figure 1.53) were shown to have an enhanced current following introduction of CO_2 into the electrochemical cell containing the complexes and 0.1 M electrolyte in dry MeCN, however, no analysis of electrolysis products was undertaken. The symmetrical ligand was stated to be more efficient for CO_2 reduction, with i/i_p of approximately 2-2.5 (at 50 mV s^{-1}). The compounds were shown to electropolymerise on the electrode but no voltammetry in monomer-free solution or heterogeneous electrolyses under CO_2 were undertaken. The complexes may only be loosely comparable as the symmetrical ligand not only contains an additional nitro group but contains an additional aromatic ring which allows for increased

conjugation. A better option for considering the effect of symmetry would be the inclusion of the aromatic ring in both complexes.

Lacy *et al*. assessed the Co cyclam-related **(180)** (Figure 1.53) [239]. An enhancement in reductive voltammetry was observed, upon the addition of CO_2 to a solution of 10 M H_2O in MeCN. This was however, very close in potential to the onset of water reduction by either complex or bare electrode. With electrolysis at -1.88 V vs Fc/Fc^+ for 40 minutes, 45% and 30% FE was achieved for CO and H_2 respectively with a charge of 22 C consumed. This catalyst was assessed for photocatalytic CO_2 reduction activity [240,241]. No TONs were reported, but CO was detected with the use of Ir trisphenylpyridine photosensitiser.

1.3.2.2.1.5. Schiff base complexes of Ni, Cu and Co

The Schiff base complexes, **(182)** and **(183)** (Figure 1.54) were assessed as electrocatalysts for CO_2 reduction [242]. In various solvents, i/i_p values were between 1.5 and 2.1 for **(182)** and 2-3 for **(183)** without the presence of acid. With the presence of 5 mM TFA, a sharp electrocatalytic wave was demonstrated, however, i/i_p was not stated. Gas phase or chromatographic analysis of products were not undertaken but IR spectroscopy showed the presence of bands associated with CO, along with those thought to be resultant of oxalate formation. The group also assessed the Ni Schiff base complex, **(181)** (Figure 1.53) [243]. **(181)** showed some enhancement of voltammetric response (i/i_p of 1.6) at -2.1 V vs Fc/Fc^+. When electrolysed, no CO was detected. However, oxalate was identified by solution IR. In a further study of Cu Schiff bases, **(184)**, **(185)** and **(186)** (Figure 1.54) were shown to demonstrate electrochemical enhancement under CO_2 [244]. However, electrolyses were not undertaken.

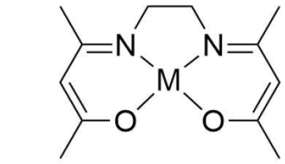

M = Ni = (182)
M = Cu = (183)

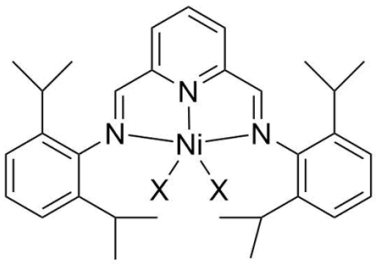

X = Cl = (190)
X = Br = (191)

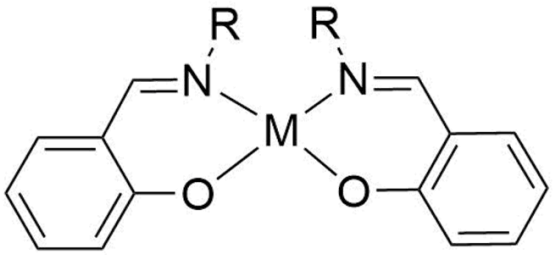

R	M	
(o-methyl)phenyl	Cu	**(184)**
(o-chloro)phenyl	Cu	**(185)**
propylene bridged	Cu	**(186)**
ethylene bridged	Co	**(187)**
o-(4-nitro)phenylene bridged	Cu	**(188)**
o-(4-nitro)phenylene bridged	Ni	**(189)**

Figure 1.54: Schiff base and related complexes studied towards CO_2 reduction

Narayanan *et al*. studied Ni bis(aldimino)pyridine complexes **(190)** and **(191)** (Figure 1.54) in MeCN and in MeCN with 1 M MeOH as proton source [245]. Though enhancement of voltammetry was observed due to the presence of CO_2 and without a proton source present, **(191)** produced H_2 (FE of 89%, TON of approximately 45) upon electrolysis at the third reduction of the complex (-2.28 V vs Fc/Fc^+) with little CO (FE < 3%) over 22 hours. Interestingly, 89% FE_{H2} was also obtained in the presence of 1 M MeOH, but a lower TON_{H2} of < 20 was obtained over 24 hours. The presence of CO_2 was required to achieve H_2 generation, akin to a previously reported manganese complex [246].

1.3.2.2.1.6. Bisterpyridyl complexes

Dicationic bisterpyridyl complexes **(192)**, **(193)**, **(194)**, **(195)**, **(196)** and **(197)** (Figure 1.55) were assessed for their CO_2 reducing capabilities by Elgrishi *et al*. [247] in DMF with 5% water (10% in the case of **(194)**). **(192)** and **(193)** showed higher i/i_p responses towards CO_2 reduction than did **(194)**, **(195)**, **(196)** or **(197)**. **(193)** was observed to produce CO with almost quantitative FE between the potentials of -1.72 and -2.14 V vs Fc/Fc^+, whereas **(192)** generated CO and H_2 in ratios dependent heavily on electrolysis

potential (between -1.93 and -2.23 V vs Fc/Fc^+). Electrolysis at -1.93 V produced a selectivity of CO/H_2 of 20, whereas at -2.23 V, the selectivity of CO/H_2 was far lower at 0.3. Over the course of 3 hours, at potentials corresponding to an optimal FE for CO generation (-1.72 and -1.93 V respectively), **(193)** produced more CO than did **(192)**, with a TON_{CO} not exceeding 2 (assuming 2 mM concentration for electrolyses).

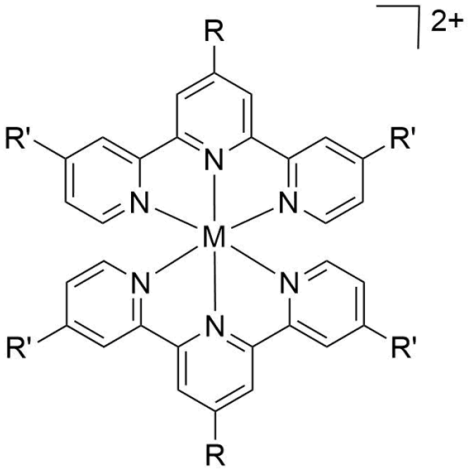

R	R'	M	
H	H	Co	**(192)**
H	H	Ni	**(193)**
H	H	Zn	**(194)**
H	H	Mn	**(195)**
H	H	Fe	**(196)**
H	H	Cu	**(197)**
p-(Cl)C_6H_4	H	Co	**(198)**
p-(CH_3)C_6H_4	H	Co	**(199)**
OCH_3	H	Co	**(200)**
t-bu	t-bu	Co	**(201)**

Figure 1.55: Bisterpyridyl complexes as assessed for electrocatalytic CO_2 reduction

The electrocatalytic properties of four substituted Co^{2+} tpy_2 complexes, namely **(198)**, **(199)**, **(200)** and **(201)** (Figure 1.55), were reported with respect to their modifications. Their selectivities and efficiencies were assessed utilising acetic acid in DMF for H_2 generation and 5% water in DMF for CO generation [248]. The order of activity towards proton reduction was **(201)** > **(200)** > **(192)** > **(199)** > **(198)** which strongly follows a trend of higher activity based on higher degrees of electron donation from the ligand. When voltammetry was undertaken under CO_2 in the presence of 5% water, the same trend was observed, and the authors reasoned that the active catalyst formed was Co^+R-$tpy^{\cdot-}$. Electrolyses were undertaken with a mercury pool electrode (1.5 cm diameter) at a fixed current of 300 μA over the course of 4 hours. Interestingly, FE_{CO} and selectivity of CO/H_2 were in the order of **(198)** > **(199)** > **(192)** > **(200)** (FE_{CO}s of 31, 12, 11 and 4%, and with selectivities of 15.5, 2.4, 0.61 and 0.17 respectively). However, the best performer in these terms was **(201)**, bucking the trend of electron deficiency towards metal centre leading to greater efficiency. FE_{CO} and selectivity in

this case was 37% and 9.25 respectively. In the case of **(201)**, the authors proposed that bulky substituents prevented the formation of inactive dimers.

1.3.2.2.1.7. Other Complexes containing first row transition metals

Chapovetsky *et al*. explored the homogeneous use of three Co 2,2'-tetraaminopyridyl macrocyclic complexes with varied substitution of H, Me or allyl (**(202)**, **(203)** and **(204)** respectively, Figure 1.56) in DMF with bronsted acids present [249]. When **(202)** was electrolysed at -2.8 V vs Fc/Fc^+ in DMF with 1.2 M TFE, 6.2 CO TONs were generated, with a 98% Faradaic efficiency. Despite such a negative potential, preferential CO_2 reduction over H_2 generation is noteworthy. Over 300 times less CO was detected for **(203)** and **(204)** with a FE_{CO} amounting to 23% for **(203)**. Voltammograms within the study suggest that the use of methanol as Bronsted acid would lead to even higher experimental TOFs. This series of complexes accentuate the importance of proximal hydrogens as seen previously in the form of pendant amines for homogeneous electrocatalytic H_2 generation [250] and hydroxyl groups for CO_2 reduction [179]. It is worth noting that this behaviour is complex-dependent [251].

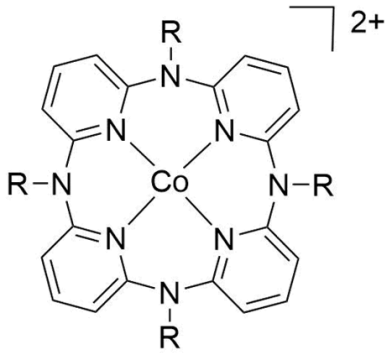

R	
H	**(202)**
Me	**(203)**
Allyl	**(204)**

Figure 1.56: Co tetrapyridyl macrocycles studied towards electrocatalytic CO_2 reduction

Five Co^{2+} complexes, **(205)**, **(206)**, **(207)**, **(208)** and **(209)** (Figure 1.57), were assessed for their electro- and photocatalytic CO_2 reducing capabilities [252]. All five complexes demonstrated catalytic current via voltammetry upon the introduction of CO_2. When electrolysed for 30 minutes at -1.7 V vs SCE in MeCN/0.1 M $TBAPF_6$, **(205)** demonstrated an FE_{CO} of up to 96%. Continuing to 4 and 8 hours, FE_{CO} dropped to 85%

and 69% respectively. Interestingly, when electrolysed under identical conditions for 4 hours, **(205)** generated almost 70 μmol CO, whereas three of the other complexes, **(206)**, **(207)** and **(208)**, generated less than 10 μmol CO. Photocatalysis of **(205)** with Ir trisphenylpyridine as PS (in 50x excess of catalyst) and TEA as sacrificial donor yielded a TON_{CO} of 368, and selectivity of 19:1 over H_2 generation. **(205)** again showed activity towards CO generation, whereas its dimethyl analogue **(206)** did not.

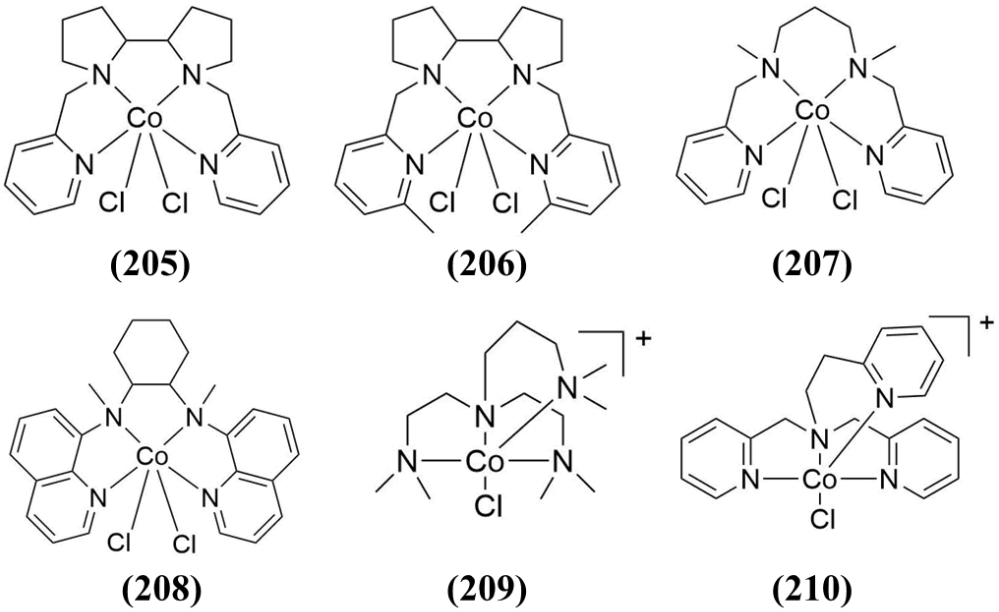

Figure 1.57: Various Co complexes assessed towards electrocatalytic CO_2 reduction

Following its reported use as a photocatalyst [89], He *et al*. demonstrated **(210)** (Figure 1.57) as a homogeneous electrocatalyst in MeCN [253]. As compared to a conventional gold electrode, Si-NW and planar Si allowed for a photovoltage of 580 and 320 mV respectively. When electrolysed (at -1.57 V vs Fc/Fc^+ for Si-NW, not specified for Si) in MeCN/0.1 M $TBAPF_6$ with 1% water, 1 mM **(210)** with Si-NW and planar Si produced FE_{CO} of 69% (4.2 $TON_{CO)}$ and 57% and FE_{H2} of 26% and 22% respectively.

Takeda *et al*. probed the voltammetric response of **(211)** (Figure 1.58) in a 5:1 ratio of DMF to TEOA [92]. Voltammetry was quoted in relation to an $Ag/AgNO_3$ reference electrode. Due to potential instability of this electrode, it is not straightforward to convert potentials versus another reference electrode. However it appears that rapid CO_2 reduction does occur electrochemically but not until close to the solvent reduction

window. The purpose of the study was photocatalysis, and with copper based photosensitisers, TEOA and BIH, the catalyst was observed to generate CO. Other diimine iron complexes (i.e. **(212)** and **(213)**, Figure 1.58) also show promise towards CO_2 binding [254] and may have potential towards electro- and photocatalytic CO_2 reduction.

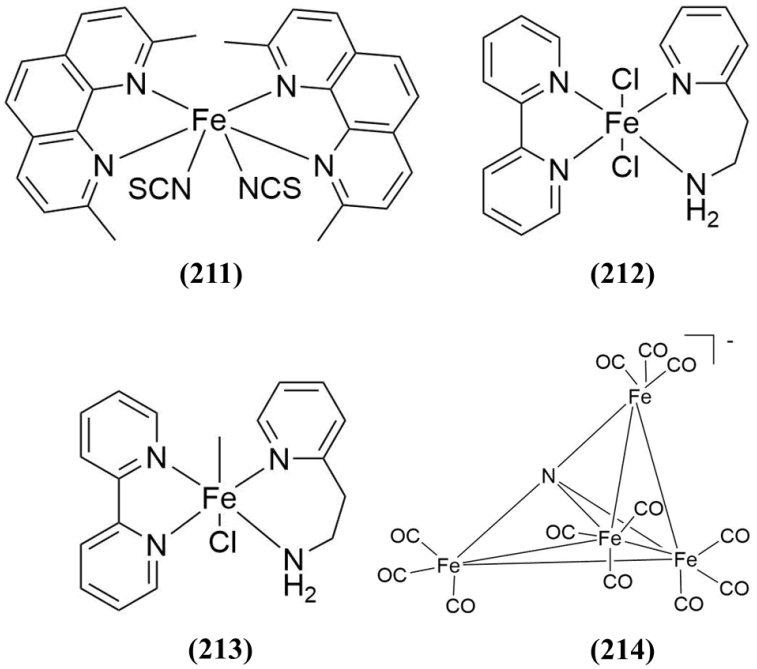

(211) **(212)**

(213) **(214)**

Figure 1.58: Various iron-centred complexes of interest to CO_2 reduction

(215) (Figure 1.59) was stated to undergo electrochemical reaction with CO_2 at -1.8 V vs Fc/Fc^+ to generate CO [255]. Quantitation of products and associated FEs was not assessed. However, a TOF calculation yielded a figure of 96 s^{-1}. This figure is not ground-breaking but the study is important in attempting to improve on infrequently reported zinc complexes for CO_2 reduction.

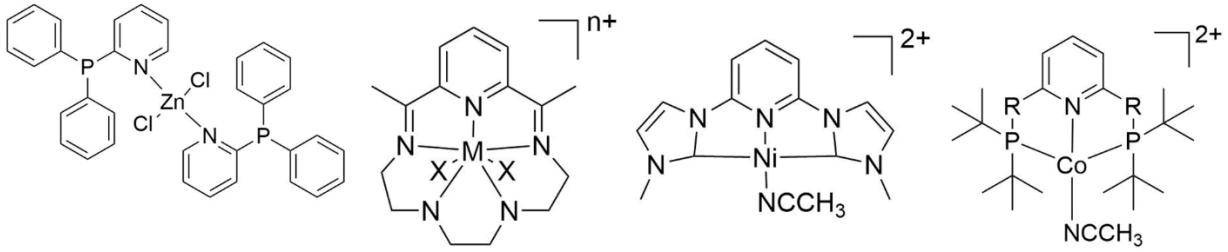

(215) M = Co, X = N/A, n = 2, = **(216)** M = Fe, X = Cl, n = 1, = **(217)** **(218)** R = CH_2 = **(219)** R = NH = **(220)** R = O = **(221)**

Figure 1.59: Various metal complexes assessed towards electrocatalytic CO_2 reduction

Chen *et al*. highlighted the change to product distribution that is possible from a change in metal centre [90]. In their study, **(216)** (Figure 1.59), containing a Co centre produced CO exclusively (FE_{CO} of 82%, 0.4 mA/cm^2) at a glassy carbon electrode, held at -1.5 V vs SCE for 1 hour in DMF with 0.1 M $TBAPF_6$. When **(217)** was assessed, a lower current density of 0.09 mA/cm^2 was obtained over the course of 3 hours at -1.25 V vs SCE, allowing for 75-80% FE_{HCOOH} with no competing H_2 or CO. The introduction of weak acids such as water and phenol were stated to make no difference to behaviour or activity observed. These catalysts were successfully incorporated into a homogeneous photocatalytic system in MeCN with TEA and $Ir(ppy)_3$ as a photosensitiser, whereby the catalysts held the same selectivities as those achieved under electrocatalytic conditions.

Research into heterocyclic carbene complexes has not been confined to that of Mn and Re carbonyl complexes, as demonstrated by Sheng *et al*. [256]. The Ni-centred **(218)** (Figure 1.59) showed two metal-based reductions followed by a CO_2-enhanced ligand based reduction at -1.79V vs Fc/Fc^+ in MeCN with 0.1 M $TBAPF_6$. Over the course of two hours, little charge was passed (~ 0.1 C) at a -1.173 V with 0.4 mM water present, however, CO with no H_2 was stated to have been generated. FE_{CO} was not reported.

Three tridentate PNP-coordinated Co complexes, **(219)**, **(220)** and **(221)** (Figure 1.59), demonstrated CO_2 binding upon their second reductions at the potentials -2.27 to -2.56V vs Fc/Fc^+ in MeCN [257]. [H^+diazabicycloundec-7-ene][BF_4] was utilised as a weak acid in electrolysis, however, no CO_2 reduction products were determined in the headspace.

Dickie *et al*. effectively highlight a point in molecular design that may often not be considered [258]. Hydrogen bonding can occur from the counter ion to amine protons, as opposed to ion pairing that is often stated within complexes. The neutral ligand of bis(diisopropylphosphino)amine was utilised to synthesise the Ni complexes **(222)**, **(223)**, **(224)**, **(225)**, **(226)** and **(227)** (Figure 1.60), sharing similarity to complexes synthesised by Simón-Manso and Kubiak [259]. In the case of the complexes bearing two of the ligands (i.e. **(225)**, **(226)** and **(227)**), the electronic properties were observed to shift, as shown by H^1- and P^{31}- NMR and IR spectra. Crystallographic data showed that the ligand's N atom is bent slightly out of plane of the P atoms, but to varied degrees, depending on X. Voltammetric data under Ar also demonstrates that there is a difference of 90 mV and 80 mV between the $E_{1/2}$ of first and second reductions of **(225)** and **(226)** respectively. Under CO_2, all three complexes demonstrate catalytic enhancement at the second reduction, but **(225)** also demonstrates an enhancement at the first reduction (i/i_p of 6.6). This shows that a seemingly subtle change in anion choice (from a synthetic aspect) can change not only at what potential, but also whether a complex binds CO_2. Furthermore, as the values of redox potentials vary in THF with 0.1 M $TBAPF_6$ (50 times excess of the counterion in the case of **(225)**, **(226)** or **(227)**), the anion avoids exchange with the PF_6 ion.

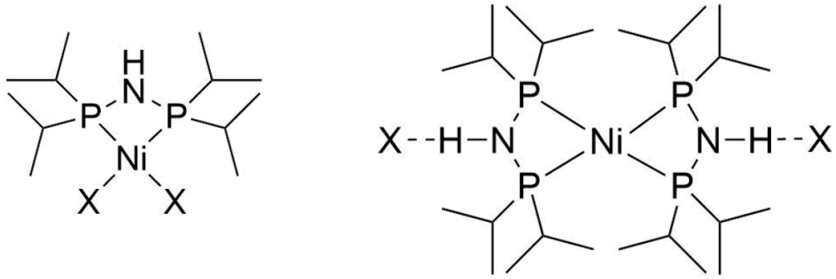

X		X	
Cl	**(222)**	BF_4	**(225)**
Br	**(223)**	NO_3	**(226)**
I	**(224)**	ClO_4	**(227)**

Figure 1.60: Ni complexes assessed towards electrocatalytic CO_2 reduction

An iron carbonyl cluster (**(214)**, Figure 1.58) was found to display excellent efficiency of approximately 95% for formic acid over the course of 50 minute electrolysis at -1.2

V vs SCE in pH 6.5 and 7 aqueous solutions (TOF_{HCOOH} of 44 and 106 hr^{-1} and TON_{HCOOH} of 36 and 88 respectively) [260]. Even at pH 5, an 80% FE_{HCOOH} was retained. Most notable with this catalyst is that the same group previously reported FE_{H2} of 98% and TON_{H2} of 34 at -1.25 V vs SCE in a N_2 purged aqueous solution of pH 5 [261]. In contrast, when under CO_2, a 24 hour electrolysis at -1.2 V vs SCE (pH 7) was shown to continually perform at > 90% FE_{HCOOH}. It is believed that an intermediate, responsible for CO_2 reduction, is that of the reduced hydride. Furthermore, the group reasoned that the driving force for C-H bond formation from CO_2 was less favourable in MeCN than in aqueous solution. A further investigation of substituted complexes showed that the addition of a pendent hydroxyl group (proton shuttle) allows for selectivity to be shifted towards H_2 generation over formate generation [262].

Biscyclopentadienyl (Cp_2) complexes **(228)**, **(229)**, **(230)**, **(231)**, **(232)**, **(233)** and **(234)** (Figure 1.61) were assessed for their ability to reduce CO_2 via cyclic voltammetry in MeCN with 0.1 M $TBAPF_6$ [263]. **(228)**, **(229)**, **(230)** and **(231)** showed voltammetric enhancement under CO_2, with **(228)** demonstrating the greatest enhancement (i/i_p of 3.6 at -2.34 V vs Fc/Fc^+ under Ar compared to -2.7 V vs Fc/Fc^+ under CO_2). **(230)** and **(231)** produced FE_{CO}s of 13% and 8% with similar efficiencies towards hydrogen, while **(228)** produced FEs for CO and H_2 of 10% and 17%.

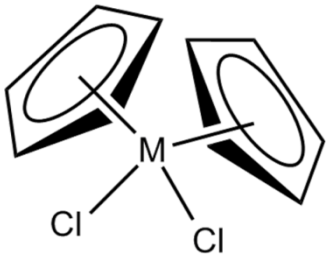

M =	**#**
Nb	**(228)**
Ti	**(229)**
Mo	**(230)**
W	**(231)**
Zr	**(232)**
Hf	**(233)**
V	**(234)**

Figure 1.61: Cyclopentadienyl complexes assessed towards electrocatalytic CO_2 reduction

1.3.2.2.2. Heterogeneous electrocatalysts towards CO_2 reduction

1.3.2.2.2.1. Manganese diimine complexes

As discussed in section 1.3.2.2.1.1, Torralba-Peñalver *et al*. undertook a feasibility assessment of silicon nanowires as a photoelectrode material with **(89)** and **(92)** (homogeneous) towards CO_2 reduction [213]. Within this study, the group also synthesised **(98)** (Figure 1.40), which they electropolymerised onto Si-NW. The system demonstrated a catalytic enhancement of voltammetry upon the addition of CO_2 and water in a monomer-free MeCN/5% H_2O solution. Electrolysis experiments of the heterogeneous film were not undertaken within the report.

In a different manganese diimine heterogenisation approach, phosphonic acid anchoring groups were introduced on the 4,4'- positions of bipyridine to immobilise **(97)** (Figure 1.40) onto a TiO_2 electrode [264]. This heterogenisation approach was previously used by the group with the Re-centred homologue [77]. After 2 hours of electrolysis at -1.7 V vs Fc/Fc^+ in MeCN/5% H_2O, a resultant FE_{CO} of 67% (equating to 112 TON_{CO}) and FE_{H2} of 12.4% was obtained. A fall of selectivity of CO over H_2 (12 to 5.4) from hours 1 to 2 is as noted, indicative of catalyst decomposition. Electrolyses were repeated with illumination at $\lambda > 420$ nm light (avoiding excitation of the TiO_2 bandgap). FEs over 2 hours for CO and H_2 drastically changed to 12% and 59% respectively (selectivity of CO/H_2 of 0.2), suggesting degradation of the catalyst. A photoanode of Cd-sensitised ZnO (with TEOA as electron donor) was implemented, with the cathodic compartment shielded from light, which somewhat circumvented the issue of preferential H_2 evolution. This approach led to an FE_{CO} of 26% (FE_{H2} of 10%), TON_{CO} of 11 and selectivity over H_2 of 2.6 with an applied potential of 0.6 V following 1 hour of electrolysis. The decrease in activity compared to the three-electrode electrocatalytic system was acknowledged.

Further heterogeneous studies were carried out using Nafion and multi-walled carbon nanotubes (MWCNTs) by dropcasting suspensions, also containing **(89)**, onto glassy carbon electrodes [164]. In pH 7 phosphate buffered aqueous solutions, the highest TON_{CO} of 471 (selectivity of 2 over H_2) and FE_{CO} of 51% were obtained at -1.5 V vs Ag/AgCl without CNTs present. More negative than this led to the generation of H_2

from the bare electrode. With CNTs also present, higher charges were registered at -1.4 V. Following 4 hours of electrolysis, 0.74 C was passed (TON_{CO} of 101 with 22% FE and selectivity of 0.5) whereas 0.064 C was passed in the absence, equating to FE_{CO} of 22, selectivity of 1 and TON_{CO} of 209. More than 20 times the amount of catalyst was dropcast with CNTs than without CNTs. It is probable that the increased surface area of CNTs allowed for more active catalytic monolayers and avoiding stacking and potential insulation of electrodes.

In a complementary study, **(94)**, **(95)** and **(96)** (Figure 1.40) were assessed [265]. Electrolysis using **(96)** immobilised using nafion and CNTs exclusively produced hydrogen in neutral 0.1 M phosphate buffer, supporting homogeneous voltammetry in MeCN with 5% water which showed little enhancement under CO_2 compared to that under Ar. Though the homogeneous **(95)** demonstrated some enhancement to voltammetry at negative potential (~ -2.4 V vs SCE, in MeCN with 5% water), and little enhancement to voltammetry as a surface confined species, it produced almost no CO at -1.4 V in pH 7 phosphate buffer. Results between **(89)** and **(94)** were not straight-forward to analyse as **(94)** required repurging with CO_2 every hour to regain higher current levels. At -1.5 V, though **(89)** achieved a higher average current density over the 4 hours, **(94)** produced 46.1 TON_{CO} (vs 35.9 for **(89)**) with higher FE_{CO} and selectivity for CO. At -1.4 V, a selectivity of 1 was achieved using **(94)** with the cost of 13 times less current density.

In homogeneous solutions, **(94)** has been stated to be 300 times more active than **(89)** homogeneously with 1.4 M TFE, however due to possessing electron donating groups, this occurs at approximately 200 mV more negative to that of **(89)** [196]. When operating close to the potential at which a bare electrode (and likely CNT) produces hydrogen, the effect of trade-off between activity of CO generation and the applied potential within catalysts becomes far more apparent in terms of controlling selective CO_2 reduction over proton reduction.

1.3.2.2.2.2. Iron, cobalt and copper porphyrins and related macrocycles

Following its use within homogeneous electrocatalytic CO_2 reduction studies [228], **(150)** (Figure 1.49) was incorporated into a Nafion/carbon paste layer and spray deposited onto carbon paper [266]. At -0.86 V vs SHE in a 0.1 M KCl/0.5 M $KHCO_3$ aqueous solution, the cathodic compartment demonstrated 90% Faradaic efficiency for conversion to CO and a selectivity of 9 over H_2 generation. In a test of stability at longer timescales, the cell was electrolysed for 30 hours at -0.96 V vs SHE. Selectivity and continuous charge were retained over the timescale, contrary to the inclusion of **(143)** in place of **(150)**.

Blakemore *et al*. investigated π-stacking between carbon black/pyrolytic graphite and a rhenium bipyridine appended with a pyrene unit for CO_2 reduction in MeCN [267]. The use of pyrene appended to an Ir-pincer complex was also investigated for CO_2 reduction in aqueous solutions [268]. Non-covalent immobilisation was further pursued by Maurin and Robert [269] using **(156)** (Figure 1.50) and MWCNT. Surface confined electrochemistry was demonstrated for the $Fe^{3+/2+}$ process in aqueous solution, with the current of forward and reverse scans proportional to the scan rate. In pH 7.3 (0.5 M $NaHCO_3$) at -1.03 V vs NHE, a TON_{CO} of 432 was obtained over the course of three hours with a 24-fold selectivity over H_2, accounting for 97% total FE. Over 12 hours, a TON_{CO} of 813 was obtained, however selectivity dropped to 5.7, as the rate of catalysis halved. With the fall in selectivity, stability at longer timescale does not appear to be present, although degradation is not as rapid as an alternative approach to heterogeneous CO_2 reduction containing an iron porphyrin, namely electropolymerisation of **(153)** (Figure 1.49) [270]. Maurin and Robert later reported binding the mono-carboxylated **(157)** (Figure 1.50) to the surface of aminophenyl-functionalised MWCNT [271]. Electrolyses at -1.06 V vs SHE in pH 7.3 aqueous solutions of 0.5 M $NaHCO_3$, CO was produced with FE_{CO} of 95% (following 1 hour), with a maximum TON_{CO} of 750 obtained (TOF_{CO} of 178 hr^{-1} over 3 hours). Through isotopic labelling, CO_2 was confirmed to be the source of CO. Furthermore, the mono-carboxylated **(158)** (Figure 1.50) was also assessed and showed lower activity and efficiency (generating almost half of the CO as **(157)** with FE_{CO} of 77 and 51 % after 1 and 3 hours respectively). Over 2.5 μmol of H_2 (compared to 8.5 and 4.5 μmol CO for **(157)** and **(158)** respectively after 3 hours) was generated in under 1 hour of electrolysis without catalyst

present. Therefore, the lower surface coverage obtained for **(158)** (2×10^{-9} mol cm^{-2}) as compared to **(157)** (6.4×10^{-9} mol cm^{-2}) could account for both the loss of efficiency to sites where catalyst wasn't present and to the lower activity.

A further heterogeneous approach using Fe porphyrins and inclusion within aqueous electrolytes was employed by Hod *et al*. [272]. **(151)** (Figure 1.49) was incorporated into a ZrO/ZrOH MOF (MOF-525, i.e. $Zr_6O_4(OH)_4(TCPP\text{-}H_2)_3$, TCPP = tetracarboxyphenylporphyrin [273]) on an FTO electrode through the use of electrophoretic deposition. Following a 4 hour electrolysis at -1.3 V vs NHE in MeCN (1 M $TBAPF_6$) without the addition of trifluoroethanol (TFE), FEs for CO and H_2 were 54% and 45%, and TON_{CO} was stated to be 272. The source of protons was likely from residual water in the solvent. Upon the addition of 1 M TFE, 3.2 hours of electrolysis yielded FEs of 41% and 60% of CO and H_2 respectively, with TON_{CO} amounting to 1520. There was a 5.6-fold increase in the amount of CO generated, however, at the cost of selectivity. A 1 mM homogeneous solution of **(143)** was electrolysed at FTO in DMF with 1 M TFE for comparison, whereby over 50 TON_{CO} and approximately 85-90% FE_{CO} and ~10% FE_{H2} was achieved. TONs are not a fair comparison (due to a larger concentration of catalyst within the bulk solution), however, the heterogeneous system suffered in terms of selectivity.

Quezada *et al*. combined the use of electropolymerisation of **(154)** (Figure 1.49) to an indium tin oxide (ITO) semiconductor and a dry ionic liquid medium of $BMIMBF_4$ [274]. Electropolymerised **(154)** was observed to retain catalytic activity as observed in comparison of voltammetry in N_2 and CO_2. At -0.8 V vs Ag/AgCl, a 4 hour electrolysis produced CO with an efficiency of 65%. The TON_{CO} was estimated to be 69 with no H_2 detected, before catalyst deactivation. This approach was also extended to Zn and Fe and **(155)** (Figure 1.49) was additionally found to retain some activity towards electrocatalytic CO_2 reduction (TON_{CO} ~9) [275].

The heterogeneous reduction of CO_2 by **(235)** (Figure 1.62) physisorbed onto graphite was reported by Shen *et al*. in varied pH (1-3) $HClO_4$ and $NaClO_4$ 0.1 M electrolytes [70]. At pH 3 (and a pressure of 10 atm of CO_2), ~60% efficiency was achieved for CO generation at -0.6 V vs RHE. At -0.8 V, this became ~50%, but with approximately 2.5% FE_{CH4}. H_2 was stated to account for the remaining efficiency. With further negative potentials of -0.8 V, H_2 is expected to dominate product distribution. Charges

passed or TONs generated in experiments were not specified. However current densities of 0.3 mA cm^{-2} were achieved, in line with that achieved by Costentin *et al*. pertaining to **(145)** in DMF with 10% water [179]. Despite the increase in pressure, selectivity of CO_2 over water reduction in very acidic solutions remains an issue for molecular electrocatalysts. A density functional theory study was undertaken following this, and concluded that the Co^{1+} metal oxidation state gives rise to binding of the carbon of CO_2, leading to CO and CH_4 as major and minor products respectively [276]. Formate was also concluded as a likely minor product, which was thought to proceed through the binding of an oxygen of CO_2 to the metal centre.

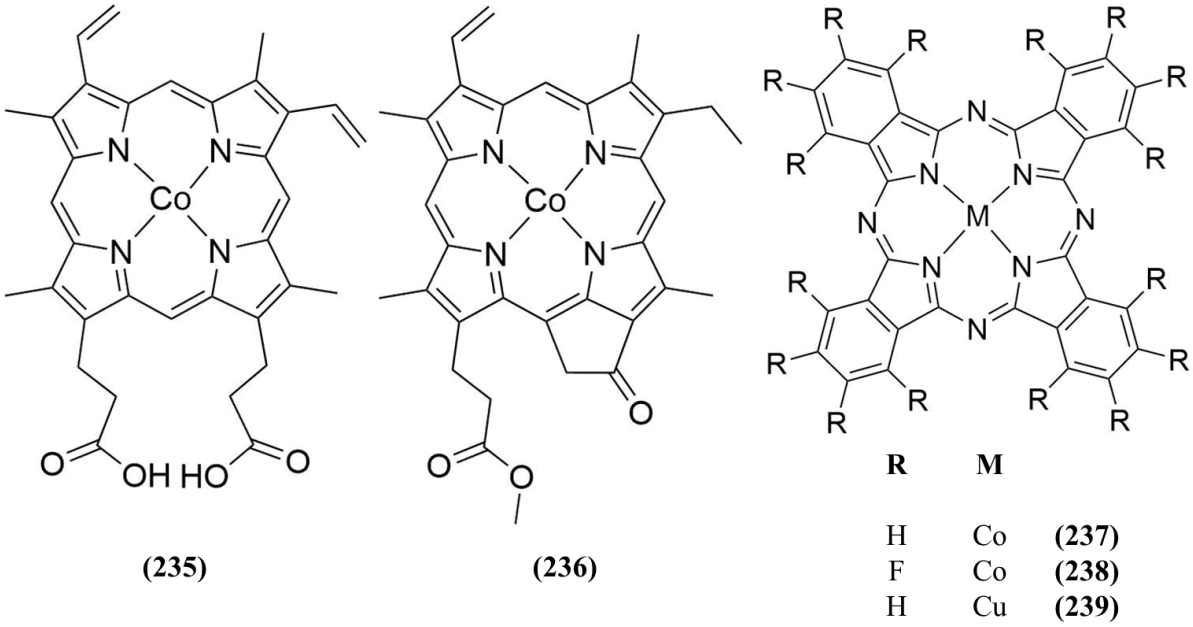

(235) **(236)**

Figure 1.62: Various Co and Cu macrocycles as assessed towards heterogeneous electrocatalytic CO_2 reduction

A metal organic framework (MOF) was created from aluminium oxide rods and **(152)** (Figure 1.49) and deposited onto glassy carbon via atomic layer deposition and microwave reaction [277]. Following electrolyses in aqueous bicarbonate electrolyte, optimal results for Faradaic efficiency of 76% CO and 25% H_2 were obtained at -0.75 V vs RHE. A TON_{CO} of 1400 was achieved over 7 hours of electrolysis. MOFs containing Co porphyrin units were also utilised in the photocatalytic reduction of CO_2 [278].

Lin *et al*. synthesised covalent organic frameworks (COF) by condensation of **(154)** and also mixtures of **(154)**/Cu tetraaminotetraphenylporphyrin in mole ratios of 1/9 and 1/99 with 4-formylbenzaldehyde or biphenyldicarboxaldehyde, creating COF 1-Co, COF 2-Co, COF 2-1/9 and COF 2-1/99 respectively) followed by deposition onto carbon fabric [279]. For the film containing only Co metal centres, 4% of the metal centres of COF 1-Co were estimated as active through the $Co^{2+/1+}$ electrochemical reduction. At -0.67 V vs RHE in a pH 7.3 bicarbonate buffer, COF 1-Co and COF 2-Co produced CO and H_2 with FE_{CO}s of 89 and 90% and FE_{H2}s of 14 and 20% respectively within the first 4 hours. After 24 hours, COF 1-Co retained efficiency, where as COF 2-Co's selectivity fell somewhat to 83 and 23% for CO and H_2 respectively, though COF 2-Co generated almost 3 times as much CO as COF 1-Co with approximately 10% more Co centres. When decreasing the Co/Cu ratio within COF 2, TOF_{CO} per cobalt centre was observed to increase, at the expense of FE_{CO}, whereby COF 2-Co, COF 2-1/9 and COF 2-1/99 generated TOF_{CO} of 165, 360 and 764 hr^{-1} per cobalt centre with FE_{CO} falling from 91% to 67% and then to 48% respectively. A range of control electrolysis experiments, including with COF 1-Cu, COF 1-H_2, Co_3O_4 and **(154)** produced significantly less CO. To accompany the examples of Co porphyrins as applied heterogeneous electrocatalysts, it may also be of note that Co porphyrin nanotubes have been studied theoretically for the electrocatalytic reduction of CO_2 [280].

In a further assessment of Cu porphyrins, and the approach of local proton sources, Weng *et al.* incorporated **(147)** and **(148)** (Figure 1.49) with carbon nanoparticles onto carbon paper [281]. In a 0.5 M $KHCO_3$ electrolyte, a very high current density of 49 mA cm^{-2} was recorded at -0.976 V vs RHE. Following an hour of electrolysis, CO, methane, ethylene (C_2H_4), formic acid and H_2 were detected with FE_{CO} of 10%, FE_{CH4} of 27%, FE_{C2H4} of 13% and FE_{HCOOH} of 5% and the remainder of Faradaic efficiency within the experiments stated to be H_2. This equated to TOF_{CH4} and TOF_{C2H4} of 4.3 s^{-1} and 1.8 s^{-1} respectively. The proximal hydrogens due to the o,o'-hydroxy groups of **(147)** appear to have a crucial role in catalysis, with **(148)** demonstrating an average current density of approximately 2.5 mA cm^{-2}, with < 30% FE towards CO_2 reduction products (FE_{CO} of approximately 20%). This report is very interesting from the aspects of very high current density towards CO_2 reduction products, generation of methane and ethylene, and heterogeneous CO_2 reduction in an aqueous environment.

(236) (Figure 1.62) in conjunction with MWCNT was recently dropcast onto a glassy carbon electrode with a Nafion proton-exchange membrane [182]. A TON_{CO} of 1100 and TOF_{CO} of 140 hr^{-1} was generated with a Faradaic efficiency of 89% at -1.1 V vs NHE (in a pH 4.6, 5 mM aqueous solution of Na_2SO_4). It was suggested that the remaining 11% efficiency was lost to H_2 generation (with formation of trace formic acid). The average of experiments conducted at pH 4.6 (-1.1 V vs NHE) resulted in a CO/H_2 selectivity of 4.3. The combination of **(236)** with MWCNT was later used for photocatalytic CO_2 reduction [282] in the presence of water to generate CO and H_2.

Following on from studies of Co phthalocyanine and modified phthalocyanines [184,283], Morlanés *et al*. reported the concurrent heterogeneous reduction of CO_2 and oxidation of water by **(238)**, (Figure 1.62) in a two-compartment electrolysis cell [284]. At -0.8 V vs RHE in a 0.5 M $NaHCO_3$ solution, the dip-coated carbon cloth electrode generated a Faradaic efficiency of up to 93% with 4-5% contribution from H_2. Current densities with **(237)** in the same system were lower and led to 45-63% FE_{H2}. It is likely that the electron withdrawing effect of the fluorine groups allows for a more easily reducible $Co^{2+/1+}$ state. Stability within the system (over 10 hours) was also ascribed by the researchers to a reduced affinity of the cobalt centre to CO (via the inductive effect of the fluorine groups), to which they believe poisons the catalyst, such as is the case with Ni cyclams (Figure 1.52) [187]. Furthermore, addition of Na_2EDTA did not influence activity, suggesting that cobalt ions and cobalt oxide did not play a role in catalysis.

(237) (Figure 1.62) has previously been studied heterogeneously with the use of poly-4-vinylpyridine (P4VP) [285,286]. Kramer and McCrory further probed as to why the polymer interacted favourably with the complex [287]. Solutions containing **(237)**, **(237)** with pyridine (py), **(237)** with P4VP or P2VP and **(237)** with P2VP were dropcast onto edge-plane graphite electrodes and the results of electrolyses at -1.25 V vs SCE in pH 4.7 aqueous buffer reaffirmed the enhancement for CO generation as a result of axial coordination from the pyridine. The order of activity relating to TON_{CO} was **(237)**-P4VP ≈ **(237)**(py)-P2VP > **(237)**(py) > **(237)**-P2VP ≈ **(237)** with **(237)**-P4VP and **(237)**(py)-P2VP generating 34,000 and 30,000 TONs respectively (also the highest FE_{CO}s of 89 and 83%) over the course of two hour electrolyses. It was postulated with **(237)**-P4VP and to a lesser extent **(237)**(Py)-P2VP, that a protonated pyridine within PVP stabilised the CO_2-bound intermediate trans to the axial binding pyridine, i.e. an

effect of the primary and outer coordination sphere interaction. **(237)** was also studied on vapour-grown carbon fiber by Yamanaka *et al*., achieving a maximum FE_{CO} of 70% (TOF_{CO} of 1100 hr^{-1}) with 14 mA cm^{-2} at 0 ^0C and -0.9 V vs Ag/AgCl in a nafion separated polymer electrolyte membrane cell [288].

(239) (Figure 1.62) was dip coated onto carbon cloth and incorporated as a gas diffusion electrode in the cathode of a modified polymer electrolyser [289]. CO_2 (5 bar pressure) was passed through the cathodic compartment which contained aqueous electrolyte to maintain electrical contact between the working and reference electrodes. CO_2 reduction products were observed at potentials of between -1.6 and -1.75 V vs Ag/AgCl (Sat'd KCl). When -1.75 V was applied to the cathode for 6 hours, methane, ethylene and formate were detected with FE_{CH4}, FE_{C2H4} and FE_{HCOOH} of 7.7%, 0.7% and 3% respectively. Hydrogen was however, the main product detected with FE_{H2} of 88.6%. CO was not detected.

1.3.2.2.2.3. Nickel cyclams and related complexes containing Cu and Co

Neri *et al*. demonstrated **(175)** (Figure 1.52) as a homogeneous electrocatalyst towards CO_2 reduction [234]. Using the added carboxyl group, the complex was further anchored to nanocrystalline TiO_2. Although an increase in cathodic current was observed upon the introduction of CO_2, accompanied by an anodic shift in the $Ni^{2+/1+}$ compared to that at a mercury surface, stability was observed as an issue. Murase *et al*. explored the substitution of the Cl^- counterions in **(171)**Cl_2 with the hydrophobic tetraphenylborate ($[BPh_4]^-$) [290]. When dropcast onto Sn, **(171)**$(BPh_4)_2$ produced CO in a stable manner for 20 minutes with stirred electrolysis at -1.4 V vs Ag/AgCl in pH 10 0.1 M KCl buffer. Approximately 25 TON_{CO} was reached before the catalyst was removed from the surface and/or began to deactivate. FE_{CO} and FE_{H2} amounted to 60% and 35% respectively following 30 minute electrolyses. A direct comparison to **(171)**Cl_2 was not shown but **(171)**Cl_2 is known to dissolve in water. Furthermore, the Sn surface was stated to show a greater surface confined response in conjunction with **(171)**$(BPh_4)_2$ than did glassy carbon.

(172) (Figure 1.52) was deposited onto FTO through voltammetric cycling in aqueous solutions or with potentiostatic conditions in 3% H_2O in DMF under a CO_2 atmosphere

[291]. X-ray absorption spectra showed the presence of ligand within the film. The catalytic onset in CO_2 reduction potential appears at approximately 100 mV more positive to that of FTO alone. Formic acid was resultant in 88% efficiency with the remainder accounted for by hydrogen. Values from experiments displaying electrolysis with FTO alone were not specified, but were stated to be lower than with the deposited material.

Due to their demonstration as electrocatalysts [239], cobalt cyclams also hold interest as CO_2 photoelectrocatalysts. With this in mind, Jin *et al*. covalently attached Co(cyclam) to mesoporous silica by bonding an alkylsilanol group to either a binding nitrogen of the cyclam or directly to the cobalt centre [292]. Similar to earlier studies with **(171)** for electrocatalytic CO_2 reduction [101,174], attachment to the nitrogen resulted in a detrimental effect to activity, whereas photocatalytic activity was retained with alkyl bonding to the cobalt centre. Co(cyclam) was also bound via Ti – O – Co bonds to P25, Anatase and Rutile TiO_2 by microwave reaction in the presence of triethylamine, resulting in Co(cyclam)/P25, Co(cyclam)/Anatase, and Co(cyclam)/Rutile [293]. The TiO_2-bound complexes were assessed photocatalytically and produced CO and H_2 in approximately a 1:1 ratio (UV irradiation, 25:3 MeCN/TEOA).

1.3.2.2.2.4. Cu, Ni and Co Schiff base complexes

Copper and nickel nitrosalophens (**(188)** and **(189)** respectively, Figure 1.54) were reported by Singh *et al*. [294] in the electrocatalytic conversion of CO_2 with H_2O, yielding CO and H_2 and smaller amounts of methane and ethane. At -1.5 V vs SHE, **(189)**, deposited on a gas diffusion electrode with Nafion, produced FEs of 40% CO, 20% H_2 and 17% for each of methane and ethane in an aqueous solution of 0.5 M $KHCO_3$ (pH 7.5). TON/TOFs or moles of products were not referred to, therefore, it is unclear as to just how effective these catalysts are.

(187) (Figure 1.54) was first reported for the homogeneous electrocatalytic reduction of CO_2 to CO by Pearce and Pletcher [295]. Recently, Fu *et al*. dispersed this catalyst through carbon black and deposited the mixture with Nafion onto carbon paper [296]. At -0.9 V vs SHE in a 0.5 M $KHCO_3$ aqueous solution, a FE_{HCOOH} of 27% was achieved over the course of an hour, with substantially larger current registered under CO_2 than

under Ar. As more negative potentials were utilised, FE_{HCOOH} suffered and bubbles, likely due to H_2 generation, were noted. The largest amount of formate was generated at -1.1 V, with approximately 0.47 mM formate present within the electrolyte.

1.3.2.2.2.5. Tetraruthenated pyridyl porphyrins

(240), **(241)** and **(242)** (Figure 1.63), based on a tetrapyridylporphyrin bound to four units of [Ru(bpy$_2$)Cl] (with a polyoxotungstate anion) were assessed for electro- and photoelectrochemical reduction of CO_2 in a 0.1 M $NaClO_4$ aqueous solution on the surface of indium tin oxide [297]. The method of deposition was layer-by-layer, wherein the electrode was dip-coated in a solution of complex, rinsed and dried, and following this, dipped in a solution of POM, rinsed, dried and the process repeated twice more. Following 6 hour electrolyses at -0.8V vs Ag/AgCl without irradiation, formic acid and methanol were detected (10,600 and 500 TONs respectively) with **(240)**. FEs were not reported, however, no H_2 was detected.

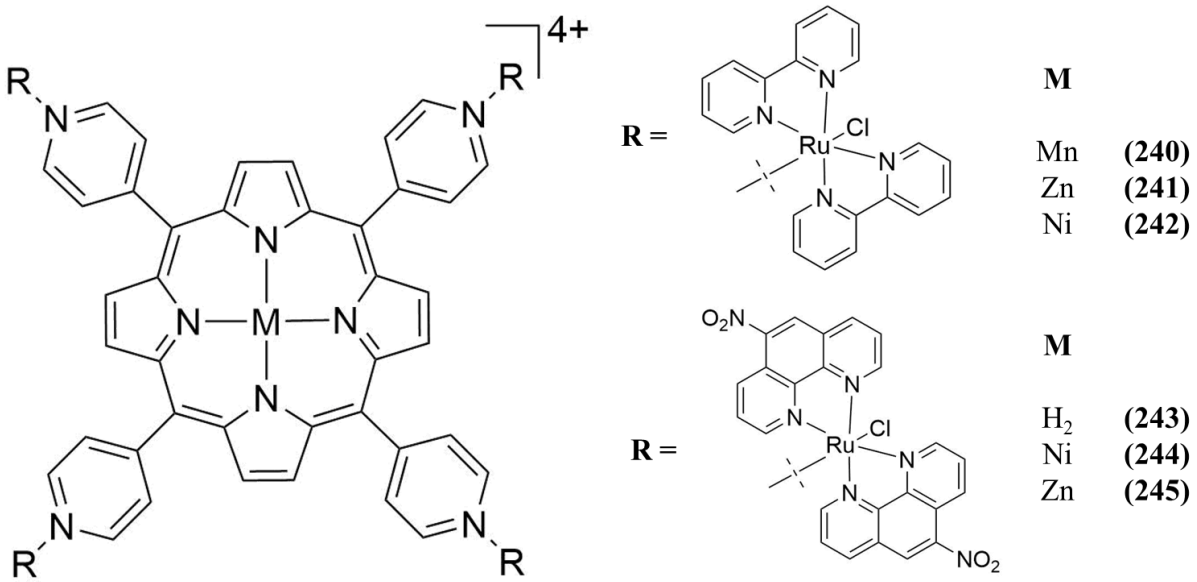

Figure 1.63: Tetraruthenated porphyrin complexes assessed for their electrocatalytic CO_2 reduction ability

A similar approach was utilised by Dreyse *et al*. [298]. **(243)**, **(244)** and **(245)** (Figure 1.63) were electropolymerisable onto glassy carbon, producing a heterogeneous film.

Each of the complexes was investigated at -0.8 V vs Ag/AgCl in 0.1 M $NaClO_4$ solutions. TOFs for MeOH with **(245)** and **(244)** were found to be 15 and 4.5 s^{-1} equating to 56 and 55% FE. Less than substantial amounts of H_2, formate and formaldehyde were also detected over the experiments including that with bare electrode. However, in each case, the polymer film appreciably surpassed the bare electrode.

1.3.2.2.2.6: Surface-bound chelating ligand

Phenylterpyridine has more recently been covalently bound to an electrode surface through voltammetric cycling of glassy carbon in a solution of the diazo-substituted ligand [299]. Metallation and demetallation of this electrode-bound ligand appears to be at will with chelation of the metal centre by EDTA in aqueous solution. Preliminary results for H_2 generation were positive with Co metallation. Optimisation of the system is however still required in the interest of CO_2 reduction to CO.

1.3.3. Cobalt based metal complexes towards H_2 generation in organic media

Substitution of rare metals and metal-centred complexes for first row transition metal complexes as catalysts for H_2 production from protons has become a very active area of research, owing to the scarcity [300] and expense of the highly active metals such as platinum [301,302]. From the 1960s [303,304], cobalt complexes have been utilised towards electrocatalytic proton reduction. Particularly from the 2000s [305], they have gathered interest within the areas of photocatalytic and electrocatalytic H_2 generation [52,301,305–310]. This section focuses on cobalt complexes as assessed for electrocatalytic proton reduction in organic solvents, with the aim of complementing the research undertaken in chapter four. A range of organic and inorganic acids have been used as proton sources (including acetic [311], trifluoroacetic [312], chloroacetic [313], tosic [314], triflic [315], benzoic [316], tetrafluoroboric [317] and perchloric acid [318], unsubstituted [319] and methoxy- [320], bromo, cyano, and dichloro-substituted anilinium [321] and triethyl- [322] and ammonium salts [323] in addition to water

[324]). Futher to this, the introduction to chapter four provides a brief overview of Co-based heterogeneous catalysts of a non-molecular nature towards water splitting.

The Co complexes reported in the literature are grouped in terms of heteromacrocycles, such as porphyrins, corroles, phthalocyanines, cobaloximes, diimine-dioximes and BF_2 analogues, polypyridyl complexes, phosphines and cyclopentadienyl complexes, dithiolates and other Co containing complexes.

1.3.3.1. Co-centred heteromacrocycles

An early report of molecular electrocatalytic H_2 evolution by a cobalt centred complex focussed on the reduction of CO_2 to CO in either water or water/MeCN 2:1 v/v (0.1 M KNO_3) [324]. When electrolysed at -1.6 V vs SCE at a mercury electrode under a CO_2 atmosphere, **(246)** (Figure 1.64) produced CO and H_2 in a 1:1 ratio with FE_{H2} of 46.5% and TOF_{H2} of 1.95 hr^{-1}. When electrolysed at -1.5 V, **(247)** generated 45% FE_{H2} with TOF_{H2} of 2.25. At a longer electrolysis time (19 hrs), **(247)** generated TON_{H2} of 52 with 75% FE_{H2} (and 21% FE_{CO}). In the absence of CO_2, **(247)** operated with an approximate FE_{H2} of 80%.

Hu *et al*. later explored the use of **(248)**, **(249)**, **(250)** and **(251)** (Figure 1.64) at vitreous carbon in MeCN [320]. With the addition of approximately 21 mM tosic acid monohydrate, a 30 minute electrolysis of **(248)** and **(249)** produced FEs of 100% and 90% respectively at -0.58 V vs SCE. Approximately 5 TON_{H2} were generated without any observed degradation of catalyst. Substitution of two methyl groups with phenyl groups (i.e. **(250)** and **(251)**) served to shift the $Co^{2+/1+}$ reduction to more positive potentials. However, electrolyses at -0.48 V vs SCE generated poorer Faradaic efficiencies of 20-25 % with tetrafluoroboric acid monodiethylether. Appreciable deactivation was noted beyond 2 turnover numbers.

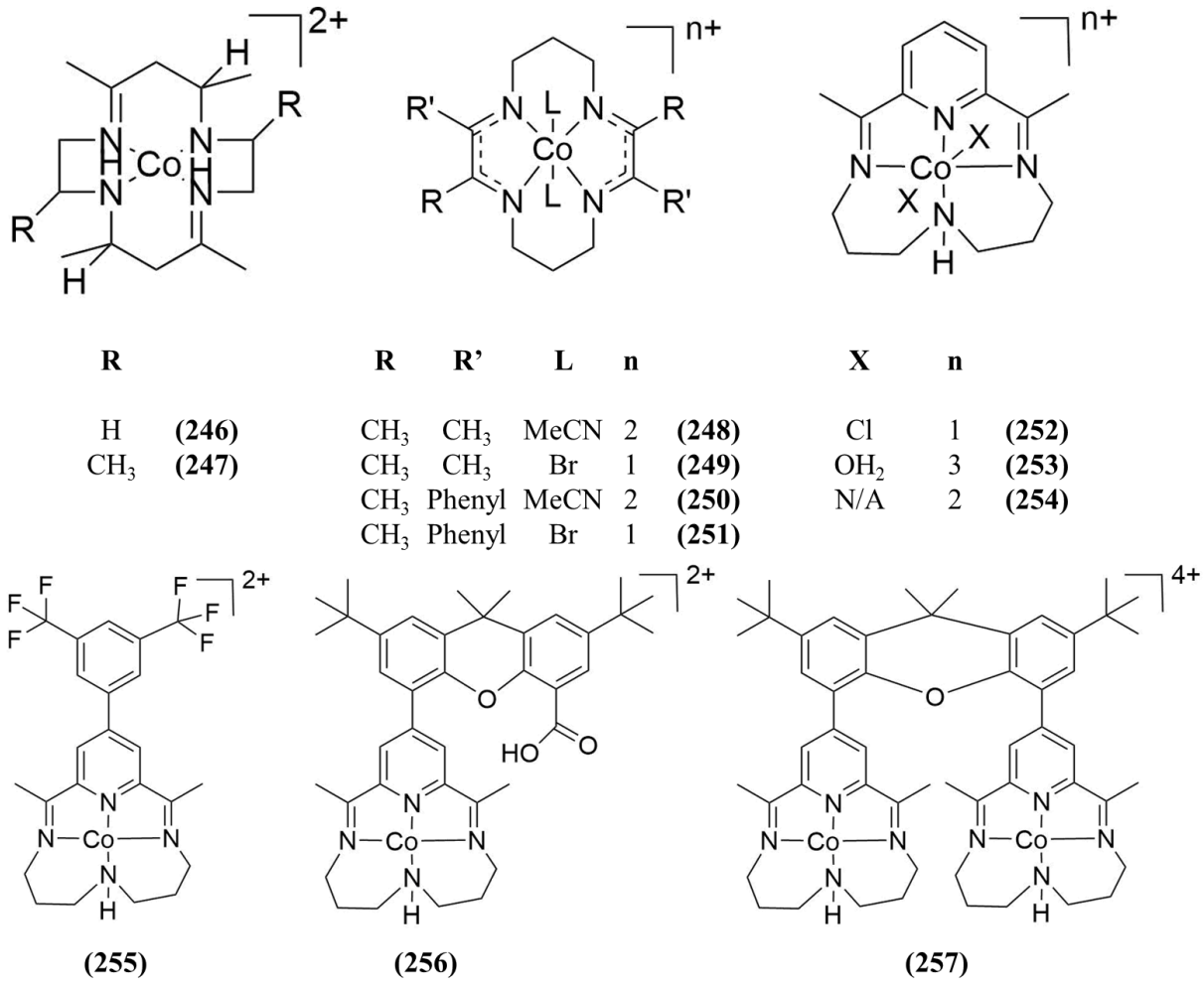

R		R	R'	L	n		X	n	
H	**(246)**	CH_3	CH_3	MeCN	2	**(248)**	Cl	1	**(252)**
CH_3	**(247)**	CH_3	CH_3	Br	1	**(249)**	OH_2	3	**(253)**
		CH_3	Phenyl	MeCN	2	**(250)**	N/A	2	**(254)**
		CH_3	Phenyl	Br	1	**(251)**			

(255) **(256)** **(257)**

Figure 1.64: Various Co macrocycles assessed towards electrocatalytic H_2 generation

Leung *et al*. assessed the ability of **(252)** (Figure 1.64) in aqueous and MeCN electrolytes [311]. Electrolysis of the complex was undertaken at -0.65 V vs SCE (catalytic current onset was observed at approximately -0.4 V) in the presence of 0.2 M p-cyanoanilinium tetrafluoroborate in MeCN. Greater than 90% FE was achieved towards proton reduction, with at least 50 TONs observed. A catalytic wave was also observed with the addition of triflic acid, but not with the relatively weaker acids of tosic acid, TFA or acetic acid. In aqueous solution, the complex was active towards proton reduction (with the use of acetic acid), whereby the $Co^{2+/1+}$ reduction was 0.28 V more negative in aqueous solution. Electrolyses in aqueous electrolyte at -0.95 V vs SCE produced > 90% FE and > 50 TON. The complex was also found to be photocatalytically active.

McCrory *et al*. further assessed the complex in the form of **(253)** (Figure 1.64) in aqueous solutions [325]. A 92% efficiency and 17 TON were achieved when the complex was electrolysed for 2 hours at -0.93 V vs SCE in a pH 2, 0.1 M phosphate buffer. The stability of the twice reduced (electrogenerated) Co^{1+} complex was assessed by Varma *et al*. [326]. Under strictly anaerobic conditions, complete stability of the Co^{1+} species was noted in MeCN over several weeks. The group also showed that with aquo complex, as with the Cl axial ligands, enhancement of voltammetric current was observed upon addition of p-cyanoanilinium tetrafluoroborate, an organic acid to the complex in MeCN. The onset occurred at approximately -0.7 V vs Ag/Ag^{+}, concurrent with the beginning of the $Co^{2+/1+}$ reduction.

The complex was substituted further on the pyridyl group, as **(255)**, **(256)** and **(257)** (Figure 1.64) were explored in addition to **(254)** [315]. The dinuclear **(257)** was however, not assessed in an electrocatalytic manner. In MeCN, **(255)**'s $Co^{2+/1+}$ reduction demonstrated an anodic shift of 90 mV relative to the same process of **(254)**, although its enhancement of voltammetric current upon additions of tosic acid was stated to be greatly attenuated in comparison. Triflic acid allowed for a catalytic increase in voltammetry, though successive additions showed the catalytic peak potential to shift cathodically. Despite the observation of a catalytic current, the complex was not found to be stable in the presence of higher concentrations of the stronger acid. The hangman complex **(256)** was shown to be active for proton reduction by voltammetry in the presence of tosic acid. However, SEM with EDX analysis of the electrode used for electrolysis of the complex showed the presence of small particles containing Pd, believed to originate from a coupling reagent used in the synthesis of the complex. Upon reusing the electrode, heterogeneous activity was noted, and therefore, it was deemed inconclusive as to whether the complex (or the deposited Pd) accounted for the H_2 detected. A 1.5 hour electrolysis of 1 mM **(254)** was also undertaken in MeCN with 20 equivalents of tosic acid present and a glassy carbon rod held at -1.2 V vs Fc/Fc^{+}, whereby quantitative FE_{H2} was obtained with a TON_{H2} of 7.

Kal *et al*. synthesised and assessed two dinuclear cobalt complexes, **(258)** and **(259)** (Figure 1.65), bearing structural similarity to the salen ligand [327]. In MeCN, catalytic enhancements appeared in the voltammetry of both complexes in the presence of both stronger (TFA) and weaker (acetic) acids. In the presence of TFA, **(258)**'s enhancement appeared at approximately -1.3 V vs Fc/Fc^{+} (close to what is believed to be the

$Co^{2+}Co^{1+}/Co^{1+}Co^{1+}$ reduction). Electrolyses of **(258)** at -1.88 V vs Fc/Fc^{+} and at a carbon paper working electrode in MeCN with 100 equivalents of acetic acid produced Faradaic efficiencies of between 72 and 94%. In the presence of up to 65 equivalents of TFA, the complexes appeared to be chemically stable over the course of several hours. Following a voltammogram of **(258)** in a homogeneous solution containing 5 equivalents of acid, the electrode was assessed for heterogeneous activity. Within the voltammogram (in the absense of catalyst), a reduction wave was not observed in the voltammetric region of homogeneous electrocatalysis.

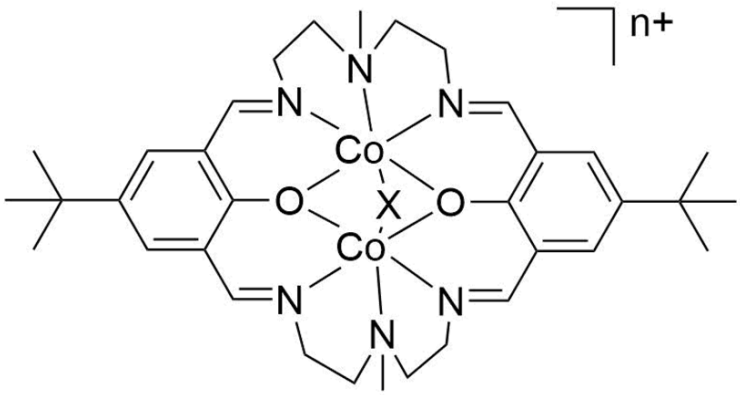

X	n	
N/A	2	**(258)**
CH_3COO	1	**(259)**

Figure 1.65: Co Schiff base dinuclear complexes assessed towards electrocatalytic H_2 generation

1.3.3.1.1. Co porphyrins, corroles and phthalocyanines

Kellett and Spiro originally studied the activity of three water soluble Co porphyrins (**(260)**, **(261)** and **(262)**, Figure 1.66) in an aqueous 0.1 M trifluoroacetic acid (TFA) solution [328]. In addition to electrolyses undertaken in water with TFA present, the complexes were assessed for voltammetric enhancement in DMSO. Upon the addition of water, an enhancement was observed at the $Co^{2+/1+}$ reduction, indicating the complexes' ability to reduce protons without the presence of TFA in a non-aqueous solvent. Natali *et al*. later incorporated **(262)** into a photocatalytic proton reduction system [329]. Voltammetry of the complex in MeCN additionally showed cathodic current enhancement (below approximately -1.4 V vs SCE) upon the addition of up to 13 equivalents of benzoic acid.

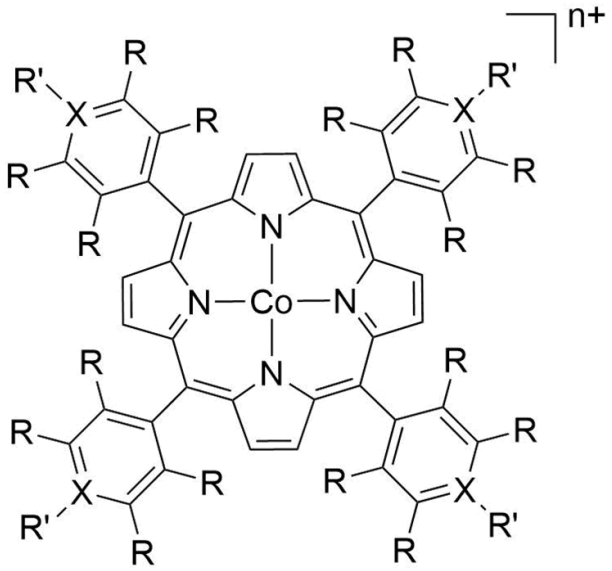

X	R	R'	n	
N	H	N/A	0	**(260)**
N	H	CH_3	4+	**(261)**
C	H	$N(CH_3)_3$	4+	**(262)**
C	F	F	0	**(263)**
C	H	SO_3H	0	**(264)**
C	H	Cl	0	**(265)**
C	H	OCH_3	0	**(266)**

Figure 1.66: Various Co porphyrins utilised in electrocatalytic H_2 generation

Inclusion of a peripheral hydrogen and its effect on electroreduction of protons was the focus of Lee *et al*. [316], through the development of a hangman-type Co porphyrin. The group synthesised **(267)** and **(268)** (Figure 1.67) and their behaviour towards the reduction of strongly and weakly acidic protons was investigated in MeCN. Introduction of the peripheral acidic group allowed for an anodic shift in potential (of approximately 200 mV) of the $Co^{1+/0}$ reduction as compared to **(268)** ($E_{1/2}$ of -2.14 V vs Fc/Fc^+). However, reversibility of the process at 100 mV s^{-1} was also strongly diminished, as compared to the behaviour observed with **(268)**. Inclusion of the weaker, benzoic acid showed that reduction to the Co^0 state was required in both cases to enact proton reduction. Electrolysis of 0.4 mM **(267)** at -2.05 V vs Fc/Fc^+ in MeCN with 37.5 equivalents of benzoic acid produced a FE of 80%, whereas electrolysis of 0.5 mM **(268)** at -2.2 V vs Fc/Fc^+ in the presence of 30 equivalents of benzoic acid rendered a FE of 85%. The introduction of the stronger, tosic acid showed the growth of catalytic waves appearing less negative than -1.5 V, proceeding the $Co^{2+/1+}$ reduction. This led to the conclusion that utilisation of the stronger acid allowed for protonation following the $Co^{2+/1+}$ reduction. In a further study, **(263)** (Figure 1.66) showed a catalytic enhancement to voltammetry (E_p of approximately -2 V vs Fc/Fc^+) in MeCN, with the introduction of benzoic acid [330].

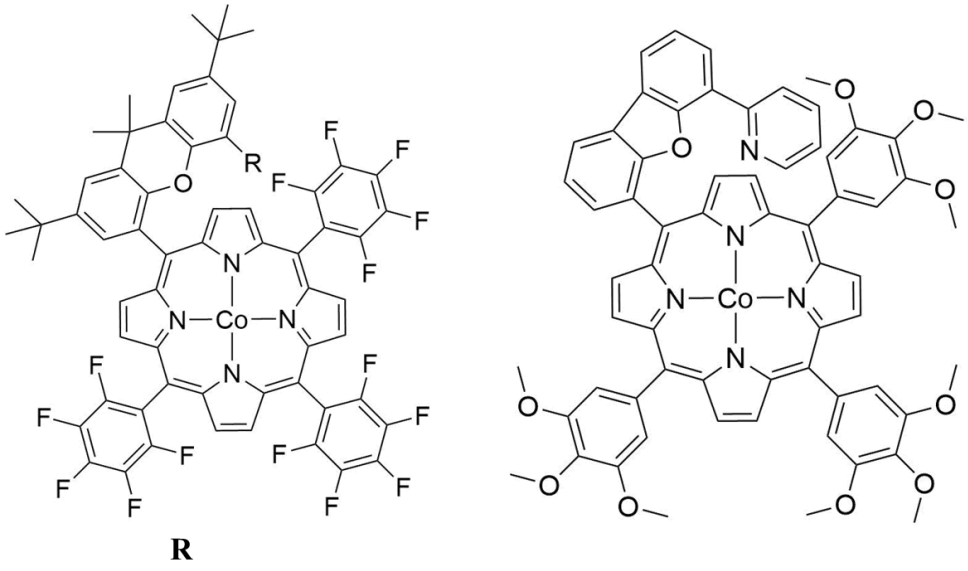

Figure 1.67: Co hangman porphyrin complexes assessed towards electrocatalytic H_2 generation

The group also showed the benefit of a hanging pyridyl group in the form of **(269)** (Figure 1.67) [314]. A voltammetric enhancement of the complex' $Co^{2+/1+}$ reduction (approximately -1.2 V vs Fc/Fc^{+}) was observed in MeCN (0.1 M tetraethylammonium tosylate), upon the introduction of tetrafluoroboric acid diethylether (thereby generating tosic acid in-situ).

Beyene *et al*. synthesised the water-soluble **(264)** (Figure 1.66) for the purpose of electrocatalytic H_2 production in neutral aqueous solution [331]. Electrochemistry of the complex was also undertaken in DMSO. A significant voltammetric enhancement was observed upon the addition of up to 10 equivalents of acetic acid (at the potential of the $Co^{1+/0}$ reduction, -1.45 V vs SHE). The complex was found to be active in neutral aqueous electrolyte, and a quantitative Faradaic efficiency was achieved at -1.39 V vs SHE. No loss of charge was observed over the course of 73 hours of electrolysis at -1.29 V vs SHE.

In DMF, Liu *et al*. compared the ability of **(265)** and **(266)** (Figure 1.66) to react with protons derived from acetic acid [332]. As shown by voltammetry, **(265)** only displayed

catalytic enhancement at the potential of the $Co^{1+/0}$ reduction (approximately -1.9 V vs Ag/Ag^{+}), whereas the methoxy substitution in **(266)** allowed for an increase in current at the potential of the $Co^{2+/1+}$ reduction. **(235)** (Figure 1.62) was also shown by Sommer *et al*. to exhibit a significant current enhancement to voltammetry, upon the addition of 28 equivalents of tosic acid in MeCN [333]. The onset of catalytic current occurred at about -1 V vs SHE, coinciding with the complex' $Co^{1+/0}$ reduction.

(270) (Figure 1.68) was probed as an electrocatalyst for hydrogen evolution from aqueous solution [312]. To gain an understanding towards the mechanism of operation, Mondal *et al*. assessed the electrochemical behaviour of the complex in MeCN. Upon the introduction of 0.13 M TFA, a dramatic increase in potential was shown with onset at approximately -0.75 V vs Ag/AgCl. Through evidence from spectroelectrochemical experiments, it was deduced that the Co^{1+} species was responsible for reaction with protons prior to H_2 generation. A further study compared the catalytic enhancements observed in the voltammetry of **(270)**, **(271)** and **(272)** (Figure 1.68) [334]. The order of reactivity of the corroles with protons derived from TFA in MeCN was determined to be F > Cl > Br substitution, however, no electrolyses were undertaken.

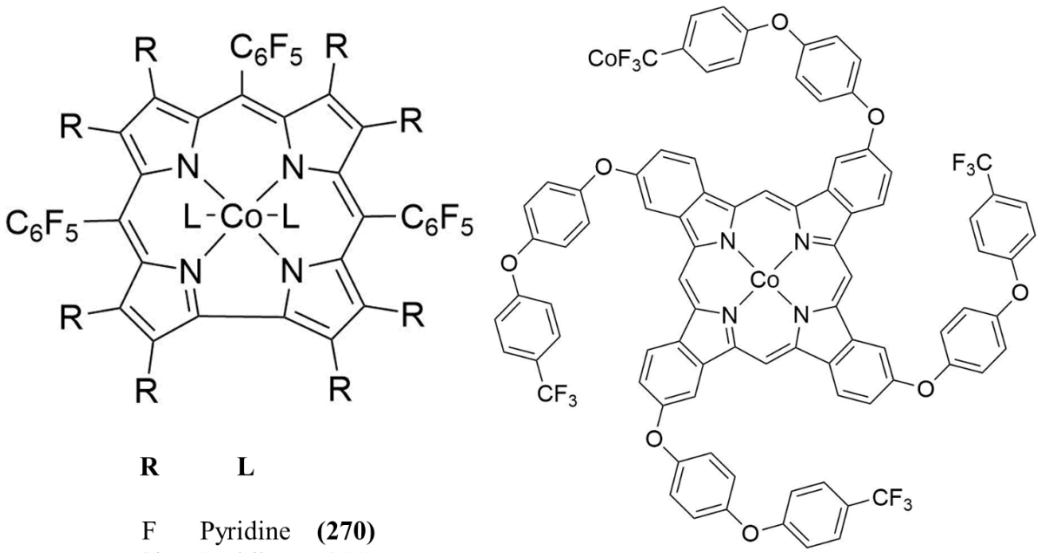

Figure 1.68: Co corroles and phthalocyanine assessed towards electrocatalytic H_2 generation

Co phthalocyanines are heterogeneously active electrocatalysts in the generation of hydrogen from aqueous solution. The first report of the family for the electrocatalytic HER originated in the 1960s [303]. Additional research, focussed on further tuning of the family, was undertaken by Koca *et al*. [318]. Within this study, voltammetry of **(273)** (Figure 1.68) was undertaken in MeCN. Additions of perchloric acid showed enhancements to voltammetry, beginning at approximately 0 V vs SCE. Further enhancements were observed at more cathodic potentials. The complex dropcast (with Nafion) onto a glassy carbon electrode allowed for the generation of H_2 at -1.08 V vs SCE (as compared to -1.31 V vs SCE at bare electrode) in a pH 9.2 phosphate buffered (0.1 M NaCl) electrolyte.

1.3.3.2. Cobaloximes, Co diimine-dioximes and BF_2 analogues

Cobaloximes, diimine-dioximes and BF_2 analogues have been widely studied and largely contribute to the area of cobalt-centred molecular electrocatalytic hydrogen evolution [329]. However, questions as to the identity of the true active species within these complexes arose through the studies of Saveant *et al*. [335], and following this, the work of Artero's group [336,337]. Co particles have been noted to deposit from reduction of complexes in organic [335,338–340] and aqueous media [336,337,341] (structures available in Figure 1.69). The loss of Co^{2+} from a BF_2 analogue had been noticed upon catalytic generation of H_2 [342], prior to observations of heterogeneously active deposits. The FE of a Co bisiminopyridyl complex in aqueous solution was found to greatly diminish at potentials cathodic of -1.5 V vs SCE [343], whereby the authors believed that reduction of the imine bond, and reactivity of the resulting radical may be responsible for catalyst degradation. Ligand exchange within Co dimethylglyoxime and diphenylglyoxime has also been shown under photocatalytic conditions [344]. Additionally, similar depositions were observed within a nickel diimine-dioxime under acidic aqueous conditions of electrolysis [345].

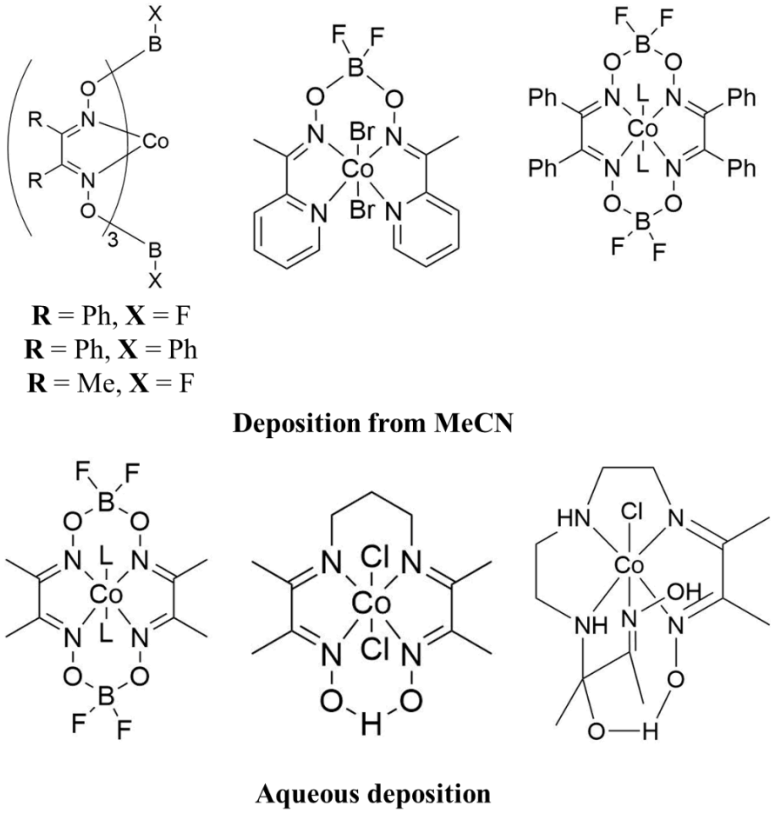

Figure 1.69: Cobalt imine-oxime complexes reported to deposit onto electrode surfaces

However, when a Co diimine-dioxime complex was covalently attached to the surface of MWCNTs [346] remarkable stability was observed. Following 7 hours of electrolysis in aqueous solution, a TON_{H2} of 56,000 was achieved. Proceeding this, X-ray photoelectron spectroscopy (XPS) analysis of the electrode showed no evidence for Co or Co oxide formation. Therefore, stability of this family of complexes may be significantly improved with surface immobilisation, prior to electrolyses.

Relatively recent reviews exist on Co glyoxyl complexes towards the hydrogen evolution reaction (HER) [309,347]. In addition, the review by Artero and Fontecave further discusses the issue of heterogeneity within molecular proton reduction [185].

1.3.3.3. Co polypyridyl complexes

In 1981, Krishnan and Sutin reported the first molecular photocatalytic water reducing system involving a cobalt bipyridyl catalyst [348]. The primary $[Co(bpy)_n]^{2+}$ complexes

under their catalytic conditions include n=1 and n=2 species. **(274)** has only recently been assessed towards homogeneous electrocatalytic proton reduction in organic electrolyte, in addition to **(275)** (Figure 1.70) [349]. In MeCN and with 20% water and p-cyanoanilinium tetrafluoroborate, electrolysis of **(274)** at -1.3 V vs Ag/AgCl produced just over 1 TON_{H2} over the course of an hour. **(275)** was not as active, whereby < 1 TON_{H2} was achieved (-0.75 V vs Ag/AgCl). Colloid metal was observed on an electrode involved in a similar electrolysis, whereby the electrolysis potential was -1.1 V.

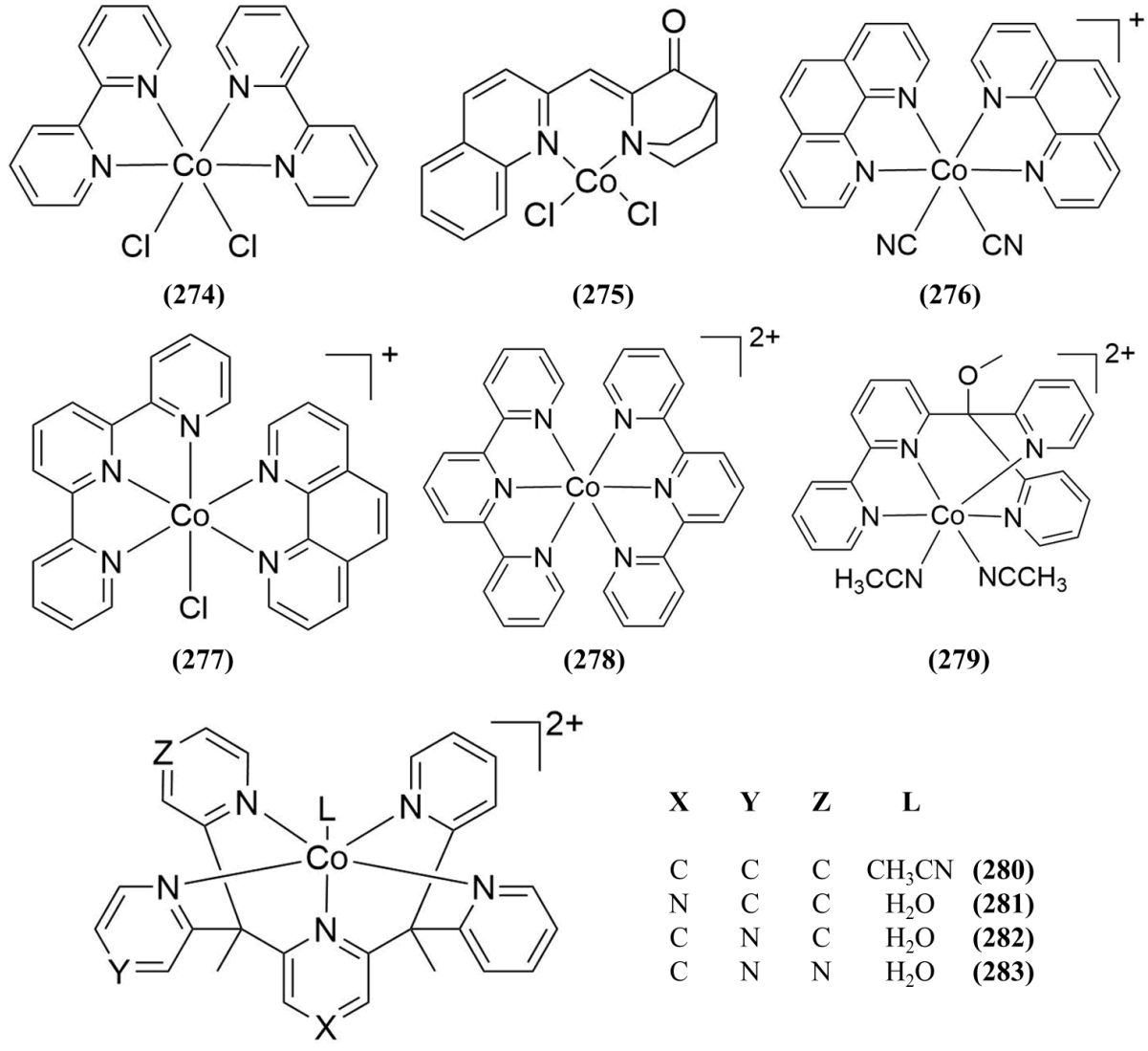

Figure 1.70: Various Co polypyridyl complexes reported for electrocatalytic H_2 generation

Peng *et al*. reported the electrocatalytic generation of hydrogen from a neutral aqueous solution and also from MeCN with acetic acid using a similar bisdiimine Co complex, **(276)** (Figure 1.70) [350]. Electrolysis of 3.44 μM **(276)** in the presence of 2 mM acetic acid at -1.4 V vs Ag/Ag^{+} produced a 49 μl H_2 over the course of two hours. Over a 2 minute electrolysis, the authors, assuming that the system was 100% efficient, stated that 1.85 TON was achieved. However, Faradaic efficiencies were not reported. In a separate study by Chen *et al*. [351], **(277)** (Figure 1.70) showed a voltammetric enhancement (up to i/i_p of 23) at its $Co^{2+/1+}$ reduction (approximately -1.5 V vs Fc/Fc^{+}) in MeCN with additions of tosic acid. The complex was polymerised onto a Cu_2O photocathode for heterogeneous photoelectrochemical reduction in aqueous solution. The molecular nature of the electrodeposit was evident through XPS, whereby Co^{2+} and N signals were observed.

Within its report as a heterogeneous catalyst, **(278)** (Figure 1.70) demonstrated a homogeneous voltammetric enhancement in dimethylacetamide (DMA) [352]. With the introduction of 20% water, a catalytic onset was shown to coincide with the complex' $Co^{1+/0}$ reduction (beginning at approximately -1.5 V vs Ag/AgCl). Electrolysis at -1.7 V vs Ag/AgCl for 30 minutes produced 125 TON, with FE > 80%. It is not clear as to whether these figures are the result of homogeneous or heterogeneous catalysis.

Bigi *et al*. [353] assessed the ability of the tetrapyridyl **(279)** (Figure 1.70) at -1 V vs SCE at glassy carbon in MeCN with TFA present. Following a 30 minute electrolysis, the complex was found to be 99% efficient, producing approximately 20 TON (TOF of approximately 40 hr^{-1}). Voltammetric studies showed that the $Co^{2+/1+}$ redox couple was reversible up to a ratio of 1:1 MeCN to water. Therefore, the catalyst may only be active for the reduction of protons from TFA in MeCN.

Proceeding the advent of **(280)** (Figure 1.70) as an electrocatalyst towards H_2 generation in pH 7 aqueous solutions [354], the catalyst was also shown by voltammetry to be active towards proton reduction in MeCN and in the presence of acetic acid [355]. An onset of proton reduction occurred cathodic of the $Co^{2+/1+}$ reduction (approximately -0.8 V vs SHE). At a region more positive of direct acetic acid reduction (i.e. > -1.4 V vs SHE), **(280)** produced quantitative Faradaic efficiency in the presence of both acetic acid and acetic acid/TBAOAc (1:1) over 2 hour electrolyses.

With the aim of lowering the potential of H_2 reduction by **(280)**, Jurss *et al*. pursued the introduction of one (both axially and equatorially coordinated) and two pyrazine units to the ligand, resulting in the complexes of **(281)**, **(282)** and **(283)** respectively (Figure 1.70) [313]. The addition of up to 20 equivalents of chloroacetic acid to each complex in MeCN enacted a cathodic current increase within the voltammetry of each complex. The onset potential of catalytic current was -1.7 V, -1.5 V and -1.15 V vs Fc/Fc^+ for **(281)**, **(282)** and **(283)** respectively, despite the similar E_{pc} of the axial and equatorial complex' second reductions (-1.4 V and -1.42 V vs Fc/Fc^+ respectively). Upon electrolysing the complexes at -1.5 V vs Fc/Fc^+ in MeCN with 100 equivalents of chloroacetic acid at a carbon rod, it was found that **(282)** was approximately twice as active as **(283)**. It was also surprising that despite the relatively cathodic onset potential observed within **(281)**, the complex performed with similar activity to that of **(283)**. All three complexes performed with Faradaic efficiencies > 90%. TONs were not reported for experiments in organic solvents. **(281)**, **(282)** and **(283)** were further assessed with a Hg pool electrode in aqueous pH 7 buffer, whereby all complexes operated with 100% efficiency. **(283)** produced H_2 with similar or 17% greater levels of activity to **(282)**, depending on the applied potential of between -1 V and -1.2 V vs SHE. However, the activity of **(281)** was appreciably lower than that of the other complexes analysed.

Two tripyridyldiamino Co complexes, **(284)** and **(285)** (Figure 1.71), were found to display electrocatalytic behaviour via voltammetry in MeCN upon the addition of triethylammonium chloride and acetic acid [356]. In the presence of 100 equivalents of acetic acid, the complexes were electrolysed at -1.7 V vs Ag/AgCl with a Hg pool electrode. A 3 hour electrolysis of 0.2 mM **(284)** led to 90% FE and 15 TON (TOF of 5 hr^{-1}) with the same electrolysis of **(285)** producing 75% efficiency and TON of 14 (TOF of 5 hr^{-1}). Under these conditions, the charge-time profile of electrolysis suggests a possible instability in MeCN with acid present (particularly in the case of **(285)**). However, electrolysis in aqueous solutions was the intended purpose. In 1 M pH 7 phosphate buffer, a three hour electrolysis of 10 μM **(284)** at -1.7 V vs Ag/AgCl produced 1615 TON with 95% efficiency, with **(285)** amassing 1400 TON, also at a 95% efficiency. Electrolyses in aqueous buffer were extended to 18 hours, whereby **(284)** produced 7150 TON (95% FE) and **(285)** produced 6000 TON (95% FE). No degradation was observed as assessed with UVs of the electrolysis solution. Additionally, the charge-time profiles in aqueous conditions showed a far more linear

response to those in organic solution. Gas generated within blank experiments was also deducted from electrolyses with the catalysts present.

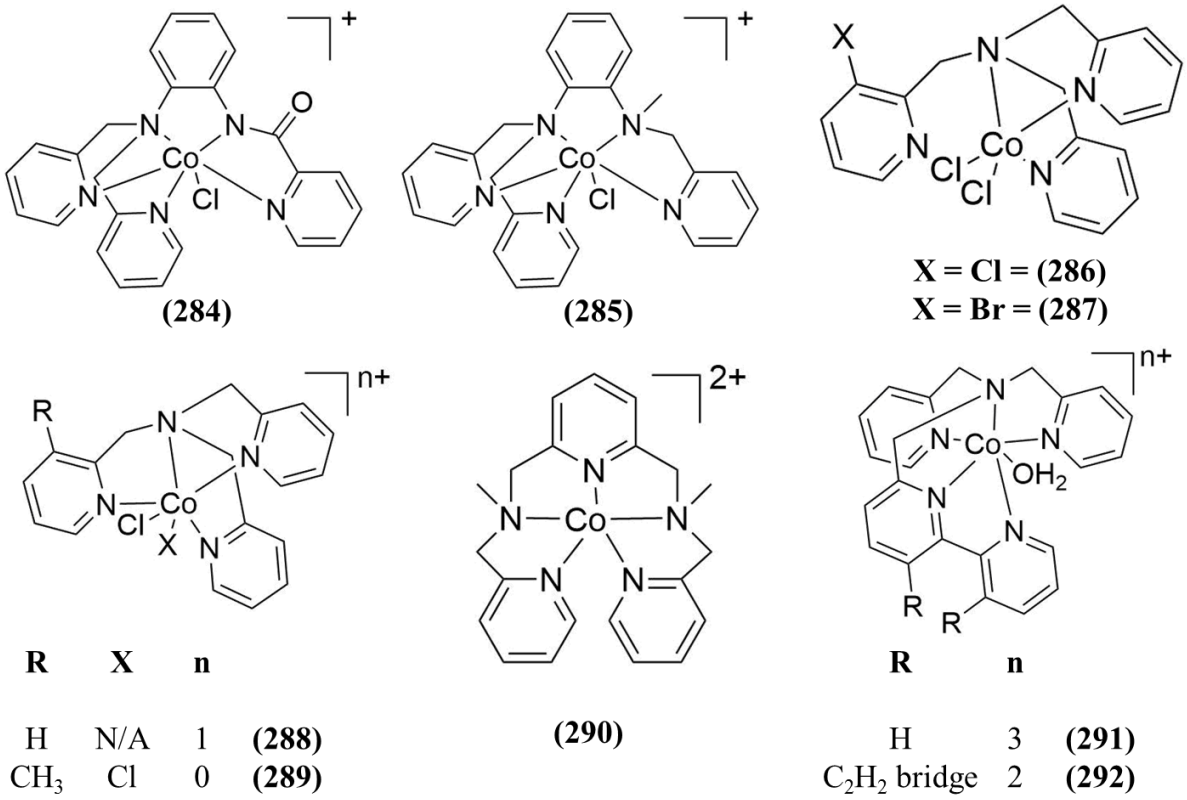

Figure 1.71: Various Co polypyridyl complexes utilised for electrocatalytic H_2 generation

Wang *et al*. studied **(286)**, **(287)**, **(288)** and **(289)** (Figure 1.71) bearing tripyridyl tri- or tetra-coordinating ligands in MeCN [357], whereby all complexes showed a catalytic response to voltammetry with additions of acetic acid. All four complexes demonstrated two electrochemical reductions, at approximately -1.55 and -1.8 V vs SCE, which were ascribed to the $Co^{2+/1+}$ and $Co^{1+/0}$ processes. However, as compared to **(288)** and **(289)** (tetra-coordinated ligand), **(286)** and **(287)** (tri-coordinated ligand) both showed an additional reduction (at -1.45 and -1.34 V respectively), which was attributed to reduction of the pendent halo-substituted pyridyl group. Bulk electrolyses at -2 V vs SCE in the presence of acetic acid yielded FE values of 95, 94, 92 and 93 % respectively. It is worth noting that at this potential, the contribution of the bare electrode to H_2 generation may be large [358]. Despite acid dependent behaviour of its

first reduction, electrolysis of **(287)** at -1.34 V with 10 equivalents of acetic acid did not produce any H_2. At -1.35 and -1.45 V however, electrolysis of **(286)** in the presence of acid permitted the generation of H_2. The authors concluded that the bromo-substituted pyridyl group may act as a proton relay but was not a proton reduction site, whereas the Cl-substituted group may act in the capacity of a H_2 evolving site.

A further pentadentate complex, **(290)** (Figure 1.71) was shown to be active towards photocatalytic water reduction in a mixed MeCN/H_2O (1:1) with 10% TEA system containing $[Ir(ppy)_2(bpy)]^+$ as PS [359]. Upon addition of up to 4% water, an enhancement of reductive current was observed at approximately 100 mV negative of the first reduction (where the couple's $E_{1/2}$ appeared at -1.6 V vs Fc/Fc^+). Unusually, despite enhancement of the reductive current, a slight cathodic shift in the oxidation of the couple was observed, but disappearance of the wave did not occur. Electrolyses were not undertaken.

Singh *et al*. demonstrated the ability of **(291)** (Figure 1.71) towards electrocatalytic proton reduction in an aqueous solution [360]. Following from this, Song explored a phenanthrolinyl analogue, **(292)** in MeCN [361]. The addition of up to 10 equivalents of acetic acid showed the appearance of a catalytic wave associated with H_2 generation, with an onset potential at -1.7 V vs Fc/Fc^+ in the presence of 2 equivalents of acetic acid.

Natali *et al*. assessed the voltammetry of **(293)**, **(294)**, **(295)**, **(296)** and **(297)** (Figure 1.72) in MeCN/H_2O 1:1 with up to 2.5 mM TFA, preceeding their incorporation into photocatalytic experiments [362]. Each of the complexes showed a current enhancement beginning at approximately -1 V vs SCE (prior to the $Co^{2+/1+}$ reduction). When electrolysed at -1.2 V with carbon foil, **(296)** demonstrated a Faradaic efficiency of 90%.

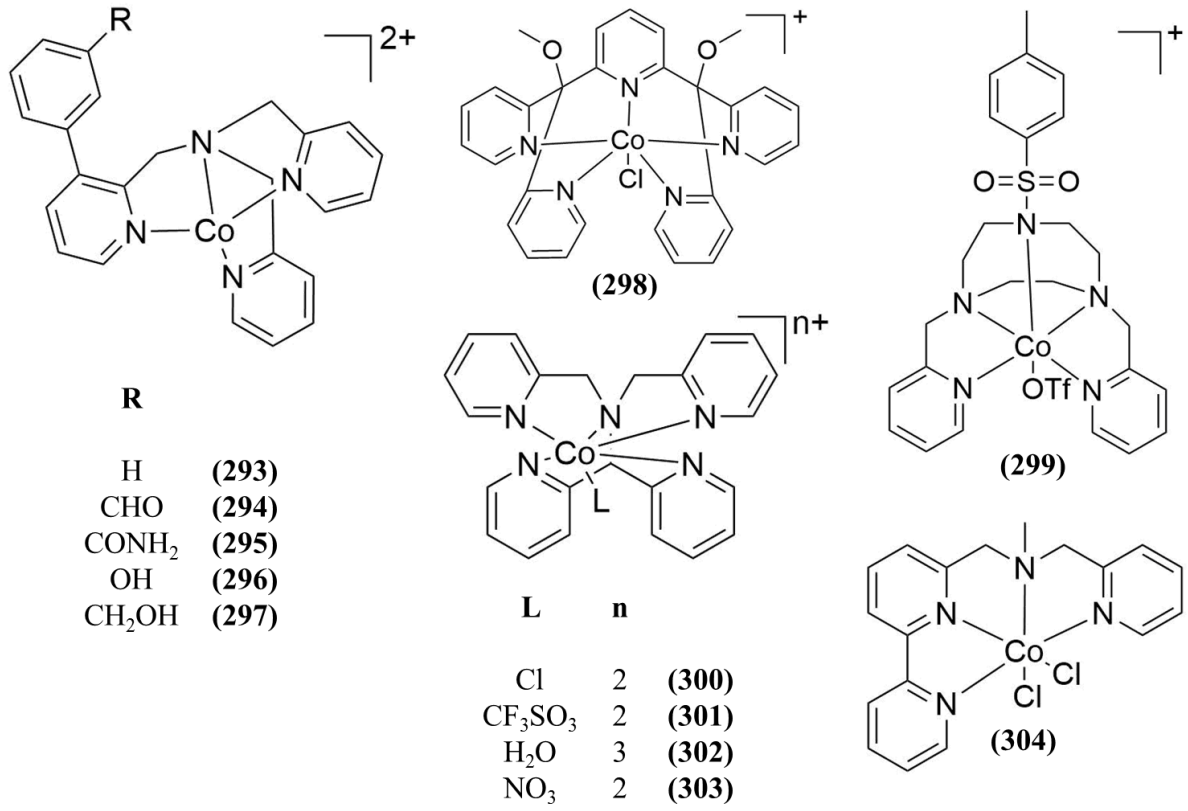

Figure 1.72: Polypyridyl Co complexes assessed towards electrocatalytic H_2 generation

The electrocatalytic response of **(298)** (Figure 1.72) was shown in MeCN with TFA present [363]. Call *et al*. also showed a catalytic current enhancement to the voltammetry of **(299)** (Figure 1.72) in MeCN, upon the addition of TFA [364]. Xie *et al*. utilised up to 10 mM acetic acid in MeCN and showed the enhancement of the $Co^{2+/1+}$ reduction (beginning < -1.4 V vs SCE) within **(300)**, **(301)** and **(302)**, whereas the reduction of **(303)** was not enhanced [365]. The complexes were varied only by the monodentate axial ligand and photocatalytic experiments showed that **(303)** also imparted poor activity. Within a mechanistic study, Singh *et al*. reported a current enhancement at the potential of the $Co^{2+/1+}$ process in **(304)** (Figure 1.72) (with onset potential as positive as -1.25 V vs Fc/Fc^{+}) in MeCN with 450 equivalents of TFA [366].

Tong *et al*. originally reported **(305)** (Figure 1.73), bearing a tetradentate phenanthrolyl-pyridylquinoline ligand towards photocatalytic hydrogen generation in a pH 4 aqueous system [367]. A subsequent photocatalytic study focussed on three additional and similar complexes, **(306)**, **(307)** and **(308)** (Figure 1.73) [368]. The voltammetry of

(305) in addition to **(307)** (which was found to display superior photocatalytic activity with 0.3 M ascorbic acid, $[Ru(bpy)_3]^{2+}$) was assessed in DMF/H_2O (4:1 ratio). Upon the introduction of 100 equivalents of acetic acid, a catalytic wave was observed following **(305)** and **(307)**'s $Co^{2+/1+}$ reductions (with onset cathodic of -1.1/-1.2 V and E_ps of approximately -1.7 V vs Fc/Fc^+). With respect to the voltammetry undertaken in DMF relative to DMF with 20% water, the complexes did not appear to exhibit catalytic behaviour towards water reduction in DMF prior to the addition of acid.

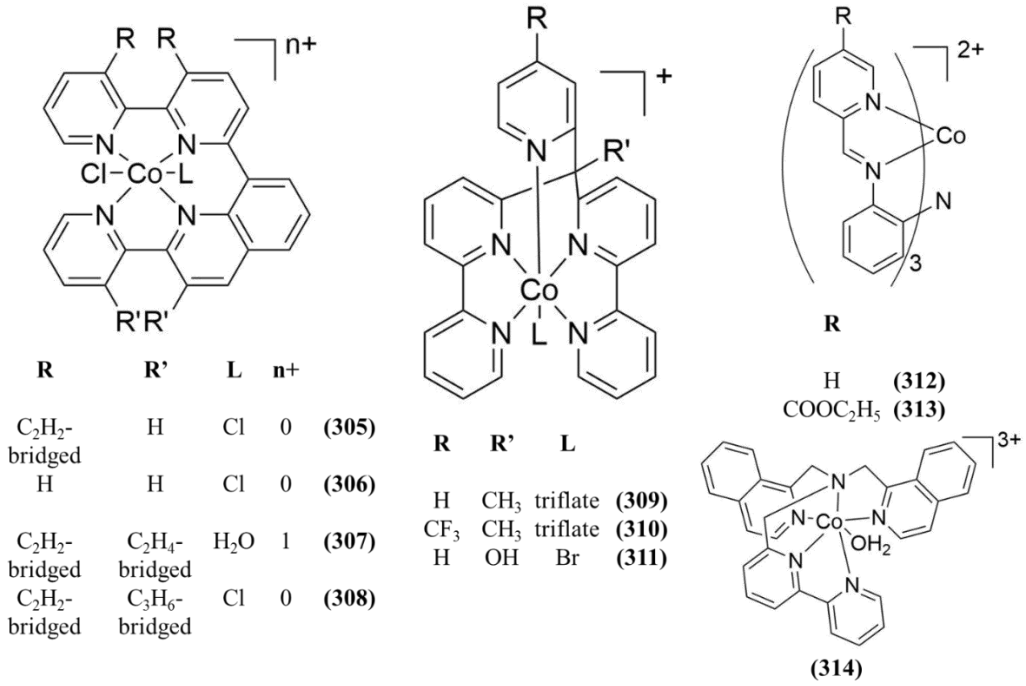

Figure 1.73: Co polypyridyl complexes assessed towards electro- and/or photocatalytic H_2 generation

Nippe *et al*. explored pentadentate ligands as bound to the complexes **(309)** and **(310)** (Figure 1.73) [369]. In addition to the $Co^{2+/1+}$ reduction, two ligand based reductions were observed. In MeCN and at a glassy carbon electrode, the addition of acetic acid showed a large current enhancement in the case of **(309)**, at the approximate E_{pc} of the ligand-based reduction. The perfluoromethyl analogue similarly showed an enhancement at the first reduction, however, far less pronounced than that of the unsubstituted ligand. In the case of **(309)**, the enhancements occurred with approximate E_{pc} of -1.75 and -1.9 V vs Fc/Fc^+, whereby the bpy-based reductions appeared at -1.79 and -1.94 V vs Fc/Fc^+. A 90% FE was achieved for **(309)** at an unspecified potential.

The voltammetric response of the dinuclear **(315)** (Figure 1.74) was assessed in MeCN with the addition of tosic acid [370]. When the potential was cycled to approximately -1.4 V vs SCE, an anodic feature (potentially relating to a heterogeneous species) was observed on the reverse scan. Electrolysis of the solution at -0.75 V vs SCE with a glassy carbon electrode produced a relatively low Faradaic efficiency of 40% (with the absense of catalyst generating 1/8 of the H_2 that in the presence). In conjunction with the voltammetry shown, it is possible that part of the current was consumed to form Co^0 or a cobalt oxide. Within photocatalytic experiments, whereby the complex was active as a catalyst, higher concentrations (55 μM) led to the detection of nanoparticulate matter. The inspiration for **(315)** came from **(316)** (Figure 1.74), a catalyst and electrocatalyst towards proton reduction [371]. In MeCN with TFA present, **(316)**'s voltammetry also showed a catalytic enhancement at potentials lower than approximately -0.7 V vs SCE (at approximately the potential of the complex' third reduction, $Co^{2+}Co^{2+}/Co^{2+}Co^{1+}$). A ten minute electrolysis at -1.1 V vs SCE allowed for a Faradaic efficiency of 79% towards H_2 generation.

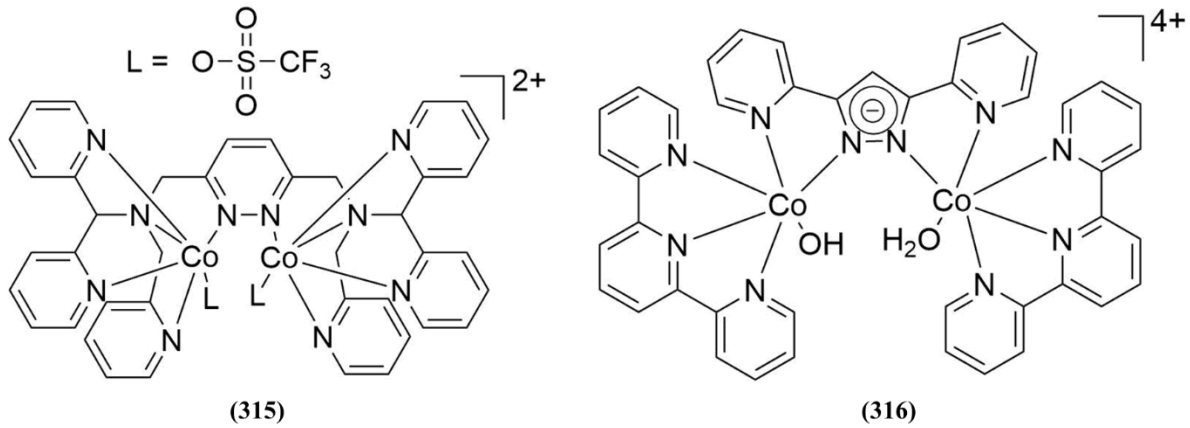

Figure 1.74: Dinuclear Co complexes assessed for activity towards electrocatalytic H_2 generation

Song *et al.* assessed two hexadentate iminopyridyl complexes, **(312)** and **(313)** (Figure 1.73) [372]. With up to approximately 12 equivalents of acetic acid, **(312)** displayed an i/i_p of 3.3 at the second reduction (~ -1.7 V vs Fc/Fc^+) in MeCN. Photocatalysis was achieved in a system containing $[Ir(ppy)_2(bpy)]^+$ and 10% TEA in 1:1 MeCN/H_2O.

(313), which varied by the inclusion of ethyl ester groups, showed some, but very little enhancement comparatively.

Within the Co polypyridyl complexes studied, complexes such as **(309)** [369], a related complex **(311)** [373] and **(314)** (Figure 1.73) [374] were shown to be active in photocatalytic systems. The introduction of approximately 1 ml of Hg was introduced into the reaction setup in each case and H_2 amounts and rates were stated to be unaffected. At least under the conditions assessed, the complexes were not assumed to form nanoparticles over the course of photocatalysis.

1.3.3.4. Co phosphines and cyclopentadienyl complexes

Original reports of cobalt cyclopentadienyl complexes as catalysts and electrocatalysts towards H^+ reduction surfaced in the early 80s. **(317)** in addition to **(318)** (Figure 1.75) was reported for H^+ reduction in a phthalate buffered aqueous KCl solution [375]. Further to this, a series of cyclopentadienyl phosphine Co complexes (**(319)**, **(320)**, **(321)**, **(322)**, **(323)** and **(324)**, Figure 1.75) were reported as H^+ reduction catalysts by Koelle and Paul [323] and were initially assessed in propylene carbonate and DCM with NH_4PF_6 as proton source. Electrolyses were undertaken in aqueous solutions.

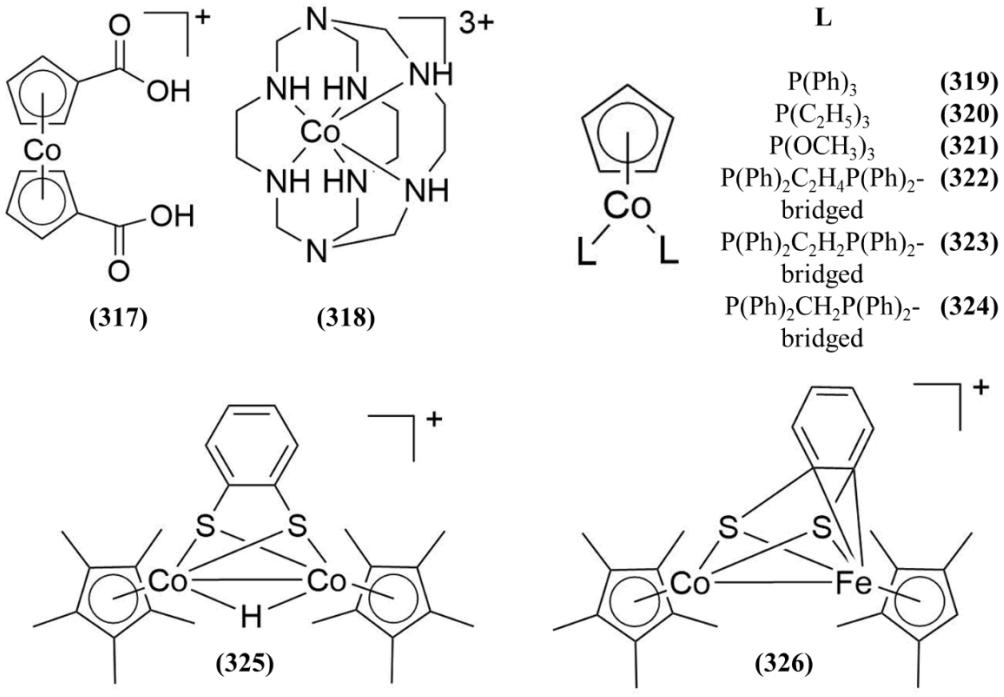

Figure 1.75: Co and Co-Fe complexes assessed as electrocatalyts towards H_2 generation

Homo- and heterodinuclear complexes **(325)** and **(326)** (Figure 1.75) were assessed in the presence of the strong acids, TFA and HBF_4 [317]. Both complexes exhibited a rise in catalytic current (beginning at approximately -1.33 V and -1.23 V vs Fc/Fc^+ for **(325)** and **(326)** respectively with TFA) in DCM. **(325)** produced a FE of 90% when electrolysed at -1.6 V vs Fc/Fc^+ in the presence of 30 equivalents of TFA, whereas typical FEs for the complexes in MeCN with HBF_4 were 80-90%. However, no voltammetric enhancement for either complex was observed upon addition of the weaker acetic acid, suggesting an acid strength dependence on activity.

Jacobsen *et al*. explored a cobalt complex with two diphos ligands in MeCN with added triflic acid [376]. The authors discovered that under these conditions, one ligand was removed, producing **(327)** (Figure 1.76). The reductive current of **(327)** in MeCN was enhanced in the presence of bromoanilinium tetrafluoroborate, with its half peak potential (-0.99 V vs Fc/Fc^+) corresponding to the complex' $Co^{2+/1+}$ reduction. A controlled potential electrolysis of the complex at -1.1 V produced H_2 with a Faradaic efficiency of 101 ± 5%. A related complex, **(330)**, was synthesised and the complex demonstrated relatively poor activity to that of **(327)**. It was reasoned that the pendant base plays an important role in the activity of the complex.

A follow-on study by Wiedner *et al*. probed the Co complexes **(328)** and **(329)** (Figure 1.76) in addition to analogous nickel complexes [321]. Upon the additions of p-cyano-, p-bromo- and dichloroanilinium tetrafluoroborate, a rise associated with catalytic current was observed in the voltammetry of **(328)** in MeCN. However, as detected by UV-monitoring, a ratio of 75:1 acid to complex led to the complex' decomposition to $[Co(CH_3CN)_6]^{2+}$ with half-lives of approximately 40, 18 and 190 minutes in the presence of cyano-, dichloro- and bromoanilinium tetrafluoroborate respectively. **(329)** also appeared to show deligation with less than 15 equivalents of bromo- and cyanoanilinium tetrafluoroborate. It was suspected that protonation of the more basic nitrogen of **(329)** led to more rapid ligand loss. Furthermore, the introduction of the more sterically demanding tert-butyl group may impart greater instability on the complexes. Bulk electrolysis of 1 mM **(328)** in the presence of 230 mM bromoanilinium tetrafluoroborate was undertaken at -1.11 V vs Fc/Fc^+ with a reticulated vitreous carbon electrode. Following the consumption of 42 C, H_2 was evolved with a 96% FE, equating to approximately 16 TON. Electrolyses of $[Co(CH_3CN)_6]^{2+}$ were not undertaken, though

the half wave potential of proton reduction within voltammograms including **(328)** (-1.1 V) occurs close to the $Co^{2+/1+}$ $E_{1/2}$ of $[Co(CH_3CN)_6]^{2+}$ (at -1.21 V).

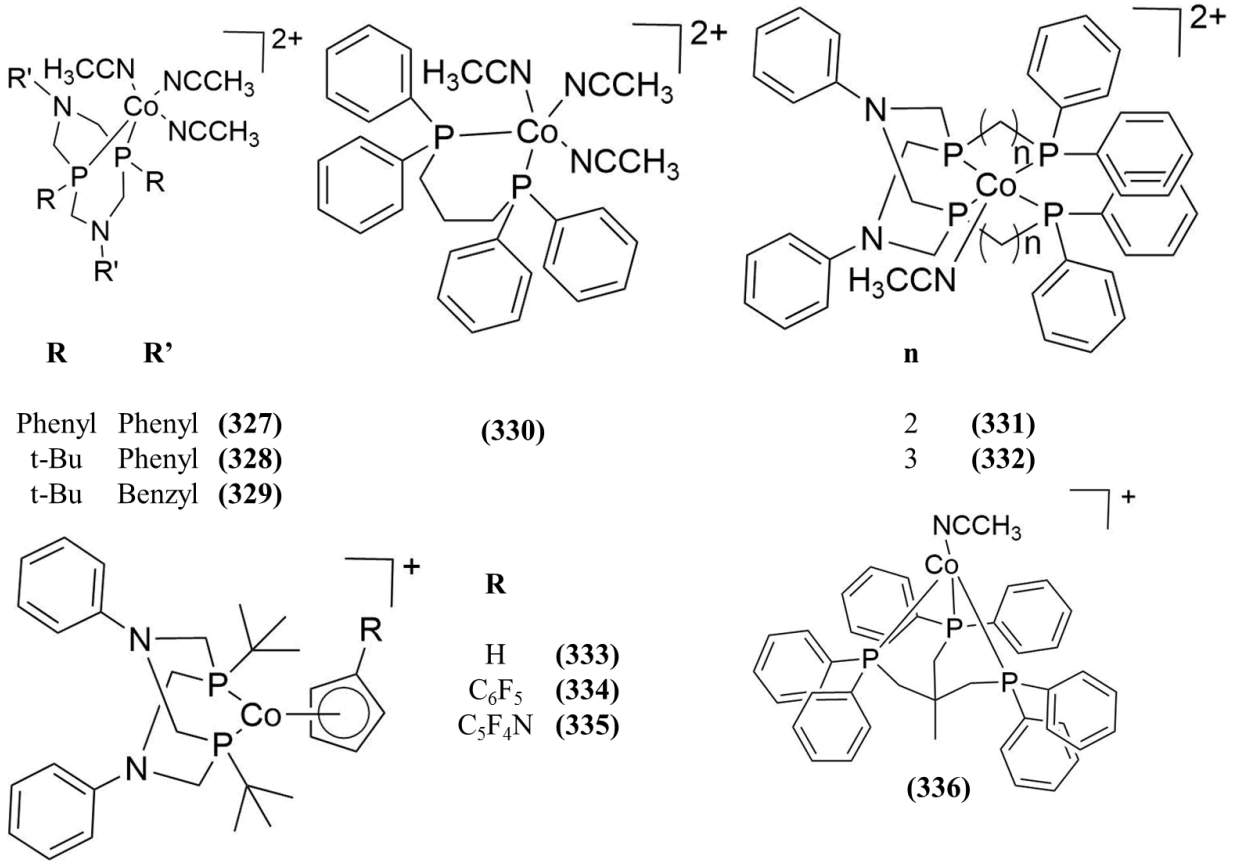

Figure 1.76: Co di-, tri- and tetraphos complexes studied towards electrocatalytic H^+ reduction

Following the aforementioned study, the focus shifted to developing a more stable Co phosphine catalyst [377]. The group synthesised two new Co complexes bearing tetraphosphine ligands (Figure 1.76), namely **(331)** and **(332)**. **(331)** was chemically reduced with potassium graphite (KC_8), yielding the Co^{1+} complex. The reduced complex further reacted with bromoanilinium tetrafluoroborate to yield the H-Co^{3+} **(331)** complex. The hydride was stated to be indefinitely stable in solid form or in N_2-purged MeCN, vastly contrasting to the behaviour of **(328)** and **(329)**. **(332)** was also stated to react with KC_8, and subsequently, with bromoanilinium tetrafluoroborate.

In a later publication, the group reported the electrocatalysis of H^+ by **(331)** and **(332)** (Figure 1.76) [378]. Both complexes exhibited catalytic enhancement, with onsets at

approximately -1.4 or -1.2 V vs Fc/Fc^+ respectively with the additions of dimethylformamide-trifluoromethanesulfonic acid/DMF ($[(DMF)H^+]$:DMF), 1:1 ratio or bromoanilinium tetrafluoroborate. The addition of water to the solvent mix allowed for further enhancement of catalytic current. **(332)** produced 101% (± 5%) FE upon electrolysis at -1.4 V vs Fc/Fc^+ using a reticulated vitreous carbon electrode in MeCN with 0.25 M $[(DMF)H^+]$ and 0.25 M DMF. The TON, based on bulk concentration, equates to 10.6.

A further approach to the improvement of Co phosphines combines those of Wiedner *et al*. [321] with the earlier work of Koelle *et al*. regarding Co cyclopentadienyl phosphines [323]. This resulted in the electrocatalytic activity assessment of **(333)**, **(334)** and **(335)** (Figure 1.76) [379]. Introduction of the more electron withdrawing perfluoropyridyl and perfluorophenyl groups on the Cp ligand shifted the $Co^{3+/2+}$ $E_{1/2}$ from -0.51 V to -0.26 V and -0.35 V vs Fc/Fc^+ respectively, with the $Co^{2+/1+}$ $E_{1/2}$ shifting from -1.25 V to -0.95 and -1.07 V respectively. The complexes were observed to undergo the same chemical reductions and protonations of **(331)** and **(332)** (*vide supra*). However, the Co^{3+} hydride of **(335)**, in contrast to the other complexes, appeared to show slow decomposition in MeCN at room temperature. A blue colour was noted in addition to NMR signals associated with a paramagnetic species.

Voltammetry of **(335)** in MeCN with 10 equivalents of [DMF(H)]OTf monitored over 100 minutes showed that degradation of the complex to $[Co(CH_3CN)_6]^{2+}$ occurred. This degradation shifted the catalytic current positively (from E_{pc} of -1.53 to -1.26 V vs Fc/Fc^+). With the use of a weaker acid, p-anisidium tetrafluoroborate, decomposition was not observed. A four minute electrolysis of **(335)** in MeCN with 100-fold excess of p-anisidium tetrafluoroborate at -1.6 V vs Fc/Fc^+ with a reticulated carbon electrode produced a FE of 97%. **(333)** and **(334)** were stated to show an enhancement for H^+ reduction in MeCN with the addition of [DMF(H)]OTf at the reduction potential of the Co^{3+}-hydride species (approximately -1.96 and -1.73 V vs Fc/Fc^+ respectively). As these potentials overlapped with that of [DMF(H)]OTf's reduction at the bare electrode, the complexes were not further investigated. Furthermore, **(333)** did not show any voltammetric enhancement with 110 equivalents of water alone.

Marinescu *et al*. studied **(336)** (Figure 1.76) in MeCN [380]. Additions of up to 11.3 equivalents of tosic acid monohydrate resulted in a catalytic current enhancement at the

$Co^{1+/0}$ reduction with i/i_p of 9.5 at approximately -1.8 V vs Fc/Fc^+. Some current enhancement was also shown at approximately -1 V (negative of the $Co^{2+/1+}$ reduction). Electrolysis of the complex in the presence of 20 equivalents of tosic acid produced a Faradaic efficiency of 99%. 9.5 C was consumed, corresponding to approximately 2.5 TONs over the course of the 2 hours at a glassy carbon plate electrode.

Van der Meer *et al*. assessed the voltammetric responses of **(337)**, **(338)** and **(339)** (Figure 1.77) in MeCN with the addition of acetic acid [381]. The first reduction within each complex occurred with E_{pc} of -1.13, -1.09 and -1.05 V vs Fc/Fc^+ respectively. The second reductions however appeared at more varied potentials ($E_{1/2}$ of -1.58 and -1.38 V for **(337)** and **(338)** and E_{pc} of -1.84 V for **(339)**), leading to the assignation of the first reduction as $Co^{3+/2+}$, with the second as a ligand-based reduction. Despite the structural similarity between **(337)** and **(338)**, **(338)** displayed a poor response upon the introduction of acid whereas **(337)** showed a current enhancement at approximately the potential of the second reduction in the presence of acid. A voltammetric enhancement of **(339)** was also apparent approximately the second reduction, but this was attributed to direct proton reduction at the glassy carbon electrode. Bulk electrolysis of **(337)** at -1.54 V vs Fc/Fc^+ in MeCN with a 20-37 fold excess of acetic acid produced an average FE of 80%. Furthermore, stability of the catalyst in the presence of up to 50 equivalents of acetic acid was monitored by NMR and cyclic voltammetry. The complex was stated to show no decomposition up to 24 hours.

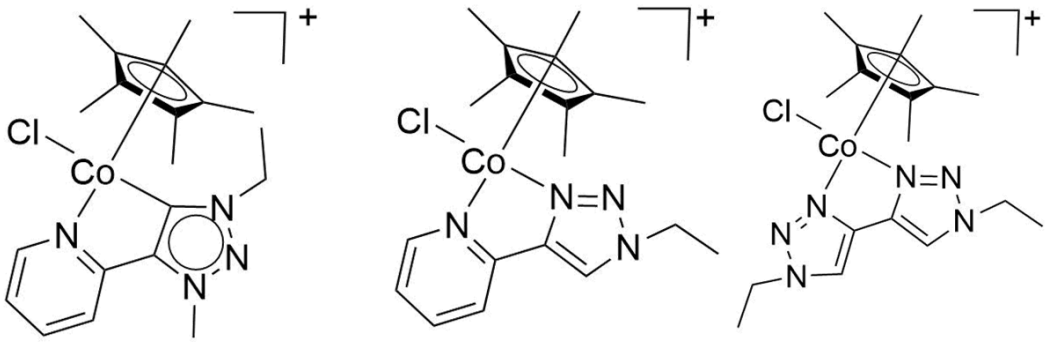

(337) **(338)** **(339)**

Figure 1.77: Co cyclopentadienyl triazolylidine complexes assessed towards electrocatalytic proton reduction

1.3.3.5. Co dithiolate complexes

In 2011, the ability of Co benzene dithiolate (**(340)**, Figure 1.78) to photocatalyse and electrocatalyse the reduction of protons was first reported by McNamara *et al*. [382]. The complex displayed a reversible reduction in MeCN with $TBAPF_6$. In MeCN/water (1:1) with 0.1 M KNO_3, the reduction (observed with $E_{1/2}$ at -1.01 V vs Fc/Fc^+) appeared to be quasireversible, though no enhancement due to the presence of water alone was apparent. Additions of TFA and tosic acid resulted in a catalytic current at -1.01 V vs Fc/Fc^+ in the MeCN/water solution. 0.2 mM of the complex produced a 99.7% Faradaic efficiency upon electrolysis at -1 V vs SCE with 65 mM tosic acid in a 0.1 M KNO_3, MeCN/H_2O 1:1 system. Smaller current enhancements were also stated in dry MeCN than that observed in the MeCN/H_2O 1:1 solution.

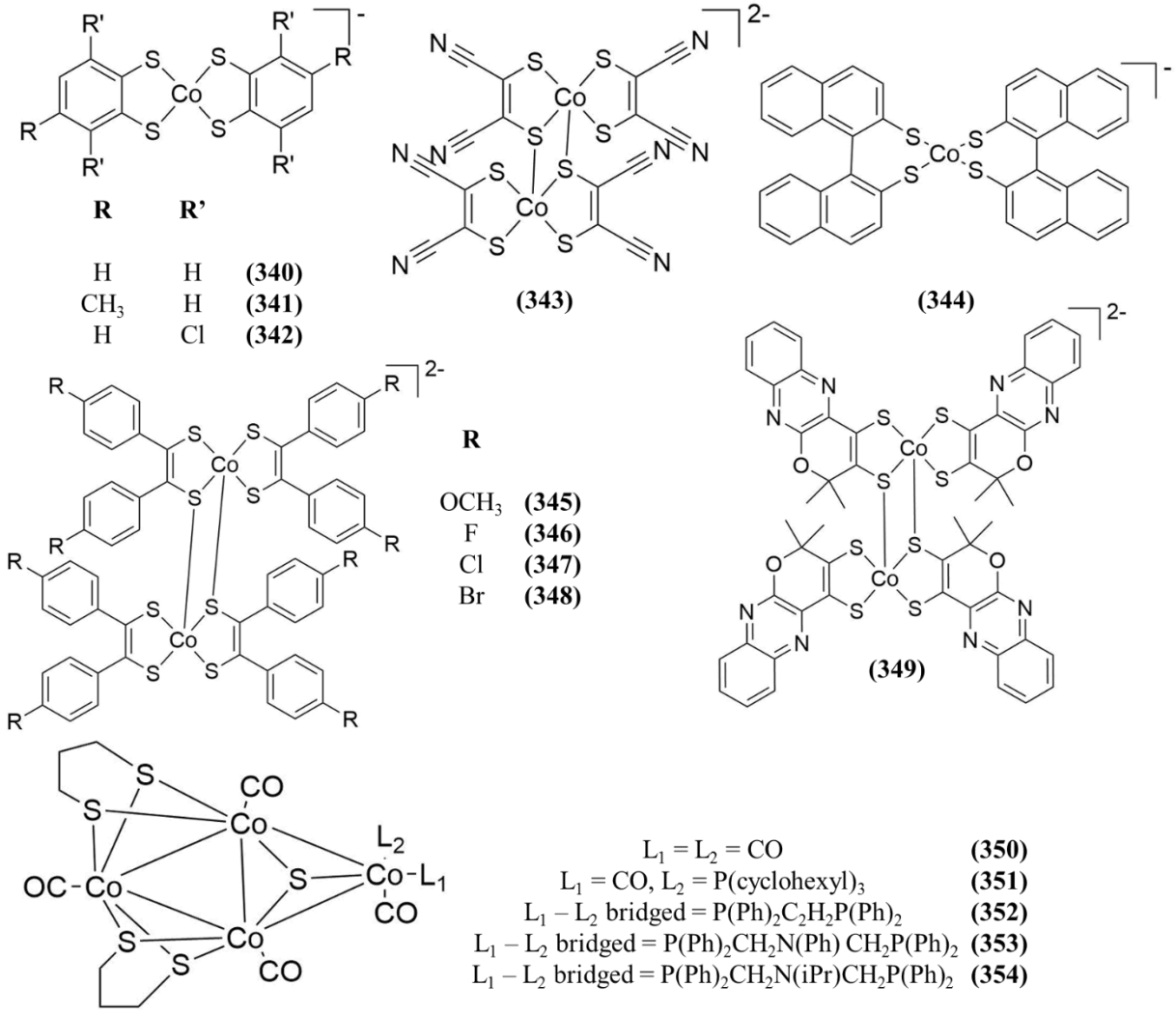

Figure 1.78: Co dithiolene complexes assessed towards electrocatalytic H_2 generation

A following report by the group assessed both the photo- and electrocatalytic activity of **(341)**, **(342)** and **(343)** (Figure 1.78) [383]. It was noted based on preceeding literature that although **(343)** crystallised as a dimer, when in solution and reduced, the complex existed predominantly as the monomeric dianion. The first reduction of **(340)**, **(341)**, **(342)** and **(343)** were observed with $E_{1/2}$ of -0.64, -0.7, -0.51 and -0.04 V vs SCE respectively in MeCN/H_2O 1:1 v/v. Upon the addition of TFA, both **(342)** and **(343)** demonstrated catalytic behaviour, albeit cathodic of the potential of the first reduction (at approximately -0.76 and -1.4 V vs SCE respectively). **(341)**, akin to **(340)**, exhibited a catalytic onset at approximately the first reduction. Electrolyses were undertaken at -1 V vs SCE with 0.2 mM of complex and 65 mM tosic acid in MeCN/H_2O 1:1 with 0.1 M KNO_3, whereby > 95% FEs were stated.

Rao *et al*. modified the structure, producing **(344)** (Figure 1.78) and its nickel analogue [384]. To gain a greater understanding of the complex' activity in a photocatalytic system, electrochemistry of the complex was undertaken initially in a 1:1 MeCN/H_2O solution containing 0.1 M KNO_3. A reversible reduction was observed with $E_{1/2}$ of -0.72 V vs SCE. Upon the introduction of TFA, a catalytic wave was observed at potentials more negative than the initial reduction (as was observed within the cases of **(342)** and **(343)**, *vide supra* [383]). A previous computational study on **(340)** and **(343)** concluded that a second reduction, resultant from the protonation of two or one sulphur atom(s) respectively, was likely required for catalysis to occur [385]. No electrolyses were undertaken with **(344)**.

Dimeric Co dithiolate complexes **(345)**, **(346)**, **(347)** and **(348)** (Figure 1.78) were assessed for their electrocatalytic ability to reduce protons to H_2 [386]. Cyclic voltammetry of the complexes revealed three reductions, with the third reduction occurring with $E_{1/2}$ of -1.48, -1.33, -1.28 and -1.27 V vs Fc/Fc^+ in DMF for the MeO-, F-, Cl-, and Br-substituted complexes respectively. Upon the introduction of anilinium tetrafluoroborate to **(348)** in DMF, a catalytic current was observed with E_p of -1.45 V. Electrolysis at -1.47 V vs Fc/Fc^+ under these conditions produced H_2 with a FE of 90%. The electrocatalytic behaviour of **(347)** was stated to be identical to the bromo analogue. For the same catalyst and acid addition concentrations, **(345)** and **(346)** appeared to show a higher degree of catalytic current by voltammetry than did **(348)**, although at more negative potentials ($E_{p/2}$ values of -1.46 and -1.37 V vs Fc/Fc^+ respectively). **(348)** did not show a catalytic response by voltammetry when up to 130 equivalents of the

weaker dichloroacetic acid was utilised. In contrast, catalytic enhancement was observed in the voltammetry of **(345)**, though a cathodic shift of 60 mV was observed in the $E_{p/2}$.

Fogeron *et al*. assessed the photocatalytic and electrocatalytic ability of **(349)** (Figure 1.78) [387]. In MeCN, the complex exhibited three reductions (with $E_{1/2}$s of 0.03 V, -0.51 V and -2 V vs Ag/AgCl). Upon the addition of acetic acid, a catalytic current was observed, with the E_p, $E_{p/2}$ and onset potentials of -1.75 V, -1.45 V and -1 V. Protonation of the ligand, following the second reduction, was believed to be responsible for the potential at which catalysis occurred. Electrolysis of the complex (1 mM) was undertaken at -1.6 V vs Ag/AgCl, using a mercury electrode in MeCN with 100 equivalents of acetic acid. Over the course of 6 hours, an 88% efficiency was recorded following 40 TONs. A lower concentration of catalyst (0.1 mM) produced 270 and 700 TONs following 6 and 22 hours of electrolysis (i.e. TOF of 45 and 32 hr^{-1}) respectively, corresponding to 90% FE.

A tetracobalt carbonyl cluster, **(350)**, bearing propane-dithiolate linkers (Figure 1.78) and four additional complexes, bearing a further mono- (**(351)**) or di-phosphine ligand (**(352)**, **(353)** and **(354)**) were assessed by Li *et al*. [388]. Each of the complexes exhibited catalytic enhancement to voltammetry upon the addition of TFA to the complexes in THF. Enhancement occurred either at the first reduction, between the first and second reductions, or at the second reduction, whereby onset potentials spanned between -1.5 V and -2 V vs Fc/Fc^+. Electrolysis of the complexes was performed between -2.15 and -2.45 V vs Fc/Fc^+ to verify the production of H_2, however FEs were not specified.

1.3.3.6. Other Co complexes

A Co anilinosalen (**(355)**) was reported as the precursor to an active electrocatalyst (**(356)**) by Kochem *et al*. [389] (Figure 1.79). Upon the addition of two equivalents of $HBF_4.Et_2O$ to **(355)**, **(356)** was obtained quantitatively. Protonation of the complex allowed for an anodic shift in potential of approximately 1 V of the $Co^{2+/1+}$ process (-2.26 V vs Fc/Fc^+ in MeCN for **(355)**). With 200 equivalents of p-cyanoanilinium tetrafluoroborate present, **(355)** demonstrated a catalytic wave beginning at

approximately -1.2 V. Electrolysis of the complex at a 3.4 cm^2 glassy carbon electrode, poised at either -1.8 or -1.9 V for 3.7 hours in MeCN with 100 equivalents of p-cyanoanilinium tetrafluoroborate produced the charge equivalent to 60 TONs. However, though H_2 was detected, FE was not specified.

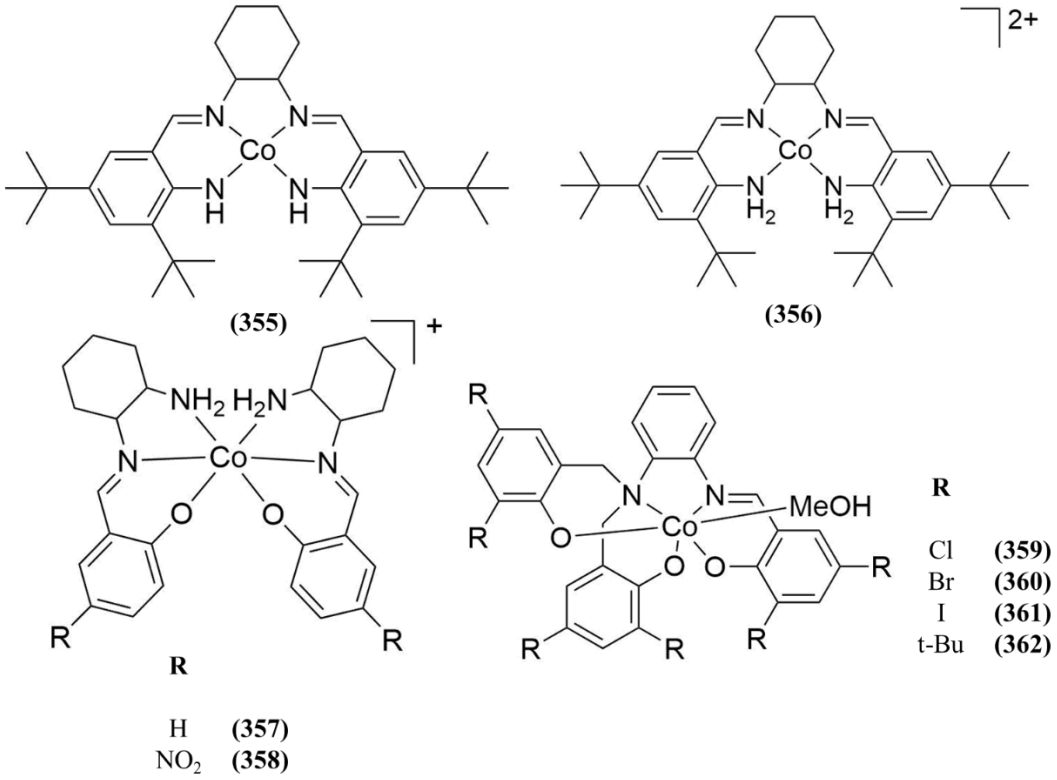

Figure 1.79: Co salen-related complexes utilised towards electrocatalytic proton reduction

Armstrong *et al*. synthesied and assessed the Schiff base complexes **(357)** and **(358)** (Figure 1.79) in MeCN [390]. The addition of TFA to **(357)** produced a slight increase in voltammetric current at approximately -1.23 V vs Fc/Fc^+. However, no H_2 was detected upon electrolysis. In contrast, **(358)** permitted a significant current enhancement at approximately -1.1 V upon the introduction of TFA. Electrolysis of the complex at -1.2 V vs Fc/Fc^+ in the presence of TFA produced H_2 with a FE of 98%. Furthermore, the inclusion of 200 μl water to the catalyst in MeCN with 11 mM TFA allowed for a further enhancement to the reduction at approximately -1.2 V. The authors suspect that protonation of the complex may occur on the phenolate or amine moieties.

Considering that the complex is initially coordinatively saturated, partial ligand dissociation may proceed, followed by catalysis.

Basu *et al*. explored the Co^{3+} phenolate-rich complexes **(359)**, **(360)**, **(361)** and **(362)** (Figure 1.79), as compared to the related Co salophens [358]. The potentials of the attributed $Co^{3+/2+}$ reduction was not shown to shift significantly with either Cl, Br, I or t-Bu substitution. However, the ligand based reduction shifted from $E_{1/2}$ of -2.03 V vs Fc/Fc^{+} for the most electron withdrawn **(359)** to -2.55 for the electron donated **(362)**. Studies focused on the Cl and t-Bu substituted complexes as a result. Upon the addition of acetic acid, a catalytic wave appeared within both complexes at approximately the potentials of their associated ligand reductions. A three hour electrolysis of **(359)** in MeCN with ten equivalents of acetic acid at a Hg pool electrode held at -2.2 V vs Fc/Fc^{+} produced a TON of 10.8 with 85% efficiency. Under identical conditions, the blank experiment generated 16 times less H_2. UV-visible spectra of **(359)** reduced electrochemically (prior to the ligand based reduction) and the solution of **(359)** with acetic acid following electrocatalysis both showed a similar band in the region greater than 400 nm. No deposit was stated to be observed on the electrode following electrolysis. Enhancement with **(362)** occurred at potentials too negative to allow for CPE experiments in the presence of acids.

The group of Zhan have reported several complexes for the electrocatalytic reduction of protons in both MeCN/DMF and aqueous solution. The reports are summarised together due to the close degree of similarity of the studies. The complexes assessed were of **(363)** [391], **(364)** [392], **(365)** [393], **(366)** [394], **(367)** [395], **(368)** [396], **(369)** [397], **(370)** [398], **(371)** [399], **(372)** [400], **(373)** [401], **(374)** [402], **(375)** [403], **(376)** [404], **(377)** [405] and **(378)** [406] (Figure 1.80). All of the complexes were shown by voltammetry to undergo some enhancement of current following the addition of acetic acid.

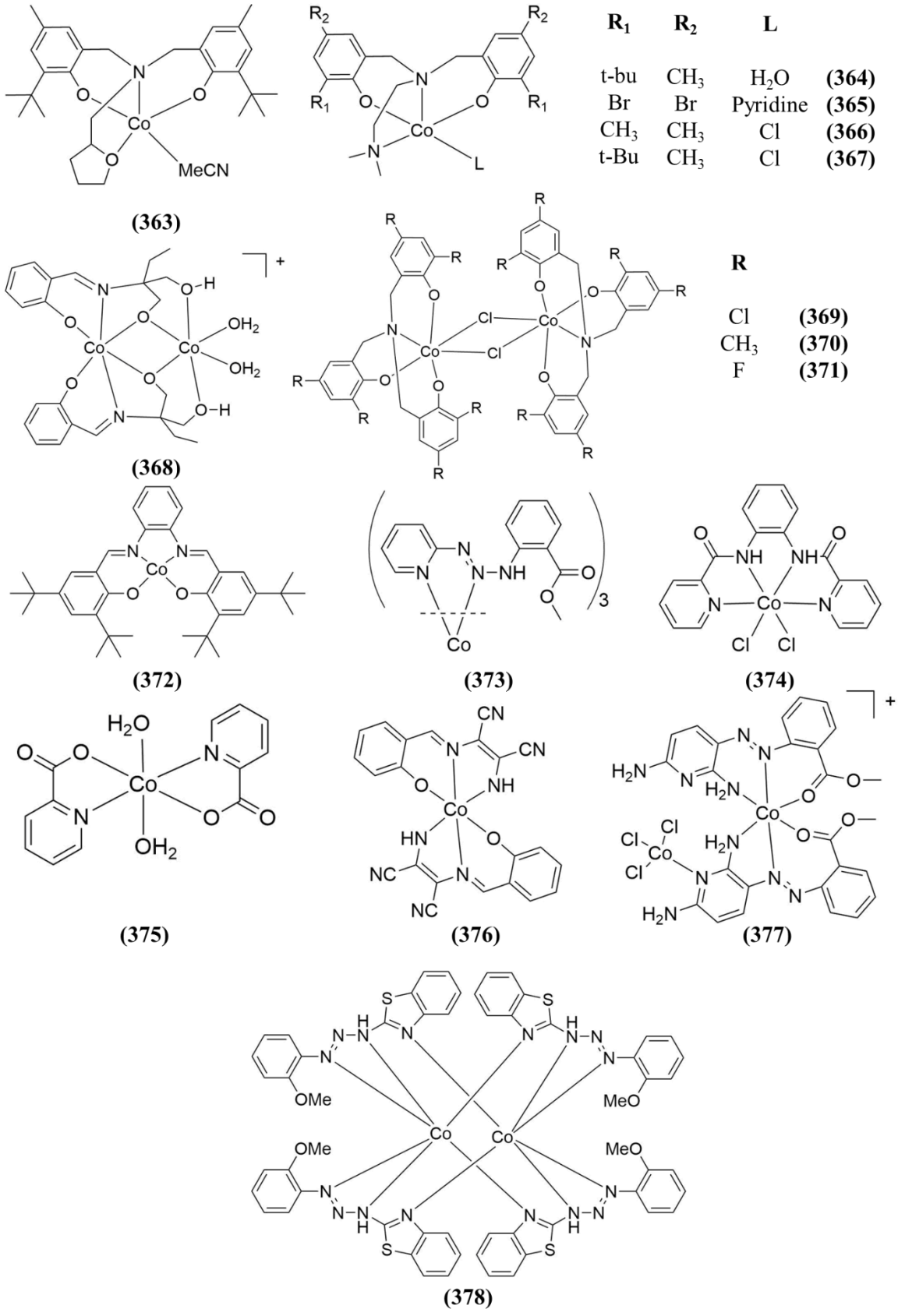

Figure 1.80: The similarly reported Co complexes of Zhan *et al*. [391–406] towards electrocatalytic H^+ reduction

Section 1.3.1 provided a summary of intramolecular approaches as utilised towards photocatalytic CO_2 reduction. Particularly relevant to the research undertaken within chapter two is section 1.3.1.1.2, which summarises Ru-Re systems for this purpose. Ru-Re approaches constitute a large proportion of intramolecular CO_2 reduction photocatalysts.

Section 1.3.2 provided a backdrop to the molecularly defined electrocatalytic CO_2 reduction studies undertaken within chapter three. As is shown by the volume of publications included within this review, with particular emphasis on recent studies (2014 -) of first row transition metal complexes, the area of molecular electrocatalytic CO_2 reduction has become increasingly active. Researchers have shown a particularly strong interest in Mn diimine based complexes.

Section 1.3.3 provided an overview of Co-centred complexes towards electrocatalytic H_2 generation, primarily in organic electrolytes. Particularly pertinent to the work within chapter four are examples of deligation, with the production of active heterogeneous electrocatalysts (see for example section 1.3.3.2).

1.4. References

[1] S. Solomon, D. Qin, M. Manning, Z. Chen, M. Marquis, K. Averyt, M. Tignor, *Climate Change 2007: The Physical Science Basis - Contribution of Working Group I to the Fourth Assessment Report of the Intergovernmental Panel on Climate Change*, **2007**.

[2] W. C. Wang, Y. L. Yung, A. A. Lacis, T. Mo, J. E. Hansen, *Science* **1976**, *194*, 685–690.

[3] R. T. Pierrehumbert, *Principles of Planetary Climate*, Cambridge University Press, **2010**.

[4] J. K. Casper, *Greenhouse Gases: Worldwide Impacts*, Infobase Publishing, **2010**.

[5] *Intergovernmental Panel on Climate Change). 2013. Climate Change 2013: The Physical Science Basis. Working Group I Contribution to the IPCC Fifth Assessment Report. Cambridge, United Kingdom: Cambridge University Press. Available Online at: Https://Www.ipcc.ch/Pdf/Assessment-Report/ar5/wg1/WG1AR5_SPM_FINAL.pdf, Last Accessed 16 Mar 2017*

[6] US National Oceanographic and Atmospheric Administration, "ESRL Global Monitoring Division - Global Greenhouse Gas Reference Network," can be found under https://www.esrl.noaa.gov/gmd/ccgg/trends/full.html and ftp://aftp.cmdl.noaa.gov/products/trends/co2/co2_annmean_mlo.txt, last accessed 16 Mar 2017

[7] United Nations Framework Convention on Climate Change, "Kyoto Protocol Reference Manual on Accounting of Emissions and Assigned Amounts," can be found under http://unfccc.int/kyoto_protocol/items/3145.php last accessed 17 Mar 2017

[8] NASA, Goddard Institute for Space Studies (GISS), "Global surface temperature | NASA Global Climate Change," can be found under https://climate.nasa.gov/vital-signs/global-temperature, Last accessed 17 Mar 2017

[9] C. Field, V. Barros, D. Dokken, K. Mach, M. Mastrandrea, T. Bilir, M. Chatterjee, K. Ebi, Y. Estrada, R. Genova, et al., **2014**.

[10] World Meterological Organisation, *WMO Statement on the State of the Global Climate in 2016*, **2017**.

[11] P. U. Clark, J. D. Shakun, S. A. Marcott, A. C. Mix, M. Eby, S. Kulp, A. Levermann, G. A. Milne, P. L. Pfister, B. D. Santer, et al., *Nat. Clim. Change* **2016**, *6*, 360–369.

[12] European Union, "Climate change consequences," can be found under https://ec.europa.eu/clima/change/consequences_en, Last accessed 17 Mar 2017, **2016**.

[13] National Oceanic and Atmospheric Administration (NOAA), "Ocean Acidification," can be found under https://www.pmel.noaa.gov/co2/story/Ocean+Acidification, Last accessed 17 Mar 2017

[14] D. Cressey, *Nat. News* **2016**, DOI 10.1038/nature.2016.19747.

[15] United Nations, Department of Economic and Social Affairs, Population Division, *World Population Prospects: The 2015 Revision, Key Findings and Advance Tables.*, **2015**.

[16] US Energy Information Administration (EIA), *International Energy Outlook 2016*, **2016**.

[17] World Bank Group, *World Development Indicators 2016: Highlights*, **2016**.

[18] *European Commission, 2015, 2020 Climate and Energy Package, Available Online at Http://Ec.europa.eu/Clima/Policies/Roadmap/Index_en.htm*
[19] European Comission, *Communication from the Commission to the European Parliament, the Council, the European Economic and Social Committee and the Committee of the Regions: Taking Stock of the Europe 2020 Strategy for Smart, Sustainable and Inclusive Growth*, **2014**.
[20] European Commission, *Communication from the Commission to the European Parliament, the Council, the European Economic and Social Committee and the Committee of the Regions: A Policy Framework for Climare and Energy in the Period from 2020 to 2030*, **2014**.
[21] European commission, *Eurostat Demography Report*, **2015**.
[22] "World Energy Statistics | World Energy Consumption & Stats," can be found under https://yearbook.enerdata.net/ Last accessed 19 Mar 2017
[23] European Commission, "Paris Agreement," can be found under https://ec.europa.eu/clima/policies/international/negotiations/paris_en Last assessed 19 Mar 2017, **2016**.
[24] V. Ramanathan, Y. Xu, *Proc. Natl. Acad. Sci.* **2010**, *107*, 8055–8062.
[25] J. Tollefson, *Nat. News* **2009**, DOI 10.1038/news.2009.1156.
[26] Irish Government, "Summary of Budget Measures for 2010," can be found under http://www.budget.gov.ie/Budgets/2010/Summary.aspx Last accessed 20 Mar 2017, **2009**.
[27] Irish Government, "Budget 2012 - Financial Statement by the Minister for Finance," can be found under http://www.budget.gov.ie/Budgets/2012/FinancialStatement.aspx#section18 Last accessed 20 Mar 2017, **2011**.
[28] Irish Government, "Budget 2013 - Financial Statement by the Minister for Finance," can be found under http://www.budget.gov.ie/Budgets/2013/FinancialStatement.aspx Last accessed 20 Mar 2017, **2012**.
[29] British Petroleum, *BP Statistical Review of World Energy 2016 - BP Global*, **2016**.
[30] C. Sun, X. Zhu, *Energy Policy* **2014**, *69*, 397–405.
[31] M. Rahu, *Eur. J. Cancer* **2003**, *39*, 295–299.
[32] T. Perko, *J. Environ. Radioact.* **2014**, *133*, 86–91.
[33] C. Keller, V. Visschers, M. Siegrist, *Risk Anal.* **2012**, *32*, 464–477.
[34] Irish Government, Dept of Health, "Decision to Discontinue the Future Distribution of Iodine Tablets | Department of Health," can be found under http://health.gov.ie/blog/press-release/decision-to-discontinue-the-future-distribution-of-iodine-tablets/ Last accessed 20 Mar 17, **2008**.
[35] Irish Government, "Irish Statute Book, Electricity Regulation Act, 1999, Section 18," can be found under http://www.irishstatutebook.ie/eli/1999/act/23/section/18/enacted/en/html#sec18 Last accessed Mar 2017, **1999**.
[36] Economic and Social Research Institute (ESRI), J Curtis, E Morgenroth and B Coyne, *The Potential Economic Impact of a Nuclear Accident - An Irish Case Study*, **2017**.
[37] Sustainable Energy Authority of Ireland (SEAI), *Energy in Ireland - 2016 Report*, **2016**.
[38] C. Maeda, Y. Miyazaki, T. Ema, *Catal. Sci. Technol.* **2014**, *4*, 1482.
[39] C. Riplinger, E. A. Carter, *ACS Catal.* **2015**, *5*, 900–908.
[40] K. Li, A. D. Handoko, M. Khraisheh, J. Tang, *Nanoscale* **2014**, *6*, 9767–9773.

[41] S. Sato, T. Arai, T. Morikawa, *Inorg. Chem.* **2015**, *54*, 5105–5113.
[42] R. D. Richardson, E. J. Holland, B. K. Carpenter, *Nat Chem* **2011**, *3*, 301–303.
[43] F. Sarsekeyeva, B. K. Zayadan, A. Usserbaeva, V. S. Bedbenov, M. A. Sinetova, D. A. Los, *Photosynth. Res.* **2015**, *125*, 329–340.
[44] Dept. of Communications, Energy and natural resources, *Ireland's Transition to a Low Carbon Energy Future – 2015-2030*, **2015**.
[45] Energy Research Strategy Group, *Energy Innovation Ireland: A Strategy Document Produced by The Energy Research Strategy Group For the Minister for Communications, Energy and Natural Resources*, **2016**.
[46] Sustainable Energy Authority of Ireland (SEAI), *Best Practice Guide - Photovoltaics (PV)*, **2010**.
[47] NASA, "Measuring Solar Insolation : Image of the Day," can be found under https://earthobservatory.nasa.gov/IOTD/view.php?id=1355 Last accessed 20 Mar 2017, **2001**.
[48] S. Meister, R. O. Reithmeier, M. Tschurl, U. Heiz, B. Rieger, *ChemCatChem* **2015**, *7*, 690–697.
[49] M. Pschenitza, S. Meister, A. von Weber, A. Kartouzian, U. Heiz, B. Rieger, *ChemCatChem* **2016**, *8*, 2688–2695.
[50] Y. Shi, B. Zhang, *Chem. Soc. Rev.* **2016**, *45*, 1529–1541.
[51] N. Armaroli, V. Balzani, *ChemSusChem* **2011**, *4*, 21–36.
[52] W. T. Eckenhoff, W. R. McNamara, P. Du, R. Eisenberg, *Biochim. Biophys. Acta BBA - Bioenerg.* **2013**, *1827*, 958–973.
[53] "Toyota recalls all fuel-cell Mirai vehicles," can be found under https://phys.org/news/2017-02-toyota-recalls-fuel-cell-mirai-vehicles.html Last accessed 21 Mar 2017, **2017**.
[54] US Department of energy, "Alternative Fuels Data Center: Hydrogen Fueling Infrastructure Development," can be found under http://www.afdc.energy.gov/fuels/hydrogen_infrastructure.html Last accessed 21 Mar 2017
[55] R. O. Reithmeier, S. Meister, B. Rieger, A. Siebel, M. Tschurl, U. Heiz, E. Herdtweck, *Dalton Trans.* **2014**, *43*, 13259–13269.
[56] H. Rao, J. Bonin, M. Robert, *Chem. Commun.* **2017**, DOI 10.1039/C6CC09967J.
[57] A. B. Ricks, G. C. Solomon, M. T. Colvin, A. M. Scott, K. Chen, M. A. Ratner, M. R. Wasielewski, *J. Am. Chem. Soc.* **2010**, *132*, 15427–15434.
[58] G. Sahara, O. Ishitani, *Inorg. Chem.* **2015**, *54*, 5096–5104.
[59] H. Takeda, K. Koike, T. Morimoto, H. Inumaru, O. Ishitani, in *Adv. Inorg. Chem.* (Ed.: R. van E. and G. Stochel), Academic Press, **2011**, pp. 137–186.
[60] H. Takeda, K. Koike, H. Inoue, O. Ishitani, *J. Am. Chem. Soc.* **2008**, *130*, 2023–2031.
[61] T. Morimoto, T. Nakajima, S. Sawa, R. Nakanishi, D. Imori, O. Ishitani, *J. Am. Chem. Soc.* **2013**, *135*, 16825–16828.
[62] Y. Yamazaki, H. Takeda, O. Ishitani, *J. Photochem. Photobiol. C Photochem. Rev.* **2015**, *25*, 106–137.
[63] A. J. Morris, G. J. Meyer, E. Fujita, *Acc. Chem. Res.* **2009**, *42*, 1983–1994.
[64] S. Rau, D. Walther, J. G. Vos, *Dalton Trans.* **2007**, 915–919.
[65] V. Balzani, A. Juris, M. Venturi, S. Campagna, S. Serroni, *Chem. Rev.* **1996**, *96*, 759–834.
[66] K. Koike, S. Naito, S. Sato, Y. Tamaki, O. Ishitani, *J. Photochem. Photobiol. Chem.* **2009**, *207*, 109–114.

[67] J. Schneider, H. Jia, J. T. Muckerman, E. Fujita, *Chem Soc Rev* **2012**, *41*, 2036–2051.
[68] J. Y. Becker, B. Vainas, R. E. (née Levin), L. K. (Née Orenstein), *J. Chem. Soc., Chem. Commun.* **1985**, 1471–1472.
[69] D. J. Boston, Y. M. F. Pachón, R. O. Lezna, N. R. de Tacconi, F. M. MacDonnell, *Inorg. Chem.* **2014**, *53*, 6544–6553.
[70] J. Shen, R. Kortlever, R. Kas, Y. Y. Birdja, O. Diaz-Morales, Y. Kwon, I. Ledezma-Yanez, K. J. P. Schouten, G. Mul, M. T. M. Koper, *Nat. Commun.* **2015**, *6*, 8177.
[71] K. Kobayashi, T. Kikuchi, S. Kitagawa, K. Tanaka, *Angew. Chem. Int. Ed.* **2014**, *53*, 11813–11817.
[72] M. B. Chambers, X. Wang, N. Elgrishi, C. H. Hendon, A. Walsh, J. Bonnefoy, J. Canivet, E. A. Quadrelli, D. Farrusseng, C. Mellot-Draznieks, et al., *ChemSusChem* **2015**, *8*, 603–608.
[73] H. Fei, M. D. Sampson, Y. Lee, C. P. Kubiak, S. M. Cohen, *Inorg. Chem.* **2015**, *54*, 6821–6828.
[74] B. H. Mahan, *J. Chem. Phys.* **1960**, *33*, 959–965.
[75] R. R. Reeves, P. Harteck, B. A. Thompson, R. W. Waldron, *J. Phys. Chem.* **1966**, *70*, 1637–1640.
[76] P. Warneck, *J. Chem. Phys.* **1964**, *41*, 3435–3439.
[77] C. D. Windle, E. Pastor, A. Reynal, A. C. Whitwood, Y. Vaynzof, J. R. Durrant, R. N. Perutz, E. Reisner, *Chem. – Eur. J.* **2015**, *21*, 3746–3754.
[78] K. Sekizawa, K. Maeda, K. Domen, K. Koike, O. Ishitani, *J. Am. Chem. Soc.* **2013**, *135*, 4596–4599.
[79] *JC Hummelen, University of Groningen, Http://Www.rug.nl/Sciencelinx/Nieuws/20120702hummelen_natpho?lang=en Date Last Accessed 23 Mar 2017*
[80] Y. Tamaki, K. Koike, T. Morimoto, O. Ishitani, *J. Catal.* **2013**, *304*, 22–28.
[81] Y. Tamaki, K. Watanabe, K. Koike, H. Inoue, T. Morimoto, O. Ishitani, *Faraday Discuss.* **2012**, *155*, 115–127.
[82] Y. Kuramochi, K. Fukaya, M. Yoshida, H. Ishida, *Chem. – Eur. J.* **2015**, *21*, 10049–10060.
[83] J. Bonin, M. Robert, M. Routier, *J. Am. Chem. Soc.* **2014**, *136*, 16768–16771.
[84] T. Ogata, S. Yanagida, B. S. Brunschwig, E. Fujita, *J. Am. Chem. Soc.* **1995**, *117*, 6708–6716.
[85] T. Ogata, Y. Yamamoto, Y. Wada, K. Murakoshi, M. Kusaba, N. Nakashima, A. Ishida, S. Takamuku, S. Yanagida, *J. Phys. Chem.* **1995**, *99*, 11916–11922.
[86] Y. Tamaki, K. Koike, T. Morimoto, Y. Yamazaki, O. Ishitani, *Inorg. Chem.* **2013**, *52*, 11902–11909.
[87] J. Rohacova, O. Ishitani, *Chem. Sci.* **2016**, *7*, 6728–6739.
[88] V. S. Thoi, N. Kornienko, C. G. Margarit, P. Yang, C. J. Chang, *J. Am. Chem. Soc.* **2013**, *135*, 14413–14424.
[89] S. L.-F. Chan, T. L. Lam, C. Yang, S.-C. Yan, N. M. Cheng, *Chem. Commun.* **2015**, *51*, 7799–7801.
[90] L. Chen, Z. Guo, X.-G. Wei, C. Gallenkamp, J. Bonin, E. Anxolabéhère-Mallart, K.-C. Lau, T.-C. Lau, M. Robert, *J. Am. Chem. Soc.* **2015**, *137*, 10918–10921.
[91] A. Rosas-Hernández, P. G. Alsabeh, E. Barsch, H. Junge, R. Ludwig, M. Beller, *Chem. Commun.* **2016**, *52*, 8393–8396.
[92] H. Takeda, K. Ohashi, A. Sekine, O. Ishitani, *J. Am. Chem. Soc.* **2016**, *138*, 4354–4357.

[93] A. Rosas-Hernández, C. Steinlechner, H. Junge, M. Beller, *Green Chem.* **2017**, DOI 10.1039/C6GC03527B.
[94] J. Bonin, M. Chaussemier, M. Robert, M. Routier, *ChemCatChem* **2014**, *6*, 3200–3207.
[95] H. Takeda, H. Koizumi, K. Okamoto, O. Ishitani, *Chem. Commun.* **2014**, *50*, 1491–1493.
[96] Y. Kuramochi, J. Itabashi, K. Fukaya, A. Enomoto, M. Yoshida, H. Ishida, *Chem. Sci.* **2015**, *6*, 3063–3074.
[97] J. L. Grant, K. Goswami, L. O. Spreer, J. W. Otvos, M. Calvin, *J. Chem. Soc. Dalton Trans.* **1987**, 2105–2109.
[98] E. Kimura, S. Wada, M. Shionoya, T. Takahashi, Y. Litaka, *J. Chem. Soc. Chem. Commun.* **1990**, 397–398.
[99] E. Kimura, X. Bu, M. Shionoya, S. Wada, S. Maruyama, *Inorg. Chem.* **1992**, *31*, 4542–4546.
[100] E. Fujita, S. J. Milder, B. S. Brunschwig, *Inorg. Chem.* **1992**, *31*, 2079–2085.
[101] K. Bujno, R. Bilewicz, L. Siegfried, T. A. Kaden, *J. Electroanal. Chem.* **1998**, *445*, 47–53.
[102] E. Kimura, S. Wada, M. Shionoya, Y. Okazaki, *Inorg. Chem.* **1994**, *33*, 770–778.
[103] C. Herrero, A. Quaranta, S. E. Ghachtouli, B. Vauzeilles, W. Leibl, A. Aukauloo, *Phys. Chem. Chem. Phys.* **2014**, *16*, 12067–12072.
[104] N. Komatsuzaki, Y. Himeda, T. Hirose, H. Sugihara, K. Kasuga, *Bull. Chem. Soc. Jpn.* **1999**, *72*, 725–731.
[105] B. Gholamkhass, H. Mametsuka, K. Koike, T. Tanabe, M. Furue, O. Ishitani, *Inorg. Chem.* **2005**, *44*, 2326–2336.
[106] Z.-Y. Bian, K. Sumi, M. Furue, S. Sato, K. Koike, O. Ishitani, *Inorg. Chem.* **2008**, *47*, 10801–10803.
[107] Z.-Y. Bian, K. Sumi, M. Furue, S. Sato, K. Koike, O. Ishitani, *Dalton Trans.* **2009**, 983–993.
[108] S. Meister, R. O. Reithmeier, A. Ogrodnik, B. Rieger, *ChemCatChem* **2015**, *7*, 3562–3569.
[109] H. Hori, O. Ishitani, K. Koike, F. P. A. Johnson, T. Ibusuki, *Energy Convers. Manag.* **1995**, *36*, 621–624.
[110] H. Hori, F. P. A. Johnson, K. Koike, O. Ishitani, T. Ibusuki, *J. Photochem. Photobiol. Chem.* **1996**, *96*, 171–174.
[111] K. Koike, H. Hori, M. Ishizuka, J. R. Westwell, K. Takeuchi, T. Ibusuki, K. Enjouji, H. Konno, K. Sakamoto, O. Ishitani, *Organometallics* **1997**, *16*, 5724–5729.
[112] S. Sato, K. Koike, H. Inoue, O. Ishitani, *Photochem. Photobiol. Sci.* **2007**, *6*, 454–461.
[113] A. Nakada, K. Koike, T. Nakashima, T. Morimoto, O. Ishitani, *Inorg. Chem.* **2015**, *54*, 1800–1807.
[114] A. Nakada, K. Koike, K. Maeda, O. Ishitani, *Green Chem.* **2016**, *18*, 139–143.
[115] Z.-Y. Bian, S.-M. Chi, L. Li, W. Fu, *Dalton Trans.* **2010**, *39*, 7884–7887.
[116] Z.-Y. Bian, H. Wang, W.-F. Fu, L. Li, A.-Z. Ding, *Polyhedron* **2012**, *32*, 78–85.
[117] K. Koike, J. Tanabe, S. Toyama, H. Tsubaki, K. Sakamoto, J. R. Westwell, F. P. A. Johnson, H. Hori, H. Saitoh, O. Ishitani, *Inorg. Chem.* **2000**, *39*, 2777–2783.
[118] H. Tsubaki, A. Sekine, Y. Ohashi, K. Koike, H. Takeda, O. Ishitani, *J. Am. Chem. Soc.* **2005**, *127*, 15544–15555.

[119] K. Ohkubo, Y. Yamazaki, T. Nakashima, Y. Tamaki, K. Koike, O. Ishitani, *J. Catal.* **2016**, *343*, 278–289.
[120] Y. Yamazaki, T. Morimoto, O. Ishitani, *Dalton Trans.* **2015**, *44*, 11626–11635.
[121] Y. Yamazaki, A. Umemoto, O. Ishitani, *Inorg. Chem.* **2016**, *55*, 11110–11124.
[122] E. Kato, H. Takeda, K. Koike, K. Ohkubo, O. Ishitani, *Chem Sci* **2015**, *6*, 3003–3012.
[123] T. Nakajima, Y. Tamaki, K. Ueno, E. Kato, T. Nishikawa, K. Ohkubo, Y. Yamazaki, T. Morimoto, O. Ishitani, *J. Am. Chem. Soc.* **2016**, *138*, 13818–13821.
[124] Y. Ueda, H. Takeda, T. Yui, K. Koike, Y. Goto, S. Inagaki, O. Ishitani, *ChemSusChem* **2015**, *8*, 439–442.
[125] K. Wada, M. Eguchi, O. Ishitani, K. Maeda, *ChemSusChem* **2017**, *10*, 287–295.
[126] G. Sahara, R. Abe, M. Higashi, T. Morikawa, K. Maeda, Y. Ueda, O. Ishitani, *Chem. Commun.* **2015**, *51*, 10722–10725.
[127] G. Sahara, H. Kumagai, K. Maeda, N. Kaeffer, V. Artero, M. Higashi, R. Abe, O. Ishitani, *J. Am. Chem. Soc.* **2016**, *138*, 14152–14158.
[128] J. Dietrich, U. Thorenz, C. Förster, K. Heinze, *Inorg. Chem.* **2013**, *52*, 1248–1264.
[129] Y. Tamaki, T. Morimoto, K. Koike, O. Ishitani, *Proc. Natl. Acad. Sci. U. S. A.* **2012**, *109*, 15673–15678.
[130] H. Ishida, T. Terada, K. Tanaka, T. Tanaka, *Inorg. Chem.* **1990**, *29*, 905–911.
[131] Y. Tamaki, K. Koike, O. Ishitani, *Chem. Sci.* **2015**, *6*, 7213–7221.
[132] Y. Tamaki, O. Ishitani, *ACS Catal.* **2017**, *7*, 3394–3409.
[133] A. Nakada, T. Nakashima, K. Sekizawa, K. Maeda, O. Ishitani, *Chem. Sci.* **2016**, *7*, 4364–4371.
[134] F. Yoshitomi, K. Sekizawa, K. Maeda, O. Ishitani, *ACS Appl. Mater. Interfaces* **2015**, *7*, 13092–13097.
[135] K. Maeda, K. Sekizawa, O. Ishitani, *Chem. Commun.* **2013**, *49*, 10127–10129.
[136] R. Kuriki, K. Sekizawa, O. Ishitani, K. Maeda, *Angew. Chem. Int. Ed.* **2015**, *54*, 2406–2409.
[137] R. Kuriki, H. Matsunaga, T. Nakashima, K. Wada, A. Yamakata, O. Ishitani, K. Maeda, *J. Am. Chem. Soc.* **2016**, *138*, 5159–5170.
[138] K. Muraoka, H. Kumagai, M. Eguchi, O. Ishitani, K. Maeda, *Chem. Commun.* **2016**, *52*, 7886–7889.
[139] Y. Kuramochi, O. Ishitani, *Inorg. Chem.* **2016**, *55*, 5702–5709.
[140] G. A. Andrade, A. J. Pistner, G. P. A. Yap, D. A. Lutterman, J. Rosenthal, *ACS Catal.* **2013**, *3*, 1685–1692.
[141] A. Loudet, K. Burgess, *Chem. Rev.* **2007**, *107*, 4891–4932.
[142] J. J. Teesdale, A. J. Pistner, G. P. A. Yap, Y.-Z. Ma, D. A. Lutterman, J. Rosenthal, *Catal. Today* **2014**, *225*, 149–157.
[143] C. Bruckmeier, M. W. Lehenmeier, R. Reithmeier, B. Rieger, J. Herranz, C. Kavakli, *Dalton Trans.* **2012**, *41*, 5026–5037.
[144] Y. Tamaki, D. Imori, T. Morimoto, K. Koike, O. Ishitani, *Dalton Trans.* **2016**, *45*, 14668–14677.
[145] J. Shakeri, H. Hadadzadeh, H. Tavakol, *Polyhedron* **2014**, *78*, 112–122.
[146] J. Hawecker, J.-M. Lehn, R. Ziessel, *Helv. Chim. Acta* **1986**, *69*, 1990–2012.
[147] T. Morimoto, C. Nishiura, M. Tanaka, J. Rohacova, Y. Nakagawa, Y. Funada, K. Koike, Y. Yamamoto, S. Shishido, T. Kojima, et al., *J. Am. Chem. Soc.* **2013**, *135*, 13266–13269.
[148] Y. Yamamoto, Y. Tamaki, T. Yui, K. Koike, O. Ishitani, *J. Am. Chem. Soc.* **2010**, *132*, 11743–11752.

[149] K. Kiyosawa, N. Shiraishi, T. Shimada, D. Masui, H. Tachibana, S. Takagi, O. Ishitani, D. A. Tryk, H. Inoue, *J. Phys. Chem. C* **2009**, *113*, 11667–11673.
[150] K. Kiyosawa, Ph. D dissertation, Tokyo Metropolitan University, **2009**.
[151] Y. Kou, S. Nakatani, G. Sunagawa, Y. Tachikawa, D. Masui, T. Shimada, S. Takagi, D. A. Tryk, Y. Nabetani, H. Tachibana, et al., *J. Catal.* **2014**, *310*, 57–66.
[152] C. D. Windle, M. V. Câmpian, A.-K. Duhme-Klair, E. A. Gibson, R. N. Perutz, J. Schneider, *Chem. Commun.* **2012**, *48*, 8189.
[153] C. D. Windle, M. W. George, R. N. Perutz, P. A. Summers, X. Z. Sun, A. C. Whitwood, *Chem. Sci.* **2015**, *6*, 6847–6864.
[154] J. Schneider, K. Q. Vuong, J. A. Calladine, X.-Z. Sun, A. C. Whitwood, M. W. George, R. N. Perutz, *Inorg. Chem.* **2011**, *50*, 11877–11889.
[155] C. Matlachowski, M. Schwalbe, *Dalton Trans.* **2015**, *44*, 6480–6489.
[156] C. Matlachowski, B. Braun, S. Tschierlei, M. Schwalbe, *Inorg. Chem.* **2015**, *54*, 10351–10360.
[157] Y. Kitagawa, H. Takeda, K. Ohashi, T. Asatani, D. Kosumi, H. Hashimoto, O. Ishitani, H. Tamiaki, *Chem. Lett.* **2014**, *43*, 1383–1385.
[158] Y. Kitagawa, S. Ogasawara, D. Kosumi, H. Hashimoto, H. Tamiaki, *Bull. Chem. Soc. Jpn.* **2015**, *88*, 346–351.
[159] Y. Kitagawa, S. Ogasawara, D. Kosumi, H. Hashimoto, H. Tamiaki, *J. Photochem. Photobiol. Chem.* **2015**, *311*, 104–111.
[160] R. O. Reithmeier, S. Meister, A. Siebel, B. Rieger, *Dalton Trans.* **2015**, *44*, 6466–6472.
[161] Y. Hori, R. Takahashi, Y. Yoshinami, A. Murata, *J. Phys. Chem. B* **1997**, *101*, 7075–7081.
[162] R. Senthil Kumar, S. Senthil Kumar, M. Anbu Kulandainathan, *Electrochem. Commun.* **2012**, *25*, 70–73.
[163] A. Bassegoda, C. Madden, D. W. Wakerley, E. Reisner, J. Hirst, *J. Am. Chem. Soc.* **2014**, *136*, 15473–15476.
[164] J. J. Walsh, G. Neri, C. L. Smith, A. J. Cowan, *Chem. Commun.* **2014**, *50*, 12698–12701.
[165] J. A. Ramos Sende, C. R. Arana, L. Hernandez, K. T. Potts, M. Keshevarz-K, H. D. Abruna, *Inorg. Chem.* **1995**, *34*, 3339–3348.
[166] E. Portenkirchner, J. Gasiorowski, K. Oppelt, S. Schlager, C. Schwarzinger, H. Neugebauer, G. Knör, N. S. Sariciftci, *ChemCatChem* **2013**, *5*, 1790–1796.
[167] J. Qiao, Y. Liu, F. Hong, J. Zhang, *Chem. Soc. Rev.* **2013**, *43*, 631–675.
[168] R. Angamuthu, P. Byers, M. Lutz, A. L. Spek, E. Bouwman, *Science* **2010**, *327*, 313–315.
[169] O. R. Inderwildi, S. J. Jenkins, D. A. King, *J. Phys. Chem. C* **2008**, *112*, 1305–1307.
[170] "Mantra Energy", available at: http://mantraenergy.com/mantra-energy/technology/erc-technology/. Last accessed 30 Jul 2015,
[171] "Liquid Light | Make carbon dioxide a practical feedstock for multi-carbon chemicals," can be found under http://llchemical.com/technology/ Last accessed 27 Mar 2017
[172] B. Kumar, J. M. Smieja, A. F. Sasayama, C. P. Kubiak, *Chem Commun* **2012**, *48*, 272–274.
[173] P. Kang, Z. Chen, A. Nayak, S. Zhang, T. J. Meyer, *Energy Environ. Sci.* **2014**, *7*, 4007–4012.
[174] J. D. Froehlich, C. P. Kubiak, *Inorg. Chem.* **2012**, *51*, 3932–3934.

[175] Z. Chen, P. Kang, M.-T. Zhang, T. J. Meyer, *Chem. Commun.* **2013**, *50*, 335–337.
[176] C. Delacourt, P. L. Ridgway, J. B. Kerr, J. Newman, *J. Electrochem. Soc.* **2008**, *155*, B42–B49.
[177] C. Costentin, S. Drouet, M. Robert, J.-M. Savéant, *J. Am. Chem. Soc.* **2012**, *134*, 11235–11242.
[178] N. Yang, S. R. Waldvogel, X. Jiang, *ACS Appl. Mater. Interfaces* **2015**, *8*, 28357–28371.
[179] C. Costentin, S. Drouet, M. Robert, J.-M. Savéant, *Science* **2012**, *338*, 90–94.
[180] C. Costentin, G. Passard, M. Robert, J.-M. Savéant, *Proc. Natl. Acad. Sci.* **2014**, *111*, 14990–14994.
[181] C. W. Machan, M. D. Sampson, C. P. Kubiak, *J. Am. Chem. Soc.* **2015**, *137*, 8564–8571.
[182] S. Aoi, K. Mase, K. Ohkubo, S. Fukuzumi, *Chem. Commun.* **2015**, *51*, 10226–10228.
[183] M. Bourrez, F. Molton, S. Chardon-Noblat, A. Deronzier, *Angew. Chem. Int. Ed.* **2011**, *50*, 9903–9906.
[184] S. Meshitsuka, M. Ichikawa, K. Tamaru, *J. Chem. Soc. Chem. Commun.* **1974**, 158–159.
[185] V. Artero, M. Fontecave, *Chem. Soc. Rev.* **2013**, *42*, 2338–2356.
[186] M. Fujihira, Y. Hirata, K. Suga, *J. Electroanal. Chem. Interfacial Electrochem.* **1990**, *292*, 199–215.
[187] J. D. Froehlich, C. P. Kubiak, *J. Am. Chem. Soc.* **2015**, *137*, 3565–3573.
[188] B. J. McNicholas, J. D. Blakemore, A. B. Chang, C. M. Bates, W. W. Kramer, R. H. Grubbs, H. B. Gray, *J. Am. Chem. Soc.* **2016**, *138*, 11160–11163.
[189] F. P. A. Johnson, M. W. George, F. Hartl, J. J. Turner, *Organometallics* **1996**, *15*, 3374–3387.
[190] P. Kalck, *Homo- and Heterobimetallic Complexes in Catalysis: Cooperative Catalysis*, Springer, **2016**.
[191] C. Riplinger, M. D. Sampson, A. M. Ritzmann, C. P. Kubiak, E. A. Carter, *J. Am. Chem. Soc.* **2014**, *136*, 16285–16298.
[192] M. Bourrez, M. Orio, F. Molton, H. Vezin, C. Duboc, A. Deronzier, S. Chardon-Noblat, *Angew. Chem. Int. Ed.* **2014**, *53*, 240–243.
[193] D. C. Grills, J. A. Farrington, B. H. Layne, S. V. Lymar, B. A. Mello, J. M. Preses, J. F. Wishart, *J. Am. Chem. Soc.* **2014**, *136*, 5563–5566.
[194] J.-D. Compain, M. Bourrez, M. Haukka, A. Deronzier, S. Chardon-Noblat, *Chem. Commun.* **2014**, *50*, 2539–2542.
[195] C. W. Machan, C. P. Kubiak, *Dalton Trans.* **2016**, *45*, 17179–17186.
[196] J. M. Smieja, M. D. Sampson, K. A. Grice, E. E. Benson, J. D. Froehlich, C. P. Kubiak, *Inorg. Chem.* **2013**, *52*, 2484–2491.
[197] M. D. Sampson, A. D. Nguyen, K. A. Grice, C. E. Moore, A. L. Rheingold, C. P. Kubiak, *J. Am. Chem. Soc.* **2014**, *136*, 5460–5471.
[198] M. D. Sampson, C. P. Kubiak, *Inorg. Chem.* **2015**, *54*, 6674–6676.
[199] M. D. Sampson, C. P. Kubiak, *J. Am. Chem. Soc.* **2016**, *138*, 1386–1393.
[200] M. Hammouche, D. Lexa, M. Momenteau, J. M. Saveant, *J. Am. Chem. Soc.* **1991**, *113*, 8455–8466.
[201] A. A. Isse, A. Gennaro, E. Vianello, C. Floriani, *J. Mol. Catal.* **1991**, *70*, 197–208.
[202] F. Franco, C. Cometto, F. Ferrero Vallana, F. Sordello, E. Priola, C. Minero, C. Nervi, R. Gobetto, *Chem. Commun. Camb. Engl.* **2014**, *50*, 14670–14673.

[203] J. Agarwal, T. W. Shaw, H. F. Schaefer, A. B. Bocarsly, *Inorg. Chem.* **2015**, *54*, 5285–5294.
[204] K. T. Ngo, M. McKinnon, B. Mahanti, R. Narayanan, D. C. Grills, M. Z. Ertem, J. Rochford, *J. Am. Chem. Soc.* **2017**, *139*, 2604–2618.
[205] C. W. Machan, S. A. Chabolla, J. Yin, M. K. Gilson, F. A. Tezcan, C. P. Kubiak, *J. Am. Chem. Soc.* **2014**, *136*, 14598–14607.
[206] C. W. Machan, C. P. Kubiak, *Dalton Trans.* **2016**, *45*, 15942–15950.
[207] M. V. Vollmer, C. W. Machan, M. L. Clark, W. E. Antholine, J. Agarwal, H. F. S. III, C. P. Kubiak, J. R. Walensky, *Organometallics* **2015**, *34*, 3–12.
[208] Q. Zeng, J. Tory, F. Hartl, *Organometallics* **2014**, *33*, 5002–5008.
[209] J. Agarwal, T. W. Shaw, C. J. Stanton, G. F. Majetich, A. B. Bocarsly, H. F. Schaefer, *Angew. Chem. Int. Ed Engl.* **2014**, *53*, 5152–5155.
[210] J. Agarwal, C. J. Stanton III, T. W. Shaw, J. E. Vandezande, G. F. Majetich, A. B. Bocarsly, H. F. Schaefer III, *Dalton Trans* **2015**, *44*, 2122–2131.
[211] C. J. Stanton, J. E. Vandezande, G. F. Majetich, H. F. Schaefer, J. Agarwal, *Inorg. Chem.* **2016**, *55*, 9509–9512.
[212] Y. C. Lam, R. J. Nielsen, H. B. Gray, W. A. Goddard, *ACS Catal.* **2015**, *5*, 2521–2528.
[213] E. Torralba-Peñalver, Y. Luo, J.-D. Compain, S. Chardon-Noblat, B. Fabre, *ACS Catal.* **2015**, *5*, 6138–6147.
[214] G. K. Rao, W. Pell, I. Korobkov, D. Richeson, *Chem. Commun.* **2016**, *52*, 8010–8013.
[215] J. A. Cabeza, P. García-Álvarez, R. Gobetto, L. González-Álvarez, C. Nervi, E. Pérez-Carreño, D. Polo, *Organometallics* **2016**, *35*, 1761–1770.
[216] J.-X. Zhang, C.-Y. Hu, W. Wang, H. Wang, Z.-Y. Bian, *Appl. Catal. Gen.* **2016**, *522*, 145–151.
[217] Y. Pellegrin, F. Odobel, *Comptes Rendus Chim.* **2017**, *20*, 283–295.
[218] P. L. Cheung, C. W. Machan, A. Y. S. Malkhasian, J. Agarwal, C. P. Kubiak, *Inorg. Chem.* **2016**, *55*, 3192–3198.
[219] C. W. Machan, C. J. Stanton, J. E. Vandezande, G. F. Majetich, H. F. Schaefer, C. P. Kubiak, J. Agarwal, *Inorg. Chem.* **2015**, *54*, 8849–8856.
[220] J. Tory, B. Setterfield-Price, R. A. W. Dryfe, F. Hartl, *ChemElectroChem* **2015**, *2*, 213–217.
[221] M. L. Clark, K. A. Grice, C. E. Moore, A. L. Rheingold, C. P. Kubiak, *Chem. Sci.* **2014**, *5*, 1894.
[222] D. Sieh, D. C. Lacy, J. C. Peters, C. P. Kubiak, *Chem. – Eur. J.* **2015**, *21*, 8497–8503.
[223] R. N. Dominey, B. Hauser, J. Hubbard, J. Dunham, *Inorg. Chem.* **1991**, *30*, 4754–4758.
[224] F. Franco, C. Cometto, F. Sordello, C. Minero, L. Nencini, J. Fiedler, R. Gobetto, C. Nervi, *ChemElectroChem* **2015**, *2*, 1372–1379.
[225] K. A. Grice, C. Saucedo, *Inorg. Chem.* **2016**, *55*, 6240–6246.
[226] K. Alenezi, *Int. J. Electrochem. Sci.* **2015**, *10*, 4279–4289.
[227] K. Alenezi, K. Alenezi, *J. Chem. J. Chem.* **2016**, *2016*, *2016*, e1501728.
[228] C. Costentin, M. Robert, J.-M. Savéant, A. Tatin, *Proc. Natl. Acad. Sci.* **2015**, *112*, 6882–6886.
[229] E. A. Mohamed, Z. N. Zahran, Y. Naruta, *Chem. Commun.* **2015**, *51*, 16900–16903.
[230] Z. N. Zahran, E. A. Mohamed, Y. Naruta, *Sci. Rep.* **2016**, *6*, 24533.

[231] J. Choi, T. M. Benedetti, R. Jalili, A. Walker, G. G. Wallace, D. L. Officer, *Chem. – Eur. J.* **2016**, *22*, 14158–14161.
[232] J. Song, E. L. Klein, F. Neese, S. Ye, *Inorg. Chem.* **2014**, *53*, 7500–7507.
[233] C. R. Schneider, H. S. Shafaat, *Chem. Commun.* **2016**, *52*, 9889–9892.
[234] G. Neri, J. J. Walsh, C. Wilson, A. Reynal, J. Y. C. Lim, X. Li, A. J. P. White, N. J. Long, J. R. Durrant, A. J. Cowan, *Phys. Chem. Chem. Phys.* **2014**, *17*, 1562–1566.
[235] G. Neri, I. M. Aldous, J. J. Walsh, L. J. Hardwick, A. J. Cowan, *Chem. Sci.* **2016**, *7*, 1521–1526.
[236] P. V. Bernhardt, G. K. Boschloo, F. Bozoglian, A. Hagfeldt, M. Martínez, B. Sienra, *New J. Chem.* **2008**, *32*, 705–711.
[237] S.-J. Kang, A. Dale, S. Sarkar, J. Yoo, H. Lee, *J. Electrochem. Sci. Technol.* **2015**, *6*, 106–110.
[238] H. Khoshro, H. R. Zare, A. Gorji, M. Namazian, *Electrochimica Acta* **2014**, *117*, 62–67.
[239] D. C. Lacy, C. C. L. McCrory, J. C. Peters, *Inorg. Chem.* **2014**, *53*, 4980–4988.
[240] M. Zhang, M. El-Roz, H. Frei, J. L. Mendoza-Cortes, M. Head-Gordon, D. C. Lacy, J. C. Peters, *J. Phys. Chem. C* **2015**, *119*, 4645–4654.
[241] H. Sheng, H. Frei, *J. Am. Chem. Soc.* **2016**, *138*, 9959–9967.
[242] M. Y. Udugala-Ganehenege, N. M. Dissanayake, Y. Liu, A. M. Bond, J. Zhang, *Transit. Met. Chem.* **2014**, *39*, 819–830.
[243] M. Y. Udugala-Ganehenege, Y. Liu, C. Forsyth, A. M. Bond, J. Zhang, *Transit. Met. Chem.* **2014**, *39*, 883–891.
[244] H. Khoshro, H. R. Zare, R. Vafazadeh, *J. CO2 Util.* **2015**, *12*, 77–81.
[245] R. Narayanan, M. McKinnon, B. R. Reed, K. T. Ngo, S. Groysman, J. Rochford, *Dalton Trans.* **2016**, *45*, 15285–15289.
[246] T. K. Mukhopadhyay, N. L. MacLean, L. Gan, D. C. Ashley, T. L. Groy, M.-H. Baik, A. K. Jones, R. J. Troyitch, *Inorg. Chem.* **2015**, *54*, 4475–4482.
[247] N. Elgrishi, M. B. Chambers, V. Artero, M. Fontecave, *Phys. Chem. Chem. Phys.* **2014**, *16*, 13635–13644.
[248] N. Elgrishi, M. B. Chambers, M. Fontecave, *Chem. Sci.* **2015**, *6*, 2522–2531.
[249] A. Chapovetsky, T. H. Do, R. Haiges, M. K. Takase, S. C. Marinescu, *J. Am. Chem. Soc.* **2016**, *138*, 5765–5768.
[250] M. L. Helm, M. P. Stewart, R. M. Bullock, M. R. DuBois, D. L. DuBois, *Science* **2011**, *333*, 863–866.
[251] L. Duan, G. F. Manbeck, M. Kowalczyk, D. J. Szalda, J. T. Muckerman, Y. Himeda, E. Fujita, *Inorg. Chem.* **2016**, *55*, 4582–4594.
[252] F. Wang, B. Cao, W.-P. To, C.-W. Tse, K. Li, X.-Y. Chang, C. Zang, S. L.-F. Chan, C.-M. Che, *Catal. Sci. Technol.* **2016**, *6*, 7408–7420.
[253] D. He, T. Jin, W. Li, S. Pantovich, D. Wang, G. Li, *Chem. – Eur. J.* **2016**, *22*, 13064–13067.
[254] C. E. Roth, A. Dibenedetto, M. Aresta, *Eur. J. Inorg. Chem.* **2015**, *2015*, 5066–5073.
[255] E. S. Donovan, B. M. Barry, C. A. Larsen, M. N. Wirtz, W. E. Geiger, R. A. Kemp, *Chem. Commun.* **2016**, *52*, 1685–1688.
[256] M. Sheng, N. Jiang, S. Gustafson, B. You, D. H. Ess, Y. Sun, *Dalton Trans.* **2015**, *44*, 16247–16250.
[257] D. W. Shaffer, S. I. Johnson, A. L. Rheingold, J. W. Ziller, W. A. Goddard, R. J. Nielsen, J. Y. Yang, *Inorg. Chem.* **2014**, *53*, 13031–13041.

[258] D. A. Dickie, B. E. Chacon, A. Issabekov, K. Lam, R. A. Kemp, *Inorganica Chim. Acta* **2016**, *453*, 42–50.
[259] E. Simón-Manso, C. P. Kubiak, *Organometallics* **2005**, *24*, 96–102.
[260] A. Taheri, E. J. Thompson, J. C. Fettinger, L. A. Berben, *ACS Catal.* **2015**, *5*, 7140–7151.
[261] A. D. Nguyen, M. D. Rail, M. Shanmugam, J. C. Fettinger, L. A. Berben, *Inorg. Chem.* **2013**, *52*, 12847–12854.
[262] N. D. Loewen, E. J. Thompson, M. Kagan, C. L. Banales, T. W. Myers, J. C. Fettinger, L. A. Berben, *Chem. Sci.* **2016**, *7*, 2728–2735.
[263] K. A. Grice, C. Saucedo, M. A. Sovereign, A. P. Cho, *Electrochimica Acta* **2016**, *218*, 110–118.
[264] T. E. Rosser, C. D. Windle, E. Reisner, *Angew. Chem. Int. Ed.* **2016**, *55*, 7388–7392.
[265] J. J. Walsh, C. L. Smith, G. Neri, G. F. S. Whitehead, C. M. Robertson, A. J. Cowan, *Faraday Discuss.* **2015**, *183*, 147–160.
[266] A. Tatin, C. Comminges, B. Kokoh, C. Costentin, M. Robert, J.-M. Savéant, *Proc. Natl. Acad. Sci.* **2016**, *113*, 5526–5529.
[267] J. D. Blakemore, A. Gupta, J. J. Warren, B. S. Brunschwig, H. B. Gray, *J. Am. Chem. Soc.* **2013**, *135*, 18288–18291.
[268] P. Kang, S. Zhang, T. J. Meyer, M. Brookhart, *Angew. Chem. Int. Ed.* **2014**, *53*, 8709–8713.
[269] A. Maurin, M. Robert, *J. Am. Chem. Soc.* **2016**, *138*, 2492–2495.
[270] X.-M. Hu, Z. Salmi, M. Lillethorup, E. B. Pedersen, M. Robert, S. U. Pedersen, T. Skrydstrup, K. Daasbjerg, *Chem. Commun.* **2016**, *52*, 5864–5867.
[271] A. Maurin, M. Robert, *Chem. Commun.* **2016**, *52*, 12084–12087.
[272] I. Hod, M. D. Sampson, P. Deria, C. P. Kubiak, O. K. Farha, J. T. Hupp, *ACS Catal.* **2015**, *5*, 6302–6309.
[273] W. Morris, B. Volosskiy, S. Demir, F. Gándara, P. L. McGrier, H. Furukawa, D. Cascio, J. F. Stoddart, O. M. Yaghi, *Inorg. Chem.* **2012**, *51*, 6443–6445.
[274] D. Quezada, J. Honores, M. García, F. Armijo, M. Isaacs, *New J. Chem.* **2014**, *38*, 3606–3612.
[275] D. Quezada, J. Honores, M. J. Aguirre, M. Isaacs, *J. Coord. Chem.* **2014**, *67*, 4090–4100.
[276] J. Shen, M. J. Kolb, A. J. Göttle, M. T. M. Koper, *J. Phys. Chem. C* **2016**, *120*, 15714–15721.
[277] N. Kornienko, Y. Zhao, C. S. Kley, C. Zhu, D. Kim, S. Lin, C. J. Chang, O. M. Yaghi, P. Yang, *J. Am. Chem. Soc.* **2015**, *137*, 14129–14135.
[278] H. Zhang, J. Wei, J. Dong, G. Liu, L. Shi, P. An, G. Zhao, J. Kong, X. Wang, X. Meng, et al., *Angew. Chem. Int. Ed.* **2016**, *55*, 14310–14314.
[279] S. Lin, C. S. Diercks, Y.-B. Zhang, N. Kornienko, E. M. Nichols, Y. Zhao, A. R. Paris, D. Kim, P. Yang, O. M. Yaghi, et al., *Science* **2015**, *349*, 1208–1213.
[280] G. Zhu, Y. Li, H. Zhu, H. Su, S. H. Chan, Q. Sun, *ACS Catal.* **2016**, *6*, 6294–6301.
[281] Z. Weng, J. Jiang, Y. Wu, Z. Wu, X. Guo, K. L. Materna, W. Liu, V. S. Batista, G. W. Brudvig, H. Wang, *J. Am. Chem. Soc.* **2016**, *138*, 8076–8079.
[282] S. Aoi, K. Mase, K. Ohkubo, S. Fukuzumi, *Catal. Sci. Technol.* **2016**, *6*, 4077–4080.
[283] C. M. Lieber, N. S. Lewis, *J. Am. Chem. Soc.* **1984**, *106*, 5033–5034.
[284] N. Morlanés, K. Takanabe, V. Rodionov, *ACS Catal.* **2016**, *6*, 3092–3095.

[285] T. Abe, T. Yoshida, S. Tokita, F. Taguchi, H. Imaya, M. Kaneko, *J. Electroanal. Chem.* **1996**, *412*, 125–132.
[286] T. Yoshida, K. Kamato, M. Tsukamoto, T. Iida, D. Schlettwein, D. Wöhrle, M. Kaneko, *J. Electroanal. Chem.* **1995**, *385*, 209–225.
[287] W. W. Kramer, C. C. L. McCrory, *Chem. Sci.* **2016**, *7*, 2506–2515.
[288] I. Yamanaka, K. Tabata, W. Mino, T. Furusawa, *Isij Int.* **2015**, *55*, 399–403.
[289] M. Bevilacqua, J. Filippi, A. Lavacchi, A. Marchionni, H. A. Miller, W. Oberhauser, E. Vesselli, F. Vizza, *Energy Technol.* **2014**, *2*, 522–525.
[290] M. Murase, G. Kitahara, T. M. Suzuki, R. Ohta, *ACS Appl. Mater. Interfaces* **2016**, *8*, 24315–24318.
[291] T. N. Huan, E. S. Andreiadis, J. Heidkamp, P. Simon, E. Derat, S. Cobo, G. Royal, A. Bergmann, P. Strasser, H. Dau, et al., *J. Mater. Chem. A* **2015**, *3*, 3901–3907.
[292] T. Jin, C. Liu, G. Li, *J. Coord. Chem.* **2016**, *69*, 1748–1758.
[293] C. Liu, T. Jin, M. E. Louis, S. A. Pantovich, S. L. Skraba-Joiner, T. Rajh, G. Li, *J. Mol. Catal. Chem.* **2016**, *423*, 293–299.
[294] S. Singh, B. Phukan, C. Mukherjee, A. Verma, *RSC Adv* **2015**, *5*, 3581–3589.
[295] D. J. Pearce, D. Pletcher, *J. Electroanal. Chem. Interfacial Electrochem.* **1986**, *197*, 317–330.
[296] Y. Fu, Y. Liu, Y. Li, J. Li, J. Qiao, J. Zhang, *J. Solid State Electrochem.* **2015**, *19*, 3355–3363.
[297] M. García, M. J. Aguirre, G. Canzi, C. P. Kubiak, M. Ohlbaum, M. Isaacs, *Electrochimica Acta* **2014**, *115*, 146–154.
[298] P. Dreyse, J. Honores, D. Quezada, M. Isaacs, *ChemSusChem* **2015**, *8*, 3897–3904.
[299] N. Elgrishi, S. Griveau, M. B. Chambers, F. Bedioui, M. Fontecave, *Chem. Commun.* **2015**, *51*, 2995–2998.
[300] J. R. McKone, S. C. Marinescu, B. S. Brunschwig, J. R. Winkler, H. B. Gray, *Chem. Sci.* **2014**, *5*, 865–878.
[301] V. S. Thoi, Y. Sun, J. R. Long, C. J. Chang, *Chem Soc Rev* **2013**, *42*, 2388–2400.
[302] D. Z. Zee, T. Chantarojsiri, J. R. Long, C. J. Chang, *Acc. Chem. Res.* **2015**, *48*, 2027–2036.
[303] R. Jasinski, *Nature* **1964**, *201*, 1212–1213.
[304] R. Jasinski, *J. Electrochem. Soc.* **1965**, *112*, 526–528.
[305] N. Queyriaux, R. T. Jane, J. Massin, V. Artero, M. Chavarot-Kerlidou, *Coord. Chem. Rev.* **2015**, *304–305*, 3–19.
[306] J. L. Inglis, B. J. MacLean, M. T. Pryce, J. G. Vos, *Coord. Chem. Rev.* **2012**, *256*, 2571–2600.
[307] S. Losse, J. G. Vos, S. Rau, *Coord. Chem. Rev.* **2010**, *254*, 2492–2504.
[308] V. Artero, M. Chavarot-Kerlidou, M. Fontecave, *Angew. Chem. Int. Ed.* **2011**, *50*, 7238–7266.
[309] N. Kaeffer, M. Chavarot-Kerlidou, V. Artero, *Acc. Chem. Res.* **2015**, *48*, 1286–1295.
[310] X. Zhao, P. Wang, M. Long, *Comments Inorg. Chem.* **2016**, *0*, 1–33.
[311] C.-F. Leung, Y.-Z. Chen, H.-Q. Yu, S.-M. Yiu, C.-C. Ko, T.-C. Lau, *Int. J. Hydrog. Energy* **2011**, *36*, 11640–11645.
[312] B. Mondal, K. Sengupta, A. Rana, A. Mahammed, M. Botoshansky, S. G. Dey, Z. Gross, A. Dey, *Inorg. Chem.* **2013**, *52*, 3381–3387.

[313] J. W. Jurss, R. S. Khnayzer, J. A. Panetier, K. A. E. Roz, E. M. Nichols, M. Head-Gordon, J. R. Long, F. N. Castellano, C. J. Chang, *Chem. Sci.* **2015**, *6*, 4954–4972.
[314] D. J. Graham, S.-L. Zheng, D. G. Nocera, *ChemSusChem* **2014**, *7*, 2449–2452.
[315] C. H. Lee, D. Villágran, T. R. Cook, J. C. Peters, D. G. Nocera, *ChemSusChem* **2013**, *6*, 1541–1544.
[316] C. H. Lee, D. K. Dogutan, D. G. Nocera, *J. Am. Chem. Soc.* **2011**, *133*, 8775–8777.
[317] P. Tong, W. Xie, D. Yang, B. Wang, X. Ji, J. Li, J. Qu, *Dalton Trans.* **2016**, *45*, 18559–18565.
[318] A. Koca, A. Kalkan, Z. A. Bayır, *Electrochimica Acta* **2011**, *56*, 5513–5525.
[319] P.-A. Jacques, V. Artero, J. Pécaut, M. Fontecave, *Proc. Natl. Acad. Sci.* **2009**, *106*, 20627–20632.
[320] X. Hu, B. S. Brunschwig, J. C. Peters, *J. Am. Chem. Soc.* **2007**, *129*, 8988–8998.
[321] E. S. Wiedner, J. Y. Yang, W. G. Dougherty, W. S. Kassel, R. M. Bullock, M. R. DuBois, D. L. DuBois, *Organometallics* **2010**, *29*, 5390–5401.
[322] C. Baffert, V. Artero, M. Fontecave, *Inorg. Chem.* **2007**, *46*, 1817–1824.
[323] U. Koelle, S. Paul, *Inorg. Chem.* **1986**, *25*, 2689–2694.
[324] B. J. Fisher, R. Eisenberg, *J. Am. Chem. Soc.* **1980**, *102*, 7361–7363.
[325] C. C. L. McCrory, C. Uyeda, J. C. Peters, *J. Am. Chem. Soc.* **2012**, *134*, 3164–3170.
[326] S. Varma, C. E. Castillo, T. Stoll, J. Fortage, A. G. Blackman, F. Molton, A. Deronzier, M.-N. Collomb, *Phys. Chem. Chem. Phys.* **2013**, *15*, 17544–17552.
[327] S. Kal, A. S. Filatov, P. H. Dinolfo, *Inorg. Chem.* **2014**, *53*, 7137–7145.
[328] R. M. Kellett, T. G. Spiro, *Inorg. Chem.* **1985**, *24*, 2373–2377.
[329] M. Natali, A. Luisa, E. Iengo, F. Scandola, *Chem. Commun.* **2014**, *50*, 1842–1844.
[330] M. M. Roubelakis, D. K. Bediako, D. K. Dogutan, D. G. Nocera, *Energy Environ. Sci.* **2012**, *5*, 7737–7740.
[331] B. B. Beyene, S. B. Mane, C.-H. Hung, *Chem. Commun.* **2015**, *51*, 15067–15070.
[332] Y. Liu, L.-Z. Fu, L.-M. Yang, X.-P. Liu, S.-Z. Zhan, C.-L. Ni, *J. Mol. Catal. Chem.* **2016**, *417*, 101–106.
[333] D. J. Sommer, M. D. Vaughn, G. Ghirlanda, *Chem. Commun.* **2014**, *50*, 15852–15855.
[334] A. Mahammed, B. Mondal, A. Rana, A. Dey, Z. Gross, *Chem. Commun.* **2014**, *50*, 2725–2727.
[335] E. Anxolabéhère-Mallart, C. Costentin, M. Fournier, S. Nowak, M. Robert, J.-M. Savéant, *J. Am. Chem. Soc.* **2012**, *134*, 6104–6107.
[336] N. Kaeffer, A. Morozan, J. Fize, E. Martinez, L. Guetaz, V. Artero, *Acs Catal.* **2016**, *6*, 3727–3737.
[337] S. Cobo, J. Heidkamp, P.-A. Jacques, J. Fize, V. Fourmond, L. Guetaz, B. Jousselme, V. Ivanova, H. Dau, S. Palacin, et al., *Nat. Mater.* **2012**, *11*, 802–807.
[338] S. El Ghachtouli, M. Fournier, S. Cherdo, R. Guillot, M.-F. Charlot, E. Anxolabéhère-Mallart, M. Robert, A. Aukauloo, *J. Phys. Chem. C* **2013**, *117*, 17073–17077.
[339] S. E. Ghachtouli, R. Guillot, F. Brisset, A. Aukauloo, *ChemSusChem* **2013**, *6*, 2226–2230.
[340] E. Anxolabéhère-Mallart, C. Costentin, M. Fournier, M. Robert, *J. Phys. Chem. C* **2014**, *118*, 13377–13381.

[341] D. Basu, S. Mazumder, X. Shi, R. J. Staples, H. B. Schlegel, C. N. Verani, *Angew. Chem. Int. Ed.* **2015**, *54*, 7139–7143.
[342] E. Szajna-Fuller, A. Bakac, *Eur. J. Inorg. Chem.* **2010**, *2010*, 2488–2494.
[343] B. D. Stubbert, J. C. Peters, H. B. Gray, *J. Am. Chem. Soc.* **2011**, *133*, 18070–18073.
[344] T. M. McCormick, Z. Han, D. J. Weinberg, W. W. Brennessel, P. L. Holland, R. Eisenberg, *Inorg. Chem.* **2011**, *50*, 10660–10666.
[345] S. Cherdo, S. El Ghachtouli, M. Sircoglou, F. Brisset, M. Orio, A. Aukauloo, *Chem. Commun.* **2014**, *50*, 13514–13516.
[346] E. S. Andreiadis, P.-A. Jacques, P. D. Tran, A. Leyris, M. Chavarot-Kerlidou, B. Jousselme, M. Matheron, J. Pécaut, S. Palacin, M. Fontecave, et al., *Nat. Chem.* **2013**, *5*, 48–53.
[347] J. L. Dempsey, B. S. Brunschwig, J. R. Winkler, H. B. Gray, *Acc. Chem. Res.* **2009**, *42*, 1995–2004.
[348] C. V. Krishnan, N. Sutin, *J. Am. Chem. Soc.* **1981**, *103*, 2141–2142.
[349] M. A. W. Lawrence, A. A. Holder, *Inorganica Chim. Acta* **2016**, *441*, 157–168.
[350] Q.-X. Peng, L.-Z. Tang, S.-T. Ren, L.-P. Ye, Y.-F. Deng, S.-Z. Zhan, *Chem. Phys. Lett.* **2016**, *662*, 152–155.
[351] X. Chen, H. Ren, W. Peng, H. Zhang, J. Lu, L. Zhuang, *J. Phys. Chem. C* **2014**, *118*, 20791–20798.
[352] T. Abe, M. Kaneko, *J. Mol. Catal. Chem.* **2001**, *169*, 177–183.
[353] J. P. Bigi, T. E. Hanna, W. H. Harman, A. Chang, C. J. Chang, *Chem. Commun.* **2010**, *46*, 958–960.
[354] Y. Sun, J. P. Bigi, N. A. Piro, M. L. Tang, J. R. Long, C. J. Chang, *J. Am. Chem. Soc.* **2011**, *133*, 9212–9215.
[355] A. E. King, Y. Surendranath, N. A. Piro, J. P. Bigi, J. R. Long, C. J. Chang, *Chem. Sci.* **2013**, *4*, 1578–1587.
[356] D. Basu, S. Mazumder, X. Shi, H. Baydoun, J. Niklas, O. Poluektov, H. B. Schlegel, C. N. Verani, *Angew. Chem. Int. Ed.* **2015**, *54*, 2105–2110.
[357] J. Wang, C. Li, Q. Zhou, W. Wang, Y. Hou, B. Zhang, X. Wang, *Catal. Sci. Technol.* **2016**, *6*, 8482–8489.
[358] D. Basu, M. M. Allard, F. R. Xavier, M. J. Heeg, H. B. Schlegel, C. N. Verani, *Dalton Trans.* **2015**, *44*, 3454–3466.
[359] X.-W. Song, Y. Meng, C.-L. Zhang, C.-B. Ma, C.-N. Chen, *Inorg. Chem. Commun.* **2017**, *76*, 52–54.
[360] W. M. Singh, T. Baine, S. Kudo, S. Tian, X. A. N. Ma, H. Zhou, N. J. DeYonker, T. C. Pham, J. C. Bollinger, D. L. Baker, et al., *Angew. Chem. Int. Ed.* **2012**, *51*, 5941–5944.
[361] X. Song, H. Wen, C. Ma, H. Chen, C. Chen, *New J. Chem.* **2015**, *39*, 1734–1741.
[362] M. Natali, E. Badetti, E. Deponti, M. Gamberoni, F. A. Scaramuzzo, A. Sartorel, C. Zonta, *Dalton Trans.* **2016**, *45*, 14764–14773.
[363] E. Deponti, A. Luisa, M. Natali, E. Iengo, F. Scandola, *Dalton Trans.* **2014**, *43*, 16345–16353.
[364] A. Call, Z. Codolà, F. Acuña-Parés, J. Lloret-Fillol, *Chem. – Eur. J.* **2014**, *20*, 6171–6183.
[365] J. Xie, Q. Zhou, C. Li, W. Wang, Y. Hou, B. Zhang, X. Wang, *Chem. Commun.* **2014**, *50*, 6520–6522.
[366] W. M. Singh, M. Mirmohades, R. T. Jane, T. A. White, L. Hammarström, A. Thapper, R. Lomoth, S. Ott, *Chem. Commun.* **2013**, *49*, 8638–8640.

[367] L. Tong, R. Zong, R. P. Thummel, *J. Am. Chem. Soc.* **2014**, *136*, 4881–4884.
[368] L. Tong, A. Kopecky, R. Zong, K. J. Gagnon, M. S. G. Ahlquist, R. P. Thummel, *Inorg. Chem.* **2015**, *54*, 7873–7884.
[369] M. Nippe, R. S. Khnayzer, J. A. Panetier, D. Z. Zee, B. S. Olaiya, M. Head-Gordon, C. J. Chang, F. N. Castellano, J. R. Long, *Chem. Sci.* **2013**, *4*, 3934–3945.
[370] C. Di Giovanni, C. Gimbert-Suriñach, M. Nippe, J. Benet-Buchholz, J. R. Long, X. Sala, A. Llobet, *Chem. – Eur. J.* **2016**, *22*, 361–369.
[371] S. Mandal, S. Shikano, Y. Yamada, Y.-M. Lee, W. Nam, A. Llobet, S. Fukuzumi, *J. Am. Chem. Soc.* **2013**, *135*, 15294–15297.
[372] X. Song, H. Wen, C. Ma, C. Chen, *Polyhedron* **2014**, *81*, 639–645.
[373] C. Bachmann, M. Guttentag, B. Spingler, R. Alberto, *Inorg. Chem.* **2013**, *52*, 6055–6061.
[374] M. Vennampalli, G. Liang, L. Katta, C. E. Webster, X. Zhao, *Inorg. Chem.* **2014**, *53*, 10094–10100.
[375] V. Houlding, T. Geiger, U. Kölle, M. Grätzel, *J. Chem. Soc., Chem. Commun.* **1982**, 681–683.
[376] G. M. Jacobsen, J. Y. Yang, B. Twamley, A. D. Wilson, R. M. Bullock, M. R. DuBois, D. L. DuBois, *Energy Environ. Sci.* **2008**, *1*, 167–174.
[377] E. S. Wiedner, J. A. S. Roberts, W. G. Dougherty, W. S. Kassel, D. L. DuBois, R. M. Bullock, *Inorg. Chem.* **2013**, *52*, 9975–9988.
[378] E. S. Wiedner, A. M. Appel, D. L. DuBois, R. M. Bullock, *Inorg. Chem.* **2013**, *52*, 14391–14403.
[379] M. Fang, E. S. Wiedner, W. G. Dougherty, W. S. Kassel, T. Liu, D. L. DuBois, R. M. Bullock, *Organometallics* **2014**, *33*, 5820–5833.
[380] S. C. Marinescu, J. R. Winkler, H. B. Gray, *Proc. Natl. Acad. Sci.* **2012**, *109*, 15127–15131.
[381] M. van der Meer, E. Glais, I. Siewert, B. Sarkar, *Angew. Chem. Int. Ed.* **2015**, *54*, 13792–13795.
[382] W. R. McNamara, Z. Han, P. J. Alperin, W. W. Brennessel, P. L. Holland, R. Eisenberg, *J. Am. Chem. Soc.* **2011**, *133*, 15368–15371.
[383] W. R. McNamara, Z. Han, C.-J. (Madeline) Yin, W. W. Brennessel, P. L. Holland, R. Eisenberg, *Proc. Natl. Acad. Sci.* **2012**, *109*, 15594–15599.
[384] H. Rao, Z.-Y. Wang, H.-Q. Zheng, X.-B. Wang, C.-M. Pan, Y.-T. Fan, H.-W. Hou, *Catal. Sci. Technol.* **2015**, *5*, 2332–2339.
[385] B. H. Solis, S. Hammes-Schiffer, *J. Am. Chem. Soc.* **2012**, *134*, 15253–15256.
[386] C. S. Letko, J. A. Panetier, M. Head-Gordon, T. D. Tilley, *J. Am. Chem. Soc.* **2014**, *136*, 9364–9376.
[387] T. Fogeron, J.-P. Porcher, M. Gomez-Mingot, T. K. Todorova, L.-M. Chamoreau, C. Mellot-Draznieks, Y. Li, M. Fontecave, *Dalton Trans.* **2016**, *45*, 14754–14763.
[388] P. Li, R. Zaffaroni, B. de Bruin, J. N. H. Reek, *Chem. – Eur. J.* **2015**, *21*, 4027–4038.
[389] A. Kochem, F. Thomas, O. Jarjayes, G. Gellon, C. Philouze, T. Weyhermüller, F. Neese, M. van Gastel, *Inorg. Chem.* **2013**, *52*, 14428–14438.
[390] J. E. Armstrong, P. M. Crossland, M. A. Frank, M. J. V. Dongen, W. R. McNamara, *Dalton Trans.* **2016**, *45*, 5430–5433.
[391] C.-N. Lin, L.-L. Zhou, L.-Z. Fu, S.-Z. Zhan, C.-H. Chen, *Inorg. Chem. Commun.* **2015**, *61*, 97–99.
[392] L.-L. Zhou, L.-Z. Fu, Q.-N. Liang, C. Fang, S.-Z. Zhan, *J. Coord. Chem.* **2016**, *69*, 628–637.

[393] L.-Z. Tang, C.-N. Lin, S.-Z. Zhan, *Transit. Met. Chem.* **2016**, *41*, 819–825.
[394] T. Fang, L.-Z. Fu, L.-L. Zhou, S.-Z. Zhan, S. Chen, *Electrochimica Acta* **2015**, *178*, 368–373.
[395] L.-L. Zhou, L.-Z. Fu, S.-Z. Zhan, *J. Mol. Catal. Chem.* **2015**, *404–405*, 227–232.
[396] L.-Z. Tang, C.-N. Lin, Y.-X. Zhang, S.-Z. Zhan, *Int. J. Hydrog. Energy* **2016**, *41*, 14676–14683.
[397] L.-Z. Fu, L.-L. Zhou, S.-Z. Zhan, *RSC Adv.* **2015**, *5*, 84770–84775.
[398] L.-Z. Fu, L.-L. Zhou, Q.-N. Liang, C. Fang, S.-Z. Zhan, *Polyhedron* **2016**, *107*, 83–88.
[399] Y.-X. Zhang, L.-Z. Fu, L.-L. Zhou, S.-Z. Zhan, W. Li, *Synth. Met.* **2016**, *212*, 69–74.
[400] Y.-X. Zhang, L.-Z. Tang, Y.-F. Deng, S.-Z. Zhan, *Inorg. Chem. Commun.* **2016**, *72*, 100–104.
[401] L.-Z. Fu, L.-L. Zhou, S.-Z. Zhan, *Catal. Commun.* **2015**, *70*, 26–29.
[402] Z.-Q. Wang, L.-Z. Tang, Y.-X. Zhang, S.-Z. Zhan, J.-S. Ye, *J. Power Sources* **2015**, *287*, 50–57.
[403] L.-Z. Fu, L.-Z. Tang, Y.-X. Zhang, Q.-N. Liang, C. Fang, S.-Z. Zhan, *Int. J. Hydrog. Energy* **2016**, *41*, 249–254.
[404] J.-P. Cao, L.-Z. Fu, L.-L. Zhou, S.-Z. Zhan, *J. Power Sources* **2015**, *279*, 107–113.
[405] L.-Z. Fu, L.-L. Zhou, L.-Z. Tang, Y.-X. Zhang, S.-Z. Zhan, *J. Power Sources* **2015**, *280*, 453–458.
[406] L.-L. Zhou, L.-Z. Fu, L.-Z. Tang, Y.-X. Zhang, S.-Z. Zhan, *Int. J. Hydrog. Energy* **2015**, *40*, 5099–5105.

Chapter 2: The intramolecular photocatalytic activity of bis-2,2'-bipyridyl ruthenium 2,2':5',3'':6'',2'''-quaterpyridine rhenium tricarbonyl chloride bishexafluorophosphate (RuRe) towards CO_2 reduction

2.1. Introduction

Within this chapter, the assessment of RuRe (Figure 2.1) towards photocatalytic CO_2 reduction was undertaken for the first time. Section 1.3.1.1.2 summarises previously assessed Ru-Re based systems for this purpose, with the theme of varied linkers between two bipyridyl chelators frequently occurring. Contrasting this, RuRe contains two bipyridyl groups directly bonded to each other.

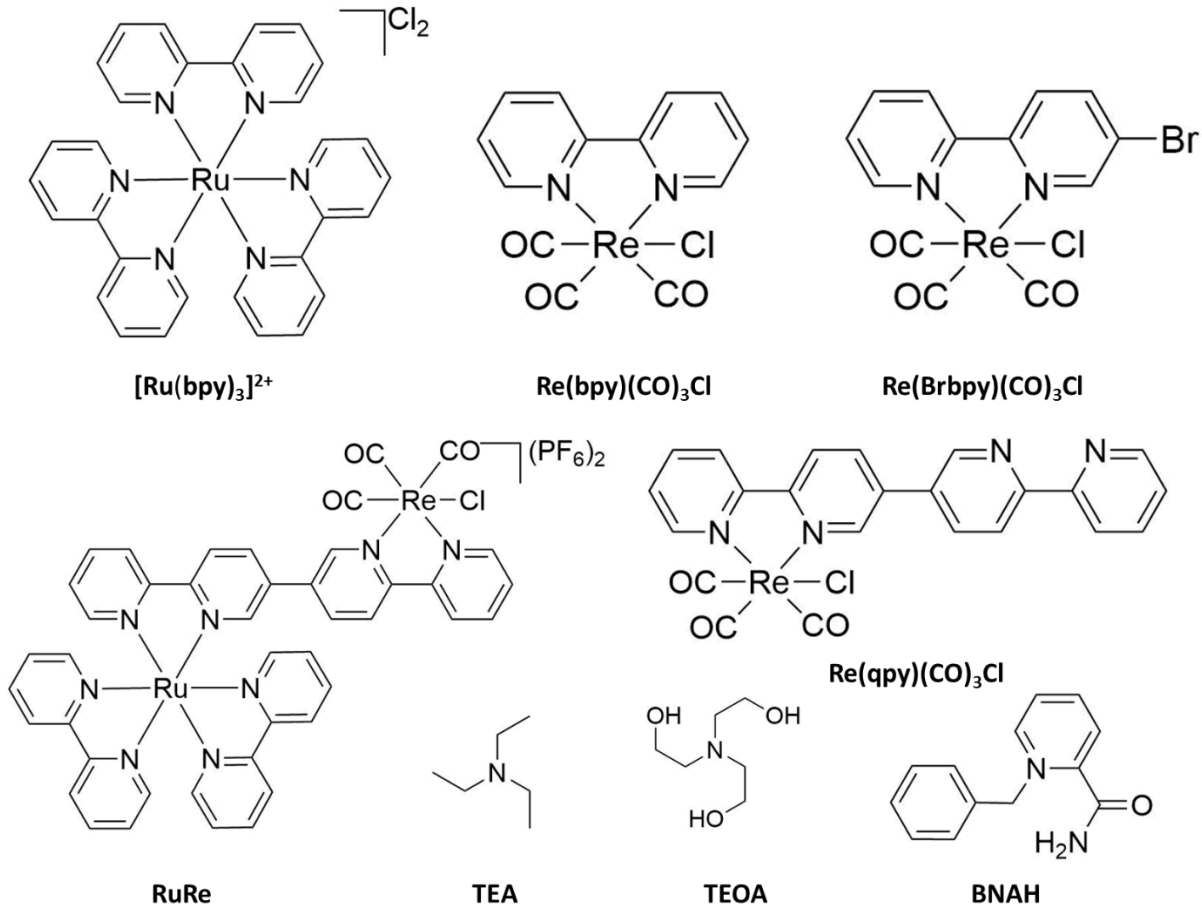

Figure 2.1: $[Ru(bpy)_3]^{2+}$, $Re(bpy)(CO)_3Cl$, $Re(Brbpy)(CO)_3Cl$, $Re(qpy)(CO)_3Cl$, RuRe complexes and TEA, TEOA and BNAH sacrificial electron donors studied within this chapter

The photocatalytic activity of 100 μM RuRe towards CO_2 reduction was determined at three different light sources of λ = 355 nm, λ = 470 nm and λ > 400 nm. Further to this, the solvent and sacrificial electron donor were optimised. Results in each case were compared with the mononuclear systems of 134 μM $[Ru(bpy)_3]^{2+}$ with either 100 μM $Re(bpy)(CO)_3Cl$ or 100 μM $Re(qpy)(CO)_3Cl$, whereby bpy = 2,2'-bipyridine and qpy = 2,2':5',3'':6'',2'''-quaterpyridine. Later within the chapter, another intermolecular photocatalytic experiment was undertaken, incorporating 134 μM $[Ru(bpy)_3]^{2+}$ with 100 μM $Re(Brbpy)(CO)_3Cl$ (Brbpy = 5-bromo-2,2'-bipyridine) in DMF with TEOA as the sacrificial electron donor.

A comparison of the UV-vis spectra (in MeCN) of each of the five complexes assessed within the study are shown Figure 2.2. At higher energy (and not shown in Figure 2.2) within $[Ru(bpy)_3]^{2+}$, $Re(bpy)(CO)_3Cl$, $Re(Brbpy)(CO)_3Cl$ and RuRe is a bpy (or Brbpy) π–π* transition, appearing at 287, 295, ~ 300 and 287 nm respectively. The feature of lowest energy shown within the spectra (371, 382, ~ 395, 450 and 451 nm for $Re(bpy)(CO)_3Cl$, $Re(Brbpy)(CO)_3Cl$, $Re(qpy)(CO)_3Cl$, RuRe and $[Ru(bpy)_3]^{2+}$ respectively) is a metal to ligand charge transfer (MLCT) band. Additionally $Re(qpy)(CO)_3Cl$ and RuRe demonstrate a qpy π–π* transition at 332 and 323 nm respectively with RuRe featuring a further (tentatively assigned and discussed later) Re -> qpy MLCT at ~ 398 nm.

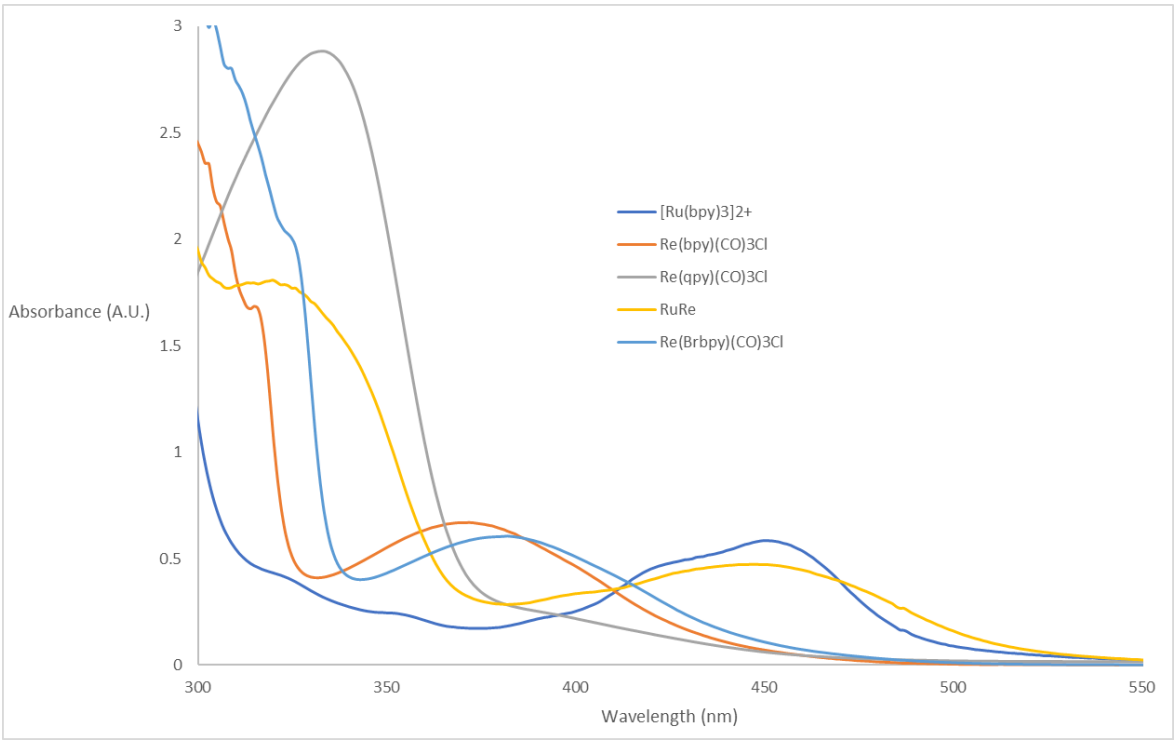

Figure 2.2: A comparison of UV-visible spectra of $[Ru(bpy)_3]^{2+}$, $Re(bpy)(CO)_3Cl$, $Re(qpy)(CO)_3Cl$, $Re(Brbpy)(CO)_3Cl$ and RuRe, undertaken at room temperature in MeCN.

The voltammetry of RuRe, $[Ru(bpy)_3]^{2+}$, $Re(bpy)(CO)_3Cl$ and $Re(qpy)(CO)_3Cl$ was assessed to determine the potentials at which reductions and oxidations occur prior to UV-visible and IR- spectroelectrochemical (SEC) experiments. In addition to this, the potential and reversibility of processes (with reference to homologues) can often provide information regarding the identity of reduced and oxidised species. Particularly relevant to di- and multinuclear species, a level of communication between metal centres in the ground state may be inferred, with reference to the mononuclear counterparts [1].

Oxidative UV-visible SEC was undertaken to clarify whether an intervalence charge transfer (IVCT) band occurred upon the preferential oxidation of one metal centre. Where an IVCT band is present, internuclear interaction between mixed valence states is suggested [2]. Further to this, IR-SEC was undertaken to elucidate the effect of oxidation of one or both metal centres. The reduction and oxidation potentials and

spectrofluorometric data were additionally utilised to assess whether reductive or oxidative quenching pathways were feasible.

2.2. Results and Discussion

2.2.1. Photocatalytic assessment of RuRe towards CO_2 reduction

MeCN and TEA were initially selected as solvent and sacrificial electron donor respectively. 100 μM RuRe showed an increase in detected CO as compared to mixtures employing 134 μM $[Ru(bpy)_3]^{2+}$ + 100 μM $Re(bpy)(CO)_3Cl$, 134 μM $[Ru(bpy)_3]^{2+}$ + 100 μM $Re(qpy)(CO)_3Cl$ and 100 μM $Re(qpy)(CO)_3Cl$ only (as shown in Appendix A.1). Optimisation of the solvent and electron donor was undertaken.

2.2.1.1. Optimisation of the solvent/sacrificial electron donor system

Optimisation of the solvent and electron donor was undertaken with the solvents, acetonitrile (MeCN), dimethylformamide (DMF) and dimethylacetamide (DMA), using the pairing of 134 μM $[Ru(bpy)_3]^{2+}$ as PS and 100 μM $Re(bpy)(CO)_3Cl$ as catalyst. DMA is not a commonly used solvent for CO_2 electro- or photochemical reduction. However, it has gained interest recently following a study reporting that in the presence of water and a base (such as TEOA), DMF can produce formate spontaneously [3]. DMA has been studied in this context and it has been reported not to exhibit this behaviour in the presence of BNAH as sacrificial donor [4]. Acetone and tetrahydrofuran were of interest as solvents also due to high level of solubility of CO_2 [5] and often for dissolving compounds. However, in both cases, the chloride salt of $[Ru(bpy)_3]^{2+}$ was poorly or not soluble. Furthermore, both TEA and TEOA were assessed as sacrificial electron donors (in a 1:5 v/v ratio to the solvent). Figure 2.3 displays the averaged results obtained from the experiments. All photocatalytic experiments were undertaken in triplicate.

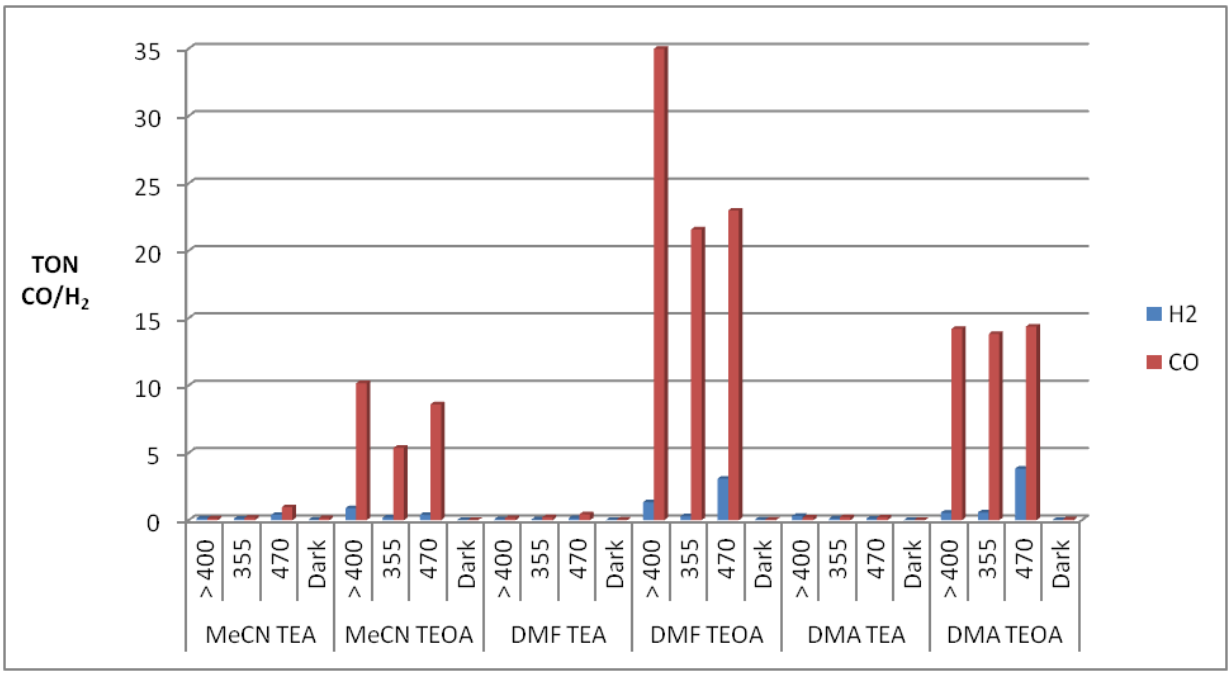

Figure 2.3: The effect of different solvents and sacrificial donors on H_2 and CO production from CO_2 in 134 μM $[Ru(bpy)_3]^{2+}$ with 100 μM $Re(bpy)(CO)_3Cl$ (at λ = 355, 470 and > 400 nm), with an irradiation time of 21 hours

Two key observations were made following the study. With this intermolecular pairing, TEOA is superior to TEA as a sacrificial donor in each solvent system (in agreement with the literature stating that the one-component system $Re(bpy)(CO)_3Cl$ is most active in the presence of TEOA as compared to other sacrificial electron donors. This may be due to the ability of $[Re(bpy)(CO)_3MeCN]^+$ in conjunction with TEOA to bind CO_2 [6]. It is evident also that activity for CO production is superior in DMF to that in DMA or MeCN.

To exclude solvent degradation as a source of CO, DMF/TEOA samples of $[Ru(bpy)_3]^{2+}$ + $Re(bpy)(CO)_3Cl$ were irradiated under an argon atmosphere. As is displayed in Appendix A.2, negligible levels of CO were produced in the absence of CO_2. Therefore, it is unlikely that in DMF/TEOA, the source of CO is from solvent or electron donor degradation or indeed catalytic degradation by either $[Ru(bpy)_3]^{2+}$ or $Re(bpy)(CO)_3Cl$. As the TON of CO generation in DMF/TEOA under a CO_2 atmosphere is 35 (>> 3), at least the vast majority of CO was generated catalytically as opposed to originating from the carbonyl groups of $Re(bpy)(CO)_3Cl$. Further to this observation, even under a CO_2

atmosphere with TEA, $[Ru(bpy)_3]^{2+}$ and $Re(bpy)(CO)_3Cl$ present, minimal amounts of CO were produced from DMF (see Figure 2.3). Dark samples were found to produce a maximum of 0.04 TON_{CO}.

BNAH has previously been used in conjunction with DMF/TEOA and has been found to enhance CO generation [7]. In this case however, λ = 355 nm and > 400 nm produced minimal amounts of CO and λ = 470 nm irradiation produced 3 times less CO in the presence of BNAH than in its absense, as is shown in Appendix A.3. This is potentially due to an inner filter effect [8] owing to the high concentration of BNAH (0.1 M, in keeping with the literature [7,9]). Previously the group of Ishitani noted a decrease in TON_{HCOOH} and Φ_{HCOOH} for Ru and Mn bipyridyl based catalysts with a trinuclear Re bipyridyl PS in the presence of BI(OH)H as compared to the absence [10]. The decreases were assumed to also be due to an inner filter effect, however caused by the oxidised product of BI(OH)H.

Under a CO_2 atmosphere in DMF/TEOA without the photosensitiser or catalyst present, BNAH produced negligible CO at each light source (maximally 0.1 TON_{CO}). As DMF/TEOA was shown to be the optimal solvent/donor system, the intramolecular complex RuRe (100 μM) was investigated for catalytic activity in addition to 134 μM $[Ru(bpy)_3]^{2+}$ only and 100 μM $Re(bpy)(CO)_3Cl$ only.

2.2.1.2. Photocatalytic reduction of CO_2 using RuRe and intermolecular system of $[Ru(bpy)_3]^{2+}$ with $Re(bpy)(CO)_3Cl$ in DMF/TEOA (5:1 v/v)

Figure 2.4 displays the performance of 100 μM RuRe, 134 μM $[Ru(bpy)_3]^{2+}$ + 100 μM $Re(bpy)(CO)_3Cl$, 134 μM $[Ru(bpy)_3]^{2+}$ only and 100 μM $Re(bpy)(CO)_3Cl$ only in DMF/ TEOA. It is evident that at each light source, the intramolecular approach with the quaterpyridyl (qpy) bridging ligand does not perform as efficiently as the $[Ru(bpy)_3]^{2+}$ + $Re(bpy)(CO)_3Cl$ mixture, or even as efficiently as the $Re(bpy)(CO)_3Cl$ alone. Various possibilities for the poorer activity of RuRe exist, including that the PS subunit might pass an electron to another molecule's catalytic centre, the ligand may be responsible for lowering the catalytic ability of the catalyst subunit through a lowering of the catalyst subunit's reducing power, or that passing an electron from the PS to the catalyst

subunits may become energetically unfavourable and that the catalytic subunit acts as a photocatalyst.

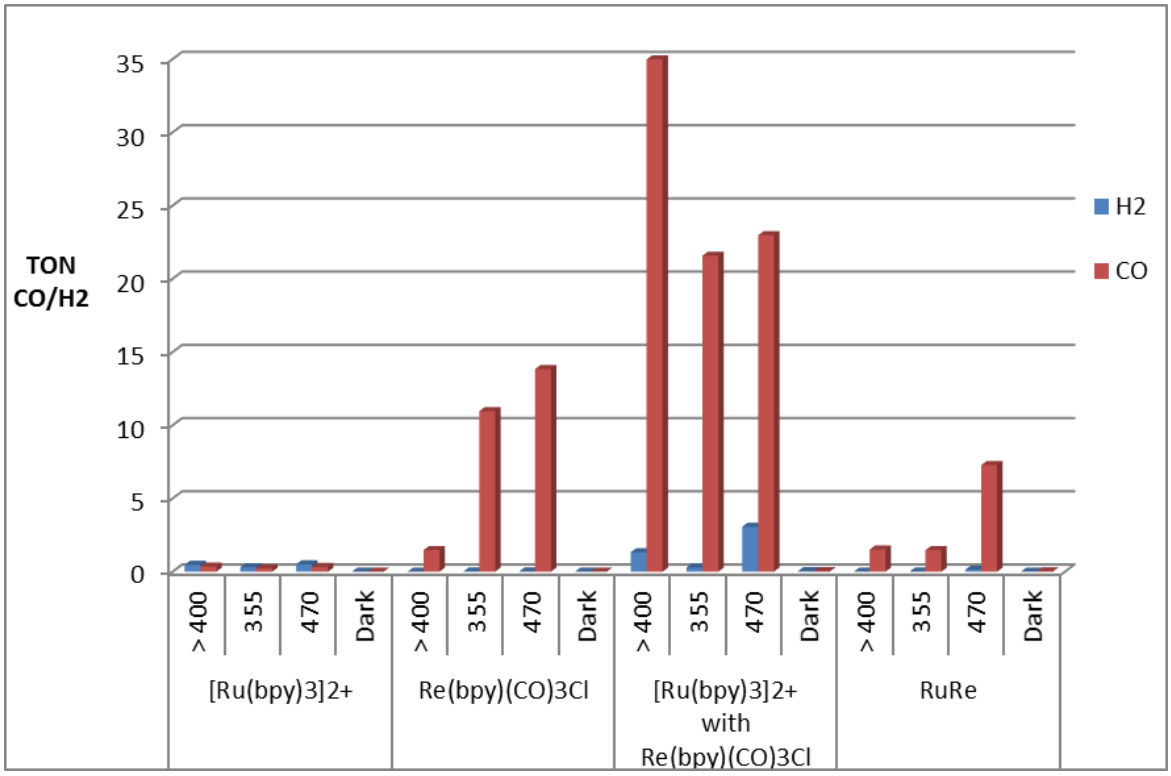

Figure 2.4: Intermolecular vs intramolecular photocatalytic CO_2 reductive performance of 100 μM RuRe, 134 μM $[Ru(bpy)_3]^{2+}$ + 100 μM $Re(bpy)(CO)_3Cl$, 134 μM $[Ru(bpy)_3]^{2+}$, and 100 μM $Re(bpy)(CO)_3Cl$ in DMF/TEOA (5:1 v/v)

From the wavelength dependence study, RuRe is quite inactive at 355 nm as compared to $Re(bpy)(CO)_3Cl$ only and $[Ru(bpy)_3]^{2+}$ + $Re(bpy)(CO)_3Cl$, suggesting that the quaterpyridyl bridge might significantly alter the electron density to the Re centre. $Re(bpy)(CO)_3Cl$ demonstrates higher activity at 470 nm. The MLCT of $Re(bpy)(CO)_3Cl$ occurs with λ_{max} at 370 nm in MeCN, however the band tails to beyond 500 nm. Further to this, there is a considerable difference between the spectral irradiance of the λ = 470 nm and the λ = 355 nm and λ > 400 nm LEDs (see chapter five).

Quenching experiments of $[Ru(bpy)_3]^{2+}$ were undertaken in DMF with TEA and TEOA to infer whether a reductively quenched catalytic cycle could account for an increase in activity of the system. TEOA partially quenched $[Ru(bpy)_3]^{2+}$* (Appendix A.4, in line

with the literature [11]), whereas TEA additions showed no significant difference to the acquired fluorescence spectra (Appendix A.5, as previously stated in both MeOH [12] and water [13]). As shown in Appendix A.6, CO_2 purging did not quench $[Ru(bpy)_3]^{2+}$*. TEOA appears to be a superior sacrificial donor to TEA for the reduction of $[Ru(bpy)_3]^{2+}$, following ^{1}MLCT excitation.

2.2.2. Voltammetric assessment of the complexes

2.2.2.1. Reductive voltammetry of RuRe, $Re(qpy)(CO)_3Cl$, $[Ru(bpy)_3]^{2+}$ and $Re(bpy)(CO)_3Cl$

Prior to spectroelectrochemical experiments, the electrochemistry of RuRe and $Re(qpy)(CO)_3Cl$ was assessed. The reductive electrochemistry of the compounds is shown in Figure 2.5.

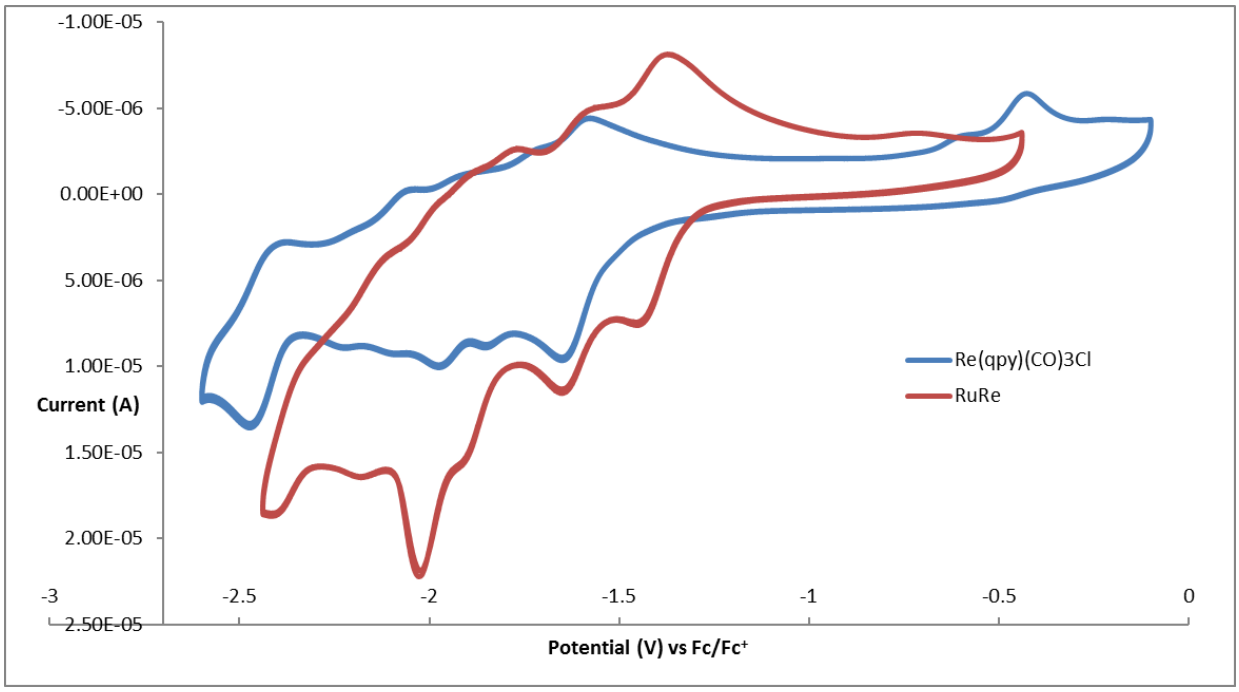

Figure 2.5: Reductive voltammetry of Ar-purged RuRe and $Re(qpy)(CO)_3Cl$ (0.75 mM) in MeCN with 0.1 M $TBAPF_6$, ν = 100 mV s^{-1}

The electrochemistry of $[Ru(bpy)_3]^{2+}$ was also undertaken in MeCN and appears in Appendix A.7. In agreement with the literature [14–17], three reversible bpy-based reductions with $E_{1/2}$ of -1.74, -1.92 and -2.17 V vs Fc/Fc^+ were observed for $[Ru(bpy)_3]^{2+}$. Following these reversible reductions, an irreversible reduction with E_{pc} of -2.77 V vs Fc/Fc^+ led to the formation of two irreversible oxidations with E_{pa} of -1.35 and -1.19 V. This reduction (and subsequent oxidations) has previously been shown for a substituted Ru trisbipyridyl complex in MeCN [14], in addition to $[Ru(bpy)_3]^{2+}$ in DMF [18].

As is shown in Figure 2.5, multiple reductions occur within $Re(qpy)(CO)_3Cl$ and RuRe (as compared to $Re(bpy)(CO)_3Cl$, Appendix A.8) and the voltammetric behaviour is assumed to be further complicated by the irreversible nature of the Re-metal centred reduction. Additional processes occurred more negative to the voltammograms shown in Figure 2.5. However, such a negative potential gives rise to irreversible oxidations at -1, -0.8 and -0.2 V vs Fc/Fc^+ for $Re(qpy)(CO)_3Cl$ and -1.04 and -0.92 V vs Fc/Fc^+ for RuRe, akin to oxidations found with $[Ru(bpy)_3]^{2+}$. These irreversible oxidations have not been analysed further. Therefore, processes more negative to those shown are not discussed. The redox behaviour of $Re(qpy)(CO)_3Cl$ is ill defined following the quasireversible first reduction at $E_{1/2}$ of -1.62 V. However, the $E_{1/2}$ matches that of the second reversible process that occurs in RuRe, suggesting that the second reduction of RuRe may be attributed to the Re ligand based reduction. Therefore, communication between the metal centres is likely to be poor as the reduction of the mononuclear species of $Re(qpy)(CO)_3Cl$ does not differ to that of the same process within the dinuclear species of RuRe [1]. The first reduction of RuRe occurs at -1.4 V vs Fc/Fc^+. Further to the close $E_{1/2}$ values within $Re(qpy)(CO)_3Cl$ and RuRe, Halpin *et al.* previously reported the electrochemistry of $[(bpy)_2Ru(qpy)Ru(bpy)_2]^{4+}$, whereby the first and second reductions of the complex (with $E_{1/2}$s of ~ -1 V and -1.2 V vs SCE, i.e. ~ -1.4 V and -1.6 V vs Fc/Fc^+) were stated as qpy based reductions.

Assuming that no strong communication between the subunits of RuRe is present, the rhenium moiety's quaterpyridyl based one electron reduced (OER) species occurs negative to that of the ruthenium moiety's quaterpyridyl based reduction. As detailed in section 2.2.5, a reductive quenching photocatalytic mechanism may not be permitted as the first reduction of the Ru subunit does not have the reducing power to pass an electron to the Re centre [19].

The voltammetry of $Re(bpy)(CO)_3Cl$ in MeCN appears in Appendix A.8 and the voltammograms of $Re(bpy)(CO)_3Cl$ with $Re(qpy)(CO)_3Cl$ appear in Appendix A.9. A contrast between electrochemical behaviour of the first cathodic redox couple (ligand->ligand$^{\bullet-}$) of $Re(qpy)(CO)_3Cl$ and $Re(bpy)(CO)_3Cl$ supports the behaviour observed of the Re-L MLCT in absorbance spectra (~395 to 371 nm respectively, Figure 2.2). The first reduction of $Re(qpy)(CO)_3Cl$ occurs with $E_{1/2}$ of -1.62 V (as observed for the Re-ligand based reduction of RuRe), whereas that of $Re(bpy)(CO)_3Cl$ occurs at -1.75 V vs Fc/Fc^+. It has been stated previously that production of the OER species should occur with an $E_{1/2}$ more cathodic than -1.4 V vs $Ag/AgNO_3$ (-1.49 V vs Fc/Fc^+ [20]) with Re diimine-based complexes so as not to hinder photocatalysis [20,21]. Absorbance spectra of the complexes show the MLCT band at 400 nm for $Re(qpy)(CO)_3Cl$ and 370 nm for $Re(bpy)(CO)_3Cl$ in MeCN. Due to increased conjugation within the ligand, the reducing power of $Re(qpy)(CO)_3Cl$ towards CO_2 is decreased as compared to the $Re(bpy)(CO)_3Cl$ analogue [19]. This has also been reported to explain activity for non-Re-based catalysts [22].

For comparison/contrast, the overlaid voltammetry of $[Ru(bpy)_3]^{2+}$ and RuRe appears in Appendix A.10 and the overlaid voltammetry of $[Ru(bpy)_3]^{2+}$ with $Re(bpy)(CO)_3Cl$ appears in Appendix A.11.

2.2.2.2. Oxidative voltammetry of RuRe and $Re(qpy)(CO)_3Cl$

The oxidative electrochemistry of RuRe and $Re(qpy)(CO)_3Cl$ appears in Figure 2.6. A reversible process and irreversible process is evident, however, the attribution of which oxidation leads to the reduction is not straightforward. To verify reversibility of the ruthenium-centred oxidation, $[Ru(bpy)_3]^{2+}$ voltammetry was undertaken which showed one reversible process with $E_{1/2}$ of 0.89 V vs Fc/Fc^+ (associated with $Ru^{2+/3+}$) [14,23]). Therefore, it is expected that $[Ru(bpy)_2(qpy)]^{2+}$, and by extension, the $[Ru(bpy)_2(qpy)]^{2+}$ portion of RuRe would lead to a $Ru^{2+/3+}$ reversible oxidation approximately within this region. For comparison, Halpin *et al.* reported a single reversible oxidation of $[(bpy)_2Ru(qpy)Ru(bpy)_2]^{2+}$ with $E_{1/2}$ of approximately 0.95 V vs Fc/Fc^+ [2]. Both $Re(qpy)(CO)_3Cl$ and $Re(bpy)(CO)_3Cl$ have a single irreversible oxidation (assessed up to 10 V/s in the case of $Re(qpy)(CO)_3Cl$, see Appendix A.12) at 1.01 V and 0.98 V respectively (associated with $Re^{1+/2+}$ [24]), compounding the behaviour observed of a

reversible couple with an irreversible oxidation. For comparison, the first oxidation of $[Ru(bpy)_3]^{2+}$ occurs at less positive potentials than does the first oxidation of $Re(bpy)(CO)_3Cl$ (E_{pa} of 0.94 V and 0.98 V vs Fc/Fc^+ respectively, Appendix A.11). It is noted that the first oxidation in Ru-Re complexes is often that of the Ru centred oxidation [25].

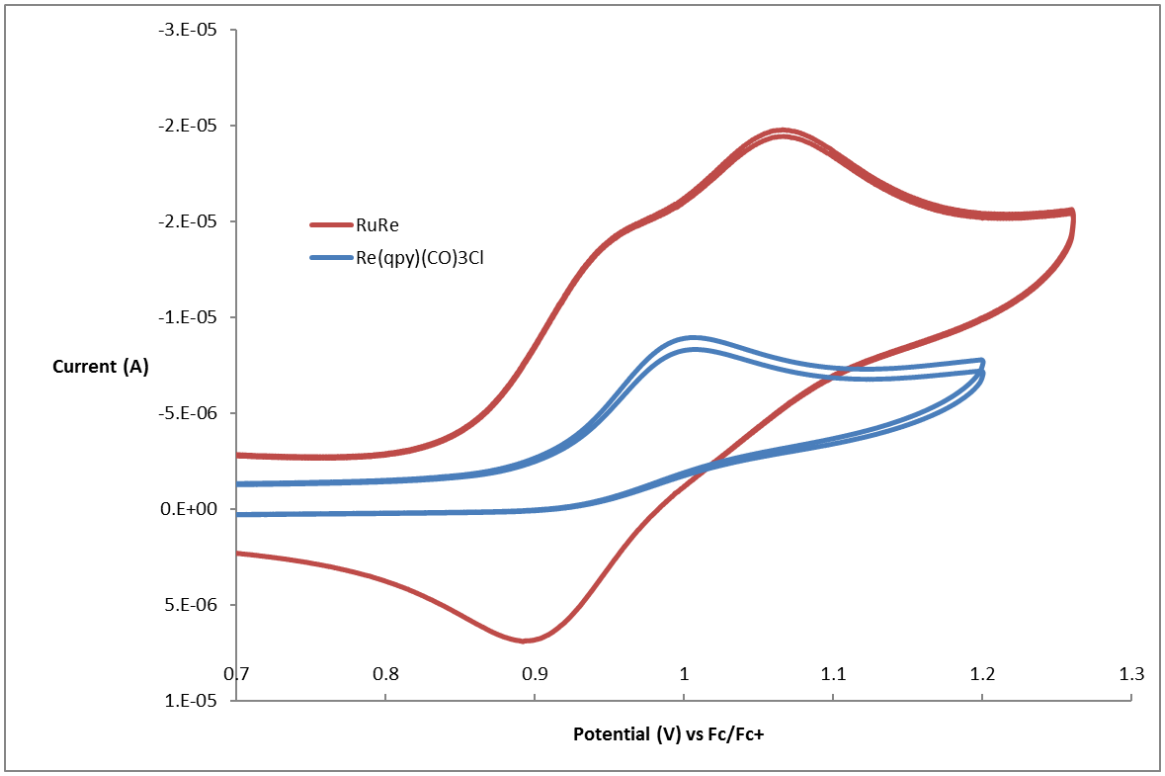

Figure 2.6: Oxidative voltammetry of RuRe dinuclear and $Re(qpy)(CO)_3Cl$ mononuclear complex (0.75 mM) in MeCN with 0.1M $TBAPF_6$, ν = 100 mV s^{-1}

2.2.2.3. Summary of electrochemical data

A summary of electrochemical data obtained for RuRe, $Re(qpy)(CO)_3Cl$, $[Ru(bpy)_3]^{2+}$ and $Re(bpy)(CO)_3Cl$ is presented in Table 2.1.

Table 2.1: Summary of the first oxidation and reduction potentials vs Fc/Fc^+ of the assessed complexes at 100 mV s^{-1} in MeCN/0.1 M $TBAPF_6$

Complex	Ru $(L/L^{\cdot-})_1$ (V)	$ReL/L^{\cdot-}$ (V)	$Ru^{2+/3+}$ (V)	$Re^{1+/2+}$ (V)
$[Ru(bpy)_3]^{2+}$	-1.74	-	0.89	-
$Re(bpy)(CO)_3Cl$	-	-1.74	-	0.98 [i]
$Re(qpy)(CO)_3Cl$	-	-1.62 [q]	-	1.01 [i]
RuRe	-1.4 [q]	-1.62 [q]	0.93*	1.07 [i]

i = irreversible oxidation, E_{pa} displayed. q = quasireversible process, $E_{1/2}$ displayed. All other values are $E_{1/2}$s. * = Assumed that the first oxidation gives rise to the $Ru^{3+/2+}$ reduction

From the electrochemistry of RuRe and $Re(qpy)(CO)_3Cl$, it is clear that the direct bonding of the two bipyridyl units of qpy results in a decrease of both Ru- and Re-ligand based reduction potentials as compared to the monomeric species of $[Ru(bpy)_3]^{2+}$ and $Re(bpy)(CO)_3Cl$ [2]. This may be caused by both extended pi-bonding overlap (increased conjugation) and/or by electronegativity of a group.

The potential of the first reductive process in $Re(qpy)(CO)_3Cl$ matches that of the second reductive process within RuRe. This suggests not only that the second reduction of RuRe is that of the $[Re(bpy)(CO)_3Cl]$ / $[Re(bpy^{\cdot-})(CO)_3Cl]$ moiety, but also the two bipyridyl units within both RuRe and $Re(qpy)(CO)_3Cl$ may be out of plane, so that communication due to conjugation between the bipyridyl groups does not occur [1]. In the case of RuRe, steric hindrance between Re and the remaining two bipyridyl groups on Ru may occur. For example, where the 2,2':3',2'':6'',2'''-qpy ligand was utilised, x-ray crystallography has previously shown that $[(bpy)_2Os(qpy)Ru(bpy)_2]^{4+}$, $[Ru((qpy)Re(CO)_3Cl))_3]^{2+}$, and even $[Ru(\kappa^3\text{-qpy})(\kappa^2\text{-qpy})Cl]^+$ (whereby the second bipyridyl moiety of qpy wasn't metallated) demonstrate significant distortion of the

second bipyridyl moieties as compared to the first [26]. The 2,2':4',4'':2'',2'''-qpy bridged complex $[(bpy)_2Ru(qpy)Ru(bpy)_2]^{4+}$ was also believed to twist between the two bpy units, thereby weakening metal to metal centre interaction [27].

Steric hindrance within the monomer of $Re(qpy)(CO)_3Cl$ may be less expected than in the case of RuRe. The crystal structures of analogous [Re/$Mn(CO)_3$]-based complexes bearing 5-phenyl, pyridyl or bipyridyl-substituted bipyridines (where p orbital overlap could occur) were not found within the literature. Somewhat analogous examples are however discussed. $Mn(tpy)(CO)_3Br$ and $Re(tpy)(CO)_3Cl$ (tpy = κ^2-2,2':6',2''-terpyridine) show non-coplanarity of the third (unbound) pyridyl unit [28,29]. 6'-substitution as compared to 5' substitution within $Re(qpy)(CO)_3Cl$ is however expected to place the group closer to a carbonyl ligand. [Iron(κ^3-2,2':6',2''-terpyridine)$_2$]$^{2+}$ complexes bearing either a 2-, 3-, or 4-pyridyl substitution from the 4' position of tpy, in addition to a Ru analogue showed out of plane twisting of the pyridyl units [30]. It is noted in the case of Zn(κ^3-(4'-(2-pyridyl))-2,2':6',2''-terpyridine)diazide for example, that the pyridyl substituent crystallised in a planar manner to the tpy [31]. $[Ru(4,4':2',2'':4'',4'''-qpy)_3]^{2+}$, i.e. bpy with 4-pyridyl from the 4,4'- positions, crystallised with the 4-pyridyl groups demonstrating a twist angle of 30^0 to the bpy units [32]. $[(Ru(bpy)_2)_2(4,4':2',2'':4'',4'''-qpy)_2(Re(CO)_3Cl)_2]^{4+}$, whereby each Re centre is bound by a 4-pyridyl unit from each of the qpy ligands, was crystallised and showed non-planarity of the pyridyl units with the linking bpy ligand [33]. DFT-optimised structures of six 4,4':2',2'':4'',4'''-qpy or bispyridiniumbipyridine containing structures of $[Re(CO)_3MeCN]$, $[Ru(phen)_2]$ and [Ir(bpy/phen/cyclometallating analogues)$_2$] also assume skewed geometry with respect to planarity of the bpy [34,35]. The ligand of 2,2':6',2'':6'',2'''-qpy crystallised with a planar structure [36], whereas 2,2':3',2'':6'',2'''-qpy demonstrates significant distortion between the second, third and fourth pyridyl rings [37]. Additionally, DFT studies of $[(bpy)_2Ru(qpy)PdCl_2]^{2+}$ (qpy as utilised in this study) assume a 17^o torsion angle between both bipyridine subunits of the qpy ligand [38].

In contrast to this, $[Ru(dmb)_2$(3,3'-bisphenanthroline)$]^{2+}$ (phen version of the qpy ligand utilised in this work) was believed through photophysical and electrochemical data to show planarity of the second phen moiety, whereas the 2,2'- version of the complex was believed to display distortion [39]. Furthermore, Re(3,3'-

diphenylphenanthroline)$(CO)_3Cl$ was the subject of DFT calculations, whereby the structure assumed planarity of the phenyl rings with phenanthroline [40].

From the literature, it is certainly possible that the mononuclear qpy ligand as used in this research could adopt a non-planar structure when bound to $[Re(CO)_3Cl]$. Both $[Ru(bpy)_2(qpy)]^{2+}$ and $[Ru(dceb)_2(qpy)]^{2+}$ (dceb = dicarboxyethylbpy) have previously shown 2 nm and 0 nm shifts to the Ru -> qpy MLCT w.r.t. their Ru-Re dinuclear species [41], thus strengthening the argument that a lower level of communication may be present [1] due to distortion of the bpy planes. A very weak spectral feature within the spectrum of RuRe is apparent at approximately 398 nm. This feature is tentatively ascribed to the Re -> qpy MLCT, as a weak absorbance at approximately 395 nm within $Re(qpy)(CO)_3Cl$ is also ascribed to the Re -> qpy MLCT [42] (see Figure 2.2 and Figure 2.8, inset). In terms of electron withdrawal by the second (non-chelated) bpy portion on the bound bpy of $Re(qpy)(CO)_3Cl$, even where extended π-conjugation may not occur (through misalignment of p-orbitals), pyridyl groups remain as electron withdrawing groups [32,43]. By extension, it is assumed that a bpy substituent is also electron withdrawing, even when π-conjugation is interrupted.

2.2.3. Oxidative UV-visible spectroelectrochemistry (SEC)

Prior to discussing the UV-vis spectral changes associated with oxidation of the complexes, the features of the spectra of RuRe, $Re(qpy)(CO)_3Cl$ and $[Ru(bpy)_3]^{2+}$, obtained in MeCN, are summarised in Table 2.2.

Table 2.2: UV-visible spectral features associated with ligand π–π* and MLCTs in MeCN with 0.1 M $TBAPF_6$

Complex	bpy π–π*	qpy π–π*	Ru bpy/qpy MLCT	$Re(qpy)(CO)_3Cl$ MLCT
RuRe	287 nm	323 nm	450 nm	~ 398 nm[a]
$Re(qpy)(CO)_3Cl$	-	332 nm	-	~ 395 nm
$[Ru(bpy)_3]^{2+}$	287 nm	-	451 nm	-

a. Tentatively assigned through comparison with MLCT of $Re(qpy)(CO)_3Cl$

2.2.3.1. RuRe oxidative UV-visible spectroelectrochemistry

To determine the level of communication between both metal centres, UV-visible spectroelectrochemistry was undertaken. Of particular interest was whether an IVCT band was present. The IVCT band is a broad feature, typically observed between 850 to 2000 nm for polypyridyl-bridged metal centres upon the preferential oxidation of one metal centre [44,45]. Previously, the metals in the ground state of $[(bpy)_2Ru(qpy)Ru(bpy)_2]^{4+}$ and $[(bpy)_2Os(qpy)Os(bpy)_2]^{4+}$ were reported to not demonstrate communication [2].

UV-visible spectroelectrochemistry was undertaken as outlined in chapter five. Particularly relevant for RuRe, the controlled potential was increased incrementally and fixed at potentials at which changes were observed. When no further changes were observed, the potential was further increased.

Figure 2.7 displays the UV-vis spectra obtained upon electrolysis of RuRe at 1.38 V and 1.65 V vs Ag wire, and gradual changes with electrolysis at 1.75 V vs Ag wire. The 600-2500 nm region was monitored, though as no IVCT band was noted, the region is not shown. The Ru and Re metal centred E_{pa}s are separated by approximately 100 mV. Therefore a selective and exhaustive 1 e^- oxidation was not obtained. Further to this, as the IVCT is expected to be much weaker than the Ru -> ligand MLCT [2], the absence of communication between the centres in the ground state may not be inferred.

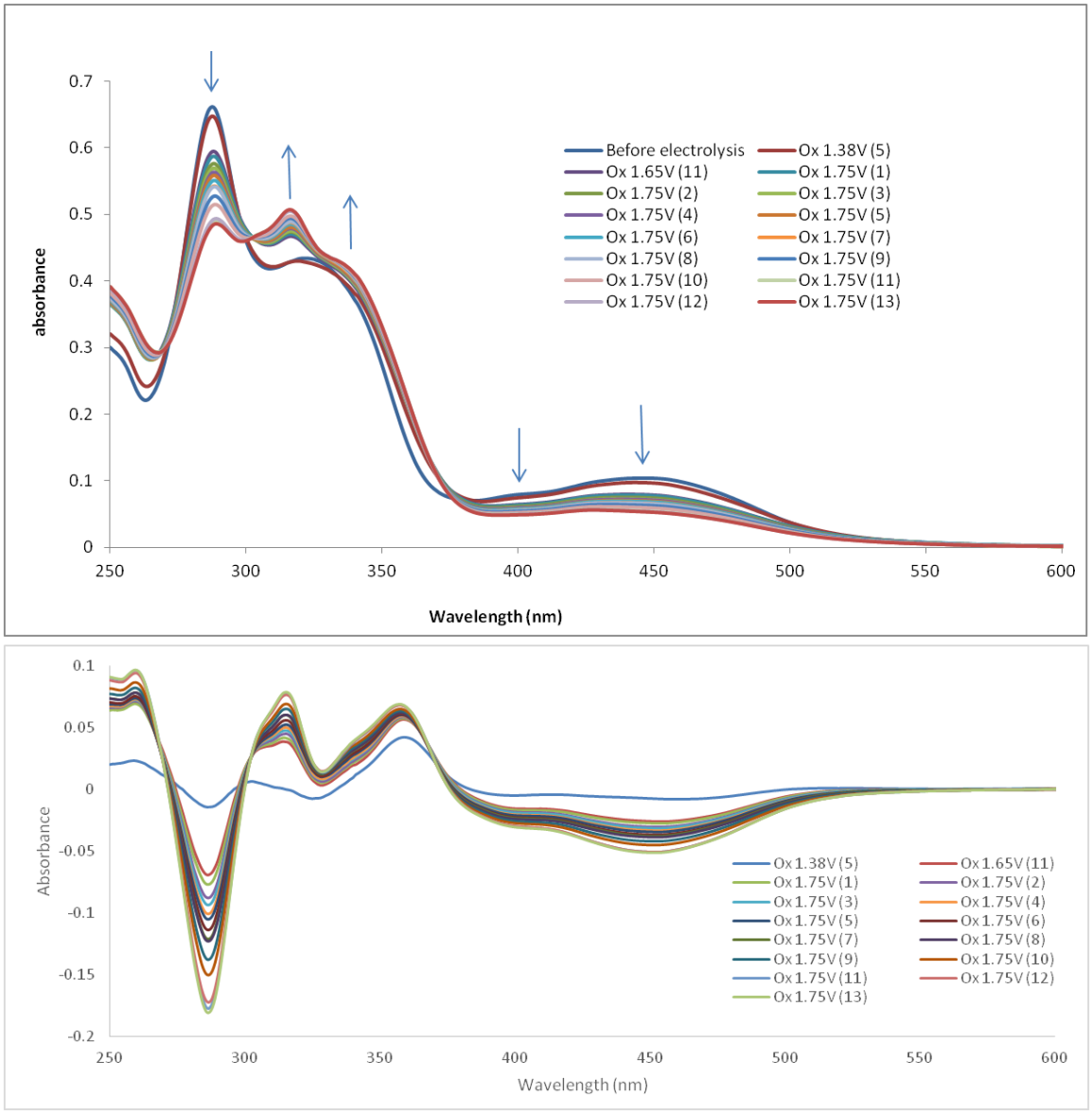

Figure 2.7: Top: UV-vis SEC spectra of RuRe bulk-oxidised at 1.38 V, 1.65 V, and after the second oxidation (1.75 V vs Ag wire) in MeCN with 0.1 M $TBAPF_6$ and at a Pt gauze working electrode. Bottom: Difference spectra from pre-electrolysis spectrum. Successive UV-vis scans were recorded 3.5 minutes apart with the number in the parenthesis representing the spectral scan number

Minor changes within spectra were observed at 1.38 V vs Ag wire. Increasing the potential to 1.65 V and further to 1.75 V vs Ag wire resulted in more pronounced changes to spectra. A peak with λ_{max} = 316 nm became defined at close to but higher energy of the qpy π–π* transition (λ = 323 nm). This was accompanied by a decrease in

bpy π–π* and Ru MLCT. The tentatively assigned Re -> qpy MLCT at approximately 400 nm was also observed to decrease, suggesting the simultaneous oxidation of both metal centres.

In addition to monitoring at 1.38 V, no IVCT band was observed during the electrolyses at 1.65 or 1.75 V. However, upon electrolysing at 1.65 and 1.75 V, a weak and broad band (attributed to the Ru^{3+} ligand-to-metal charge transfer [46]) was observed. This spectral feature is displayed in Appendix A.13. Following the oxidation at 1.75 V, the potential was returned to 0 V and the resulting spectra are displayed in Appendix A.14. Significant reversibility was observed, suggesting that Re oxidation (irreversible) bears little effect on the electronic nature of the $[(bpy)_2(qpy)Ru]^{2+}$ portion of the compound.

2.2.3.2. Re(qpy)(CO)$_3$Cl oxidative UV-visible SEC

One irreversible oxidation was observed at 1 V vs Fc/Fc^+ for $Re(qpy)(CO)_3Cl$ at a glassy carbon electrode in MeCN with 0.1 M $TBAPF_6$, corresponding to the Re metal-centred oxidation (Figure 2.6). As only a single oxidation is observed before solvent oxidation occurs, spectral changes due to electrolysis at 1.65 V vs Ag wire (available in Figure 2.8) were solely that of $Re^{1+/2+}$ (and potential products formed from chemical steps following the oxidation). Upon oxidation of the metal centre, there is a growth in the region of the qpy π–π* feature (from 332 to 338 nm) with loss of the MLCT associated with Re -> qpy (approximately 395 nm). Subsequent electrolysis at 0 V led to partial recovery of the non-oxidised spectrum. However, this behaviour was slow and diffusion from the reservoir cannot be ruled out in explaining the observation.

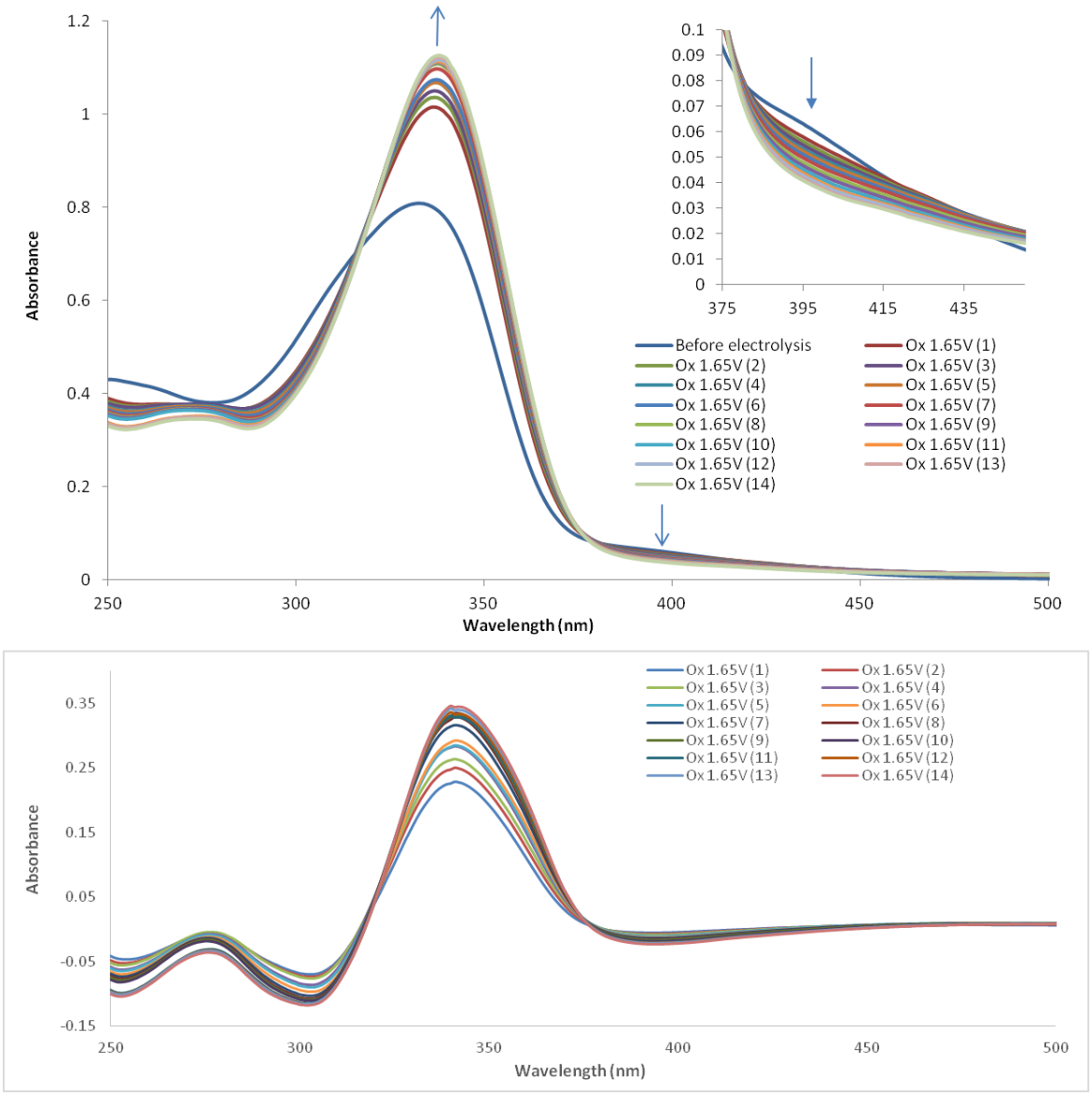

Figure 2.8: Top: UV-vis SEC spectra of $Re(qpy)(CO)_3Cl$ bulk-oxidised at 1.65 V vs Ag wire) and at a Pt gauze working electrode in MeCN with 0.1 M $TBAPF_6$. Inset: Depletion of Re -> qpy MLCT. Bottom: Difference spectra from pre-electrolysis spectrum

2.2.3.3. $[Ru(bpy)_3]^{2+}$ oxidative UV-visible SEC

As stated previously, $[Ru(bpy)_3]^{2+}$ shows one metal-centred reversible oxidation with $E_{1/2}$ of 0.89 V vs Fc/Fc^+. Figure 2.9 shows the UV-visible spectra obtained from bulk electrolysing a solution of $[Ru(bpy)_3]^{2+}$ beyond the $Ru^{2+/3+}$ oxidation (1.6 V vs Ag wire)

and following this, electrolysing below the E_{pc} (0 V vs Ag wire) to assess reversibility of observed changes.

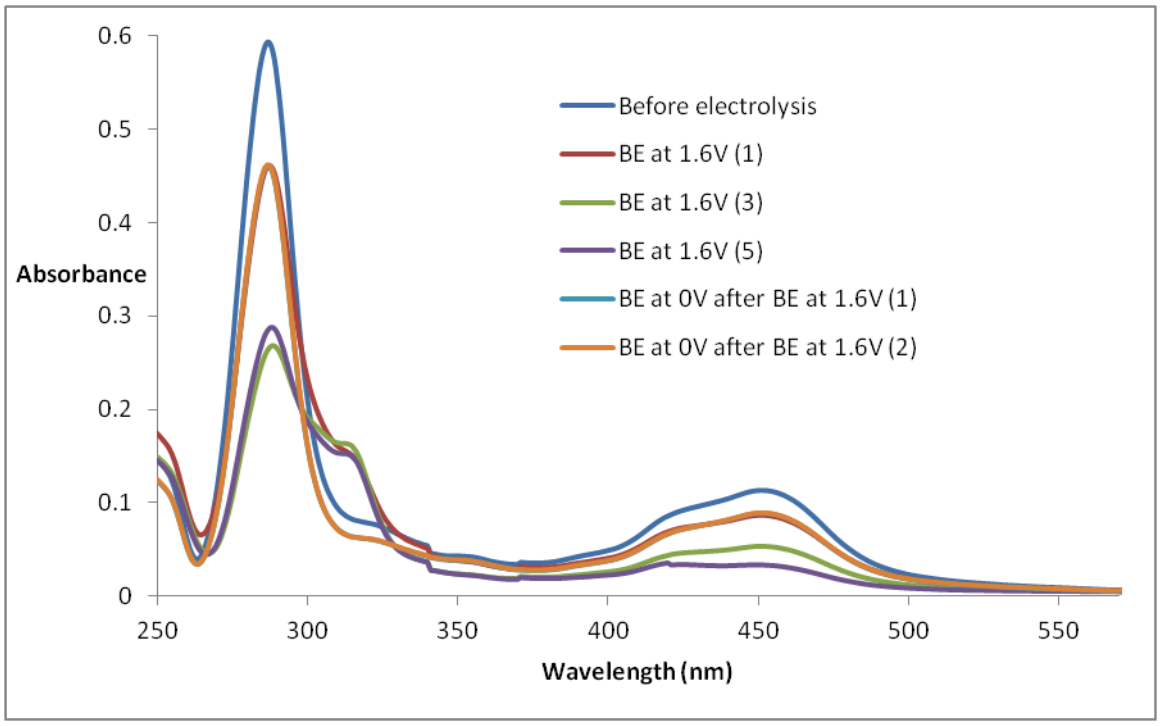

Figure 2.9: Oxidative UV-visible SEC of $[Ru(bpy)_3]^{2+}$, oxidised with Pt mesh electrode at 1.6 V vs Ag wire and 0 V following oxidation at 1.6 V, in MeCN with 0.1 M $TBAPF_6$. BE = bulk electrolysis or controlled potential electrolysis

Complete reversibility of the $Ru^{2+/3+}$ species was not obtained (timescale of 17.5 mins at 1.6 V and 7 mins at 0 V), as observed in the comparison of the pre-electrolysis spectrum and spectra obtained at 0 V following electrolysis at 1.6 V. However, a significant proportion of the complex was returned to $[Ru^{2+}(bpy)_3]^{2+}$. Similar behaviour was observed in the reversibility of RuRe following its second oxidation (Appendix A.14). It is noted, however, that integrated areas of differential pulsed voltammograms (displayed in Appendix A.15) regarding the $Ru^{2+/3+}$ couple of $[Ru(bpy)_3]^{2+}$ are equivalent. Key observations within Figure 2.9 include the depletion of bpy π–π* and Ru -> bpy MLCT transitions at 287 and 451 nm respectively, with the formation of a band at 315 nm. This depletion/formation at 287/315 nm holds similarity to RuRe, whereby RuRe bpy π–π* depletes at 288 nm and formation of a band at 316 nm.

2.2.3.4. Comparison of RuRe UV-visible SEC results with those of $Re(qpy)(CO)_3Cl$ and $[Ru(bpy)_3]^{2+}$

The spectral changes upon oxidation of RuRe cannot be explained without comparing the spectrum of RuRe to $[(bpy)_2(qpy)Ru]^{2+}$. Such a comparison of the spectrum of RuRe with $[(bpy)_2(qpy)Ru]^{2+}$ [41] shows that the contribution of $[(bpy)_2(qpy)Ru]^{2+}$ to the RuRe spectrum is dominant, with bpy $\pi-\pi^*$ unshifted at 288 nm between mono- and dinuclear complexes. The qpy $\pi-\pi^*$ shifts from 318 to 322 nm upon the addition of the $[Re(CO)_3Cl]$ moiety. Furthermore, a shift of the Ru -> ligand MLCT to marginally higher energy (from 452 to 450 nm) occurs.

To compare the spectral changes of both RuRe and $Re(qpy)(CO)_3Cl$, both complexes show a rise in intensity at approximately 350 nm. However, as the qpy $\pi-\pi^*$ overlaps in this region, it is difficult to attribute the changes of this feature in the case of RuRe to Ru oxidation or both metal centre oxidations. Disappearance of the Re MLCT is noted within $Re(qpy)(CO)_3Cl$. Within RuRe, the tentatively ascribed Re MLCT also decreases/becomes insignificant upon electrolysis at 1.65/1.75 V.

There is strong evidence to suggest that any changes observed in the absorbance spectra of RuRe are solely or greatly due to the $[(bpy)_2(qpy)Ru]^{2+}$ moiety, and therefore, apparent reversibility of spectra is not surprising even though an irreversible oxidation ($Re^{1+/2+}$) is occurring.

2.2.4. Oxidative IR-SEC of $Re(bpy)(CO)_3Cl$, $Re(qpy)(CO)_3Cl$ and RuRe

Metal carbonyls have characteristic fingerprints in the metal carbonyl region in the IR spectrum and can be used to monitor electron density. Therefore, oxidative IR-spectroelectrochemistry was performed on the complexes of $Re(bpy)(CO)_3Cl$, $Re(qpy)(CO)_3Cl$ and RuRe*.

* It is emphasised that potentials vs Ag wire in IR-SEC experiments may vary to that of UV-vis SEC experiments as a different cell and Ag wire was used. Additionally, the Ag wire pseudo-reference electrode is known to be unstable.

2.2.4.1. Oxidative IR-SEC of $Re(bpy)(CO)_3Cl$

The results of IR-SEC oxidation of $Re(bpy)(CO)_3Cl$ are available in Figure 2.10. Regarding $Re(bpy)(CO)_3Cl$, cyclic voltammetric sweeps (3 cycles, 100 mV/s) were undertaken at a platinum gauze working electrode, extending from lower (0 to 0.8 V) to higher (0 to 1.6 V) potential.

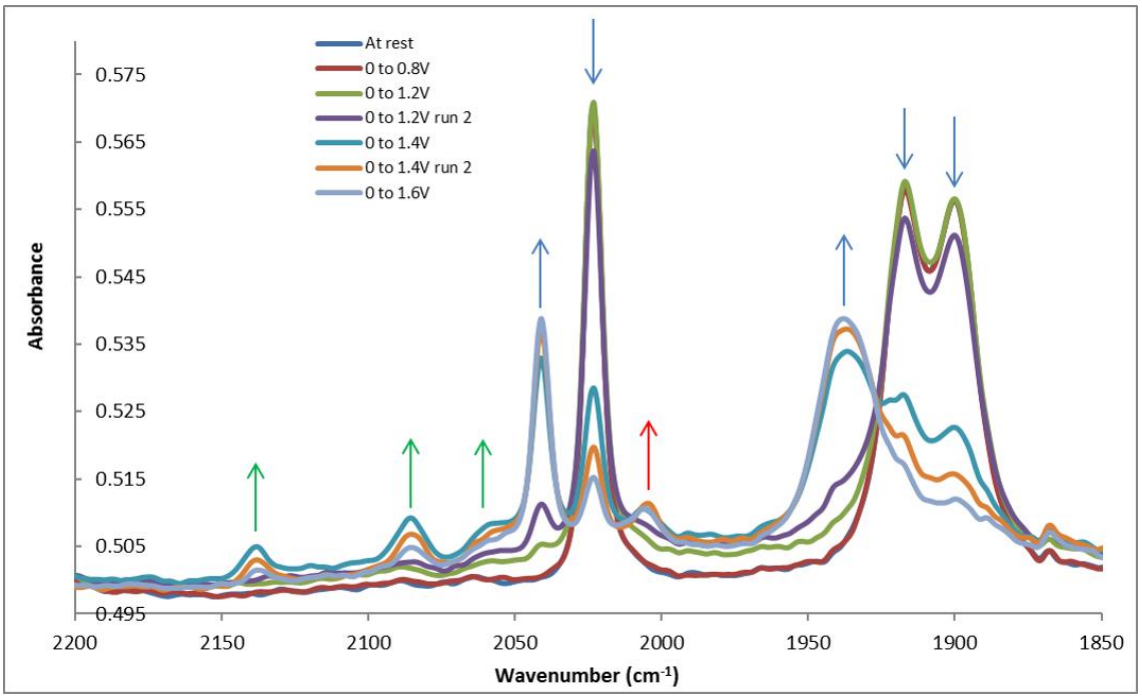

Figure 2.10: Oxidative IR-SEC of $Re(bpy)(CO)_3Cl$, cyclic voltammetric scans at Pt mesh to 1.6V vs Ag wire in MeCN, 0.1M $TBAPF_6$

Upon oxidation of the Re centre, the three ν(CO) stretches of $Re(bpy)(CO)_3Cl$ at 2023, 1917 and 1900 cm^{-1} (downward blue arrow) changed considerably, showing a slender band at 2041 cm^{-1} and a broad band at 1938 cm^{-1} (upward blue arrow). This spectrum is in very close agreement with values quoted for $[Re(bpy)(CO)_3MeCN]^+$ [47,48], suggesting that oxidation of the Re centre results in loss of chloride, followed by solvolysis with MeCN [49]. The shift to higher energy of the stretches is explained by the π-backbonding ability of M-CO decreasing due to the overall positive charge on the complex. Accompanied with this change is observation of a species which was previously attributed as a disproportionation 7-coordinate product ($Re^{3+}(bpy)(CO)_3Cl_2$), with bands at 2138, 2084 and 2057 cm^{-1} (green arrows) [49]. A further weak band also

appears at 2005 cm^{-1} (red arrow), however, this feature is unassigned. An irreversibility of the electrochemical process up to 500 mV s^{-1} was observed at glassy carbon and is displayed in Appendix A.16. Slight quasireversible reductive behaviour was observed at higher scan rates, up to 20 V s^{-1}. However, a return of the original species due to cycling of potential at 100 mV s^{-1}, as per IR-SEC, is not expected.

2.2.4.2. Oxidative IR-SEC of $Re(qpy)(CO)_3Cl$

Figure 2.11 shows the oxidative IR-SEC behaviour of $Re(qpy)(CO)_3Cl$ following voltammetry from 0 to 1.4 V vs Ag wire. A difference spectrum is included to elucidate the changes observed. Due to solubility issues associated with the complex in acetonitrile, the new bands formed upon the cycling of potential were more difficult to detect than with experiments involving $Re(bpy)(CO)_3Cl$. Precipitation of the product may also not be excluded as a possibility. Gradual changes were elucidated upon electrolyses with incremented potential from 0.7 to 1.1 V vs Ag wire and show the same formations. The difference spectra associated with this appear in Figure 2.12. Shown also is electrolysis at 1.2 V, whereby degradation of the complex was noted.

Upon oxidation with either the voltammetric or electrolytic method, $Re(qpy)(CO)_3Cl$ undergoes a decrease of intensity of the parent ν_{CO} bands at 2024, 1918 and 1901 cm^{-1} and the growth of a slender peak at 2042 cm^{-1} and a broad feature at 1940 cm^{-1}. These figures very closely match that observed with $Re(bpy)(CO)_3Cl$, suggesting that the irreversible oxidation that occurs with $Re(qpy)(CO)_3Cl$ is akin to that of $Re(bpy)(CO)_3Cl$, with loss of chloride and solvolysis to produce $[Re(qpy)(CO)_3MeCN]^+$. Formation of the 7-coordinate $Re^{3+}(qpy)(CO)_3Cl_2$ was not apparent as was the case with $Re(bpy)(CO)_3Cl$ [49].

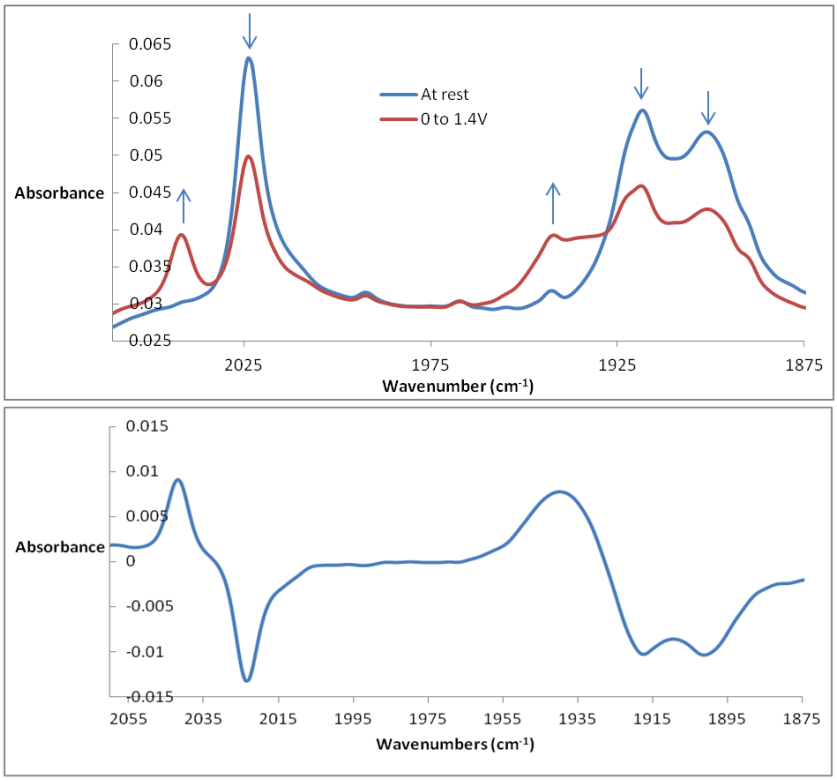

Figure 2.11: Above: Oxidative IR-SEC of $Re(qpy)(CO)_3Cl$. at rest and with cyclic voltammetry (ν = 100 mV s^{-1}) from 0 to 1.4 V vs Ag wire in MeCN, 0.1 M $TBAPF_6$. Below: Difference spectrum of changes occurring (0 to 1.4 V – rest)

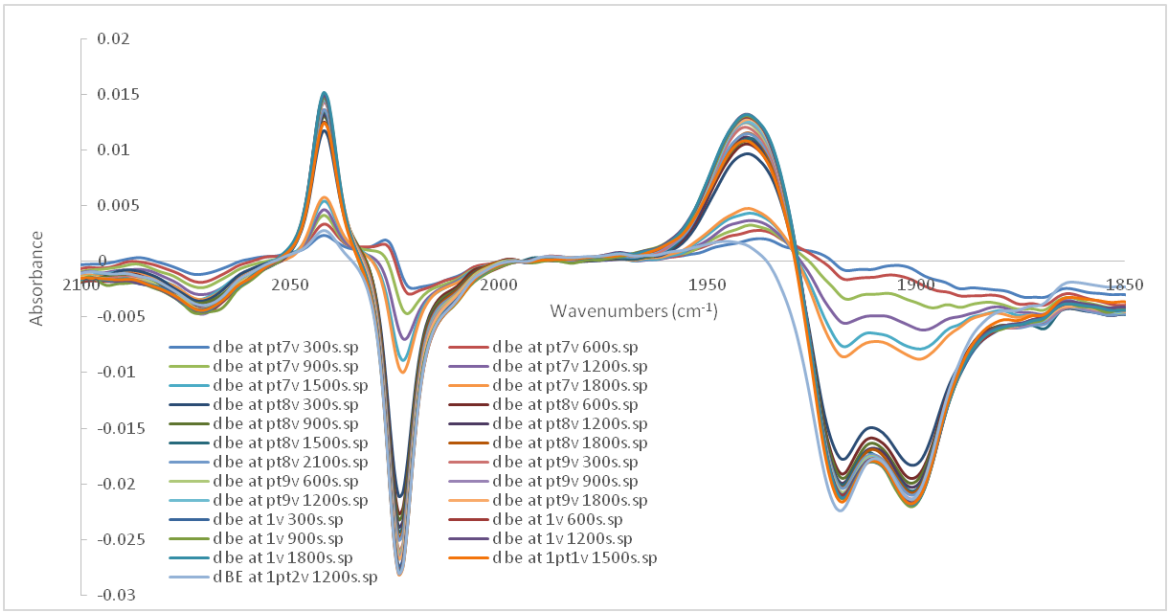

Figure 2.12: IR-SEC difference spectra of $Re(qpy)(CO)_3Cl$ in MeCN with controlled potential electrolyses from 0.7 V to 1.2 V vs Ag wire. Spectra are baseline corrected to 1995 cm^{-1}

2.2.4.3. Oxidative IR-SEC of RuRe

The oxidation of RuRe (Figure 2.13) was investigated through the gradual increase of electrolysis potential. Two spectral changes were observed at potentials of 0.5 V vs Ag wire and higher.

The bands associated with the three Re-CO bonds of the parent complex (at 2024, 1918 and 1903 cm^{-1}, blue arrows) depleted with the formation of a sharp feature at 2036 cm^{-1} along with the formation of a further band at approximately 1933 cm^{-1} (green arrows). The peak of the parent complex at 1918 cm^{-1} decreases less rapidly than the peaks at 2024 or 1903 cm^{-1}, suggesting that the feature at approximately 1933 cm^{-1} is broad and extends under the parent band at 1918 cm^{-1}. Though the energy of the new peaks isn't shifted to as high in frequency, as in the cases of $Re(bpy)(CO)_3Cl$ and $Re(qpy)(CO)_3Cl$, a slender and broad peak was again observed, consistent with the formation of the $[(bpy)_2Ru(qpy)Re(CO)_3MeCN]^{3+}$.

The second change observed is the formation of two bands, at 2055 and 2042 cm in addition to a broader feature at 1949 cm^{-1} (orange arrows). These bands are very weak with respect to the parent bands. In addition to this, other associated bands may be obscured by residual parent and first oxidation bands. It does appear, however, that the bands of the second oxidation (orange arrows) form together. Analogous oxidative IR SEC studies of dinuclear metal carbonyl complexes have not been found within the literature to base a comparison from.

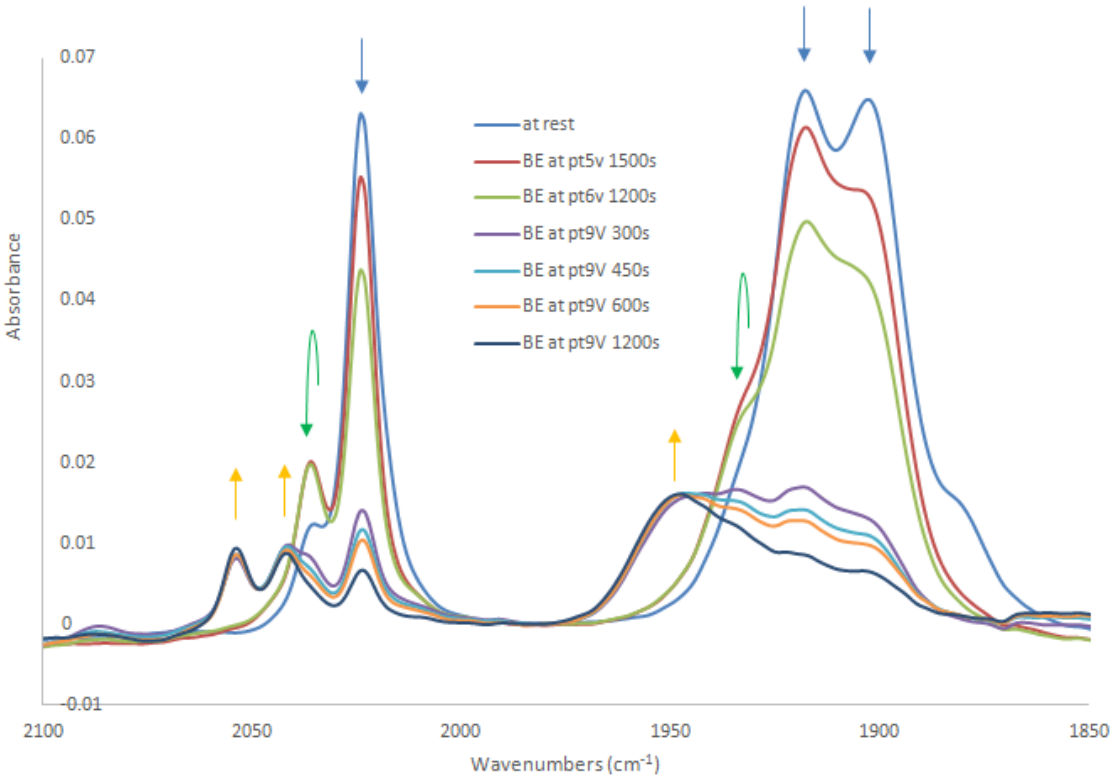

Figure 2.13: IR SEC of the first and second changes observed for RuRe, controlled potential electrolysis at Pt gauze electrode in MeCN with 0.1 M $TBAPF_6$, potentials vs Ag wire

In a separate experiment, following production of the first change, a switching of the potential to 0 V showed no significant changes. This irreversibility suggests a Re based oxidation of the compound, (scan rates of up to 10 V/s does not lead to reversibility within $Re(qpy)(CO)_3Cl$, Appendix A.12). As previously stated, irreversibility of the first process is in contrast to the literature [50–52] whereby Ru centred oxidation is often less positive to that of Re in similar complexes.

Potentials positive of 0.9 V led to diminishing of all signals, akin to the behaviour observed within $Re(qpy)(CO)_3Cl$ IR SEC.

2.2.5. Energetic feasibility of the systems towards the generation of a Re(ligand) based one electron reduced species

To better understand the lower photocatalytic ability of RuRe as compared to the intermolecular approach of $[Ru(bpy)_3]^{2+}$ with $Re(bpy)(CO)_3Cl$, examination of ground and excited state potentials was performed on both systems. For each system, there is the potential for either an oxidative or reductive quenching mechanism, as explained in Figure 2.14.

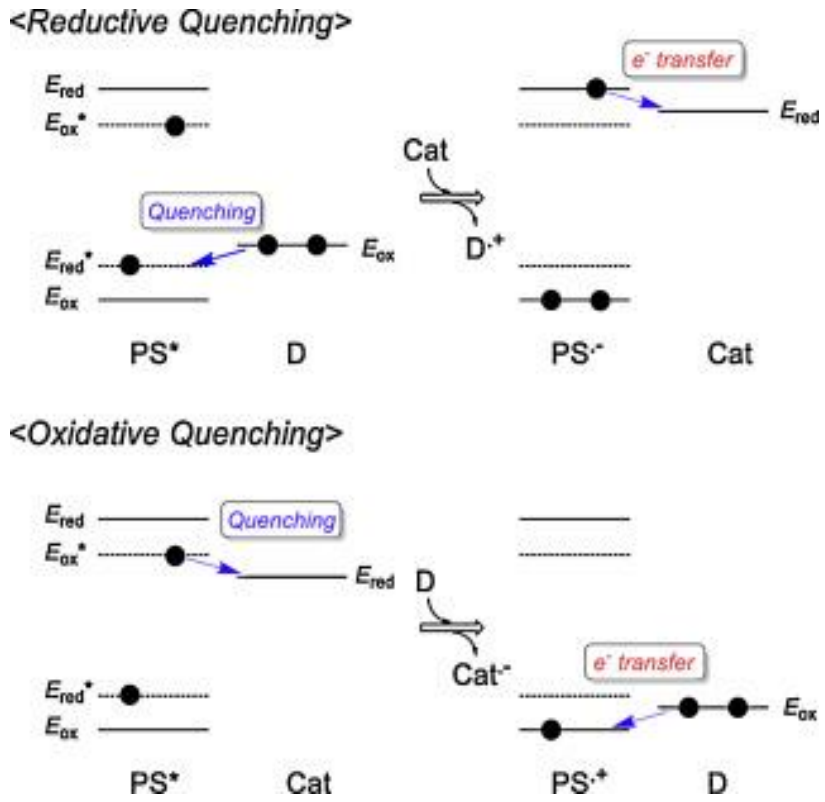

Figure 2.14: Oxidative and reductive quenching scenarios related to photocatalytic reduction reactions, reproduced from Yamazaki *et al*. [53]

Both paths, leading to a OER catalyst, involve two key steps. In the oxidative quenching pathway, the PS* reduces the catalyst. Following this, PS^+ is re-reduced to PS by the sacrificial electron donor. In the reductive quenching pathway, PS* is first reduced by the sacrificial donor. Subsequently, $PS^{\cdot-}$ reduces the catalyst. Electron transfer has been stated as feasibile if the $E_{1/2}$ of the electron accepting species is similar to or more

negative than the oxidation potential of the electron donor (either PS to catalyst, or electron donor to PS) [53,54].

Within section 2.2.5, $[Ru(bpy)_3]^{2+}$ is referred to as PS and $Re(bpy)(CO)_3Cl$ is referred to as Cat. For example, PS^+ refers to the singly oxidised species $[Ru(bpy)_3]^{3+}$.

2.2.5.1. Oxidative quenching scenario of the $[Ru(bpy)_3]^{2+}$, $Re(bpy)(CO)_3Cl$ and TEOA system

In the oxidative quenching scenario, PS is first excited. PS* passes an electron to the Cat, prior to the oxidised PS^+ receiving an electron from TEOA. In order to calculate the thermodynamic feasibility of electron transfer, the excited state oxidation potential of the PS is first calculated with Equation 2.1 [17,55].

$$E(PS^*/PS^+) = E(PS/PS^+) - E_{0\text{-}0} \qquad \text{Equation 2.1}$$

Whereby the $E_{0\text{-}0}$ is 0-0 excitation energy in electron volts, i.e. the energy difference between the ground and excited states, taken at zero vibrational level [55].

The $E_{1/2}$ of PS/PS^+ was found to be 0.89 V vs Fc/Fc^+ in MeCN (see Table 2.1). The $E_{0\text{-}0}$ may be approximated as the energy at the intersection between normalised absorption and emission spectra [56]. Absorption and emission spectra were acquired for the PS in DMF (as shown in Appendix A.17) and the $E_{0\text{-}0}$ was determined as 548 nm, equating to 2.26 eV. Therefore, the excited state oxidation potential of PS^*/PS^+ is -1.37 V vs Fc/Fc^+. The $E_{1/2}$ of Cat/Cat^- (as shown in Table 2.1) is -1.74 V. Therefore, from a thermodynamic aspect, it is not feasible for PS* to reduce Cat.

The second step of the oxidative quenching pathway would however be feasible. The $E_{1/2}$ of the first oxidation of the PS is 0.89 V vs Fc/Fc^+ (see Table 2.1). Therefore, the reduction potential of the PS^+/PS reversible couple is also assumed as 0.89 V vs Fc/Fc^+. The oxidation potential of TEOA is stated in the literature as the more negative potential of 0.33 V vs Fc/Fc^+ [54]. As the reduction potential of PS^+/PS is more positive than the oxidation potential of TEOA, electron transfer may proceed [53].

2.2.5.2. Reductive quenching scenario of the $[Ru(bpy)_3]^{2+}$, $Re(bpy)(CO)_3Cl$ and TEOA system

In the reductive quenching system, PS is first excited. PS* gains an electron from the SD, prior to reduction of the Cat. The first step requires calculation of the PS^*/PS^- couple. This is calculated as per Equation 2.2 [17,55].

$$E(PS^*/PS^-) = E(PS/PS^-) + E_{0\text{-}0} \qquad \text{Equation 2.2}$$

The first reduction of the PS occurs with $E_{1/2}$ of -1.74 V vs Fc/Fc^+ (see Table 2.1). As previously stated (and shown in Appendix A.17), the $E_{0\text{-}0}$ of the PS was found to be 2.26 eV. Therefore, the excited state reduction potential amounts to 0.52 V. (Note: the oxidation potential of TEOA is stated in the literature as +0.33 V vs Fc/Fc^+). Therefore, electron transfer from TEOA to the PS may proceed from a thermodynamic aspect.

The second step of electron transfer occurs with PS^- reducing Cat. The $E_{1/2}$ of these processes are equal at -1.74 V vs Fc/Fc^+ (Table 2.1), meaning that electron transfer may proceed [53].

2.2.5.3. Oxidative quenching scenario of RuRe and TEOA system

Quenching experiments of RuRe with TEOA were not undertaken. However, excitation of the complex was undertaken at 470 nm, thereby selectively irradiating the Ru-L MLCT. The resulting emission and excitation spectra, as acquired in MeCN, are shown in Appendix A.18. An approximate $E_{0\text{-}0}$ value of 571 nm was obtained. This value equates to 2.17 eV. The first oxidation of RuRe occurs with $E_{1/2}$ of 0.93 V vs Fc/Fc^+. Therefore, as per Equation 2.1, the $[RuRe]^*/ [Ru^+Re^-]$ excited state oxidation potential occurs at -1.24 V vs Fc/Fc^+. The first two ground state reduction potentials of RuRe are -1.4 V and -1.62 V vs Fc/Fc^+ (Table 2.1). These processes, with comparison to $Re(qpy)(CO)_3Cl$, are Ru-L based and Re-L based reductions respectively. Therefore, intramolecular oxidative quenching of Ru by Re subunits is thermodynamically not feasible. Furthermore, intermolecular oxidative quenching of [RuRe]* by the Ru subunit of a ground state RuRe molecule is unfavoured.

The second step would be whether TEOA could replenish the electron within $[RuRe]^+$. As the potential of $[RuRe]^+$ (0.93 V) is more positive than that of TEOA (0.33 V),

electron transfer could proceed. However, as stated, it is not thermodynamically feasible for $[Ru^{+}Re^{-}]$ to be generated.

2.2.5.4. Reductive quenching scenario of RuRe and TEOA system

The first (and Ru-L based) reduction of RuRe occurs at -1.4 V vs Fc/Fc^{+} and the $E_{0\text{-}0}$ was approximated as 2.17 eV (see Appendix A.18). The excited state reduction potential of RuRe, i.e. $[RuRe]^{*}/[Ru^{-}Re]$ is +0.77 V vs Fc/Fc^{+}. As the oxidation potential of TEOA is 0.33 V, this reaction is expected to proceed.

The second step is a comparison of Ru-L and Re-L first reduction potentials. As electrochemical results for $Re(qpy)(CO)_3Cl$ heavily imply that the second reduction within RuRe is that of the Re subunit's ligand based reduction, the Re-L based reduction occurs at 0.22 V more negative to that of the Ru-L based reduction (-1.62 V and -1.4 V vs Fc/Fc^{+} respectively). Therefore, though quenching of the excited state of RuRe by TEOA is likely, the subsequent reduction of the Re-L moiety may not occur.

It is noted within these calculations that only the first reduction of Re-L is considered. When CO_2 was introduced to $Re(bpy)(CO)_3Cl$ in DMF (however, in the absence of TEOA), voltammetric enhancement, i.e. catalytic current was only observed at approximately the potential of its first reduction (see Appendix B.5**ii**). In an active Ru-Re intramolecular complex, voltammetric enhancement was, however, shown to occur at the first reduction upon the introduction of CO_2 [57]. $Re(bpy)(CO)_3Cl$ additionally demonstrates activity at 470 nm (see Figure 2.4). Therefore, partial activity of the $[Ru(bpy)_3]^{2+}$ + $Re(bpy)(CO)_3Cl$ system is due to $Re(bpy)(CO)_3Cl$ acting in a photosensitiser capacity. Increasing the concentration of $Re(dmb)(CO)_3Cl$ has previously shown to not only increase TON_{CO}, but also TOF_{CO}, implying a bimolecular reaction within $Re(dmb)(CO)_3Cl$ upon the reduction of CO_2 [58].

2.2.6. Photocatalytic reduction of CO_2 using Re(Brbpy)(CO)$_3$Cl with $[Ru(bpy)_3]^{2+}$ in DMF/TEOA (5:1 v/v)

Further to RuRe as an intramolecular approach, Re(Brbpy)(CO)$_3$Cl was assessed as a potential photocatalyst towards CO_2 reduction. Calculations based on electrochemical data and photophysical data (within section 2.2.5) suggest that a potential reason for the relatively low activity of the $[Ru(bpy)_3]^{2+}$ PS with Re(bpy)(CO)$_3$Cl may be due to their similar first reduction potentials, thereby hindering efficient transfer from $[Ru(bpy)_3]^{\bullet-}$ to Re(bpy)(CO)$_3$Cl. In an effort to increase the driving force of this step, Re(Brbpy)(CO)$_3$Cl was synthesised. Though electrochemistry of the complex was not undertaken, a lower energy shift in the MLCT λ_{max} of 12 nm (to λ_{max} of 482 nm in MeCN) within the UV-visible spectra (Appendix A.19) indicates that the Br group has an electron withdrawing effect on the complex, with the expected effect of shifting the reduction potential of both the bpy based and metal centred reductions to more positive values.

The results of 134 μM $[Ru(bpy)_3]^{2+}$ + 100 μM Re(Brbpy)(CO)$_3$Cl as compared to 134 μM $[Ru(bpy)_3]^{2+}$ + 100 μM Re(bpy)(CO)$_3$Cl are shown in Figure 2.15.

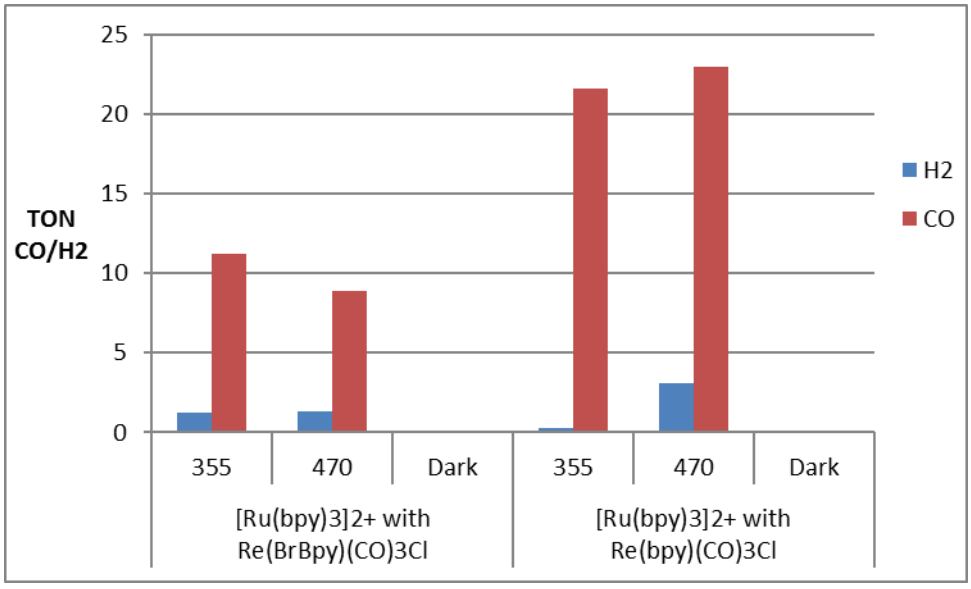

Figure 2.15: Photocatalytic reduction of CO_2 with 134 μM $[Ru(bpy)_3]^{2+}$ and either 100 μM Re(Brbpy)(CO)$_3$Cl or 100 μM Re(bpy)(CO)$_3$Cl in DMF/TEOA (5:1). Samples were irradiated for 21 hours

The new system of $[Ru(bpy)_3]^{2+}$ with $Re(Brbpy)(CO)_3Cl$ is catalytically active towards CO_2 reduction to CO, however at a decreased rate compared to with $Re(bpy)(CO)_3Cl$ present. Despite increasing the reducing power of $[Ru(bpy)_3]^{2+}$ relative to the Re-based catalyst, an approximate halving of the TON_{CO} within the complexes was observed. This accentuates the importance of the reducing power of the reduced Re species towards the reduction of CO_2. The same effect is assumed in the case of the Re portion of RuRe with respect to $Re(bpy)(CO)_3Cl$.

2.3. Concluding remarks

Within this chapter, a Ru-Re intramolecular complex bridged by two directly linked bipyridyl units was assessed for the first time in the interest of photocatalytic CO_2 reduction. A solvent and electron donor optimisation was undertaken. Within this study, the TON_{CO} of RuRe was increased from ~ 1 in MeCN/TEA to ~ 7 in DMF/TEOA with λ = 470 nm. Significantly poorer TON_{CO} values were obtained with λ = 355 nm and λ > 400 nm sources. However, the intermolecular system of $[Ru(bpy)_3]^{2+}$ + $Re(bpy)(CO)_3Cl$ under the same conditions in DMF/TEOA produced up to 35 TON_{CO}.

The voltammetry of RuRe and $Re(qpy)(CO)_3Cl$ revealed that the first reductions of the RuRe complex were at a less negative potential than those within the mononuclear $[Ru(bpy)_3]^{2+}$ and $Re(bpy)(CO)_3Cl$, with the first reduction of $Re(qpy)(CO)_3Cl$ matching the potential of the second reduction of RuRe. Due to the very similar potentials of the first reduction within $Re(qpy)(CO)_3Cl$ and second reduction of RuRe, communication between the two metal centres appeared to be weak.

UV-Vis-NIR spectroelectrochemistry of RuRe did not show the presence of an intervalence charge transfer band in the NIR region, however, the ~ 100 mV separation between E_{pa}s of the $Ru^{2+/3+}$ and $Re^{1+/2+}$ metal centred oxidations provided difficulty in selective oxidation of one metal centre over simultaneous oxidation of both centres. The dominant changes occurring within UV-visible spectroelectrochemistry may however be attributable to the oxidation of the Ru centre. Within IR-SEC, two sets of stretching vibrations were apparent. It is uncertain as to whether these sets of peaks arose from oxidation of the Ru and then the Re centres, or from the oxidation of the Re centre and then of a product formed from the Re oxidation. However, despite the first formation

resembling that of a Re *fac*-tricarbonyl complex as in the oxidations of $Re(bpy)(CO)_3Cl$ and $Re(qpy)(CO)_3Cl$, the second formation resulted in a pattern atypical of a tricarbonyl species.

The energetic feasibility of the inter- and intramolecular systems was explored using electrochemical data and approximations of $E_{0\text{-}0}$ values. It was found that the only energetically feasible catalytic scenario was that of reductive quenching within the intermolecular system, which supports the observations of TON_{CO} obtained, and that TEOA quenches the fluorescence of $[Ru(bpy)_3]^{2+}$.

Furthermore, the energy assessment (and reductive cyclic voltammetry) within the first two stages of photocatalytic reaction revealed the similarity of the first reductions within both $Re(bpy)(CO)_3Cl$ and $[Ru(bpy)_3]^{2+}$. To increase the potential difference involved in the reduction of the catalyst by $[Ru(bpy)_3]^{2+}$, the electron withdrawn $Re(Brbpy)(CO)_3Cl$ was assessed in the system in place of $Re(bpy)(CO)_3Cl$. The results of this were however, inferior to that of $Re(bpy)(CO)_3Cl$, heavily suggesting that the critical potential within the first two steps of catalysis is that of the Re-based catalysts first or second reduction, i.e. the driving force behind CO_2 binding and reduction.

2.4. References

[1] L. Moreira, J. Calbo, J. Aragó, B. M. Illescas, I. Nierengarten, B. Delavaux-Nicot, E. Ortí, N. Martín, J.-F. Nierengarten, *J. Am. Chem. Soc.* **2016**, *138*, 15359–15367.
[2] Y. Halpin, L. Cleary, L. Cassidy, S. Horne, D. Dini, W. R. Browne, J. G. Vos, *Dalton Trans.* **2009**, 4146.
[3] A. Paul, D. Connolly, M. Schulz, M. T. Pryce, J. G. Vos, *Inorg. Chem.* **2012**, *51*, 1977–1979.
[4] Y. Kuramochi, M. Kamiya, H. Ishida, *Inorg. Chem.* **2014**, *53*, 3326–3332.
[5] M. B. Miller, D.-L. Chen, D. R. Luebke, J. K. Johnson, R. M. Enick, *J. Chem. Eng. Data* **2011**, *56*, 1565–1572.
[6] T. Morimoto, T. Nakajima, S. Sawa, R. Nakanishi, D. Imori, O. Ishitani, *J. Am. Chem. Soc.* **2013**, *135*, 16825–16828.
[7] B. Gholamkhass, H. Mametsuka, K. Koike, T. Tanabe, M. Furue, O. Ishitani, *Inorg. Chem.* **2005**, *44*, 2326–2336.
[8] H. Takeda, K. Koike, H. Inoue, O. Ishitani, *J. Am. Chem. Soc.* **2008**, *130*, 2023–2031.
[9] Y. Tamaki, T. Morimoto, K. Koike, O. Ishitani, *Proc. Natl. Acad. Sci. U. S. A.* **2012**, *109*, 15673–15678.
[10] J. Rohacova, O. Ishitani, *Chem. Sci.* **2016**, *7*, 6728–6739.
[11] R. Ziessel, J. Hawecker, J.-M. Lehn, *Helv. Chim. Acta* **1986**, *69*, 1065–1084.
[12] O. Ishitani, K. Ishii, S. Yanagida, C. Pac, T. Ohno, A. Yoshimura, *Chem. Lett.* **1989**, *18*, 217–220.
[13] C. R. Rivarola, S. G. Bertolotti, C. M. Previtali, *Photochem. Photobiol.* **2006**, *82*, 213–218.
[14] M. Zhou, J. Roovers, *Macromolecules* **2001**, *34*, 244–252.
[15] M. Zhou, G. P. Robertson, J. Roovers, *Inorg. Chem.* **2005**, *44*, 8317–8325.
[16] K. Kalyanasundaram, *Coord. Chem. Rev.* **1982**, *46*, 159–244.
[17] A. Juris, V. Balzani, F. Barigelletti, S. Campagna, P. Belser, A. von Zelewsky, *Coord. Chem. Rev.* **1988**, *84*, 85–277.
[18] T. Saji, S. Aoyagui, *J. Electroanal. Chem. Interfacial Electrochem.* **1975**, *58*, 401–410.
[19] G. Sahara, O. Ishitani, *Inorg. Chem.* **2015**, *54*, 5096–5104.
[20] H. Takeda, K. Koike, T. Morimoto, H. Inumaru, O. Ishitani, in *Adv. Inorg. Chem.* (Ed.: R. van E. and G. Stochel), Academic Press, **2011**, pp. 137–186.
[21] H. Takeda, O. Ishitani, *Coord. Chem. Rev.* **2010**, *254*, 346–354.
[22] Y. Kuramochi, K. Fukaya, M. Yoshida, H. Ishida, *Chem. – Eur. J.* **2015**, *21*, 10049–10060.
[23] T. M. Pappenfus, K. R. Mann, *Inorg. Chem.* **2001**, *40*, 6301–6307.
[24] A. Juris, S. Campagna, I. Bidd, J. M. Lehn, R. Ziessel, *Inorg. Chem.* **1988**, *27*, 4007–4011.
[25] G. Sahara, H. Kumagai, K. Maeda, N. Kaeffer, V. Artero, M. Higashi, R. Abe, O. Ishitani, *J. Am. Chem. Soc.* **2016**, *138*, 14152–14158.
[26] R. L. Cleary, K. J. Byrom, D. A. Bardwell, J. C. Jeffery, M. D. Ward, G. Calogero, N. Armaroli, L. Flamigni, F. Barigelletti, *Inorg. Chem.* **1997**, *36*, 2601–2609.
[27] A. J. Downard, G. E. Honey, L. F. Phillips, P. J. Steel, *Inorg. Chem.* **1991**, *30*, 2259–2260.
[28] J.-D. Compain, M. Bourrez, M. Haukka, A. Deronzier, S. Chardon-Noblat, *Chem. Commun.* **2014**, *50*, 2539–2542.

[29] P. A. Anderson, F. R. Keene, E. Horn, E. R. T. Tiekink, *Appl. Organomet. Chem.* **1990**, *4*, 523–533.
[30] J. E. Beves, E. L. Dunphy, E. C. Constable, C. E. Housecroft, C. J. Kepert, M. Neuburger, D. J. Price, S. Schaffner, *Dalton Trans.* **2008**, 386–396.
[31] L. Gou, *Z. Für Krist. - New Cryst. Struct.* **2014**, *224*, 561–562.
[32] E. Rousset, D. Chartrand, I. Ciofini, V. Marvaud, G. S. Hanan, *Chem. Commun.* **2015**, *51*, 9261–9264.
[33] P. de Wolf, P. Waywell, M. Hanson, S. L. Heath, A. J. H. M. Meijer, S. J. Teat, J. A. Thomas, *Chem. – Eur. J.* **2006**, *12*, 2188–2195.
[34] H. Ahmad, A. Wragg, W. Cullen, C. Wombwell, A. J. H. M. Meijer, J. A. Thomas, *Chem. – Eur. J.* **2014**, *20*, 3089–3096.
[35] H. Ahmad, A. J. H. M. Meijer, J. A. Thomas, *Chem. – Asian J.* **2011**, *6*, 2339–2351.
[36] E. C. Constable, S. M. Elder, J. Healy, D. A. Tocher, *J. Chem. Soc., Dalton Trans.* **1990**, 1669–1674.
[37] R. L. Cleary, D. A. Bardwell, M. Murray, J. C. Jeffery, M. D. Ward, *J. Chem. Soc., Perkin Trans. 2* **1997**, 2179–2184.
[38] N. Das, G. S. Bindra, A. Paul, J. G. Vos, M. Schulz, M. T. Pryce, *Chem. – Eur. J.* **2017**, *23*, 5330–5337.
[39] Y.-Z. Hu, Q. Xiang, R. P. Thummel, *Inorg. Chem.* **2002**, *41*, 3423–3428.
[40] X. Li, D. Zhang, G. Lu, G. Xiao, H. Chi, Y. Dong, Z. Zhang, Z. Hu, *J. Photochem. Photobiol. Chem.* **2012**, *241*, 1–7.
[41] A. Paul, Synthesis and Characterisation of Polypyridyl Metal Complexes for New Fuels, doctoral, Dublin City University. School of Chemical Sciences, **2012**.
[42] N. Das, Metal Carbonyl Complexes and Porphyrin Macrocyles: Photochemistry and Potential Therapeutic Applications, doctoral, Dublin City University. School of Chemical Sciences, **2014**.
[43] C. Hansch, A. Leo, R. W. Taft, *Chem. Rev.* **1991**, *91*, 165–195.
[44] D. M. D'Alessandro, F. R. Keene, *Chem. Rev.* **2006**, *106*, 2270–2298.
[45] D. M. D'Alessandro, P. H. Dinolfo, M. S. Davies, J. T. Hupp, F. R. Keene, *Inorg. Chem.* **2006**, *45*, 3261–3274.
[46] K. Kalyanasundaram, S. M. Zakeeruddin, M. K. Nazeeruddin, *Coord. Chem. Rev.* **1994**, *132*, 259–264.
[47] A. Klein, C. Vogler, W. Kaim, *Organometallics* **1996**, *15*, 236–244.
[48] F. P. A. Johnson, M. W. George, F. Hartl, J. J. Turner, *Organometallics* **1996**, *15*, 3374–3387.
[49] J. P. Bullock, E. Carter, R. Johnson, A. T. Kennedy, S. E. Key, B. J. Kraft, D. Saxon, P. Underwood, *Inorg. Chem.* **2008**, *47*, 7880–7887.
[50] Z.-Y. Bian, S.-M. Chi, L. Li, W. Fu, *Dalton Trans.* **2010**, *39*, 7884–7887.
[51] V. Balzani, A. Juris, M. Venturi, S. Campagna, S. Serroni, *Chem. Rev.* **1996**, *96*, 759–834.
[52] Z.-Y. Bian, K. Sumi, M. Furue, S. Sato, K. Koike, O. Ishitani, *Dalton Trans.* **2009**, 983–993.
[53] Y. Yamazaki, H. Takeda, O. Ishitani, *J. Photochem. Photobiol. C Photochem. Rev.* **2015**, *25*, 106–137.
[54] S. Jasimuddin, T. Yamada, K. Fukuju, J. Otsuki, K. Sakai, *Chem. Commun.* **2010**, *46*, 8466–8468.
[55] P. Ceroni, V. Balzani, in *Explor. Supramol. Syst. Nanostructures Photochem. Tech.* (Ed.: P. Ceroni), Springer Netherlands, **2012**, pp. 21–38.
[56] W. Xu, B. Peng, J. Chen, M. Liang, F. Cai, *J. Phys. Chem. C* **2008**, *112*, 874–880.

[57] K. Wada, M. Eguchi, O. Ishitani, K. Maeda, *ChemSusChem* **2017**, *10*, 287–295.
[58] S. Meister, R. O. Reithmeier, M. Tschurl, U. Heiz, B. Rieger, *ChemCatChem* **2015**, *7*, 690–697.

Chapter 3. The electrocatalytic activity of a series of Cobalt salicylidene (Salen) complexes towards CO_2 reduction

3.1. Introduction

As outlined in chapter one, significant progress has been made in indentifying cheaper and sustainable catalysts for the purpose of electrocatalytic CO_2 reduction, and particularly so, within the past three years. However, many of these complexes have some downfalls. For example, the highly touted family of iron porphyrins currently suffer from an often low-yielding synthesis (with typical yields < 25% for the unsubstituted and symmetrical TPP ligand [1–3]), manganese tricarbonyl complexes are often air- and photosensitive [4,5], nickel cyclams are known to be less active at carbon than Hg electrodes [6], and over time, Ni-CO poisoning of the mercury surface occurs [7,8]. Furthermore, it would be advantageous to discover a set of conditions for a family of catalysts or indeed a new family of catalysts that could operate at even lower overpotentials, and/or operate with greater speed than iron porphyrins.

One premise of the research presented subsequently, is to further explore other electrocatalysts that are regarded as being sustainable. The salen and salophen ligands, in contrast to porphyrins, are typically very high-yielding condensations of 1,2-diamines and a salicylaldehyde (symmetrical ligands not uncommonly synthesised in > 95% yield [9–13]), both relatively commercially cheap starting materials. Synthesis is generally straight-forward with pure ligand in most cases, precipitating from alcohol, requiring only further washing with alcohol. Additionally, reactions are quite often not reported to require inert conditions. The metallation of such ligands with a Co(II) salt is often reported in > 70% yield, utilising recrystallisation and/or washing as purification method [14–17]. Cobalt as a metal centre is far more abundant than that of the often studied rhenium and other third row transition metals, and as a result, would offer a reasonable alternative in terms of low cost and sustainability.

Cobalt salens and salophens have been reported widely as CO_2/epoxide co-polymerisation [18] and water oxidation [14,19] catalysts among other applications, with sparsely reported applications for heterogeneous photo- [20] and electrocatalytic water reduction [21]. Co salen [22] and Co salophen [23] have been explored as CO_2

reducing electrocatalysts with the use of a mercury electrode (0.1 M $LiClO_4$ in MeCN). The alkali metal ion as lewis acid has been emphasised as pertinent to CO_2 reduction within these complexes, as has been mentioned previously for Fe porphyrins [24] and more recently, Mn tricarbonyls [25] with the addition of the alkaline earth metal of Mg^{2+}. A polypyrrole-Co schiff base film was also reported for heterogeneous electrocatalytic CO_2 reduction at a gold electrode in MeCN with 0.1 M TBAP [26]. Recently, Co salen was incorporated with carbon black and nafion to generate formate heterogeneously in an aqueous $KHCO_3$ electrolyte [27].

In terms of the use of alkali metal cation electrolytes, a study probing the potential of electrolyte catalysis towards CO_2 electroreduction found that while tetraalkylammonium ions are not catalysts, Li^+ actually inhibited reduction [28]. Therefore, it may be more beneficial to avoid the use of Li^+ where alternative additives can be utilised. To this end, a more recent advent within the area is the full extent to which the addition of bronsted acids can boost catalysts' activity towards CO_2 reduction (though water as a Bronsted acid has been used early in molecular CO_2 reduction [29,30]). How drastic a positive effect water can have on molecular electrocatalytic CO_2 reduction (e.g. with many Mn diimine complexes requiring a proton source to have any activity) was not common knowledge at the time of the studies by Pearce and Isse. In the interest of probing a potential benefit relating to bronsted acid interactions with salens, the inclusion of 5% water has been rationalised. This could circumvent any potential inhibition, as witnessed with the use of Li^+ [28]. It is also of particular interest to further assess the salen complexes with an inexpensive and abundant electrode material such as carbon. This has been achieved with the Co salen complex in carbon black in a heterogeneous manner, but has not been explored homogeneously.

Moreover, Co salens or salophens have not previously been incorporated into a molecular-based photocatalytic CO_2 reduction system. With the correct choice of photosensitiser and sacrificial donor, this aim is feasible, provided that the complexes display an adequate reducing ability and stability towards electrocatalysis of CO_2.

3.2. Results and discussion:

3.2.1. Electrocatalytic CO_2 reduction by Cobalt Salen complexes, cyclic voltammetry

Four Salen complexes of varying electron density to the Co centre were assessed for homogeneous electrocatalytic CO_2 reduction ability. These include CoSal, CobdtChexSal, CodBrSal and CopdSal as depicted in Figure 3.1. CoSal, CobdtChexSal and CopdSal were procured from Sigma Aldrich, whereas CodBrSal was synthesised (see Chapter 5). Unless otherwise stated, all of the potentials quoted are in reference to the $E_{1/2}$ of the $Fe^{2+/3+}$ couple of ferrocene (Fc/Fc^{+}).

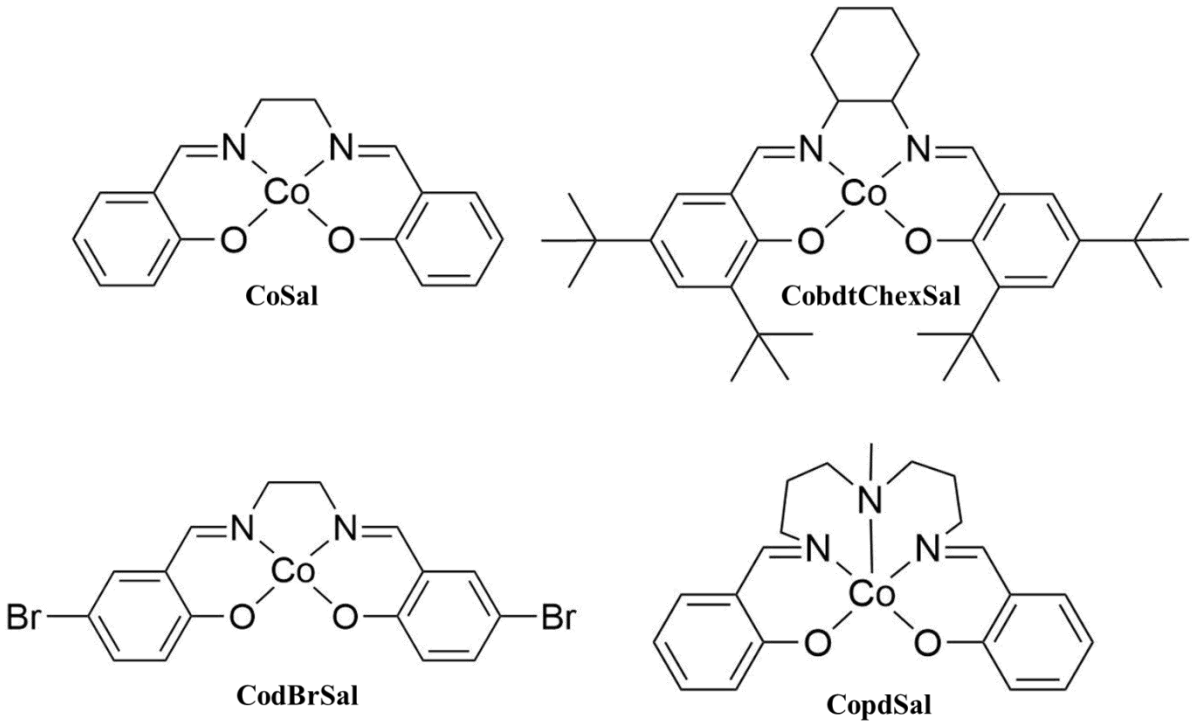

Figure 3.1: Cobalt salen structures; CoSal, CobdtChexSal, CodBrSal and CopdSal assessed for electrocatalytic CO_2 reduction.

3.2.1.1. Voltammetry of the complexes as reported within the literature

Of the four complexes studied within this chapter, reductive electrochemistry does not appear to have been reported for CodBrSal. Typically, cobalt salens exhibit a $Co^{2+/1+}$ reversible reduction and what has been commonly reported as a $Co^{2+/3+}$ reversible oxidation. There is evidence to suggest a sharing of charge upon oxidation between the Co^{3+} and the phenolate moiety of the ligand bound to Co^{2+} [31,32]. The ligand-centred oxidation may be precluded at the potential of the $Co^{2+/3+}$ oxidation with the use of coordinating solvents such as DMF [33].

Further oxidations are reported [34], however, as these processes are not featured in voltammograms within this chapter, values relating to these processes within the literature are not reported. The values of the $Co^{2+/1+}$ and $Co^{2+/3+}$ processes reported in the literature appear in Table 3.1. The literature values have been converted to the Fc/Fc^{+} couple, with the conversion factors explained as notes proceeding the Table. Ferrocene was employed as an internal standard within this research. Mistakes within conversion of potentials between NHE or SCE and Fc/Fc^{+} can arise, which may lead to discrepancies between values reported within the literature [35].

A further reduction beyond that of $Co^{2+/1+}$ has been observed for CoSal [36]. At a less negative potential, Co salophen exhibits what is proposed to be a ligand based reduction [37] (~ -2.4 to -2.5 V vs Fc/Fc^{+}), negative of its $Co^{2+/1+}$ reduction. This, more negative, second reduction within salophens exhibits reversibility under Ar. However, in the presence of a proton source, i.e. residual water, the reduction is observed to become irreversible. The second reduction observed for CoSal is also assumed to be a ligand-based reduction [36].

Table 3.1: Redox values within the literature related to the first reduction and first oxidation of cobalt salens appearing within chapter three.

Complex	$E_{1/2}$ $Co^{2+/1+}$ (vs Fc/Fc^{+})	$E_{1/2}$ $Co^{2+/3+}$ (vs Fc/Fc^{+})	Solvent	Reference	Note
CoSal	-1.695 V -1.75 V -1.685 V	-	DMF	[36] [38] [39]	A
	-1.74 V	-0.43 V	DMF	[40]	A
	-1.65 V *E_{pc}	-	MeCN	[41]	B, C
CobdtChexSal	-1.95 V	-	DMF	[42]	D
	-2.04 V	-	DMF	[43]	E
	-	0 +0.01 +0.11 V	DCM	[33] [31] [34]	
	-	+0.66 V * E_{pa} by DPV	DCM	[44]	F
CopdSal	-2.72 V	-0.7 V	DMSO	[45]	G
	-2.39 V	-0.58 V	DMSO	[46]	H

Notes:

A. Quoted vs Hg amalgam (Cd satd) which was specified as -0.76 V vs SCE [36,38–40], SCE is stated to be -0.45 V vs Fc/Fc^{+} in DMF [47].

B. Quoted vs Ag/Ag^{+} in MeCN. Ag/Ag^{+} was specified as +0.35 V vs SCE [41], SCE is stated as -0.4 V vs Fc/Fc^{+} in MeCN [47].

C. It has been shown that the solvent utilised affects the oxidation and reduction potential observed with CoSal [48].

D. Quoted vs SCE, SCE is stated as -0.45 V vs Fc/Fc^{+} in DMF [47].

E. Quoted vs Ag/Ag^{+}, stated to be +0.35 V vs SCE [41]. The SCE is stated as -0.45 V vs Fc/Fc^{+} in DMF [47].

F. Quoted vs Ag/Ag^{+}. The electrode is +0.35 V vs SCE [41], the SCE is stated to be -0.46 V vs Fc/Fc+ in DCM [47].

G. The electrolyte was either TEAP or $TBAPF_6$ (not specified). Values for these electrolytes have not been obtained. Conversion of SCE to Fc^{+} in DMSO is therefore assumed to be -0.44 V (average of values in $TEAPF_6$ and TBAP) [47].

H. The electrolyte was DMSO with TEAP and values were referenced vs SCE. As per G, -0.44 V conversion was applied to the values.

CoSal's first reduction occurs with $E_{1/2}$ of approximately -1.72 V with the first reduction of CobdtChexSal occurring with an $E_{1/2}$ of approximately -2.0 V (see Table 3.1) in DMF. This cathodic shift in reduction potential is expected as the contribution of electron donation from the cyclohexylene bridge and tertiary butyl groups of the bdtChexSal ligand towards the cobalt centre increases the energy required for the cobalt centre to further gain an electron [35,46]. There is a discrepancy within the literature ($E_{1/2}$ of -2.39 and -2.72 V) [45,46] as to at what potential the first reduction of CopdSal occurs within DMSO. This has also been stated as the $Co^{2+/1+}$ reduction [46]. No other reduction values were obtained within the literature for CopdSal, particularly none in DMF. Assuming an average value of -2.55 V, the $Co^{2+/1+}$ reduction is approximately 500 mV more negative than that of CobdtChexSal. This is evidence as to a strong electron donation arising from the lone pair of the additional nitrogen datively bound to the cobalt centre in CopdSal. One further reduction has been observed for CopdSal in DMSO, which has been attributed to a $Co^{1+/0}$ metal centred reduction [46]. In comparison to what is observed in CoSal [36] and Co salophen [37], a ligand based reduction may not be ruled out.

3.2.1.2. Voltammetry of the complexes under Ar in DMF/0.1 M $TBAPF_6$

DMF was utilised as the solvent as acetonitrile did not allow for adequate dissolution of CobdtChexSal. Achieving a concentration of 1 mM CoSal in DMF or DMF/5% water was not possible due to insolubility. CobdtChexSal experienced partial insolubility only with the use of 10% water in DMF. CodBrSal experienced partial insolubility in DMF with 5% water. The level of solubility of the Co salens was not further assessed where the complexes were not fully dissolved. Background reductive scans (in the absence of compound) of Ar- and CO_2-purged DMF with and without 5% water appear in Appendix B.1 for reference.

The cyclic voltammetry of CoSal, CobdtChexSal, CodBrSal and CopdSal appear in Figure 3.2

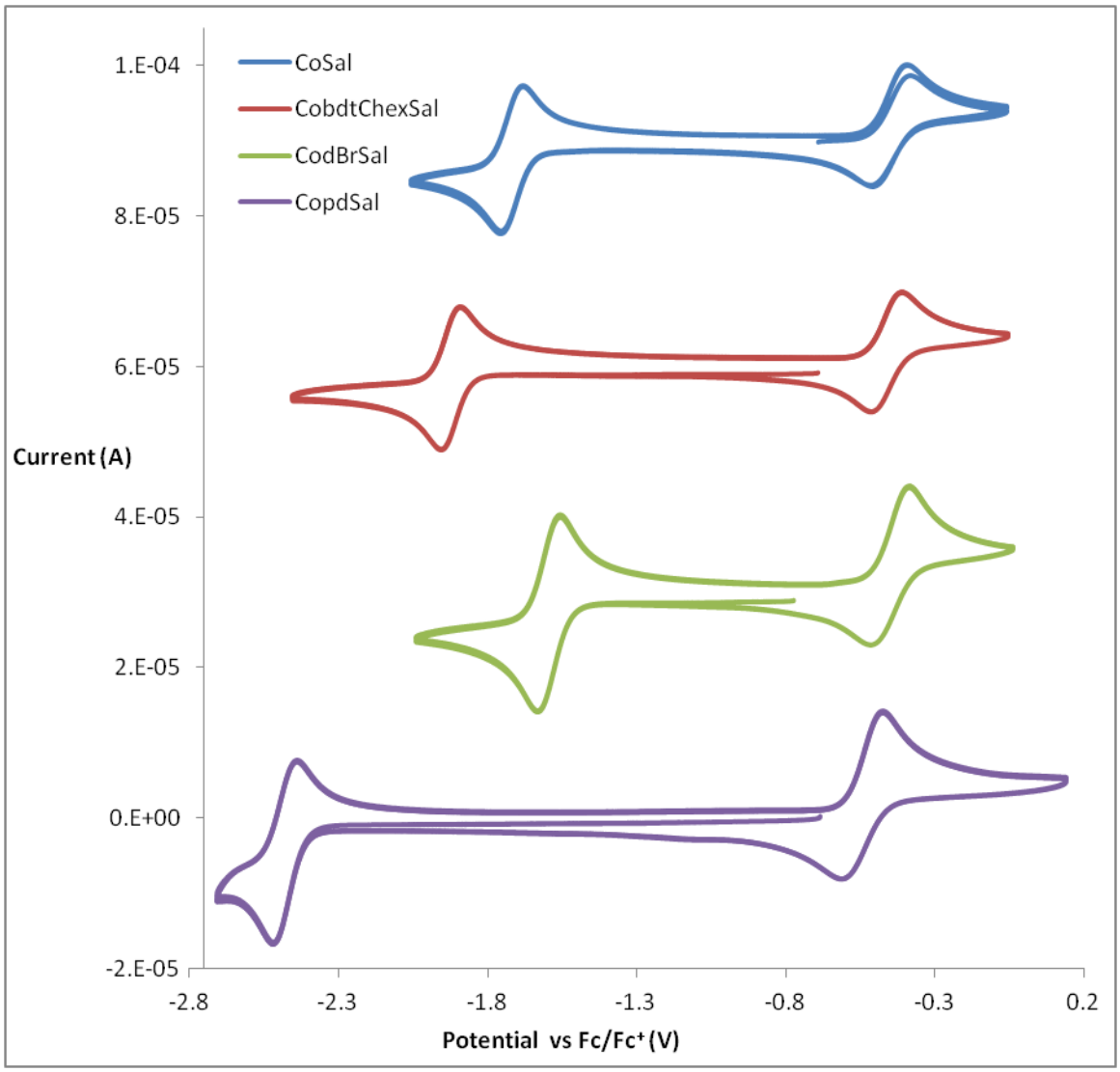

Figure 3.2: Cyclic voltammetry of approximately 1 mM CoSal, 1 mM CobdtChexSal, CodBrSal and CopdSal in DMF with 0.1 M $TBAPF_6$ under Ar (ν = 100 mV s^{-1}). The voltammograms are offset by 30 μA. The initial scanning direction was positive for CoSal and negative for CobdtChexSal, CodBrSal and CopdSal from an OCP of approximately -0.7 V.

The $E_{1/2}$ values of the first oxidations and first reductions as acquired in DMF/0.1 M $TBAPF_6$ appear in Table 3.2.

Table 3.2. Redox potentials associated with the first oxidation and first reduction of the cobalt salens assessed in DMF/0.1 M $TBAPF_6$

Complex	$E_{1/2}$ $Co^{3+/2+}$	$E_{1/2}$ $Co^{2+/1+}$
CoSal	-0.45 V	-1.72 V
CobdtChexSal	-0.46 V	-1.92 V
CodBrSal	-0.45 V	-1.60 V
CopdSal	-0.54 V	-2.48 V

In keeping with standard cobalt salen electrochemistry under Ar, a quasireversible oxidative process and quasireversible reductive process are observed [49]. No further oxidative processes were investigated. Regarding CoSal, no other reduction process was observed up to -2.86 V vs Fc/Fc^+. Skljarevski *et al*. have shown that in DMF, another reduction occurs at a more negative potential than that examined within this thesis [36]. The second reduction is assumed to be ligand based. The first oxidative and reductive processes in CoSal were found to occur with $E_{1/2}$s of -0.45 V and -1.72 V respectively. These are in line with the literature values in DMF (see Table 3.1).

CobdtChexSal also exhibits a quasireversible oxidation and reduction relating to $Co^{3+/2+}$ and $Co^{2+/1+}$ respectively. These processes are found to occur at -0.46 V and -1.92 V respectively. The $E_{1/2}$ of $Co^{2+/1+}$ is in line with the literature (Table 3.1), however the oxidative processes from the literature are in DCM and may not be directly comparable. Not only are values for ferrocene [47] and cobalt salens [48] solvent dependent, but the first oxidation occurring (metal or ligand based) may change, depending on the choice of solvent [31–33].

Upon extending the potential window to -3.49 V, CobdtChexSal shows a second, irreversible reduction, shown in Figure 3.3.

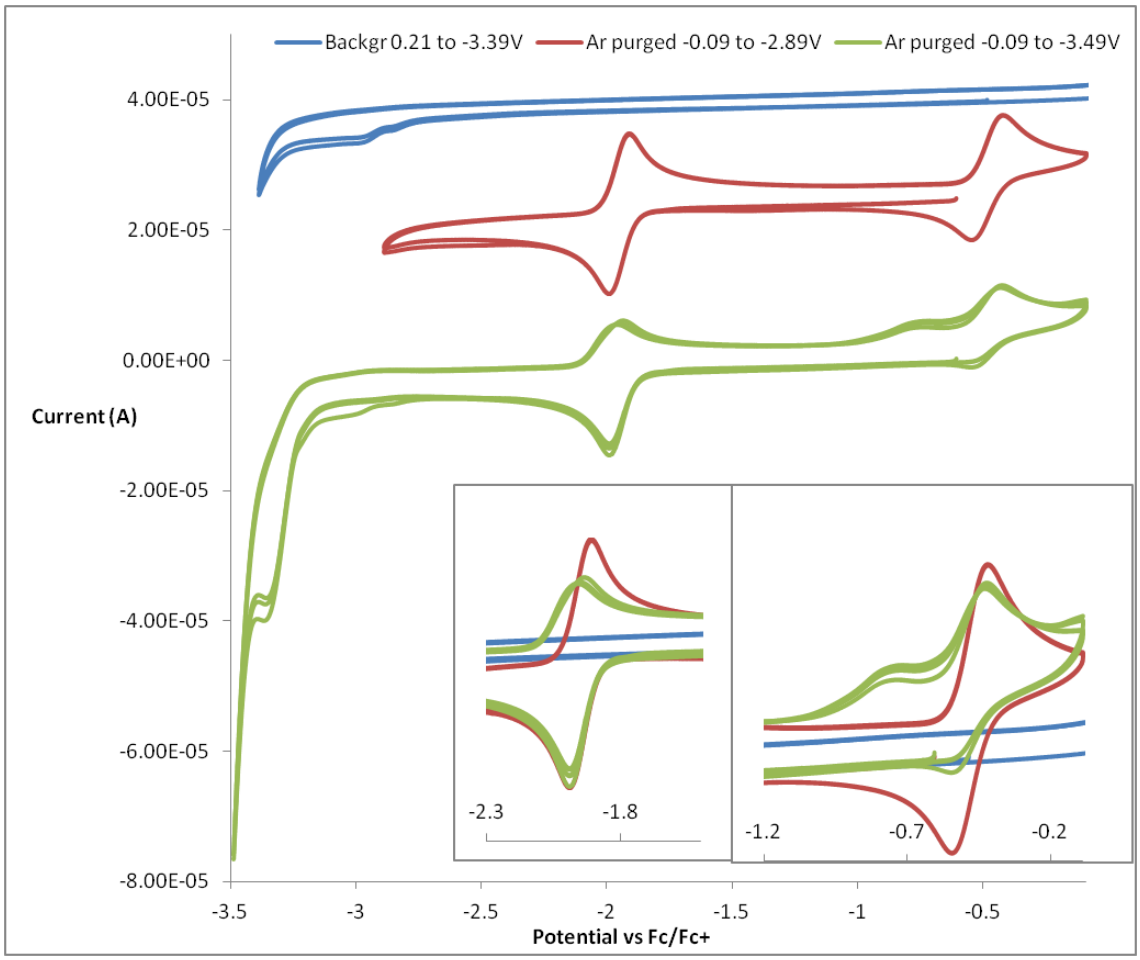

Figure 3.3: Cyclic voltammetry of 1 mM CobdtChexSal to -2.89 V and to -3.49 V under Ar in DMF/0.1 M $TBAPF_6$, including background DMF/0.1 M $TBAPF_6$ under Ar, (ν = 100 mV s^{-1}). CobdtChexSal to -2.89 V and background scans are offset by 25 and 40 μA respectively. Inset: no current offset and magnified, scans of regions containing the first reduction (left) and first oxidation (right)

The irreversible second reduction of CobdtChexSal, occurring with E_{pc} of -3.36 V and shown in Figure 3.3, has not been found within the literature. However, a similar reduction has been observed in the case of CoSal (at -3.10 V vs Fc/Fc^{+}) and Co salophen, and has been attributed to a ligand-based reduction [36,37]. It was shown within Co salophen that the second reduction became fully irreversible with the introduction of one molar equivalent of phenol (as proton source) but demonstrates reversibility in the absence of protons in DMF. CoSal however demonstrates

irreversibility in the absence of a proton source [36]. Voltammetry of the H_2bdtChexSal ligand also demonstrates an irreversible reduction (at -2.45 V vs Fc/Fc^+) in DCM [50].

Accessing the ligand reduction results in a slight but noticeable cathodic shift in the reoxidation of the $Co^{1+/2+}$ species, along with decreasing the level of reversibility of the oxidation. Similar behaviour was also observed by Skljarevski *et al*. upon inclusion of the ligand reduction of CoSal [36]. At -0.74 V, a new oxidation occurs. In the presence of one equivalent of phenol, Co salophen also demonstrates a similar oxidative feature (prior to the $Co^{2+/3+}$ oxidation) once the potential is extended to the ligand reduction [37]. The irreversibility of the second reductive process shown in Figure 3.3 could arise from trace water that may be contained in DMF[1].

No electrochemistry of CodBrSal could be found within the literature. Again however, a quasireversible oxidation and reduction appear (at -0.45 V and -1.59 V) and are attributed to the $Co^{2+/3+}$ oxidation and $Co^{2+/1+}$ reduction. Extending the potential of the voltammetric scan to more negative values results in the appearance of two more reductive processes before solvent/electrolyte reduction occurs.

Cyclic voltammograms obtained through a window opening experiment containing CodBrSal appear in Figure 3.4. The level of reversibility of the $Co^{2+/1+}$ and $Co^{2+/3+}$ processes is affected when the reduction potential is extended to -2.84 V. Following the first sweep to -2.84 V, a weak oxidation is observed at -1.77 V, prior to the reoxidation of $Co^{1+/2+}$dBrSal. This is accompanied by a more pronounced oxidation at -0.62V leading to the $Co^{3+/2+}$ reduction becoming less reversible. On the second and third reductive sweeps, an additional weak reduction occurs at -2.48 V.

[1] It is accepted that although efforts are taken in ensuring that the anhydrous DMF remains dry, the solvent will contain trace water.

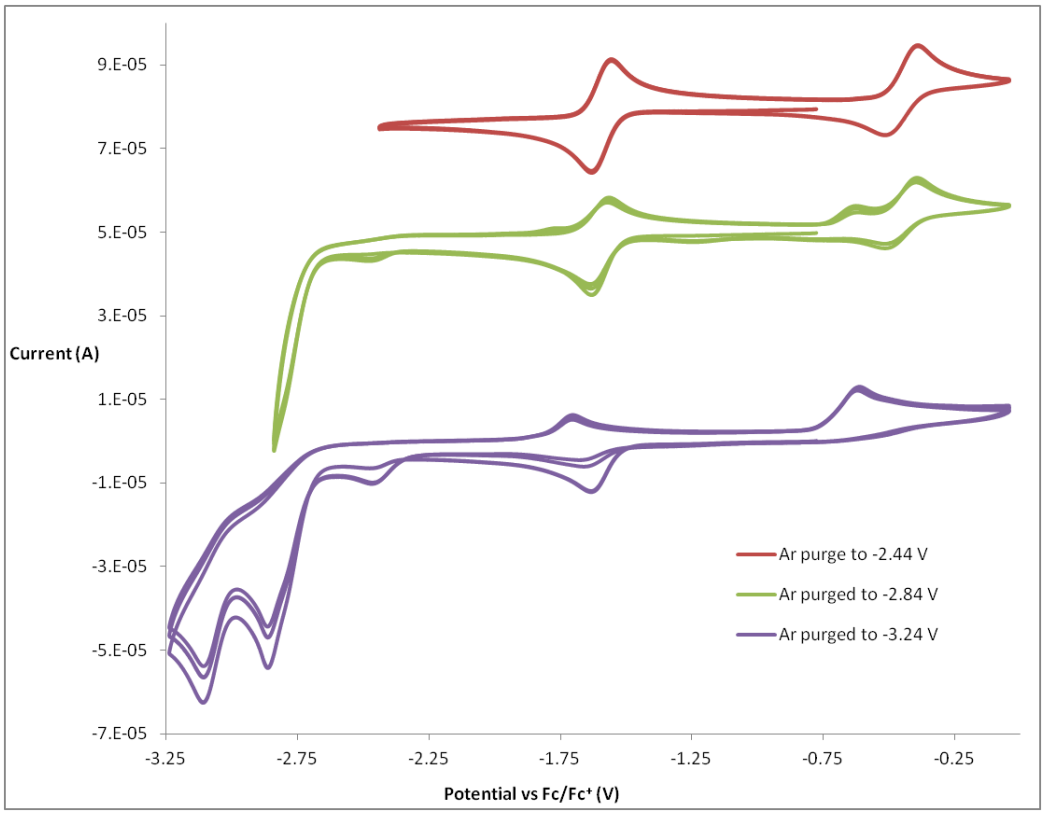

Figure 3.4: Cyclic voltammetry of CodBrSal under Ar in DMF/0.1 M $TBAPF_6$, (ν = 100 mV s^{-1}). Scans to -2.84 V and -2.44 V are offset by 50 and 80 μA respectively.

Upon cycling from -0.04 to -3.24 V, the observed changes become more pronounced. An irreversible reduction wave with E_{pc} of -2.86 V is followed by an additional irreversible reduction with E_{pc} of -3.11 V. The original $Co^{2+/3+}$ redox couple is no longer observed, accompanied by a drastic decrease in the reduction wave associated with the $Co^{2+/1+}$ state. It also appears as though the reduction wave at -2.86 V may contain a reduction process at approximately -2.77 V, suggesting the occurrence of two overlapping processes. The feature at -2.46 V (appearing in sweeps two and three when the potential was reversed at -2.84 V) is also apparent on the first reductive scan of -0.04 to -3.24 V, but grows in intensity on the second cycle. This is unexpected as its absence within the first scan to -2.84 V provides evidence as to the feature arising from the complex being reduced at the first irreversible process (with E_{pc} of -2.86 V). The reduction may be a surface confined process resulting from the earlier scan of -0.04 to -2.84 V. Between scans, the solution was momentarily stirred with the aim of replenish the diffusion layer at the electrode surface, though the electrode was not cleaned.

Reasonable possibilities for the reductions observed at -2.86 and -3.11 V are reduction of the ligand imine bonds, followed by protonation due to residual water [37] and bromide losses from the ligand [51,52]. The loss of multiple halides from a compound may show successively negative reductions as each halide is removed [38].

Akin to the behaviour observed in DMSO within the literature (see Table 3.1), CopdSal exhibits a quasireversible oxidation and reduction in DMF with $E_{1/2}$ of -0.54 V and -2.48 V respectively (Figure 3.2). Cycles were reversed at -2.71 V as a second (irreversible) reduction occurs at more negative potentials (as shown in Figure 3.5). Complete reversibility at 100 mV s^{-1} was not observed under Ar (i_{pa}/i_{pc} = 0.695).

Cyclic voltammograms obtained from a window opening experiment with CopdSal are available in Figure 3.5. When the potential of cycling is extended to further negative values of -2.76 V (to -3.06 and -3.21 V), additional electrochemical processes are observed. Figure 3.5 shows the presence of two additional reductions at -2.88 and -3.08 V, accompanied by an oxidation at -2.62 V and possibly a second, weak oxidation at -2.83 V. Unsurprisingly, due to the level of irreversibility of the reduction at -2.88 V, further reversibility of the $Co^{1+/2+}$ oxidation is lost, as is the case with reduction of the original $Co^{3+/2+}$ species. The level of irreversibility of the reduction at -2.88 V could suggest that there is some water present in the solvent and that the cause of irreversibility is protonation of the reduced imine bond in an EC mechanism [37]. This species could further undergo a reduction at -3.08 V [37]. The second reductive species of CopdSal has previously been suggested as $Co^{1+/0}$ [46], however, the focus of the study by Zanello *et al*. was on oxidative electrochemistry.

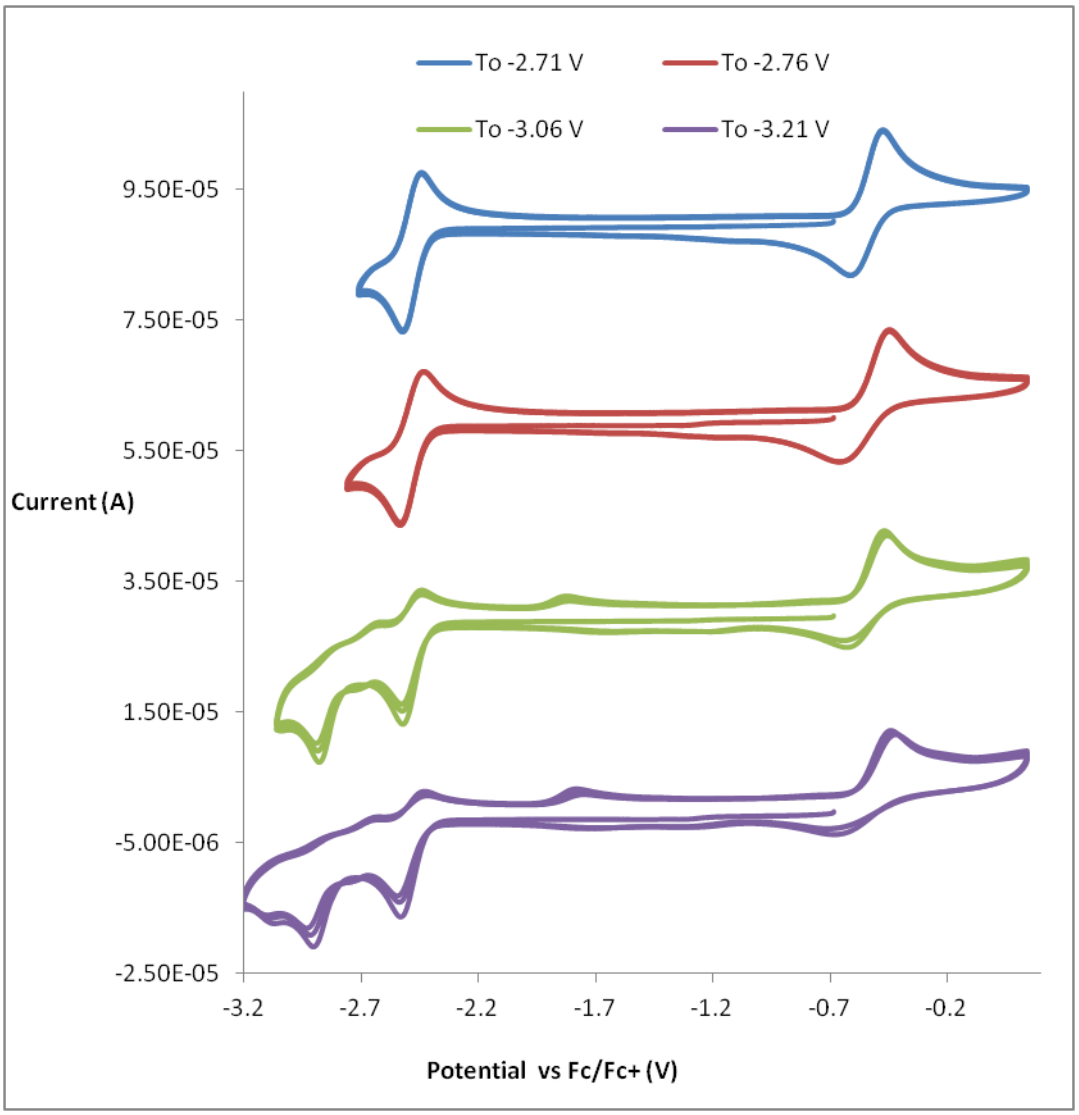

Figure 3.5: Cyclic voltammetry of 1 mM CopdSal under Ar in DMF with 0.1 M $TBAPF_6$ (100 mV s^{-1}), switching potential of -2.71, -2.76, -3.06 and -3.21 V.

The trend in $E_{1/2}$ values for the $Co^{2+/3+}$ and $Co^{2+/1+}$ redox couples obtained under Ar in DMF (Table 3.2) are consistent with the behaviour expected. The $Co^{2+/3+}$ redox couple shows an increase in potential from electron donating groups to electron withdrawing groups. The variation in $Co^{2+/3+}$ $E_{1/2}$ between the four compounds is 93 mV from the ligand with the most electron donation (pdSal) to the ligand with most electron withdrawing groups (dBrSal). The $E_{1/2}$ of the $Co^{2+/1+}$ reduction within the four compounds also show the same trend related to the level of electron donating or withdrawing power of the ligand. The variation between $E_{1/2}$ values is far more pronounced than with the $Co^{2+/3+}$ couple, with a difference of 0.89 V measured between

the $Co^{2+/1+}$ $E_{1/2}$ of CopdSal and CodBrSal and has been observed previously for cobalt salen/salophen complexes [53] in DMF and tetraazamacrocyclic cobalt complexes [54] in MeCN.

The remarkably cathodic $Co^{2+/1+}$ redox couple shift shown by CopdSal is evidence of the binding of the central nitrogen within the pdSal ligand to the cobalt centre. The first reduction is deemed to be the $Co^{2+/1+}$ reduction as discussed previously. Discussion of electron donating and withdrawing effects of CobdtChexSal as compared to CoSal and CodBrSal is relatively straightforward in comparison to CopdSal. The electron donation within CopdSal comes directly from an additional nitrogen atom datively bound to the cobalt centre, whereas the electron donation of CobdtChexSal is not directly to the metal centre. Donation of two electrons from the nitrogen's lone pair results in a decreased stabilisation on the reduced metal centre, therefore pushing it to more negative potentials. In the case of the $Co^{2+/3+}$ couple, the donation of additional lone pair electrons stabilises the oxidised metal centre, thus lowering the energy required for oxidation.

3.2.1.3. Voltammetric response of homogeneous Co salens towards CO_2 reduction in DMF/0.1 M $TBAPF_6$.

Each complex was assessed with the use of cyclic voltammetry and bulk electrolysis for their capability towards CO_2 reduction to CO. The voltammetry of the complexes under CO_2 with and without water as a proton source are discussed within this section.

3.2.1.3.1. Voltammetric response of CoSal towards CO_2 reduction

The voltammetric behaviour of CoSal under Ar, CO_2 and CO_2 with 5% water is displayed in Figure 3.6.

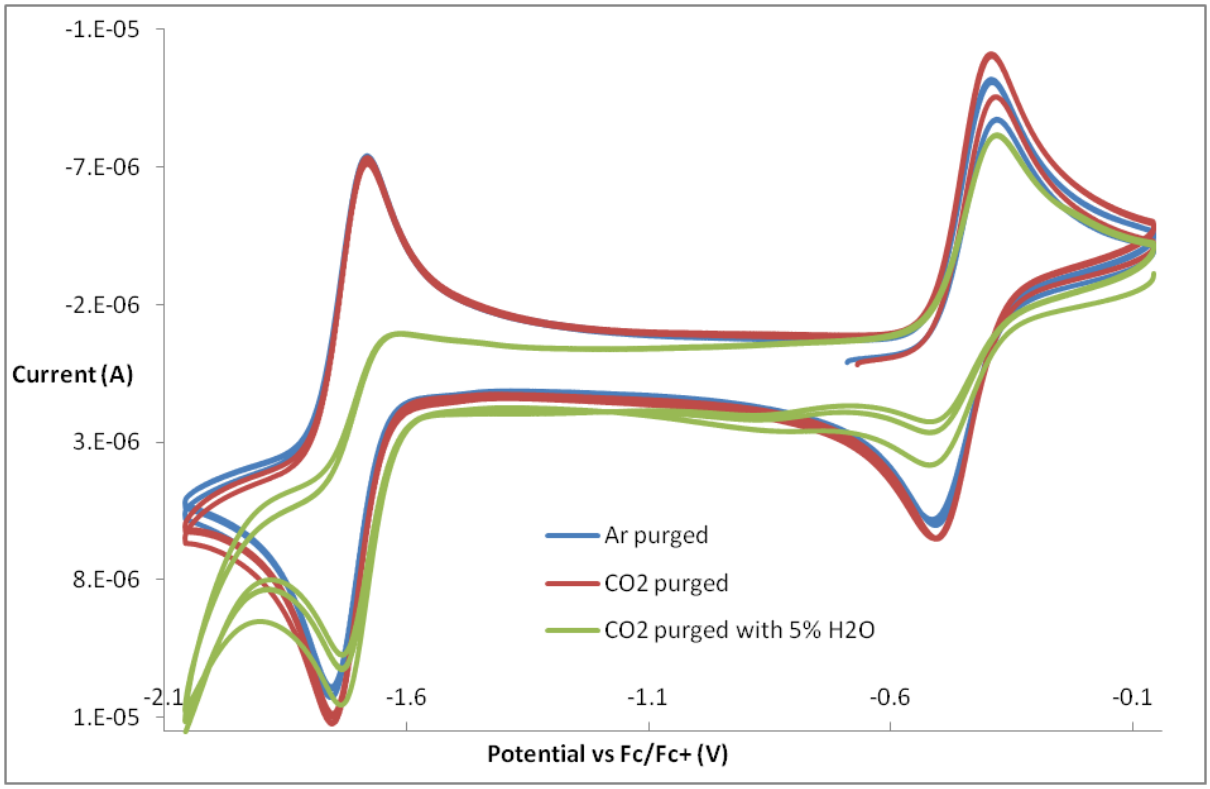

Figure 3.6: Cyclic voltammetry of approximately 1mM CoSal in DMF with 0.1 M $TBAPF_6$ under Ar, CO_2 and CO_2 with 5% H_2O (ν = 100 mV sec^{-1}). The initial scanning direction was positive from an OCP of approximately -0.7 V.

The voltammetry of CoSal under Ar in DMF/0.1 M $TBAPF_6$ is discussed in section 3.2.1.2. Following a purge with CO_2, there is almost no change observed in the $Co^{2+/3+}$ and $Co^{2+/1+}$ couples compared to that under argon (shown previously for the $Co^{2+/1+}$ reduction under CO_2 [36]). With the introduction of 5% water, the $Co^{2+/1+}$ redox couple is no longer reversible. Accompanying this is the substantial loss of reduction current associated with the $Co^{3+/2+}$ couple. It is to be noted that this complex was not fully soluble in DMF (at 1 mM), even before the addition of 5% water. A range of solvents

were utilised, however no suitable solvent was found. Bulk electrolyses were undertaken at -1.86 V and due to inactivity, at -2.10 V vs Fc/Fc^{+}.

The substantial loss of reversibility regarding the $Co^{2+/1+}$ redox couple strongly suggests chemical conversion of the reduced complex, enacted by the presence of CO_2 and water. However, an enhancement of reductive current at -1.75 V (indicative of electrocatalysis) was not observed. Following the $Co^{2+/1+}$ reduction under CO_2 with 5% water, there is an increase in current that does not feature in voltammograms under Ar or CO_2 only. This may be due to electrocatalytic CO_2 reduction, proton reduction, or the reduction of a species formed from Co^{1+}Sal's interaction with water or with CO_2 and water. CoSal was not examined with water but without the presence of CO_2.

The decrease in oxidative current observed with the $Co^{2+/3+}$ redox process could be due to the aforementioned solubility issue, of which the presence of water is expected to further decrease the solubility of the complex. Instability of the complex is possible in the presence of water. However, stability issues leading to precipitate were not observed for CobdtChexSal or CopdSal. Furthermore, the oxidative current associated with the $Co^{2+/3+}$ oxidation of CoSal was not observed to decrease more than that observed initially, over the course of the experiment.

Upon probing the re-reduction of the $Co^{2+/3+}$ oxidation, it is clear that the previously reversible process has become quasi-reducible. Experiments were undertaken in a "window-opening manner" and scans of $Co^{2+/3+}$ oxidation-only and of $Co^{2+/3+}$ oxidation and $Co^{2+/1+}$ reduction are featured in Figure 3.7. It is observed, only under a CO_2 atmosphere with water present, that the re-reduction of the $Co^{3+/2+}$ oxidation becomes less reversible when the irreversible reduction associated with $Co^{2+/1+}$ is reached. Accompanying the irreversible reduction is the very weak formation of a species at approximately -0.25 V. A further note on voltammetry of CoSal is that a weak reduction process at approximately -0.86 V accompanies the $Co^{2+/3+}$ oxidation (independent to the $Co^{2+/1+}$ reduction). This feature does not appear under Ar or CO_2 only and could be due to the oxidised complex reacting very slowly with water. Indeed, complexes such as this have previously been explored as precursors for and demonstrated electro- and photocatalytic behaviour towards water oxidation [19,55].

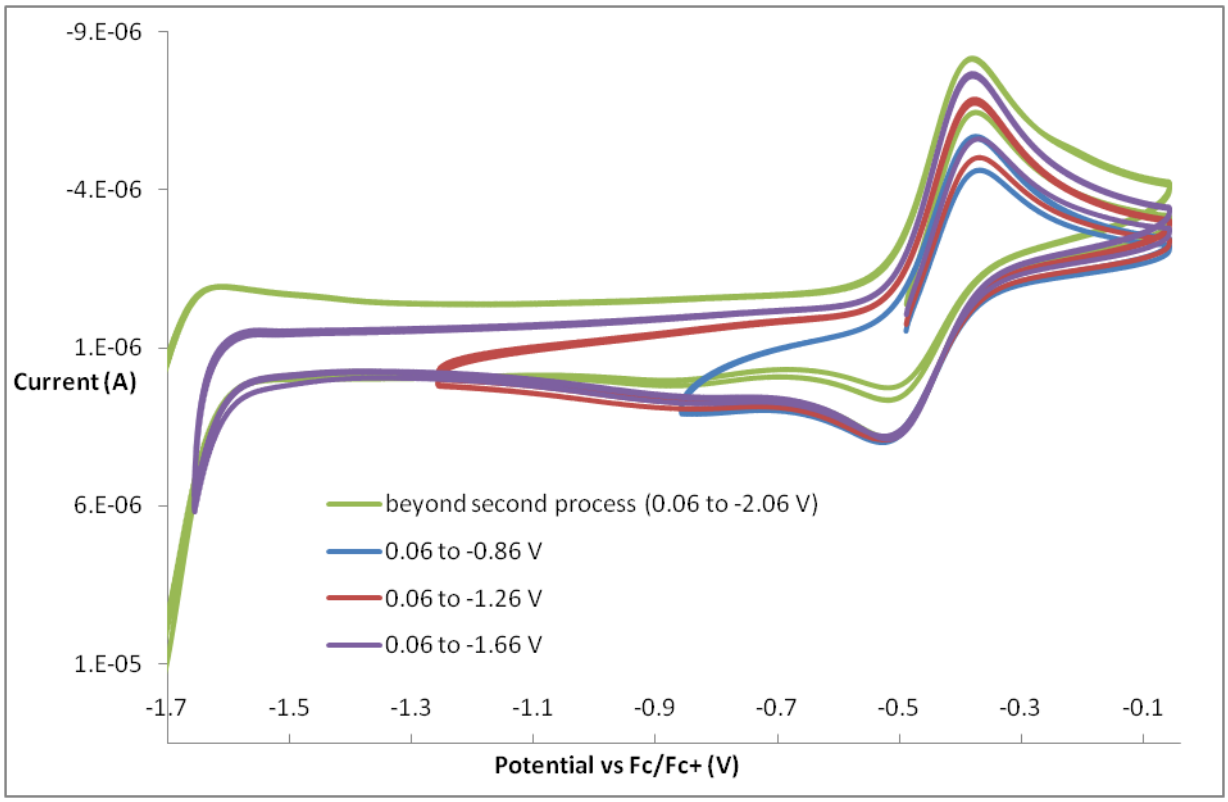

Figure 3.7: Cyclic voltammetry of approximately 1mM CoSal in DMF with 0.1M $TBAPF_6$ under CO_2 with 5% H_2O (ν = 100 mV s^{-1}), 0.06 to -0.86, -1.26, -1.66 and -2.06 V vs Fc/Fc^+. The initial scanning direction was positive from an OCP of approximately -0.5 V.

3.2.1.3.2. Voltammetric response of CobdtChexSal towards CO_2 reduction

Figure 3.8 shows the voltammetry of CobdtChexSal under argon, CO_2 and CO_2 with 5% water. The voltammetry of CobdtChexSal under Ar in DMF/0.1 M $TBAPF_6$ is discussed in section 3.2.1.2.

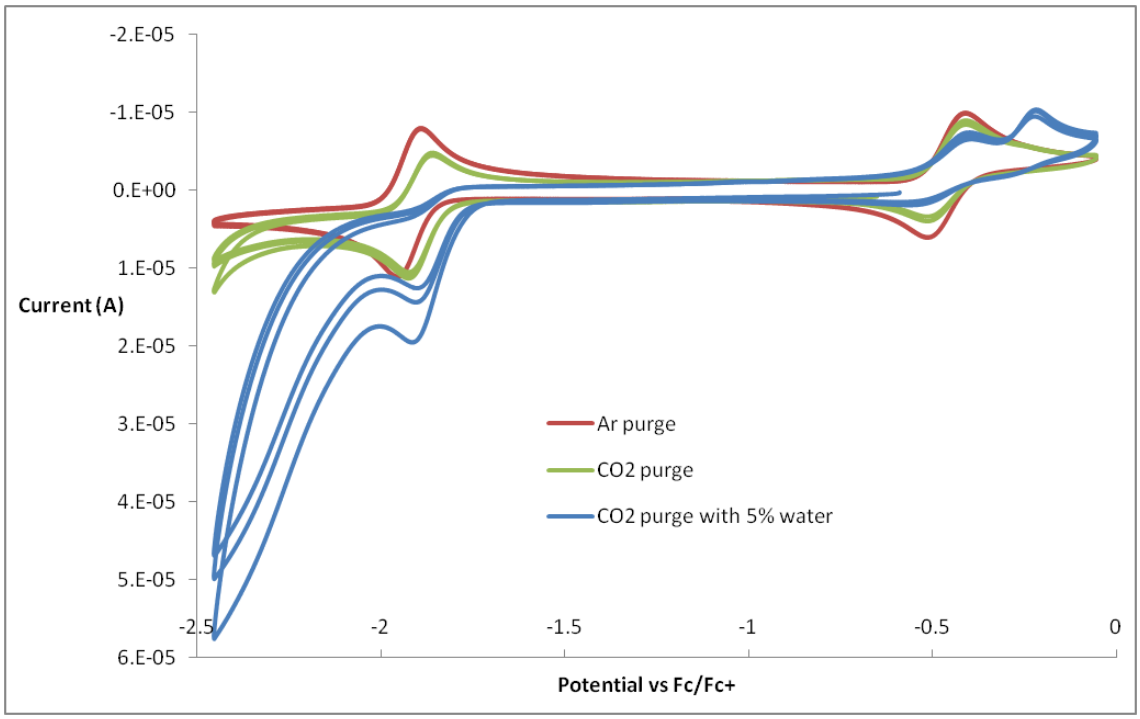

Figure 3.8: Cyclic voltammetry of 1 mM CobdtChexSal in DMF with 0.1 M $TBAPF_6$ under Ar, CO_2 and CO_2 with 5% H_2O (ν = 100 mV s^{-1}). The initial scan direction is negative.

Upon the introduction of CO_2, the re-oxidation associated with the $Co^{2+/1+}$ couple becomes less reversible as does the reduction associated with the $Co^{3+/2+}$ couple. It is possible that potential trace water in the solvent may aid with such irreversibility in conjunction with the presence of CO_2. If the voltammetry is halted before the 2+/1+ state is reached, the electrochemical reversibility remains for the $Co^{3+/2+}$ redox couple (as demonstrated with CoSal with 5% water, Figure 3.7). Therefore, the quasireversibility of the $Co^{3+/2+}$ couple is affected by binding of CO_2 (potentially aided by residual protons) to the $[CobdtChexSal]^-$ state.

The behaviour is corroborated by the quasireversible reduction associated with $Co^{2+/1+}$. CO_2 appears to bind to the metal-centred one-electron reduced (OER) species as the presence of CO_2 imparts a loss of reversible oxidation within the redox couple. Loss of reversibility implies that the one electron reduced form of CobdtChexSal undergoes chemical reaction with CO_2. Various compounds require the presence of protons in order to reduce CO_2 [56]. For example, though bipyridyl complexes of Re demonstrate

an enhancement of current without the addition of a proton source [57], homologous manganese complexes require protons to allow demonstration of activity [58].

Within the voltammograms presented in Figure 3.8, a far more pronounced change is observed upon the introduction of 5% water. At the scan rate of 100 mV/s, reversibility of the $Co^{2+/1+}$ reduction is completely lost, suggesting that CO_2 (aided by the presence of protons) or H^+ binding to Co^{1+}bdtChexSal occurs. It is evident also that the $Co^{2+/3+}$ oxidation is no longer reversible and following this, a new prominent irreversible oxidation appears with E_{pa} of -0.22 V. Figure 3.9 contains cyclic voltammograms of CobdtChexSal under CO_2 with 5% water present, however isolating the $Co^{2+/3+}$ oxidation in the potential window examined.

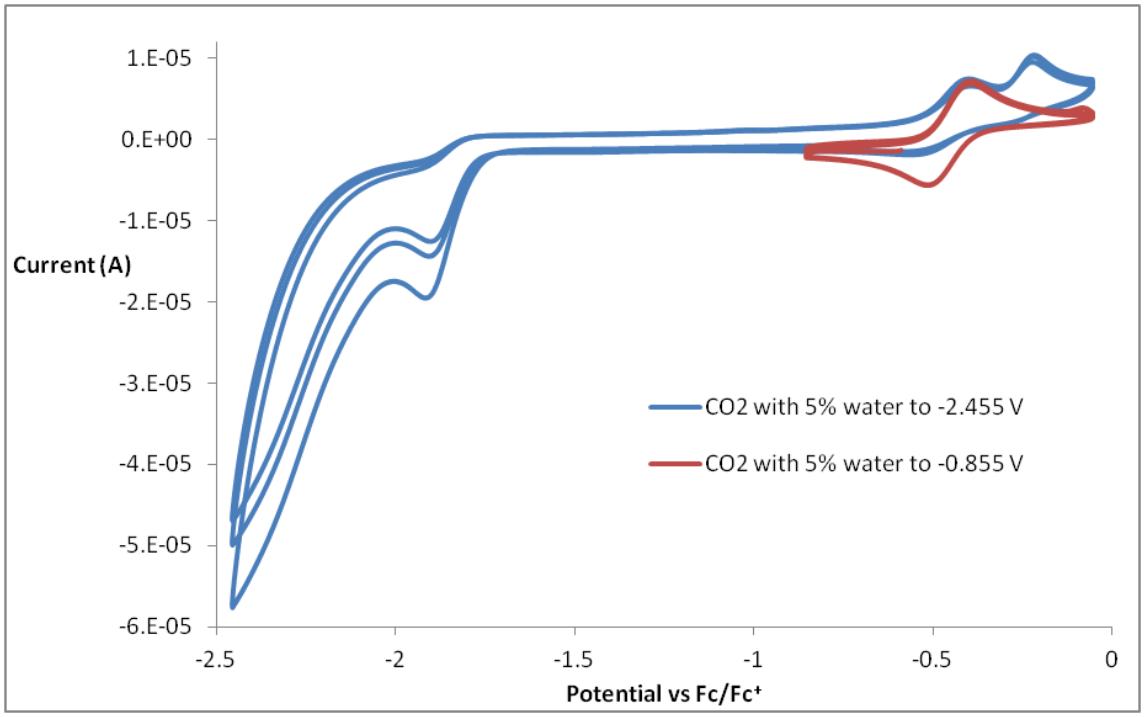

Figure 3.9: Cyclic voltammetry of CO_2 purged 1 mM CobdtChexSal in DMF with 5% water (ν = 100 mV s^{-1}) with potential sweeps to -0.85 V and -2.45 V. The initial scanning direction is negative.

From Figure 3.9, it is evident that the additional oxidation appearing at -0.22 V in Figure 3.8 is a result of the irreversible reduction of $Co^{2+/1+}$. If the irreversible $Co^{2+/1+}$ reduction is not undertaken, the $Co^{2+/3+}$ oxidation appears as a reversible couple.

The voltammetry of CobdtChexSal was continued to the reductive solvent window (to -3.49 V) under Ar and CO_2 as shown in Figure 3.10.

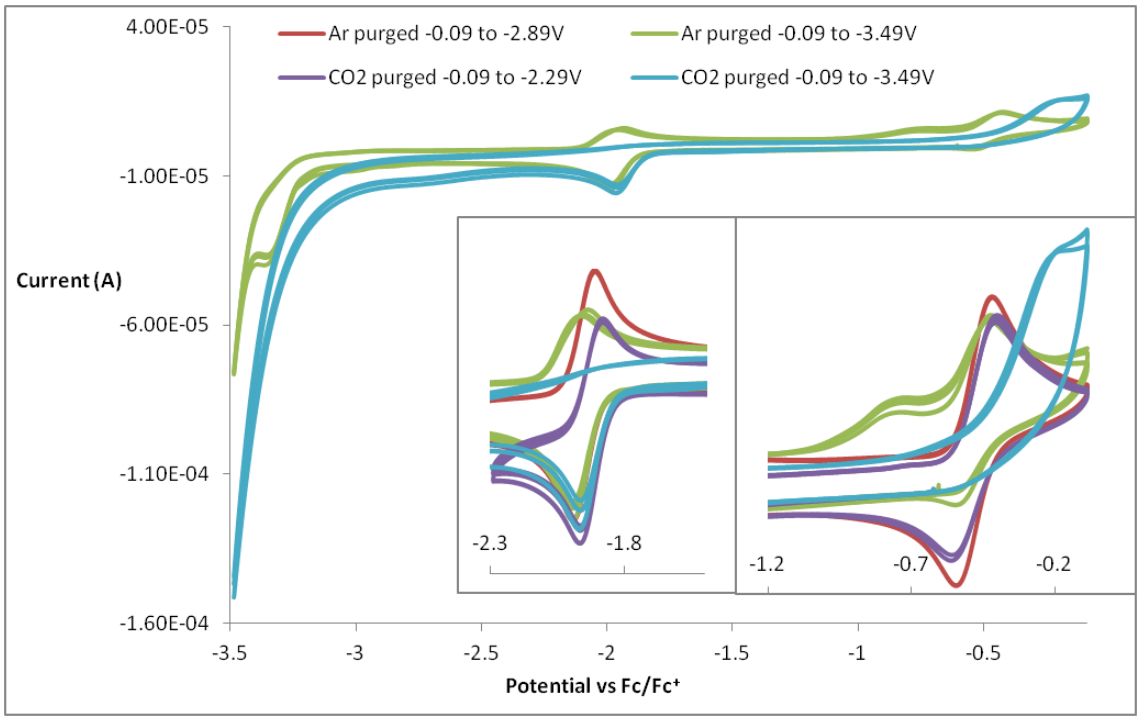

Figure 3.10: Cyclic voltammetry of 1 mM CobdtChexSal featuring the second reduction, in DMF with 0.1 M $TBAPF_6$ under Ar and CO_2 (ν = 100 mV s^{-1}). The insets include voltammograms halted before the second reduction.

Figure 3.10 contains the voltammetry of CobdtChexSal that was undertaken in the same manner as in Figure 3.3, however with the addition of a scan under CO_2. Upon the introduction of CO_2, a slightly earlier solvent/electrolyte reduction onset exists (~ -3.0 V) (also shown in Appendix B.1 without complex present). The earlier onset is accompanied by the complete irreversibility of $Co^{1+/2+}$ and the $Co^{2+/3+}$ oxidations, instead exclusively producing an oxidative wave at ~ -0.24 V (see Figure 3.10). The oxidation at -0.74 V under Ar is not present under CO_2. The significance of the disappearance of this unidentified process is so far unclear. It is not apparent as to whether the species responsible for the oxidation at -0.24 V is that of the species giving rise to the oxidation at -0.22 V, when the first reduction is undertaken under CO_2 with 5% water present (see Figure 3.8/Figure 3.9).

Under CO_2 and without water present, Skljarevski *et al*. noted an enhancement of current at CoSal's ligand based reduction [36]. However, in the case of CoSal, the $Co^{1+/2+}$ oxidation was present following the ligand based reduction. The enhancement was stated as likely being due to formic acid generation, with comparison to Co polypyridyl [59–61] complexes. In terms of electrolysis at such a negative potential as -3.36 V, carbon electrodes have been reported to generate butane from the tetrabutylammonium cation [62]. Due to electrolyte decomposition by the electrode, the Faradaic efficiency of the system towards CO_2 reduction may decrease.

In order to assess whether the species observed at -0.24 V is a product of the introduction of both CO_2 and water, or of the presence of water alone, electrochemistry was undertaken with the addition of 10% water under Ar and under CO_2, as shown in Figure 3.11.

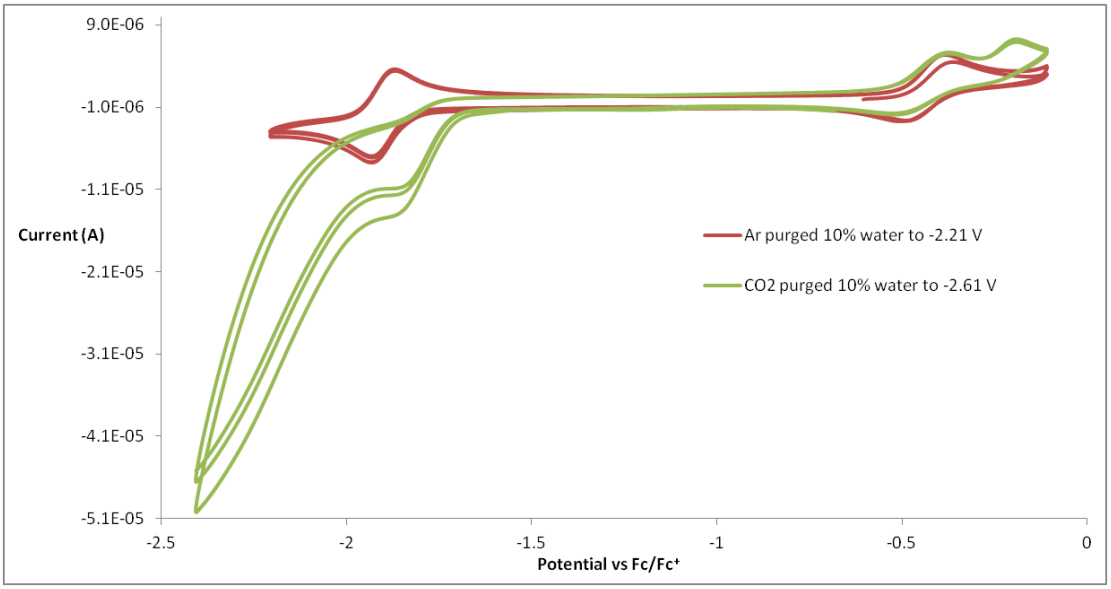

Figure 3.11: Cyclic voltammetry of approximately 1 mM CobdtChexSal under Ar with 10% H_2O, CO_2 with 10% H_2O (ν = 100 mV s^{-1}). Initial scan direction from OCP (approximately -0.6 V) is positive for Ar purged, negative for CO_2 purged.

It is noted that the level of solubility of CobdtChexSal decreased in DMF with the addition of 10% water. Within the voltammetry obtained in Figure 3.11, no oxidative feature at -0.24 V is observed with water but without the presence of CO_2 (in contrast to that observed in Figure 3.8). Upon the introduction of CO_2 with 10% water present, the

oxidative feature shifts slightly, appearing at -0.23 V. Therefore, the appearance of the irreversible oxidative feature with E_{pa} of -0.23/-0.24 V is due to the joint presence of CO_2 and H_2O.

3.2.1.3.3. Voltammetric response of CodBrSal towards CO_2 reduction

The voltammetric behaviour of CodBrSal under Ar, CO_2 and CO_2 with 5% water appears in Figure 3.12.

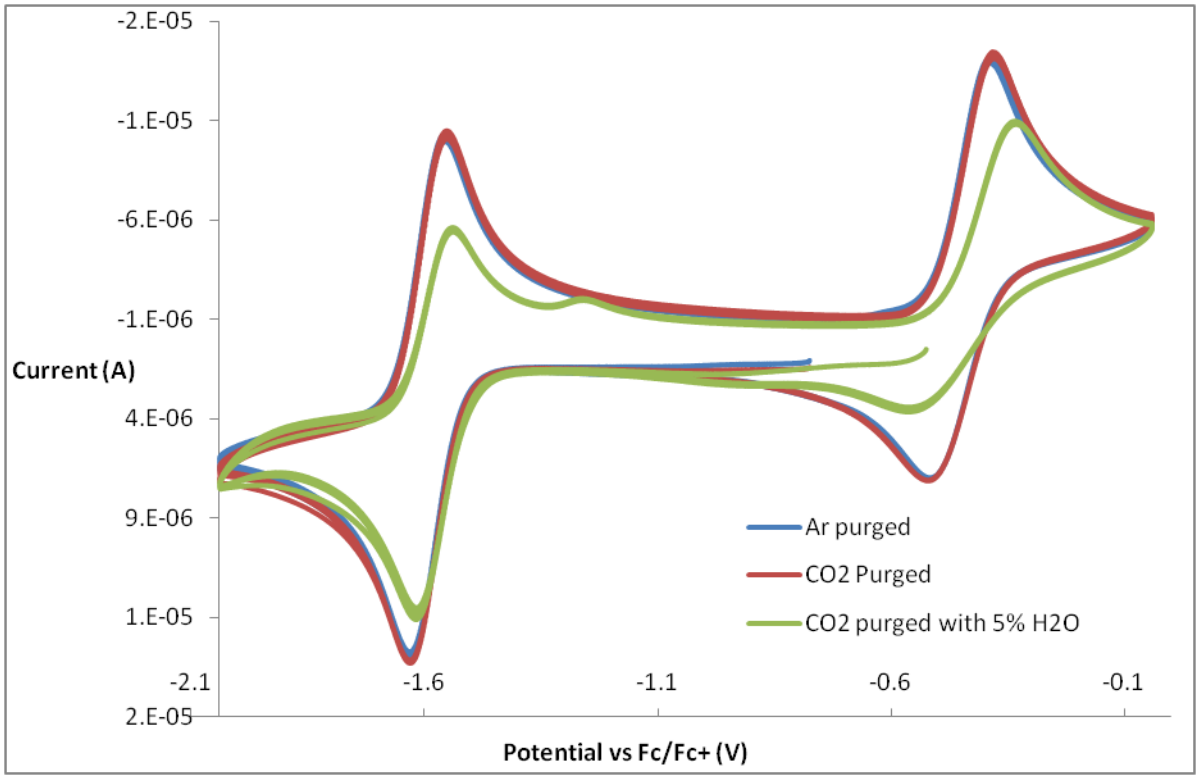

Figure 3.12: Cyclic voltammetry of 1 mM CodBrSal in DMF with 0.1 M $TBAPF_6$ under Ar, CO_2 and CO_2 with 5% H_2O (ν = 100 mV s^{-1}). The initial scanning direction is negative.

As is the case with CoSal and CobdtChexSal, the introduction of CO_2 does not cause irreversibility to either the first reductive or first oxidative process. A loss in redox peak height is observed for CodBrSal with CO_2 present upon the introduction of 5% water. This is partially due to solubility issues with the complex in DMF with water present. However, other changes can still be noted. The reversibility of the $Co^{2+/1+}$ process is

partially lost due to binding of CO_2 or H_2O to the Co^{1+} species. A weak irreversible oxidation is shown at -1.26 V, resulting from the $Co^{2+/1+}$ reduction process. The species is unknown, however a similar species was not present upon examining CoSal or CobdtChexSal under CO_2 with 5% water. A key difference between CodBrSal and CoSal or CobdtChexSal is that even under CO_2 with 5% water, CodBrSal still exhibits a quasireversible oxidative process related to $Co^{1+/2+}$.

Figure 3.13 shows the voltammetry obtained with potential cycling between -0.04 and -3.24 V under Ar, CO_2 and CO_2 with 5% H_2O present. It is noted, akin to the ligand reduction of CobdtChexSal (Figure 3.10), that electrolysis experiments close to the onset of solvent/electrolyte reduction may not be feasible. At such negative potentials, Faradaic efficiency towards catalysed CO_2 reduction may be lost due to electrolyte decomposition.

When cycling to such negative potentials as -3.24 V, the presence of CO_2 shows an irreversible oxidative process at approximately -0.32 V, or 70 mV anodically shifted of the E_{pa} $Co^{2+/3+}$ under Ar. In contrast, under Ar, no such peak was immediately evident. A second irreversible oxidation appears immediately following this (at approximately -0.16 V) under anodic scan. Both features occur with the presence of 5% water under CO_2, however, the oxidation at -0.32 V becomes very weak. With 5% water, the first oxidation decreases and second oxidation increases in intensity. This suggests that the second oxidation (with E_{pa} of -0.16 V) is not the direct oxidation of the electrochemical species formed at the first oxidation (with E_{pa} of -0.32 V). Species at similar oxidation potentials show when halting the cycles at -2.84 V. A similar second oxidation was observed for CobdtChexSal, requiring the $Co^{2+1/+}$ reduction in the presence of CO_2 and water (Figure 3.11), or the ligand reduction in the presence of CO_2 only (Figure 3.10).

Within the scans presented in Figure 3.13, the addition of CO_2 appears to return the $Co^{2+/1+}$ redox couple's shape (as that under Ar, without cycling the potential to the ligand based reductions), despite accessing the ligand based reductions. Furthermore, the reductive feature occurring at -2.48 V under Ar is absent under CO_2.

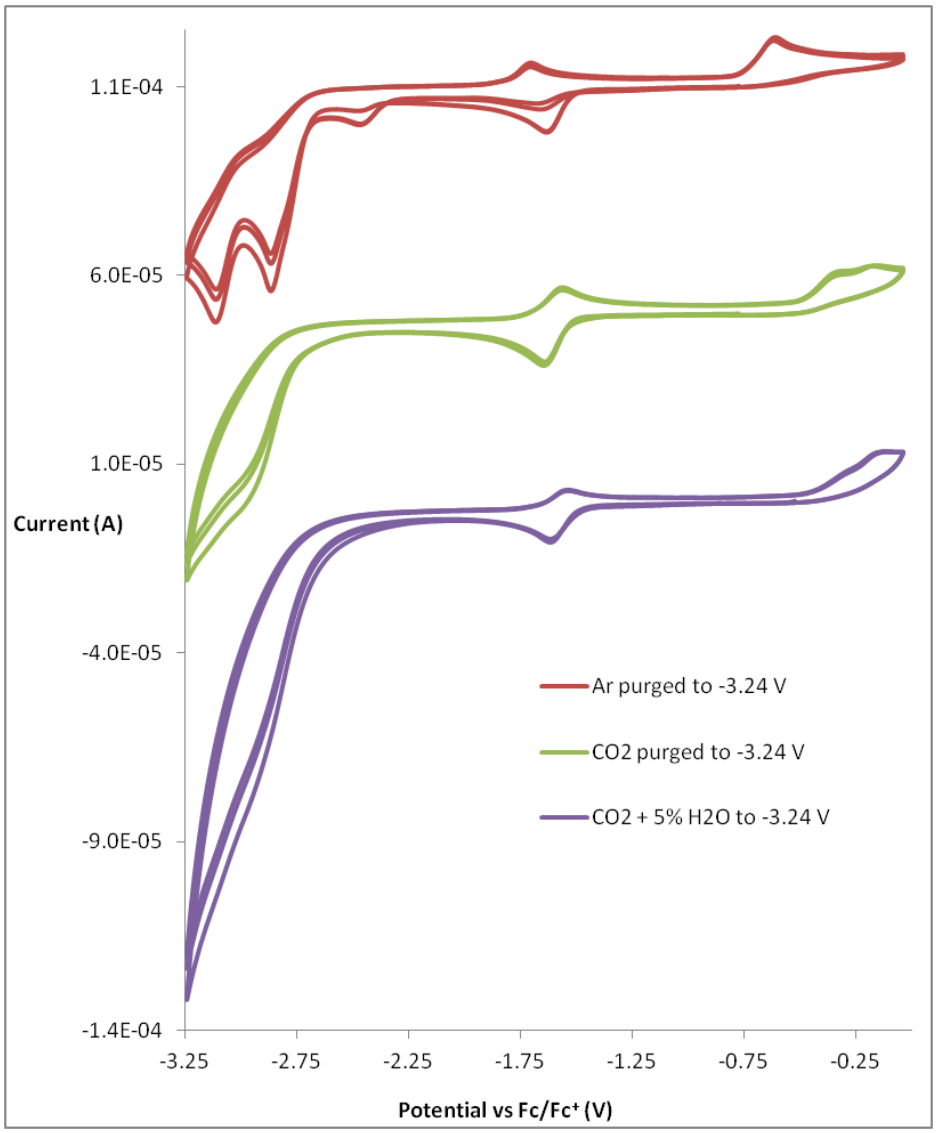

Figure 3.13: Cyclic voltammetry of 1 mM CodBrSal in DMF with 0.1 M $TBAPF_6$ under Ar, CO_2 and CO_2 with 5% water (ν = 100 mV s^{-1}), -0.04 to -3.24 V vs Fc/Fc^+. The initial scanning direction was negative. CVs under Ar and under CO_2 are offset by 110 and 50 μA respectively.

3.2.1.3.4. Voltammetric response of CopdSal towards CO_2 reduction

The cyclic voltammetry of CopdSal's $Co^{2+/1+}$ and $Co^{2+/3+}$ redox couples under Ar, CO_2 and CO_2 with 5% water appears in Figure 3.14.

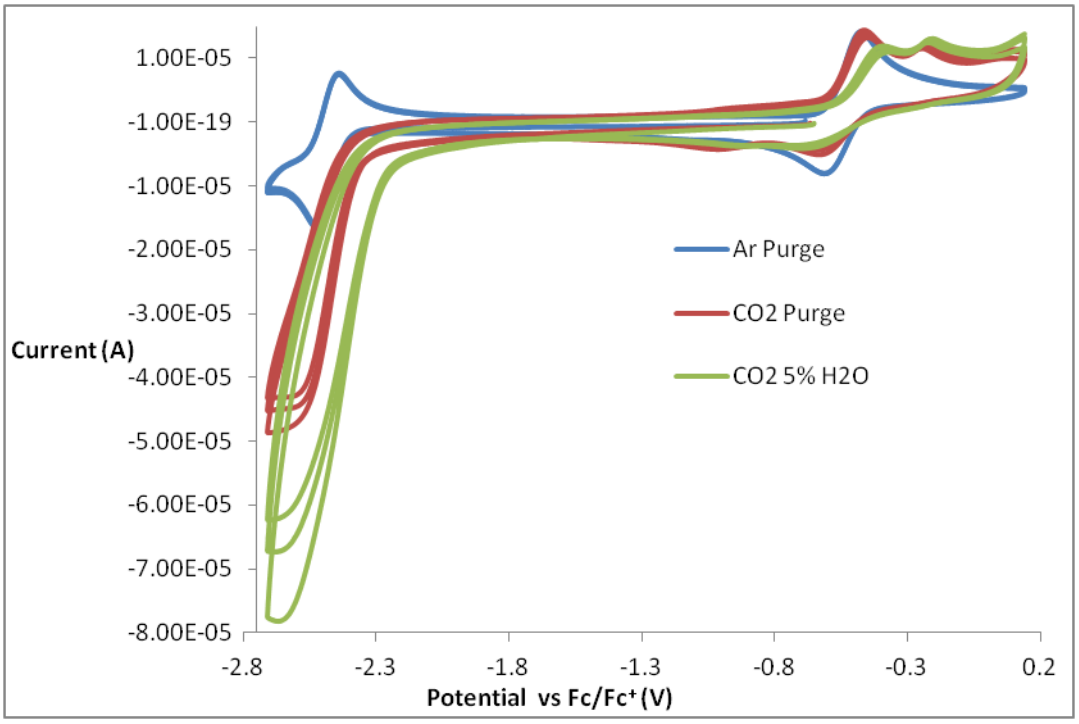

Figure 3.14: Cyclic voltammetry of 1 mM CopdSal in DMF with 0.1 M $TBAPF_6$ under Ar, CO_2 and CO_2 with 5% H_2O, ν = 100 mV s^{-1}. The initial scanning direction is negative.

As is displayed in Figure 3.14, the E_{pc} of the $Co^{2+/1+}$ process under Ar occurs at -2.52 V. Under CO_2, a current enhancement is obtained (i/i_p of 2.9) accompanied by a complete loss of reversibility of the couple. A further enhancement is observed with the addition of water, with the i/i_p reaching a 4.8-fold enhancement with 5% H_2O under CO_2. It is again noted that the DMF may contain some water before known additions, and the enhancement acquired under CO_2 may be due to a combined CO_2 and water presence. In terms of potentially allowing for a more selective system towards CO_2 reduction as opposed to H_2 generation (which occurs from the bare electrode non-catalytically at sufficiently negative potentials), the effect of a lower amount of water (0.167%) with

CO_2 was assessed by cyclic voltammetry and appears in Appendix B.2. The addition of 0.167 % water allows for an increase in catalytic current as compared to CO_2 only, but not as much as that witnessed with 5% water.

CopdSal demonstrates, similarly to CobdtChexSal, that with reductive current enhancement at $Co^{2+/1+}$ and irreversibility of this couple, a new irreversible oxidation is observed at -0.22 V, at a potential anodic to the $Co^{2+/3+}$ oxidation. Under CO_2 and in the absence of water, weak reduction and oxidation processes appear at approximately -1.01 V and -1.02 V respectively. The oxidative feature disappears with 5% water present, however the weak reductive feature remains.

Figure 3.15 displays the voltammetry of CopdSal at 10 mV s^{-1} under Ar, CO_2 and CO_2 with 5% water. Interestingly at the slower scan rate of 10 mV s^{-1}, the irreversible oxidation observed at -0.22 V is only very weakly present under CO_2 only, but is more apparent with the presence of water. This may suggest that with a slow scan rate, the species (produced by EC mechanism) at the first reduction diffuses away from the surface of the electrode.

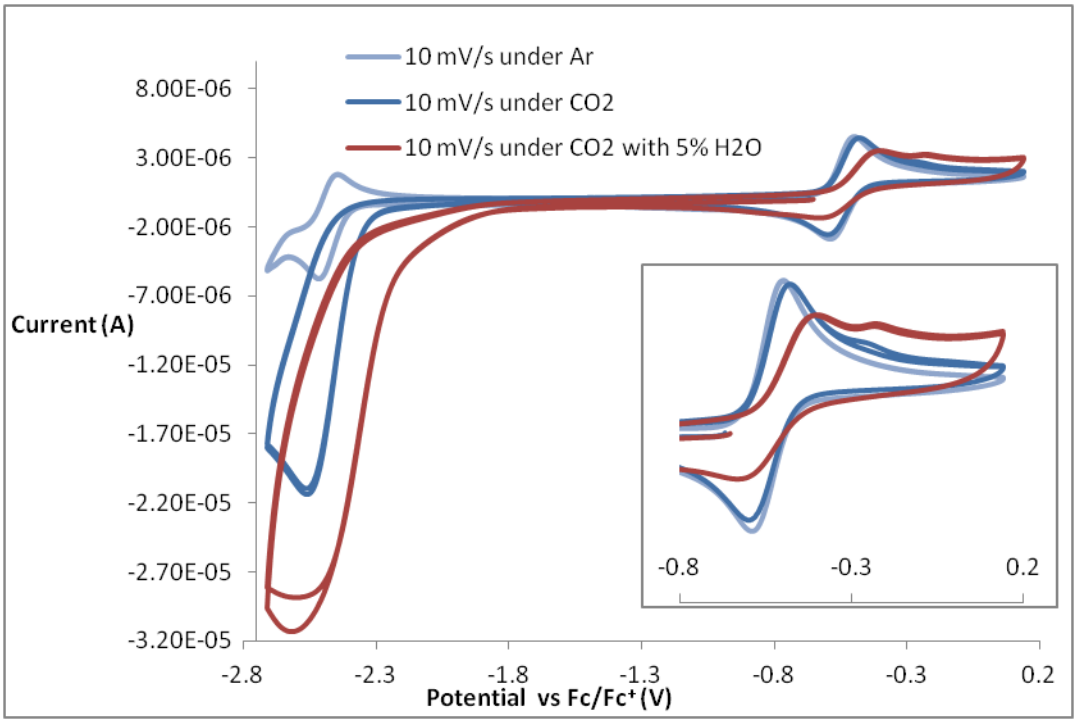

Figure 3.15: Cyclic voltammetry of 1 mM CopdSal at slower scan rate of 10 mV s^{-1} in DMF with 0.1 M $TBAPF_6$ under Ar, CO_2 and CO_2 with 5% H_2O. The initial scanning direction is negative

Reversibility within the $Co^{2+/1+}$ reduction of CopdSal was assessed under CO_2 and CO_2 with 5% water with varied scan rate. However, up to a scan rate of 10,000 mV s^{-1}, no level of reversibility was returned to the $Co^{1+/2+}$ oxidation under either CO_2 only (Appendix B.3) or CO_2 with 5% water (Appendix B.4). Examination of the $Co^{2+/3+}$ oxidation and the oxidation appearing anodic to the $Co^{2+/3+}$ oxidation under CO_2 only (Appendix B.3) shows that as the scan rate increases, this more anodic oxidation appears with greater intensity relative to the $Co^{2+/3+}$ oxidation. This corroborates the behaviour shown in Figure 3.15, whereby at the slow scan rate of 10 mV s^{-1}, the feature is very weak.

As shown in Figure 3.5, CopdSal is further reduced beyond the $Co^{2+/1+}$ reduction. However, no additional enhancement to the catalytic wave was observed at more negative potentials than sweeps to -2.71 V prior to the solvent/electrolyte reduction.

3.2.1.4. Summary of the $Co^{2+/3+}$ and $Co^{2+/1+}$ redox potentials under Ar and under CO_2 with 5% water

Table 3.3 displays the redox potentials of $Co^{2+/3+}$ and $Co^{2+/1+}$ couple under argon and E_{pc} of the Co^{2+} reduction process under argon and CO_2 with 5% water.

As is shown in Figure 3.14, the E_{pc} of the $Co^{2+/1+}$ process for CopdSal under CO_2 with 5% water is not as clearly defined as in the case of the other three compounds. Upon the introduction if CO_2 with water present, the E_{pc} of $Co^{2+/1+}$ is observed to shift anodically for each of CodBrSal, Sal and bdtChexSal. This behaviour does not feature with CopdSal. The anodic shift observed for CodBrSal, Sal and bdtChexSal has been noted previously for CoSal at a Hg electrode in CO_2-purged MeCN with 0.1 M $NaClO_4$ [22] and for Co cyclams at a graphite electrode in CO_2-purged DMSO with 0.1 M TBAP [63].

Table 3.3: Redox potentials of $Co^{2+/3+}$ and $Co^{2+/1+}$ couple under argon and E_{pc} of the Co^{2+} reduction process under Ar and CO_2 with 5% water (ν = 100mV s^{-1})

Complex	$E_{1/2}$ $Co^{2+/3+}$	$E_{1/2}$ $Co^{2+/1+}$	E_{pc} $Co^{2+/1+}$ Ar	E_{pc} $Co^{2+/1+}$ CO_2 + 5% H_2O
CoSal	-0.45 V	-1.72 V	-1.75 V	-1.73 V
CobdtChexSal	-0.46 V	-1.92 V	-1.96 V	-1.90 V
CodBrSal	-0.45 V	-1.59 V	-1.63 V	-1.56 V
CopdSal	-0.54 V	-2.48 V	-2.52 V	~ -2.66 − -2.71 V

3.2.2. Homogeneous controlled-potential electrolysis (CPE) under CO_2 in DMF with 5% water at a 0.071 cm^2 glassy carbon electrode

Tables 3.1 and 3.2 contain the results obtained from 1 hour CPE of CoSal, bdtChexSal, dBrSal and pdSal at a glassy carbon electrode (0.071 cm^2). The assessment includes a comparison of CO and H_2 (and CH_4 in the case of CopdSal) from the aspects of moles produced[2], Faradaic efficiencies (FE) and selectivity of CO over H_2. The electrolysis potentials are referenced versus the ferrocene/ferrocenium couple and the fixed potentials of electrolysis were more negative than the potential at which the $Co^{2+/1+}$ reduction occurred within each compound.

[2] Within the electrolyses involving 1 mM of dissolved catalyst, nmol of the product may be converted to TON (assuming bulk concentration) by dividing by 15,000, whereas μmol of the product may be converted to TON by dividing by 15.

Table 3.4: Bulk electrolyses undertaken at a 0.071 cm^2 glassy carbon working electrode in DMF/0.1 M $TBAPF_6$ under CO_2 with 5% H_2O in the presence and absence of 1 mM CoSal, bdtChexSal and dBrSal

Complex	**Potential (V)**	**Charge (C)**	**nmol CO**	**FE CO (%)**	**nmol H_2**	**FE H_2 (%)**	**Selectivity (CO/H_2)**
CoSal	-1.86	0.073	8	2	11	3	0.7
CoSal	-2.1	0.083	34	9	13	3	2.65
none	-2.1	0.024	2	1.5	53	43	0.03
CobdtChexSal	-2.1	0.117	130	23	18	3	7.2
CodBrSal	-1.78	0.131	4	0.5	11	2	0.3
none	-1.78	0.016	< 1	0.5	46	54	0.007
CodBrSal	-2.84	0.139	140	20	44	6	3.3
none	-2.84	0.014	1	2	10	14	0.1

Table 3.5: Bulk electrolyses undertaken in DMF/0.1 M $TBAPF_6$ under CO_2 with varied water in the presence and absence of 1 mM CopdSal, results in triplicate for varied potential electrolyses, all other electrolyses in singlicate

Complex / % H_2O	**Potential (V)**	**Charge (C)**	**nmol CO**	**FE CO (%)**	**nmol H_2**	**FE H_2 (%)**	**CO /H_2**	**nmol CH_4**	**FE CH_4 (%)**
CopdSal / 5%	-2.71	0.361	24	1.5	1100	55	0.02	4	1
CopdSal / 5%	-2.51	0.182	18	2	420	46	0.044	3	1
CopdSal / 5%	-2.39	0.136	10	1.5	330	47	0.03	5	3
CopdSal / 0%	-2.71	0.048	27	11	0	0	-	0	0
CopdSal / 0.167 %	-2.71	0.046	76	32	3	1	24	0	0
None / 0 %	-2.71	0.005	2	8	0	0	-	0	0
None / 0.167 %	-2.71	0.003	3	15	0	0	-	0	0
None / 5 %	-2.71	0.006	0	0	19	60	0	0	0

From the results in Table 3.4 and Table 3.5, it is evident that a higher charge is obtained in the presence than in the absence of catalyst. In all cases, it is also evident that the production of CO is higher with than without catalyst present.

The total Faradaic efficiency is less in most cases where a complex is present than in its absence. Solubility of CO is higher than hydrogen in water [64,65] and the ionic liquid 1-butyl-3-methylimidazolium tetrafluoroborate [66], and may also hold true to a polar aprotic solvent. However, comparable figures in DMF have not been found to support this. As H_2 is often generated preferentially to CO in the experiments without complex, the proportion of gas that is detected within the headspace as compared to that remaining in the solution may be higher. Though total FE suffers, FE_{CO} is far greater where a complex is present than without. Furthermore, selectivity towards CO production is higher with CoSal, CobdtChexSal and CodBrSal. In comparing CodBrSal, CoSal and CobdtChexSal as tetradentate homologous complexes with varied degrees of electron donation to the metal centre, it appears that CobdtChexSal is superior as a CO_2 reduction catalyst (Table 3.4).

When electrolysed after its relatively positive first reduction potential (-1.78 V), CodBrSal demonstrates a greater selectivity towards CO_2 reduction than does the bare electrode (with a CO/H_2 selectivity of 0.3 compared to 0.007 produced solely using a bare electrode). This equates to approximately 10 times more CO produced in the presence of a catalyst than at the bare electrode only. Interestingly, the bare electrode hydrogen generation was suppressed, with a 54 % FE_{H2} generated at -1.78 V at the bare electrode decreasing to 2 % FE_{H2} upon the introduction of CodBrSal.

Electrolysing after the second reduction potential of CodBrSal (1.06 V more negative, at -2.84 V) led to the formation of a far greater amount of CO with 20% efficiency being accounted for by the 140 nmol of detected CO (greatest amount of CO generated within salen electrolysis experiments) in contrast to < 1% FE_{CO} with 4 nmol at -1.78 V. A selectivity of 3.3 was achieved with compound at -2.84 V in contrast to 0.1 and 0.3 at the bare electrode at the same potential and with catalyst at -1.78 V respectively. Very interestingly, the amount and efficiency of hydrogen generation without catalyst in solution decreased from 46 nmol and 54% to 10 nmol and 14% from -1.78 V to -2.84 V. Passivation of the electrode was suspected (particularly due to slightly lower charge passed at 1.06 V more negative). Though an off-white coating was observed on the

surface of the electrode following electrolysis at -2.86 V and not on the electrode utilised at -1.76 V, this did not affect the voltammetry in a ferrocene solution (as compared with a freshly polished electrode). It is possible that reduction of the background electrolyte to butane [62] becomes a competing process with H_2 evolution. In the presence of the catalyst at -2.86 V though, the currently unidentified second reduction of CodBrSal appears to have slight affinity towards H_2 generation, generating > 4 times the H_2 that the bare electrode generates. However, for CO and especially H_2 generation, this potential is more negative than competitive electrocatalysts.

CoSal was assessed at two different potentials of -1.87, and -2.1 V when it became apparent that electrolysis at -1.87 V was not sufficient for selective CO_2 reduction. At both potentials, similar amounts of H_2 (11 and 13 nmol, with approximate FEs of 3% respectively) were generated with similar charges of 73 and 83 mC passed. Without complex present at -2.1 V, the bare electrode was capable of generating 53 nmol of H_2 (FE_{H2} of 43%). As with CodBrSal, the presence of CoSal served to suppress H_2 evolution, with > 4 times less H_2 produced when the complex was present. At -2.1 V, CoSal showed potential as a CO_2 reduction catalyst, surpassing the bare electrode and the complex at -1.86 V in terms of selectivity, CO generated and FE_{CO}. 34 nmol CO (FE_{CO} of 9%) was generated with CoSal at -2.1 V, which amounted to > 4 and almost 20 times more than that at -1.86 V or without complex (FE_{CO}s of 2 and 1.5%) respectively. A selectivity of 2.65 for CO over H_2 generation was observed, greater than 0.7 and 0.03 achieved at -1.86 V and without catalyst at -2.1 V respectively.

However, of the cobalt salen complexes studied, CobdtChexSal yielded the better results. Electrolysis following the $Co^{2+/1+}$ reduction revealed the greatest amount of CO (130 nmol) generated between the compounds electrolysed at the $Co^{2+/1+}$ process. With approximately the same potential negative of its $Co^{2+/1+}$ process, CoSal generated 16 times less CO, and with a further 240 mV cathodic shift in electrolysis potential to -2.1 V, CoSal still generated almost 4 times less CO. The stronger performance of CobdtChexSal is accentuated by comparison to the electron withdrawn CodBrSal with electrolyses just negative of the $Co^{2+/1+}$ process. In this case, CobdtChexSal exceeded CodBrSal, producing > 30 times more CO. The complex attained a FE_{CO} of 23%, surpassing that of the three other complexes examined with 5% water. This further led to the highest selectivity of CO to H_2 attained of 7.2. Electrolysis of the blank solution was evidently not the source of the CO produced, accounting for just 2 nmol or 65 times

less CO (FE_{CO} of 1.5). As with CodBrSal and CoSal, the presence of CobdtChexSal suppressed H_2 generation. 53 nmol or approximately 3 times the H_2 was generated at the bare electrode as compared to with CobdtChexSal, accounting for 43% FE_{H2} (FE_{H2} of 3% with catalyst). This diminished selectivity within the blank (0.03) leading to a 240 times more selective system with than without catalyst.

Three different potentials (-2.71, -2.51 and -2.39 V) with 5% water and three different water percentages (0, 0.167 and 5%) were assessed at -2.71 V under a CO_2 environment. The most surprising result of this was that at -2.71 V with 5% water present, CopdSal strongly demonstrated its potential as a H_2 evolution catalyst. Under these conditions, a charge 2-fold larger than any other experiment was consumed and a strong FE_{H2} of 55.2% was produced. This equated to 1100 nmol, almost 60 times greater than that generated by the bare electrode (19 nmol, 60% FE_{H2}). With reference to the voltammetry shown in Figure 3.5, under potentiostatic conditions the second reduction of the complex under Ar should not occur prior to potentials negative of -2.71 V.

Reducing the overpotential by 200 mV (electrolysis at -2.51 V) led to a lower rate of formation of H_2. Half of the charge was passed, with over 2 times less H_2 produced. This could be due to a negative potential allowing for a faster rate of catalysis, but also points towards the possibility of a second reduction of the complex. Indeed, when analysed at 10 mV s^{-1} under Ar (Figure 3.15), following the first reduction, the current is observed to increase again briefly before the scan is returned. This indicates that under CPE conditions, the second reduction process begins at -2.71 V. At -2.51 V, less CO was produced than at -2.71 V (18 and 24 nmol respectively). This is not competitive compared to that of CobdtChexSal in terms of the amount generated and the more negative potential required.

Bringing the potential less negative to -2.39 V resulted in passing 75% of the charge that was passed at -2.51 V, accompanied by a fall in the amount of CO and H_2 and resulting FE_{CO} produced. Reduction of the complex still occurs but the added driving force behind the reduction aids the formation of both CO and H_2. In all three cases, some CH_4 was observed but in low amounts, the highest of which was at -2.39 V which generated 5 nmol (FE_{CH4} of 3%).

When comparing experiments with varied water content at -2.71 V, no hydrogen was produced where no water was added. This provides a good indication that the DMF utilised within the experiment was relatively dry. Without water, CO was obtained as the sole product (27 nmol) in comparison to the 24 nmol obtained with 5% water. Interestingly, introduction of 0.167% water resulted in approximate 3-fold increase (76 nmol with FE_{CO} of 32%) in the amount of CO generated while maintaining a 24-fold selectivity over H_2. It is worth noting that although 0.167% may appear as a low amount of water, it equates to 93 mM. This is 93 times the amount of catalyst and approximate 0.4 mole ratio as compared to the concentration of CO_2 in solution [56,67,68]. The blank solutions do not account for much of the products detected, as can be observed within Table 3.5. Furthermore, no methane was detected within these experiments.

The best performing complex for CO_2 reduction in the presence of 5% water is CobdtChexSal. This has operated at -2.1 V with a selectivity of 7.2 over H_2 generation and generated the most CO of any complex assessed at the 2+/1+ Co-based reduction with 5% water. Based on these findings, the electrochemical system was optimised with CobdtChexSal in terms of working electrode material, size and potential.

3.2.3. Optimisation of electrocatalytic conditions pertaining to CobdtChexSal

In the study of the Co salens, CobdtChexSal demonstrated potential as a CO_2 reduction electrocatalyst. In terms of selectivity of CO over H_2 (7.2), the amount of CO (130 nmol, and at a more feasible potential of -2.1 V) and FE_{CO} (23%), the behaviour observed for CobdtChexSal was superior to that observed for CodBrSal, CoSal and CopdSal.

In order to allow for a more exhaustive approach to electrolysis, the use of larger glassy carbon was envisaged. Benefits to glassy carbon include high strength and low-porosity [69] as compared to other forms of carbon such as carbon felt [70] and extruded graphite [71]. Two different types of glassy carbon rods were procured, a 3 mm diameter x 15 cm Tokai Carbon and a 6.6 mm diameter x 9 cm Sigradur G. Efforts to shorten the rods to 3 cm length were halted by both failure to recreate a smooth glassy

surface of the freshly cut face and the complications associated with cleaning three-dimentional electrodes.

Due to this, another material was sought. A graphitic carbon rod[3] of 0.7 cm diameter x 2 cm submerged and Tokai FE250 extruded graphite plate of dimensions 0.5 x 1 x 2 cm allowed for selective CO/H_2 generation from 1 mM $Re(bpy)(CO)_3Cl$ in MeCN with 10% H_2O at -2 V vs Fc/Fc^+ while affording TONs greater than unity. The choice of $Re(bpy)(CO)_3Cl$ as electrocatalyst stems from its ability to selectively convert CO_2 to CO homogeneously with high FE, even in the presence of added water [29,30].

Within the material tests, the graphite rod was visibly less porous than the plate and as a result, a FE_{CO} of 74% was obtained. The plate generated an efficiency of 21%, however, bubbles were observed to evolve from the electrode for some time following the end of electrolysis (and injection of headspace). A partial reason for loss of efficiency within this material was likely gas generated in electrolysis becoming trapped within the pores. However, with TONs above unity, both materials demonstrated their ability as possible electrode materials.

As with the three dimensional glassy carbon, both of these electrode materials could not be reliably reused, as a three dimensional procedure (comparable to the polishing undertaken with conventional glassy carbon electrodes) could not ensure adequate cleaning. Graphite is a cheaper alternative to glassy carbon, however the cost was not yet at the point of single-use experiments with the option of disposability. Thus, the exploration of carbon paper (Toray) began. The material consists of a carbon fiber composite and has garnered the interest of esteemed groups working in electrocatalysis [72], including that of CO_2 reduction [73]. The particular carbon paper is Toray paper 120, 5% PTFE wet-proofing. No other types of carbon paper (or different levels of wet-proofing) were trialled. It was believed that a low level of wet-proofing could aide with gas diffusion while still allowing the solution to move through the pores and also not so significantly affecting conductivity throughout the electrode.

[3] Obtained from Prof. W. Browne, University of Groningen, NL

3.2.3.1. Homogeneous electrocatalytic CO_2 reduction utilising $Re(bpy)(CO)_3Cl$ with carbon paper working electrode

In order to assess the feasibility of carbon paper as an electrode material for electrocatalytic CO_2 reduction and to ensure that the material could function selectively without hydrogen generation from added water, $Re(bpy)(CO)_3Cl$ was electrolysed at -2.21 V vs Fc/Fc^+. The electrolyte was 5% water in DMF with 0.1 M $TBAPF_6$, in keeping with the Co salen electrolysis experiments. A 3 x 1 cm rectangular cut of carbon paper (370 μm thickness) was employed, with 2 cm of the length submerged in solution (4.2 cm^2 apparent submerged area). These results were compared to 0.071 cm^2 glassy carbon electrodes and the results appear in Table 3.6.

Table 3.6. One hour bulk electrolyses of CO_2-purged 1 mM $Re(bpy)(CO)_3Cl$ in DMF/5% H_2O/0.1 M $TBAPF_6$ at -2.21 V vs Fc/Fc^+. Large = 1 cm x 2 cm x 370 μm carbon paper, of 4.2 cm^2 apparent submerged surface area), small = 0.071 cm^2 glassy carbon electrode. n = 3

Experiment	Charge (C)	nmol CO	FE CO (%)	nmol H_2	FE H_2 (%)
Large $Re(bpy)(CO)_3Cl$	10.9	20,800	37	0	0
Large blank	0.55	41	1.5	172	6.4
Small $Re(bpy)(CO)_3Cl$	0.15	126	17	3	0.4
Small blank	0.009	2	4	23	48

As was expected in Table 3.6, very selective (CO/H_2) formation was detected at the carbon paper electrode. Quantitative FE_{CO}s were not achieved, contrary to the original work of Hawecker *et al*. [29,30] utilising a DMF/10% H_2O/0.1 M TBAP solution with 10 cm^2 glassy carbon working electrode (FE_{CO} of 98%) at a potential of -1.25 V vs NHE. The apparent surface area (not accounting for porosity or roughness) that is submerged in solution is 4.2 cm^2. In comparison to the 0.071 cm^2 glassy carbon electrode, this is a 59 time scale up of area. > 70 times the charge was however consumed in the electrolysis compared to $Re(bpy)(CO)_3Cl$ with the 0.071 cm^2 glassy carbon. In addition to this, no hydrogen was detected with the carbon paper. Therefore,

the material is applicable to homogeneous electrocatalysis under these conditions in terms of activity and potential for selectivity.

Potential sources of loss/unaccounted CO within the $Re(bpy)(CO)_3Cl$/carbon paper experiment may include the following. The carbon paper electrode is porous, and may retain CO within its pores at time of injection. The GC within these studies employs the use of a sampling loop which alleviates to atmospheric pressure, despite a greater pressure introduced with the valve syringe. In the calculations of the number of moles, pressure is assumed to be atmospheric. In a direct injection scenario, a greater number of moles of gas per volume would be introduced to the GC, thereby allowing the 1 atm assumption. 5% water with a controlled potential of -2.21 V vs Fc/Fc^+ was utilised within this study, varying from the 10% water and -1.94 V vs Fc/Fc^+ as used by Hawecker *et al*.'s [29,30]. The electrocatalytically active species has been stated to be the doubly-reduced $[Re(bpy)(CO)_3]^-$ [58,74] in agreement with the electrochemistry obtained (Appendix B.5). Therefore, the electrolysis potential chosen within this study should be adequate for quantitative CO generation. CO solubility in DMF could potentially account for a significant loss, where experiments generate less CO. An alternative approach to quantitation of CO in MeCN/ 0.1 M $TBAPF_6$ has recently been employed by Narayanan *et al.* [75]. Within their study, a known volume of gaseous standard was introduced into the electrolysis cell and following 15 minutes of stirring (to equilibrate), a sample of the headspace was undertaken to quantify against.

The 37% FE_{CO} achieved with passing a greater charge due to larger surface area, although still not ideal, indicates that either or both greater electrode size and longer electrolyses allow for a higher detected efficiency. The doubling of charge accounted for within experiment through larger electrode size validates the potential of CO being retained due to dissolution. In summation, carbon paper allowed for a higher FE_{CO} than did the smaller conventional glassy carbon electrode. Furthermore, selectivity for CO over H_2 was retained, in line with the literature. Through this study and from a cost perspective, carbon paper demonstrates its potential as an inert electrode for use in conjunction with a catalytically active material towards electrocatalytic CO_2 reduction.

3.2.3.2. Electrode size optimisation for CobdtChexSal

Following addressing whether the electrode material could maintain selectivity towards CO_2 reduction over background electrolyte/proton reduction with the use of $Re(bpy)(CO)_3Cl$, optimisation of the electrode geometry was undertaken. The fixed potential of -2.00 V vs Fc/Fc^+ was incorporated with the aim of reducing the potential required. Though -2.10 V was utilised within the small-scale electrolyses, enhancement of voltammograms of CobdtChexSal under CO_2 with water was observed to begin at potentials positive of -2.00 V.

The design of the electrodes incorporated within this study include a groove of 1cm length to limit subjectivity pertaining to the amount of electrode submerged. Electrodes were sonicated in acetone, dried and contained an additional cut of carbon paper on each side of the groove to protect the carbon paper being torn by the crocodile clip within the cell. The dimensions of electrodes assessed are available in Figure 3.16.

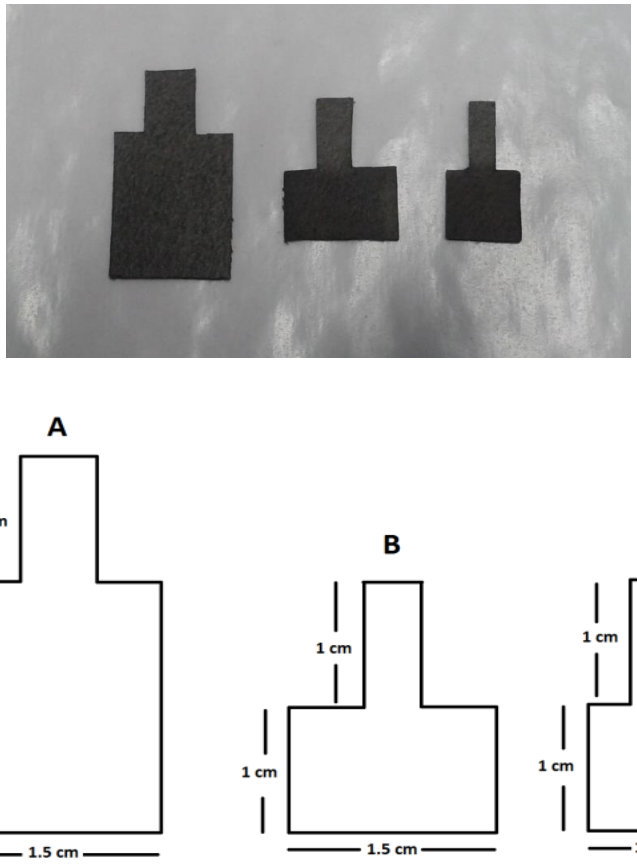

Figure 3.16: Electrode sizes utilised within size optimisation for CobdtChexSal, the third dimension is 370 μm. The apparent electrode areas submerged are A = 6.2 cm^2, B = 3.1 cm^2, C = 2.1 cm^2

The results of homogeneous electrolyses at -2.00 V with electrodes A, B and C are available in Table 3.7 and are additionally displayed in Figure 3.17. Electrolyses were undertaken for more than one hour. The cell was purged with CO_2 prior to the commencement of each hour of electrolysis. Therefore, the system remains at atmospheric pressure at the beginning of each hour. At the end of the hour, a 1 ml aliquot of gas is removed from the headspace. Without this repurge, the 1 ml removal from a 15.2 ml headspace would upset the pressure within the cell, therefore not allowing an accurate figure for headspace content with any injections beyond the first hour. Furthermore, a large fraction of the gas content not removed from prior hours of electrolyses would be analysed consecutively, artificially inflating figures and not allowing for a representative Faradaic efficiency.

Table 3.7: Varied working electrode size (with dimensions shown in Figure 3.16) for electrocatalytic CO_2 reduction with 1 mM CobdtChexSal at -2.00 V vs Fc/Fc^+. Electrolyte: 5% H_2O in DMF containing 0.1 M $TBAPF_6$. n = 3. The apparent electrode areas submerged are A = 6.2 cm^2, B = 3.1 cm^2, C = 2.1 cm^2

Electrode	H_2 μmol	H_2 FE (%)	CO μmol	CO FE (%)	Selectivity CO/H_2	Charge (C)
A Hr 1	5.23	16.8	1.83	6.1	0.35	5.92
A Hr 2	21.31	62.9	0.19	0.7	0.01	6.38
A blank Hr 1	0.92	26.6	0.03	1.1	0.033	0.61
A blank Hr 2	1.55	46.1	< 0.01	0.3	0.006	0.67
A without CO_2, Hr 1	< 0.01	< 0.1	< 0.01	< 0.1	0.19	2.25
A without CO_2, Hr 2	< 0.01	< 0.1	< 0.01	< 0.1	0.062	2.37
B Hr 1	1.76	7.5	1.92	8.1	1.096	4.63
B Hr 2	11.17	45.7	0.55	2.3	0.049	4.70
B Hr 3	34.20	80.1	0.10	0.2	0.003	8.18
C Hr 1	0.89	4.4	1.56	7.8	1.798	3.60
C Hr 2	6.55	29.6	0.79	3.5	0.12	4.31
C Hr 3	13.41	66.8	0.09	0.4	0.007	3.90

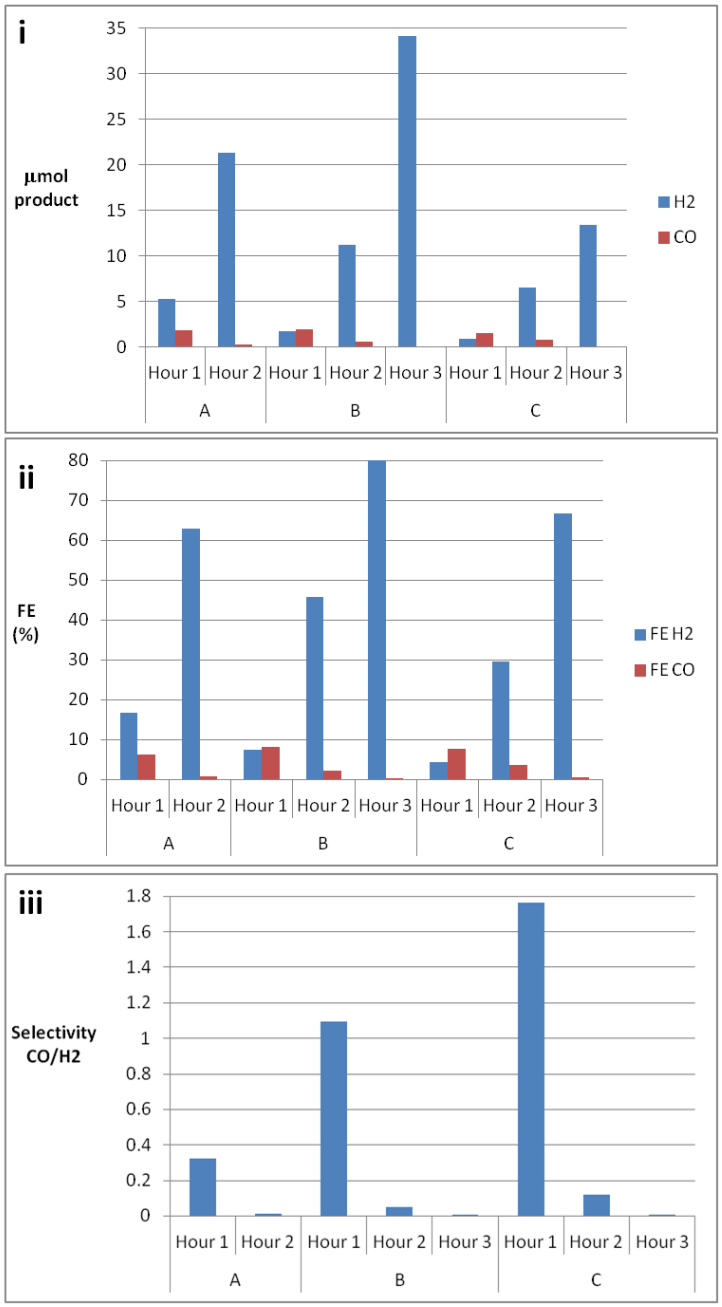

Figure 3.17: **i**. µmol of product , **ii**. FE (%) and **iii**. selectivity of CO/H_2 generated upon electrolysis of 1 mM CobdtChexSal in CO_2 purged DMF/0.1 M $TBAPF_6$/5% H_2O at varied carbon paper electrode sizes and at -2.00 V vs Fc/Fc^+

The figures in Table 3.7 show that a fall in charge is concurrent with a decrease of the surface area of the electrode. This behaviour is to be expected as even if there was no electrocatalytic activity, the compound would be reduced. For a diffusion controlled

species, this can be explained by the Randles-Sevcik equation, whereby current (and therefore charge) is directly proportional to the area of an electrode [76]. For a surface-confined process, with a greater surface area, more molecules (precatalyst or substrate) may access the electrode surface.

As the electrodes B and C were of smaller area to that of A, it was evident that a longer time would be required to pass similar amounts of charge. Hence, electrodes B and C each contained a third hour of electrolysis. It quickly became evident that successive electrolyses led to increased H_2 generation and decreased CO generation (see Figure 3.17). This trend was observed with all three electrodes and each of the three time points for electrodes B and C. For example in B, a CO/H_2 selectivity of approximately 1.1 decreased to 0.003 from hour one to hour three.

The complex undergoes reduction and appears to react with CO_2. The complex however, appears to requires reaction with CO_2 prior to forming hydrogen as evidenced by Figure 3.11, whereby doubling the water percentage to 10% v/v doesn't appear to show any loss of reversibility towards the $Co^{2+/1+}$ reduction, until the introduction of CO_2. Further evidence is held within the electrolysis figures. When the solution with 5% water is electrolysed in the absence of CO_2, (Table 3.7 "A without CO_2"), 14 times less H_2 is observed following the second hour in contrast to that in the presence of CO_2. The decrease in selectivity of CO/H_2 as charge is consumed suggests that the complex needs to be reduced and interact with CO_2 prior to taking part in proton reduction.

To assess if the complex decomposes to liberate the $[bdtChexSal]^{2-}$ ligand, UVs were taken of the solution following electrolysis one and two under CO_2 with electrode A and compared to the starting complex. The spectra acquired appear in Figure 3.18. UVs of the compound electrolysed under Ar were unsuccessful. As the cell was opened to air, the green colour associated with Co^{1+} [77] immediately reverted to a red colour. This behaviour has previously been attributed to the reoxidation of Co^{1+} by molecular oxygen. As an effective demonstration of reversion of colour, air was bubbled through the electrolysed solution, as can be seen in Appendix B.6. It is evident that the composition of the solution is not the same as the starting complex. The Co^{3+} acetate species shows no distinguishable features at 360 nm [78], whereas the starting complex shows a band with λ_{max} of 356 nm [79,80] (attributed through analogous complexes to either ligand-based $\pi-\pi^*$ [81] or n-π^* [49] transitions). Though the presence of Co^{3+}

cannot be completely ruled out, neither electrolysis 1 or 2 show evidence for a feature at 360 nm. The presence of free ligand cannot be ruled out either, with an absorption due to free ligand occurring with λ_{max} of 330 nm in DCM [82].

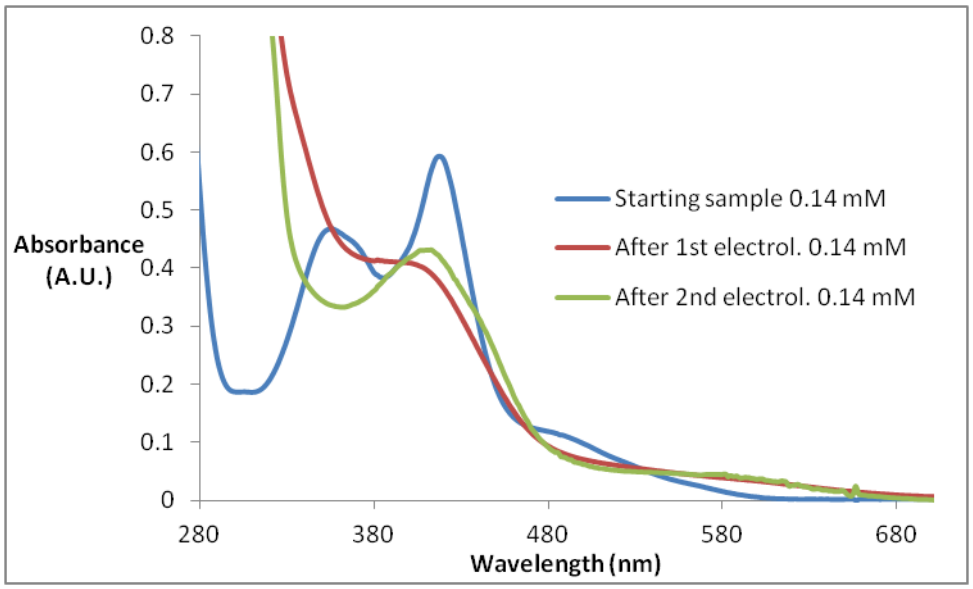

Figure 3.18: UV-visible spectra of 1 mM CobdtChexSal in DMF with 0.1 M $TBAPF_6$ and 5% water (diluted to 0.14 mM with the same electrolyte), acquired in aerated samples following electrolysis one and two (two hours) and pre-electrolysis, experimental conditions as per Table 3.7 "A"

The capability of the catalyst/pre-catalyst begins to tell a different story with larger surface area as compared to the more conventional 0.071 cm^2 electrodes. No longer is it possible to achieve a large selectivity towards CO_2 products over H_2 generation. The attention therefore shifts to determination of the optimal size based on amount and FE of H_2 generated. Of the time points undertaken, electrode size B, hour 3 showed the greatest Faradaic efficiency, number of moles and charge for H_2. With an approximate 330-fold selectivity of H_2 over CO, it is also the most selective for H_2. For these reasons, voltage optomisation continues based on size B.

3.2.3.3. Voltage optimisation for CobdtChexSal

Optimisation of potential for the CobdtChexSal system was undertaken at three potentials in addition to -2.00 V utilised in the size optimisation experiment. The additional potentials assessed include -1.83, -1.91 and -2.10 V, the results of which are available in Table 3.8.

As can be seen in Table 3.8, -2.00 V remains the optimal potential of electrolysis. It holds true that as the potential is increased from -1.83 to -2.00 V, a greater amount of products, charges and FEs are passed/accounted for by the third hour. In each case, the selectivity of CO/H_2 is observed to fall from the first to the third hours, in agreement with the behaviour observed with the electrode size study. The same behaviour is also observed at -2.10 V, however by the third hour, both H_2 FE and amount (~ 71% and 24.4 μmol respectively) are lower than that at -2.00 V (~ 80% and 34.2 μmol respectively). Selectivity of CO/H_2 within the first hour for -1.91 and -2.00 V are almost identical at 1.1, however, double the CO was generated at -2.00 than at -1.91 V (1.92 vs 0.99 μmol). This is also the same amount of CO generated within the first hour at -2.10 V. In hours 2 and 3, -2.10 V experiences a decrease in the amount of H_2 generated relative to that at -2.00 V. This may be reasoned in part as other Faradaic processes creating different, unmonitored products from either the electrolyte or CO_2. Some methane (< 5% FE_{CH4}) was detected in most experiments (less prevalent at -1.83 V) with catalyst present. It is worth noting that though H^1 NMR did not show the presence of formic acid, the technique is not sensitive relative to the amount of product that could have possibly been generated. Oxalic acid was not assessed.

Table 3.8: Varied electrolysis potential (using Figure 3.16 "Electrode B", 3.1 cm^2) for electrocatalytic CO_2 reduction with 1 mM CobdtChexSal. Potentials: -1.83, -1.91, -2.00 and -2.10 V vs Fc/Fc^+. Electrolyte: 5% H_2O in DMF containing 0.1 M $TBAPF_6$. n = 3 with blanks n = 1

Potential	Hour	H_2 μmol	H_2 FE (%)	CO μmol	CO FE (%)	Selectivity CO/H_2	Charge (C)
-1.83 V	1	0.33	3.5	0.16	1.7	0.486	1.82
	2	1.56	13.0	0.23	1.9	0.146	2.28
	3	3.72	31.5	0.10	0.8	0.026	2.20
-1.83 V blank	1	0.21	10.5	0	0	0	0.38
	2	0.38	20.1	0	0	0	0.36
	3	0.53	26.7	< 0.01	0.1	0.004	0.38
-1.91 V	1	0.90	4.8	0.99	5.6	1.1	3.42
	2	5.98	28.1	0.60	2.9	0.101	4.05
	3	17.85	68.7	0.12	0.4	0.007	5.02
-1.91 V blank	1	0.59	36.1	< 0.01	0.1	0.003	0.32
	2	1.19	40.1	< 0.01	< 0.1	0.002	0.57
	3	3.96	69.3	< 0.01	< 0.1	< 0.001	1.10
-2.00 V	1	1.76	7.5	1.92	8.1	1.096	4.63
	2	11.17	45.7	0.55	2.3	0.049	4.70
	3	34.20	80.1	0.10	0.2	0.003	8.18
-2.00 V blank	1	1.14	39.8	0.01	0.3	0.008	0.57
	2	1.98	45.2	< 0.01	0.1	0.003	0.82
	3	4.44	67.3	< 0.01	0.1	0.002	1.36
-2.1 V	1	1.90	7.1	1.92	7.2	1.01	5.14
	2	10.66	36.0	0.53	1.8	0.05	5.64
	3	24.42	71.1	0.11	0.3	0.005	6.61
-2.1 V blank	1	1.66	39.4	0.02	0.5	0.013	0.82
	2	3.90	52.4	0.01	0.1	0.003	1.43
	3	5.37	62.3	0.01	0.1	0.002	1.66

In terms of relating charge passed to electrocatalytic H_2 generation, it appears that approximately one or two mole equivalents of electrons (1.447 and 2.895 C respectively) may be required to create the electroactive species for H_2 generation. This observation is not straight-forward as there is certainly evidence to suggest that CobdtChexSal may be a CO_2 reduction catalyst but that deactivation of the complex occurs.

In an effort to assess the active species within experiments, SEM was undertaken on the carbon paper utilised for a three hour electrolysis at -2.00 V.

3.2.3.4. SEM of electrode utilised within 3-hour electrolysis at -2.00 V

Field emission scanning electron microscopy with secondary electron detection was undertaken[4]. Both an electrode utilised within the 3-hour electrolysis of CobdtChexSal at -2.00 V and a blank electrode electrolysed under the same conditions but without compound present were imaged. The results appear in Figure 3.19, with further images of the modified electrode appearing in Appendix B.7.

A striking dissimilarity is observed between the two samples imaged in Figure 3.19. It is clear that the surface of the electrode containing the complex has experienced a growth of particulate matter. It can be witnessed in Appendix B.7 row three (1000x) that these particles are spread throughout the electrode material. The particles are not uniform in size however, as observed in Appendix B.7 row one. The formation of these particles coincides with electrocatalytic H_2 generation. Electrolysis in blank electrolyte was not undertaken with the same electrodes that were used to electrolyse the CobdtChexSal solution. Therefore, it cannot be stated with certainty as to whether the heterogeneous deposit, or the electrolysed solution is responsible for H_2 generation.

[4] SEM Micrographs were acquired within DCU on a Hitachi S5500 FESEM, and with help from Mr. Colm Montgomery

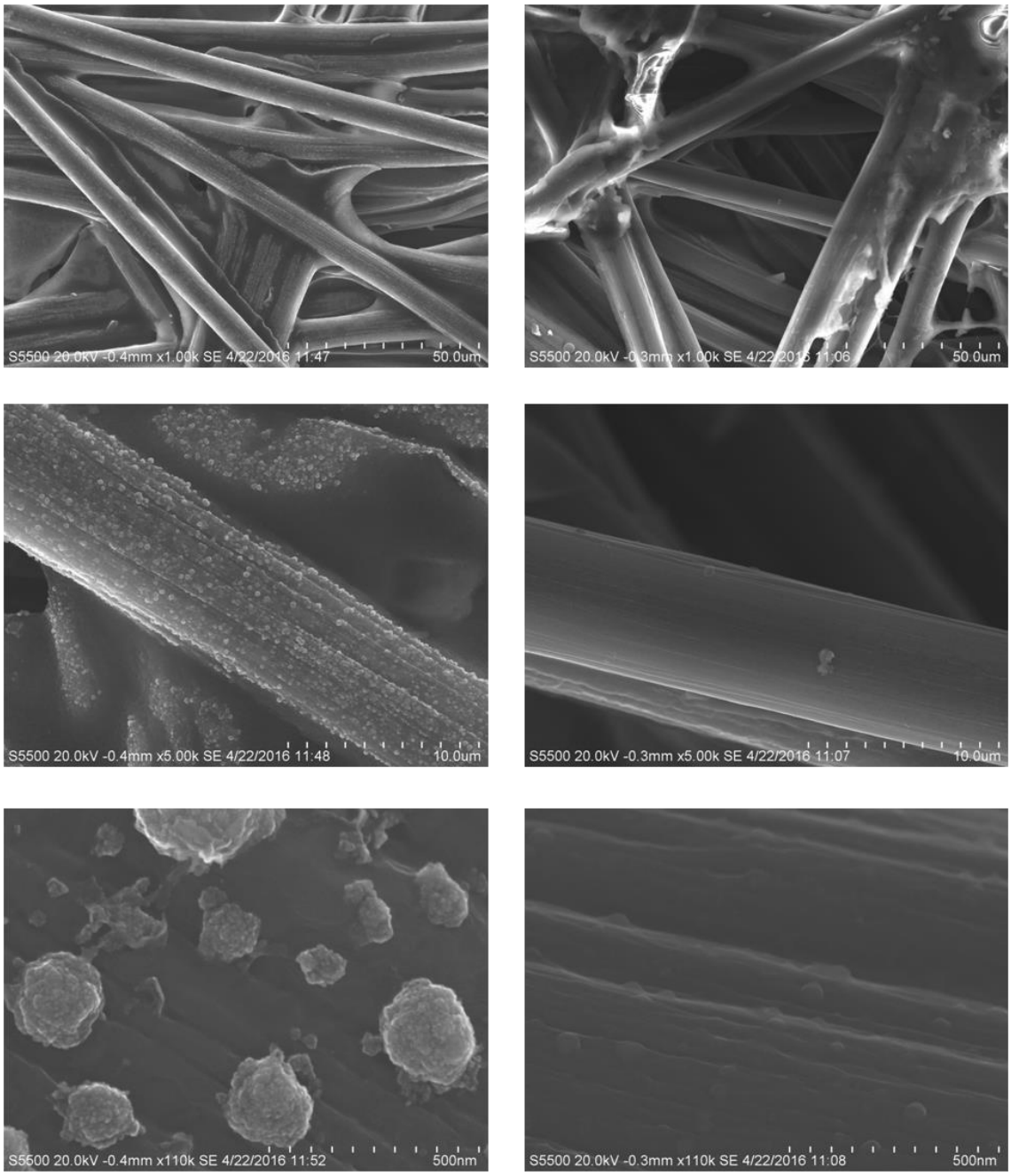

Figure 3.19: SEM images at 1000, 5000 and 110000x magnification (top, middle and bottom respectively) of carbon paper utilised in electrolysis at -2.00 V vs Fc/Fc^+ with CobdtChexSal (left) and without (right) in CO_2 purged DMF/0.1 M $TBAPF_6$/5% H_2O, 20 kV accelerating voltage, 19 μA probe current

In order to encourage further growth of heterogeneous material onto the electrode with the aim of acquiring EDX, another electrode was prepared by electrolysing the solution at -2.20 V. With further negative driving force, it was hoped that more material would deposit on the electrode and that EDX would become feasible. A film-coated electrode

resulted. SEM images of this prepared electrode along with those of an electrode prepared in the absence of catalyst appear in Figure 3.20. An EDX spectrum was acquired and features in Figure 3.21 along with an SEM image of the region analysed. The electrode shows a signal in the EDX spectrum associated with the presence of cobalt. However, due to the high contribution of carbon and the close proximity of carbon, nitrogen and oxygen signal locations (one each), it cannot be stated with any certainty that either nitrogen or oxygen exist within the deposit. At this time, cobalt oxides, which have previously been reported to catalyse CO_2 reduction to formate [83,84] as well as H_2 from water [85–88], cannot be ruled out as the identity of the deposited material.

To ensure that this material observed by SEM did not spontaneously deposit from either fresh solution or previously electrolysed solution, carbon paper was soaked overnight in the presence of 1 mM complex, 5% H_2O in DMF with $TBAPF_6$ and CO_2 and also in the solution previously electrolysed at -2.20 V. The results appear in Appendix B.8 and Appendix B.9. In neither case is a deposited material observed. This confirms in both cases that the material is electrodeposited onto the electrode.

A further check was undertaken to ensure that this behaviour was atypical of simply passing a larger charge across an electrode, potentially causing surface modification. In this endeavour, $Re(bpy)(CO)_3Cl$ was employed. The SEM images acquired following 3 hours of electrolysis at -2.20 V in the same electrolyte as that used for CobdtChexSal are found in Appendix B.10. As can be seen with these images, no deposit was observed, thus ruling out a larger charge passed as a reason for the deposit/modified surface.

In an effort to rule out the presence of Cobalt oxides and free cobalt [89,90], electrolysis was repeated at -2.00 V in the presence of approximately 0.4 mM H_2EDTA [91]. The same trend of H_2 evolution was observed with the addition of EDTA as compared to in the absence of EDTA. SEM was undertaken on the electrode utilised and micrographs appear in Appendix B.11. As can be observed, a deposition still occurred. Due to the uncertainty with the level of dissolution of H_2EDTA, the presence of Co oxide may however, not be eliminated.

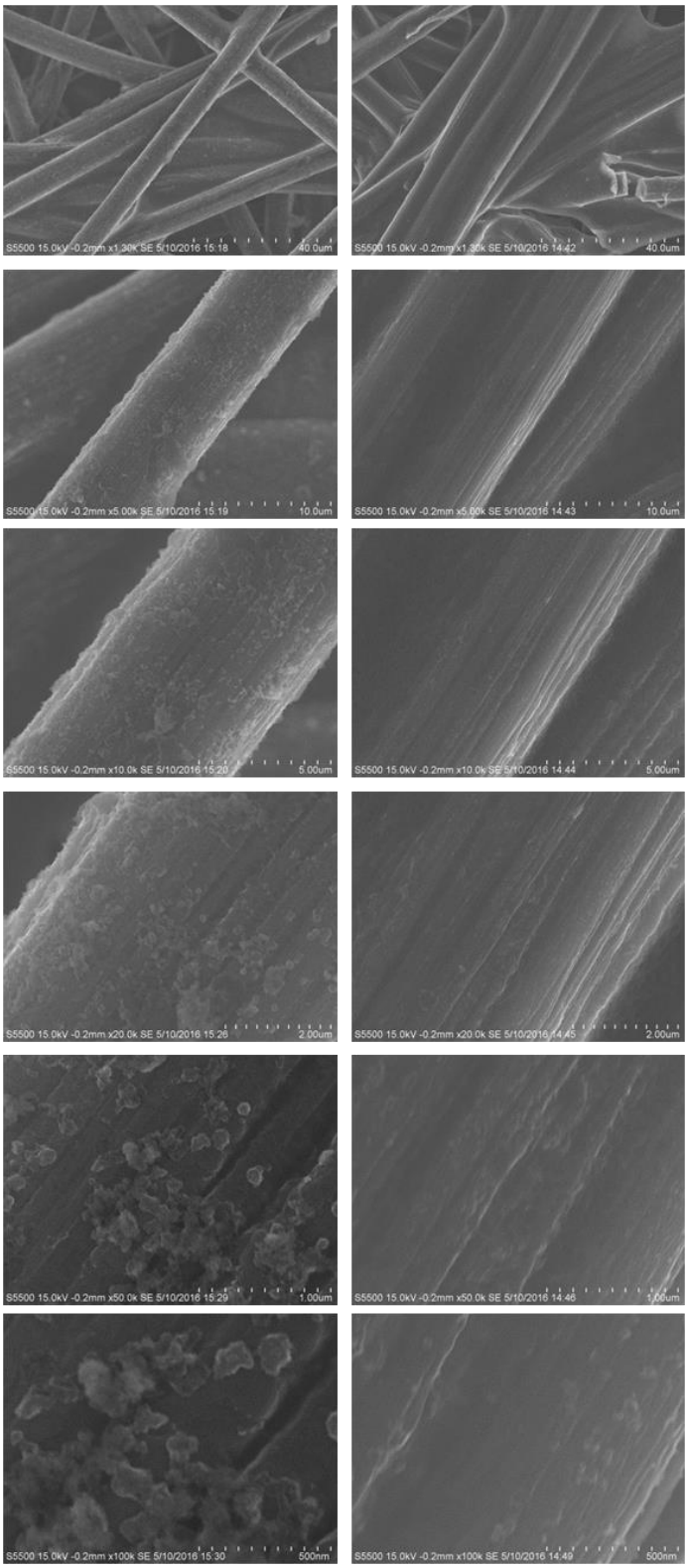

Figure 3.20: Left: Carbon paper electrode used to electrolyse 1 mM CobdtChexSal at -2.20 V under CO_2 in DMF/5% H_2O. Right: Without compound present. Top to bottom: 1300, 5000, 10000, 20000, 50000 and 100000x magnification. 15 kV accelerating voltage, 4.7 μA probe current

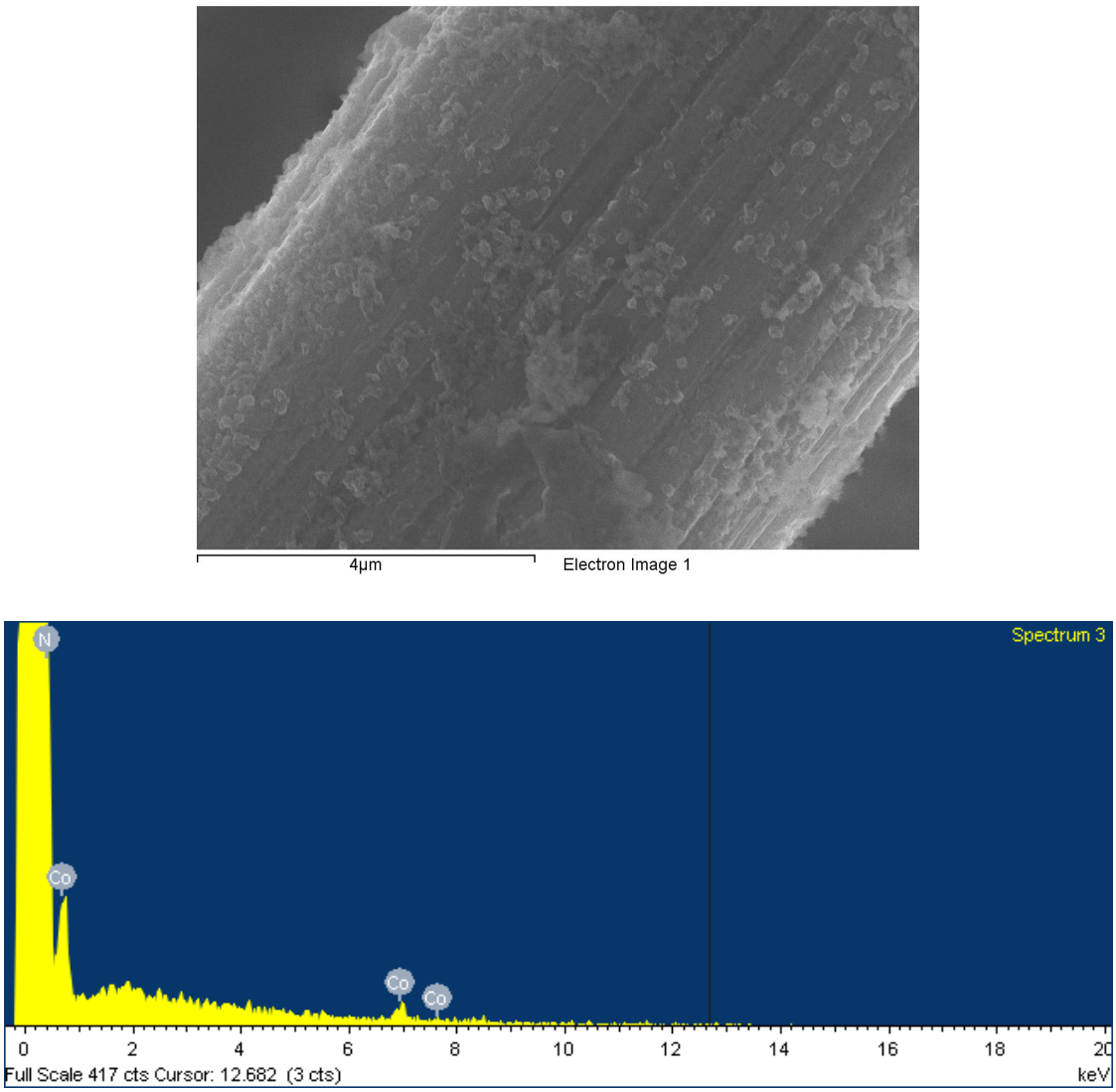

Figure 3.21: EDX spectrum of electrode used in electrolysis at -2.2 V for three hours under CO_2 with 1 mM CobdtChexSal, DMF with 5% water and 0.1 M $TBAPF_6$, including image of region examined

3.3. Concluding remarks

The experiments initiated with assessing a variety of cobalt complexes as potential electrocatalysts for CO_2 reduction. Of the four complexes analysed, CobdtChexSal showed promise in terms of selectivity towards CO generation over that of H_2. Mn Cl and Al Cl homologues of this cobalt complex were assessed to see if the ligand may display non innocence to assist the metal centre in stabilising adducts or allowing for the storage of an electron equivalent on the ligand for conversion. This approach did not prove successful. However, electrochemical evidence suggests passivation of the electrode material may play a role in the poor results obtained.

The next step focussed on larger scale optimisation of the cell so that catalytic turnover numbers could be achieved. It was reasoned that carbon paper was an ideal candidate for this purpose through the selective CO generation over H_2 with a known catalyst, $Re(bpy)(CO)_3Cl$, in addition to the cost of the material.

The electroactive area of the carbon paper was optimised with electrolyses of CobdtChexSal at -2.00 V. It was clear that preferential H_2 generation occurred in successive hours of electrolysis. UV-vis spectra of solutions taken following electrolyses suggest that neither free ligand nor Co^{3+}- ligand species are present in clear abundance within the solution as compared to UVs within the literature. Without free ligand observed, the existence of CoO_x species is less likely to be present to play a role in H_2 generation. No [Co^{1+}bdtChexSal] spectra were apparent within the literature for comparison. However, as observed under Ar, the Co^{1+} species is green in colour, whereas when electrolysed in CO_2, this green colour is not observed. The free ligand may itself undergo a reduction positive of -2.00 V, which would likely result in different UV bands in comparison to what would be expected for H_2bdtChexSal.

A very interesting point within these electrolyses is that CO_2 is required for H_2 generation. This has been observed previously in the literature for a manganese complex [92] (within the area of molecular electrocatalysts). However, the authors attributed this to the decrease in pH caused by CO_2 dissolution as carbonic acid, thus aiding the potential at which H^+ reduction occurs. Another possibility is that the complex could have difficulty in releasing CO during its cycle of converting CO_2 to CO. This new complex could also potentially convert H_2O to H_2 at its formation potential. A further report has observed H_2 generation, proposed to proceed through a formate intermediate

[93]. Additionally Narayanan *et al*. observed similar CO_2-promoted H_2 generation with a nickel bisiminopyridyl complex [75].

Optimisation continued to explore the electrolysis potential as a parameter. Following this, SEM was undertaken and showed the growth of material on the electrode. In a further electrolysis at more negative potential (-2.20 V) to acquire greater growth, EDX showed the presence of cobalt. As the electrode material is carbon, it was not feasible to view signals associated with nitrogen and oxygen. Therefore, EDX could not supply adequate proof as to the presence of either Co-L or CoO_x, or indeed discount either.

3.4. References

[1] Y. Han, H. Fang, H. Jing, H. Sun, H. Lei, W. Lai, R. Cao, *Angew. Chem. Int. Ed.* **2016**, *55*, 5457–5462.
[2] J. Liu, X. Yang, L. Sun, *Chem. Commun.* **2013**, *49*, 11785–11787.
[3] Y. Chen, L. Fu, Z. Liu, *Chem. Commun.* **2015**, *51*, 16637–16640.
[4] M. D. Sampson, A. D. Nguyen, K. A. Grice, C. E. Moore, A. L. Rheingold, C. P. Kubiak, *J. Am. Chem. Soc.* **2014**, *136*, 5460–5471.
[5] J. Agarwal, C. J. Stanton III, T. W. Shaw, J. E. Vandezande, G. F. Majetich, A. B. Bocarsly, H. F. Schaefer III, *Dalton Trans* **2015**, *44*, 2122–2131.
[6] J. D. Froehlich, C. P. Kubiak, *Inorg. Chem.* **2012**, *51*, 3932–3934.
[7] K. Bujno, R. Bilewicz, L. Siegfried, T. A. Kaden, *J. Electroanal. Chem.* **1998**, *445*, 47–53.
[8] J. D. Froehlich, C. P. Kubiak, *J. Am. Chem. Soc.* **2015**, *137*, 3565–3573.
[9] A. Mary Imelda Jayaseeli, A. Ramdass, S. Rajagopal, *Polyhedron* **2015**, *100*, 59–66.
[10] J. M. Fraile, N. García, C. I. Herrerías, J. A. Mayoral, *Catal. Sci. Technol.* **2013**, *3*, 436–443.
[11] A. S. Ogunlaja, W. Chidawanyika, E. Antunes, M. A. Fernandes, T. Nyokong, N. Torto, Z. R. Tshentu, *Dalton Trans.* **2012**, *41*, 13908–13918.
[12] A. Coletti, P. Galloni, A. Sartorel, V. Conte, B. Floris, *Catal. Today* **2012**, *192*, 44–55.
[13] L. Mishra, R. Prajapati, K. K. Pandey, *Spectrochim. Acta. A. Mol. Biomol. Spectrosc.* **2008**, *70*, 79–85.
[14] S. Fu, Y. Liu, Y. Ding, X. Du, F. Song, R. Xiang, B. Ma, *Chem. Commun.* **2014**, *50*, 2167–2169.
[15] D. Chen, A. E. Martell, *Inorg. Chem.* **1987**, *26*, 1026–1030.
[16] G. B. Gill, G. Pattenden, S. J. Reynolds, *J. Chem. Soc. [Perkin 1]* **1994**, 369–378.
[17] L. N. Rusere, T. Shalumova, J. M. Tanski, L. A. Tyler, *Polyhedron* **2009**, *28*, 3804–3810.
[18] D. J. Darensbourg, *Chem. Rev.* **2007**, *107*, 2388–2410.
[19] H. Chen, Z. Sun, X. Liu, A. Han, P. Du, *J. Phys. Chem. C* **2015**, *119*, 8998–9004.
[20] H. Chen, Z. Sun, S. Ye, D. Lu, P. Du, *J. Mater. Chem. A* **2015**, *3*, 15729–15737.
[21] I. Yamanaka, K. Tabata, W. Mino, T. Furusawa, *Isij Int.* **2015**, *55*, 399–403.
[22] D. J. Pearce, D. Pletcher, *J. Electroanal. Chem. Interfacial Electrochem.* **1986**, *197*, 317–330.
[23] A. A. Isse, A. Gennaro, E. Vianello, C. Floriani, *J. Mol. Catal.* **1991**, *70*, 197–208.
[24] M. Hammouche, D. Lexa, M. Momenteau, J. M. Saveant, *J. Am. Chem. Soc.* **1991**, *113*, 8455–8466.
[25] M. D. Sampson, C. P. Kubiak, *J. Am. Chem. Soc.* **2016**, *138*, 1386–1393.
[26] J. Losada, I. del Peso, L. Beyer, J. Hartung, V. Fernández, M. Möbius, *J. Electroanal. Chem.* **1995**, *398*, 89–93.
[27] Y. Fu, Y. Liu, Y. Li, J. Li, J. Qiao, J. Zhang, *J. Solid State Electrochem.* **2015**, *19*, 3355–3363.
[28] T. C. Berto, L. Zhang, R. J. Hamers, J. F. Berry, *Acs Catal.* **2015**, *5*, 703–707.
[29] J. Hawecker, J.-M. Lehn, R. Ziessel, *Helv. Chim. Acta* **1986**, *69*, 1990–2012.
[30] J. Hawecker, J.-M. Lehn, R. Ziessel, *J. Chem. Soc. Chem. Commun.* **1984**, 328–330.
[31] A. Kochem, H. Kanso, B. Baptiste, H. Arora, C. Philouze, O. Jarjayes, H. Vezin, D. Luneau, M. Orio, F. Thomas, *Inorg. Chem.* **2012**, *51*, 10557–10571.

[32] T. Kurahashi, H. Fujii, *Inorg. Chem.* **2013**, *52*, 3908–3919.
[33] W.-H. Leung, E. Y. Y. Chan, E. K. F. Chow, I. D. Williams, S.-M. Peng, *J. Chem. Soc. Dalton Trans.* **1996**, 1229–1236.
[34] L. Chiang, L. E. N. Allan, J. Alcantara, M. C. P. Wang, T. Storr, M. P. Shaver, *Dalton Trans.* **2014**, *43*, 4295–4304.
[35] M. Lanznaster, A. Neves, A. J. Bortoluzzi, A. M. C. Assumpção, I. Vencato, S. P. Machado, S. M. Drechsel, *Inorg. Chem.* **2006**, *45*, 1005–1011.
[36] S. Skljarevski, A. A. Peverly, D. G. Peters, *J. Electroanal. Chem.* **2011**, *661*, 39–43.
[37] A. A. Isse, A. Gennaro, E. Vianello, *J. Chem. Soc. Dalton Trans.* **1993**, 2091.
[38] P. C. Gach, J. A. Karty, D. G. Peters, *J. Electroanal. Chem.* **2008**, *612*, 22–28.
[39] L. J. Klein, K. S. Alleman, D. G. Peters, J. A. Karty, J. P. Reilly, *J. Electroanal. Chem.* **2000**, *481*, 24–33.
[40] P. Du, M. S. Mubarak, J. A. Karty, D. G. Peters, *J. Electrochem. Soc.* **2007**, *154*, F231–F237.
[41] J. A. Miranda, C. J. Wade, R. D. Little, *J. Org. Chem.* **2005**, *70*, 8017–8026.
[42] B.-L. Chen, H.-W. Zhu, Y. Xiao, Q.-L. Sun, H. Wang, J.-X. Lu, *Electrochem. Commun.* **2014**, *42*, 55–59.
[43] V. V. Yanilkin, E. I. Strunskaya, N. V. Nastapova, N. I. Iaksimyuk, Z. A. Bredikhina, D. R. Sharafutdinova, A. A. Bredikhin, *Russ. Chem. Bull.* **2003**, *52*, 923–928.
[44] L. A. Tavadyan, H. G. H. Tonikyan, M. V. Musaelyan, A. E. Barsegyan, S. H. Minasyan, J. R. J. Sorenson, *Int. J. Chem. Kinet.* **2007**, *39*, 431–439.
[45] I. Sasaki, D. Pujol, A. Gaudemer, A. Chiaroni, C. Riche, *Polyhedron* **1987**, *6*, 2103–2110.
[46] P. Zanello, R. Cini, A. Cinquantini, P. L. Orioli, *J. Chem. Soc. Dalton Trans.* **1983**, 2159–2166.
[47] N. G. Connelly, W. E. Geiger, *Chem. Rev.* **1996**, *96*, 877–910.
[48] A. Kapturkiewicz, B. Behr, *Inorganica Chim. Acta* **1983**, *69*, 247–251.
[49] B. Ortiz, S. M. Park, *Bull. Korean Chem. Soc.* **2000**, *21*, 405–411.
[50] D. Tomczyk, L. Nowak, W. Bukowski, K. Bester, P. Urbaniak, G. Andrijewski, B. Olejniczak, *Electrochimica Acta* **2014**, *121*, 64–77.
[51] O. Fussa-Rydel, H. T. Zhang, J. T. Hupp, C. R. Leidner, *Inorg. Chem.* **1989**, *28*, 1533–1537.
[52] K. Jong Lee, I. Yoon, S, Sung Lee, B, Yong Lee, *Bull. Korean Chem. Soc.* **2002**, *23*, 399–403.
[53] D. F. Rohrbach, W. R. Heineman, E. Deutsch, *Inorg. Chem.* **1979**, *18*, 2536–2542.
[54] A. M. Tait, F. V. Lovecchio, D. H. Busch, *Inorg. Chem.* **1977**, *16*, 2206–2212.
[55] E. Pizzolato, M. Natali, B. Posocco, A. M. López, I. Bazzan, M. D. Valentin, P. Galloni, V. Conte, M. Bonchio, F. Scandola, et al., *Chem. Commun.* **2013**, *49*, 9941–9943.
[56] A. Chapovetsky, T. H. Do, R. Haiges, M. K. Takase, S. C. Marinescu, *J. Am. Chem. Soc.* **2016**, *138*, 5765–5768.
[57] K.-Y. Wong, W.-H. Chung, C.-P. Lau, *J. Electroanal. Chem.* **1998**, *453*, 161–170.
[58] C. Riplinger, M. D. Sampson, A. M. Ritzmann, C. P. Kubiak, E. A. Carter, *J. Am. Chem. Soc.* **2014**, *136*, 16285–16298.
[59] H. C. Hurrell, A. L. Mogstad, D. A. Usifer, K. T. Potts, H. D. Abruna, *Inorg. Chem.* **1989**, *28*, 1080–1084.
[60] C. Arana, S. Yan, M. Keshavarz-K., K. T. Potts, H. D. Abruna, *Inorg. Chem.* **1992**, *31*, 3680–3682.

[61] C. Arana, M. Keshavarz, K. T. Potts, H. D. Abruña, *Inorganica Chim. Acta* **1994**, *225*, 285–295.
[62] C. E. Dahm, D. G. Peters, *J. Electroanal. Chem.* **1996**, *402*, 91–96.
[63] M. H. Schmidt, G. M. Miskelly, N. S. Lewis, *J. Am. Chem. Soc.* **1990**, *112*, 3420–3426.
[36] IUPAC Solubility Data Series, 1981 and 1990, data available from https://srdata.nist.gov/solubility/IUPAC/iupac.aspx, Last accessed 03 Nov 2016
[65] U. J. Jáuregui-Haza, E. J. Pardillo-Fontdevila, A. M. Wilhelm, H. Delmas, *Lat. Am. Appl. Res.* **2004**, *34*, 71–74.
[66] J. Jacquemin, M. F. Costa Gomes, P. Husson, V. Majer, *J. Chem. Thermodyn.* **2006**, *38*, 490–502.
[67] I. Hod, M. D. Sampson, P. Deria, C. P. Kubiak, O. K. Farha, J. T. Hupp, *ACS Catal.* **2015**, *5*, 6302–6309.
[68] L. Chen, Z. Guo, X.-G. Wei, C. Gallenkamp, J. Bonin, E. Anxolabéhère-Mallart, K.-C. Lau, T.-C. Lau, M. Robert, *J. Am. Chem. Soc.* **2015**, *137*, 10918–10921.
[69] F. C. Cowlard, J. C. Lewis, *J. Mater. Sci.* **1967**, *2*, 507–512.
[70] M.-N. Collomb-Dunand-Sauthier, A. Deronzier, R. Ziessel, *Inorg. Chem.* **1994**, *33*, 2961–2967.
[71] S. Oh, J. R. Gallagher, J. T. Miller, Y. Surendranath, *J. Am. Chem. Soc.* **2016**, *138*, 1820–1823.
[72] A. Heinzel, C. Hebling, M. Müller, M. Zedda, C. Müller, *J. Power Sources* **2002**, *105*, 250–255.
[73] A. Tatin, C. Comminges, B. Kokoh, C. Costentin, M. Robert, J.-M. Savéant, *Proc. Natl. Acad. Sci.* **2016**, *113*, 5526–5529.
[74] E. E. Benson, M. D. Sampson, K. A. Grice, J. M. Smieja, J. D. Froehlich, D. Friebel, J. A. Keith, E. A. Carter, A. Nilsson, C. P. Kubiak, *Angew. Chem. Int. Ed.* **2013**, *52*, 4841–4844.
[75] R. Narayanan, M. McKinnon, B. R. Reed, K. T. Ngo, S. Groysman, J. Rochford, *Dalton Trans.* **2016**, *45*, 15285–15289.
[76] C. G. Zoski, *Handbook of Electrochemistry*, Elsevier, **2006**.
[77] E. Duñach, A. P. Esteves, M. J. Medeiros, D. Pletcher, S. Olivero, *J. Electroanal. Chem.* **2004**, *566*, 39–45.
[78] S. Jain, X. Zheng, C. W. Jones, M. Weck, R. J. Davis, *Inorg. Chem.* **2007**, *46*, 8887–8896.
[79] C.-M. Liao, C.-C. Hsu, F.-S. Wang, B. B. Wayland, C.-H. Peng, *Polym. Chem.* **2013**, *4*, 3098–3104.
[80] F.-S. Wang, T.-Y. Yang, C.-C. Hsu, Y.-J. Chen, M.-H. Li, Y.-J. Hsu, M.-C. Chuang, C.-H. Peng, *Macromol. Chem. Phys.* **2016**, *217*, 422–432.
[81] C. J. Hipp, W. A. Baker, *J. Am. Chem. Soc.* **1970**, *92*, 792–798.
[82] T. Kurahashi, M. Hada, H. Fujii, *J. Am. Chem. Soc.* **2009**, *131*, 12394–12405.
[83] S. Gao, Y. Lin, X. Jiao, Y. Sun, Q. Luo, W. Zhang, D. Li, J. Yang, Y. Xie, *Nature* **2016**, *529*, 68–71.
[84] S. Gao, X. Jiao, Z. Sun, W. Zhang, Y. Sun, C. Wang, Q. Hu, X. Zu, F. Yang, S. Yang, et al., *Angew. Chem.* **2016**, *128*, 708–712.
[85] E. Anxolabéhère-Mallart, C. Costentin, M. Fournier, S. Nowak, M. Robert, J.-M. Savéant, *J. Am. Chem. Soc.* **2012**, *134*, 6104–6107.
[86] S. E. Ghachtouli, R. Guillot, F. Brisset, A. Aukauloo, *ChemSusChem* **2013**, *6*, 2226–2230.
[87] H. Jin, J. Wang, D. Su, Z. Wei, Z. Pang, Y. Wang, *J. Am. Chem. Soc.* **2015**, *137*, 2688–2694.

[88] N. Kaeffer, A. Morozan, J. Fize, E. Martinez, L. Guetaz, V. Artero, *Acs Catal.* **2016**, *6*, 3727–3737.
[89] N. Morlanés, K. Takanabe, V. Rodionov, *ACS Catal.* **2016**, *6*, 3092–3095.
[90] D. Wang, J. T. Groves, *Proc. Natl. Acad. Sci.* **2013**, *110*, 15579–15584.
[91] S. C. Moon, *Rev. Polarogr.* **1971**, *17*, 93–100.
[92] T. K. Mukhopadhyay, N. L. MacLean, L. Gan, D. C. Ashley, T. L. Groy, M.-H. Baik, A. K. Jones, R. J. Troyitch, *Inorg. Chem.* **2015**, *54*, 4475–4482.
[93] M. R. Norris, S. E. Flowers, A. M. Mathews, B. M. Cossairt, *Organometallics* **2016**, *35*, 2778–2781.

Chapter 4. Electrocatalytic proton reduction with Cobalt(II) bis[3-(salicylidenamino)propyl]methylamine (*(1)*)

4.1. Introduction

In the previous chapter, four cobalt complexes were assessed for their ability as CO_2 reduction electrocatalysts. Under a CO_2 atmosphere with 5 % water, one of the four complexes, CopdSal, operated at -2.39 to -2.71 V with a large selectivity towards H_2 generation from the available protons. It was, therefore, of interest to assess whether or not CO_2 facilitates proton reduction in the presence of CopdSal and to identify the active catalyst towards proton reduction. These interests shaped the work undertaken within chapter four. For ease, CopdSal (Figure 4.1) is herein referred to as ***(1)***, not to be confused with the method of denoting complexes in the literature surveys of chapter one. Where a varied oxidation state of the metal is discussed, the ***(1)***-Co^{n+} convention is used.

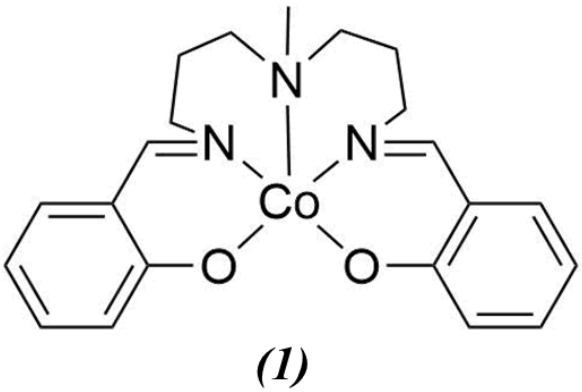

(1)

Figure 4.1: ***(1)***, formerly referred to as CopdSal, as assessed towards proton reduction in chapter four

To gain a deeper understanding into Co complexes as utilised towards electrocatalytic proton reduction in organic electrolytes, the reader is directed to chapter one. Within the experiments detailed in this chapter, it became apparent that ***(1)*** deposited as a heterogeneous material, and furthermore, evidence of deligation was observed. Therefore, Co and Co oxides are briefly discussed within this introduction. Regarding

water splitting, Co oxides have been primarily studied with respect to the oxygen evolution reaction (in addition to oxygen reduction). As this is beyond the scope of the introduction, the reader is directed to a recent review of the area by Osgood *et al*. [1] with further applications summarised by Vittal and Ho [2].

The use of cobalt oxides towards proton reduction has been studied in a lesser capacity than that of water oxidation. An earlier study involving Co metal as a working electrode was undertaken by Bicelli *et al*. in alkaline aqueous solution [3]. Through galvanostatic measurements, a spontaneously formed layer of Co oxide was believed to reduce prior to/during hydrogen evolution. To eliminate the perceived oxide, hydrogen overpotential measurements were preceded by an additional cathodic galvanostatic electrolysis. Jiang and Tseung anodically (galvanostatically) deposited porous Co from $CoCl_2$ with the concurrent bubbling of O_2 through the solution, allowing for greater porosity of the deposit [4]. A trend was observed, in that a higher loading % of Co led to a decrease in the potential required to reach 1 mA cm^{-2} current density towards H_2 evolution. Rojas *et al*. [5], employing a similar electrodeposition technique, found that the high flow rate of O_2 during preparation was beneficial in terms of surface activity towards the HER as compared to without O_2 and also with the bubbling of N_2. Cl^- anions were stated to be crucial to the porosity of the deposit, in that the solubility of the Co oxides/hydroxides was increased in the presence of chloride.

Recently, diimine-dioxime Co complexes have been enthusiastically pursued as molecular electrocatalysts with significant activity and modest overpotentials towards the HER [6]. However, numerous studies have emerged, questioning the nature of the true active catalyst with respect to some of the complexes (see section 1.3.3.2). A common assessment of whether a cobalt complex is homogeneously or heterogeneously electrocatalytically active is to transfer the working electrode used in "homogeneous" electrolysis conditions to an electrolyte that doesn't contain the dissolved catalyst and to continue electrolysis under the same conditions. Between electrolyses, often, a rinse of the electrode with water or electrolyte is undertaken, such as was employed by McCrory *et al*. [7].

Kaeffer *et al*. showed however, that the complex utilised by McCrory *et al*. led to reductive deposition of a heterogeneous species that was readily soluble in the phosphate buffered electrolyte, thus contributing to the incorrect assumption of

homogeneous activity towards H_2 generation [8]. XPS analysis of the nanoparticulate matter showed that Co (both Co^{2+} and metallic), P and O signals were evident, with the absence of N. The XPS measurements bore resemblance to those described by the group for tentatively described Janus particles (also prepared from two Co diimine-dioximes in addition to the primary method of using $Co(NO_3)_2$) [9]. The particles consisted of a metallic cobalt centre and a Co^{2+} oxo/hydroxo-phosphate layer. With these particles, anodic and potentiostatic equilibration of the particles at +1.16 V vs Ag/AgCl (with concomitant O_2 evolution) also resulted in the detection of a different ratio of Co:P.

4.2. Results and discussion

Prior to the presentation and discussion of results, the following terminology is provided.

- Solution hour 1 (soln hr 1) pertains to electrolysis in a solution consisting of 1 mM of ***(1)*** in the specified electrolyte.
- Solution hour 2 (soln hr 2) refers to electrolyses undertaken with a clean electrode with reuse of the solution following solution hour 1.
- All "surface" experiments were undertaken in DMF/0.1 M $TBAPF_6$ with the water content specified, and in the absence of ***(1)***.
    - Surface-1 hours 1 and 2 refer specifically to reusing the electrode generated following the end of the solution hour 1, for the first and second hour respectively. Surface-1 2 hours refers to two continuous hours of electrolysis, whereas Surface-1 hrs 1+2 refer to electrolyses analysed and repurged following hour 1 and restarted for a subsequent hour.
    - Surface-2 refers to reuse of the electrode following preparation during solution hour 2.
- Control/Blank is used to denote electrolysis with a previously unused electrode in the specified electrolyte, and in the absence of ***(1)***

The terms "solution" and "surface" are used as opposed to homogeneous and heterogeneous respectively, as the active catalyst in both cases may be heterogeneous in nature. Where mentioned, the glassy carbon electrodes were of 3 mm diameter (0.071

cm^2). Furthermore, the Toray carbon paper is stated as having an apparent surface area of 3.13 cm^2. This is calculated by assuming a flat surface area and negating the porosity and surface roughness of the material. As per chapters two and three, all potentials are reported with respect to the Fc/Fc^+ redox couple. In order to convert moles of H_2 produced into turnover numbers based on the concentration of the bulk solution, the moles of H_2 may be divided by 1.5×10^{-5}.

4.2.1. Electrochemical experiments at glassy carbon

4.2.1.1. Homogeneous electrolyses of *(1)* under Ar vs CO_2 at glassy carbon in the presence of water

To determine the effect of CO_2 on H_2 generation, a 1 mM solution of ***(1)*** in DMF/5% H_2O/0.1 M $TBAPF_6$ was electrolysed at -2.71 V with a glassy carbon working electrode under an argon atmosphere. The results obtained under Ar and under CO_2 appear in Table 4.1.

Table 4.1: Results obtained from one hour-long electrolyses in the presence and absence of ***(1)*** and in the presence and absence of CO_2. Electrolyses were carried out at -2.71 V in a DMF/5% H_2O/$TBAPF_6$ solution with a glassy carbon electrode

Experiment	Charge (C)	nmol H_2	FE H_2 (%)	nmol CO	FE CO (%)	nmol CH_4	FE CH_4 (%)
(1) CO_2, 1 Hour	0.361	1100	55	24	1.5	3.9	1
Control, CO_2	0.006	19	60	0	0	0	0
(1) Ar, 1 Hour	1.610	6580	79	0	0	0	0
Control, Ar	0.049	27	10	0	0	0	0

As is shown in Table 4.1, the complex under an Ar environment produces 6 times more H_2 than that observed under a CO_2 atmosphere. The behaviour of CO_2-promoted proton reduction had previously been noted with manganese- [10] and nickel-centred catalysts [11] and was attributed to the alteration of pH by dissolved CO_2. However, contrary to these reports, the production of H_2 from ***(1)*** was hindered with the potential acidification of the electrolyte, through dissolved CO_2.

The reason for the 6-fold increase in H_2 generation is not understood. The control experiments clearly demonstrate that background CO and CH_4 generation is absent and background H_2 generation is negligible. To account for the charge passed in background experiments (maximally 3% of the experiments with catalyst present), it is possible that solvent or electrolyte reduction may occur. For example, when $TBABF_4$ was electrolysed at glassy carbon with an applied potential of -2.2 V vs Cd amalgam, (approximately -3.41 V vs Fc/Fc^+) in DMF with trace water, Dahm and Peters observed the formation of butane [12].

The voltammograms obtained within Chapter 3 (see Figure 3.14) shows that that even without the presence of a known volume of water in the electrolyte, the complex undergoes reaction with CO_2 following the $Co^{2+/1+}$ reduction. The results in Table 4.1 show that when the electrolysis potential is more negative than that of the $Co^{2+/1+}$ reduction, an inhibition towards H_2 generation occurs in the presence of CO_2. Therefore, it is reasonable to assume that the binding of CO_2 to the complex may deactivate or decrease the activity of the complex towards proton reduction. This is contrary to the behaviour observed for the pre-catalyst CobdtChexSal (chapter three), whereby the presence of CO_2 appeared to promote H_2 generation.

4.2.1.2. Voltammetry of *(1)* under Ar and Ar with 5% water

To assess the direct interaction of ***(1)*** with water present, voltammetry of the complex was undertaken in Ar purged solutions, without and with 5% water added.

Initially, the first two reductive processes were acquired under Ar and are shown in Figure 4.2. Additionally, a previously acquired voltammogram incorporating the third reduction under Ar is shown (switching potential of -3.16 V). ***(1)*** undergoes three reductions (the first process stated in the literature to be $Co^{2+/1+}$ reduction [13,14]) with

the third reduction occurring in close proximity to the second (E_{pc} separation of 200 mV). In Figure 4.2, the returning oxidation that occurs at -1.75 V with a switching potential of -2.95 V is relatively weak, when compared to inclusion of the third reduction (switching potential of -3.16 V). This suggests that the scan to -2.95 V may include slight accession of the third, underlying reduction.

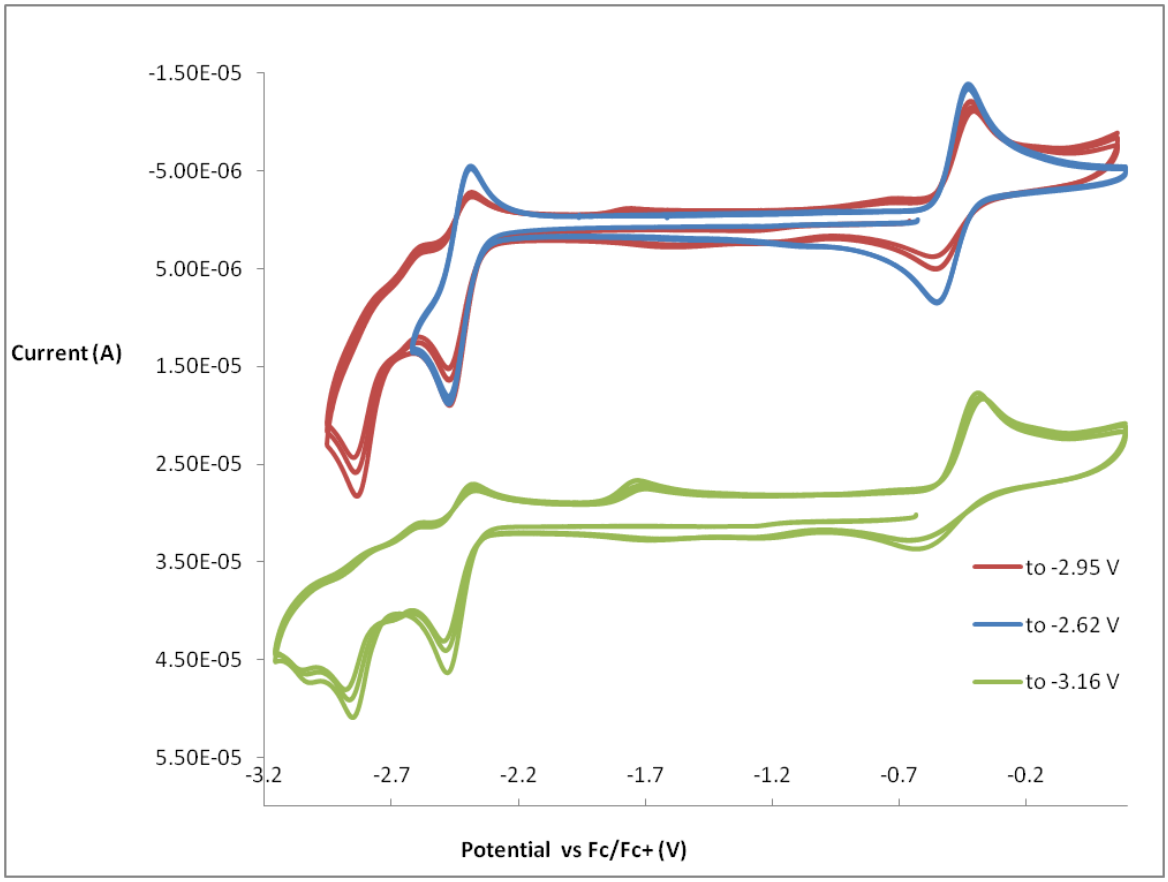

Figure 4.2: Cyclic voltammetry of 1 mM ***(1)*** in DMF with 0.1 M $TBAPF_6$ under Ar (ν = 100 mV s^{-1}), switching potential of -2.62, -2.95 V vs Fc/Fc^+ showing the first and second reduction, including the $Co^{2+/3+}$ oxidation. Also included is the third reduction (offset and switching potential of -3.16 V).

Subsequently, 5% water was introduced and the resulting voltammograms appear in Figure 4.3. Figure 4.3 shows that the presence of water imparts complete irreversibility of the first reduction. In contrast, in the absence of water, reversibility of the first reduction is only affected upon accessing the second reduction. In the presence of water, the reduction also shifts anodically by 50 mV and an enhancement in current is

observed. A second reduction also appears at approximately -2.65 V. There is no obvious match for a process of ***(1)*** in the absence of water and is likely a result of the first reductive species undergoing a chemical reaction.

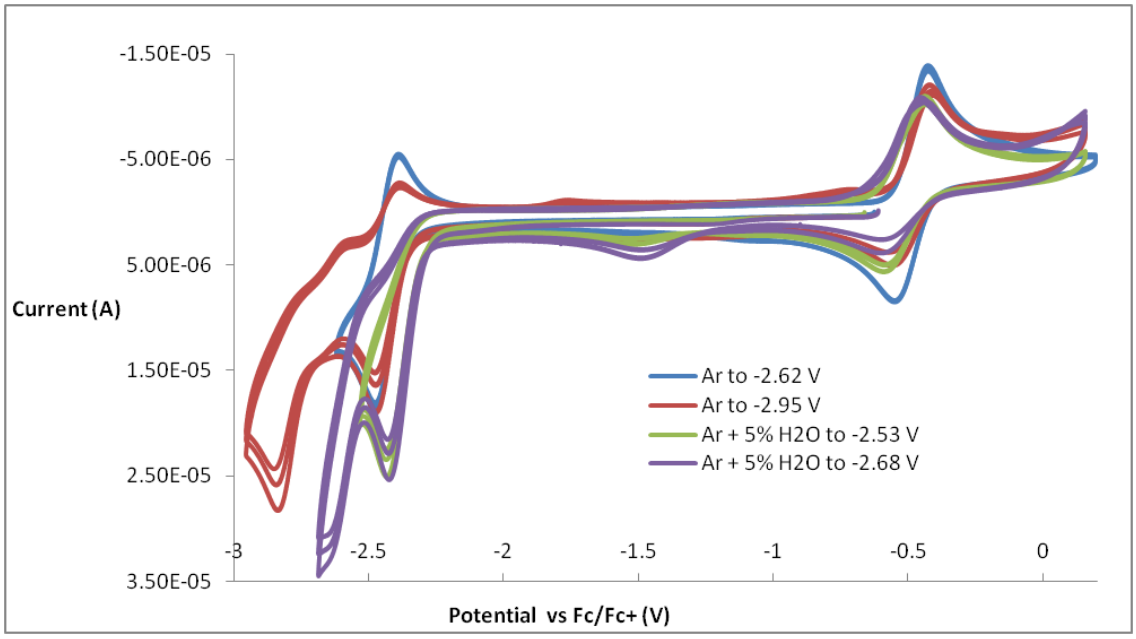

Figure 4.3: Cyclic voltammetry of 1 mM ***(1)*** displaying the first two reductions in DMF with 0.1 M $TBAPF_6$ under Ar and under Ar with 5% water (ν = 100 mV s^{-1}). The voltammograms contain the $Co^{2+/3+}$ oxidation

The irreversibility of the first reduction upon the addition of water is indicative of [***(1)***-Co^{1+}]$^{-}$ reacting with protons in solution. A scan rate study was undertaken, including both the $Co^{2+/3+}$ oxidation and the $Co^{2+/1+}$ reduction but omitting any further reductions. The results of the scan rate dependence of the first reduction with first oxidation present appear in Figures 4.3**i** and **ii** in addition to Appendix C.1**i** and **ii**. For reference, the voltammograms of ***(1)*** under Ar and in the absence of water appear in Appendix C.2.

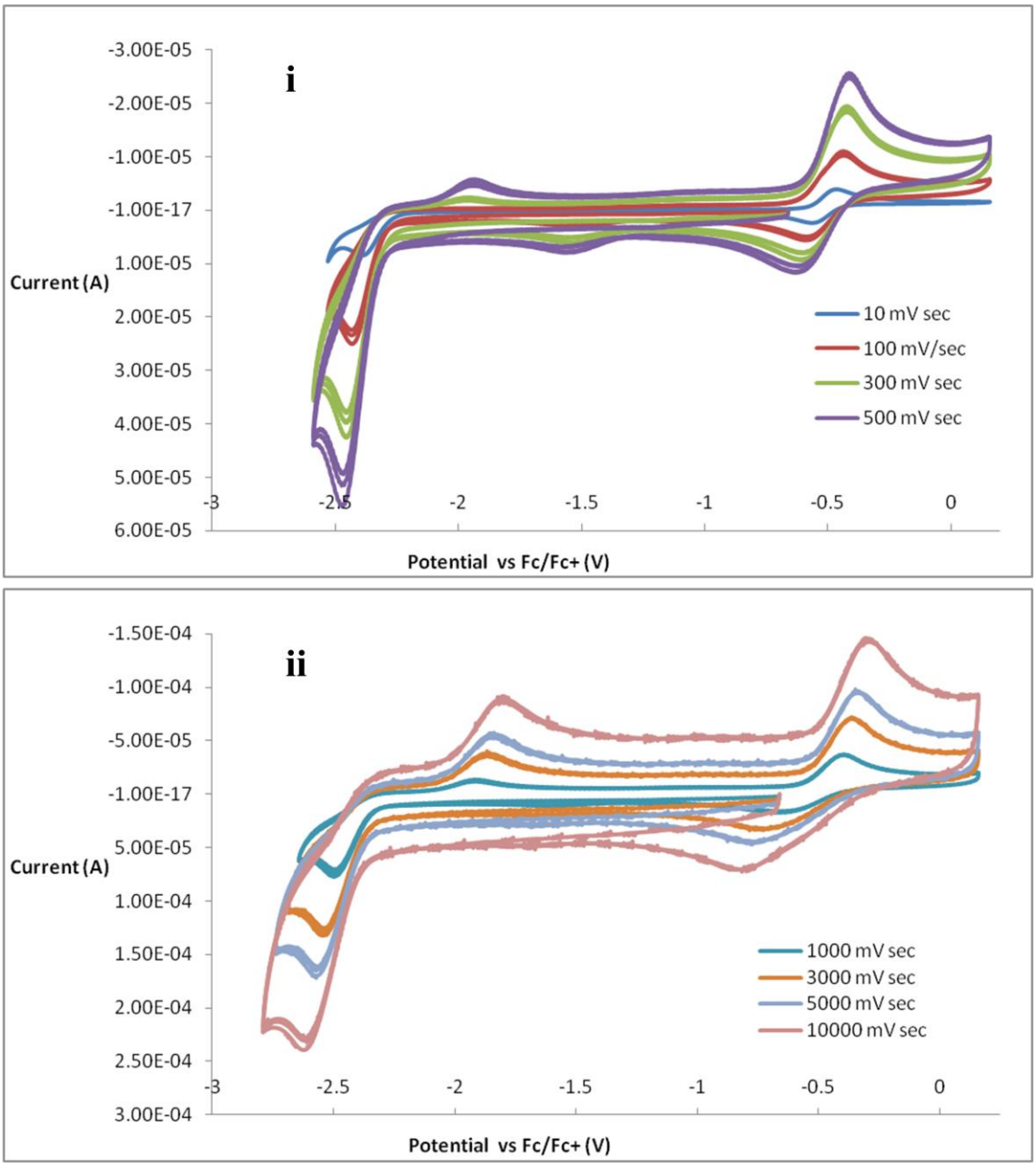

Figure 4.4: Cyclic voltammetric scan rate dependence of 1 mM ***(1)*** in DMF with 0.1 M $TBAPF_6$ and 5% H_2O under Ar, potential window encapsulating the first oxidation and first reduction only. Scan rate; **i.** 10, 100, 300 and 500 mV s^{-1} and **ii.** 1,000, 3,000, 5,000 and 10,000 mV s^{-1}. Voltammograms are separated in two plots for clarity.

It is evident from Figure 4.4 and Appendix C.1 that in the presence of water, no returning oxidation is observed at the first reduction up to a scan rate of 100 V s^{-1} when water is present. The $Co^{2+/3+}$ redox couple experiences a broadening of ΔE_p as the scan rate is increased. This behaviour may be an indicator of quasireversibility/irreversibility

[15,16]. With quasireversible redox couples, the increase in scan rate leads to an increase in separation between E_{pa} and E_{pc} [17]. At a scan rate of 10 mV s^{-1}, a 100 mV separation is observed and this separation is not improved by either the absence of water or isolation of the $Co^{2+/3+}$ couple only. At 100 mV s^{-1}, the ΔE_p increases from 125 mV to 155 mV in the presence of water. This could be indicative of the deposit of an electro-inactive layer (at the potential of the $Co^{2+/3+}$ process) on the electrode surface delaying electron transfer to the homogeneous complex [18].

Interestingly at 10 mV s^{-1}, the irreversibility of the $Co^{2+/1+}$ reduction doesn't appear to affect the reversibility of the $Co^{2+/3+}$ couple. At slower scan rates, though the reduced complex in the diffusion layer is allowed a greater time to react with water, the time allowed for diffusion of the irreversibly reduced species from the electrode to bulk solution is also greater. However, the independent behaviour of the $Co^{2+/3+}$ couple with respect to the $Co^{2+/1+}$ reduction also appears with higher scan rates. This may suggest that a catalytic cycle occurs, whereby the original Co^{2+} species is regenerated, or alternatively, the formation of another species oxidised at very similar potentials as the original $Co^{2+/3+}$.

Two additional features are observed at moderate scan rates (300, 500 and 1,000 mV s^{-1}). Figure 4.4**i** shows an oxidation at approximately -2 V and a reduction at approximately -1.6 V. When scans only probe the first reduction and exclude the $Co^{2+/3+}$ process (Appendix C.3**i**, **ii** and **iii**), the reduction at ~ -1.6 V no longer appears. This may imply that the $Co^{2+/3+}$ oxidation (with subsequent chemical reaction) accounts for the reduction at -1.6 V. However, similar experiments excluding the first reduction were not undertaken to assess whether or not the oxidised complex reacting with water was solely responsible for the reduction at -1.6 V.

A comparison of scan rate variation with current response of the $Co^{2+/3+}$ oxidation and $Co^{3+/2+}$ reduction (Appendix C.4) shows that the current for each process is linear with the square root of scan rate both in the absence and presence of water, obeying the Randles-Sevcik relationship of homogeneous redox behaviour [19]. In terms of comparative current response for the oxidation and reduction, water does not appear to significantly affect reversibility of the $Co^{2+/3+}$ redox couple. However, a broadening of peak-to-peak separation (ΔE_p) is noted for each scan rate with water when compared with water-free solutions.

The oxidation at approximately -2 V, appearing at scan rates greater than 100 mV s^{-1} in the presence of water, is linked to the $Co^{2+/1+}$ reduction. The separation between the $Co^{2+/1+}$ reduction and the oxidation is unrealistically large (ΔE_p of 510 mV at 300 mV s^{-1}) as compared to the $Co^{2+/1+}$ redox couple in the absence of water (ΔE_p of 105 mV at 300 mV s^{-1}) to assume that the oxidation at ~ -2 V could be the partial return oxidation of the reduced species occurring at ~ -2.5 V. This is further evidence that following reduction of the complex, the reduced species undergoes a chemical reaction (in addition to the lack of a reversible $Co^{1+/2+}$ oxidation), giving rise to the oxidative feature at ~ -2 V (Figure 4.4). The species at approximately -2 V potentially undergoes a further chemical reaction, or alternatively, diffuses from the electrode surface prior to its rereduction, which does not appear on the subsequent cathodic scans.

Following the reduction of $Co^{2+/1+}$ in the presence of water, another reduction occurs between the potentials at which the first and second reductions occur in the absence of water (Figure 4.3). At the first reduction, the complex could react with a proton to create a Co^{3+} hydride (Co^{3+}-H) [20]. Following this, the second reduction could be reduction of the Co^{3+}-H to Co^{2+}-H (another Co^{2+}-based H_2 evolving catalyst has recently been shown to demonstrate an additional reductive peak at a close but negative potential to the first reduction [21]). This could undergo a further reaction with a proton, returning the original catalyst and H_2 via an ECEC heterolytic mechanism [20]. A homolytic mechanism is unlikely (unless two or more mechanisms occur) as two electrochemical reductions are apparent, though enhancement of the first reduction is observed. If two Co^{3+}-H species were formed, both would form at one single potential and a second reduction potential with a new E_{pc} should not be observed. An EECC mechanism may possibly be ruled out as these processes are more positive to the processes that appear without water. Additionally, if an EECC heterolytic mechanism was occurring, the first reduction potential should not show an enhancement or shift to positive potentials, and would be expected to maintain reversibility in the presence of water. An ECCE Co^{3+}-H based heterolytic mechanism remains a possibility. When voltammetry is halted following the first reduction, a species (potentially that of Co^{3+}-H) is oxidised at approximately -2 V and scan rates of 300 mV or greater. With scan rates slower than this, the species that would have been oxidised may be further reacted with a proton to generate Co^{3+} and H_2, to be reduced electrochemically back to the Co^{2+} starting complex. It is also possible that more than one mechanism is occurring [22], including a

competing heterogeneous electrocatalytic pathway (though no peaks clearly associable with heterogeneous deposition were noted).

In the presence of water, accessing ***(1)***'s second reduction (Figure 4.3) enacts a lower level of reversibility of the reduction associated with the $Co^{3+/2+}$ oxidation. This may be an indicator of deposition onto the electrode, whereby the rate of transfer of electrons through the deposit is slower than that directly from the surface of the carbon electrode. Following the second reduction with water present, a large current enhancement takes place, as shown in the linear sweep voltammograms (LSVs) in the presence and absence of water. The LSVs appear in Figure 4.5.

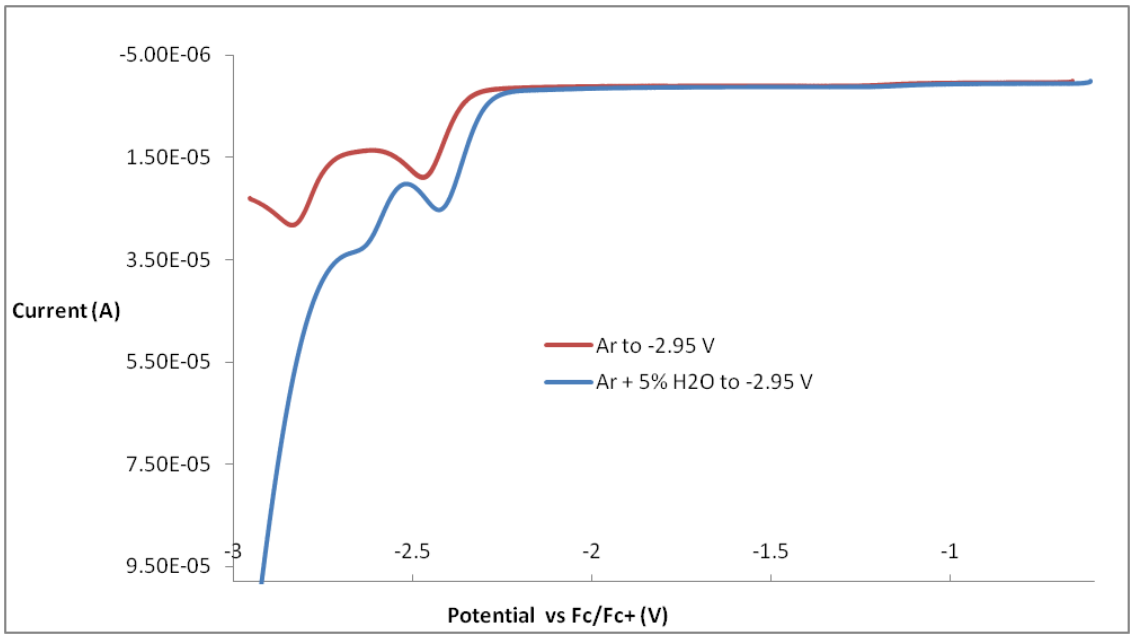

Figure 4.5: Linear sweep voltammograms of 1 mM ***(1)*** in DMF with 0.1 M $TBAPF_6$ under Ar and under Ar with 5% water (ν = 100 mV s^{-1}), scans to -2.95 V.

4.2.1.3. Reusability of the *(1)* solution beyond one hour of electrolysis at glassy carbon

To assess whether the solution was still as active for H_2 generation within the second hour, or if deactivation occurred over the course of electrocatalysis, further electrolyses were undertaken to monitor H_2 generation over the first hour and second hour of electrolysis. The results of the electrolyses (at the same potential of -2.71 V vs Fc/Fc^+ and at a glassy carbon electrode with 1 mM ***(1)*** in DMF/0.1 M $TBAPF_6$/5% water)

appear in Table 4.2. An important note is that the glassy carbon electrode was replaced prior to the second hour of electrolysis.

Table 4.2: Results of hour-long bulk electrolyses of 1 mM ***(1)*** at -2.71 V vs Fc/Fc^+ and 0.071 cm^2 glassy carbon electrode in DMF/0.1 M $TBAPF_6$/5% water under Ar. Solution hour 2 reused the solution but replaced the electrode and the cell was repurged.

Experiment	# of runs	Charge (C)	H_2 nmol	H_2 FE (%)
Solution hr 1	3	1.61	6580	79
Solution hr 2	3	0.252	86	14

An unexpected result obtained within Table 4.2 is that of a significantly lower charge consumed and H_2 detected (over 6 and 76 times lower respectively than that of the first hour) within the second hour of solution electrolysis. Consumption of 1.45 C is required in order to convert the 1 mM solution to a 1 e^- species. Though 1.61 C was consumed in the hour of electrolysis, 79% of this (1.27 C) was utilised to create H_2, thereby limiting the amount of charge available for compound conversion to 0.34 C (or approximately 23% of the charge required to quantitatively convert the solution to a 1 e^- reduced species). In this case, it is expected that approximately 77% of the precatalyst (greater if formation of the reduced species required > 1 e^-) would remain active. However, as previously stated, the H_2 detected following the second hour of electrolysis was 76 times lower or approximately only 1.3% as active.

Between the two hours of electrolyses, a freshly cleaned electrode was inserted into the cell. This excludes the possibility of passivation of the electrode due to electro-inactive material adhesion within the first hour. A possibility exists for the formation of a non-conducting material (during the first hour) that only significantly adheres to the surface of the electrode during the second hour of electrolysis. The results, however, suggest that the solution has been largely exhausted of electroactive material under such conditions of electrolysis.

4.2.1.4. Electrosynthesised product of *(1)* as a heterogeneous proton reduction electrocatalyst, heterogeneous vs homogeneous electrolysis

The results within Table 4.2 suggest either or a combination of the following; passivation of the electrode with an electroinactive material during hour 2, consumption of the homogeneous precatalyst over time, or consumption of the homogeneous catalyst to prepare a heterogeneously active catalyst. The current-time electrolysis plots for solution hours 1 and 2 are available in Figure 4.6.

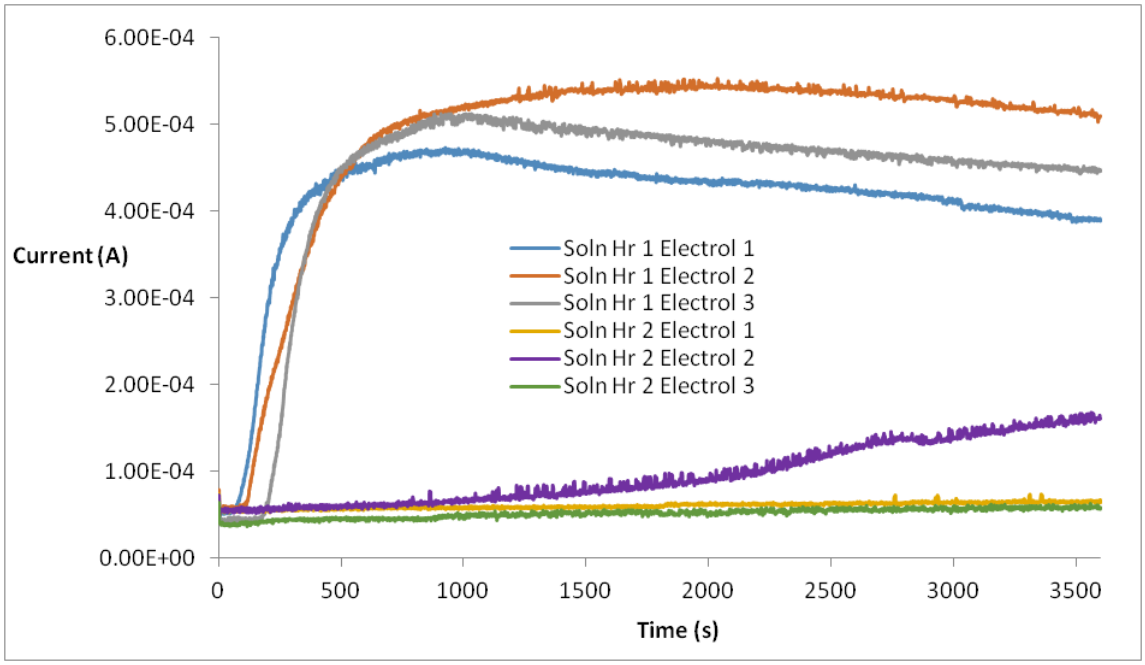

Figure 4.6: Bulk electrolysis current-time plots for 1 mM ***(1)*** electrolysed for one hour and second subsequent hour with electrode change between. Electrolysis was undertaken at -2.71 V vs Fc/Fc^+ with a glassy carbon electrode and with stirring in DMF/0.1 M $TBAPF_6$ with 5% water

There is an increase in current within each of the three solution hour 1 electrolyses (up to between ~ 800 - 1500 seconds), and following this, a gradual decrease in current. Some of the decrease in current could be explained by a decrease in availability of ***(1)*** near the electrode. If an active catalyst forms at the electrode surface, this would remain active towards H_2 generation and consumption of electrons would continue at a high rate despite consumption of ***(1)***. An additional observation within Figure 4.6 is that the "Solution" hour one experiments appear to demonstrate a lag in charge consumption of

60 - 150 seconds prior to a sharp rise in current. However, a lag period is also noted within subsequent heterogeneous experiments (as shown in Figure 4.7).

To explore the possibility of an active heterogeneous species forming, the electrodes utilised within the first hour of electrolysis (as per Table 4.1) were rinsed with DMF, allowed to air-dry, and examined in a heterogeneous capacity in DMF with 5% water and 0.1 M $TBAPF_6$, in the absence of complex. The results appear in Table 4.3. and the averaged surface-1 hours 1 and 2 with averaged solution hour 1 current-time plots are shown in Figure 4.7.

Table 4.3 shows that the "surface-1" electrodes within heterogeneous experiments also demonstrated high activity towards proton reduction. This heavily suggests that during the solution hour 1 electrolyses, a heterogeneous species is deposited, allowing the electrode to perform in a ***(1)***-free electrolyte solution containing water. An increase in the amount of H_2 and particularly FE_{H2} (6-8%) within the surface-1 experiments may be explained by the consumption of electrons to create the true catalyst within solution hour 1. Deposition of the active catalyst during solution hour 1 electrolyses would also account for a lower charge and activity shown within the solution experiments as compared to the surface-1 experiments. Assuming that the active catalyst is gradually deposited over the hour, only at the end of the solution hour 1 does the electrode contain the same amount of catalyst as surface-1 hour 1 from the start of the electrolyses.

Table 4.3: Results obtained from single hour-long electrolyses obtained in the presence and absence of 1 mM ***(1)***. Electrolyses undertaken at -2.71 V in a DMF/5% H_2O/0.1 M $TBAPF_6$ solution with a 0.071 cm^2 glassy carbon electrode. Surface experiments were undertaken in the absence of ***(1)***. The experimental descriptions of "Solution" and "Surface" are as described at the beginning of section 4.2.

Experiment	# of runs	Charge (C)	nmol H_2	FE H_2 (%)
Solution Hr 1	3	1.61	6580	79
Solution Hr 2	3	0.25	227	14.4
Surface-1 Hr 1	2	1.72	7740	87.2
Surface-1 Hr 2	1	1.88	8326	85.3
Control 1 Hr	3	0.05	26.5	10.2

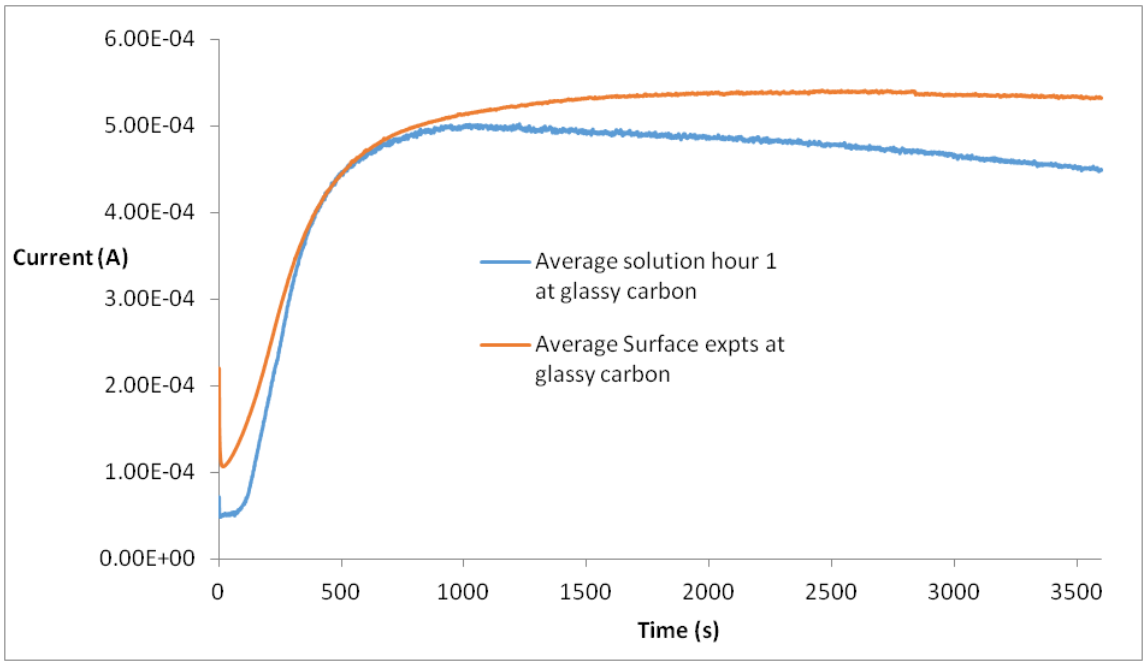

Figure 4.7: Averaged bulk electrolysis current-time plots for solution hour 1 (1 mM ***(1)***) and surface-1 hours 1 and 2. Electrolyses were undertaken at -2.71 V vs Fc/Fc^+ with a glassy carbon electrode and with stirring in DMF/0.1 M $TBAPF_6$ with 5% water

Solution hour 2 electrolyses demonstrated significantly poorer results in terms of the quantity of H_2 or FE_{H2} than did solution hour 1s. It was of interest to verify whether or not the electrodes prepared following solution hour 2 experiments were active in a heterogeneous capacity in fresh electrolyte. Table 4.4 displays the results obtained from electrolysis of DMF/0.1 M $TBAPF_6$/5% water using the same electrode prepared in "solution" hour 2 electrolyses.

Table 4.4: Results obtained during the second hour of electrolysis of 1 mM ***(1)***.and subsequent electrolysis of a DMF / 5% H_2O / 0.1 M $TBAPF_6$ solution with the same electrode (surface-2). Electrolyses were undertaken at -2.71 V with a glassy carbon electrode.

Experiment	# of runs	Charge (C)	H_2 nmol	H_2 FE (%)
Solution hr 2	3	0.25	227	14.4
Surface-2, 1 hour	1	0.073	289	76.4

Table 4.4 shows that surface-2 generates more H_2 than solution hour 2 in which the electrode is prepared, despite passing 3 times less charge. This may be at least partially explained with an additional charge required to electrodeposit the active catalytic material during the solution hour 2 experiments. With respect to surface-1 experiments, surface-2 electrodes were significantly less active, generating 27 times less H_2 (see Table 4.3).

4.2.1.5. Electrolysis of 1 mM *(1)* in the absence of water

With the aim of gaining information such as the identity or surface concentration of the active catalyst, voltammetry was undertaken in DMF/0.1 M $TBAPF_6$ without water following the "solution hour 1" and "surface" experiments. However, no processes were identified between -3.5 and 1.5 V vs Fc/Fc^+, thus quantitation of the catalyst on the surface via voltammetry was not possible. Voltammetric silence of a surface deposit active for proton reduction has been observed previously [23].

In a further measure to approximate the amount of catalyst on the electrode surface and/or to determine whether water was required to form the active catalyst, 1 mM ***(1)*** was electrolysed at -2.71 V vs Fc/Fc^+ in DMF with 0.1 M $TBAPF_6$ but in the absence of water. The electrodes were then used for electrolysis in DMF/0.1 M $TBAPF_6$/5% water at the potential of -2.71 V in the absence of ***(1)***. The results appear in Table 4.5.

Table 4.5: Results obtained from single hour-long "solution" electrolyses with 1 mM ***(1)*** in the absence of water, and subsequent "surface" experiments in the presence of 5% water. Electrolyses undertaken at -2.71 V in a DMF/0.1 M $TBAPF_6$ solution with a 0.071 cm^2 glassy carbon electrode.

Experiment	# of runs	Charge (C)	H_2 nmol	H_2 FE (%)
Solution hr 1, no water	2	0.099	0	0
Surface 1 hr following, 5% water	2	0.025	57.09	36.5

As is shown in Table 4.5, and with comparison to solution hour 1 and surface-1 hour 1 values (whereby the preparation electrolyte additionally included water) (Table 4.3), no

hydrogen gas was detected in experiments where water was not present. This result is expected, and shows that the DMF contains minimal water. However, when this electrode was subsequently utilised for electrolysis of a DMF/0.1 M $TBAPF_6$/5% water solution, over 100 times less H_2 was detected than in surface experiments where preparation of the "surface" electrode involved 5% water and yielded results similar to control experiments. This result affirms that water is required in the preparative stage of the true catalyst. Due to the lack of formation of an active catalyst, the charge passed in solution hour 1 in the absence of water could not be associated with the amount of active catalyst on the surface.

An additional experiment performed involved undertaking the "solution" hour 1 with water, and a subsequent "surface" electrolysis without water. The results, appearing in Appendix C.5 confirm that the hydrogen contributing towards H_2 is derived from the added water.

4.2.2. Electrolyses at 3.13 cm^2 (apparent surface area) Toray carbon paper

Despite not observing surface-confined voltammetry at glassy carbon electrodes, the surface electrolysis experiments imply the deposition of an electrocatalyst on the surface of the electrodes. With the aim of characterising this film in terms of appearance and molecular composition and also allowing for greater activity, electrocatalysis was undertaken using Toray carbon paper (5% PTFE) electrodes with the optimised dimensions as per chapter three of 1.5 x 1 x 0.037 cm, or apparent surface area of 3.13 cm^2.

4.2.2.1. Electrolysis results obtained following "Solution" hour 1 and hour 2, and "Surface-1" hours 1 and 2 at Toray carbon paper

A 1 mM solution of ***(1)*** was electrolysed at -2.71 V in DMF with 0.1 M $TBAPF_6$ and 5% H_2O as per the experiments at conventional glassy carbon electrodes. However, the experiments contained in this section were undertaken utilising 3.13 cm^2 apparent surface area cuts of Toray carbon paper (5% PTFE). The benefit of this material is two-fold in terms of experimental use. The material may be viewed and imaged under the

field emission scanning electron microscope (FESEM, herein referred to as SEM) and also with a greater surface area, larger amounts of H_2 may be evolved for the same electrolysis time as compared to the glassy carbon electrode. Table 4.6 shows the electrolysis values obtained with the carbon paper electrodes. The averaged surface hour one and surface hour two electrolysis current-time plots associated with the data in Table 4.6 are shown in Appendix C.6.

Table 4.6: 1 mM solutions of ***(1)*** or deposit as a result of the first hour of electrolysis in complex electrolysed at carbon paper. Electrolysis at -2.71 V in DMF, 0.1 M $TBAPF_6$ with 5% H_2O

Experiment	# of runs	Charge (C)	H_2 μmol	H_2 FE (%)
Solution hour 1	8	12.26	43.9	69
Solution hour 2	5	13.63	52.1	74
Surface hour 1	4	11.35	46.9	80
Surface Hour 2	4	13.3	57	83
Control hour 1	4	2.98	1	7
Control hour 2	3	2.46	5	39

Conditions: Solution hour 1 is the first hour of electrolysis containing 1 mM ***(1)***. Solution hour 2 reuses the solution following solution hour 1 but with a new electrode. Surface-1 hours 1 and 2 are the electrodes reused following solution hour 1 experiments only. Control is a new electrode in solution containing no ***(1)***. Control hour 2 reuses the same electrode utilised in control hour 1.

As is shown in Table 4.6 (as compared to Table 4.3) there is an approximate 7-8 fold increase in the charge consumed by the carbon paper with respect to glassy carbon, leading to a greater amount of H_2 evolved. A quite unusual observation is that the solution was reusable for a second successful electrocatalytic experiment. This contrasts the lower activity observed within solution hour 2 experiments with the glassy carbon electrodes. An inability to reuse solutions for a second electrolysis at glassy carbon electrode was assumed to be due to catalyst consumption. However, ~8 times the charge was passed within the experiment involving the carbon paper to that of the glassy

carbon electrode. If consumption of the precatalyst accounted for the inability to reuse the solution following solution hour 1 at glassy carbon, solution hour 2 with carbon paper should have demonstrated a more significant fall in activity as compared with solution hour 2 at glassy carbon (96% decrease, Table 4.3). In contrast, solution hour 2 of carbon paper generated 19% more H_2 than in the first hour. Additionally, surface-1 hours 1 and 2 produced H_2 with similarly high levels of activity as compared to the solution experiments.

4.2.2.2. Surface-2 electrolysis results at Toray carbon paper

In order to assess whether or not the solution hour 2-generated electrodes would be active towards H_2 generation in the absence of the precatalyst, the potential of -2.71 V vs Fc/Fc^+ was applied to the electrodes in DMF/0.1 M $TBAPF_6$/5% water. The results of the surface-2 electrolyses appear in Table 4.7. The results of solution hour 2 (in which the electrode was formed) and surface-1 hour 1 are reiterated in the interest of comparison. The electrodes generated from solution hours 1 and 2 (surface-1 and surface-2 respectively) both perform with very similar activity in a DMF/5% water solution.

Table 4.7: Surface-1, surface-2 and solution hour 2 electrolyses results at carbon paper. Electrolysis at -2.71 V in DMF, 0.1 M $TBAPF_6$ with 5% H_2O

Experiment	# of runs	Charge (C)	H_2 μmol	H_2 FE (%)
Surface-1 hour 1	4	11.35	46.9	80
Solution hour 2	5	13.63	52.1	74
Surface-2 1 hour	3	11.52	44.8	75

4.2.2.3. Time dependence of H_2 evolution for solution hour 1, surface-1 and control experiments

A brief lag phase of ~ 1 – 2.5 minutes was observed in the current-time plot within solution hour 1 experiments at glassy carbon electrodes (see Figure 4.6). A similar increase in current was also observed for surface experiments (Figure 4.7). The electrolysis current-time plots of solution hour one and surface-1 hours one and two at carbon paper are displayed in Figure 4.8. The same increase in current consumed is not apparent within each at carbon paper, as compared to at glassy carbon. However, the solution hour 1 and surface-1 experiments show similar variations in behaviour with respect to the appearance of an initial current growth.

It was of interest to clarify whether a lag in hydrogen generation was apparent, through monitoring the amounts of H_2 produced over the course of the hour. In this respect, solution hour one (formation of the active catalyst), surface hour one and control one hour were assessed over the course of 5, 10, 20, 40 and 60 minutes of electrolysis at -2.71 V.

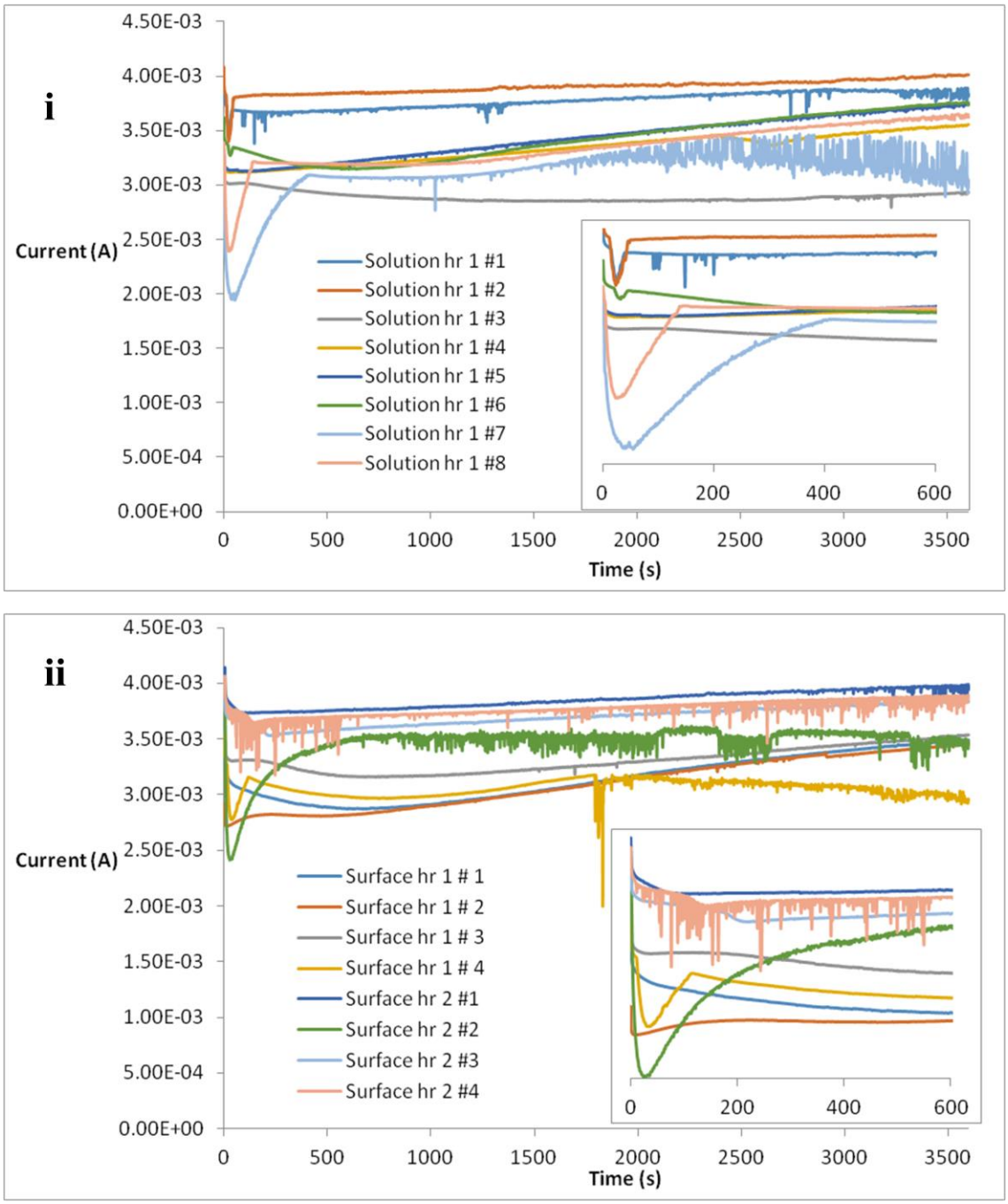

Figure 4.8: Bulk electrolysis current-time plots for **i.** solution hour one (containing 1 mM ***(1)***) and **ii.** surface-1 hours one and two at -2.71 V vs Fc/Fc^{+} with carbon paper in DMF/0.1 M $TBAPF_6$ with 5% water

The results of the time dependent H_2-monitored experiments appear in Table 4.8 with plots of moles H_2 against time, FE_{H2} against time, charge against time and moles H_2 against charge appearing within Figure 4.9 **i**, **ii**, **iii** and **iv** respectively.

Table 4.8: Time-monitored H_2 generation within solution hour 1, surface hour 1 and control electrolysis at -2.71 V vs Fc/Fc^+ and 3.13 cm^2 apparent area Toray carbon paper in DMF/0.1 M $TBAPF_6$/5% water

	Time (mins)	Charge (C)	μmol H_2	FE H_2 (%)
Solution hour one (n=3)	5	0.88	1.2	27.2
	10	1.75	3.6	40.2
	20	3.49	8.8	48.5
	40	7.05	18.7	51.2
	60	10.64	29.8	54.1
Surface hour one (n=3)	5	0.93	2.2	47
	10	1.85	6.1	63.3
	20	3.79	14.1	72.1
	40	7.29	27.9	74.8
	60	11.69	39.3	65.1
Control one hour (n=1)	5	0.54	0.03	1
	10	0.99	0.04	0.9
	20	2.15	0.09	0.8
	40	4.43	0.2	0.9
	60	6.46	0.4	1.1

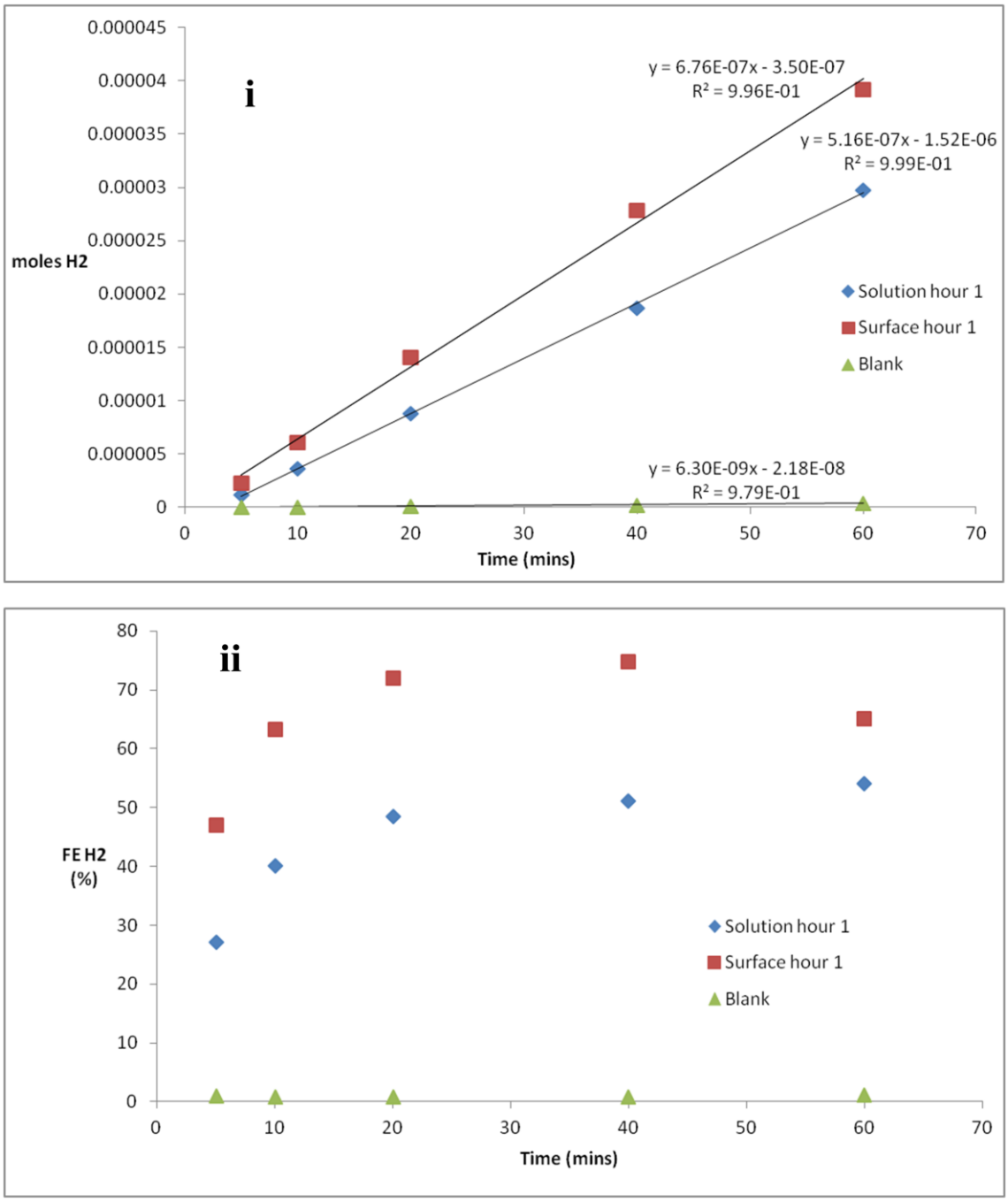

Figure 4.9: **i.** moles H_2 generated and **ii.** FE_{H2} with associated time points of 5, 10, 20, 40 and 60 minutes for solution hour 1, surface hour 1 and control 1 hour at -2.71 V vs Fc/Fc^+ and a carbon paper electrode in DMF/0.1 M $TBAPF_6$/5% water (data as per Table 4.8, average of n = 3, control n = 1)

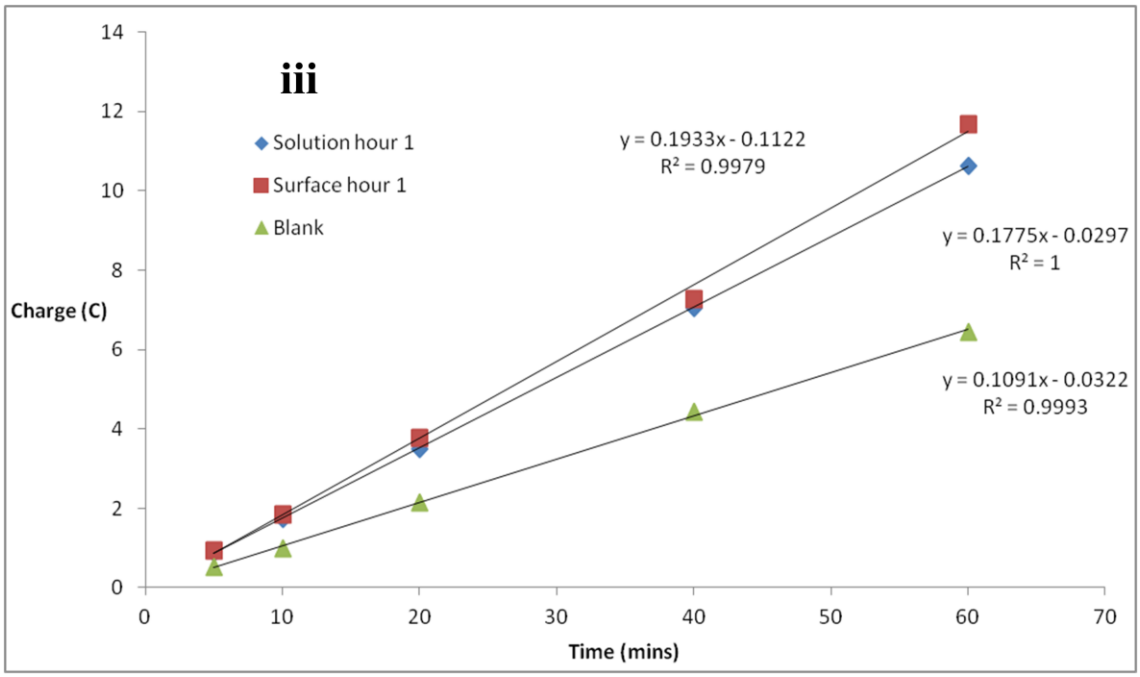

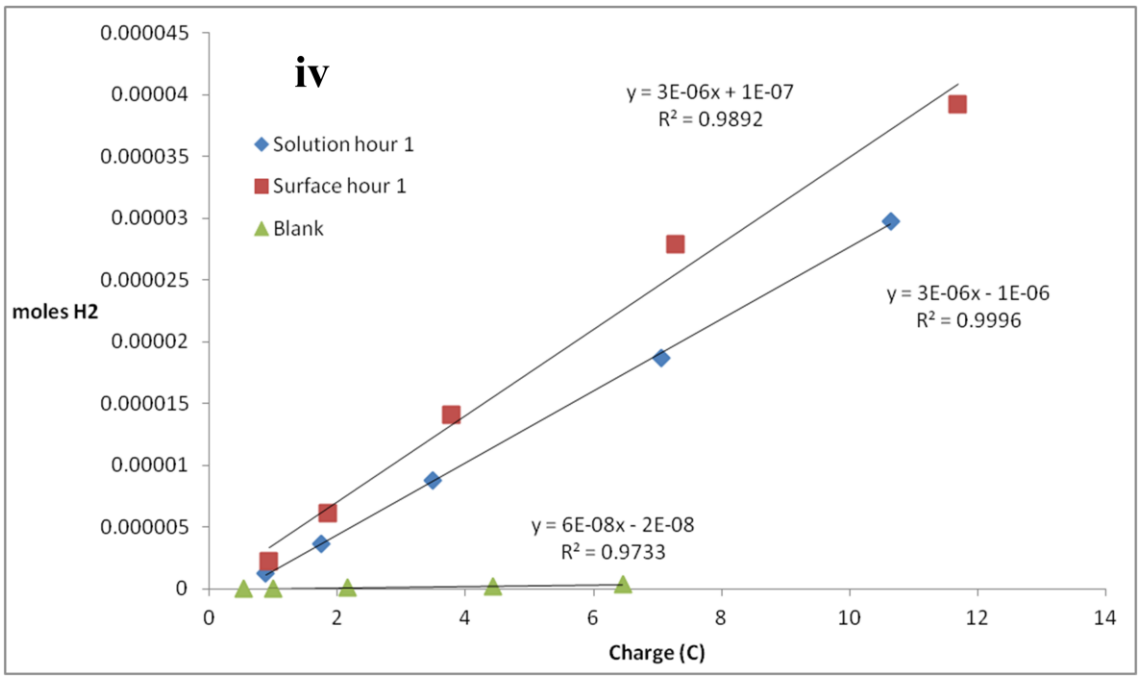

Figure 4.9 continued: **iii.** The charge passed plotted versus time points of 5, 10, 20, 40 and 60 minutes of time dependence H_2 monitoring experiment, **iv.** moles H_2 generated versus charge passed within experiment for 5, 10, 20, 40 and 60 minute time points. Curves include solution hour 1, surface hour 1 and control 1 hour. Electrolysis at -2.71 V vs Fc/Fc^+ and a carbon paper electrode in DMF/0.1 M $TBAPF_6$/5% water (data as per Table 4.8, average of n = 3, control n = 1)

As can be seen within the results (Table 4.8) and in Figure 4.9**iii**, charges within the three sets of experiments are linear with time. The moles of H_2 generated over time (Figure 4.9**i**) is shown to be linear for surface-1 hour 1 ($r^2 = 0.996$) and particularly for solution hour 1 ($r^2 = 0.999$), with the control being less linear ($r^2 = 0.979$). Surface-1 hour 1 however, shows a greater rate of generation as compared to solution hour 1.

When comparing the relationship of FE_{H2} with time (Figure 4.9**ii**), it is evident that both solution hour 1 and surface-1 hour 1 have low efficiencies initially and rise for the first 20 minutes approximately. A contribution of charging current to the charge and therefore FE is particularly evident at the beginning of the experiment, and becomes less significant at later time points as more Faradaic current is passed. However, despite poor efficiencies, the surface experiments provide better FE_{H2} throughout the hour than do the solution experiments. It is noted that the 60 minute point of the surface plot decreases in FE_{H2} as compared to the 40 minute timepoint. This is not expected. However, GC syringe withdrawals from the cell have a possibility of introducing oxygen into the cell. Oxygen is known to be reduced at potentials significantly more positive of -2.71 V vs Fc/Fc^+ at glassy carbon in DMF [24] and will compete with proton reduction if present. It can be seen that with a comparison of the values at 60 minutes within Table 4.8 with associable experiments in Table 4.6, experiments without multiple injections produce superior results in terms of moles and FE for H_2. Initially lower FEs have also been reasoned as a delay of production of H_2 bubbles on the surface of the material and also a delay of transfer of bubbles to the headspace [25].

Figure 4.9**iv** shows a plot of moles H_2 generated against charge. The slope of solution hour 1 is more linear ($r^2 = 0.9996$) than that of surface-1 hour 1 ($r^2 = 0.9892$). In this case, the intercept associated with the solution hour 1 is negative, indicating a delay in H_2 generation that is not experienced with surface-1 hour 1 (potentially a greater time is required to generate the active catalyst). Figure 4.9**iv** also accentuates how little H_2 is formed at the bare electrode.

Two further sets of experiments were undertaken. The results of electrodes soaked in 1 mM ***(1)*** prior to electrolysis in $DMF/TBAPF_6/5\%$ H_2O appear in Appendix C.7 and show that the electrocatalyst responsible for H_2 generation in surface experiments is not as a result of physisorption to the electrode. Uninterrupted 2 hour surface-1 electrolyses

were also undertaken (Appendix C.8). However, this method did not provide a benefit over the cumulative H_2 amount of Surface-1 hours 1 and 2.

4.2.3: SEM and EDX analysis of carbon paper following "solution" and "surface" experiments undertaken in section 4.2.2

Results obtained within sections 4.2.1 and 4.2.2 heavily imply that a heterogeneous deposit is formed on the surface of both glassy carbon and carbon paper. In an effort to characterise this film visually, field-emission scanning electron microscopy (FESEM, referred to as SEM herein) with secondary electron detection was undertaken (in addition to energy dispersive X-ray spectroscopy, EDX) within DCU and with the help of Mr Colm Montgomery.

4.2.3.1: SEM images of "Solution" hour 1 and control Toray carbon paper electrodes

The SEM images resulting from two electrodes analysed following the first hour of solution electrolysis (referred to as Soln hr 1 #1 and Soln hr 1 #2) appear in Figure 4.10 and Appendix C.9.

A fine surface deposit can be observed in both Figure 4.10 and Appendix C.9. to gain an understanding of the chemical composition of the deposit, EDX was undertaken on the "Soln hr 1 #1" electrode and the results appear in Appendix C.10. The deposit on the surface, however, did not show signals at greater energy than 1 kV, i.e. the Kα or Kβ lines associated with Co did not feature. As the accelerating voltage was 15kV, i.e. over double the X-Ray energy of Co Kα (6.931 kV [26]) [27], it is more likely in this case that the line at approximately 0.7 keV is that of the Kα of fluorine than the Lα of Co. The Kα spectral line associated with oxygen features in all EDX spectra herein. XPS measurements of bare Toray carbon paper within the literature have shown the presence of 2.4-2.9% [28] and 5.65% oxygen [29].

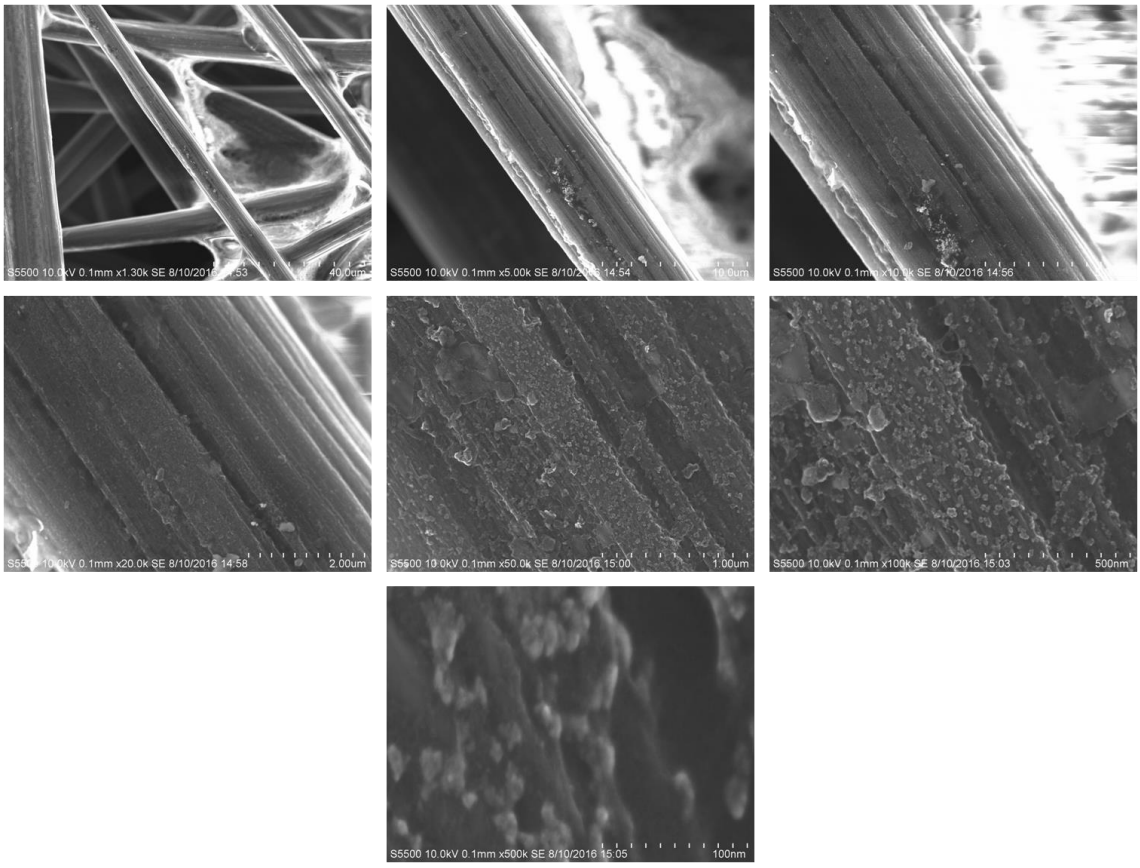

Figure 4.10: SEM images of "Soln hr 1 #1", the carbon paper used as working electrode in the first hour electrolysis of 1 mM ***(1)*** in DMF/5% H_2O/0.1 M $TBAPF_6$ at -2.71 V vs Fc/Fc^+, 10 kV accelerating voltage, 19.6 – 20 μA probe current. Magnification left to right, top to bottom: 1300, 5000, 10000, 20000, 50000 and 100000 and 500000x.

For comparison, electrodes that were used to electrolyse a control solution of DMF with 0.1 M $TBAPF_6$ and 5% H_2O for two interrupted hours (Control hr 1+2) and two continuous hours (Control 2 hrs) were analysed by SEM. The SEM micrographs for Control hr 1+2 appear in Figure 4.11 and Control 2 hrs appear in Figure 4.12.

The SEM images undertaken on Control 2 hrs (Figure 4.12) were undertaken with accelerating voltage of 10 kV, akin to the conditions of Soln hr 1 #1 and #2, and show no visible surface deposition. With a decrease of accelerating voltage to 1 kV, Control hr 1+2 (Figure 4.11) shows a fine granular and dispersed surface deposit, of approximately 100 nm width. A decrease of the accelerating voltage allows for a more defined view of the surface of the electrode, due to a decrease in depth of penetration of

the beam [30]. EDX of the sample undertaken at 15 kV accelerating voltage did not show the presence of any metals.

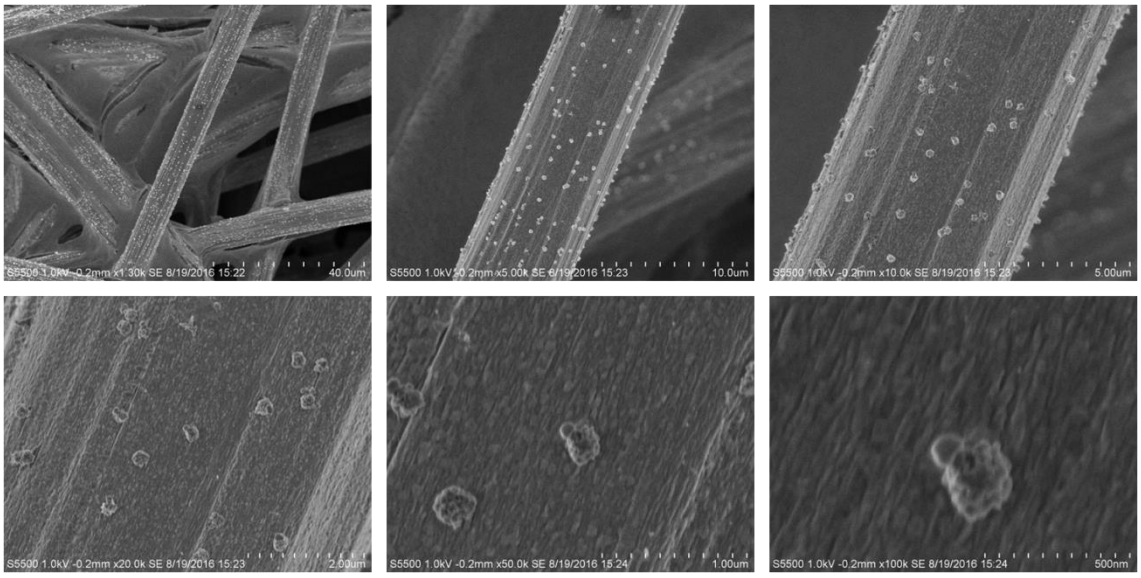

Figure 4.11: SEM images of "Control hrs 1 and 2", the carbon paper used as working electrode in the first hour electrolysis of DMF/5% H_2O/0.1 M $TBAPF_6$ at -2.71 V vs Fc/Fc^+, 1 kV accelerating voltage, 21.6 μA probe current. Magnification left to right, top to bottom: 1300, 5000, 10000, 20000, 50000 and 100000x.

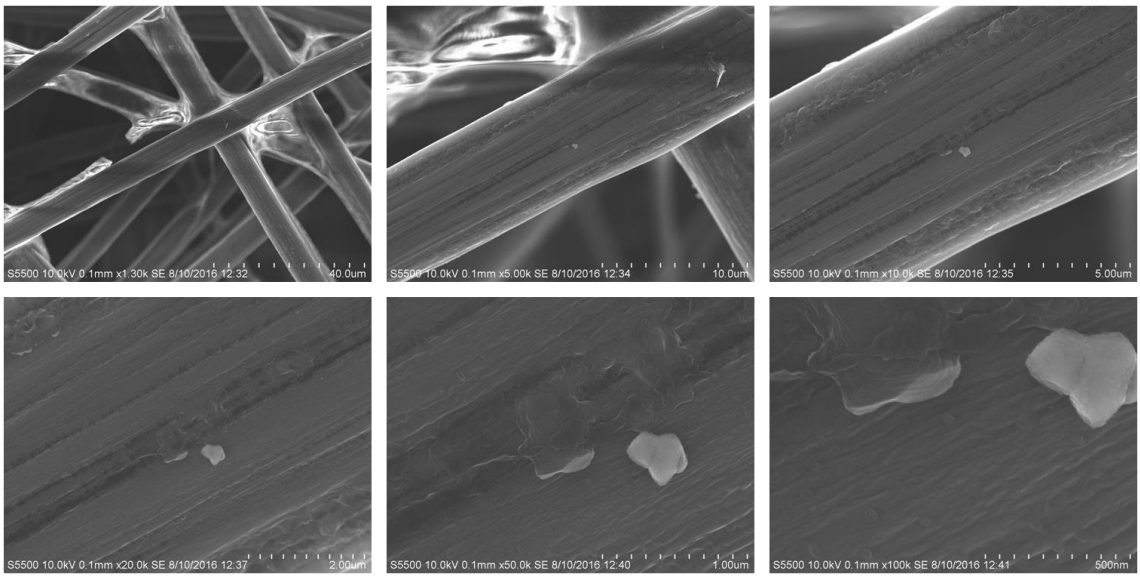

Figure 4.12: SEM images of "Control 2 hrs", the carbon paper used as working electrode for two hours of electrolysis of DMF/5% H_2O/0.1 M $TBAPF_6$ at -2.71 V vs Fc/Fc^+, 10 kV accelerating voltage, 21.6 μA probe current. Magnification left to right, top to bottom: 1300, 5000, 10000, 20000, 50000 and 100000x.

4.2.3.2: SEM images and EDX spectra of "Solution" hour 2 Toray carbon paper electrodes

As stated previously, contrary to behaviour observed at glassy carbon, hour two of electrolysis at carbon paper in the 1 mM ***(1)***, 5% H_2O, 0.1 M $TBAPF_6$ in DMF solution continued to produce H_2 at a similar rate to that of the first hour. This electrode was also active towards subsequent surface experiments. SEM micrographs of two of the electrodes involved in the second hour of solution electrolysis (Soln hr 2 #1 and Soln hr 2 #2) were acquired. Soln hr 2 #1 was undertaken with 10 kV and 1 kV accelerating voltage and appears in Figure 4.13 and Figure 4.14 respectively.

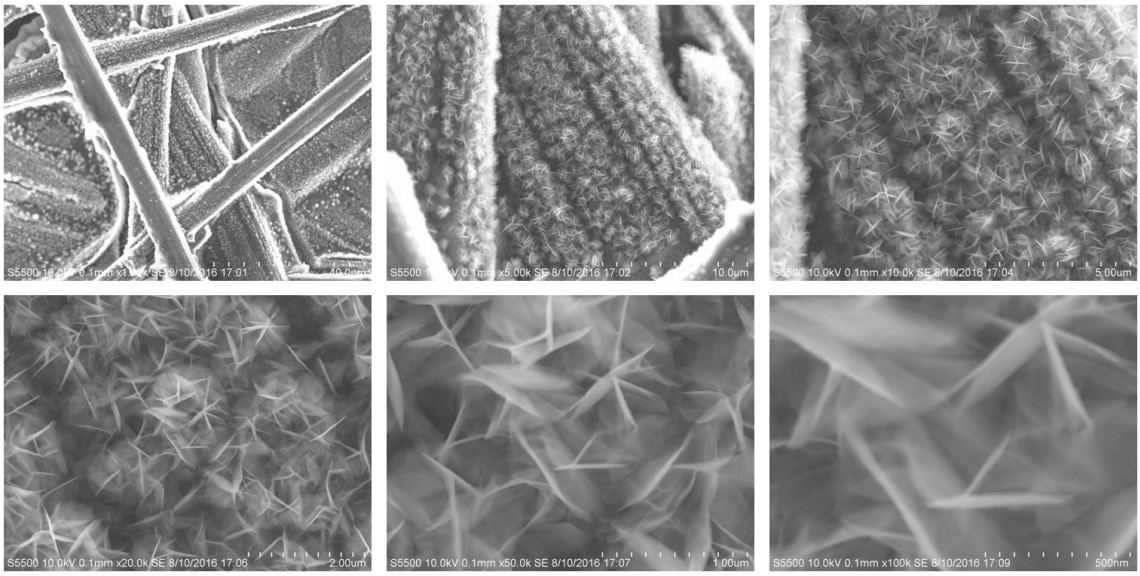

Figure 4.13: SEM images of "Soln hr 2 #1", the carbon paper used as working electrode in the second hour electrolysis of 1 mM ***(1)*** in DMF/5% H_2O/0.1 M $TBAPF_6$ at -2.71 V vs Fc/Fc^+, 10 kV accelerating voltage, 20.4 – 20.8 μA probe current. Magnification left to right, top to bottom: 1300, 5000, 10000, 20000, 50000 and 100000x

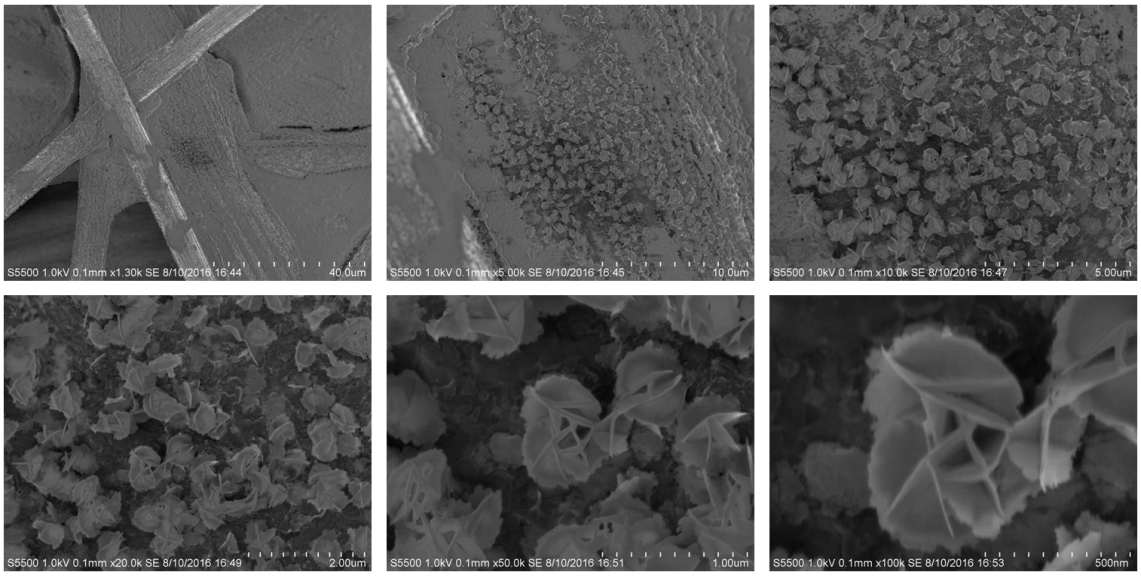

Figure 4.14: SEM images of "Soln hr 2 #1", the carbon paper used as working electrode in the second hour electrolysis of 1 mM ***(1)*** in DMF/5% H_2O/0.1 M $TBAPF_6$ at -2.71 V vs Fc/Fc^+, 1 kV accelerating voltage, 19.6 μA probe current. Magnification left to right, top to bottom: 1300, 5000, 10000, 20000, 50000 and 100000x.

From examination of Figure 4.13 and Figure 4.14, it can be seen immediately that a comprehensive deposit grows on the surface of the electrode over the second hour. The difference between both sets of micrographs also accentuates the effect of varied accelerating voltage to geometrically rich but thin structures (of sub-micron diameter). As stated previously, a decrease in accelerating voltage allows for near surface imaging and increased surface sensitivity [31]. At the lower accelerating voltage of 1 kV (Figure 4.14), the intersecting, plate-like structures become more defined. EDX analysis was undertaken on the electrode appearing in Figure 4.13 and Figure 4.14 and the resulting spectrum appears in Figure 4.15.

Within Figure 4.15, Kα, Kβ and Lα signals representative of Co are apparent in addition to F, C and O Kα signals. The C and F signals may be attributed to the carbon paper (5% PTFE). The oxygen may result from the surface deposit in addition to the contribution from carbon paper itself.

Figure 4.16 and Figure 4.17 display SEM micrographs of a second electrode (Soln hr 2 #2) under the same electrolysis and imaging conditions as that of Figure 4.14.

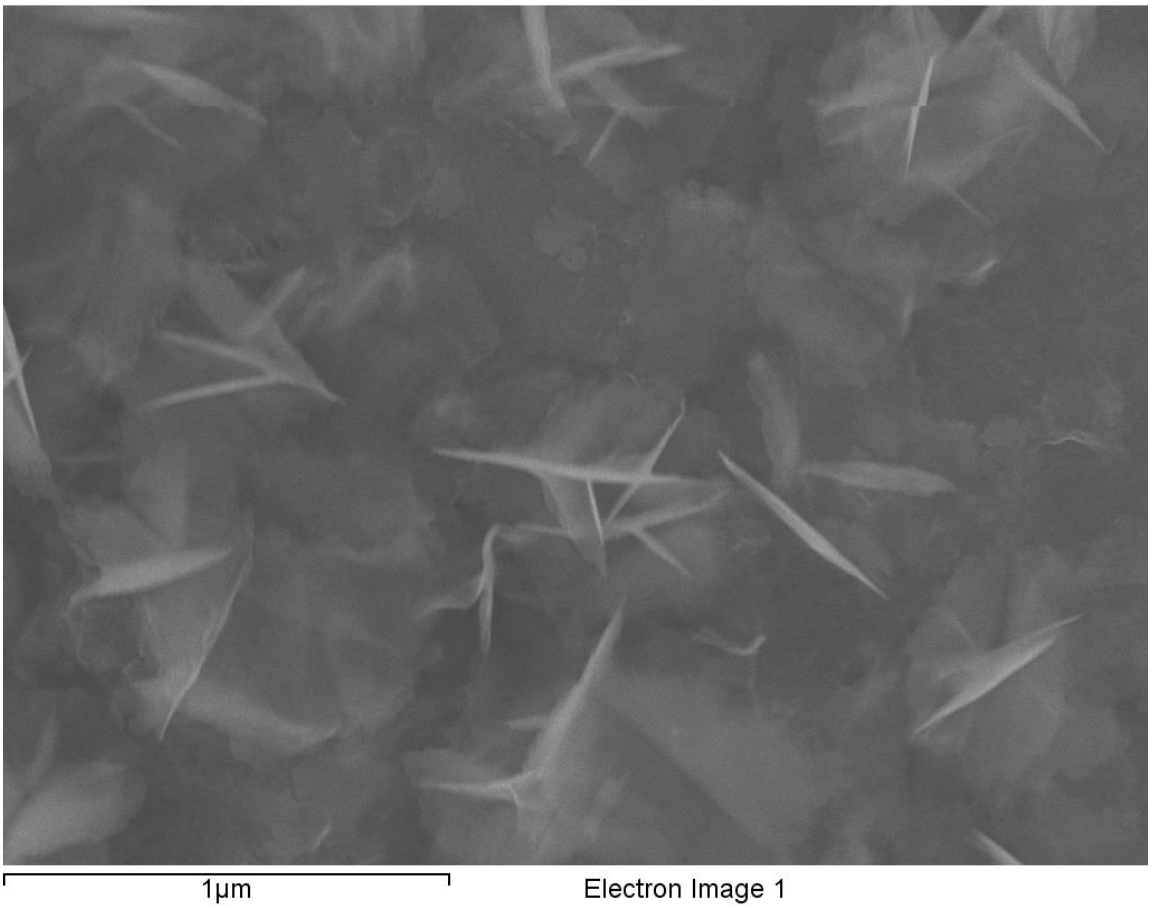

Figure 4.15: SEM image (top) and the associated EDX spectrum (bottom) of the "Soln hr 2 #1" electrode. The carbon paper used as working electrode in the second hour electrolysis of 1 mM ***(1)*** in DMF/5% H_2O/0.1 M $TBAPF_6$ at -2.71 V vs Fc/Fc^+. 15 kV accelerating voltage

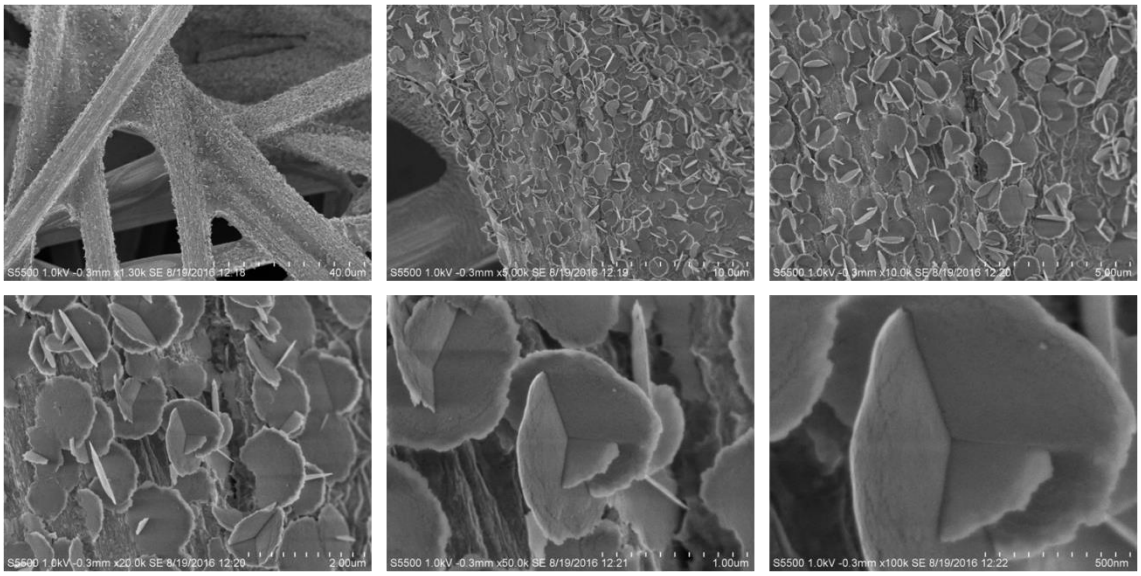

Figure 4.16: SEM images of "Soln hr 2 #2", the carbon paper used as working electrode in the second hour electrolysis of 1 mM ***(1)*** in DMF/5% H_2O/0.1 M $TBAPF_6$ at -2.71 V vs Fc/Fc^+, 1 kV accelerating voltage, 19.6 – 21.2 μA probe current. Magnification left to right, top to bottom: 1300, 5000, 10000, 20000, 50000 and 100000x.

Particularly on "Soln hr 2 #2", a remarkably ordered deposit is shown (Figure 4.16 and Figure 4.17). Almost perpendicularly bisecting discs feature commonly across the electrode surface. It is noted that the growth of the surface confined species within "Soln hr 2 #2" does appear to be greater than that obtained in "Soln hr 2 #1", i.e. in Figure 4.14, in terms of a more even surface coverage and size of features (approximate diameter closer to 1 μm vs 500 nm). Though this is not ideal in terms of reproducibility, the growth retains a very similar shape of intersecting plates, and a greater coverage allows for acquisition of an EDX spectrum of higher quality.

Though subjective, the discs appear to bare a strong likeness to those of Co_3O_4 created from the heated reaction of poly(vinylpyrrolidone) with cobalt acetate in ethylene glycol, with rinses of alcohol [32]. Additionally, the discs bare some resemblance to deposits obtained from deposition of $CoCl_2$ (specified as Co) [33], $Co(OH)_2$ sheets [34,35] and also Co_3O_4 [35]. The smooth curvature of the discs appearing in "Soln hr 2" electrodes was not obtained by Yang *et al*. [35]. The group reasoned that dissolution and reprecipitation with respect to the $Co(OH)_2$ plates may be responsible for apparent broken and uneven edges. Indeed, Jiang, Tseung and Rojas *et al*. advantageously

redissolved (*in situ*) Co oxides formed during Co deposition from $CoCl_2$, with the use of the chloride anions to form a porous Co structure in aqueous solutions [4,5]. The synthetic method of preparation also involved an aqueous environment. The method of synthesis of the bisecting plates observed within this work is a result of electrosynthesis in DMF with 5% water. Therefore, the solubility and reprecipitation effect specified by Yang *et al*. may be less applicable with a significantly different environment of synthesis.

The bisecting nature of the discs is further intriguing. Yang *et al*. also noticed that the $Co(OH)_2$ plates synthesised from reaction of $Co(NO_3)_2$ with NaOH tended to form in couples, laying flat on each other [36]. This was potentially attributed to a surface edge charge, or magnetism within the plates. It is noted however, that the bisecting plates herein are perpendicular to each other as opposed to aligned in a parallel manner.

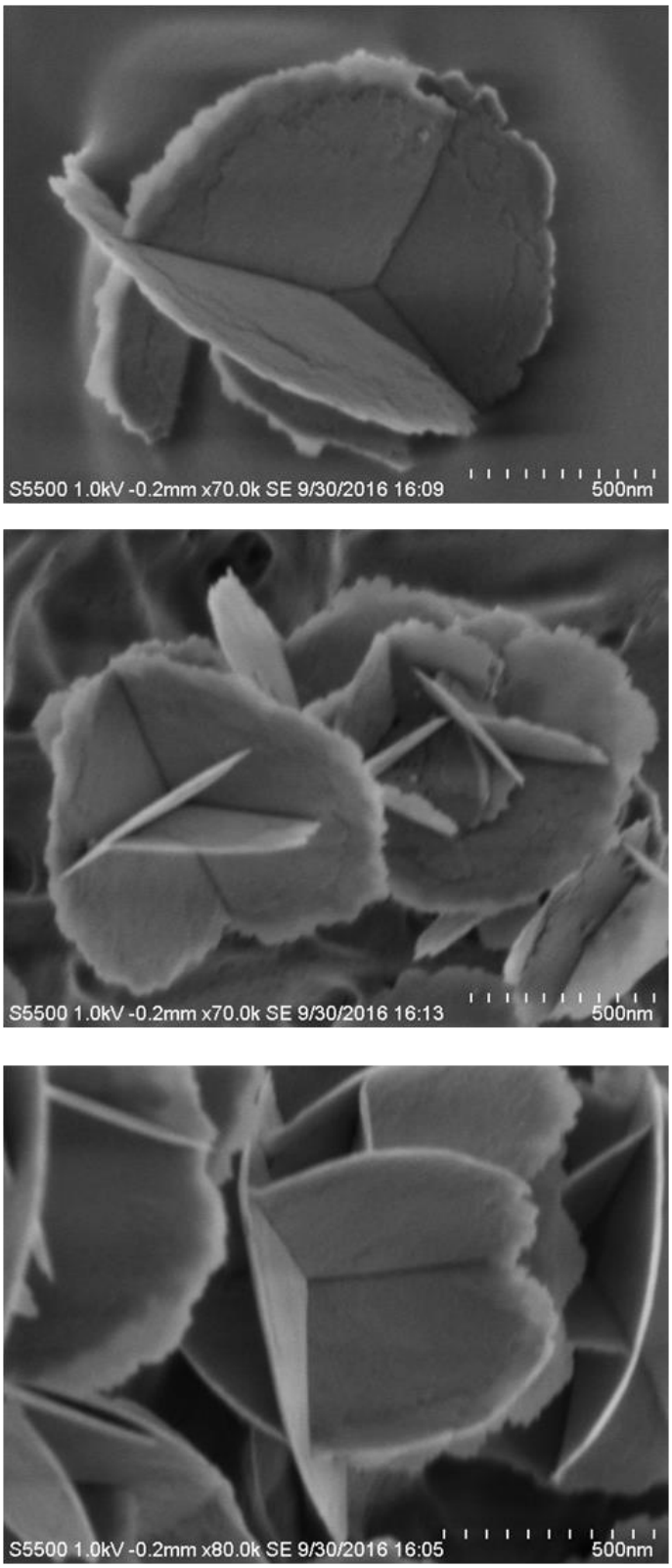

Figure 4.17: SEM images of select locations appearing on "Soln hr 2 #2", the carbon paper used as working electrode in the second hour electrolysis of 1 mM ***(1)*** in DMF/5% H_2O/0.1 M $TBAPF_6$ at -2.71 V vs Fc/Fc^+, 1 kV accelerating voltage, 18.4 – 19.2 μA probe current. Magnification top to bottom: 70000, 70000 and 80000x.

The EDX spectrum obtained from “Soln hr 2 #2” appears in Figure 4.18. The Co Lα and O Kα peaks become more prominent than the Fα signal (contrary to where a prominent surface deposit was not observed, such as that shown in Appendix C.10). It is expected that with a higher surface coverage over the electrode, the signal associated with F would decrease relative to the Co signals. The fact that the O Kα peak grows relative to the F Kα peak suggests that oxygen is also contained in the surface deposit.

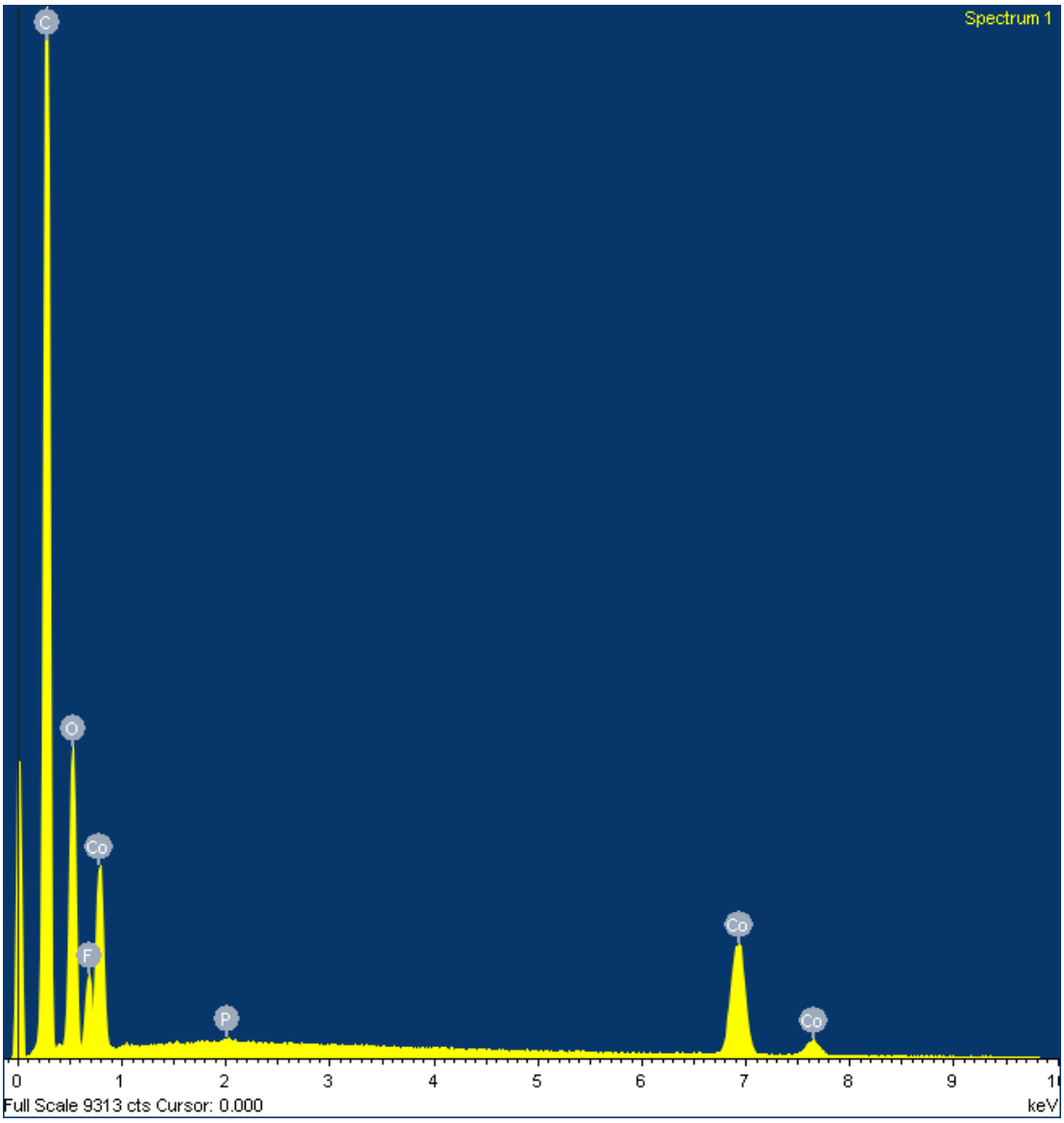

Figure 4.18: EDX spectrum of the “Soln hr 2 #2” electrode. the carbon paper used as working electrode in the second hour electrolysis of 1 mM ***(1)*** in DMF/5% H_2O/0.1 M $TBAPF_6$ at -2.71 V vs Fc/Fc^+. 15 kV accelerating voltage

4.2.3.3: SEM images and EDX spectra of Toray carbon paper electrodes, "surface-1" hours 1+2 and "surface-1" 2 hours

As shown in Table 4.6, surface-1 hours 1+2 and surface-1 two hours continuous continued to produce H_2 at a similar rate to that of the solution experiments. Two surface-1 hours 1+2 were imaged under SEM (1 kV accelerating voltage) and appear in Figure 4.19 and Appendix C.11.

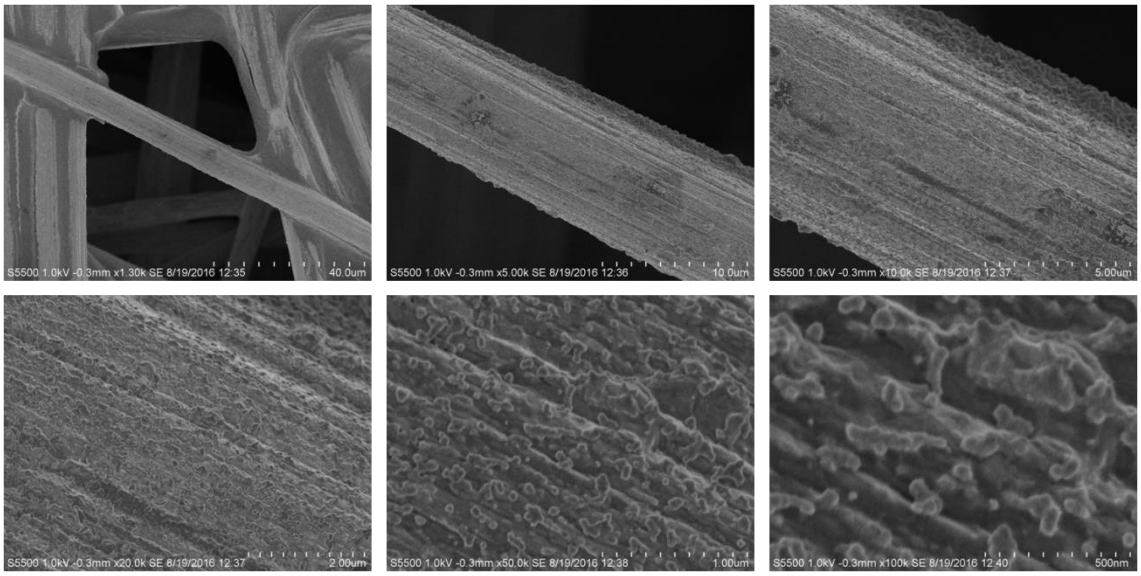

Figure 4.19: SEM images of "Surface-1 hrs 1+2 #1", the carbon paper used as working electrode following one hour electrolysis of 1 mM ***(1)*** in DMF/5% H_2O/0.1 M $TBAPF_6$ at -2.71 V vs Fc/Fc^+, and subsequent electrolysis for two interrupted hours at -2.71 V vs Fc/Fc^+ in the absence of ***(1)***. 1 kV accelerating voltage, 17.6 – 18.8 μA probe current. Magnification left to right, top to bottom: 1300, 5000, 10000, 20000, 50000 and 100000x.

As can be seen in Figure 4.19 and Appendix C.11, a light amorphous deposit is observed, which is not present in the control (Figure 4.11). EDX analysis was undertaken of the "Surface-1 hrs 1+2 #1" electrode at 15 kV accelerating voltage and the resulting EDX spectrum and associated SEM image appear in Figure 4.20.

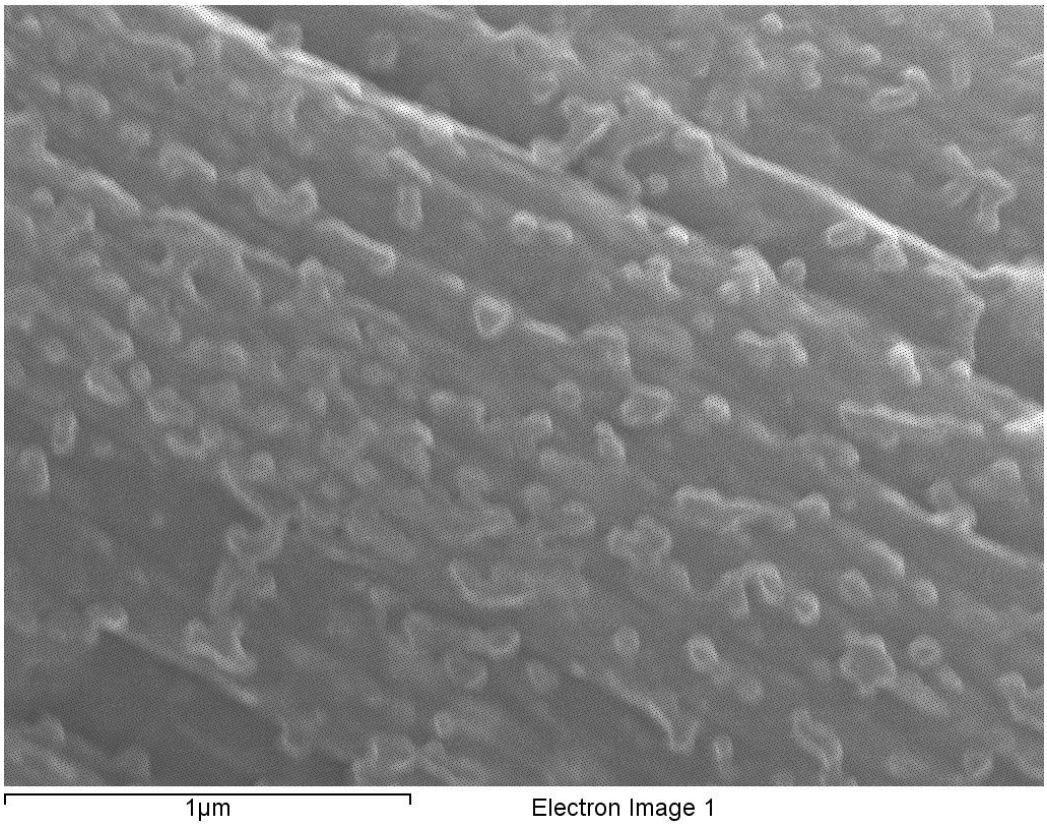

Figure 4.20: SEM image (top) and the associated EDX spectrum (bottom) of the "Surface-1 hrs 1+2 #1" electrode, the carbon paper used as working electrode following a one hour electrolysis of 1 mM ***(1)*** in DMF/5% H_2O/0.1 M $TBAPF_6$ at -2.71 V vs Fc/Fc^+, and subsequent electrolysis for two interrupted hours at -2.71 V vs Fc/Fc^+ in the absence of ***(1)***. The image and spectrum were acquired at 15 kV accelerating voltage

Within Figure 4.20, the EDX spectrum of the electrode shows the presence of cobalt within the sample. A Kβ signal associated with Co was not detected. This is not

surprising as Kβ signals generally appear with an intensity of approximately 0.1 times that of the Kα signal [37].

Two catalytically active electrodes electrolysed a solution of DMF with 0.1 M $TBAPF_6$ and 5% water for two continuous hours (Surface-1 2 hrs #1 and #2) and were imaged under SEM (1 kV accelerating voltage). The SEM images of "Surface-1 2 hrs #1" appear in Figure 4.21.

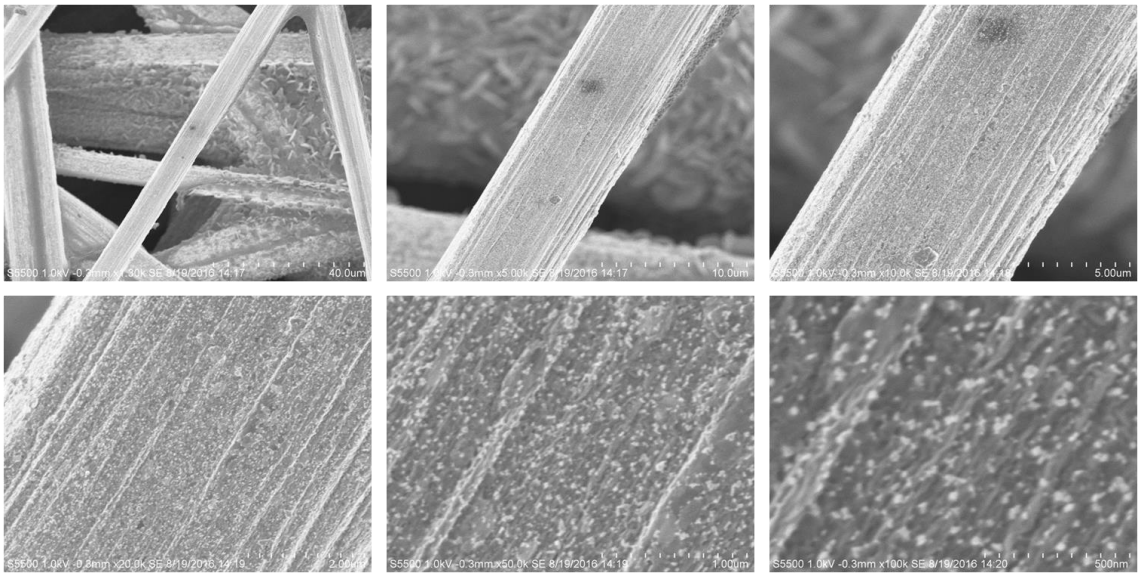

Figure 4.21: SEM images of "Surface-1 2 hrs #1", the carbon paper used as working electrode following one hour electrolysis of 1 mM ***(1)*** in DMF/5% H_2O/0.1 M $TBAPF_6$ at -2.71 V vs Fc/Fc^+, and subsequent electrolysis for two continuous hours at -2.71 V vs Fc/Fc^+ in the absence of ***(1)***. 1 kV accelerating voltage, 21.2 – 21.6 μA probe current. Magnification left to right, top to bottom: 1300, 5000, 10000, 20000, 50000 and 100000x.

"Surface-1 2 hrs #1" (Figure 4.21) appears to show less coverage of material on the outer fibres than do the interrupted surface-1 hrs 1+2 electrodes (appearing in Figure 4.19 and Appendix C.11) and also "Surface-1 2 hrs #2" (appearing following). Coupled with this is a heavier disc-shaped growth within the pores (evident from 1300x magnification), bearing resemblance to that of the growth witnessed in Soln hr 2 experiments (Figure 4.14 and Figure 4.16). EDX was undertaken of the outer fibre's surface with 15 kV accelerating voltage. The resulting EDX spectrum and associated

SEM image appear in Appendix C.12. Very weak signals exist where Co Kα and Lα peaks are expected (~ 6.931 and 0.775 kV respectively), however, these signals are very close to baseline and due to this, may not be assumed to be Co. The inner growth was further imaged by SEM and appears in Figure 4.22.

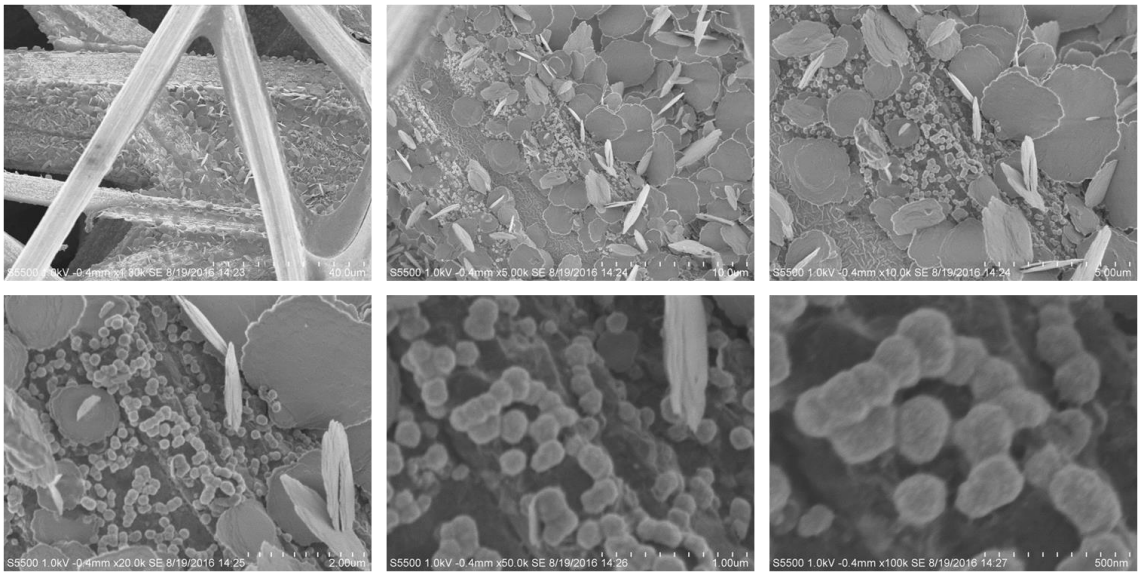

Figure 4.22: SEM images of a deeper region of "Surface-1 2 hrs #1", the carbon paper used as working electrode following one hour electrolysis of 1 mM ***(1)*** in DMF/5% H_2O/0.1 M $TBAPF_6$ at -2.71 V vs Fc/Fc^+, and subsequent electrolysis for two continuous hours at -2.71 V vs Fc/Fc^+ in the absence of ***(1)***. 1 kV accelerating voltage, 20.8 – 21.2 μA probe current. Magnification left to right, top to bottom: 1300, 5000, 10000, 20000, 50000 and 100000x.

As can be seen in Figure 4.22, relatively large disc-like growth (of varied diameter up to approximately 3-4 μm) is shown at greater depth into the electrode. At the base of the "discs" is small particulate matter of approximately 100-150 nm diameter. EDX was undertaken deeper within the electrode and the resulting spectrum and associated SEM image appear in Figure 4.23.

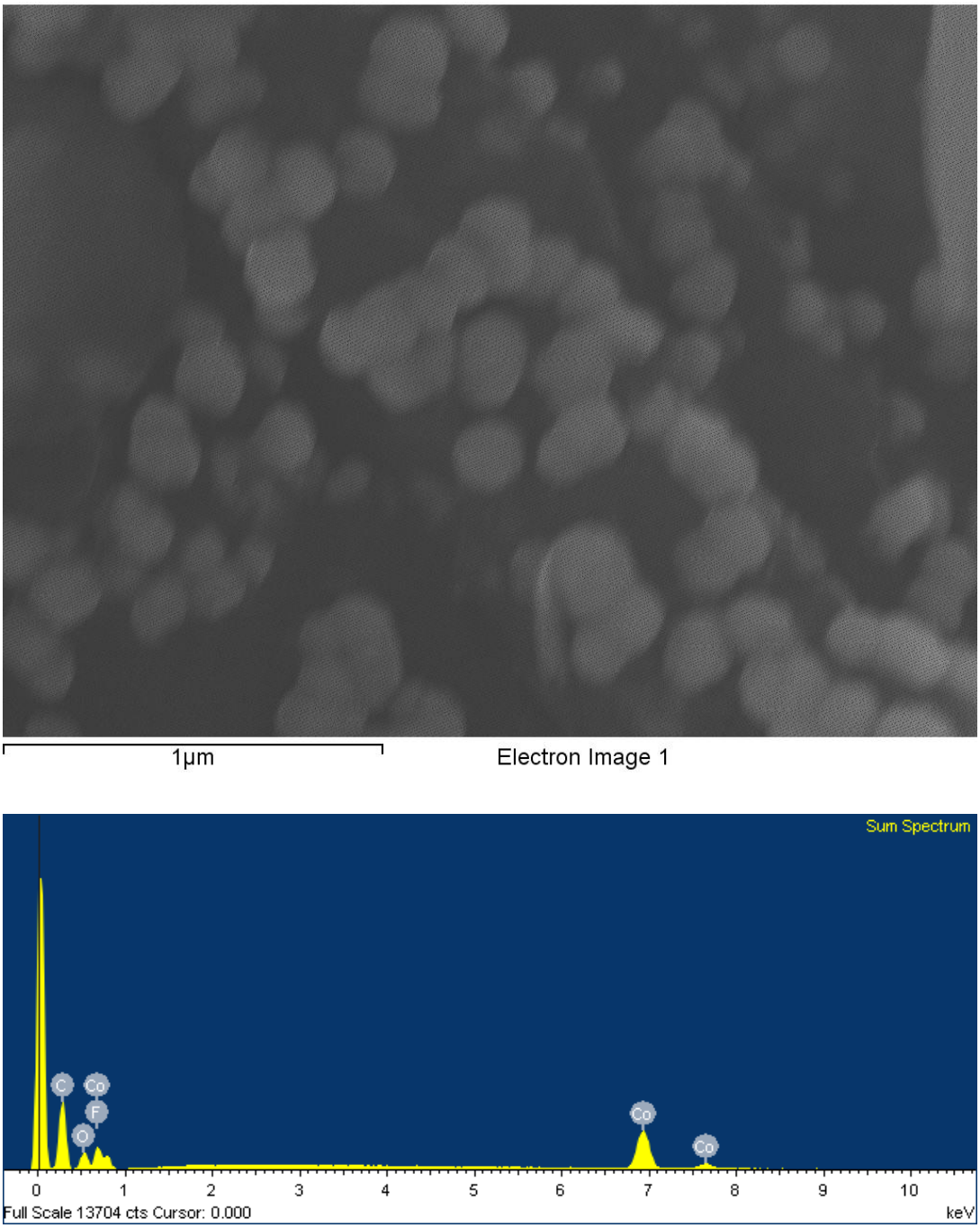

Figure 4.23: SEM image (top) and the associated EDX spectrum (bottom) of a deeper fibre within the "Surface-1 2 hrs #1" electrode, acquired at 15 kV accelerating voltage

Kα, Kβ and Lα signals associated with Co are visible within the EDX spectrum of Figure 4.23. An O Kα signal is also present (in addition to carbon and fluorine). An elemental map of Co giving rise to the EDX spectrum was obtained and appears in Figure 4.24. This elemental map quite clearly shows that a source of the Co Kα signal is

due to the spherical particulate matter imaged (see Figure 4.22, 100000x magnification and Figure 4.23).

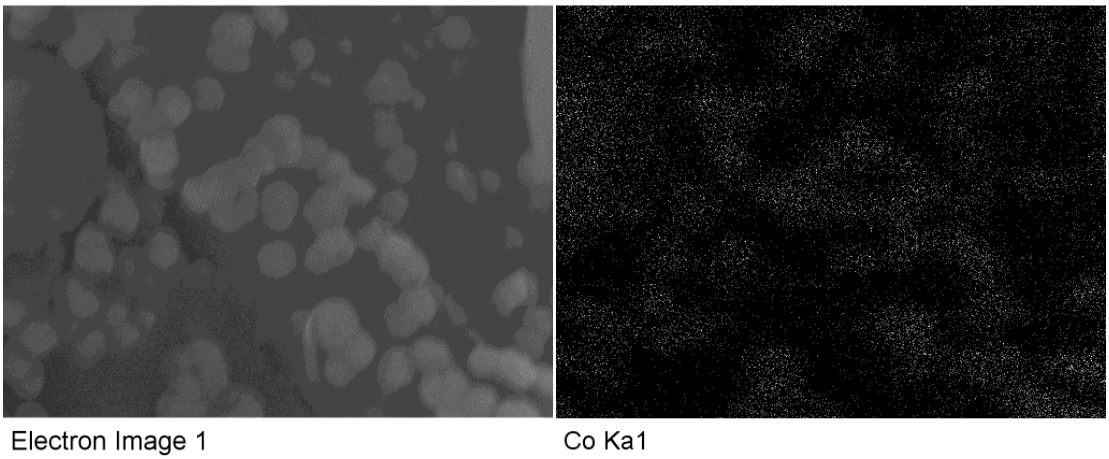

Figure 4.24: Elemental map of the inner region of a deeper fibre within the "Surface 2 hrs #1" electrode, acquired at 15 kV accelerating voltage (associated with the EDX spectrum shown in Figure 4.23).

A second electrode with the same electrochemical treatment (Surface-1 2 hrs #2) was imaged by SEM. The resulting images appear in Figure 4.25. Interestingly, "Surface-1 2 hrs #1" was the only one of the four surface electrodes that showed "disc" and particulate formation. Surface-1 2 hrs #2 (Figure 4.25) showed a light deposit (appearing richer in coverage than that of "Surface-1 2 hrs #1" outermost fibre's coverage, shown in Figure 4.21). The level of coverage is akin to that observed within the surface-1 1+2 hr electrodes (Figure 4.19 and Appendix C.11). All electrodes did however show very similar levels of activity.

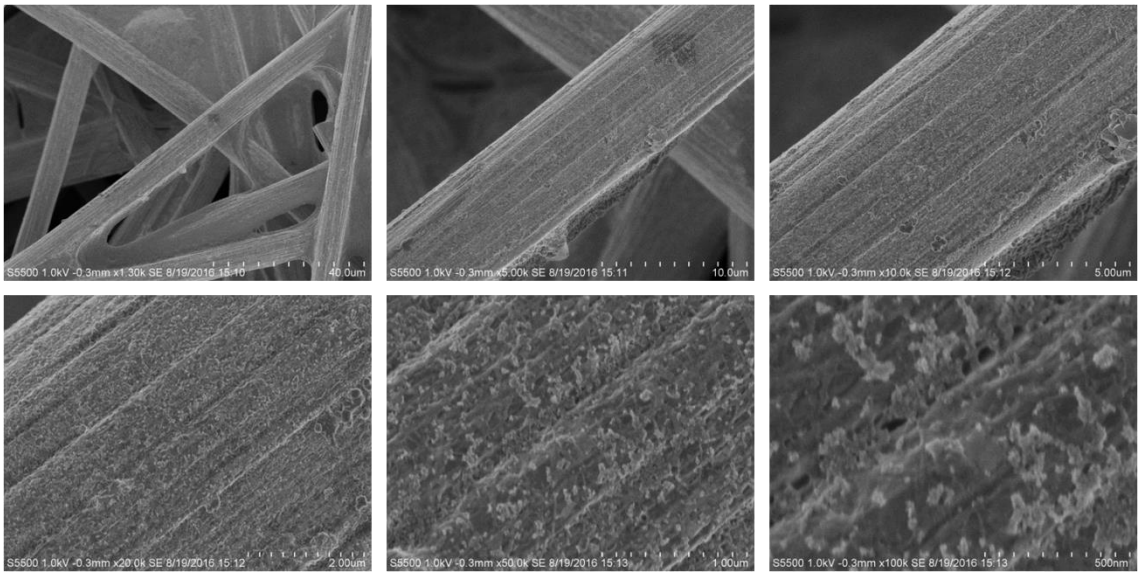

Figure 4.25: SEM images of "Surface-1 2 hrs #2", the carbon paper used as working electrode following one hour electrolysis of 1 mM ***(1)*** in DMF/5% H_2O/0.1 M $TBAPF_6$ at -2.71 V vs Fc/Fc^+, and subsequent electrolysis for two continuous hours at -2.71 V vs Fc/Fc^+ in the absence of ***(1)***. 1 kV accelerating voltage, 21.2 – 21.6 μA probe current. Magnification left to right, top to bottom: 1300, 5000, 10000, 20000, 50000 and 100000x.

4.2.3.4. SEM images of Toray carbon paper electrodes submerged in 1 mM *(1)*, non-electrolysed and electrolysed sample

SEM imaging of the electrodes soaked overnight in 1 mM ***(1)*** in DMF with 0.1 M $TBAPF_6$ and 5% water appear in Figure 4.26 (not electrolysed) and Figure 4.27 (electrolysed for 2 interrupted hours in the absence of ***(1)***). In these cases, SEM was undertaken with 10 kV accelerating voltage.

It can be seen that Figure 4.26 shows no visible coverage of the electrode resulting from soaking, demonstrating that physisorption of catalytically active species onto the surface of the electrode was not the cause of deposits witnessed on the electrode surface.

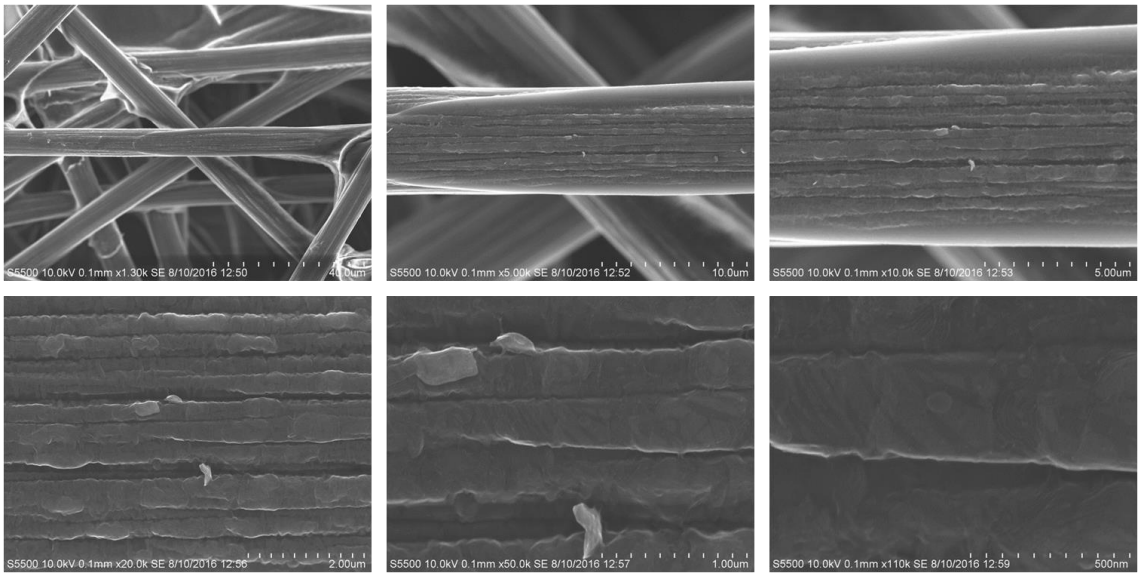

Figure 4.26: SEM images of carbon paper soaked in 1 mM ***(1)*** dissolved in DMF/5% H_2O/0.1 M $TBAPF_6$ with no electrolysis. 10 kV accelerating voltage, 18.8 – 19.2 μA probe current. Magnification left to right, top to bottom: 1300, 5000, 10000, 20000, 50000 and 100000x.

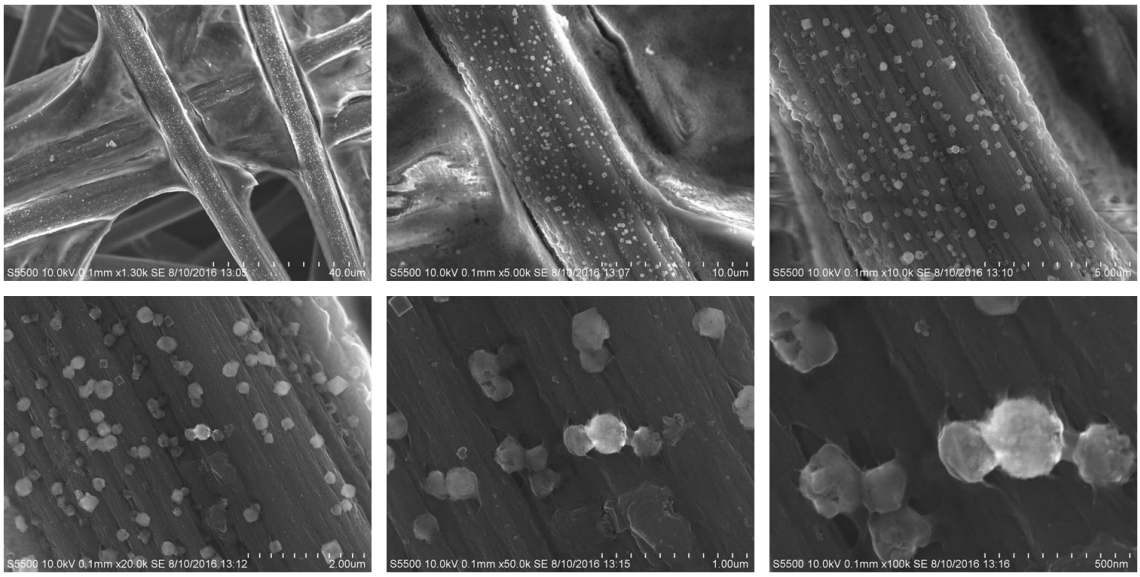

Figure 4.27: SEM images of carbon paper soaked in 1 mM ***(1)*** dissolved in DMF/5% H_2O/0.1 M $TBAPF_6$, and subsequent electrolysis for two interrupted hours at -2.71 V vs Fc/Fc^+ in the absence of ***(1)***. 10 kV accelerating voltage, 18.4 – 18.8 μA probe current. Magnification left to right, top to bottom: 1300, 5000, 10000, 20000, 50000 and 100000x

Figure 4.27 however, does show the presence of particles on the surface of carbon fibres. Though the presence of particles was observed on the electrode that was electrolysed following soaking, the results obtained in Appendix C.7 does not appear to show that a catalytically active response from the electrode. The deposit bears some resemblance to the unexpected (and not successfully characterised) deposit on the control hrs 1+2 electrode (Figure 4.11) in terms of spatial coverage. The control, alike the soaked electrode, also demonstrates a marked decrease in activity compared to the catalytically active "surface" electrodes (Appendix C.8). EDX analysis was not undertaken on the deposit due to the lower surface coverage, as compared to the coverages that allowed for qualitative analysis of Co (such as "Soln hr 2"s and "Surface-1 2 hrs #1").

Upon examination of the EDX spectra undertaken on the base material of carbon paper, it is difficult to obtain a resolved signal for nitrogen (Kα of 0.392) with the high contribution of carbon (Kα of 0.277). Therefore, the possible presence of ligand within the electrocatalytically active surface deposit cannot be definitively ruled out by EDX. In order to understand what may be forming on the surface (by understanding what forms in solution), UV-visible monitored bulk electrolyses were undertaken.

4.2.4. In-situ UV-visible spectroelectrochemistry (UV-visible monitored bulk electrolysis) of *(1)* in DMF/0.1 M $TBAPF_6$

The standard electrochemical H-cell was employed in monitoring the reduction of solutions containing ***(1)***. To permit the passage of the beam from the spectrophotometer through the working electrode compartment of the cell (containing the working and reference electrodes) without obstruction, the working electrode was angled towards the separating frit whereas the reference electrode was angled opposing the working electrode.

The spectroscopic wavelength cut-off of the cell/DMF/$TBAPF_6$ was found to be approximately 270 nm. This is adequate to view the disappearance of the complex' assumed d-d transition at 349 nm and the potential presence of a free ligand absorption, previously stated to absorb at 320 nm in $CHCl_3$ [38]. Information on the UV spectral feature at 349 nm is not available within the literature. A similar Co^{2+} complex bearing

ethylene groups between nitrogens and the amine nitrogen containing a hydrogen instead of a methyl group is stated to undergo a d-d transition at 370 nm (with two other lower energy transitions, unspecified intensities) [39]. From this, it is assumed that the transition apparent for ***(1)*** at 349 nm is also a d-d transition.

The applied potentials for electrolysis of ***(1)*** in anhydrous DMF were -2.48 V and -2.71 V vs Fc/Fc^+. In the presence of water, ***(1)*** was electrolysed at -2.42 V and -2.71 V vs Fc/Fc^+. -2.71 V was chosen as this was the electrolysis potential at which the active catalyst was formed and operated. The less negative electrolysis potential was adjusted, as the addition of water led to an anodic shift of the first reduction potential of ***(1)*** (at 100 mV s^{-1}, see Figure 4.3 and Figure 4.5). Shifting the electrolysis potential positively as compared to under anhydrous conditions minimised the possibility of entering the complex' second reduction.

4.2.4.1. *(1)* at -2.48 V vs Fc/Fc^+ without water

The complex was electrolysed at -2.48 V vs Fc/Fc^+ in anhydrous DMF with 0.1 M $TBAPF_6$ and the results appear in Figure 4.28. The difference spectra associated with the UV-visible spectra appear in Figure 4.29.

Within Figure 4.28 and Figure 4.29, an intense peak relative to the ***(1)*** d-d transition (λ_{max} of 349 nm) forms, with λ_{max} of 403 nm. Further to this, an increase in absorbance is observed beginning at approximately 310 nm. From 60 to 120 minutes, there appears to be an additional faint rise at approximately 320 nm. This cannot be ruled out as partial free ligand in solution [38]. For clarity, the spectra are separated into 0-55 min and 60-120 min electrolysis time and feature in Appendix C.13**i** and **ii** respectively. It becomes apparent that an isosbestic point is achieved at 366 nm (Appendix C.13**i**), suggesting the formation of only one species directly from the original ***(1)***, which at longer timescale (Appendix C.13**ii**, 60-120 mins), converts to a further species. It is expected that the second crossover (between 310 and 320 nm) would also be an isosbestic point. It has been previously shown that, dependent on the solvent, ***(1)*** may or may not show a second isosbestic point at higher energy in its conversion to another species [40].

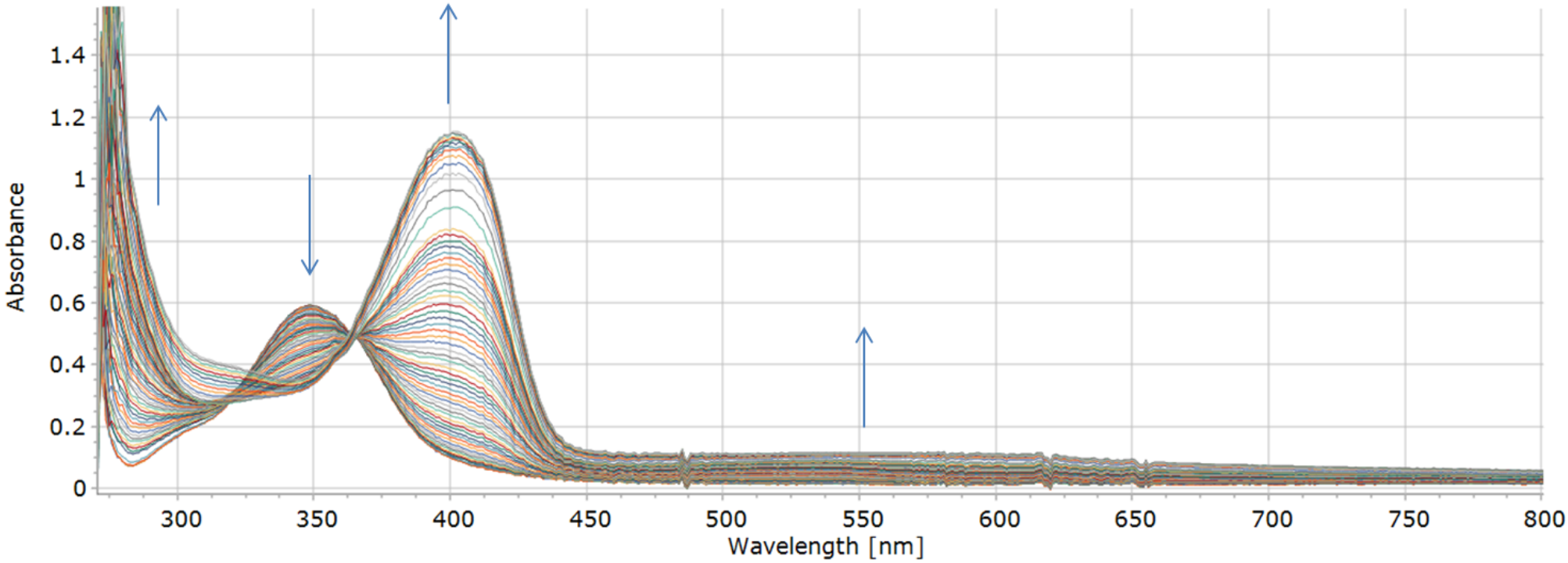

Figure 4.28: UV-visible monitored bulk electrolysis of 60 μM ***(1)*** at -2.48 V vs Fc/Fc^{+} in DMF/0.1 M $TBAPF_6$. Electrolysis was undertaken for two hours

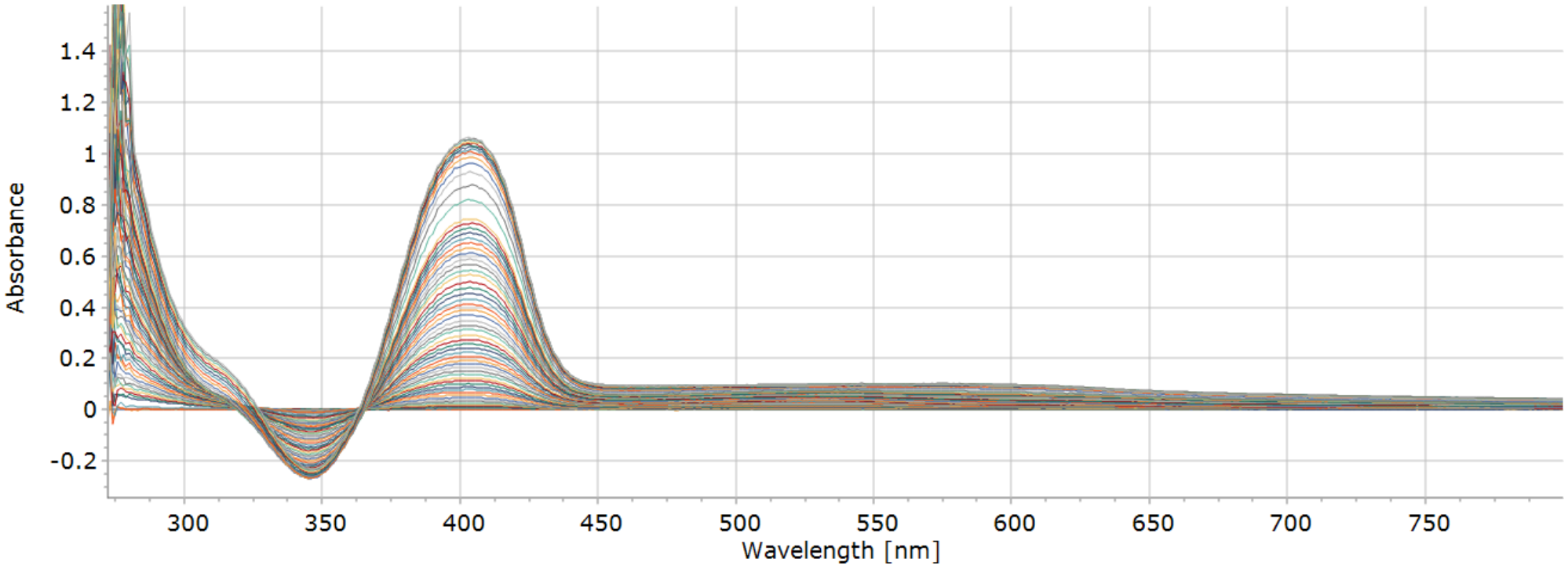

Figure 4.29: Difference spectra associated with the spectra appearing in Figure 4.28 (UV-visible monitored bulk electrolysis of 60 μM ***(1)*** at -2.48 V vs Fc/Fc^{+} in DMF/0.1 M $TBAPF_6$. Electrolysis was undertaken for two hours).

Further to the features mentioned, there also appears to be at least one broader weak feature formed between 450 and 700 nm (Figure 4.28). Spectroelectrochemistry of a similar salicylidene Co complex was not found within the literature for comparison. However, the 1 e^- metal-based reduction of Co^{2+} salen leads to the formation of a broad band extending from approximately 560 to greater than 750 nm, with λ_{max} of approximately 710 nm in DMF [41]. Co salophen and other more conjugated salicylidenes exhibited peaks extending to the near-IR region (up to ~ 1200 nm) [42]. Co^{1+} dimethylglyoxime$(BF_2)_2$ exhibits a band extending between approximately 500 nm and beyond 700 nm [43]. The H-Co^{3+} species also has the UV-spectral appearance of the Co^{1+} species [44]. The band could result from ***(1)***-Co^{1+}.

It is also noted that despite efforts to exclude water from the anhydrous DMF, trace water is likely present. As the potential is fixed below the $Co^{2+/1+}$ reduction, the Co^{1+} reduced species has greater time to potentially react with water to form a hydride, as compared to voltammetric experiments, in which the $Co^{2+/1+}$ couple appeared as reversible. Further to this, the concentration of ***(1)*** is lower in UV-visible monitored electrolyses (60 μM) than in voltammetry (1 mM). Therefore, the relative concentration of trace water becomes more significant within UV-visible monitored electrolyses. Due to this, the broad band may also not be ruled out as a H-Co^{3+} species.

4.2.4.2. Control experiments regarding UV-visible monitored bulk electrolysis of *(1)*

In order to better understand changes associated with electrolysis of ***(1)***, three control experiments were undertaken.

4.2.4.2.1. *(1)* with 15 μl water, without an applied potential

In an effort to elucidate whether chemical instability of ***(1)*** (or photoinstability from the acquisition beam of the spectrophotometer) could be accountable for skewing the higher energy isosbestic point, and indeed if any observed feature observed could be due to an alternative reaction to electroreduction of ***(1)***, a control experiment was undertaken in

DMF/0.1 M $TBAPF_6$/15 µl water, without the application of electricity to the cell. The resulting spectra appear in Figure 4.30.

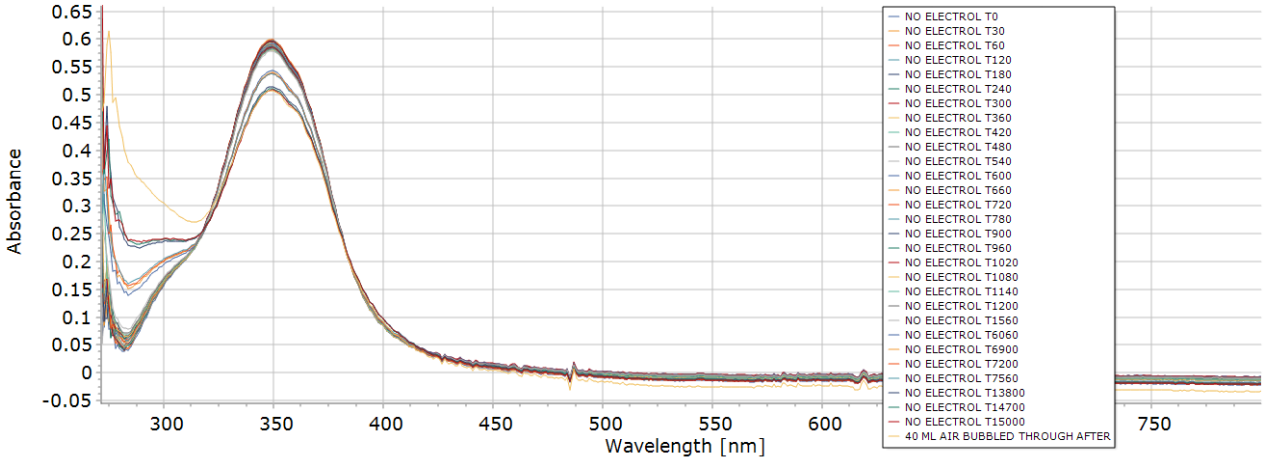

Figure 4.30: UV-visible spectra of 60 µM ***(1)*** in stirred Ar-purged DMF with 0.1 M $TBAPF_6$ and 15 µl water, monitored over time.

Figure 4.30 shows that there is a reaction of ***(1)*** with either solvent, water or potentially trace amounts of oxygen that could have entered through the septum piercing over the timescale of 250 minutes, as is evident from the drop of intensity (approximately 0.6 to 0.5 AU) of the ***(1)*** d-d band at 349 nm. Accompanying this is an increase in absorbance at higher energy of the d-d band. When air was bubbled through the solution following 250 minutes, an increase in absorbance below approximately 320 nm was noted, though there was no further change to the band at 349 nm. Drago *et al*. noted that upon monitoring the reaction of ***(1)*** with oxygen, the lower energy isosbestic point (that was observed at 329 nm in DCM) was not observed in toluene. This was reasoned as a charge transfer interaction between O_2 and toluene [40]. Contact charge transfer has been noted also for DMF [45], and results in an absorbance increase which continues to above 320 nm [46].

Interestingly, the possible presence of oxygen within the cell and the vicinity of the complex doesn't show the expected rise for the ***(1)***-O_2 superoxo complex with λ_{max} of approximately 380 nm [40]. This species has also been detected in DMF at 259 K, and was found to be 94-97% reversible in the release of O_2 [47]. However, auto-oxidation (without a specified product) of this species has been stated to occur at higher

temperatures than 253 K [48]. ***(1)***-Co^{3+} triflate has been stated to undergo a reaction with superoxide to produce ***(1)*** [49]. It is assumed that the reverse reaction may also proceed. (***(1)***-Co^{3+})$_2O_2$ has been specified as a decomposition product [47] of ***(1)***-O_2. The identity of the product of ***(1)***-O_2 auto-oxidation is unknown, but an assumption is made in that (***(1)***-Co^{3+})$_2O_2$ has a similar absorbance to that of ***(1)***-Co^{3+} triflate, which is stated to absorb with λ_{max} of 386 nm in DMSO [49]. It is also assumed that substitution of triflate with another anionic ligand (X), and also the solvent does not significantly affect its absorbance λ_{max}. With these assumptions in mind, there is no evidence for either bonding of O_2 (λ_{max} of approximately 380 nm) or formation of ***(1)***-Co^{3+}X/(***(1)***-Co^{3+})$_2O_2$ (λ_{max} assumed to be 386 nm).

4.2.4.2.2. With 15 μl water, without *(1)* or applied potential

In order to assess whether contact charge transfer in the DMF/0.1 M $TBAPF_6$/15 μl H_2O electrolyte solution may be significant enough to lead to the change observed in Figure 4.30, the Ar-purged electrolyte (containing 15 μl water) without ***(1)*** was stirred in the electrolysis cell. The results of UV-visible spectroscopy monitoring are available in Figure 4.31.

The resulting spectrum (Figure 4.31, acquired up to 150 minutes) shows that part of the rise between 250 nm and 320 nm may be attributed to oxygen slowly entering the solution, the presence of which is assumed to be from the multiply pierced (due to purging) septum. This experiment also confirms a potential source for oxygen (in addition to OH^-), should the active heterogeneous catalytic species be a form of cobalt oxide.

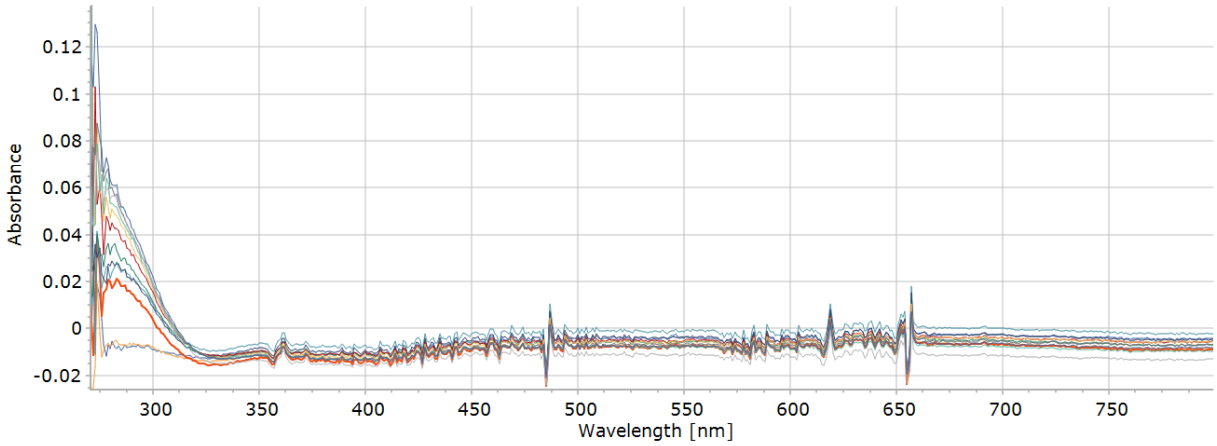

Figure 4.31: UV-visible spectra monitored up to 2.5 hours of Ar-purged and stirred electrolysis cell, containing 15 ml DMF with 0.1 M $TBAPF_6$ and 15 µl water. The solution was not electrolysed

4.2.4.2.3. 15 µl water in DMF electrolysed at -2.71 V vs Fc/Fc^+

To assess whether reductive electrolysis of the solvent/electrolyte may be responsible for any of the features observed in Figure 4.28, electrolysis of the DMF/0.1 M $TBAPF_6$ electrolyte, containing 15 µl water was undertaken at -2.71 V vs Fc/Fc^+. The resulting spectra appear in Figure 4.32.

As can be seen in Figure 4.32, the rise in spectra at higher energy (from the spectral cut-off up to approximately 350 nm) that features in Figure 4.28 (up to approximately 320 nm) can be attributed to a phenomenon that occurs through electrolysis of the solvent. This behaviour was not further examined.

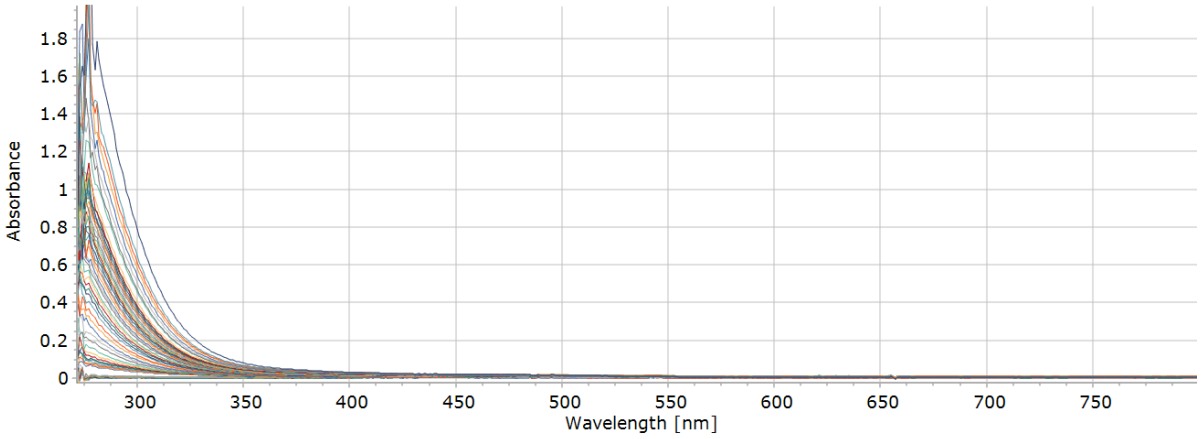

Figure 4.32: UV-visible monitored electrolysis of 15 ml DMF with 0.1 M $TBAPF_6$ and 15µl water (in the absence of ***(1)***) at -2.71 V vs Fc/Fc^+ for 120 minutes.

Within Figure 4.28, there is a rise observed from 450 nm onwards. Broad but weak bands are visible from approximately 450 nm to 750 nm with the baseline increasing with each continual scan to approximately 1000 nm (baseline increase to 0.05 AU at 1000 nm). With examination of Figure 4.30 to Figure 4.32, it is shown that this behaviour is only apparent upon electrolysis of the complex. Turbidity of the solution was not observed. However, following "solution" electrocatalytic experiments with carbon paper, occasionally a dark solid was noted, which was assumed to be derived from the carbon paper electrode. On this basis, a Tyndall effect due to turbidity may not be excluded as a possibility. Stirring of the cell, causing misalignment, and therefore deviation from baseline may be ruled out as all three control experiments were stirred at the same rate. A further comparison of the control experiments with that of Figure 4.28 also very evidently shows that the formation with λ_{max} of 403 nm is due to electrochemical reduction of the complex.

4.2.4.3. *(1)* electrolysed at -2.42 V vs Fc/Fc^+ with 15 μl water

As is shown in Figure 4.5, an anodic shift to the voltammetry of the first reduction occurred upon the introduction of water to ***(1)***. To gain an insight into what species may be forming at the first reduction with water present, ***(1)*** was electrolysed in the presence of water at the less negative potential of -2.42 V compared to in the absence of water. The associated spectra up to 120 minutes of electrolysis appear in Figure 4.33, with the difference spectra associated featuring in Figure 4.34.

Figure 4.33 shows similar changes to that without water (Figure 4.28). Subtle variation exists however. The weakly formed band/s (most prominent between approximately 450 and 650 nm), shown in Figure 4.29 in the absence of water, appear less significantly between 550 and 650 nm within Figure 4.34 with water. The intense band, shown with λ_{max} of 403 nm (Figure 4.29) without water shows a shift to 398 nm (Figure 4.34), possibly suggesting the growth of an additional band at very similar energy to that formed without water (and potentially a lower extinction coefficient to the species shown at 403 nm, with absorbance values at λ_{max} of 1.07 to 0.89 without and with water respectively). The spectra within Figure 4.28 (without water) appear to hold an isosbestic point at 366 nm. This is not apparent over the course of two hours electrolysis in the presence of water. However, two isosbestic points are noted with water at earlier electrolysis times (up to 23 minutes, Figure 4.35). These isosbestic points occur at 371 nm and 323 nm, varying from the 366 nm isosbestic point noted without water present. Due to a more rapid deviation from isosbestic behaviour, what initially forms in the presence of water is likely more unstable than that forming in the absence of water.

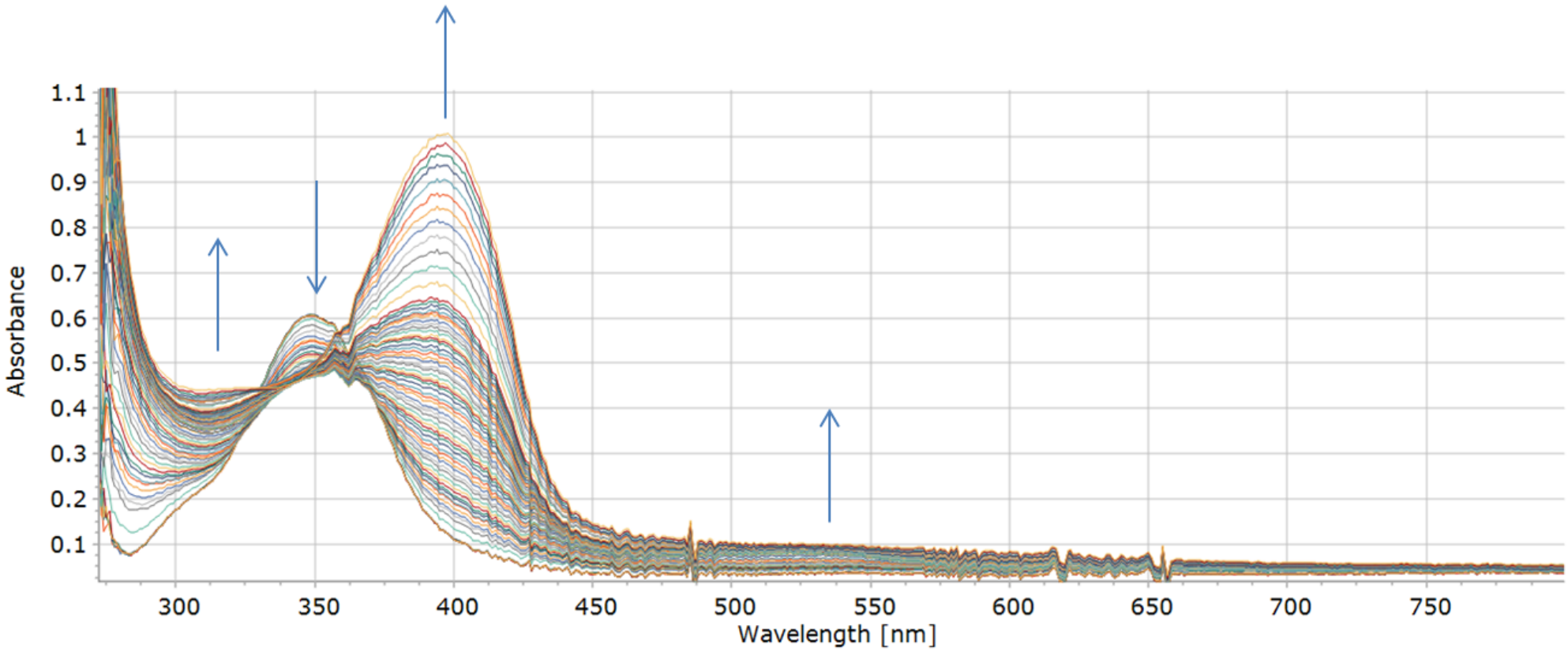

Figure 4.33: UV-visible spectra acquired during the electrolysis of 60 μM ***(1)*** in 15ml DMF/0.1 M $TBAPF_6$ with 15 μl water at -2.42 V vs Fc/Fc^+. The spectra are displayed up to 120 minutes of electrolysis.

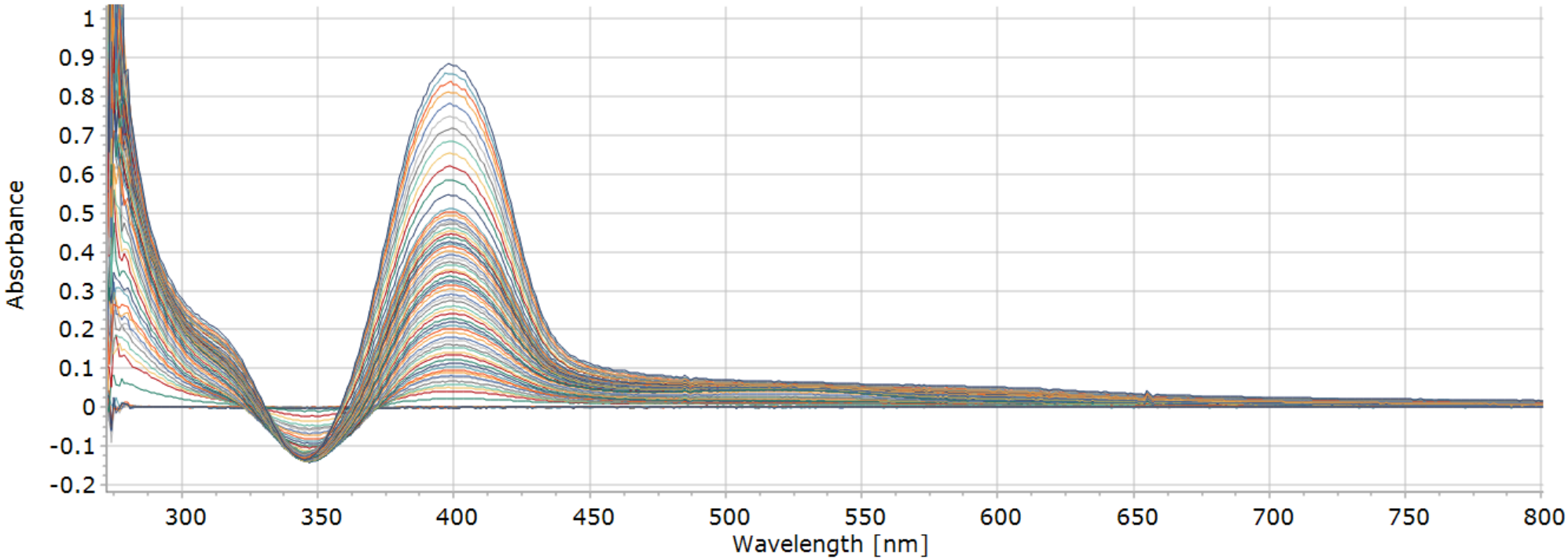

Figure 4.34: Difference spectra associated with the spectra appearing in Figure 4.33 (UV-visible monitored bulk electrolysis of 60 μM ***(1)*** at -2.42 V vs Fc/Fc^{+} in 15 ml DMF/0.1 M $TBAPF_6$ with 15μl water. The spectra are displayed up to 120 minutes of electrolysis).

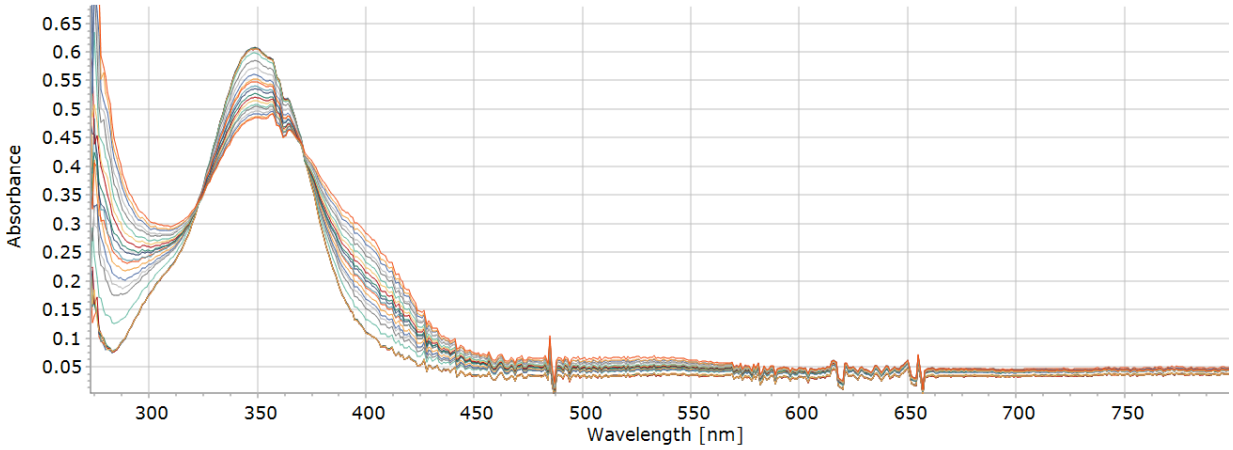

Figure 4.35: UV-visible spectra as per Figure 4.33 (electrolysis of 60 μM ***(1)*** in 15ml DMF/0.1 M $TBAPF_6$ with 15 μl water at -2.42 V vs Fc/Fc^+) up to 23 minutes of electrolysis.

The electrolysis at -2.42 V vs Fc/Fc^+ with water present was extended for an additional 30 minutes (totalling 150 minutes). The spectra acquired following 130, 140 and 150 minutes of electrolysis appear in Appendix C.14. A faint feature becomes apparent at approximately 315 nm, which is close to the λ_{max} of the H_2pdSal ligand (at 320 nm) reported in $CHCl_3$ [38].

4.2.4.4. *(1)* electrolysed at -2.71 V vs Fc/Fc^+ without water

Following electrolyses beyond the first reduction, electrolysis was undertaken at -2.71 V vs Fc/Fc^+ without water. The resulting spectra and difference spectra are featured in Figure 4.36 and Figure 4.37 respectively.

Within Figure 4.36 and Figure 4.37, a rise in absorbance is noted from the starting complex' d-d transition (λ_{max} of 349 nm) up to 9 minutes of electrolysis. For clarity, the spectra and difference spectra of the first 9 minutes are shown in Appendix C.15**i** and **ii** respectively. The non-uniformity of the rise across the spectra (shown more clearly in Appendix C.15**ii**) in conjunction with the changes occurring gradually as opposed to suddenly leads to the observation that this rise is unlikely due to a movement of the cell.

The same stirrer and speed was used within the rest of the electrolyses and no baseline shift was noted. Therefore, gradual movement of the cell is unlikely.

A band is observed to grow in at approximately 400 nm, akin to electrolysis without water at -2.48 V and with water at -2.42 V. The λ_{max} of this peak occurs at 405 nm, closer to the λ_{max} of the feature formed from electrolysis at the first reduction without water (403 nm) than with water (398 nm). Furthermore, the broad and weaker band/s occurring from approximately 450 nm to 650 nm appear to be more intense (akin to electrolysis at the first reduction potential in the absence of water, Figure 4.28 and Figure 4.29) than that achieved following the first reduction in the presence of water (Figure 4.33 and Figure 4.34). Again, the loss of ligand may not be ruled out within these experiments, with a band appearing at around 320 nm (Figure 4.37).

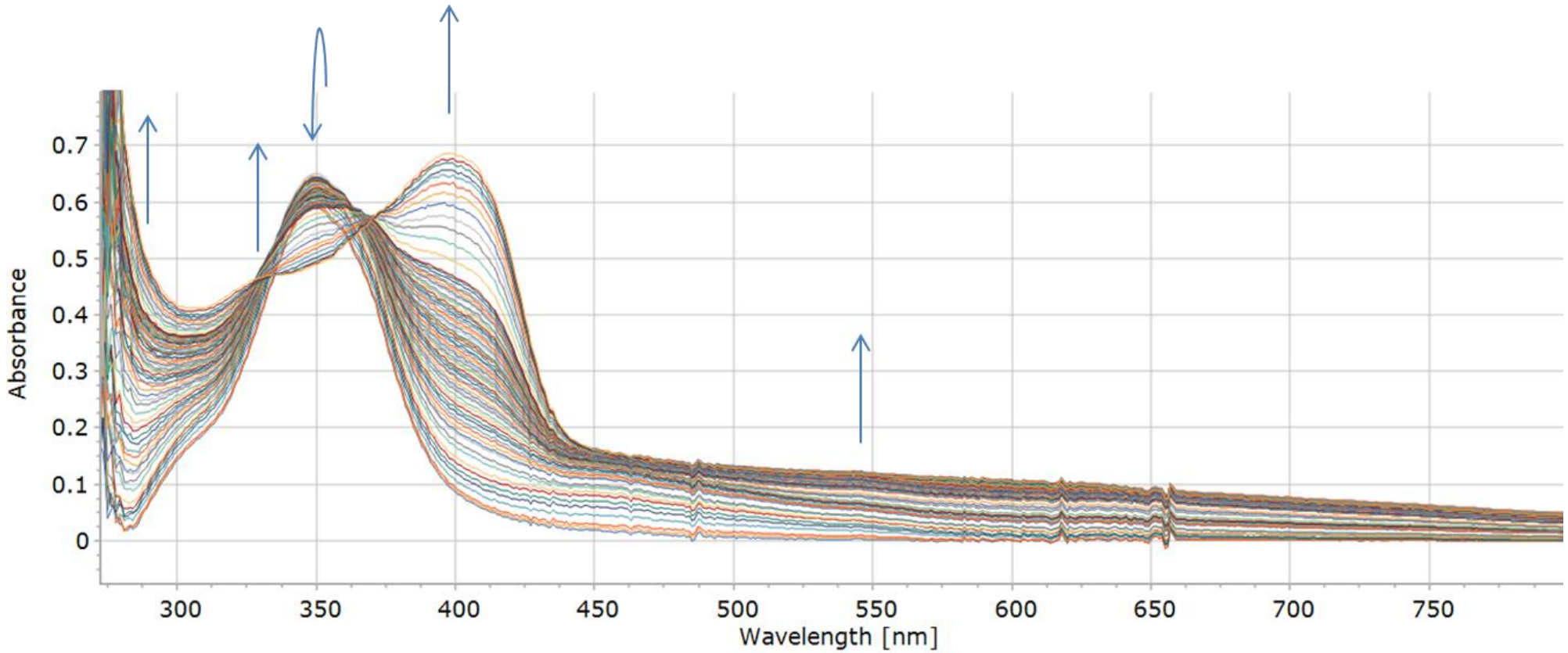

Figure 4.36: UV-visible spectra acquired during the electrolysis of 60 μM ***(1)*** in 15ml DMF/0.1 M $TBAPF_6$ at -2.71 V vs Fc/Fc^+. The spectra were undertaken up to 120 minutes of electrolysis.

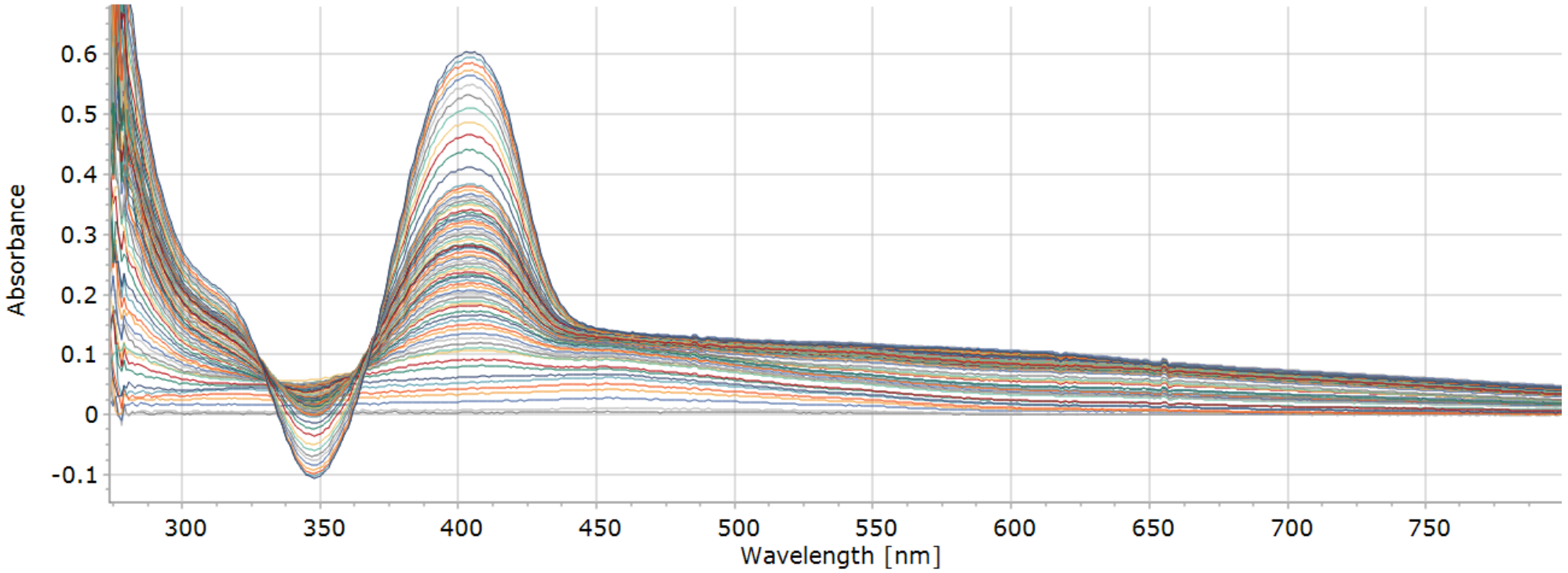

Figure 4.37: The difference UV-visible spectra associated with Figure 4.36 (as acquired during the electrolysis of 60 μM ***(1)*** in 15ml DMF/0.1 M $TBAPF_6$ at -2.71 V vs Fc/Fc^+). The spectra were undertaken up to 120 minutes of electrolysis.

Key differences between the spectral changes associated with reduction of the complex at the second reduction potential (in the absence of water) and electrolyses with and without water at the first reduction potentials are the intensity of the new band at approximately 400 nm, and the observed decrease at 349 nm. Within the two hour electrolyses, relative to the absorbance of ***(1)*** at T_0 (λ_{max} of 349 nm), the new band formed at the second reduction potential (λ_{max} = 405 nm) grew to a less intense height (0.686 AU / 0.591 AU, = 1.16 x) than did the peaks of the complex with (1.009 AU / 0.607 AU, = 1.66 x) and without water (1.154 AU / 0.591 AU, = 1.95 x) with electrolysis at the first reduction potential. Possibilities for this may include either electrochemical and/or chemical conversion of the species associated with the band/s at approximately 400 nm or the formation of another species with similar wavelength but lower extinction coefficient to that of the band at approximately 400 nm. No isosbestic points were noted during the initial stages of the experiment, unlike those observed at the first reduction potentials of ***(1)***, both with and without water.

4.2.4.5. *(1)* electrolysed at -2.71 V vs Fc/Fc^+, with 15 μl water

Electrolysis of the complex was undertaken at -2.71 V in the presence of 15 μl water. The UV-visible monitored spectra and associated difference spectra feature in Figure 4.38 and Figure 4.39 respectively.

Examination of the spectra obtained from electrolysis of ***(1)*** with 15 μl water at -2.71 V vs Fc/Fc^+ (Figure 4.38 and Figure 4.39) reveals the formation of an intense band with λ_{max} of 398 nm, identical to that formed during electrolysis of the complex at its first reduction (at -2.42 V). This contrasts with experiments undertaken in the absence of water (λ_{max} of 403 and 405 nm at -2.48 and -2.71 V respectively). The growth of one or more features between approximately 450-650 nm is evident, as with the other three electrolyses undertaken.

As with the electrolysis undertaken without water at -2.71 V, the electrolysis undertaken with water present showed a brief initial increase in the ***(1)*** d-d transition at 349 nm up to 16 minutes prior to a decrease. After 39 minutes of electrolysis, there is a further and continual rise at 349 nm, until the 120-minute electrolysis is halted.

The lack of an obvious band associated with the free ligand (around approximately 320 nm [38]) thus far suggests that what is deposited on the electrode may retain the ligand. Information regarding the energy and identity of UV-visible bands associated with cobalt metal-centred pentadentate salens is not prevalent. Therefore, drawing conclusions as to the nature of the species solely using UV-visible monitored electrolyses is not straight-forward.

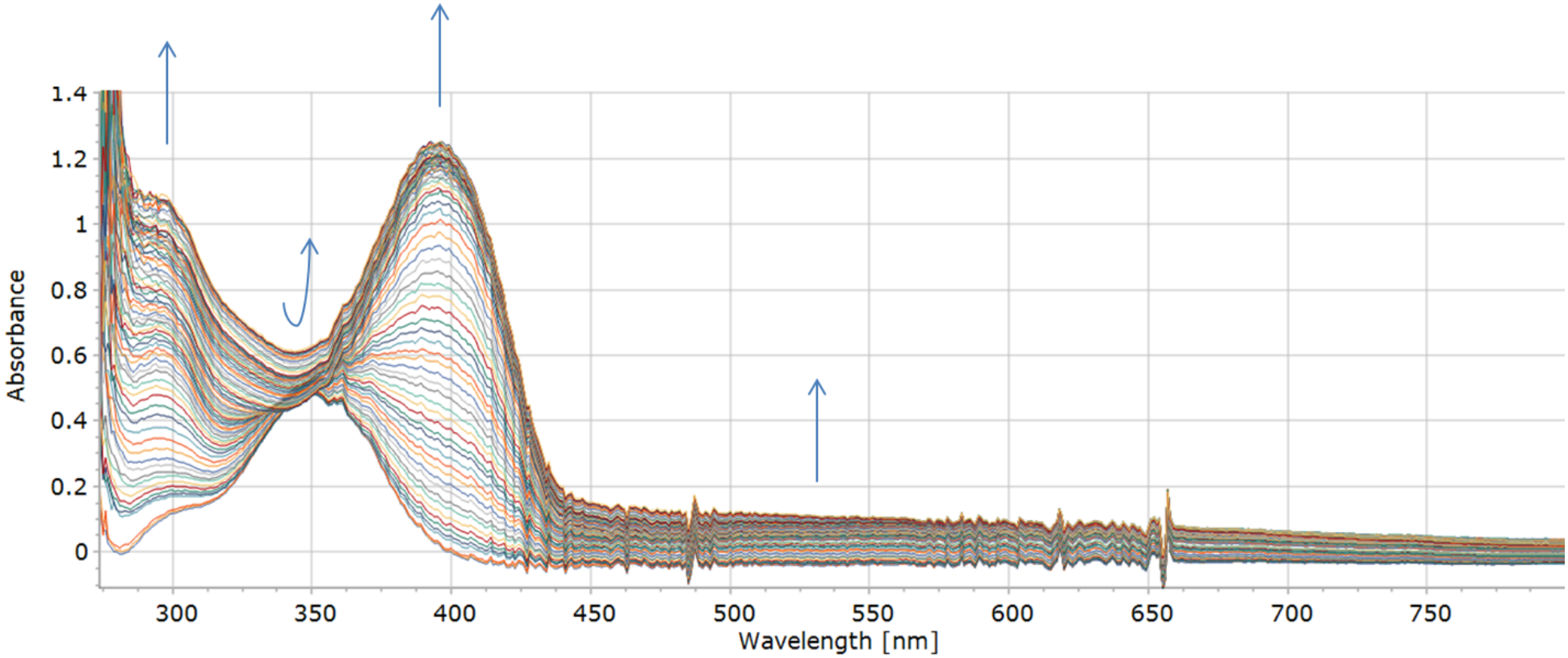

Figure 4.38: UV-visible spectra acquired during the electrolysis of approximately 60 μM ***(1)*** in 15ml DMF/0.1 M $TBAPF_6$ with 15 μl water at -2.71 V vs Fc/Fc^+. The spectra were undertaken up to 120 minutes of electrolysis.

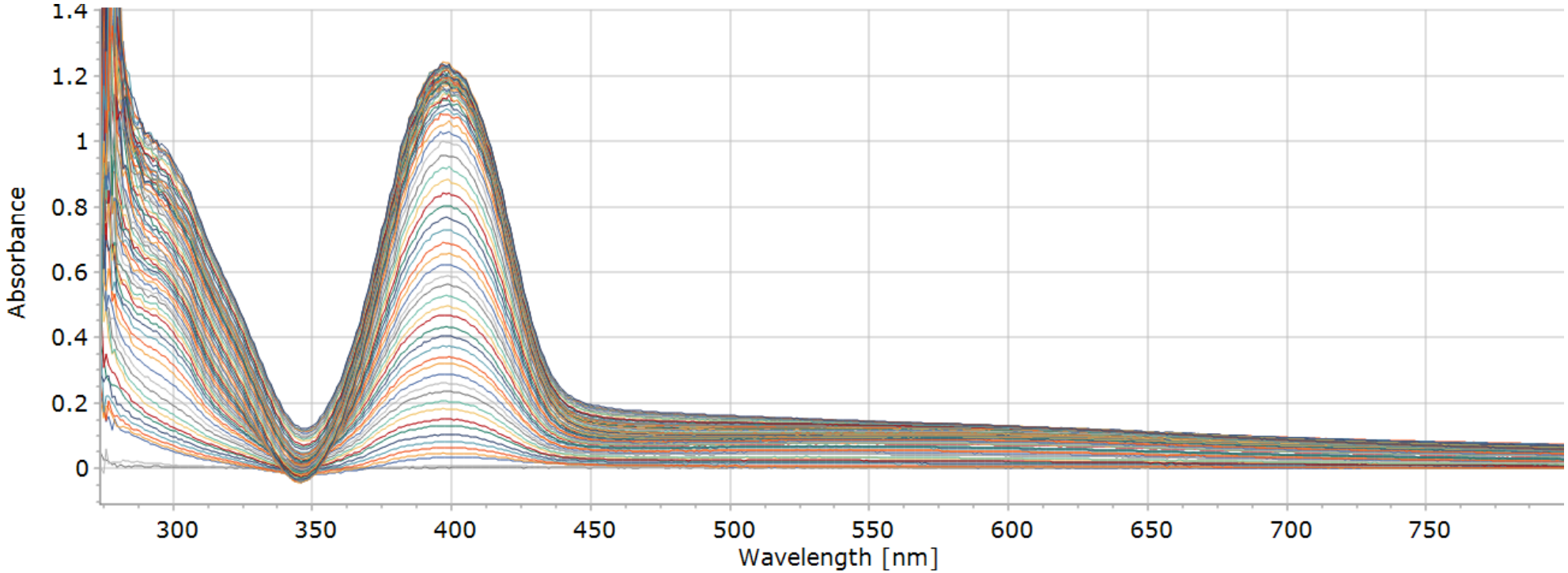

Figure 4.39: The difference UV-visible spectra associated with Figure 4.38 (as acquired during the electrolysis of 60 μM ***(1)*** in 15ml DMF/0.1 M $TBAPF_6$ with 15 μl water at -2.71 V vs Fc/Fc^+). The spectra were undertaken up to 120 minutes of electrolysis.

4.2.5. UV-visible and electrochemical experiments of H_2pdSal ligand

4.2.5.1. UV-visible spectrum of the H_2pdSal ligand

To draw conclusions from the experiment, the H_2pdSal ligand was synthesised. The UV-visible spectrum of H_2pdSal and subsequent extinction coefficient at the λ_{max} was undertaken along with that of ***(1)***. The normalised spectrum of H_2pdSal relative to ***(1)*** is displayed in Figure 4.40. The calibration curves for H_2pdSal at its λ_{max} of 315 and 408 nm appear in Appendix C.16**i** and **ii** respectively, while the calibration curves for ***(1)*** at its λ_{max} of 349 nm and also at 315 nm (for comparison to H_2pdSal) appear in Appendix C.17**i** and **ii** respectively.

The extinction coefficients for H_2pdSal were determined as approximately 7900 and 250 L mol^{-1} cm^{-1} at 315 and 408 nm respectively. The weaker band, appearing at 408 nm in DMF, has been reported at 418 nm in $CHCl_3$ [38], with the more intense band reported at 320 nm. The extinction coefficient for ***(1)*** at 349 nm (approximately 12400 L mol^{-1} cm^{-1}) is in close agreement to that previously reported in DMF [47] (12300 L mol^{-1} cm^{-1} at 349 nm). At 315 nm, ***(1)*** displays an extinction coefficient of 5200 L mol^{-1} cm^{-1}.

The UV-visible calibration curves show that the extinction coefficient of H_2pdSal at 315 nm is of similar value to ***(1)*** at 315 nm. Therefore, it remains ambiguous as to whether the free ligand could be clearly identified within electrolysis experiments.

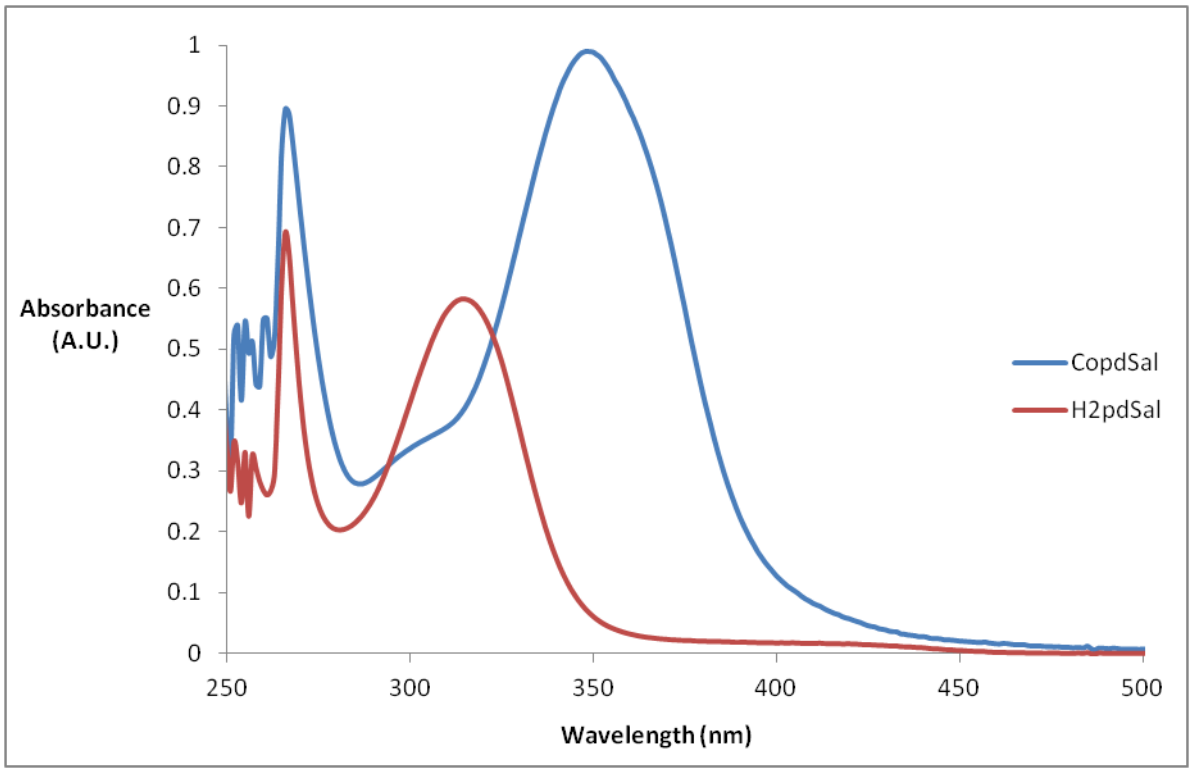

Figure 4.40: UV-visible spectra of 77.4 μM Ar-purged ***(1)*** and H_2pdSal in DMF

4.2.5.2. Cyclic voltammetry of the H_2pdSal ligand

Though the ligand was not readily apparent within UV-monitored electrolysis of ***(1)***, it is of importance to assess whether H_2pdSal undergoes any electrochemical reductions prior to -2.71 V. If this is the case, and if ***(1)*** liberates the pentadentate ligand upon reduction of the complex, the ligand would undergo reduction/s also, and therefore changes to the expected UV spectrum of H_2pdSal.

The reductive electrochemistry of H_2pdSal under Ar and Ar with 5% water appears in Figure 4.41.

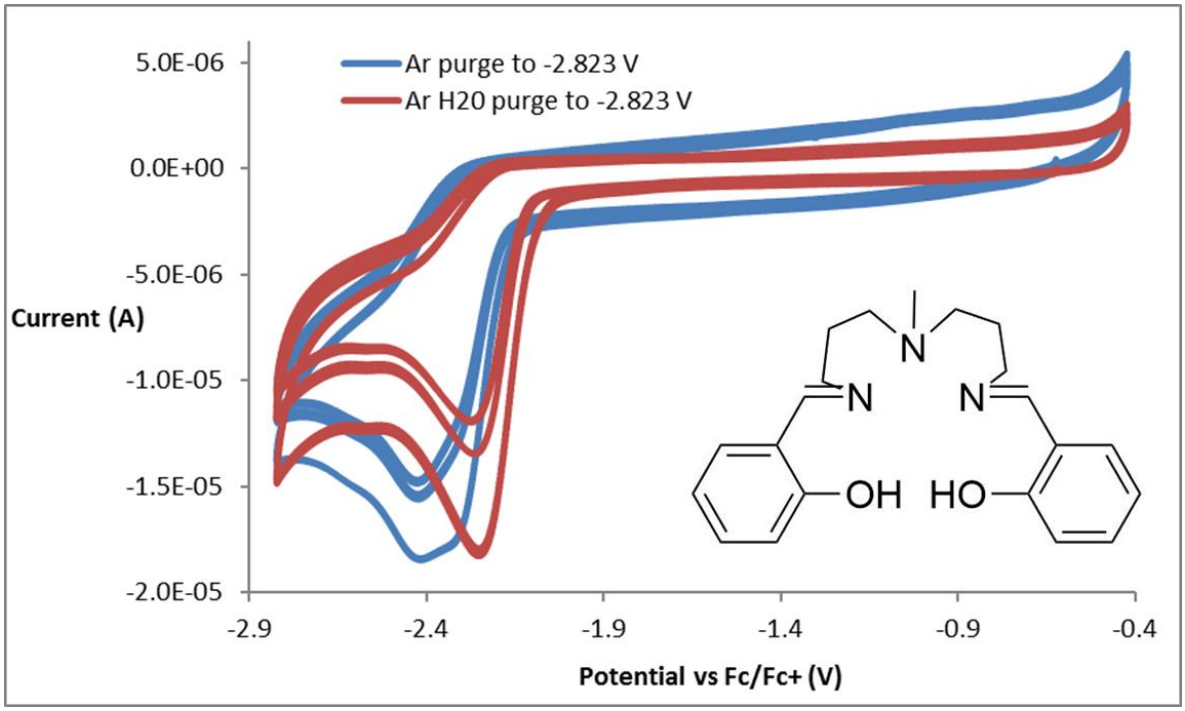

Figure 4.41: Reductive cyclic voltammetry of ~2 mM H_2pdSal in DMF with 0.1 M $TBAPF_6$ in the absence and presence of 5% water. Scans were undertaken at a glassy carbon electrode (ν = 100 mV s^{-1}) with switching potential of -2.82 V vs Fc/Fc^+.

As is shown in Figure 4.41, the absence of water shows the presence of at least two reductions with very close E_{pc}s (unresolved) at approximately -2.4 V. With the introduction of 5% water, the first reduction shifts anodically (E_{pc} of -2.25 V). No other processes were observed within the reductive window prior to solvent/electrolyte reduction. No information has been found within the literature for the same or similar pentadentate ligand. H_2pdSal is stated to be electrochemically inactive prior to -1.5 V vs SCE in MeCN [50] (i.e. -1.9 V vs Fc/Fc^+ [51]). The electrochemistry of a very similar ligand (containing hydrogen instead of the methyl group) was undertaken in DMF and an irreversible reduction is shown with E_{pc} at approximately -1.8 V vs SCE [52] (~ -2.25 V vs Fc/Fc^+ [53,54]).

The tetradentate H_2bdtChexSal ligand (appearing in chapter three) has previously been reported to be reduced at -2.45 V vs Fc/Fc^+ in DCM [55]. The authors also assessed the electrochemical behaviour of H_2ChexSal and noted an E_{pc} of -2.28 V vs Fc/Fc^+ in MeCN. Within both ligands, akin to H_2pdSal, no return anodic wave was observed. A

similar irreversible reduction was noted by Isse *et al*. regarding H_2Sal (see chapter three) and H_2Salophen in DMF in both the absence and presence of a proton source. It was noted that two equivalents of electrons per molecule were passed in the presence of excess acetic acid [56]. Prior to these reports, H_2Sal and H_2ChexSal were reduced at a lead cathode in DMF containing methanesulphonic acid. Shono *et al*. reported the formation of the respective piperazines (42% and 78% isolated yields) [57]. Open-chain diamines have also been reported from the electroreduction of diimines and it has been stated that solvent polarity may greatly affect whether open-chain or cyclised diamines are produced [58]. On the basis of the aforementioned studies, it is likely that imine reduction is occurring. The cyclised triamine (potential reduction product) of H_2pdSal has not been reported according to Scifinder. One publication exists through Scifinder, whereby the open-chain triamine reduction product of H_2pdSal was synthesised through addition of $NaBH_4$ to H_2pdSal in EtOH [59]. However, UV-visible data associated with the diamine was not provided.

The reversibility of the first reduction/s with and without water was assessed through variation of scan rate from 100 mV s^{-1} to 100 V s^{-1} and the associated voltammograms appear in Appendix C.18 and Appendix C.19 respectively. However, no reversible oxidation was observed in either case.

A further experiment undertaken involved electrolysis of the ligand at a 0.071 cm^2 glassy carbon electrode at -2.71 V vs Fc/Fc^+ in the presence of 5% water. No H_2 was detected, showing that the ligand alone was not a catalyst towards H_2 generation.

4.2.5.3. UV-visible monitored electrolysis of the H_2pdSal ligand at -2.71 V vs Fc/Fc^+, with 15 μl water

The voltammetry of H_2pdSal shows at least two reductions in the absence of water, and one reduction in the presence of 5% water at potentials positive of -2.71 V. Therefore, it was important to monitor the bulk electrolysis of H_2pdSal by UV-visible spectrophotometry. H_2pdSal was electrolysed at carbon paper in the presence of water and the resulting UV-visible and difference spectra appear in Figure 4.42 and Figure 4.43.

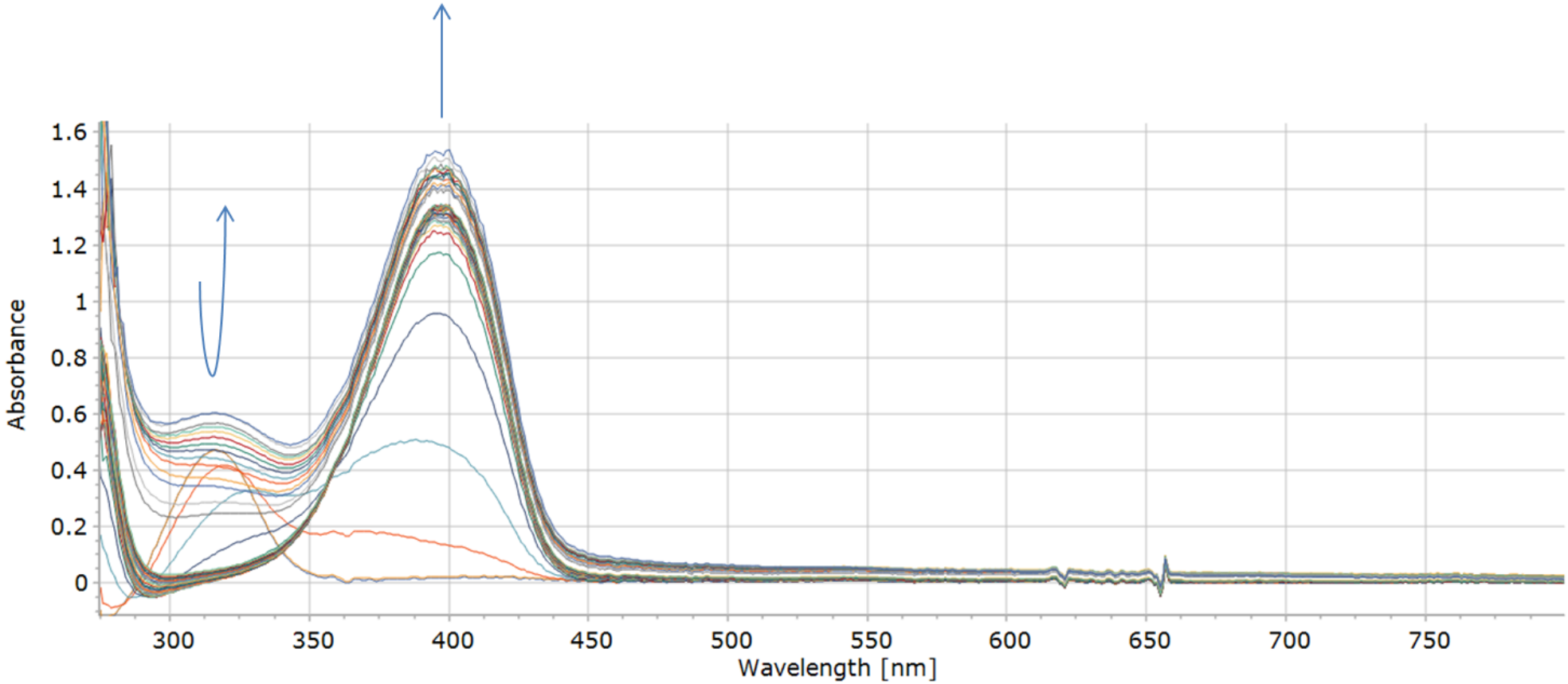

Figure 4.42: UV-visible spectra acquired during the electrolysis of approximately 60 μM H_2pdSal in 15ml DMF/0.1 M $TBAPF_6$ with 15 μl water at -2.71 V vs Fc/Fc^+. The spectra were undertaken up to 120 minutes of electrolysis

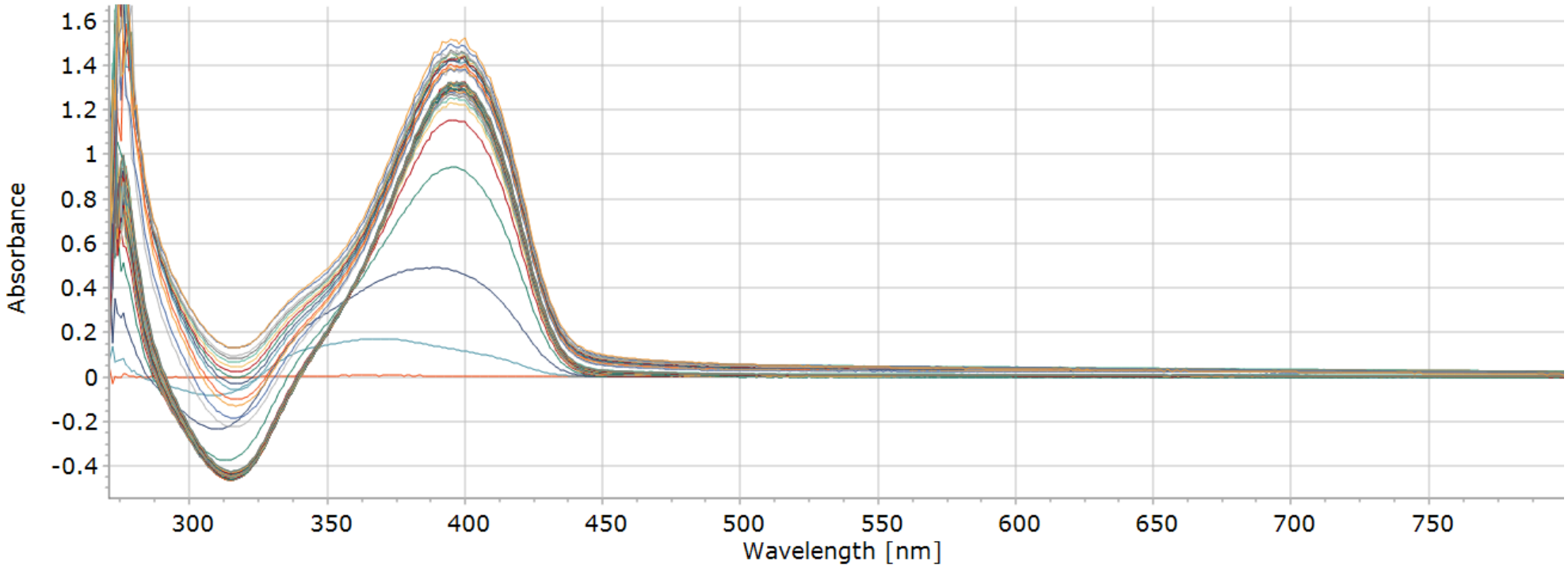

Figure 4.43: UV-visible difference spectra acquired during the electrolysis of approximately 60 μM H_2pdSal in 15ml DMF/0.1 M $TBAPF_6$ with 15 μl water at -2.71 V vs Fc/Fc^+. The spectra were undertaken up to 120 minutes of electrolysis

For clarity, Figure 4.42 is separated into 0 to 900 seconds and 900 to 7200 seconds as at least one further change is evident within spectral feature growth. The separated spectra, including legends, are shown in Appendix C.20 and Appendix C.21 respectively. Additionally, the difference spectra shown in Figure 4.43 are separated into 30 to 900 seconds and 900 to 7200 seconds and feature in Appendix C.22 and Appendix C.23.

Within Figure 4.42 and Figure 4.43, electrolysis of the ligand in the presence of water rapidly produces an intense band with λ_{max} of 396 nm, accompanied by almost full disappearance of the original band at 315 nm within 150 seconds (see Appendix C.20). The band at 396 nm is observed to increase further throughout the experiment, along with a broad increase with λ_{max} of 316 nm following the disappearance of the original band.

The disappearance of the band with λ_{max} of 315 nm occurs within 150 seconds, concomitant with the intense growth at approximately 396 nm. This spectral feature growth that occurs within the ligand was also observed upon electrolysis of ***(1)***, however, at a more prolonged timescale (see Figure 4.38 and Figure 4.39). The prolonged growth of the band with λ_{max} of 398 nm is as expected. In order for the ligand to be released from the complex, the complex must at least undergo electrochemical reduction followed by ligand loss. Electrocatalytic experiments show that the presence of water is required to generate the active catalyst and within the complex' UVs following reduction at -2.71 V, the presence of water shows a far higher growth at approximately 400 nm than that without water during the course of two hours. Furthermore, the electrochemical reduction of the complex (and also the ligand) changes in the presence of water. On the basis of these observations, the reduced (or potentially the twice reduced) complex likely undergoes at least one chemical reaction with a proton, prior to ligand loss.

4.3. Concluding remarks

Throughout chapter four, it has been shown that a heterogeneous deposit forms on glassy carbon and carbon paper electrodes, through the electrolysis of ***(1)*** dissolved in DMF with 0.1 M $TBAPF_6$ and 5% water at -2.71 V vs Fc/Fc^+. The heterogeneous

deposit at the electrode surfaces was shown to be active for the reduction of water at -2.71 V vs Fc/Fc^+.

Initially, electrolysis experiments at glassy carbon showed that dissolved ***(1)*** was more active for H_2 generation under an Ar-purged atmosphere than was the complex under an environment of CO_2. Voltammetry of the complex revealed different electrochemical processes in the presence of water than without water. Further electrolysis experiments at glassy carbon revealed an electroactive deposit on the surface of the electrode. Moreover, water was required to form the active catalyst and the production of H_2 required the presence of water. At glassy carbon, it was subsequently shown that a second hour of electrolysis of the solution containing ***(1)*** produced ~100 times less H_2 than did the first hour. In DMF/0.1 M $TBAPF_6$, surface-confined voltammetry was not observed, and quantitation of the surface active species was not determined. A 1 mM solution of the ligand, H_2pdSal (DMF with 0.1 M $TBAPF_6$ and 5% water), was additionally electrolysed at -2.71 V and the ligand did not display catalytic behaviour.

Carbon paper based experiments showed that the active heterogeneous electrocatalyst displayed no loss in activity over two hours. Similar results were additionally obtained between interrupted and continuous two hour heterogeneous electrolyses. Furthermore, the second hour of solution electrolysis demonstrated similar activity to that of freshly prepared solution. The electrode created from the second hour of electrolysis was also shown to be electrocatalytically active towards heterogeneous H_2 generation. Formation of the active catalyst through physisorption of ***(1)*** was excluded through soaking an electrode in a solution containing ***(1)***, and subsequent electrolysis in DMF/0.1 M $TBAPF_6$/5%. Within this experiment, two orders of magnitude less H_2 was evolved with a fall in FE_{H2} of 79% to 14%.

Time-dependent experiments were undertaken over the course of the first hour for solution hour one and surface-1 hour one experiments in addition to the control one hour experiment. The Faradaic efficiency towards H_2 was found to be lower in the cases of solution electrolyses than surface-1 electrolyses. Particularly poor efficiency towards H_2 generation was observed at the initial stages of the experiment (5 min time point), suggesting that the charge consumed during formation of the active catalyst is more prevalent at earlier stages of electrolyses. Each of the solution hour 1, surface-1 1 hour and control produced a linear response for charge relative to time. The number of moles

of H_2 generated over time also produced relatively linear responses. However, a more significant intercept alludes to an induction phase within solution experiments that is further suggestive of formation of the active catalyst over time.

Field emission scanning electron microscopy was undertaken on electrodes to investigate the morphology and the identity of the active catalytic species. Unusually, only a coating-like deposition was observed following preparation of the active electrode during the first hour of solution electrolysis, which was not suitable for effective EDX analysis. The second hour of solution electrolysis produced a spatially and topographically rich Co-containing deposition. SEM analysis of electrodes used towards heterogeneous electrocatalysis showed plate-like formation, of which EDX confirmed the presence of cobalt. Furthermore, nano-spheres were noted on a surface-1 2 hours electrode, and were shown by EDX (with an elemental map) to distinctively contain cobalt. In summary, extensive Co-based morphologies were formed.

(1) was electrolysed at carbon paper under varied conditions (at two potentials, both in the presence and absence of water). The *in situ* UV-visible spectroelectrochemical studies showed that an intense band was formed with a λ_{max} of ~ 400 nm.

To better understand the spectroelectrochemical results, the H_2pdSal ligand was synthesised. Voltammetry of the ligand was undertaken in the absence and presence of water and in both cases, reduction/s occurred prior to the experimental potential of -2.71 V vs Fc/Fc^+. Therefore, H_2pdSal was electrolysed at -2.71 V in the presence of water and monitored by UV-visible spectrophotometry. This experiment suggests that the band observed at approximately 400 nm during the electrolysis of ***(1)*** was due to the reduction product of the free ligand.

It is evident that a heterogeneous cobalt containing deposit is formed from the electrolysis of ***(1)*** at -2.71 V vs Fc/Fc^+ in DMF/0.1 M $TBAPF_6$/5% water. However, the above evidence suggests that the ligand is not retained in the deposit.

4.4. References

[1] H. Osgood, S. V. Devaguptapu, H. Xu, J. Cho, G. Wu, *Nano Today* **2016**, *11*, 601–625.
[2] R. Vittal, K.-C. Ho, *Catal. Rev.* **2015**, *57*, 145–191.
[3] L. Peraldo Bicelli, C. Romagnani, M. Rosania, *J. Electroanal. Chem. Interfacial Electrochem.* **1975**, *63*, 238–244.
[4] S. P. Jiang, A. C. C. Tseung, *J. Electrochem. Soc.* **1991**, *138*, 1216–1222.
[5] M. Rojas, C. L. Fan, H. J. Miao, D. L. Piron, *J. Appl. Electrochem.* **1992**, *22*, 1135–1141.
[6] N. Kaeffer, M. Chavarot-Kerlidou, V. Artero, *Acc. Chem. Res.* **2015**, *48*, 1286–1295.
[7] C. C. L. McCrory, C. Uyeda, J. C. Peters, *J. Am. Chem. Soc.* **2012**, *134*, 3164–3170.
[8] N. Kaeffer, A. Morozan, J. Fize, E. Martinez, L. Guetaz, V. Artero, *Acs Catal.* **2016**, *6*, 3727–3737.
[9] S. Cobo, J. Heidkamp, P.-A. Jacques, J. Fize, V. Fourmond, L. Guetaz, B. Jousselme, V. Ivanova, H. Dau, S. Palacin, et al., *Nat. Mater.* **2012**, *11*, 802–807.
[10] T. K. Mukhopadhyay, N. L. MacLean, L. Gan, D. C. Ashley, T. L. Groy, M.-H. Baik, A. K. Jones, R. J. Troyitch, *Inorg. Chem.* **2015**, *54*, 4475–4482.
[11] R. Narayanan, M. McKinnon, B. R. Reed, K. T. Ngo, S. Groysman, J. Rochford, *Dalton Trans.* **2016**, *45*, 15285–15289.
[12] C. E. Dahm, D. G. Peters, *J. Electroanal. Chem.* **1996**, *402*, 91–96.
[13] I. Sasaki, D. Pujol, A. Gaudemer, A. Chiaroni, C. Riche, *Polyhedron* **1987**, *6*, 2103–2110.
[14] P. Zanello, R. Cini, A. Cinquantini, P. L. Orioli, *J. Chem. Soc. Dalton Trans.* **1983**, 2159–2166.
[15] P. T. Kissinger, W. R. Heineman, *J. Chem. Educ.* **1983**, *60*, 702.
[16] G. A. Mabbott, *J. Chem. Educ.* **1983**, *60*, 697.
[17] F. G. Thomas, G. Henze, *Introduction to Voltammetric Analysis: Theory and Practice*, Csiro Publishing, **2001**.
[18] G. R. Kiani, N. Arsalani, M. G. Hosseini, A. A. Entezami, *J. Appl. Polym. Sci.* **2008**, *108*, 2700–2706.
[19] C. G. Zoski, *Handbook of Electrochemistry*, Elsevier, **2006**.
[20] N. Queyriaux, R. T. Jane, J. Massin, V. Artero, M. Chavarot-Kerlidou, *Coord. Chem. Rev.* **2015**, *304–305*, 3–19.
[21] E. S. Wiedner, R. M. Bullock, *J. Am. Chem. Soc.* **2016**, *138*, 8309–8318.
[22] S. C. Marinescu, J. R. Winkler, H. B. Gray, *Proc. Natl. Acad. Sci.* **2012**, *109*, 15127–15131.
[23] C. H. Lee, D. Villágran, T. R. Cook, J. C. Peters, D. G. Nocera, *ChemSusChem* **2013**, *6*, 1541–1544.
[24] D. T. Sawyer, G. Chiericato, C. T. Angelis, E. J. Nanni, T. Tsuchiya, *Anal. Chem.* **1982**, *54*, 1720–1724.
[25] E. Anxolabéhère-Mallart, C. Costentin, M. Fournier, S. Nowak, M. Robert, J.-M. Savéant, *J. Am. Chem. Soc.* **2012**, *134*, 6104–6107.
[26] Bruker, "Periodic_Table_and_X-ray_Energies.pdf," can be found under https://www.bruker.com/fileadmin/user_upload/8-PDF-Docs/X-rayDiffraction_ElementalAnalysis/HH-XRF/Misc/Periodic_Table_and_X-ray_Energies.pdf

[27] S. J. B. Reed, *Electron Microprobe Analysis and Scanning Electron Microscopy in Geology*, Cambridge University Press, **2005**.
[28] D. Ivnitski, K. Artyushkova, R. A. Rincón, P. Atanassov, H. R. Luckarift, G. R. Johnson, *Small* **2008**, *4*, 357–364.
[29] Y.-X. Huang, X.-W. Liu, J.-F. Xie, G.-P. Sheng, G.-Y. Wang, Y.-Y. Zhang, A.-W. Xu, H.-Q. Yu, *Chem. Commun.* **2011**, *47*, 5795–5797.
[30] E. Pretorius, *Microsc. Res. Tech.* **2010**, *73*, 225–228.
[31] R. Wuhrer, K. Moran, *IOP Conf. Ser. Mater. Sci. Eng.* **2016**, *109*, 012019.
[32] A.-M. Cao, J.-S. Hu, H.-P. Liang, W.-G. Song, L.-J. Wan, X.-L. He, X.-G. Gao, S.-H. Xia, *J. Phys. Chem. B* **2006**, *110*, 15858–15863.
[33] L. Jiang, L. Huang, Y. Sun, *Int. J. Hydrog. Energy* **2014**, *39*, 654–663.
[34] S. Gao, Y. Lin, X. Jiao, Y. Sun, Q. Luo, W. Zhang, D. Li, J. Yang, Y. Xie, *Nature* **2016**, *529*, 68–71.
[35] J. Yang, H. Liu, W. N. Martens, R. L. Frost, *J. Phys. Chem. C* **2010**, *114*, 111–119.
[36] Y. Yang, H. Fei, G. Ruan, J. M. Tour, *Adv. Mater.* **2015**, *27*, 3175–3180.
[37] J. Goldstein, D. E. Newbury, D. C. Joy, C. E. Lyman, P. Echlin, E. Lifshin, L. Sawyer, J. R. Michael, *Scanning Electron Microscopy and X-Ray Microanalysis: Third Edition*, Springer Science & Business Media, **2012**.
[38] V. T. Yilmaz, I. Degirmencioglu, O. Andac, S. Karabocek, A. M. Z. Slawin, *J. Mol. Struct.* **2003**, *654*, 125–129.
[39] A. A. Emara, A. M. Ali, E. M. Ragab, A. A. El-Asmy, *J. Coord. Chem.* **2008**, *61*, 2968–2977.
[40] R. S. Drago, J. P. Cannady, K. A. Leslie, *J. Am. Chem. Soc.* **1980**, *102*, 6014–6019.
[41] W. R. Heineman, *Anal. Chem.* **1978**, *50*, 390A–402A.
[42] D. F. Rohrbach, W. R. Heineman, E. Deutsch, *Inorg. Chem.* **1979**, *18*, 2536–2542.
[43] E. Szajna-Fuller, A. Bakac, *Eur. J. Inorg. Chem.* **2010**, *2010*, 2488–2494.
[44] V. Artero, M. Chavarot-Kerlidou, M. Fontecave, *Angew. Chem. Int. Ed.* **2011**, *50*, 7238–7266.
[45] M. F. Choi, P. Hawkins, *Talanta* **1995**, *42*, 987–997.
[46] M. F. Choi, *Spectrosc. Lett.* **1997**, *30*, 233–240.
[47] M. P. Lanci, J. P. Roth, *J. Am. Chem. Soc.* **2006**, *128*, 16006–16007.
[48] E. V. Rybak-Akimova, W. Otto, P. Deardorf, R. Roesner, D. H. Busch, *Inorg. Chem.* **1997**, *36*, 2746–2753.
[49] V. V. Smirnov, J. P. Roth, *J. Am. Chem. Soc.* **2006**, *128*, 3683–3695.
[50] Hai-Liang Zhu, Ye-Xiang Tong, Xiao-Lan Yu, Xiao-Ming Chen, *J. Coord. Chem.* **2002**, *55*, 843–852.
[51] V. Béreau, C. Duhayon, A. Sournia-Saquet, J.-P. Sutter, *Inorg. Chem.* **2012**, *51*, 1309–1318.
[52] S. S. Kim, J. H. Choe, Y. G. Choe, B. G. Jeong, *J. Korean Chem. Soc.* **1994**, *38*, 160–168.
[53] N. G. Connelly, W. E. Geiger, *Chem. Rev.* **1996**, *96*, 877–910.
[54] G. A. Andrade, A. J. Pistner, G. P. A. Yap, D. A. Lutterman, J. Rosenthal, *ACS Catal.* **2013**, *3*, 1685–1692.
[55] D. Tomczyk, L. Nowak, W. Bukowski, K. Bester, P. Urbaniak, G. Andrijewski, B. Olejniczak, *Electrochimica Acta* **2014**, *121*, 64–77.
[56] A. A. Isse, A. Gennaro, E. Vianello, *Electrochimica Acta* **1997**, *42*, 2065–2071.
[57] T. Shono, N. Kise, E. Shirakawa, H. Matsumoto, E. Okazaki, *J. Org. Chem.* **1991**, *56*, 3063–3067.
[58] R. W. Koch, R. E. Dessy, *J. Org. Chem.* **1982**, *47*, 4452–4459.

[59] M. R. A. Pillai, C. S. John, J. M. Lo, D. E. Troutner, M. Corlija, W. A. Volkert, R. A. Holmes, *Nucl. Med. Biol.* **1993**, *20*, 211–216.

Chapter 5. Materials and methods

5.1. Synthesis

5.1.1. Synthesis of rhenium 2,2'-bipyridine tricarbonyl chloride ($Re(bpy)(CO)_3Cl$)

Reaction scheme:

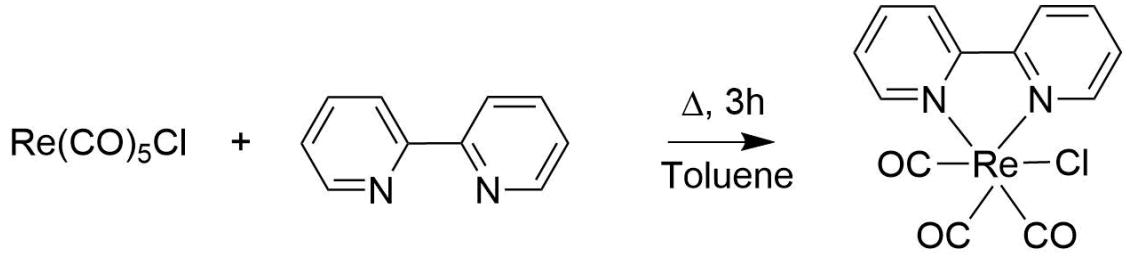

256 mg (0.71 mmol) $Re(CO)_5Cl$ and 109.6 mg (0.702 mmol) 2,2'-bipyridine were added to 35 ml spectroscopic grade toluene in a 100 ml two-neck round-bottomed flask and the solution was purged for 10 minutes with nitrogen. The solution was stirred and heated to reflux for 3 hours under an inert atmosphere. The solution was cooled to room temperature and placed in a freezer for 18 hours. The resulting yellow precipitate was collected by vacuum filtration and washed with toluene, hexane and diethyl ether to afford a yellow powder. Spectroscopic data obtained are in agreement with published data [1,2].

Yield: 300.5 mg, 0.645 mmol, 93%.

400 MHz NMR (d_6-DMSO): 7.77 (td, 2H), 8.35 (td, 2H), 8.77 (d, 2H), 9.03 (d, 2H)

IR (MeCN): υ_{CO} = 2023, 1917, 1900 cm^{-1}

Elemental analysis;

Theoretical (%), C = 33.8, H = 1.75, N = 6.06

Found (%), C = 33.71, H = 1.69, N = 6.03

5.1.2. Synthesis of 5-bromo-2,2'-bipyridine (Brbpy)

Reaction scheme:

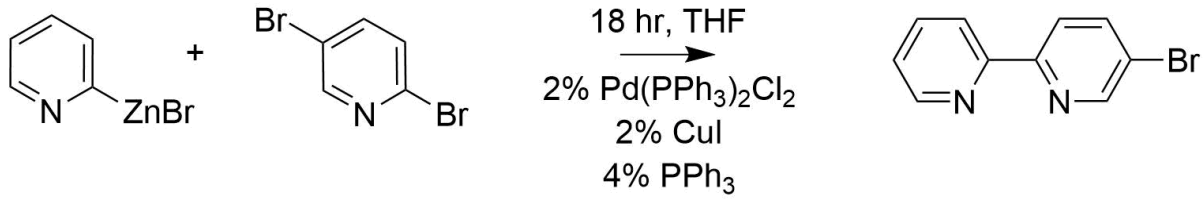

1.1808 g (5 mmol) of 2,5-dibromopyridine, 141.4 mg (0.2 mmol) $Pd(PPh_3)_2Cl_2$, 105.2 mg (0.4 mmol) triphenylphosphine and 37.9 mg (0.2 mmol) copper iodide were placed in a two-necked 25 ml round bottom flask. 10 ml of a 0.5 M 2-pyridylzinc bromide solution in THF was added to the flask through a septum and the reaction was stirred for 18 hours. The resulting light brown suspension was pipetted into 3 x 500 ml portions of saturated Na_2CO_3/EDTA aqueous solution with stirring. This suspension was extracted three times with 100 ml aliquots of dichloromethane. The organic phase was collected, dried with $MgSO_4$ and left to evaporate in ambient conditions. The resulting residue was placed on a silica column and eluted with a 9:1 ratio of hexane to ethyl acetate. Solvents were evaporated in ambient conditions to reveal white flakes. Spectroscopic data obtained is in agreement with published data [3,4].

Yield: 535.2 mg, 46%

400 MHz NMR ($CDCl_3$): 7.32 (ddd, 1H), 7.81 (td, 1H), 7.93 (dd, 1H), 8.31 (d, 1H), 8.36 (d, 1H), 8.66 (d, 1H), 8.71 (d, 1H)

5.1.3. Synthesis of rhenium 5-bromo-2,2'-bipyridine tricarbonyl chloride ($Re(Brbpy)(CO)_3Cl$)

Reaction scheme:

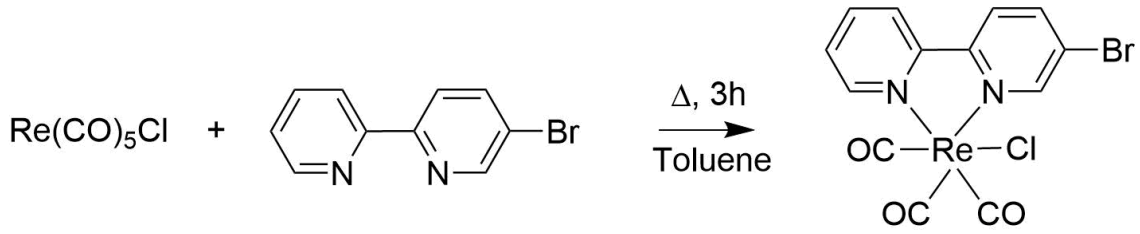

254 mg (0.7 mmol) $Re(CO)_5Cl$ and 165.2 mg (0.7 mmol) 2,2'-bipyridine were added to 35 ml spectroscopic grade toluene in a 100ml two-neck round-bottomed flask and the solution was purged for 10 minutes with nitrogen. The solution was stirred and heated to reflux for 3 hours under an inert atmosphere. The solution was cooled to room temperature and placed in a freezer for 18 hours. The resulting yellow precipitate was collected by vacuum filtration and washed with toluene, hexane and diethyl ether to afford a yellow powder. Spectroscopic data obtained are in agreement with published data of a similar complex ($Re(Brbpy)(CO)_3Br$) [5] .

Yield: 345.6 mg, 0.639 mmol, 91%.

400 MHz NMR ($CDCl_3$): 7.58 (qd, 1H), 8.03 - 8.11 (m, 2H), 8.13 – 8.2 (m, 2H), 9.07 (qd, 1H), 9.12 (d, 1H)

IR (MeCN): υ_{CO} = 2025, 1920, 1903 cm^{-1}

UV λ_{max} (MeCN): ~ 300 nm, 382 nm

5.1.4. Synthesis of bis(5-bromosalicylidene)ethylenediamine (H_2dBrSal)

Reaction scheme:

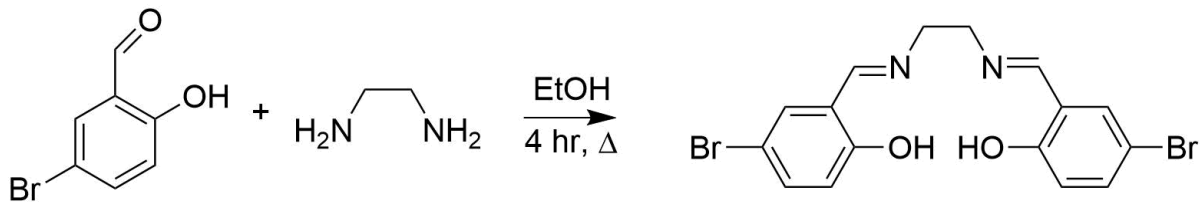

25 ml ethanol, followed by 67.5 μl (1 mmol) ethylenediamine was introduced into a dry two-necked 100 ml round bottom flask. The solution was purged with nitrogen for 10 minutes. 420.5 mg (2.1 mmol) 5-bromosalicylaldehyde was dissolved with heat in 25 ml ethanol and the solution was added dropwise to the RBF and the resulting solution was again purged with nitrogen. The reaction was refluxed for 4 hours. The solution volume was reduced under reduced pressure to approximately 10 ml and placed in the freezer overnight. The solution was vacuum filtered and washed with ethanol to reveal an orange solid. Spectroscopic data obtained are in agreement with published data [6].

Yield: 375.2 mg, 89%

400 MHz NMR (D_6-DMSO): 3.94 (s, 4H), 6.86 (d, 2H), 7.47 (dd, 2H), 7.68 (d, 2H), 8.59 (s, 2H), 13.48 (s, 2H, exchanges with D_2O)

UV λ_{max} (DMF): 411 nm, 350 nm

5.1.5. Synthesis of cobalt bis(5-bromosalicylidene)ethylenediamine monohydrate (CodBrSal)

Reaction Scheme:

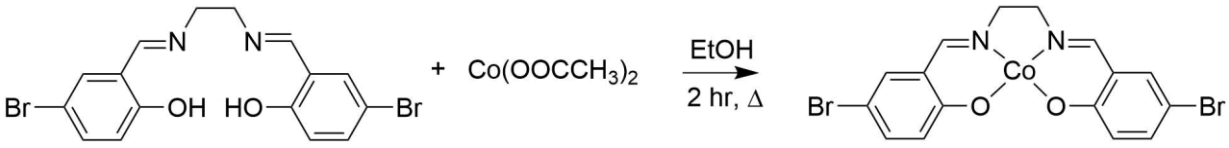

107.9 mg (0.253 mmol) 5,5'-diBrsalen was dissolved in 12.5 ml ethanol and introduced a 50 ml round bottomed flask with stirring. The solution was then heated to 50 ^{0}C. 63.1 mg (0.244 mmol) cobalt acetate tetrahydrate was dissolved in 12.5 ml ethanol and introduced into the solution containing ligand under quick dropwise addition while stirred. A brown colour was observed upon the addition. The solution was refluxed for 2 hours under nitrogen. Upon cooling of the flask, a brown suspension was observed. The contents of the flask were filtered, washed with ethanol and dried under vacuum to afford a brown solid (107.9 mg). The solid was heated to boiling in 100 ml EtOH and the hot solution was vacuum filtered, collected and placed in a vacuum desiccator overnight.

Yield: 97.1 mg, 79 %

UV λ_{max} (DMF): 412 nm (495 nm, sh.), 355 nm

MS-ESI: [M+2] m/z = 483.0 (100%)

Elemental analysis;

Theoretical (%): C = 38.35, H = 2.82, N = 5.59

Found (%): C = 38.87, H = 2.8, N = 5.31

5.1.6. Synthesis of Bis[3-(salicylidenamino)propyl]methylamine (H_2pdSal)

Reaction scheme:

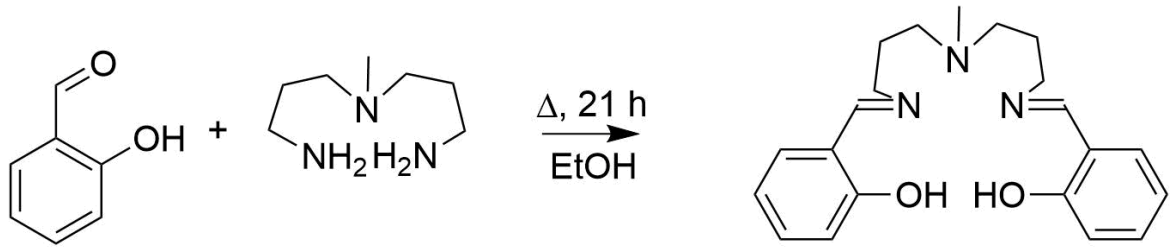

100 ml ethanol was added to a 250 ml round bottom flask, followed by 1.21 ml (11.35 mmol) salicylaldehyde. The solution was stirred. 0.915 ml (5.67 mmol) 3,3'-diamino-N-methyldipropylamine was added. The solution was purged with nitrogen for 10 minutes, prior to refluxing for 21 hours under N_2. The solvent was removed under reduced pressure to reveal an orange oil. Spectroscopic data obtained are in agreement with published data [7].

Yield: 1.9425 g, 97%

400 MHz NMR ($CDCl_3$): 1.86 (p, 4H), 2.33 (s, 3H), 2.43 (t, 4H), 3.63 (td, 4H), 6.85 (td, 2H), 6.95 (d, 2H), 7.22 (dd, 2H), 7.29 (qd, 2H), 8.34 (s, 2H), 13.59 (s, 2H, exchanges with D_2O)

UV λ_{max} (DMF): 315 nm (7,900 L mol^{-1} cm^{-1}), 408 nm (250 L mol^{-1} cm^{-1})

5.2. Instrumentation and methods

5.2.1. Gas chromatography

All gas chromatography within this thesis was undertaken with a Shimadzu GC-2010, equipped with a micropacked column (Restek ShinCarbon ST, of length 2 m and ID 0.53 mm) and a barrier ionisation detector (BID). The oven of the GC containing the column was maintained at 30 ^{0}C during the course of approximately 6 minute runs in the absence of CO_2. Where samples contained CO_2, the run time was extended to 24 minutes. The carrier gas (helium, BIP grade, Air Products) was passed through the column at a rate of 10 ml min^{-1}. Approximate retention times of the gases of interest were 0.7 mins, 2.2 mins, 5.5 mins and 17 mins for H_2, CO, CH_4 and CO_2 respectively. The BID was maintained at 220 ^{0}C. The GC contains a sample loop of approximate 250 μl volume. The injection method allows for purging the void volumes with sample, followed by filling of the loop.

5.2.1.1. Standards and sample injection

100, 1,000 and 10,000 ppm standard mixes of gases (H_2, O_2, CO, CH_4, CO_2, balance of He) were procured from Scientific and Technical Gases (STG). Approximately 1.1 ml of the standard was withdrawn with a valve-lock 1 ml syringe (Valco VICI A-2). Immediately prior to injection, the valve of the syringe was opened to remove excess gas pressure, the volume adjusted to 1 ml, and the valve was closed again. The standard was injected into the GC through the sampling loop. The standard with expected response closest to that of the sample was utilised for calculation and a minimum of two standards of this concentration were injected each day of analysis. Following standard or sample injection, at least 20 ml air was flown through the loop to exhaust to avoid gas carry-over between runs.

Injection of the headspace of samples was undertaken in the same manner as the standards, with the exception that only 1 ml was withdrawn and the pressure within the syringe was not alleviated. 1 ml of headspace was also withdrawn from the auxiliary electrode compartment to avoid movement of solution across the frit of the H-cell.

Injections of the auxiliary electrode compartment within chapter three were additionally undertaken. The frit disallowed gas movement. Therefore, the removal of gas from the auxiliary electrode compartment within chapter four experiments was solely to avoid a pressure difference across the cell.

5.2.1.2. Calculation of gas generated, TON and Faradaic efficiency

The ideal gas law was used to calculate the number of moles of gaseous product generated. The internal pressure was assumed to be 1 atm. The temperature (of the room, average of approximately 18-19 ^{0}C) was measured upon time of injection. The volume of the headspace was measured through calculating the total volume of the working electrode compartment (working and reference electrodes and stirrer bar included) and subtracting the volume of solution added.

The concentration (ppm) of the headspace of a particular gas was calculated by dividing the standard concentration (ppm) by the standard integrated area, and multiplying by the sample integrated area.

The number of moles in the headspace within the sample was calculated with Equation 5.1.

$$n = \frac{\left(\left(\frac{PV}{RT}\right) sample\ concentration\ in\ ppm\right)}{1{,}000{,}000} \qquad \text{Equation 5.1}$$

Whereby P = 101,325 Pa, V is the volume of the headspace (m^3), R is the gas constant of 8.314 Pa m^3 mol^{-1} K^{-1} and T is temperature (K).

Essentially, the sample concentration / 1,000,000 provides a decimal value of the amount of gas in the headspace.

Henry's law was not applied to account for any gaseous products remaining dissolved.

With the number of moles of gas derived, the TON was calculated by dividing the moles of gas by the number of moles of catalyst dissolved in solution. Within each "solution"/homogeneous electrolysis, a 15 ml volume and 1 mM catalyst concentration was used, thereby equating to 15 μmol catalyst. Therefore, any such experiment quoting

the number of moles generated may be converted to TON by dividing the moles generated by 1.5×10^{-5}.

Faradaic efficiency was calculated as follows. The moles of electrons consumed was obtained through division of charge (C) by Faraday's constant (96,485 C mol^{-1}). The number of moles of product (accounted for by GC) multiplied by the amount of electrons required to convert the gas (i.e. 2 H^+ to H_2 = 2, CO_2 to CO = 2, CO_2 to CH_4 = 8) accounts for the moles of electrons consumed by the specific product. The moles of electrons accounted for by the specific product is then divided by the moles of electrons consumed, x 100 calculating % Faradaic efficiency.

5.2.2. Electrochemistry

5.2.2.1. Voltammetry and bulk electrolyses (controlled potential electrolyses/Coulometry)

Voltammetry was undertaken with a CH Instruments 600E potentiostat. Glassy carbon working electrodes of 3 mm diameter (CH Instruments, CHI 104, 0.071 cm^2 area) were employed. The working electrodes were cleaned with polishing on cloth pads, using 0.3 and 0.05 μm alumina, with up to 3 minute sonications in deionised water following each grade of alumina. Finally, prior to organic experiments, the electrodes were sonicated in acetonitrile to remove residual water from the previous sonication.

Silver/silver ion (Ag/Ag^+) reference electrodes were purchased as Ag/AgCl electrodes (CH instruments, CHI 111) and conditioned. The original KCl solution was removed and the electrode was washed multiple times with deionised water (to dissolve any KCl that would otherwise precipitate upon addition of MeCN), followed by multiple washings with MeCN. The silver chloride coating on the wire was stripped physically with the use of 800 grit sandpaper (procurable from hardware stores), until a metallic wire was apparent. To minimise a liquid junction potential between the reference electrode and working electrode, it is recommended to use the same solvent utilised in electrochemical experiments as the filling solution solvent [8–10]. However, with utilisation of DMF as the internal filling solvent, a dark gray precipitate was observed.

Due to the likely scenario that DMF was reducing $AgNO_3$ to Ag^0 [11,12], the electrode filling solution contained 10 mM $AgNO_3$ and 100 mM $TBAPF_6$ dissolved in MeCN.

The inside of the fitting holding the silver wire was also filled, as it was noted that any significant gaseous voids within the electrode corresponded to filling solution leakage through the porous frit (therefore leading to the increased likelihood of Ag^+ in solution). The electrode was stored with the frit immersed in the filling solution when not in use. The electrodes were reconditioned approximately every two days when in prolonged contact with DMF, and approximately once a week in other circumstances.

The auxiliary (counter) electrode utilised was in all cases (aside from UV-visible-NIR and IR spectroelectrochemical experiments) a platinum mesh of approximate dimensions 1.5 x 1.5 cm, purchased from Goodfellow. The mesh was attached to a crocodile clip (nickel plated stainless steel, Radionics) which was soldered to a copper wire. The platinum mesh was electrochemically cleaned via cycling in 0.5 M H_2SO_4.

All connectors of electrodes (copper wire in the case of the counter electrode) were threaded through septa (Chemglass CG-3022-28), allowing for the setup of a deaerated cell.

The electrochemical cell employed for all electrolyses and all voltammetry (with the exception of UV-visible-NIR and IR spectroelectrochemistry and electrochemistry of $Re(qpy)(CO)_3Cl$ and RuRe, chapter two) was a custom-built H-cell (Yorlab) containing a sintered glass frit separating the cathode and anode. The total volume of each compartment, excluding electrode/stirrer bar/septa volumes, was approximately 34 cm^3. The electrochemical cell employed for RuRe and $Re(qpy)(CO)_3Cl$ was a V-shaped cell, whereby the working electrode was placed through one septum and the reference and counter (coiled Pt wire) electrodes through the other, allowing the working electrode to be angled towards both the reference and counter electrodes.

Every voltammetric experiment and electrolysis (with the exception of UV-visible-NIR and IR spectroelectrochemistry) was referred to an internal standard of ferrocene (Fc/Fc^+ couple), which was added following each experiment.

Voltammetric scans were initiated at the open circuit potential (OCP) and scans were undertaken with successively widening the potential window. Unless otherwise stated, the cell was not iR compensated. Where the cell was stated to be iR compensated, the

OCP was measured repeatedly to ensure stability. Once stable, an iR compensation test was undertaken at the OCP value and the scans following the test were iR compensated.

Where voltammetry was not undertaken prior to fixed potential experiments, the reference electrode was placed in a solution of the same electrolyte composition as that in which electrolysis would take place, and ferrocene. The reference electrode was deemed to be stable when a maximum of 1 mV difference was observed between the $E_{1/2}$ of Fc/Fc^+ as measured over the course of the previous hour. Ferrocene was also added post-electrolysis to verify that potential did not shift significantly.

Electrolyses (aside from within UV-visible-NIR and IR spectroelectrochemistry) were undertaken at glassy carbon, graphite rod and plate (for material suitability testing, as discussed in chapter three with the aid of $Re(bpy)(CO)_3Cl$) or carbon paper working electrodes and is specified within each section. Stirring, with uniform speed setting, was undertaken in both compartments of the cell with the use of approximately 2 cm length stirrer bars with a Bibby HB502 ceramic hotplate.

The dimethylformamide and acetonitrile utilised within voltammetric and electrolytic experiments were anhydrous (99.8 %, <0.005 % H_2O), obtained from Sigma Aldrich and used without further purification. The solvents were withdrawn using a Schlenk line with positive pressure of nitrogen.

5.2.2.1.1 Preparation of carbon paper electrodes

The carbon paper utilised throughout the experiments was Toray carbon fiber composite, containing 5% PTFE (acquired from Fuel Cell Store), with dimensions of 40 cm x 40 cm x 370 μm. The large sheet was cut into electrodes of specific dimensions with the use of a scalpel and tracing paper above (with measured markings of sizes) and below the carbon paper. Prior to their use, each electrode was sonicated in acetone for approximately 7 minutes. The acetone was decanted and the electrode was dried at 70 ^0C for approximately 13 minutes. Each electrode contained a groove (not submerged in solution) that allowed contact with a crocodile clip. Due to the thinness of the carbon paper, an additional piece of carbon paper was added between the crocodile clip and the groove to avoid breaking the material through direct clamping. The crocodile clip

remained in the cell, with copper wire wound around the handle and the copper wire was fed through the septum.

Prior to SEM analysis of the carbon paper, the working electrodes were rinsed on both sides with 3 ml DMF and the thin sides were dabbed on lens tissue. The electrodes were further allowed to dry on lens tissue in a cupboard for a minimum of three days.

5.2.2.2. UV-visible spectrelectrochemistry (UV-vis monitored bulk electrolyses) (chapter four)

UV-visible monitored electrolyses were undertaken in the same manner as standard electrolyses with the following notes/adjustments. Carbon paper (1.5 cm x 1 cm x 370 μm) was utilised as working electrode. The standard H-cell was incorporated, following an assessment of the spectral cut-off point. The sample holder of the Agilent 8453 UV-visible spectrophotometer was removed and an IKA Lab Disc S2 miniature stirring plate was propped up in a level manner to an adequate height to allow the beam to pass through the cell. Stirring of the cell was undertaken throughout each experiment.

The working electrode was wedged towards the frit between the cathodic and anodic compartments, whereas the reference electrode was inserted at approximately the opposite angle, therefore allowing the beam to pass unobstructed, through the widest part of the cell. Due to the increased path length (approximately 2.5-3 cm) of the cell as compared to a conventional 1 cm cuvette, reduced concentrations (60 μM) of the complex/ligand was used. The spectrophotometer was zeroed with the electrolyte not containing the complex/ligand and tested repeatedly to ensure that cell repositioning allowed for a smooth baseline.

Following this, an aliquot of solution containing the complex/ligand was introduced. A UV-visible spectrum was acquired to ensure that starting spectra were within range. The cell was degassed with Ar for approximately 20 minutes. The cell was placed in the path of the beam again. The cell was wired and stirring commenced. Prior to application of the fixed potential (determined from voltammetry at 100 mV s^{-1} with glassy carbon), a t_0 spectrum was undertaken. Spectra were acquired for t_{30}, t_{60} and every minute to one hour and every 5 minutes thereafter. Due to the rapid initial change within the ligand,

spectra were acquired every 30 seconds. The experiments were undertaken in the absence of light. The data was processed with Spekwin and Spectragryph softwares.

5.2.2.3. UV-visible-NIR spectroelectrochemistry (chapter two)

UV-vis SEC was undertaken with a JASCO V-670 UV-visible-NIR spectrophotometer. A custom-built 2 mm path length quartz UV cell with cylindrical reservoir was employed. The 3-electrode cell consisted of Pt mesh attached to Pt wire working electrode, placed in the window of the cell, a silver wire reference electrode and Pt wire counter electrode (both shielded from contact with a glass capillary). To trace the processes without electrolysing large amounts of solution, a glassy carbon working electrode was placed into the reservoir. Light was shielded from the solution at all times. The total volume of solution per analysis was 5 ml. The solution was not degassed. However, anhydrous MeCN was utilised.

5.2.2.4. IR spectroelectrochemistry (chapter two)

An optically transparent thin layer electrochemical (OTTLE) cell with CaF_2 plates was utilised for IR spectroelectrochemistry in conjunction with a Perkin Elmer Spectrum GX spectrometer. This cell consists of a platinum mesh working electrode placed in the IR cell window, with platinum mesh counter and silver wire reference electrodes. The electrolyte in the experiment was 0.1 M $TBAPF_6$ in MeCN. Approximately 0.1 ml of solution was required per experiment. The solutions were not prepared or introduced under an inert atmosphere, however, anhydrous MeCN was utilised.

5.2.3. Photocatalysis (chapter two)

The photocatalytic apparatus consisted of a double manifold schlenk line in which a premier grade CO_2 cylinder and vacuum pump were attached, a large sample preparation chamber containing a vial holder and schlenk flasks with concentrated sample, for each required component (Cat, PS and sacrificial donor (SD)). The viscosity of triethanolamine resulted in the requirement of its dilution in a 1:1 ratio with the

solvent utilised within experiments, prior to sample preparation. Triethylamine and MeCN were refluxed with CaH_2 and distilled prior to their uses. In the cases of DMF and DMA, anhydrous solvents (Sigma-Aldrich) were used without further purification. Triethanolamine was also used without further purification.

Following preparation of the concentrated samples in separate schlenk flasks, each of the flasks was degassed by vacuum and refilled with CO_2 for whichever was greater of either three cycles or until bubbling under vacuum was no longer apparent. The sample chamber was also evacuated and refilled three times with CO_2. The individual samples were introduced in the order of PS, Cat and SD, upon high flow of CO_2 (to avoid air entering the sample chamber). The single-piercable sample lids were applied and the vials were placed at a constant distance from the LED light sources. The process was repeated until samples (in triplicate) were prepared for each of the 355 nm, 470 nm and > 400 nm light sources and the dark control. The vial size was in total, 4.9 ml, with 2 ml occupied by the sample.

The 355 nm and 470 nm samples were irradiated with fan assistance to avoid potential heating. Ambient light was shielded from solutions at all times during preparation, irradiation and sampling. The 355 and 470 nm LED strips were manufactured in-house. The visible LED source was purchased from Halfords. The power output of the 355 nm, 470 nm and visible LED sources was measured to be 3, 62 and 12 W m^2 respectively with a Delta Ohm HD2102.2 photoradiometer equipped with either an LP471 UVA or LP471 RAD irradiance probe. Sample irradiation was undertaken for 21 hours.

As a comparative method of photocatalytic sample preparation, samples (containing $[Ru(bpy)_3]^{2+}$, $Re(bpy)(CO)_3Cl$ and TEOA (16.7 % v/v) in DMF) were purged directly with a 20 minute sparge of CO_2, whereby there was negligible difference in the amount of CO detected as compared to the Schlenk technique.

5.2.4. SEM and EDX

SEM and EDX analysis was undertaken in DCU with the help of Mr. Colm Montgomery. The field emission scanning electron microscope utilised is a Hitachi S5500, whereby secondary electron detection was undertaken. The accelerating voltage is specified with each micrograph, as is the probe current. The EDX utilised is an Oxford Instruments Pentafet detector.

5.2.5. Characterisation of synthesised complexes

NMR was undertaken with a Bruker Avance Ultrashield 400 MHz nuclear magnetic resonance spectrometer, whereby the deuterated solvents were procured from Sigma Aldrich. IR spectra were acquired with a Perkin Elmer Spectrum GX IR spectrometer. UV visible spectra were acquired with an Agilent 8453 UV-visible spectrophotometer. Elemental analyses and mass spectra were acquired within the University of Groningen.

5.3. Chemicals and materials

All chemicals related to synthesis, in addition to tetrabutylammonium hexafluorophosphate (electrochemical grade, ≥ 99%, calcium hydride (95%)), triethanolamine (≥ 99%), CobdtChexSal ((R,R)-N,N′-bis(3,5-di-tert-butylsalicylidene)-1,2-cyclohexanediaminocobalt(II)), CopdSal (bis(salicylideniminato-3-propyl)methylaminocobalt(II), 97%), CoSal (N,N′-bis(salicylidene)ethylenediaminocobalt(II), 99%), anhydrous dimethylformamide (≥ 99.8%) anhydrous dimethylacetamide (≥ 99.8%) and anhydrous acetonitrile (≥ 99.8%) were purchased from Sigma Aldrich and used as received. Triethylamine (≥ 99%) was also purchased from Sigma Aldrich, prior to distillation over CaH_2.

Premier/zero grade CO_2, Ar and N_2 were purchased from Air Products/BOC gases.

RuRe, $Re(qpy)(CO)_3Cl$ and the qpy ligand (chapter two) were synthesised in-house by Dr. Nivedita Das. $Ru(bpy)_3Cl_2$ was additionally synthesised within the group.

5.4. References

[1] E. Portenkirchner, D. Apaydin, G. Aufischer, M. Havlicek, M. White, M. C. Scharber, N. S. Sariciftci, *ChemPhysChem* **2014**, *15*, 3634–3638.
[2] S. Sato, T. Morimoto, O. Ishitani, *Inorg. Chem.* **2007**, *46*, 9051–9053.
[3] A. Paul, Synthesis and Characterisation of Polypyridyl Metal Complexes for New Fuels, doctoral, Dublin City University. School of Chemical Sciences, **2012**.
[4] N. Das, Metal Carbonyl Complexes and Porphyrin Macrocyles: Photochemistry and Potential Therapeutic Applications, doctoral, Dublin City University. School of Chemical Sciences, **2014**.
[5] R. N. Hanson, R. Kirss, E. McCaskill, E. Hua, P. Tongcharoensirikul, S. L. Olmsted, D. Labaree, R. B. Hochberg, *Bioorg. Med. Chem. Lett.* **2012**, *22*, 1670–1673.
[6] P. E. Aranha, M. P. dos Santos, S. Romera, E. R. Dockal, *Polyhedron* **2007**, *26*, 1373–1382.
[7] G. Rogez, A. Marvilliers, E. Rivière, J.-P. Audière, F. Lloret, F. Varret, A. Goujon, N. Mendenez, J.-J. Girerd, T. Mallah, *Angew. Chem. Int. Ed.* **2000**, *39*, 2885–2887.
[8] A. J. Bard, L. R. Faulkner, *Electrochemical Methods: Fundamentals and Applications*, Wiley, **2000**.
[9] G. Gritzner, in *Handb. Ref. Electrodes* (Eds.: G. Inzelt, A. Lewenstam, F. Scholz), Springer Berlin Heidelberg, **2013**, pp. 25–31.
[10] V. V. Pavlishchuk, A. W. Addison, *Inorganica Chim. Acta* **2000**, *298*, 97–102.
[11] X. Zhang, B. Shi, X. Liu, *Desalination Water Treat.* **2013**, *51*, 3762–3767.
[12] I. Pastoriza-Santos, L. M. Liz-Marzán, *Langmuir* **1999**, *15*, 948–951.

Chapter 6: Conclusion and future work

This thesis focussed on investigating complexes as catalysts towards light-assisted and electrochemically driven proton and carbon dioxide reduction.

Chapter two aimed to establish whether the two directly attached bipyridyl units of 2,2':5',3'':6'',2'''-quaterpyridine could perform as an efficient bridging ligand between a bisbipyridyl ruthenium photosensitising unit and rhenium tricarbonyl chloride catalytic centre. The resulting intramolecular complex of RuRe was assessed in a solvent- and electron donor-optimised system, and it was evident that the intermolecular system of $[Ru(bpy)_3]^{2+}$ with $Re(bpy)(CO)_3Cl$ performed with a higher level of activity than did RuRe, generating a maximal TON_{CO} of 35 as compared to 7 at $\lambda > 400$ nm and $\lambda = 470$ nm respectively.

Further experiments within the chapter focussed on why a lower level of activity was observed for RuRe than the intermolecular system. Electrochemistry was undertaken on RuRe and $Re(qpy)(CO)_3Cl$, and compared to $[Ru(bpy)_3]^{2+}$ and $Re(bpy)(CO)_3Cl$. Cyclic voltammetry revealed that the first reductions of the Ru and Re subunits of RuRe occurred significantly positive (340 and 120 mV respectively) to those of the mononuclear counterparts, $[Ru(bpy)_3]^{2+}$ and $Re(bpy)(CO)_3Cl$ respectively. With comparison to the electrochemistry of $Re(qpy)(CO)_3Cl$ (and $[(bpy)_2Ru(qpy)Ru(bpy)_2]^{4+}$ from the literature), the first and second reductions of RuRe were determined to be the Ru and Re subunit's ligand-based reductions respectively, whereas $[Ru(bpy)_3]^{2+}$ and $Re(bpy)(CO)_3Cl$ demonstrated very similar first reduction potentials.

Oxidative UV-vis-NIR spectroelectrochemistry (SEC) was undertaken to determine whether an intervalence charge transfer band was present. Unfortunately, complete and/or selective oxidation of one metal centre was not achieved, due to the similar potentials at which the Ru and Re centres were oxidised. Therefore, it was not conclusive by this method as to whether ground state communication exists between the metal centres. IR-SEC was undertaken to assess the effects of oxidising one or both metal centres. Two sets of stretching vibrations were observed. Similar to that achieved with the oxidation of $Re(qpy)(CO)_3Cl$ and $Re(bpy)(CO)_3Cl$, the first oxidation of RuRe

resulted in a formation consistent with a Re tricarbonyl complex. The second oxidation, was however, not typical of a Re tricarbonyl species.

The energies associated with oxidative and reductive quenching pathways of both RuRe and $[Ru(bpy)_3]^{2+}$ with $Re(bpy)(CO)_3Cl$ by TEOA were investigated with information derived from electrochemical and absorption/emission data and information within the literature. This analysis showed that of the two systems, $[Ru(bpy)_3]^{2+}$ with $Re(bpy)(CO)_3Cl$ may produce an OER catalytic unit under a reductive quenching scenario, where TEOA is utilised.

The more electron withdrawn $Re(Brbpy)(CO)_3Cl$ was synthesised and assessed for the first time towards photocatalytic CO_2 reduction, in the presence of $[Ru(bpy)_3]^{2+}$ and TEOA. Despite the similar first reduction potentials of $[Ru(bpy)_3]^{2+}$ and $Re(bpy)(CO)_3Cl$, this system proved to be more active in generating CO than the novel intermolecular system of $[Ru(bpy)_3]^{2+}$ with $Re(Brbpy)(CO)_3Cl$. This compounds a discussion within the literature about the benefit of an increased reducing power of the catalyst towards CO_2 reduction.

Future work from chapter two would focus on substitution of the bpy ligands bound to the Ru centre with tert-butyl or methyl groups in an effort to increase the reducing power of the OER Ru moiety, while having a less significant effect on the Re centre's reduction potential. Though synthetically more difficult, the qpy ligand may benefit from an electron donating group on the 4-/5- position (bound to on the Ru moiety), and a varied assessment of substitution on the 4'''-/5'''- position of qpy. The Ru moiety substitution would be expected to shift the first Ru ligand reduction to more negative values, while likely having little effect on that of the Re ligand-based reduction potential. As shown in section 2.2.6, substitution of the Re moiety with an electron withdrawing group may not be favourable in terms of the reducing power of the catalytic centre. Ideally, the Re ligand based reduction would remain more positive than that of the Ru based first reduction, whereby the Re moiety consists of electron donated methyl substitution. However, this is unlikely.

It is also of interest to develop IrMn complexes, as recently Mn complexes have become of purpose as a photocatalysts (in the presence of a photosensitiser) in addition to their high activities as electrocatalysts. Mn diimine tricarbonyl reductions often occur more negative to that of Re analogues, and Ir centres (particularly with cyclometalated C-N

ligands) could hold a reducing power adequate enough to reduce the Mn centre. Recent reports have also emerged of active intermolecular systems for CO_2 reduction containing Cu PS units. Cu PS units within intramolecular systems will also likely hold strong interest within the field.

Chapter three explored the potential of four cobalt salens, CoSal, CodBrSal, CobdtChexSal, and CopdSal, as CO_2 reduction electrocatalysts in the absence and presence of 5% water as a Brønsted acid. In DMF and under Ar, the voltammetry of these complexes revealed that the $E_{1/2}$ of the $Co^{2+/1+}$ process ranged between -1.6 and -1.92 V vs Fc/Fc^+ for three of the complexes, whereas dative donation of an additional lone pair to the Co centre (in the case of CopdSal) dramatically shifted the $E_{1/2}$ value cathodically to -2.48 V vs Fc/Fc^+.

Upon the introduction of CO_2 to the cell, CopdSal demonstrated a loss of the $Co^{1+/2+}$ oxidation in addition to current enhancement of the $Co^{2+/1+}$ reduction. CobdtChexSal demonstrated a partial loss of reversibility of the $Co^{2+/1+}$ redox couple, with no current enhancement observed. However, CoSal and CodBrSal did not demonstrate deviation from the voltammetric behaviour acquired under Ar. When 5% water was introduced into the cell, CoSal demonstrated almost complete loss of the $Co^{1+/2+}$ return oxidation, but no current enhancement was observed at the potential of the $Co^{2+/1+}$ reduction. CodBrSal exhibited partial loss of both the $Co^{2+/1+}$ reduction and associated oxidation. Under these conditions, CobdtChexSal showed some current enhancement of the $Co^{2+/1+}$ reduction, whereas CopdSal demonstrated further current enhancement. The appearance and extent of current enhancement to the $Co^{2+/1+}$ reduction followed the general trend of CopdSal > CobdtChexSal > CoSal > CodBrSal, in line with the trend of increased cathodic potentials associated with the $Co^{2+/1+}$ couple.

Homogeneous bulk electrolyses of the complexes under CO_2 with 5% water were carried out at 0.071 cm^2 glassy carbon electrodes to determine the amount of CO and H_2 generated, the selectivity, and the Faradaic efficiencies towards each product. Of the four complexes, CobdtChexSal (at -2.1 V vs Fc/Fc^+) demonstrated the highest selectivity towards CO generation. CopdSal, despite the highest current enhancement by voltammetry under CO_2 with and without water, selectively produced H_2 over CO.

With utilisation of $Re(bpy)(CO)_3Cl$ as a model CO_2 reducing electrocatalyst, Toray carbon paper was identified as a useful and cost-effective working electrode material,

capable of producing CO selectively over H_2. From this, size and voltage optimisations commenced with CobdtChexSal as catalyst. However, as each electrolysis was continued over time/as a greater charge was consumed, the selectivity shifted from CO and towards H_2 generation. Unusually, the presence of CO_2 was also required to generate H_2. FESEM (with secondary electron and EDX detection) images of the electrode material following three hours of electrolysis revealed a cobalt containing deposit on the electrode surface.

Regarding future work within chapter three, it is evident that further characterisation steps of this material are required. IR spectroelectrochemistry undertaken under CO_2 with water present could show peaks associated with metal carbonyl or formate bonds. However, if there is very limited solubility associated with this suggested species, this likely complicates analysis to the point that the species, though present heterogeneously, may not show by IR. The platinum grid contained as the working electrode in the IR-SEC (OTTLE) cell may not be applicable for such analysis as H_2 may result from attempting to reduce the complex in a 5% H_2O solution.

Due to the complication of the oxygen-sensitive $[Co^{1+}bdtChexSal]^-$, UV-vis SEC (as per chapter two) is not feasible for this complex. In place, UV-visible monitored experiments such as those detailed in chapter four would be more applicable. Particularly, synthesis and electrochemistry of the H_2bdtChexSal ligand would be required for comparison. Both experiments of the complex and the ligand (if ligand reductions are present at the potentials of complex reduction) containing H_2O under Ar and CO_2 are required to further address the role of CO_2 towards H_2 generation.

Heterogeneous activity towards H_2 generation has not yet been conclusively shown. Two outstanding electrolysis tests remain. The first is SEM imaging of an electrode utilised in electrolysis under Ar to verify if the particles formed require the presence of CO_2. The second is to directly verify whether these particles operate in a blank solution containing water under CO_2, and also under Ar. If the electrodes operate heterogeneously under CO_2 without operating under Ar, this would lend credence to the conclusion of Mukhopadhyay *et al*. (see chapter three) whereby CO_2 was stated to acidify the solution, thereby allowing H^+ reduction at more attractive potentials. If the electrode does not perform in fresh electrolyte, the particulate matter is not responsible for H_2 generation and that the electrochemically and chemically modified solution is.

Assuming that the electrode retains activity in a blank electrolyte, further heterogeneous characterisation is required. It may be possible to electrolyse the complex under the same conditions using a transparent and conductive material such as indium tin oxide. This would potentially allow for UV and IR heterogeneous characterisation (the latter to seek whether M-CO bonds form). Further surface characterisation would ideally include XPS measurement to ascertain whether nitrogen is present within the composition of particles. If nitrogen is present, the ligand may be retained in the deposit. If only cobalt is conclusively detected, it may be assumed that cobalt oxides or Co metal have deposited. Carbon will likely not be differentiable from the substrate which contains both carbon fibres and 5% polytetrafluoroethylene. The atomic percentages between Co and N should fit to a 1:2 ratio. As discussed in chapter four, oxygen may be detected from the carbon paper electrode.

CobdtChexSal may still have the ability to act as a CO_2 reduction catalyst. If the active catalyst within H_2 generation was either the cobalt carbonyl species or a species arising from the inability of CobdtChexSal to remove the CO, (i.e. that Co-CO led to deactivation of the system towards CO_2 reduction), an additive such as Ni(TMC) (TMC = tetramethylcyclam) as used by Kubiak *et al*. (discussed in chapter one) could be utilised. In this approach, Ni(TMC) acted as a CO scavenger and greatly boosted the rate of catalysis of Ni(cyclam). However, there is a possibility that Ni(TMC) may hold CO too efficiently, thereby acting as a sacrificial agent as opposed to an additive that could be electrochemically reconverted to the starting material. Further to this, there may be a substantial benefit to catalysis with the introduction of stronger Brønsted acids such as phenol and trifluoroethanol, as opposed to water that was included within this study. The introduction of Mg^{2+} and alkali metal cations may also provide a synergistic effect to the CO_2-reducing ability of the complex.

The work within chapter four further explored CopdSal (referred to as ***(1)*** in the chapter), due to the voltammetric enhancement to the complex under CO_2 alone, and the contrasting behaviour in which controlled potential electrolyses with CO_2 and 5% water produced H_2 selectively. An initial electrolysis experiment using 0.071 cm^2 glassy carbon held at -2.71 V vs Fc/Fc^+ showed that under Ar, ***(1)*** produced six times more H_2 than in a CO_2 purged solution at the same potential.

Further Ar-purged experiments at glassy carbon were performed. A second hour of electrolysis of the solution with a cleaned electrode produced significantly less H_2 than with a fresh solution of ***(1)***. The electrodes used within the first and second hours of solution electrolyses were rinsed, placed in DMF with 5% water, and poised at the same potential as in solution electrolyses, whereby the electrodes produced similar levels of H_2, suggesting the presence of an electroactive deposit. It was further shown that water was required for the formation of the active catalyst and as the source of H_2 respectively. The electrocatalytically active electrodes did not display surface confined voltammetry.

Electrolyses were subsequently undertaken at 3.13 cm^2 carbon paper. The terminology outlined in section 4.2 is used herein. The "surface-1" electrodes were generated in the same manner as with glassy carbon, and held similar activity in a heterogeneous capacity. Interestingly, the electrolysis of a solution of ***(1)*** with 5% water for a second hour at a new electrode resulted in similar levels of H_2 evolved, in addition to preparing an active surface-2 electrode. Time-dependent experiments were completed over the course of solution hour 1 and surface-1 hour 1, whereby solution hour 1 produced less H_2 and lower FE_{H2} at each timepoint (5, 10, 20, 40 and 60 mins) than did "surface-1".

FESEM analysis of the carbon paper electrodes was performed following the hour- and two hour-long electrolyses. Three types of deposition were noted. These included a plaque-like deposit and more defined discs (or bisecting discs) and particles. Of the three deposits, EDX could not detect cobalt within the less defined coating (observed primarily following solution hour one experiments). However, Co was determined within bisecting discs and particles.

Due to the composition of the carbon paper, nitrogen and oxygen (associable with the ligand) could not be observed. Therefore, the true nature of the active species could not be determined by SEM/EDX. To determine whether the active catalyst retains the ligand, *in situ* UV-monitored electrolyses of ***(1)*** at two potentials (-2.71 V and a more anodic potential to isolate the first reduction), with and without water were carried out. To interpret the resulting spectral changes, the ligand, H_2pdSal, was also synthesised and cyclic voltammetry was acquired. Due to the observation of a ligand based reduction prior to -2.71 V vs Fc/Fc^+, UV-monitored electrolyses were also undertaken on H_2pdSal. With comparison to spectral changes observed for the reduction of the

ligand, the spectral changes of ***(1)*** strongly suggest that the ligand is not retained within the electrocatalytically active deposit.

Future work regarding chapter four involves gaining a greater understanding as to the identity of the catalyst on the electrode. Electrochemistry of cobalt oxides has previously been determined in aqueous electrolytes. If redox processes associated with the cobalt-containing deposit were apparent in an aqueous environment, the identity and amount of electroactive catalyst may be inferred. X-ray photoelectron spectroscopy (XPS) may be used to determine the oxidation state/s of the Co. Employing a 0% PTFE commercially available carbon paper as electrode would allow EDX analysis to conclude whether or not fluorine and phosphorus (of the $[PF_6]^-$ anion) are present in the deposit.

It is of further interest to assess whether there is a chemical difference between the deposition from the first and second hours of solution electrolysis at carbon paper, due to the inability of the solution to be reused at glassy carbon and additionally, the difference in morphology following the first and second hours' electrolyses. It is unusual that the smaller glassy carbon electrode does not allow a reuse of the solution following the first hour of electrolysis of ***(1)***. It may be of interest to electrolyse the ligand under the same conditions of electrocatalysis and subsequently aim to undertake deposition under catalytic conditions in a ***(1)***/DMF/5% water solution. The ligand undergoes irreversible reduction at the potentials of deposition of the active catalyst from ***(1)***. It is possible that reduction of the ligand, following extraction of the Co centre, could lead to passivation of the electrode. If this was the case, though ***(1)*** would still be present in the solution, it may not be able to deposit as efficiently as at a clean electrode with a fresh solution of ***(1)***.

Durability of the active catalyst was only briefly assessed. It is of interest to determine the level of stability of the catalyst during multiple hours of electrolyses, particularly as there was no decrease in activity following the second hour of electrolysis as compared to the first hour. Similarly, it is of interest to see how many times the 1 mM ***(1)*** solution may be reused to generate heterogeneously active electrodes.

Variation of the proton source and concentration could increase the amount of H_2 generated. However, this may be a futile direction for future work as immediate effort following intricate identification of the deposit would ideally be focussed on the ability

of the deposit to function as a heterogeneous electrocatalyst in water. It has been stated (as discussed in section 4.1) that cobalt oxides may not withstand a rinse test with water.

Assuming that the Co-containing species is competitive for the aqueous reduction of protons, it is of interest to assess whether introduction of a Co^{2+} salt to the deposition solution containing ***(1)*** may reform the precatalyst for further use in redepositing the catalytic species. Indeed, it is also important to determine whether an effective Co deposit towards the HER may be deposited under the same conditions as ***(1)***, with the use of Co^{2+} ions.

In terms of the deposition potential, UV-visible monitored experiments suggest that deposition may occur at the first reduction, as opposed to electrolysing at -2.71 V vs Fc/Fc^{+}. Therefore, the potential required for electrodeposition may be decreased somewhat. Furthermore, the potential at which the deposit is active was not optimised, and may also be of focus.

Most importantly, similar deposits have been stated as bifunctional water oxidising/reducing catalysts (see section 4.1.2). Solubility of Co oxides within acidic solutions has been noted within the literature. Therefore, stability of the deposit would be best analysed at acidic, neutral and alkaline pH towards the HER and oxygen evolution reaction. In this respect, the electrocatalytic behaviour of the deposit under voltammetric and potentiostatic conditions in conjunction with SEM may be adequate to provisionally assess the stability of the deposit. Ideally, comparative experiments would be undertaken for the HER and oxygen evolution reaction with Pt and IrO_2 electrode materials of the same geometric area respectively.

Table of figures and tables within Appendix A

Appendix A.1: Photocatalytic CO_2 reduction experiments involving 100 μM $Re(qpy)(CO)_3Cl$, 134 μM $[Ru(bpy)_3]^{2+}$ + 100 μM $Re(qpy)(CO)_3Cl$, 134 μM $[Ru(bpy)_3]^{2+}$ + 100 μM $Re(bpy)(CO)_3Cl$ and 100 μM RuRe in MeCN with TEA (5:1 v/v). Irradiation time of 21 hours A-1

Appendix A.2: CO_2 vs Ar atmospheres for 134 μM $[Ru(bpy)_3]^{2+}$ with 100 μM $Re(bpy)(CO)_3Cl$ in DMF/TEOA (5:1). Irradiation time of 21 hours A-2

Appendix A.3: 134 μM $[Ru(bpy)_3]^{2+}$ with 100 μM $Re(bpy)(CO)_3Cl$ under CO_2 in DMF/TEOA (5:1) in the absence and presence of 0.1 M BNAH. Irradiation time of 21 hours A-2

Appendix A.4: Quenching of the emission of $[Ru(bpy)_3]^{2+}$ * (λ_{exc} = 454 nm) in the presence of TEOA, up to 5:1 DMF/TEOA (1.256 M) ratio. Inset: Stern-Volmer plot of I_0/I vs TEOA concentration A-3

Appendix A.5: Luminescence spectra of $[Ru(bpy)_3]^{2+}$ * in DMF with additions of TEA (λ_{exc} = 454 nm) A-3

Appendix A.6: The effect of deaeration, aeration and CO_2-purging on the emission of $[Ru(bpy)_3]^{2+}$ * (λ_{exc} = 454 nm) in DMF A-4

Appendix A.7: Cyclic voltammetry of 1 mM $[Ru(bpy)_3]^{2+}$ in MeCN/0.1 M $TBAPF_6$, ν = 100 mV s^{-1} A-4

Appendix A.8: Cyclic voltammetry of 1.5 mM $Re(bpy)(CO)_3Cl$ in MeCN/0.1 M $TBAPF_6$, ν = 100 mV s^{-1} A-5

Appendix A.9: Cyclic voltammetry of 1.5 mM $Re(bpy)(CO)_3Cl$ and 0.75 mM $Re(qpy)(CO)_3Cl$ in MeCN/0.1 M $TBAPF_6$, ν = 100 mV s^{-1} A-5

Appendix A.10: Cyclic voltammetry of 1 mM $[Ru(bpy)_3]^{2+}$ and 0.75 mM RuRe in MeCN/0.1 M $TBAPF_6$, ν = 100 mV s^{-1} A-6

Appendix A.11: Cyclic voltammetry of 1 mM $[Ru(bpy)_3]^{2+}$ and 1.5 mM $Re(bpy)(CO)_3Cl$ in MeCN/0.1 M $TBAPF_6$, ν = 100 mV s^{-1} A-6

Appendix A.12: Scan rate study of the first oxidation of $Re(qpy)(CO)_3Cl$ at glassy carbon electrode in MeCN with 0.1M $TBAPF_6$, data normalised by dividing by square root of scan rate A-7

Appendix A.13: The Ru^{3+} ligand-to-metal charge transfer band observed upon controlled potential UV-Vis SEC of RuRe at 1.65 and 1.75 V vs Ag wire in MeCN with 0.1 M $TBAPF_6$ A-7

Appendix A.14: UV-vis SEC Spectra obtained upon electrolysis of RuRe at 1.38, 1.65 and 1.75 V vs Ag wire, and electrolysis at 0 V vs Ag wire following, in MeCN/0.1 M $TBAPF_6$ A-8

Appendix A.15: Differential pulse voltammograms obtained for oxidative and reductive sweeps of the $Ru^{2+/3+}$ couple of $[Ru(bpy)_3]^{2+}$, undertaken in MeCN/0.1 M $TBAPF_6$ A-8

Appendix A.16: Reversibility of the $Re^{1+/2+}$ oxidation within $Re(bpy)(CO)_3Cl$. Cyclic voltammograms with scan rates of 100, 200 and 500 mV s^{-1} (top) and 1,000 – 20,000 mV s^{-1} (bottom) undertaken in MeCN with 0.1 M $TBAPF_6$. The voltammograms are normalised by current division by $\nu^{0.5}$ A-9

Appendix A.17: Absorbance and normalised (at λ_{excit} of 454 nm) emission spectra of $[Ru(bpy)_3]^{2+}$ in DMF (at RT). Inset contains magnified region of $E_{0\text{-}0}$ (548 nm) A-10

Appendix A.18: Excitation spectrum (at λ_{emm} of 657 nm) and emission spectrum (λ_{excit} of 470 nm) of RuRe in MeCN at room temperature A-10

Appendix A.19: Comparative UV-visible spectra of $Re(Brbpy)(CO)_3Cl$ and $Re(bpy)(CO)_3Cl$ in MeCN A-11

Appendix A. Pertaining to chapter two

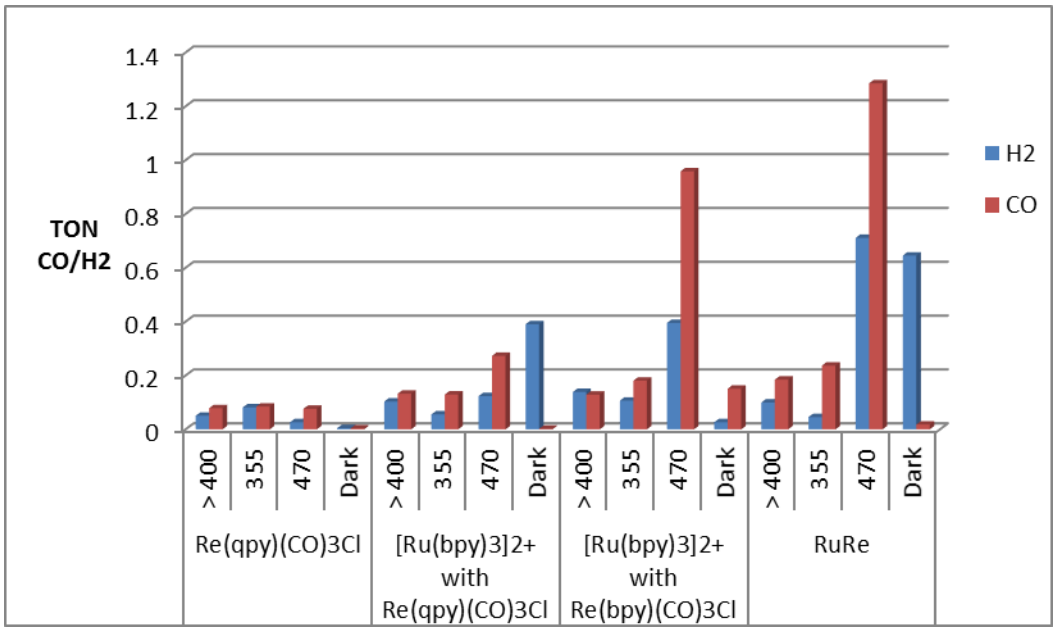

Appendix A.1: Photocatalytic CO_2 reduction experiments involving 100 μM $Re(qpy)(CO)_3Cl$, 134 μM $[Ru(bpy)_3]^{2+}$ + 100 μM $Re(qpy)(CO)_3Cl$, 134 μM $[Ru(bpy)_3]^{2+}$ + 100 μM $Re(bpy)(CO)_3Cl$ and 100 μM RuRe in MeCN with TEA (5:1 v/v). Irradiation time of 21 hours

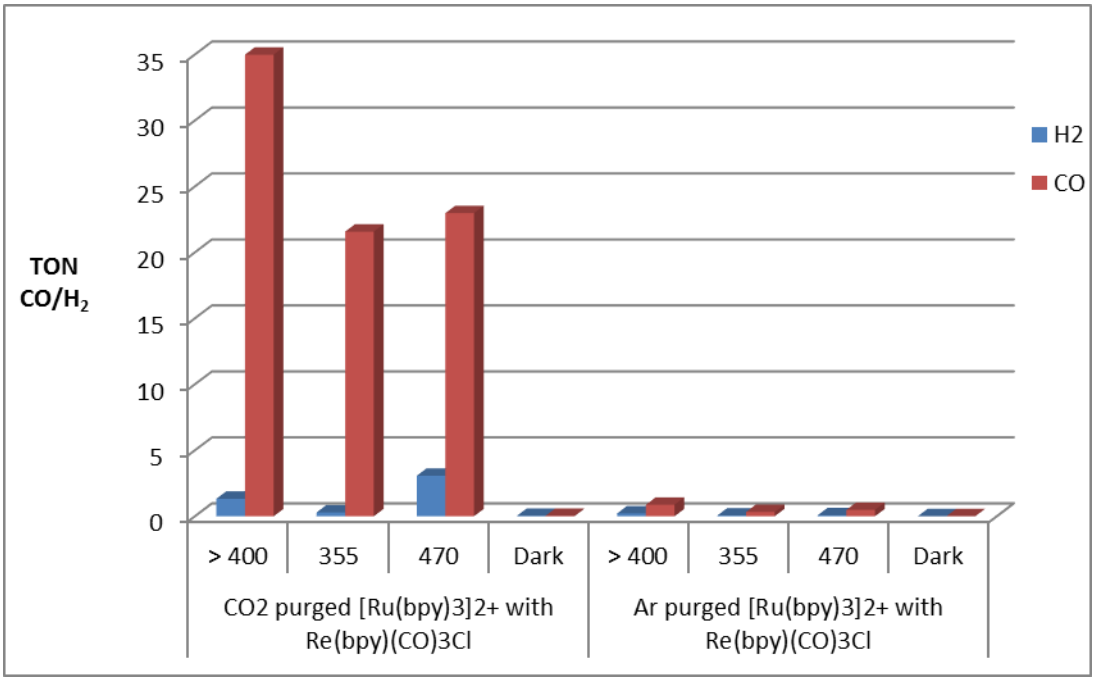

Appendix A.2: CO_2 vs Ar atmospheres for 134 μM $[Ru(bpy)_3]^{2+}$ with 100 μM $Re(bpy)(CO)_3Cl$ in DMF/TEOA (5:1). Irradiation time of 21 hours

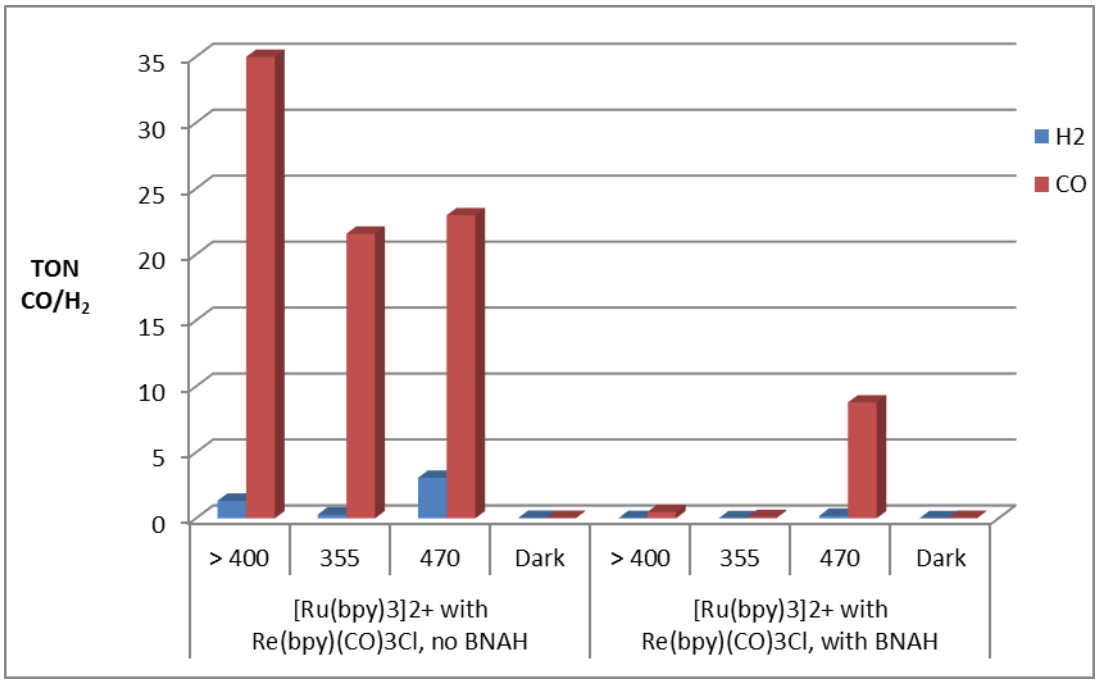

Appendix A.3: 134 μM $[Ru(bpy)_3]^{2+}$ with 100 μM $Re(bpy)(CO)_3Cl$ under CO_2 in DMF/TEOA (5:1) in the absence and presence of 0.1 M BNAH. Irradiation time of 21 hours

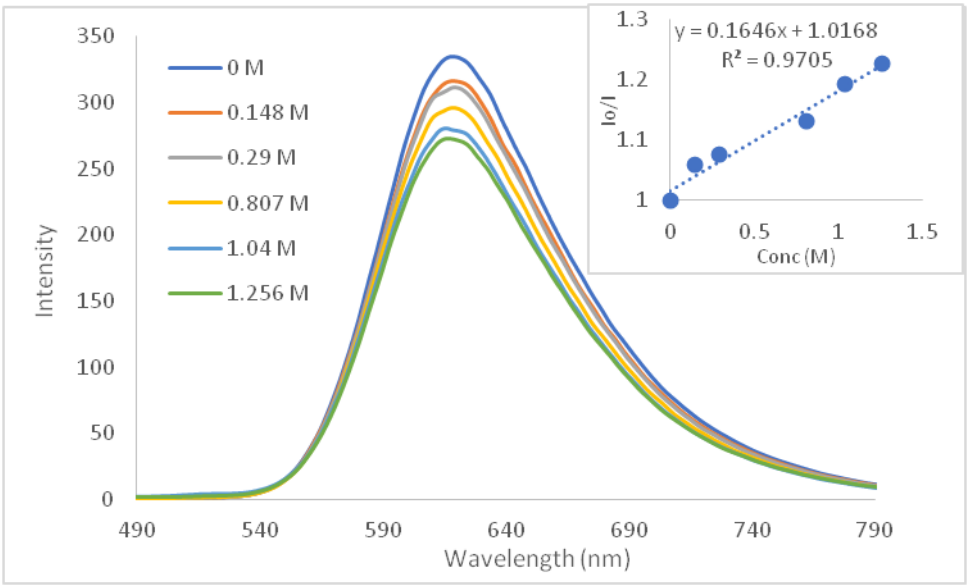

Appendix A.4: Quenching of the emission of $[Ru(bpy)_3]^{2+}$ * (λ_{exc} = 454 nm) in the presence of TEOA, up to 5:1 DMF/TEOA (1.256 M) ratio. Inset: Stern-Volmer plot of I_0/I vs TEOA concentration

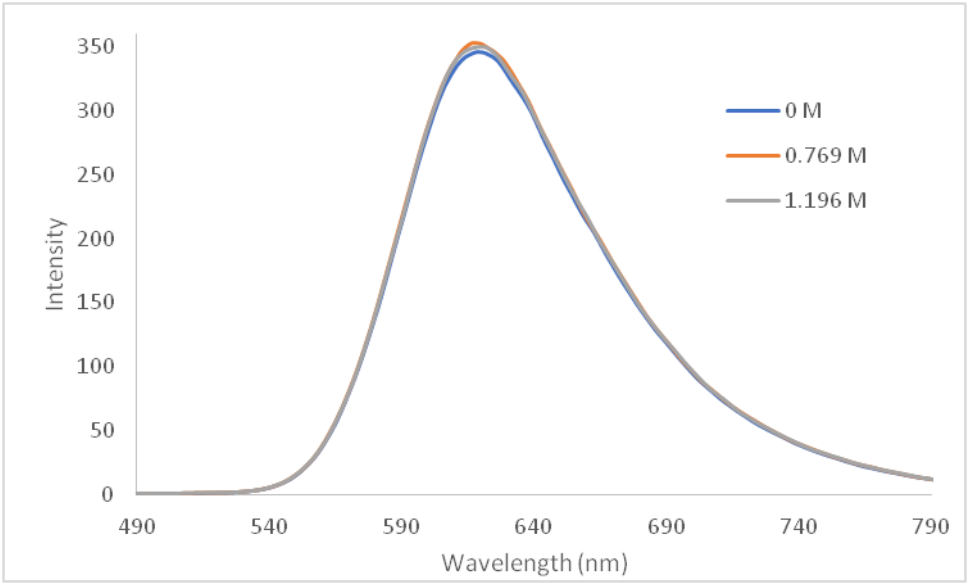

Appendix A.5: Luminescence spectra of $[Ru(bpy)_3]^{2+}$ * in DMF with additions of TEA (λ_{exc} = 454 nm)

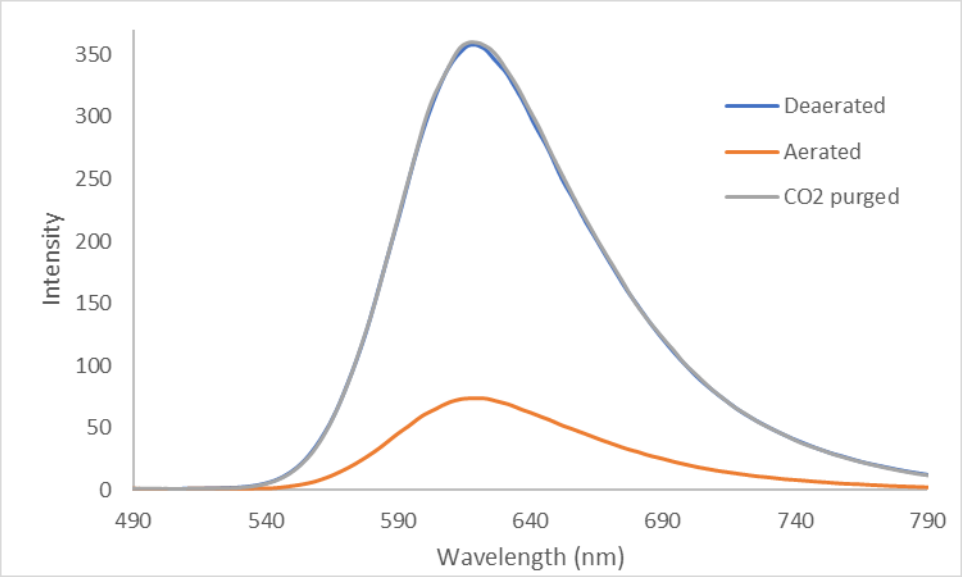

Appendix A.6: The effect of deaeration, aeration and CO_2-purging on the emission of $[Ru(bpy)_3]^{2+}$ * (λ_{exc} = 454 nm) in DMF

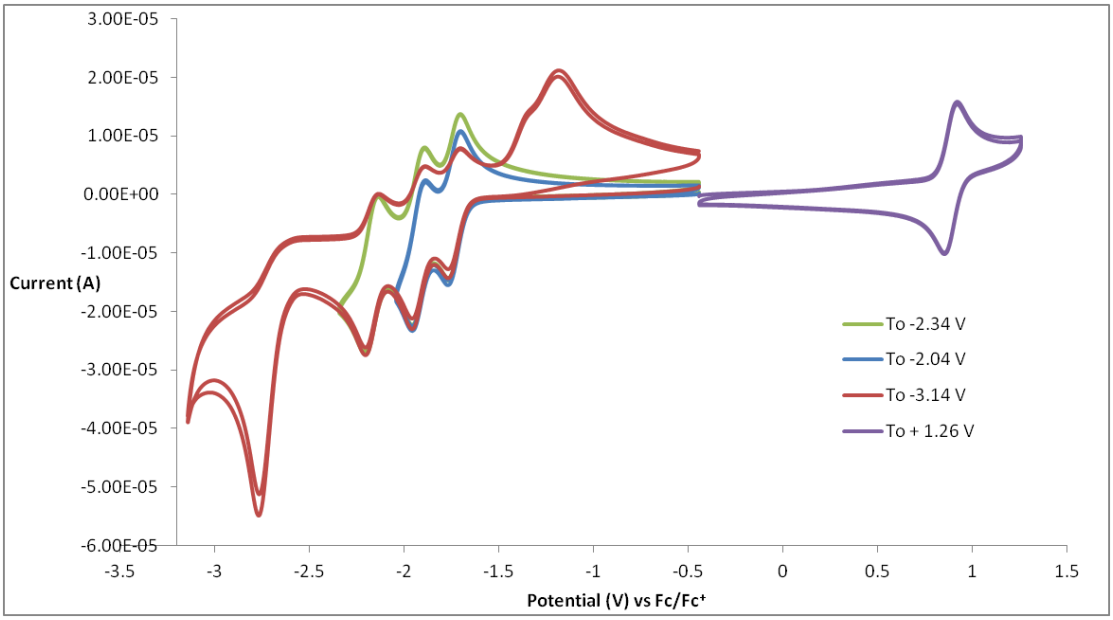

Appendix A.7: Cyclic voltammetry of 1 mM $[Ru(bpy)_3]^{2+}$ in MeCN/0.1 M $TBAPF_6$, ν = 100 mV s^{-1}

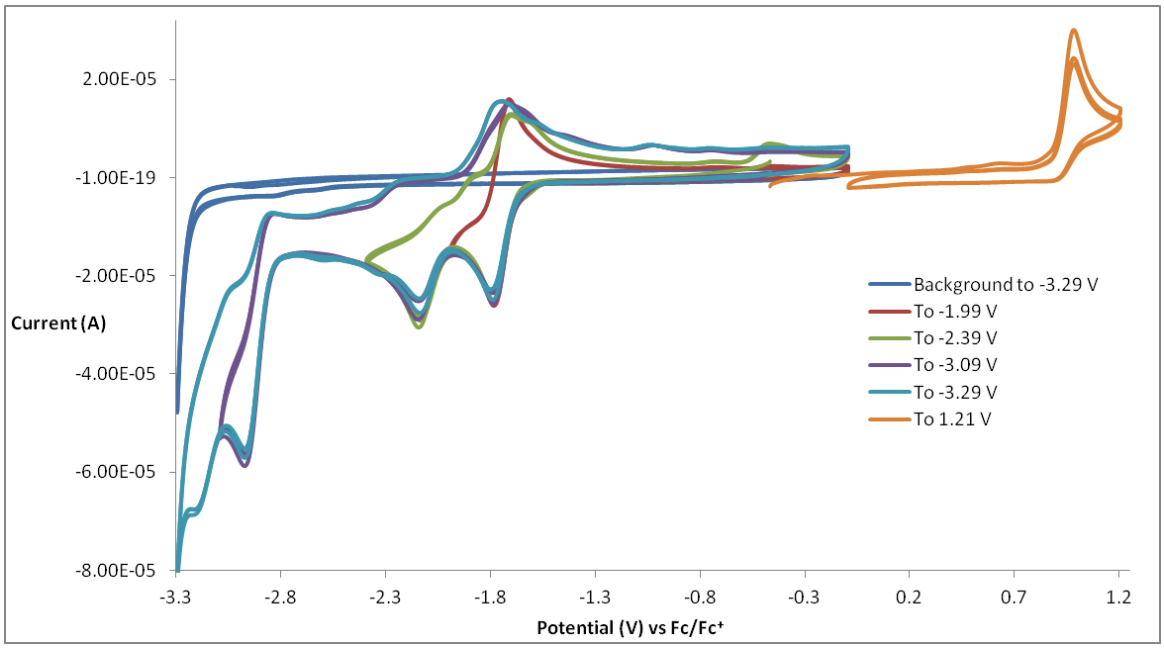

Appendix A.8: Cyclic voltammetry of 1.5 mM $Re(bpy)(CO)_3Cl$ in MeCN/0.1 M $TBAPF_6$, ν = 100 mV s^{-1}

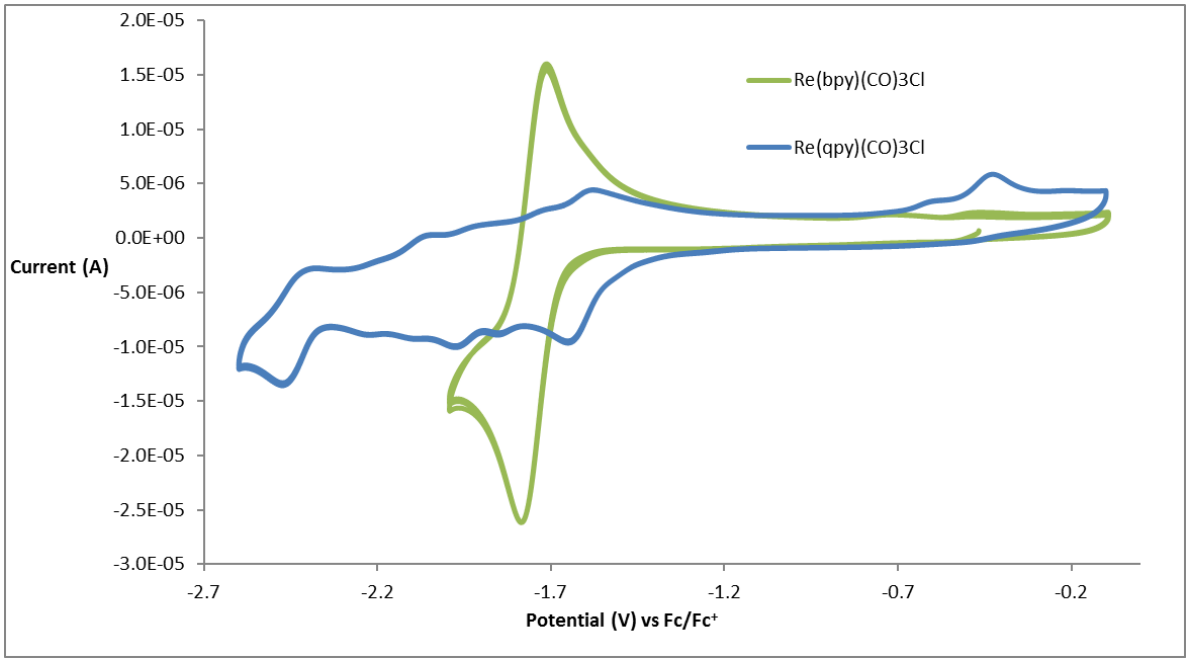

Appendix A.9: Cyclic voltammetry of 1.5 mM $Re(bpy)(CO)_3Cl$ and 0.75 mM $Re(qpy)(CO)_3Cl$ in MeCN/0.1 M $TBAPF_6$, ν = 100 mV s^{-1}

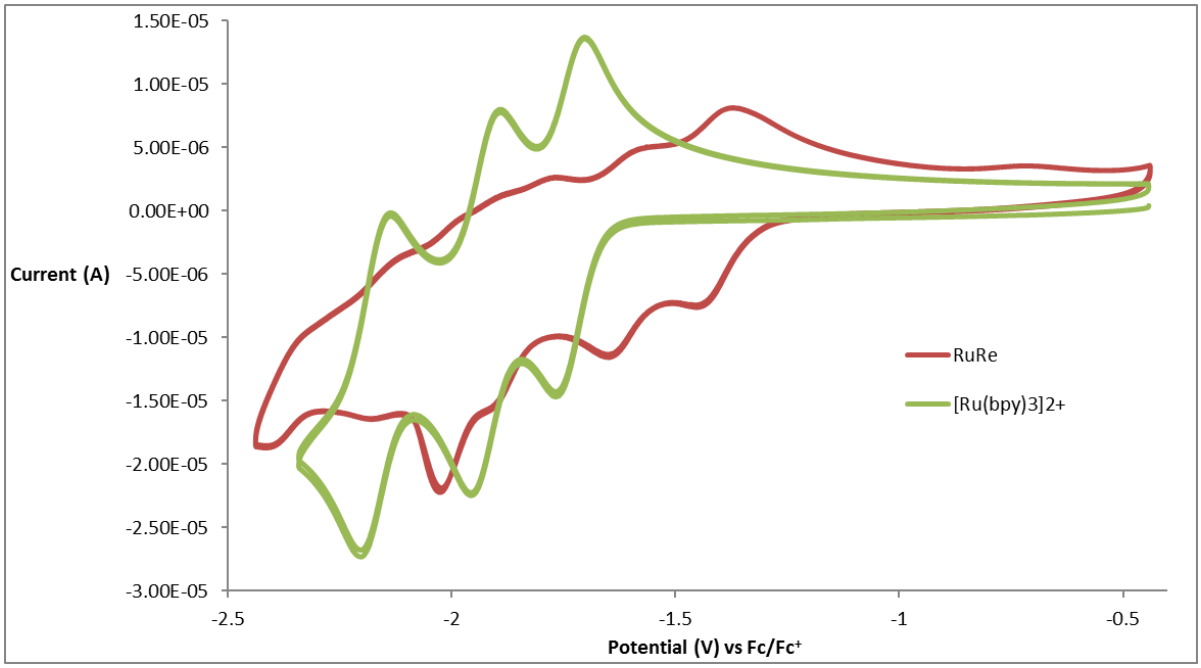

Appendix A.10: Cyclic voltammetry of 1 mM $[Ru(bpy)_3]^{2+}$ and 0.75 mM RuRe in MeCN/0.1 M $TBAPF_6$, ν = 100 mV s^{-1}

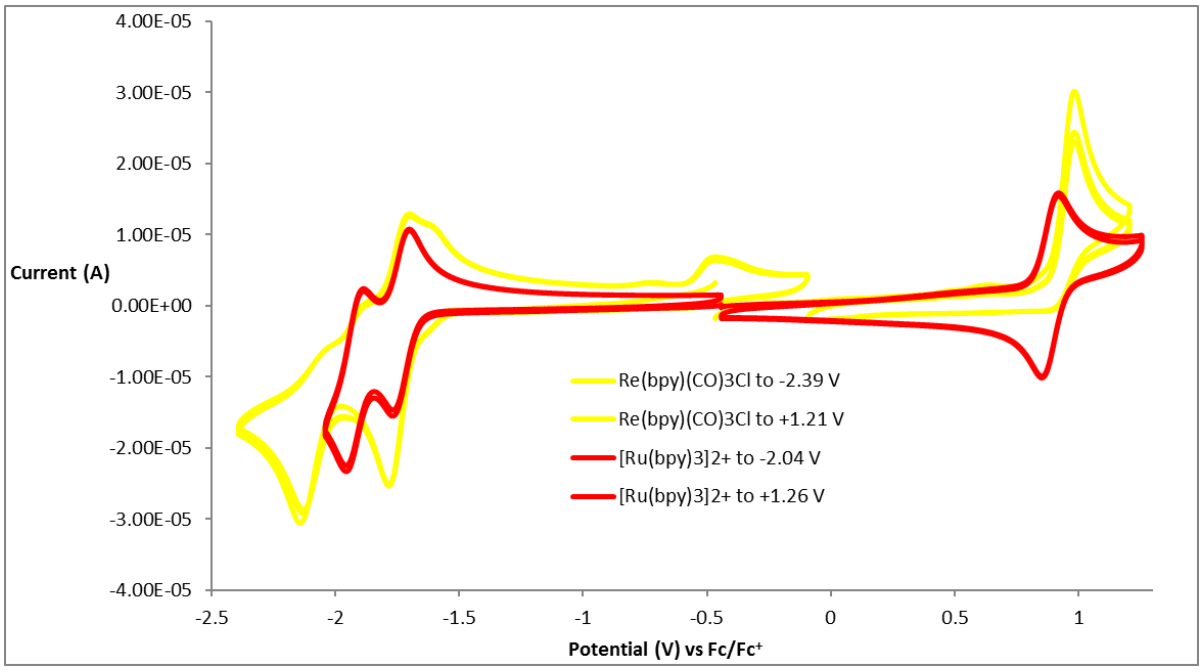

Appendix A.11: Cyclic voltammetry of 1 mM $[Ru(bpy)_3]^{2+}$ and 1.5 mM $Re(bpy)(CO)_3Cl$ in MeCN/0.1 M $TBAPF_6$, ν = 100 mV s^{-1}

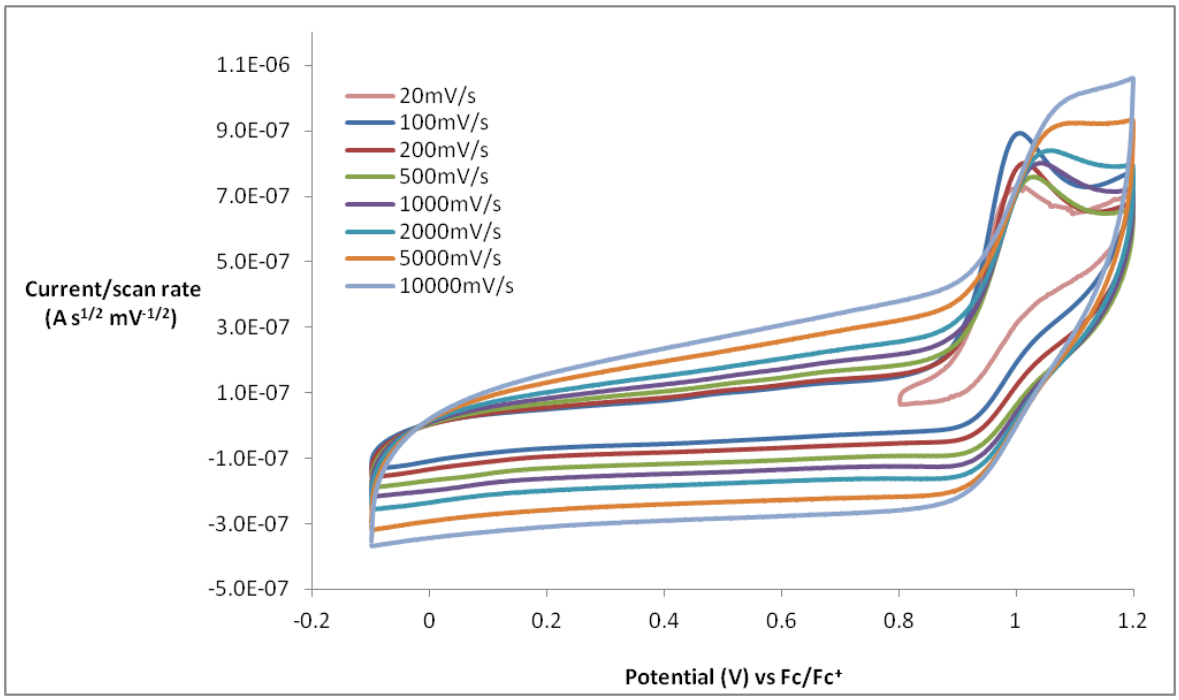

Appendix A.12: Scan rate study of the first oxidation of $Re(qpy)(CO)_3Cl$ at glassy carbon electrode in MeCN with 0.1 M $TBAPF_6$, data normalised by dividing by square root of scan rate.

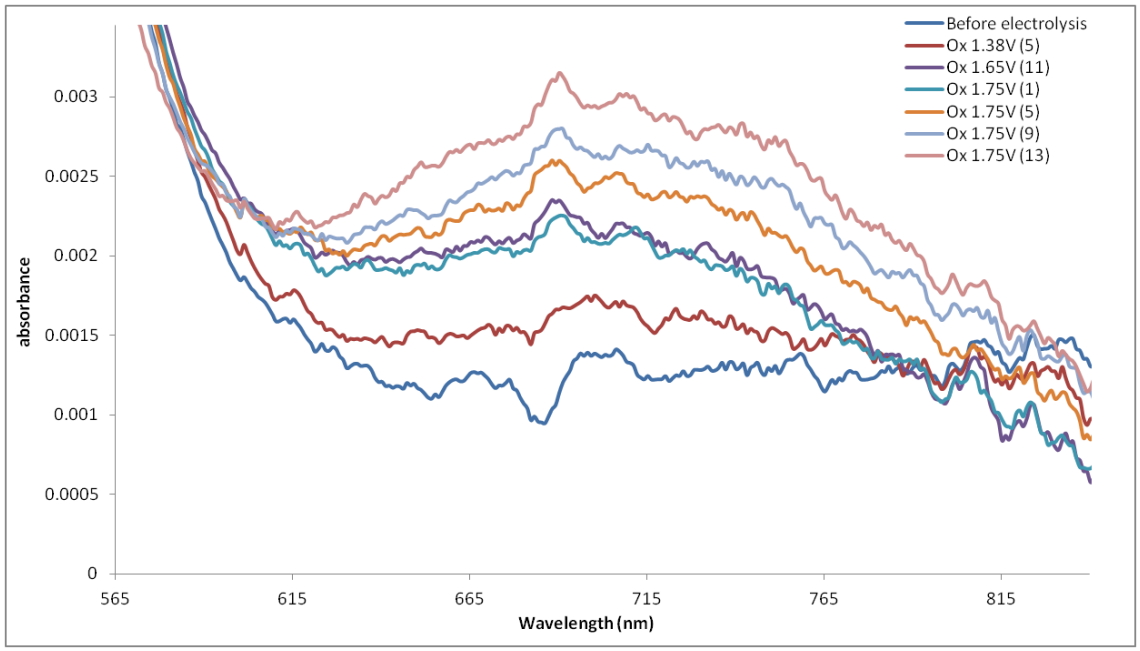

Appendix A.13: The Ru^{3+} ligand-to-metal charge transfer band observed upon controlled potential UV-Vis SEC of RuRe at 1.65 and 1.75 V vs Ag wire in MeCN with 0.1 M $TBAPF_6$

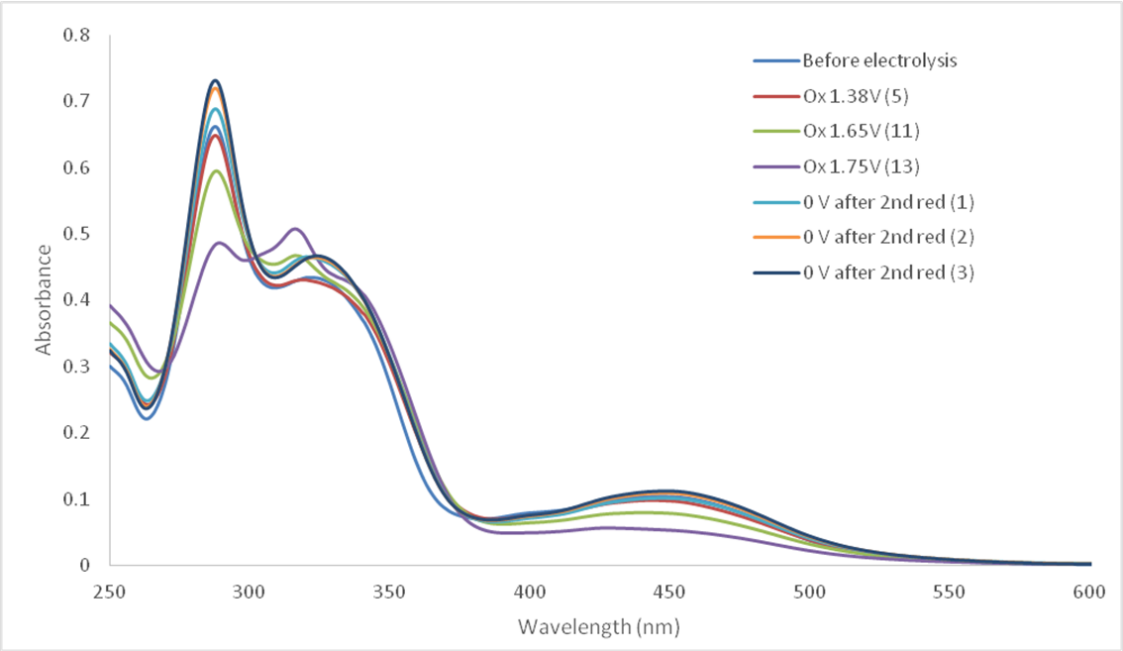

Appendix A.14: UV-vis SEC spectra obtained upon electrolysis of RuRe at 1.38, 1.65 and 1.75 V vs Ag wire, and electrolysis at 0 V vs Ag wire following, in MeCN/0.1 M $TBAPF_6$

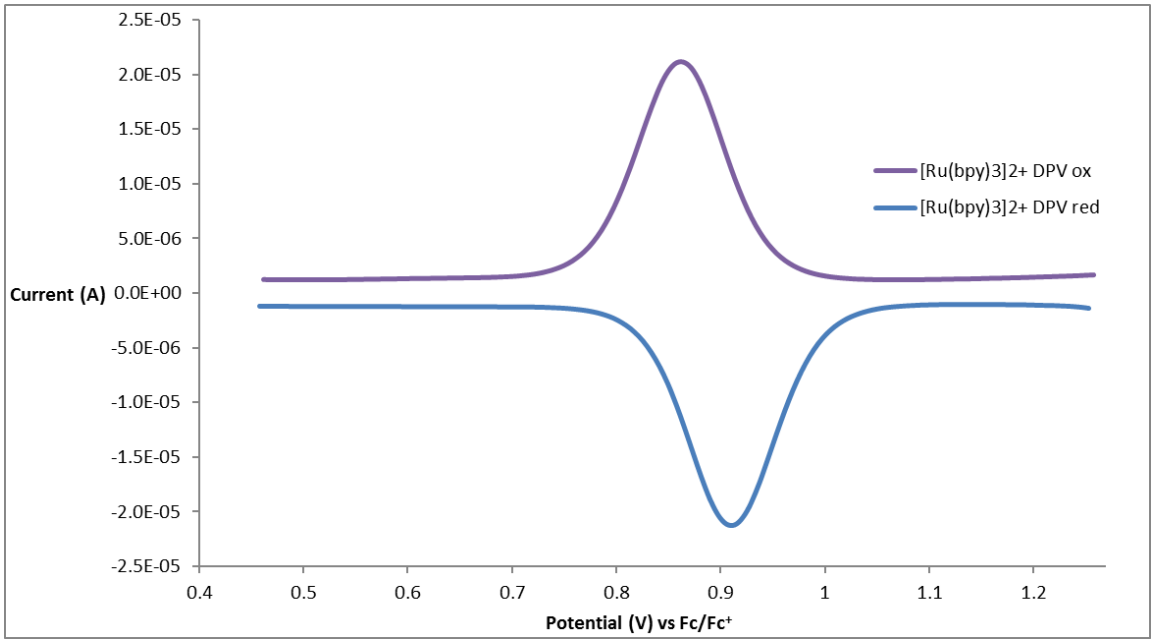

Appendix A.15: Differential pulse voltammograms obtained for oxidative and reductive sweeps of the $Ru^{2+/3+}$ couple of $[Ru(bpy)_3]^{2+}$, undertaken in MeCN/0.1 M $TBAPF_6$.

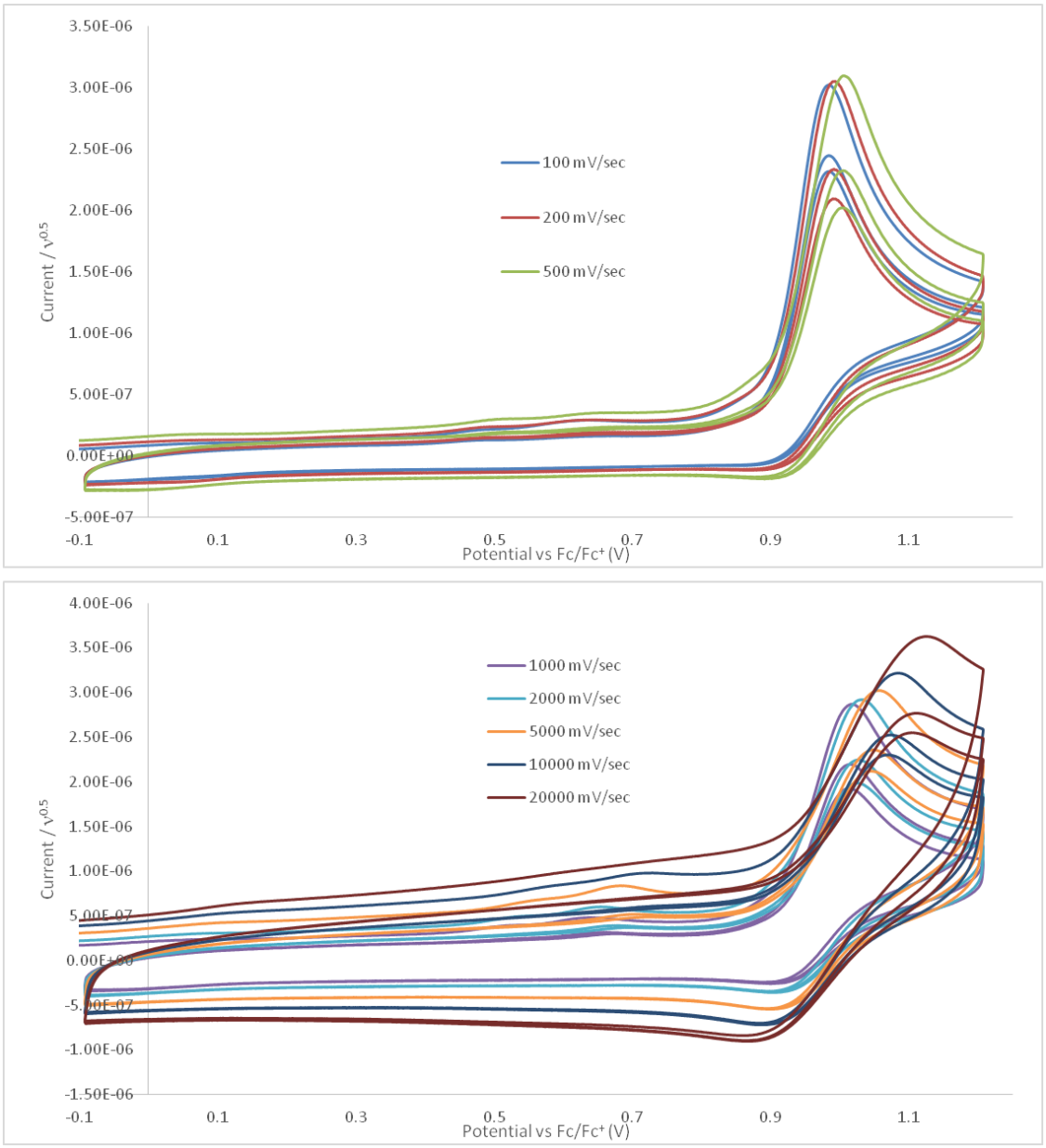

Appendix A.16: Reversibility of the $Re^{1+/2+}$ oxidation within $Re(bpy)(CO)_3Cl$. Cyclic voltammograms with scan rates of 100, 200 and 500 mV s^{-1} (top) and 1,000 – 20,000 mV s^{-1} (bottom) undertaken in MeCN with 0.1 M $TBAPF_6$. The voltammograms are normalised by current division by $v^{0.5}$

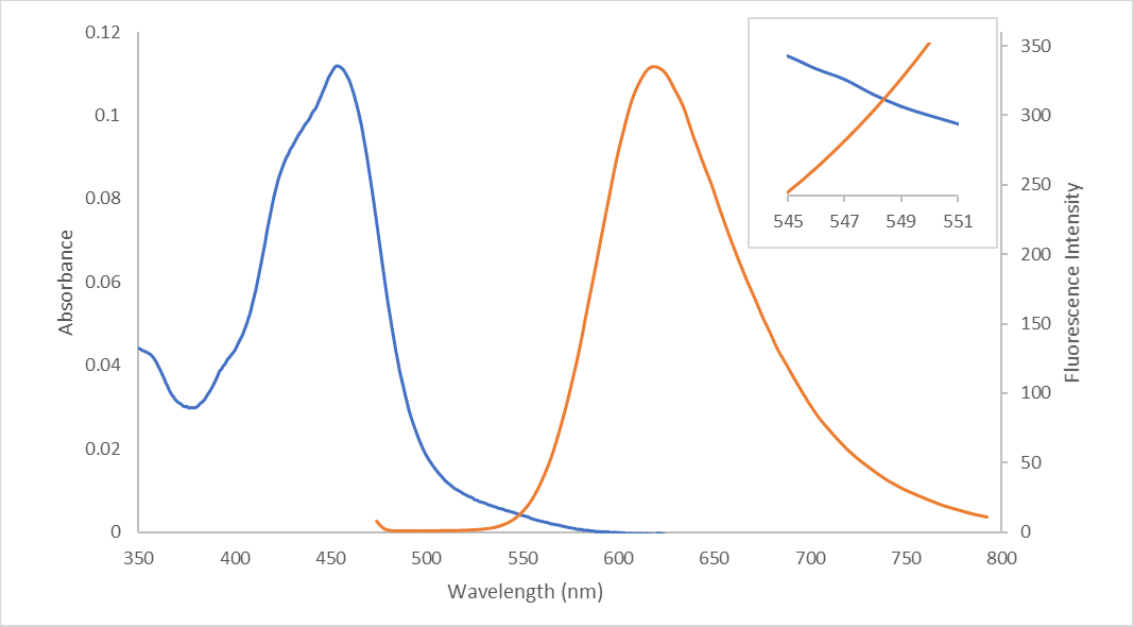

Appendix A.17: Absorbance and normalised (at λ_{excit} of 454 nm) emission spectra of $[Ru(bpy)_3]^{2+}$ in DMF (at RT). Inset contains magnified region of $E_{0\text{-}0}$ (548 nm)

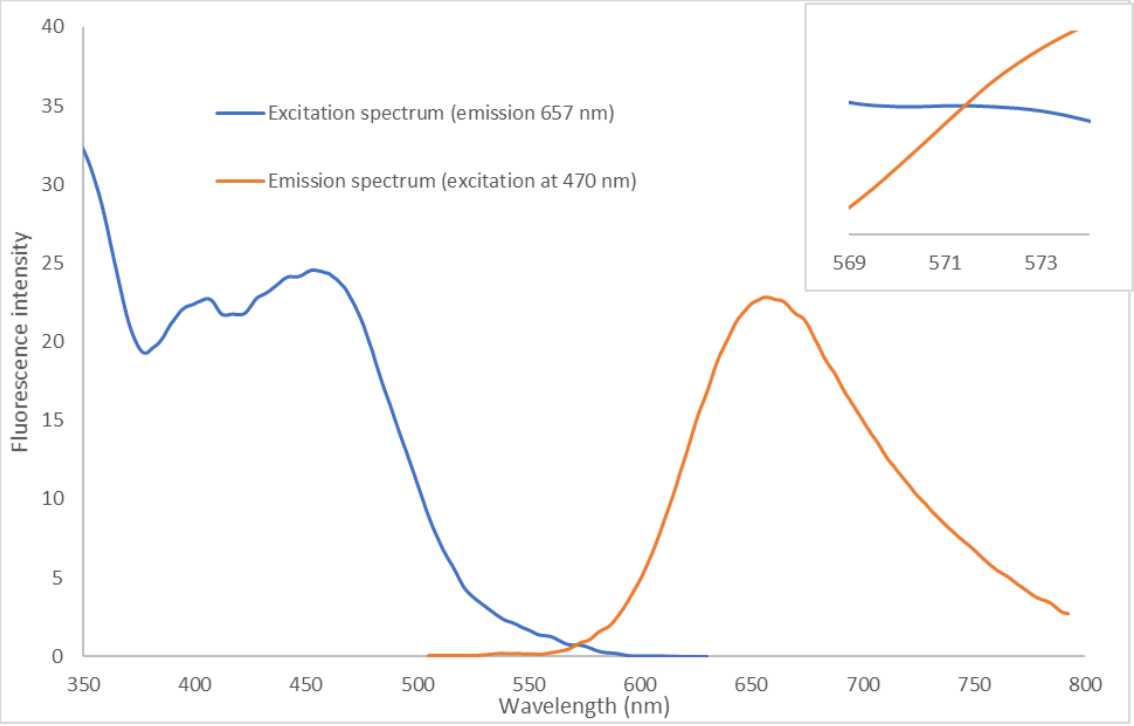

Appendix A.18: Excitation spectrum (at λ_{emm} of 657 nm) and emission spectrum (λ_{excit} of 470 nm) of RuRe in MeCN at room temperature

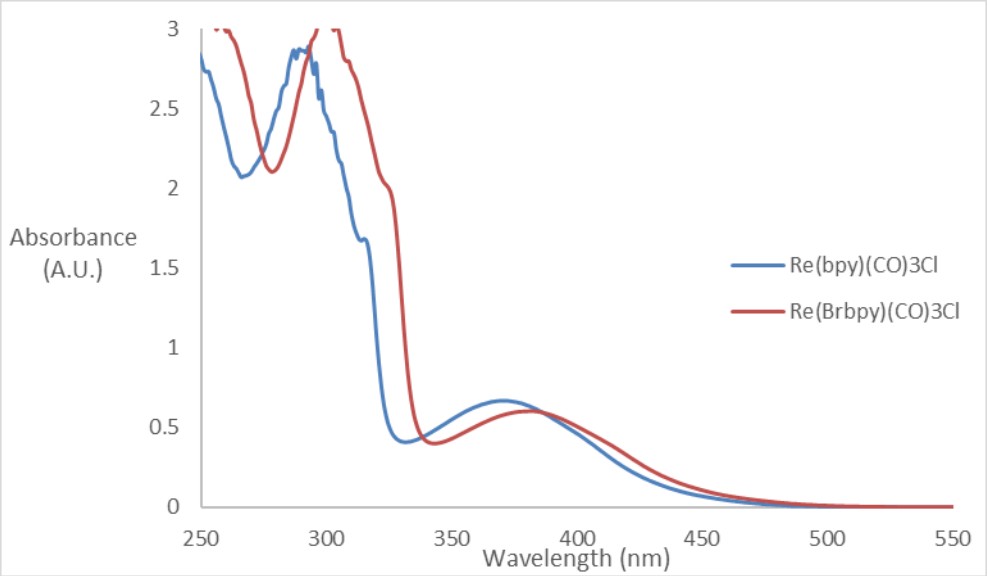

Appendix A.19: Comparative UV-visible spectra of $Re(Brbpy)(CO)_3Cl$ and $Re(bpy)(CO)_3Cl$ in MeCN

Table of figures and tables within Appendix B

Appendix B.1: Background scans of Argon- and CO_2-purged solutions of DMF/0.1 M $TBAPF_6$ with and without 5% water present. The working electrode is glassy carbon with 0.071 cm^2 area B-1

Appendix B.2: Cyclic voltammetry of 1 mM CopdSal in DMF with 0.1 M $TBAPF_6$ under CO_2, CO_2 with 0.167% H_2O and CO_2 with 5% H_2O, ν = 100 mV s^{-1}. The initial scanning direction is negative B-2

Appendix B.3: Cyclic voltammetry of 1 mM CopdSal in CO_2-purged DMF with 0.1 M $TBAPF_6$ at varied scan rate of 10, 100, 300, 500, 1,000, 5,000 and 10,000 mV s^{-1} B-2

Appendix B.4: Cyclic voltammetry of 1 mM CopdSal in CO_2-purged DMF with 5% water and 0.1 M $TBAPF_6$ at varied scan rate of 10, 100, 300, 500, 1,000, 5,000 and 10,000 mV s^{-1} B-3

Appendix B.5: Cyclic voltammetry of 1 mM $Re(bpy)(CO)_3Cl$ in DMF with 0.1 M $TBAPF_6$; **i**. Under Ar with switching potential of -1.96 and -2.36 V and **ii**. Under Ar, CO_2 and CO_2 with 5% H_2O with switching potential at -2.36 V. ν = 100 mV s^{-1} B-4

Appendix B.6: CobdtChexSal following electrolysis under conditions of Table 3.7 "A without CO_2", bubbling of air through solution B-5

Appendix B.7: SEM images of carbon paper electrode, conditions as per Table 3.8, electrolysed at -2.00 V vs Fc/Fc^+. Top four images 20 kV accelerating voltage, 19 μA probe current, as per Figure 3.19; 20000, 50000, 100000 and 1000000x magnification. Lower four images: 20 kV accelerating voltage, 4.3 μA probe current; two different regions at 1000x with one particle at 100000 and 1000000x magnification B-6

Appendix B.8: SEM images of carbon paper submerged in CO_2-purged non-electrolysed solution. 15 kV accelerating voltage, 4.7 μA probe current. Magnification left to right: 1300, 5000, 10000, 20000, 50000 and 100000x B-7

Appendix B.9: SEM images of carbon paper submerged in CO_2-purged previously-electrolysed solution. No electrolysis was undertaken with this electrode. 15 kV accelerating voltage, 4.7 μA probe current. Magnification left to right: 1300, 5000, 10000, 20000, 50000 and 100000x B-7

Appendix B.10: SEM images of carbon paper used in electrolysis of 1 mM $Re(bpy)(CO)_3Cl$ in a CO_2-purged 5% H_2O in DMF with 0.1 M $TBAPF_6$ solution at -2.2 V. 15 kV accelerating voltage, 4.7 μA probe current. Magnification left to right: 1300, 5000, 10000, 20000, 50000 and 100000x B-8

Appendix B.11: SEM images of carbon paper used in the electrolysis of CO_2 purged 1 mM CobdtChexSal with ~ 0.4 mM H_2EDTA in DMF/5% H_2O/0.1 M $TBAPF_6$ for three interrupted hours, 5 kV accelerating voltage, 9.4 – 9.8 μA probe current. Magnification left to right: 1300, 5000, 10000, 20000, 50000 and 100000x B-8

Appendix B. Pertaining to Chapter three

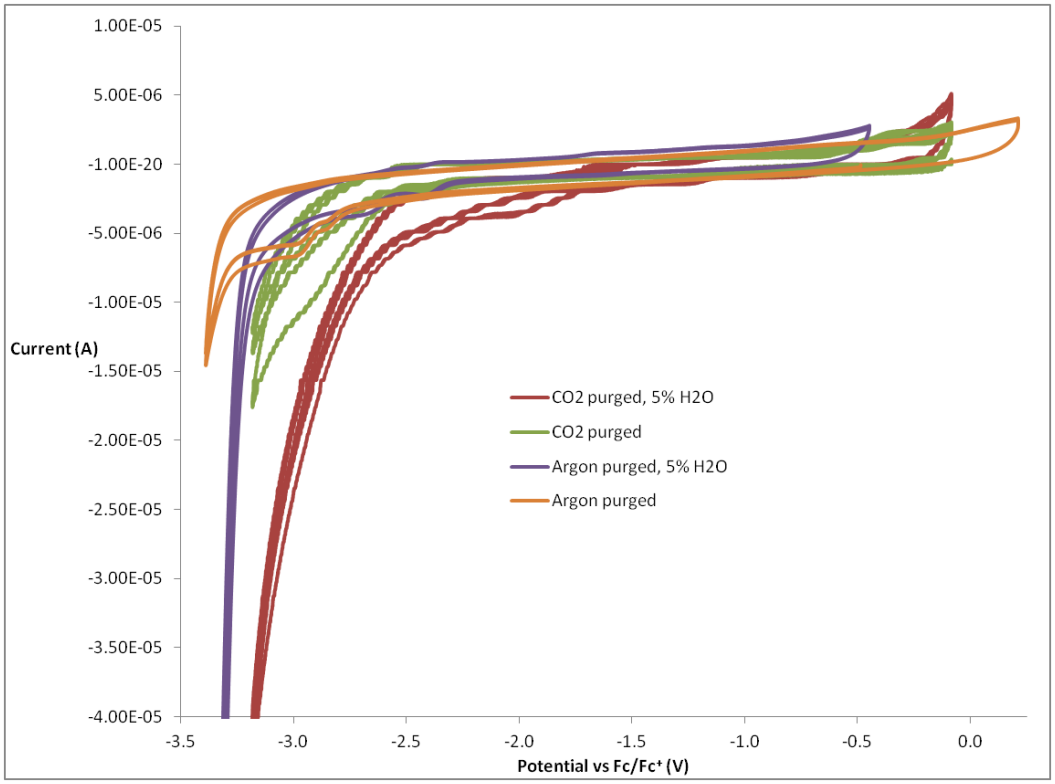

Appendix B.1: Background scans of Argon- and CO_2-purged solutions of DMF/0.1 M $TBAPF_6$ with and without 5% water present. The working electrode is glassy carbon with 0.071 cm^2 area.

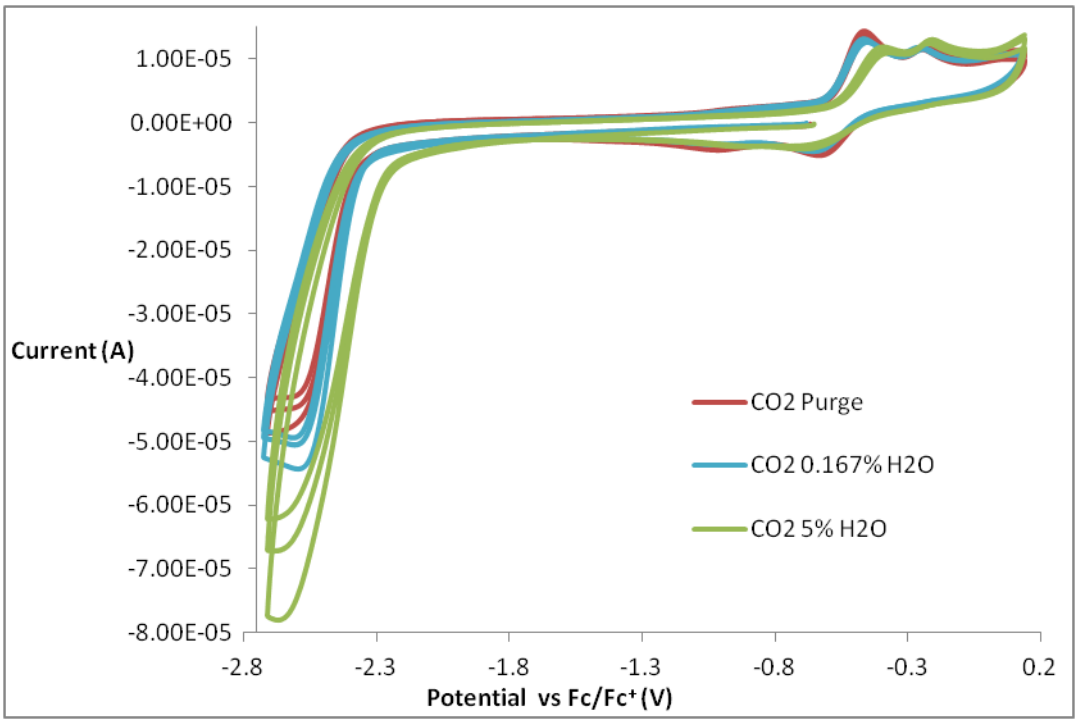

Appendix B.2: Cyclic voltammetry of 1 mM CopdSal in DMF with 0.1 M $TBAPF_6$ under CO_2, CO_2 with 0.167% H_2O and CO_2 with 5% H_2O, ν = 100 mV s^{-1}. The initial scanning direction is negative.

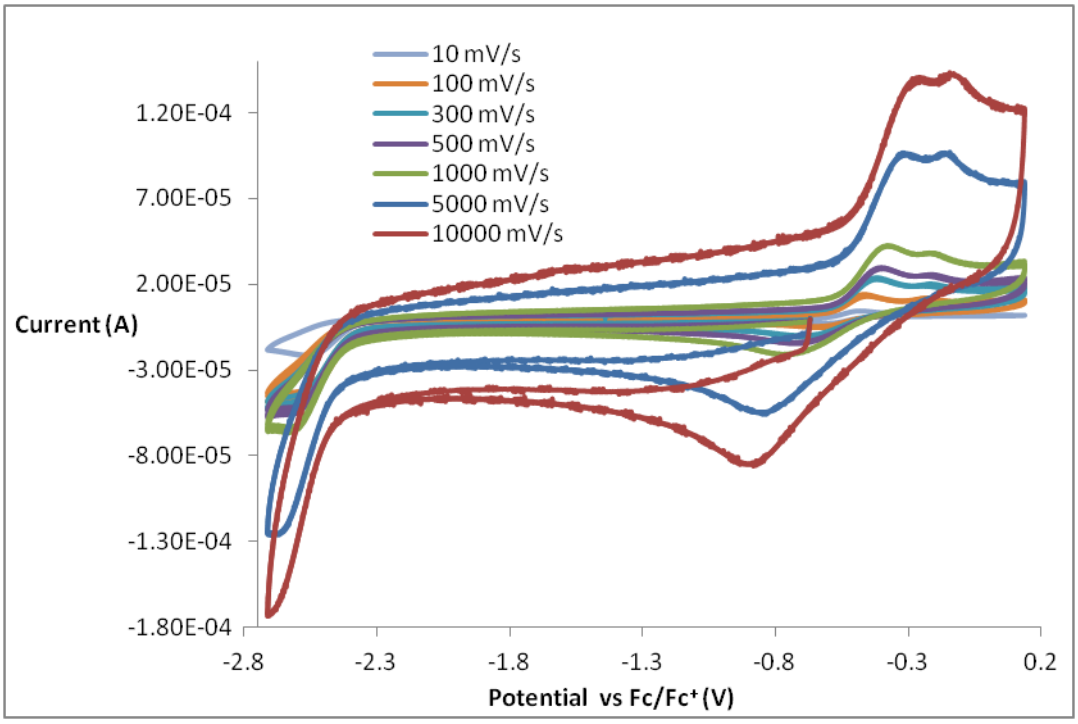

Appendix B.3: Cyclic voltammetry of 1 mM CopdSal in CO_2-purged DMF with 0.1 M $TBAPF_6$ at varied scan rate of 10, 100, 300, 500, 1,000, 5,000 and 10,000 mV s^{-1}.

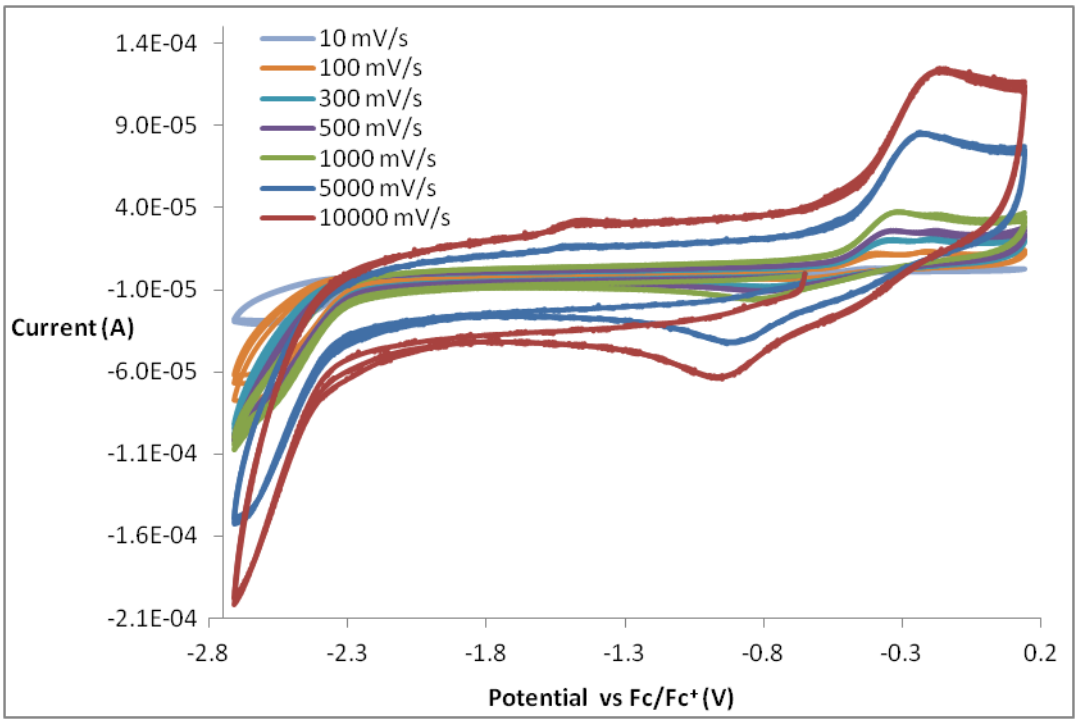

Appendix B.4: Cyclic voltammetry of 1 mM CopdSal in CO_2-purged DMF with 5% water and 0.1 M $TBAPF_6$ at varied scan rate of 10, 100, 300, 500, 1,000, 5,000 and 10,000 mV s^{-1}.

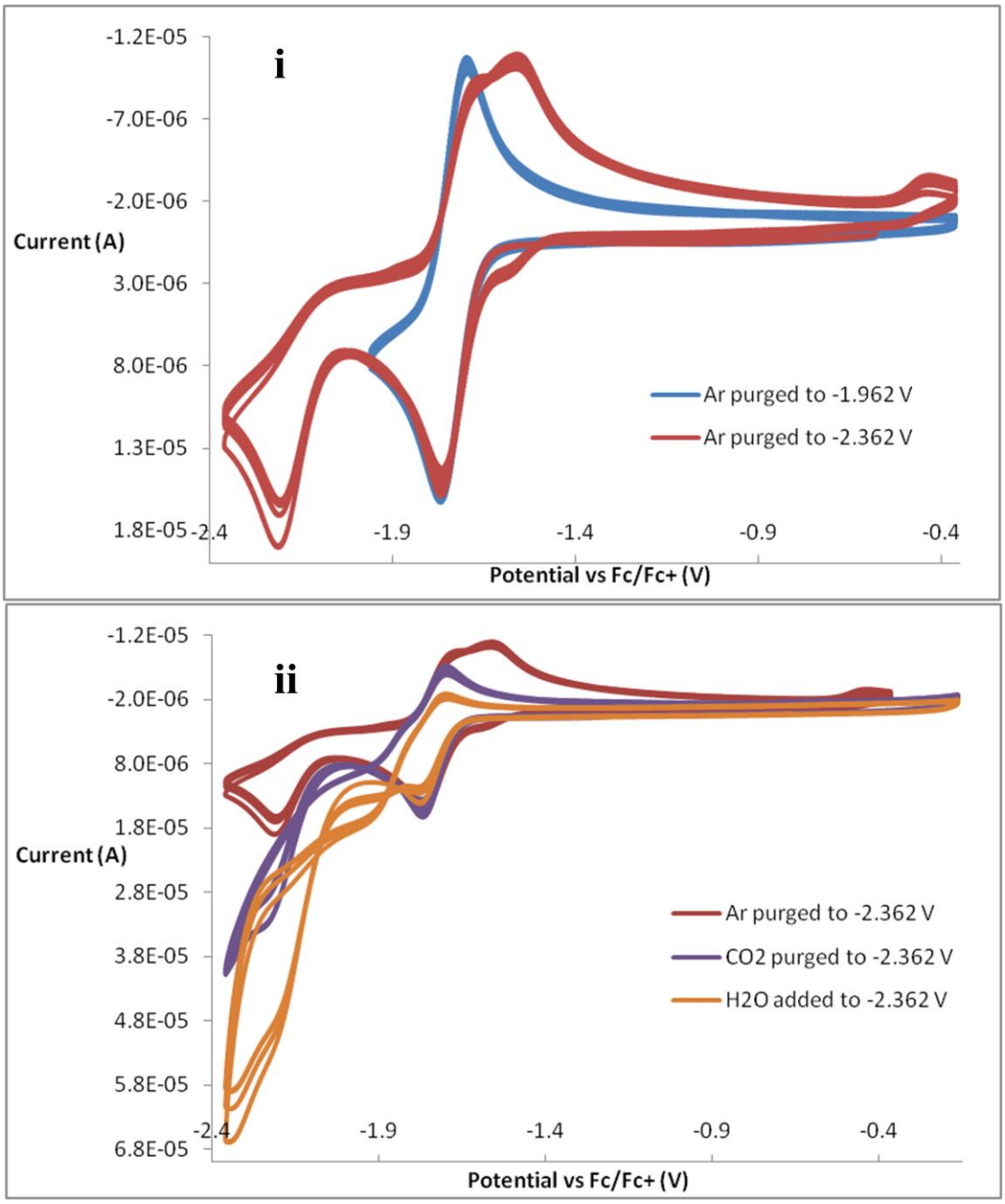

Appendix B.5: Cyclic voltammetry of 1 mM $Re(bpy)(CO)_3Cl$ in DMF with 0.1 M $TBAPF_6$; **i**. Under Ar with switching potential of -1.96 and -2.36 V and **ii**. Under Ar, CO_2 and CO_2 with 5% H_2O with switching potential at -2.36 V. ν = 100 mV s^{-1}

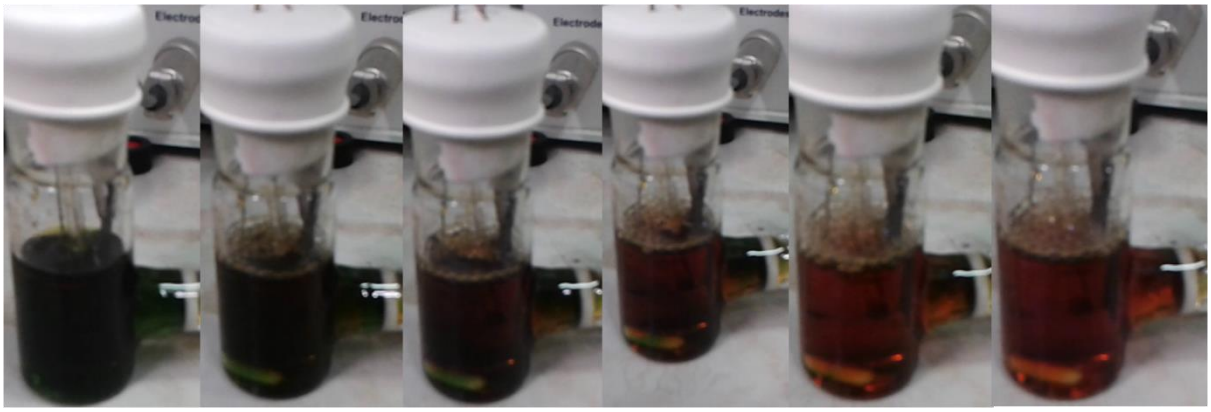

Appendix B.6: CobdtChexSal following electrolysis under conditions of Table 3.7 “A without CO_2”, bubbling of air through solution

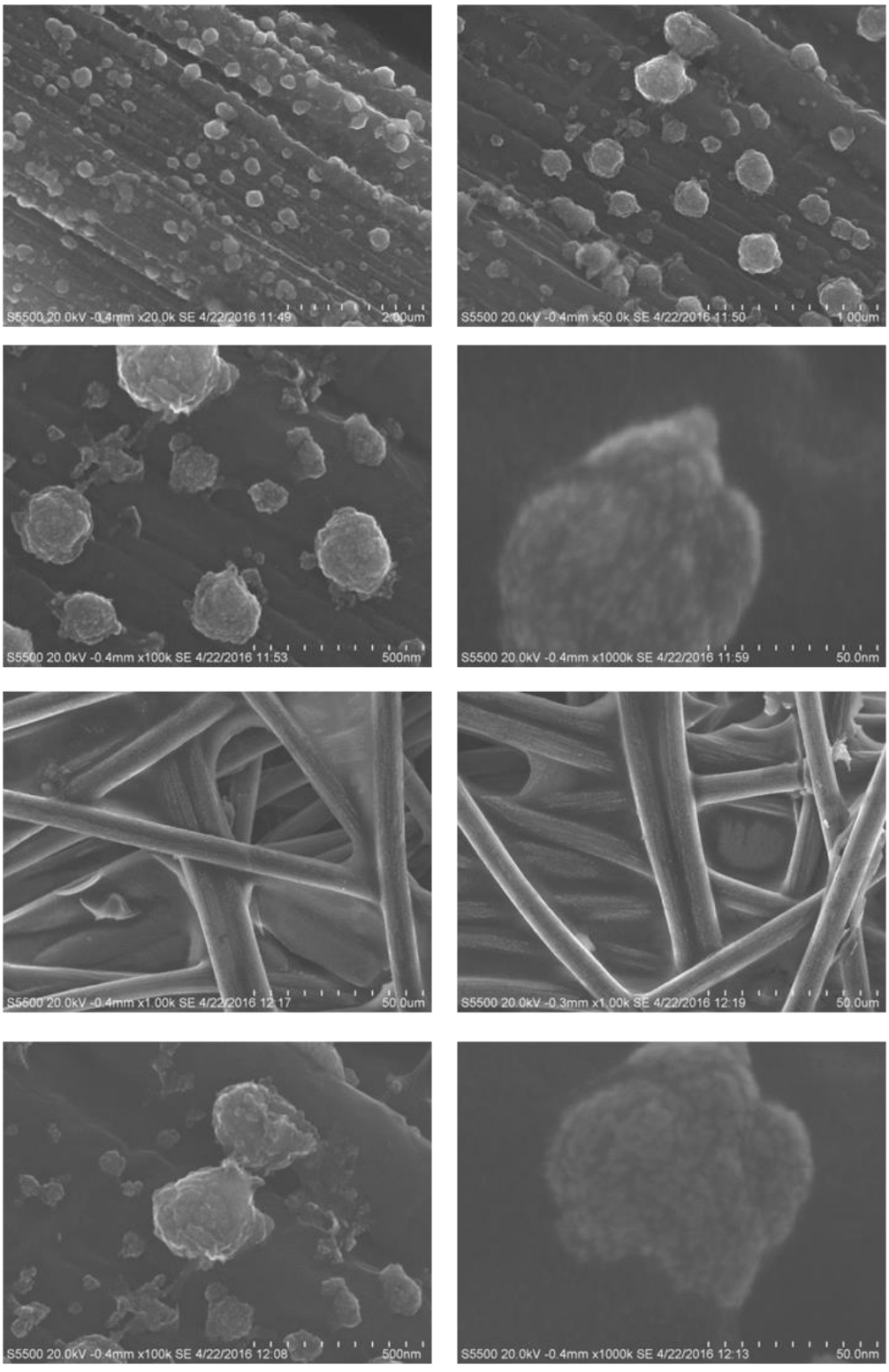

Appendix B.7: SEM images of carbon paper electrode, conditions as per Table 3.8, electrolysed at -2.00 V vs Fc/Fc^{+}. Top four images 20 kV accelerating voltage, 19 μA probe current, as per Figure 3.19; 20000, 50000, 100000 and 1000000x magnification. Lower four images: 20 kV accelerating voltage, 4.3 μA probe current; two different regions at 1000x with one particle at 100000 and 1000000x magnification

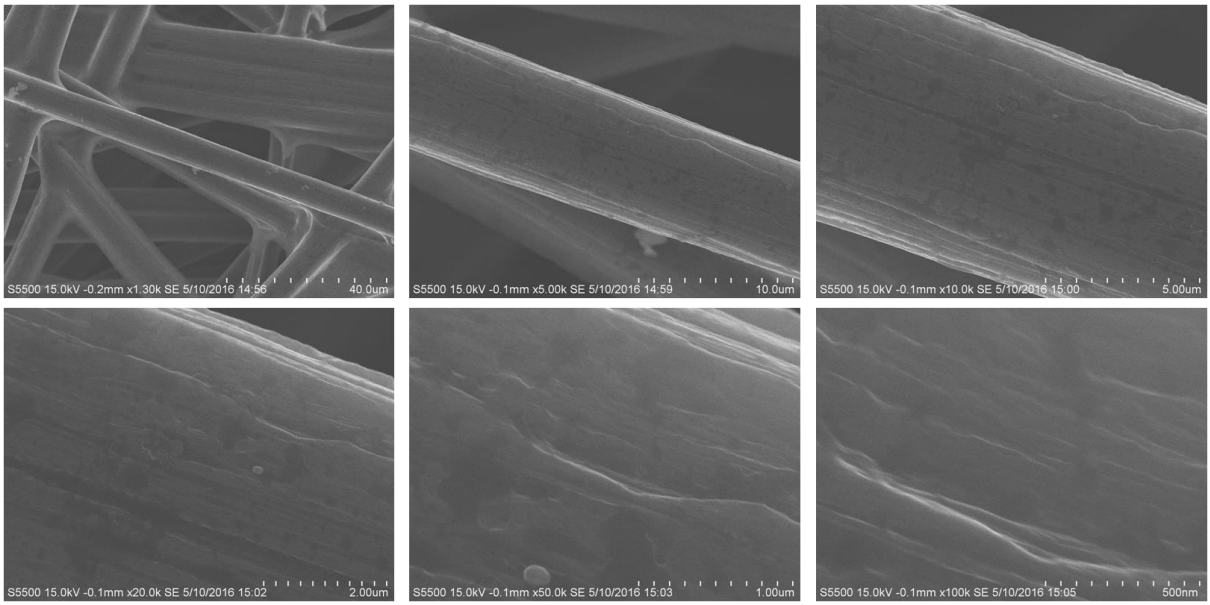

Appendix B.8: SEM images of carbon paper submerged in CO_2-purged non-electrolysed solution. 15 kV accelerating voltage, 4.7 μA probe current. Magnification left to right: 1300, 5000, 10000, 20000, 50000 and 100000x.

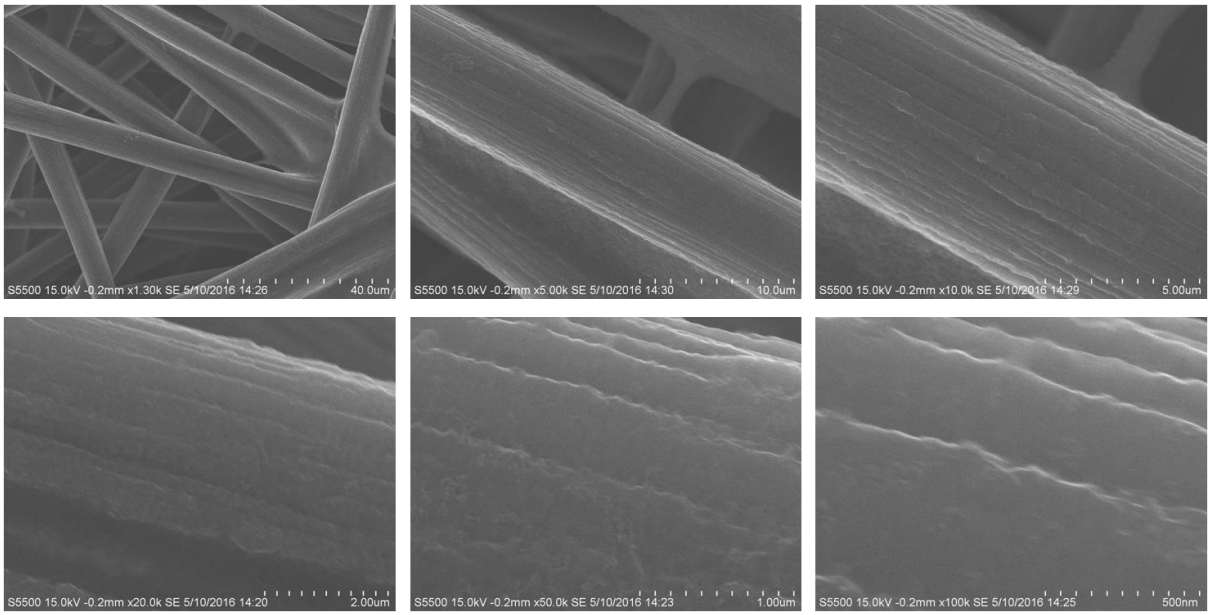

Appendix B.9: SEM images of carbon paper submerged in CO_2-purged previously-electrolysed solution. No electrolysis was undertaken with this electrode. 15 kV accelerating voltage, 4.7 μA probe current. Magnification left to right: 1300, 5000, 10000, 20000, 50000 and 100000x.

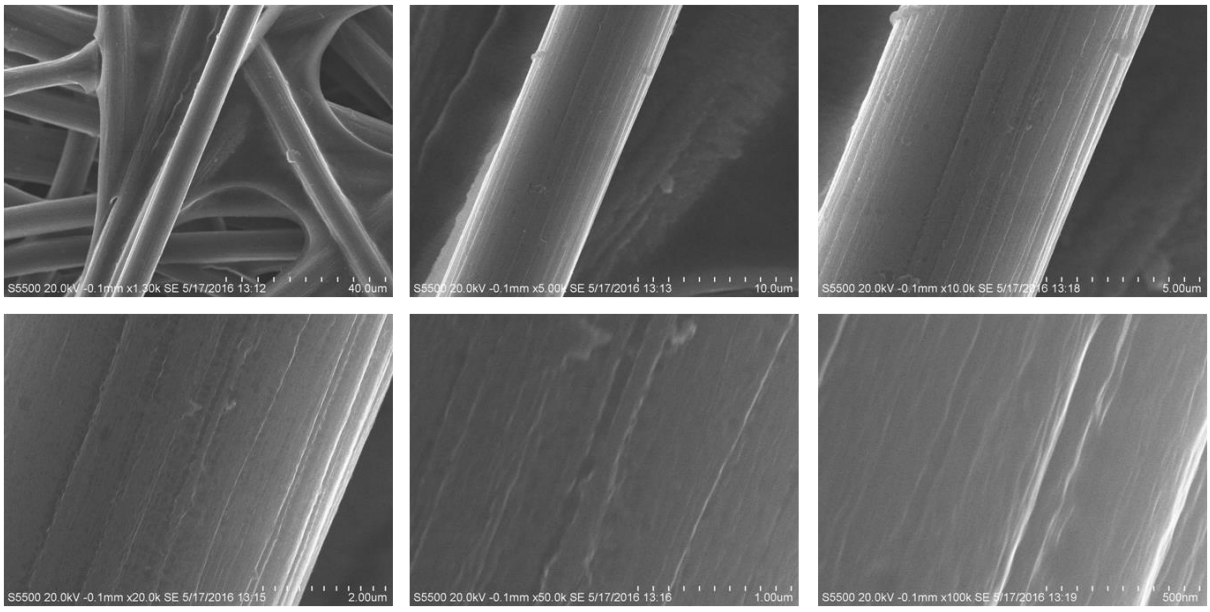

Appendix B.10: SEM images of carbon paper used in electrolysis of 1 mM $Re(bpy)(CO)_3Cl$ in a CO_2-purged 5% H_2O in DMF with 0.1 M $TBAPF_6$ solution at -2.2 V vs Fc/Fc^+. 15 kV accelerating voltage, 4.7 μA probe current. Magnification left to right: 1300, 5000, 10000, 20000, 50000 and 100000x.

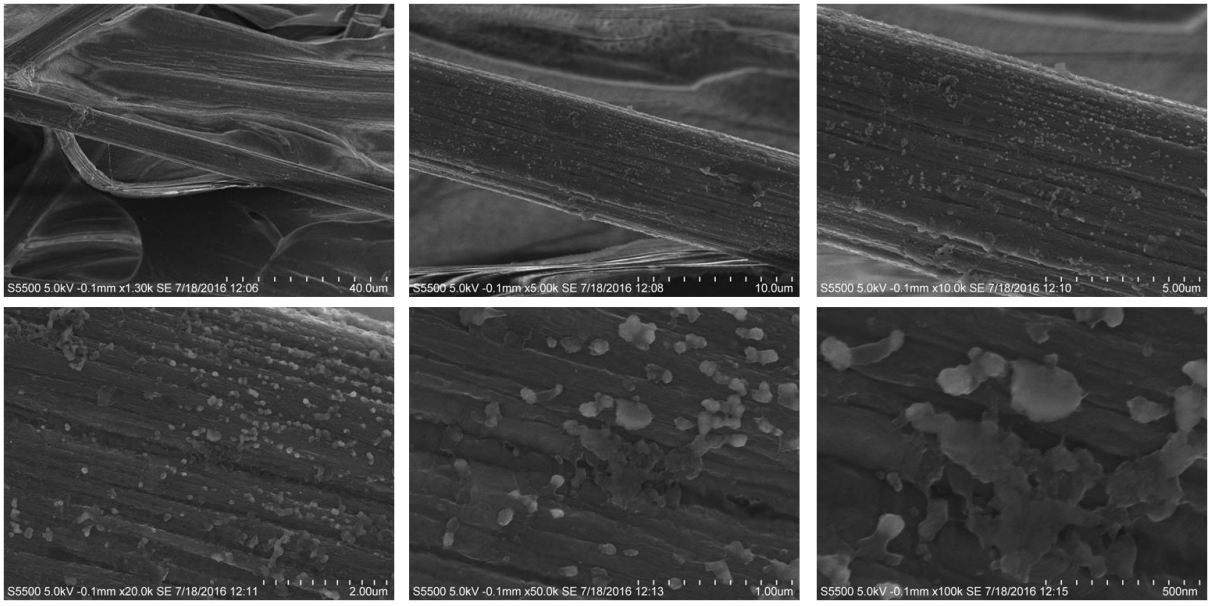

Appendix B.11: SEM images of carbon paper used in the electrolysis of CO_2 purged 1 mM CobdtChexSal with ~ 0.4 mM H_2EDTA in DMF/5% H_2O/0.1 M $TBAPF_6$ for three interrupted hours, 5 kV accelerating voltage, 9.4 – 9.8 μA probe current. Magnification left to right: 1300, 5000, 10000, 20000, 50000 and 100000x.

Table of figures and tables within Appendix C

Appendix C.1: Scan rate dependence (as per Figure 4.4) of 1 mM ***(1)*** in DMF with 0.1 M $TBAPF_6$ and 5% H_2O under Ar, potential window encapsulating the first oxidation and first reduction only. Scan rate; **i**. 10, 100, 300 and 500, 1,000, 3,000, 5,000, 10,000, 20,000, 50,000 and 100,000 mV s^{-1} and **ii**. 10 mV s^{-1} only C-1

Appendix C.2: 1 mM ***(1)*** in Ar-purged DMF with 0.1 M $TBAPF_6$ and in the absence of water, at varied scan rate of 10, 100, 300, 500 and 1,000 mV s^{-1}. A plot of current against $\nu^{0.5}$ reveals $Co^{2+/1+}$ and $Co^{1+/2+}$ R^2 values of 0.998 and 0.993 respectively C-2

Appendix C.3: Scan rate variation of the first reduction of 1 mM ***(1)*** in DMF with 0.1 M $TBAPF_6$ and 5% H_2O under Ar, including and excluding the $Co^{2+/3+}$ redox process at **i**. 100 mV s^{-1}, **ii**. 500 mV s^{-1} and **iii**. 1000 mV s^{-1} C-3

Appendix C.4: ***(1)*** first oxidative redox couple's current response with varied (square root of) scan rate under Ar, in DMF and in DMF with 5% water and associated data. *Scan rates plotted are 10, 100, 300, 500 and 1000 mV s^{-1}. 3000, 5000 and 10000 mV s^{-1} are omitted due to noise in voltammograms complicating interpretation of peak height and baseline slope C-4

Appendix C.5: Results obtained from single hour-long "solution" electrolysis with 1 mM ***(1)*** with 5% water, and subsequent "surface" experiment in the absence of water. Electrolyses undertaken at -2.71 V in a DMF/0.1 M $TBAPF_6$ solution with a glassy carbon electrode C-5

Appendix C.6: Averaged bulk electrolysis current-time plots for surface hours one and two (data as per Table 4.6) at -2.71 V vs Fc/Fc^+ with carbon paper in DMF/0.1 M $TBAPF_6$ with 5% water (electrodes generated following solution hr 1) C-5

Appendix C.7: Effect of electrolysis at -2.71 V vs Fc/Fc^+ using a carbon paper electrode soaked in a 1 mM ***(1)***, DMF, 0.1 M $TBAPF_6$ and 5% water solution. Surface and control electrolyses figures as per Table 4.6 C-6

Appendix C.8: Effect of consecutive electrolysis vs hour-long electrolyses at -2.71 V vs Fc/Fc^+ in DMF, 0.1 M $TBAPF_6$ and 5% water solution. Surface electrodes as generated in Table 4.6 C-6

Appendix C.9: SEM images of "Soln hr 1 #2", the carbon paper used as working electrode in the first hour electrolysis of 1 mM ***(1)*** in DMF/5% H_2O/0.1 M $TBAPF_6$ at -2.71 V vs Fc/Fc^+, 10 kV accelerating voltage, 21.2 – 21.6 μA probe current. Magnification left to right, top to bottom: 1300, 5000, 10000, 20000, 50000 and 100000 and 500000x C-7

Appendix C.10: SEM image (top) and the associated EDX spectrum (bottom) of the "Soln hr 1 #1" electrode. the carbon paper used as working electrode in the first hour electrolysis of 1 mM ***(1)*** in DMF/5% H_2O/0.1 M $TBAPF_6$ at -2.71 V vs Fc/Fc^+. 15 kV accelerating voltage C-8

Appendix C.11: SEM images of "Surface hrs 1+2 #2", the carbon paper used as working electrode following one hour electrolysis of 1 mM ***(1)*** in DMF/5% H_2O/0.1 M $TBAPF_6$ at -2.71 V vs Fc/Fc^+, and subsequent electrolysis for two interrupted hours at -2.71 V vs Fc/Fc^+ in the absence of ***(1)***. 1 kV accelerating voltage, 18.8 – 19.6 μA probe current. Magnification left to right, top to bottom: 1300, 5000, 10000, 20000, 50000 and 100000x C-9

Appendix C.12: SEM image (top) and the associated EDX spectrum (bottom) of the outermost fibre of "Surface 2 hrs #1" electrode (associated SEM images in Figure 4.21). 15 kV accelerating voltage C-10

Appendix C.13: UV-visible spectra acquired from 0-55 mins **(i)** and 60-120 mins **(ii)** of electrolysis, conditions and spectra as per Figure 4.28 C-11

Appendix C.14: UV-visible spectra as per Figure 4.33 (electrolysis of 60 μM ***(1)*** in 15ml DMF/0.1 M $TBAPF_6$ with 15 μl water at -2.42 V vs Fc/Fc^+) at 130, 140 and 150 minutes of electrolysis C-12

Appendix C.15: **i.** UV-visible spectra and **ii.** difference spectra associated with the first 9 minutes of electrolysis of 60 μM ***(1)*** at -2.71 V vs Fc/Fc^+ in DMF with 0.1 M $TBAPF_6$ (as per Figure 4.36 and Figure 4.37) C-12

Appendix C.16: Calibration curve of H_2pdSal in DMF at **i**. λ_{max} of 315 nm and **ii**. λ_{max} of 408 nm C-13

Appendix C.17: Calibration curve of Ar purged ***(1)*** in DMF at **i.** λ_{max} of 349 nm and **ii.** at 315 nm C-14

Appendix C.18: Cyclic voltammetry with varied scan rate of **i.** 100, 300, 500 and 1000 and **ii.** 5000, 25000 and 100000 mV s^{-1} on the first reductions of H_2pdSal at glassy carbon in DMF with 0.1 M $TBAPF_6$ in the absence of water C-15

Appendix C.19 Cyclic voltammetry with varied scan rate of **i.** 100, 300, 500 and 1000 and **ii.** 5000, 25000 and 100000 mV s^{-1} on the first reduction of H_2pdSal at glassy carbon in DMF with 0.1 M $TBAPF_6$ and 5% water C-16

Appendix C.20: As per Figure 4.42. UV-visible spectra acquired from 0 to 900 seconds during the electrolysis of approximately 60 μM H_2pdSal in 15ml DMF/0.1 M $TBAPF_6$ with 15 μl water at -2.71 V vs Fc/Fc^+ C-17

Appendix C.21: As per Figure 4.42. UV-visible spectra acquired from 900 to 7200 seconds during the electrolysis of approximately 60 μM H_2pdSal in 15ml DMF/0.1 M $TBAPF_6$ with 15 μl water at -2.71 V vs Fc/Fc^+ C-17

Appendix C.22: As per Figure 4.43. UV-visible difference spectra acquired from 30 to 900 seconds during the electrolysis of approximately 60 μM H_2pdSal in 15ml DMF/0.1 M $TBAPF_6$ with 15 μl water at -2.71 V vs Fc/Fc^+ C-18

Appendix C.23: As per Figure 4.43. UV-visible difference spectra acquired from 900 to 7200 seconds during the electrolysis of approximately 60 μM H_2pdSal in 15ml DMF/0.1 M $TBAPF_6$ with 15 μl water at -2.71 V vs Fc/Fc^+ C-18

Appendix C: Pertaining to Chapter four

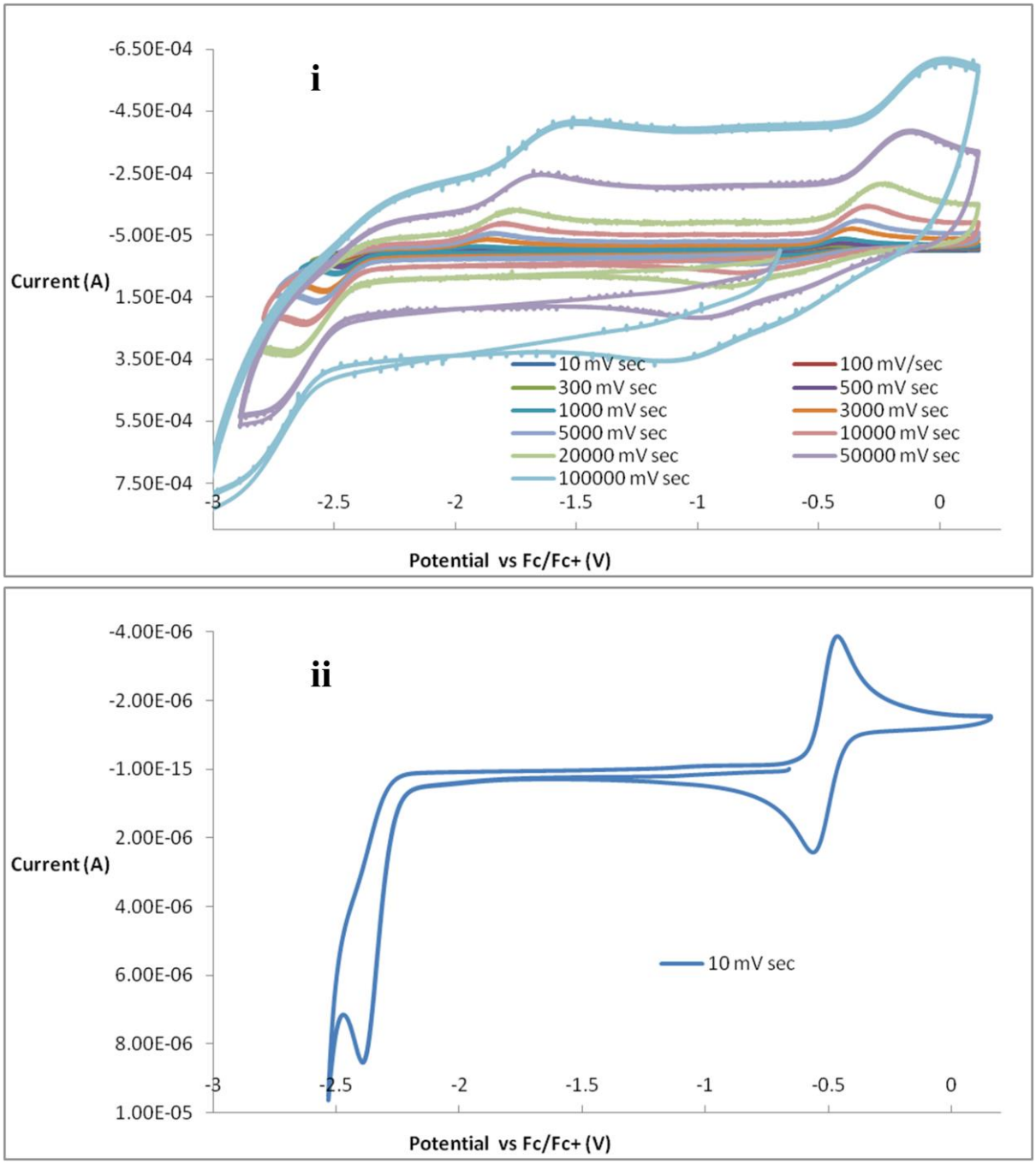

Appendix C.1: Scan rate dependence (as per Figure 4.4) of 1 mM ***(1)*** in DMF with 0.1 M $TBAPF_6$ and 5% H_2O under Ar, potential window encapsulating the first oxidation and first reduction only. Scan rate; **i**. 10, 100, 300 and 500, 1,000, 3,000, 5,000, 10,000, 20,000, 50,000 and 100,000 mV s^{-1} and **ii**. 10 mV s^{-1} only

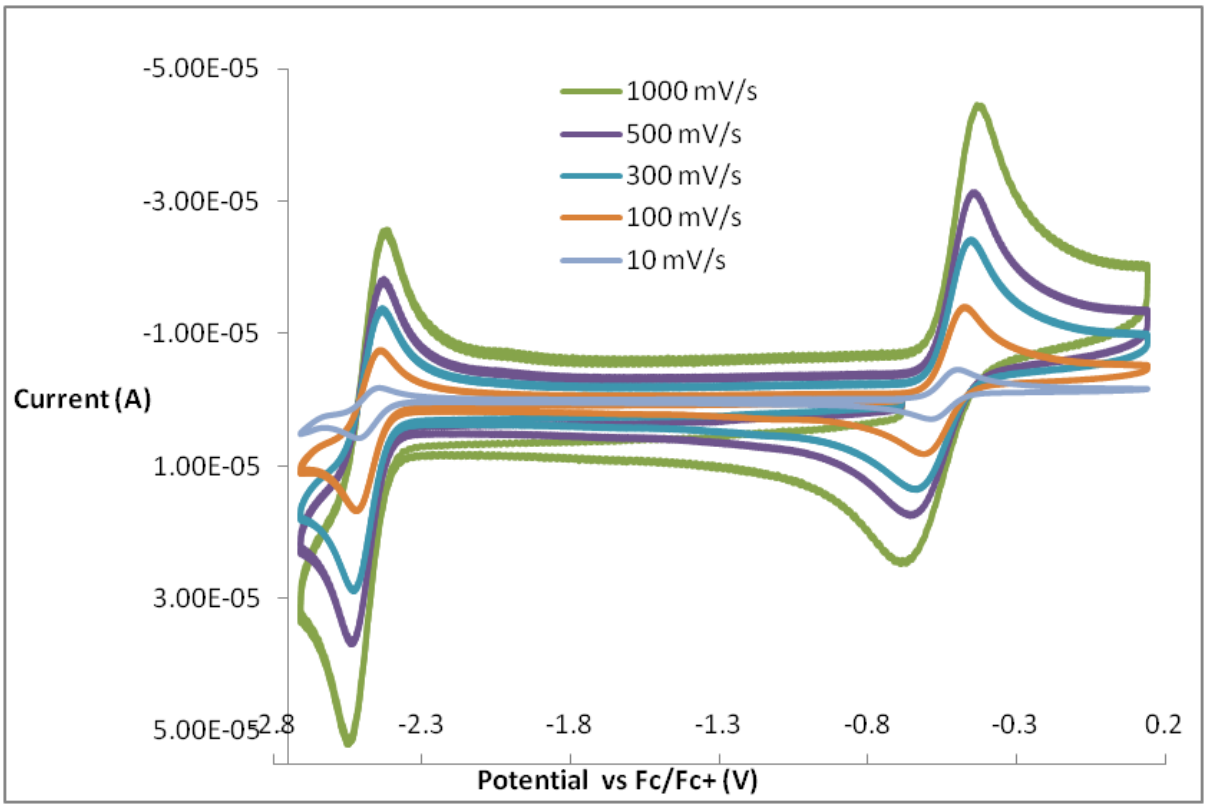

Appendix C.2: 1 mM ***(1)*** in Ar-purged DMF with 0.1 M $TBAPF_6$ and in the absence of water, at varied scan rate of 10, 100, 300, 500 and 1,000 mV s^{-1}. A plot of current against $v^{0.5}$ reveals $Co^{2+/1+}$ and $Co^{1+/2+}$ R^2 values of 0.998 and 0.993 respectively

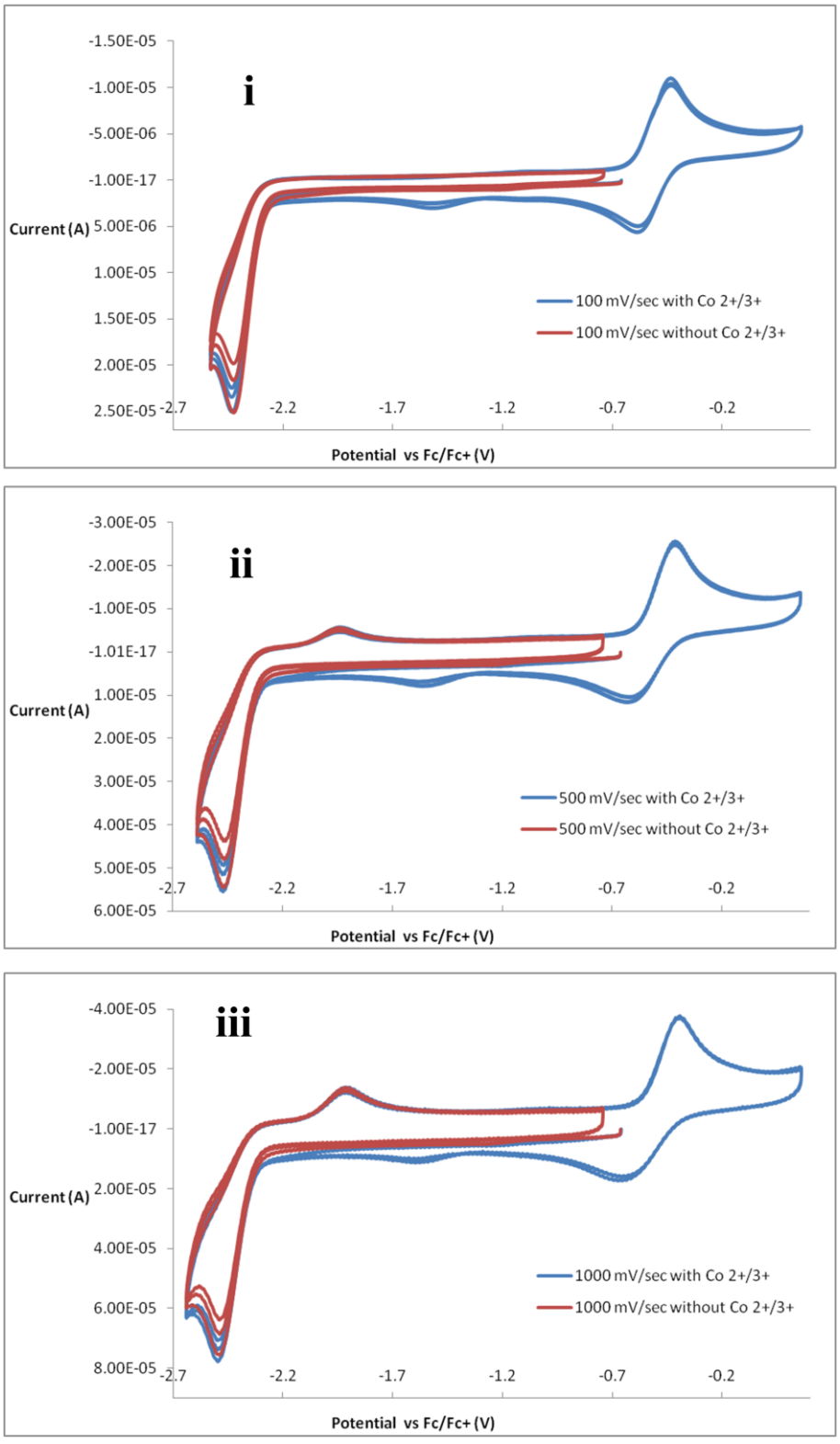

Appendix C.3: Scan rate variation of the first reduction of 1 mM ***(1)*** in DMF with 0.1 M $TBAPF_6$ and 5% H_2O under Ar, including and excluding the $Co^{2+/3+}$ redox process at **i**. 100 mV s^{-1}, **ii**. 500 mV s^{-1} and **iii**. 1000 mV s^{-1}

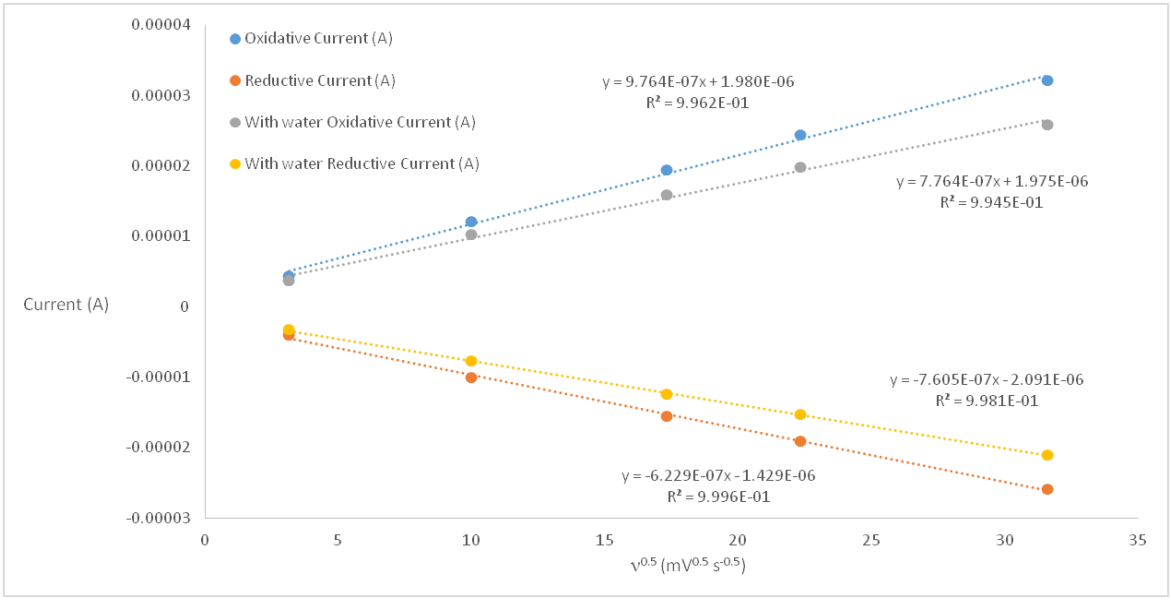

		Without 5% water			With 5% water		
ν (mV s^{-1})	$\nu^{0.5}$ ($mV^{0.5}$ $s^{-0.5}$)	$Co^{2+/3+}$ Current (μA)	$Co^{3+/2+}$ Current (μA)	ΔE_p (mV)	$Co^{2+/3+}$ Current (μA)	$Co^{3+/2+}$ Current (μA)	ΔE_p (mV)
10	3.16	4.4	4.0	102	3.7	3.3	117
100	10	12.0	10.1	166	10.2	7.8	203
300	17.32	19.4	15.6	230	15.8	12.4	287
500	22.36	24.4	19.1	264	19.8	15.3	331
1000	31.62	32.1	25.9	323	25.9	21.1	391
3000*	54.77	51.4	43.2	415	39.4	34.7	481
5000*	70.71	59.9	55.0	470	48.6	43.8	515
10000*	100	81.2	71.8	577	60.7	55.8	611

Appendix C.4: ***(1)*** first oxidative redox couple's current response with varied (square root of) scan rate under Ar, in DMF and in DMF with 5% water and associated data. *Scan rates plotted are 10, 100, 300, 500 and 1000 mV s^{-1}. 3000, 5000 and 10000 mV s^{-1} are omitted due to noise in voltammograms complicating interpretation of peak height and baseline slope

Appendix C.5: Results obtained from single hour-long "solution" electrolysis with 1 mM ***(1)*** with 5% water, and subsequent "surface" experiment in the absence of water. Electrolyses undertaken at -2.71 V in a DMF/0.1 M $TBAPF_6$ solution with a glassy carbon electrode

Experiment	# of runs	Charge (C)	H_2 nmol	H_2 FE (%)
Solution hr 1	3	1.606	6580	79
Surface 1 hr without water, following	1	0.018	3	3

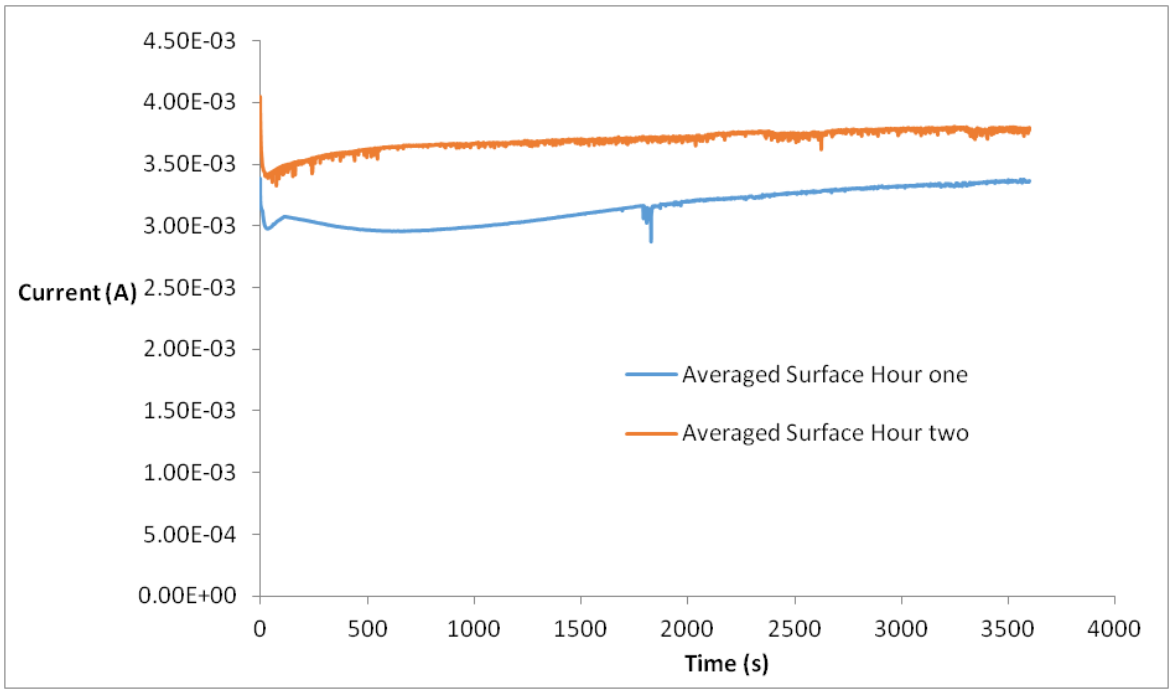

Appendix C.6: Averaged bulk electrolysis current-time plots for surface hours one and two (data as per Table 4.6) at -2.71 V vs Fc/Fc^+ with carbon paper in DMF/0.1 M $TBAPF_6$ with 5% water (electrodes generated following solution hr 1)

Appendix C.7: Effect of electrolysis at -2.71 V vs Fc/Fc^+ using a carbon paper electrode soaked in a 1 mM ***(1)***, DMF, 0.1 M $TBAPF_6$ and 5% water solution. Surface and control electrolyses figures as per Table 4.6

Experiment	# of runs	Charge (C)	H_2 μmol	H_2 FE (%)
Soaked hour 1	1	3.80	2	12
Soaked hour 2	1	2.23	4	33
Surface-1 hour 1	4	11.35	46.9	80
Surface-1 hour 2	4	13.30	57	83
Control hour 1	4	2.98	1	7
Control hour 2	3	2.46	5	39

Appendix C.8: Effect of consecutive electrolysis vs hour-long electrolyses at -2.71 V vs Fc/Fc^+ in DMF, 0.1 M $TBAPF_6$ and 5% water solution. Surface electrodes as generated in Table 4.6

Experiment	# of runs	Charge (C)	H_2 μmol	H_2 FE (%)
Surface hour 1	4	11.35	46.9	80
Surface Hour 2	4	13.30	57	83
Surface hours 1 + 2 cumulative	-	24.65	103.9	81.5
Surface 2 hours	3	24.40	91.4	72.3
Control hour 1	4	2.98	1	7
Control hour 2	3	2.46	5	39
Control hours 1 + 2 cumulative	-	5.45	6	23
Control 2 hours	4	4.66	5.5	23

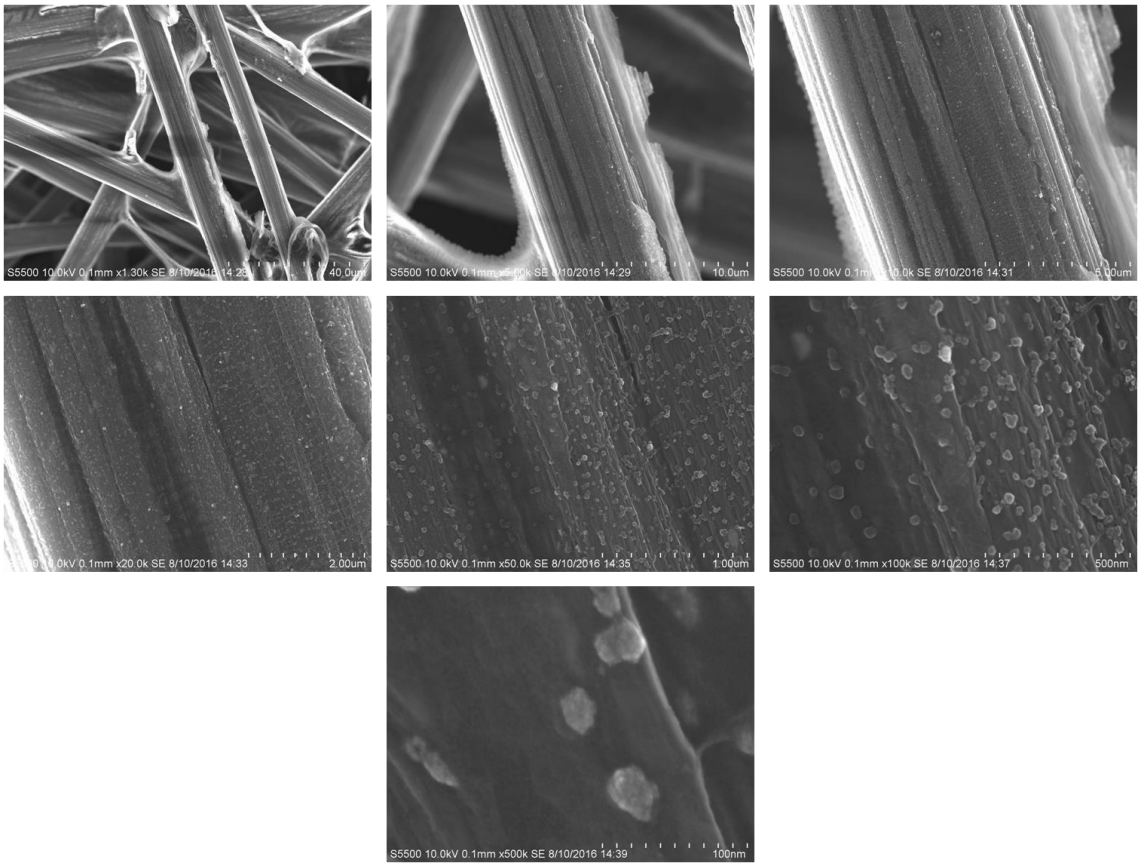

Appendix C.9: SEM images of "Soln hr 1 #2", the carbon paper used as working electrode in the first hour electrolysis of 1 mM ***(1)*** in DMF/5% H_2O/0.1 M $TBAPF_6$ at -2.71 V vs Fc/Fc^+, 10 kV accelerating voltage, 21.2 – 21.6 μA probe current. Magnification left to right, top to bottom: 1300, 5000, 10000, 20000, 50000 and 100000 and 500000x

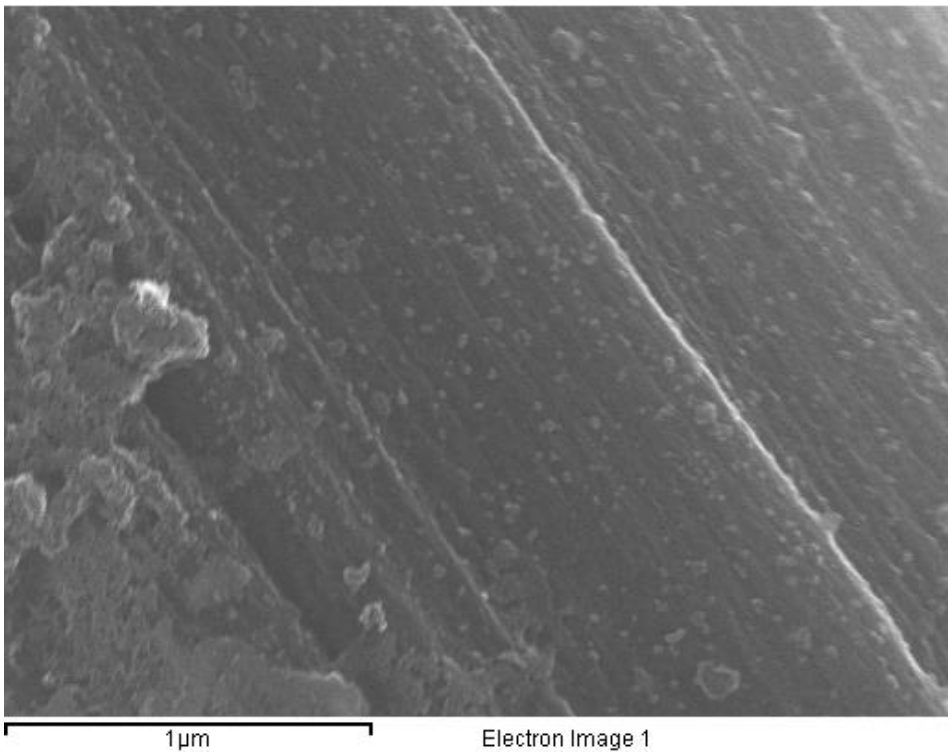

Appendix C.10: SEM image (top) and the associated EDX spectrum (bottom) of the "Soln hr 1 #1" electrode. the carbon paper used as working electrode in the first hour electrolysis of 1 mM ***(1)*** in DMF/5% H_2O/0.1 M $TBAPF_6$ at -2.71 V vs Fc/Fc^+. 15 kV accelerating voltage

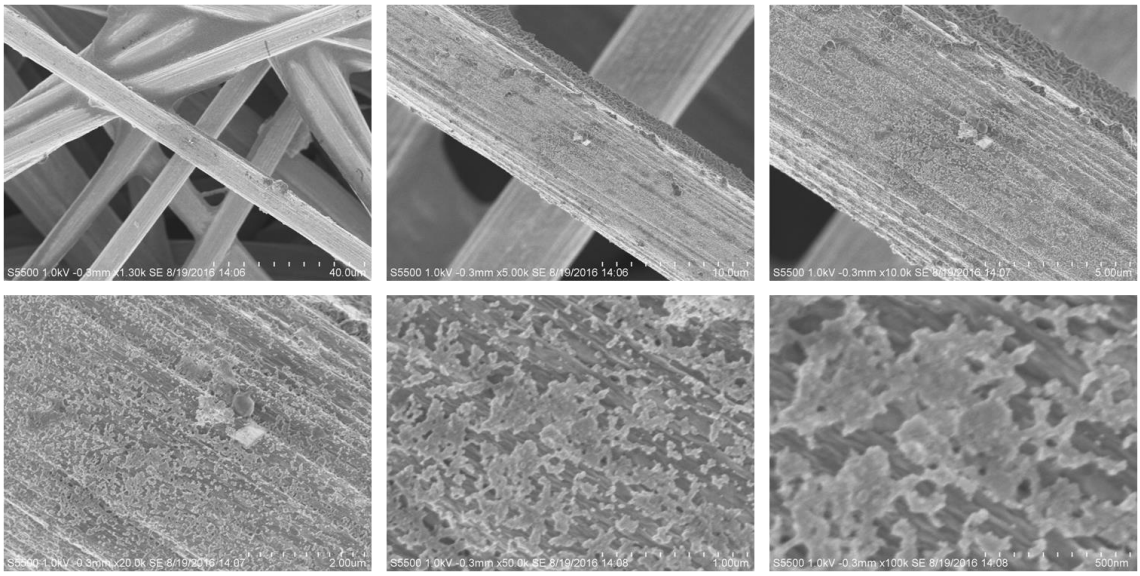

Appendix C.11: SEM images of "Surface hrs 1+2 #2", the carbon paper used as working electrode following one hour electrolysis of 1 mM ***(1)*** in DMF/5% H_2O/0.1 M $TBAPF_6$ at -2.71 V vs Fc/Fc^+, and subsequent electrolysis for two interrupted hours at -2.71 V vs Fc/Fc^+ in the absence of ***(1)***. 1 kV accelerating voltage, 18.8 – 19.6 μA probe current. Magnification left to right, top to bottom: 1300, 5000, 10000, 20000, 50000 and 100000x

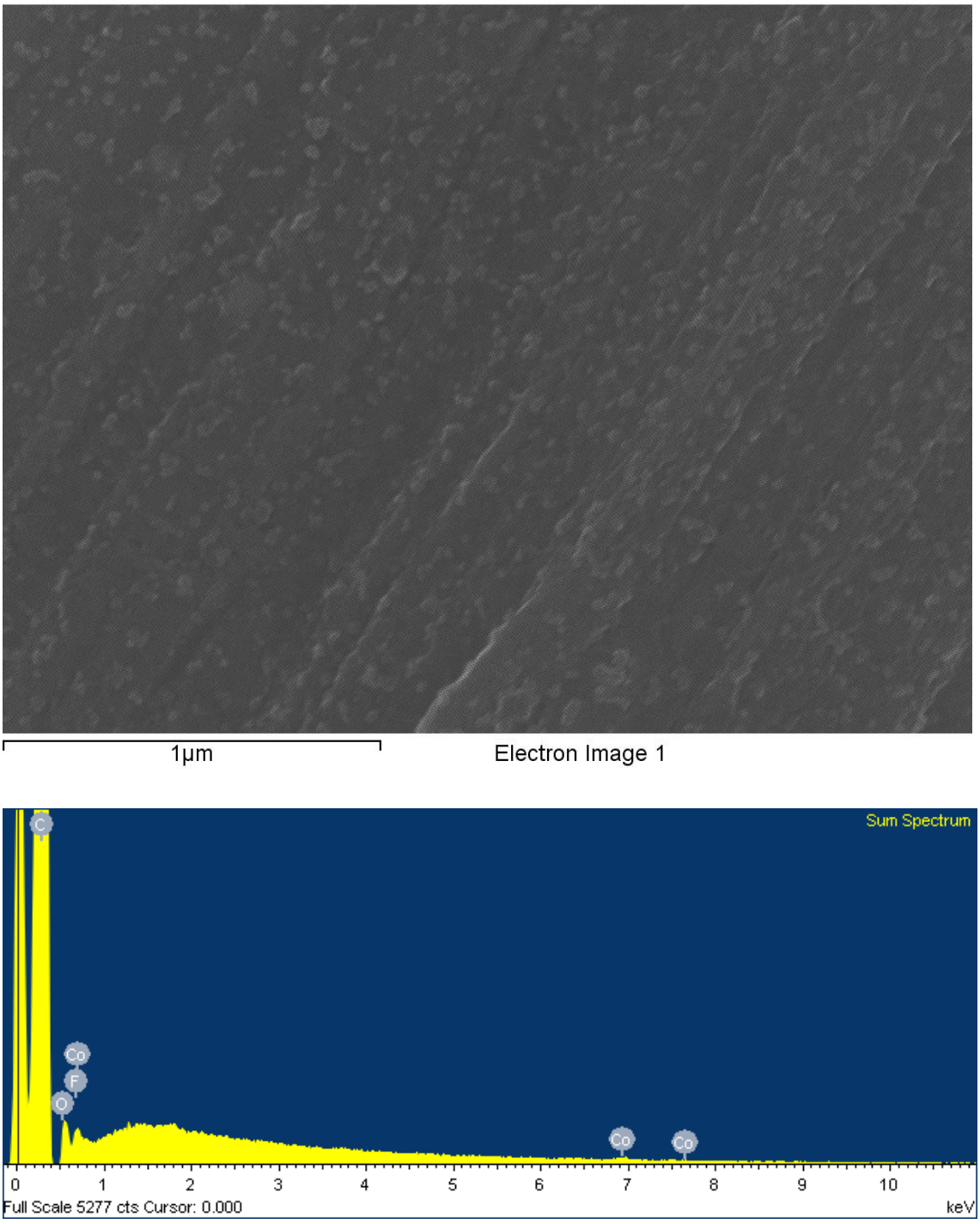

Appendix C.12: SEM image (top) and the associated EDX spectrum (bottom) of the outermost fibre of "Surface 2 hrs #1" electrode (associated SEM images in Figure 4.21). 15 kV accelerating voltage

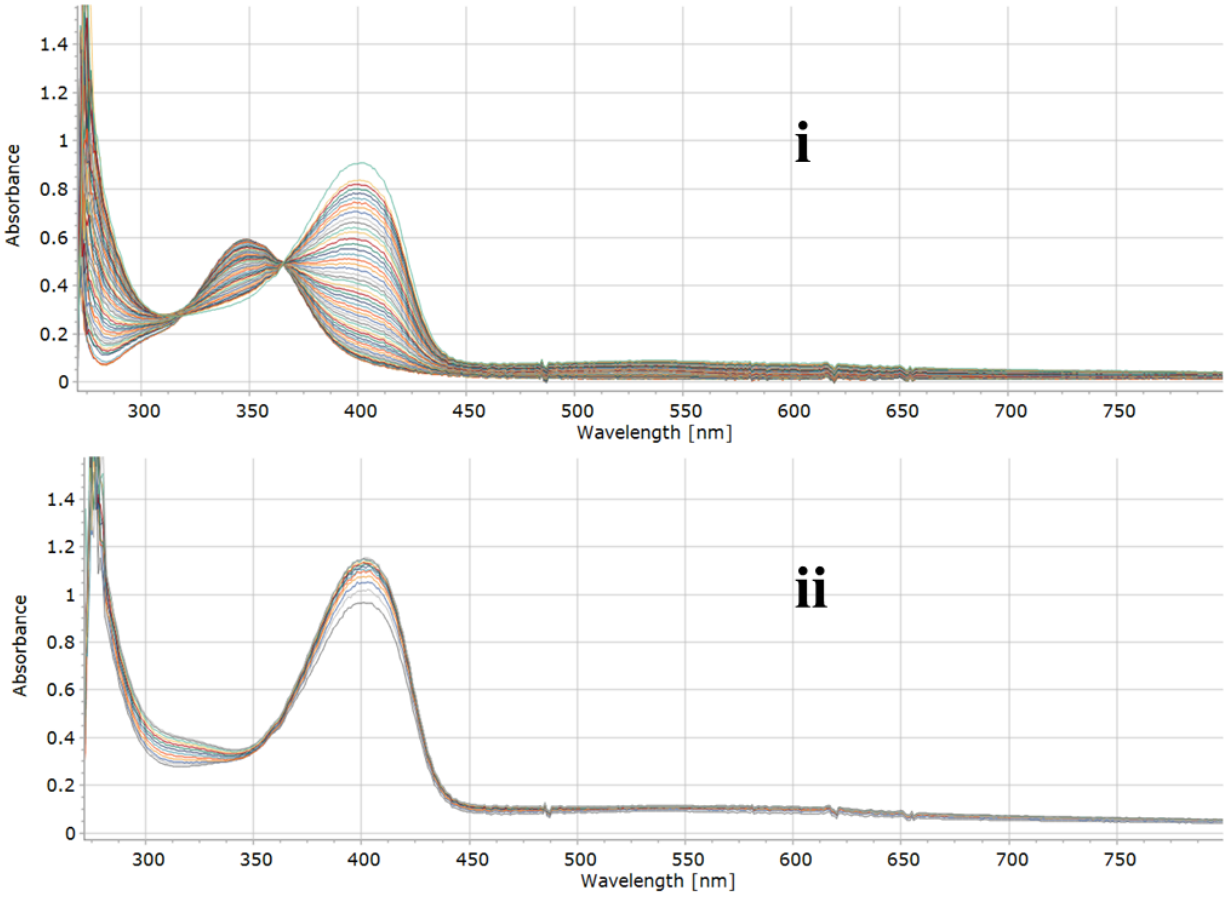

Appendix C.13: UV-visible spectra acquired from 0-55 mins **(i)** and 60-120 mins **(ii)** of electrolysis, conditions and spectra as per Figure 4.28 (electrolysis of 60 μM ***(1)*** in 15ml DMF/0.1 M $TBAPF_6$ at -2.48 V vs Fc/Fc^+)

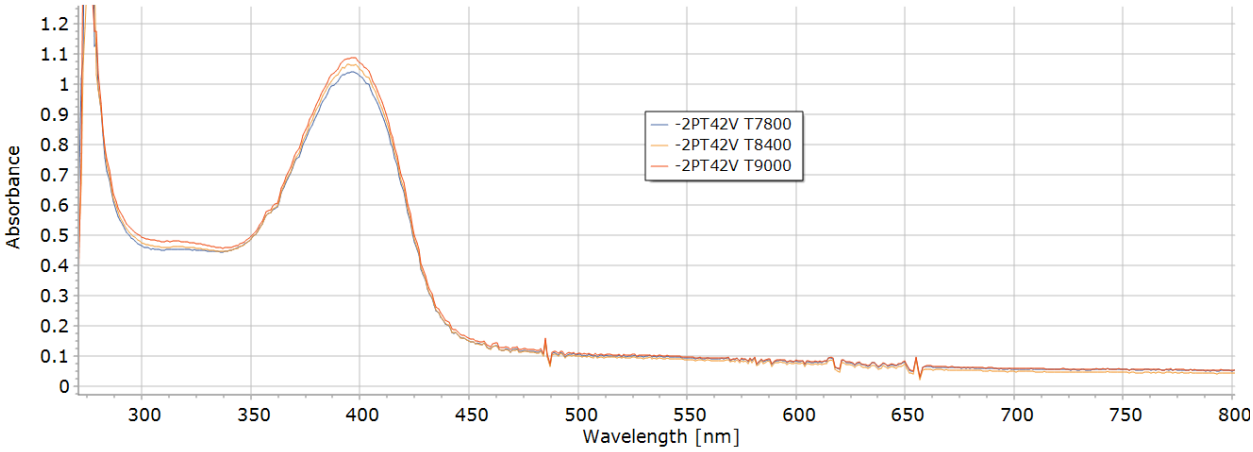

Appendix C.14: UV-visible spectra as per Figure 4.33 (electrolysis of 60 μM ***(1)*** in 15ml DMF/0.1 M $TBAPF_6$ with 15 μl water at -2.42 V vs Fc/Fc^+) at 130, 140 and 150 minutes of electrolysis

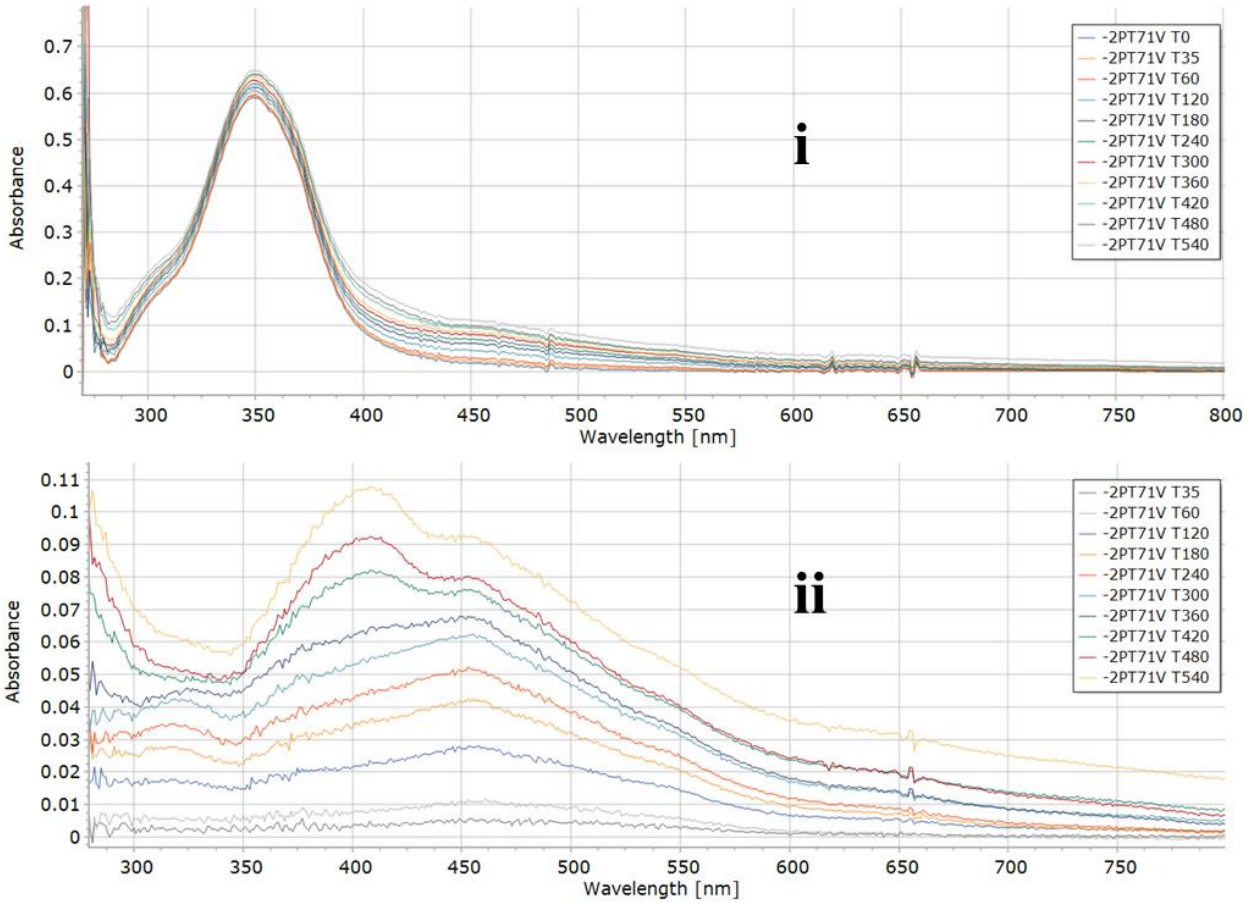

Appendix C.15: **i.** UV-visible spectra and **ii.** difference spectra associated with the first 9 minutes of electrolysis of 60 μM ***(1)*** at -2.71 V vs Fc/Fc^+ in DMF with 0.1 M $TBAPF_6$ (as per Figure 4.36 and Figure 4.37)

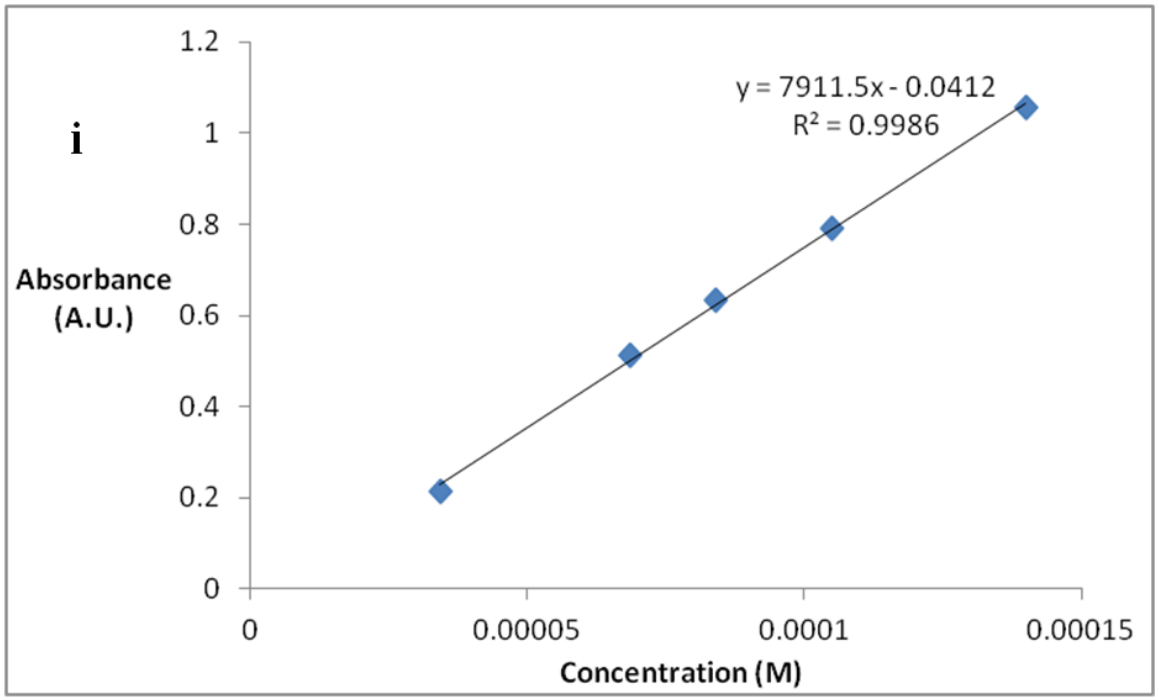

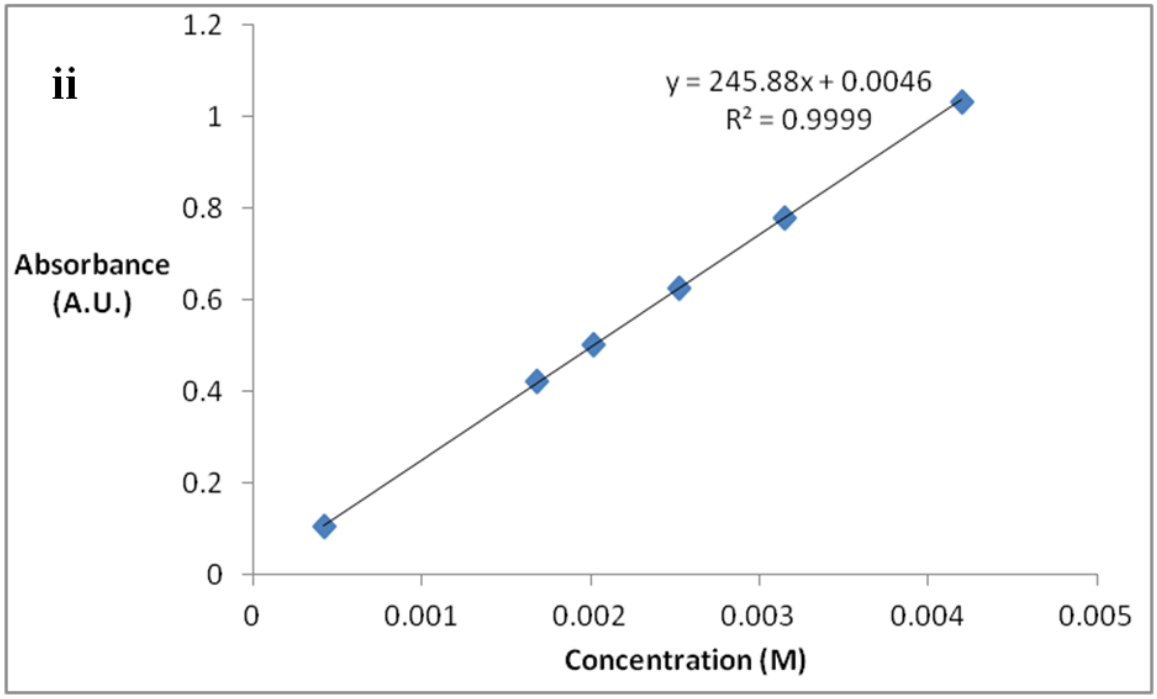

Appendix C.16: Calibration curve of H_2pdSal in DMF at **i**. λ_{max} of 315 nm and **ii**. λ_{max} of 408 nm

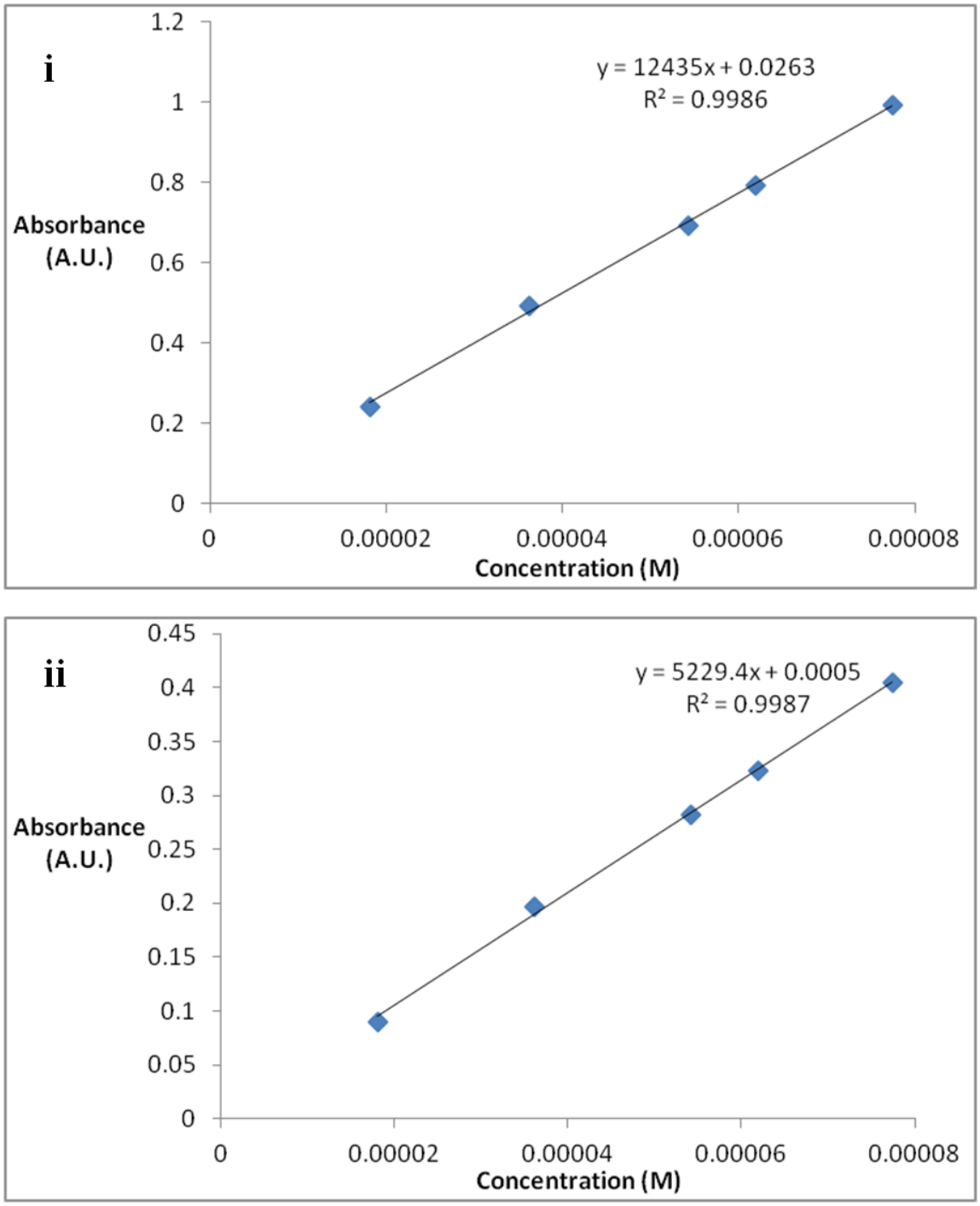

Appendix C.17: Calibration curve of Ar purged ***(1)*** in DMF at **i.** λ_{max} of 349 nm and **ii.** at 315 nm

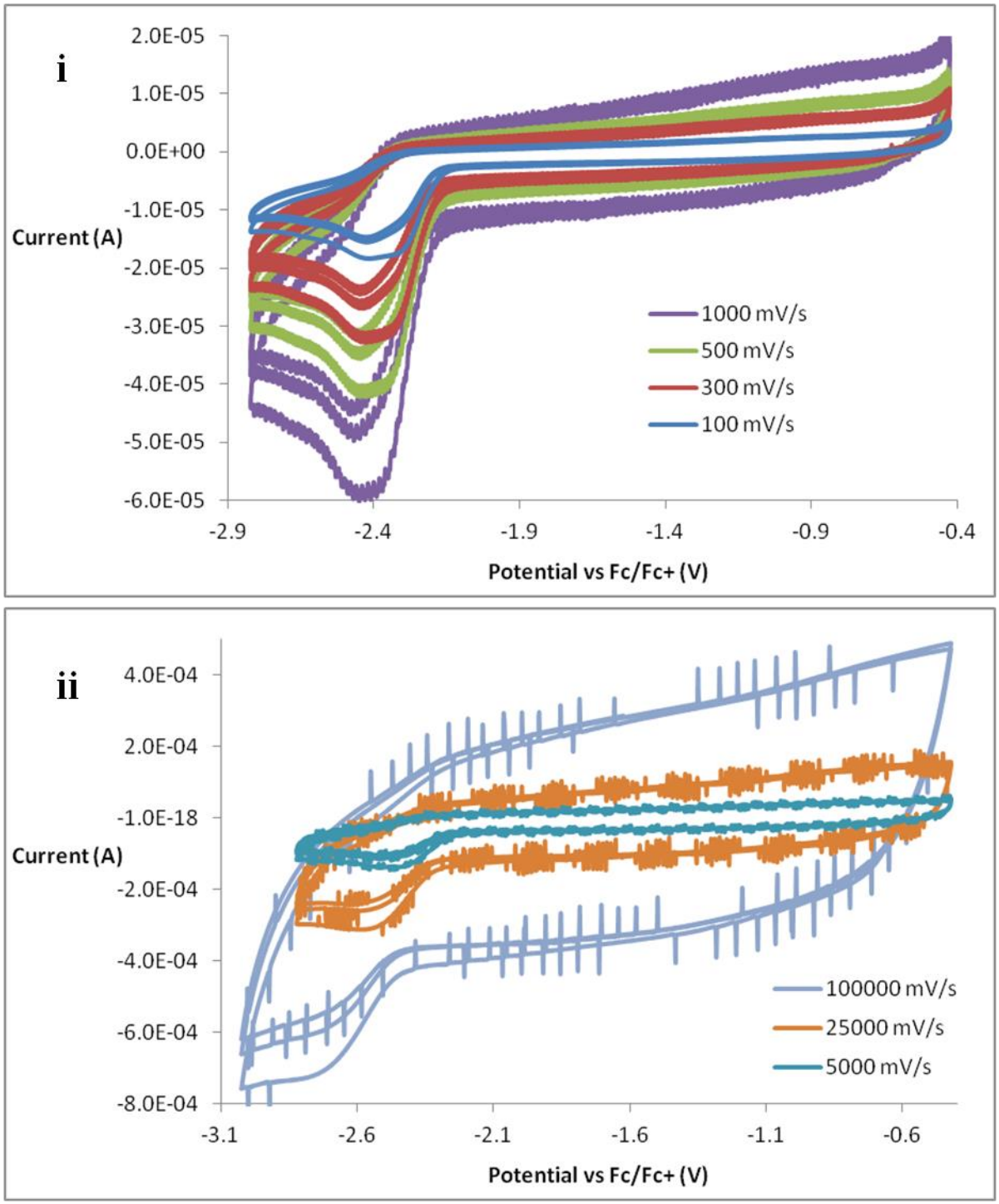

Appendix C.18: Cyclic voltammetry with varied scan rate of **i.** 100, 300, 500 and 1000 and **ii.** 5000, 25000 and 100000 mV s^{-1} on the first reductions of H_2pdSal at glassy carbon in DMF with 0.1 M $TBAPF_6$ in the absence of water

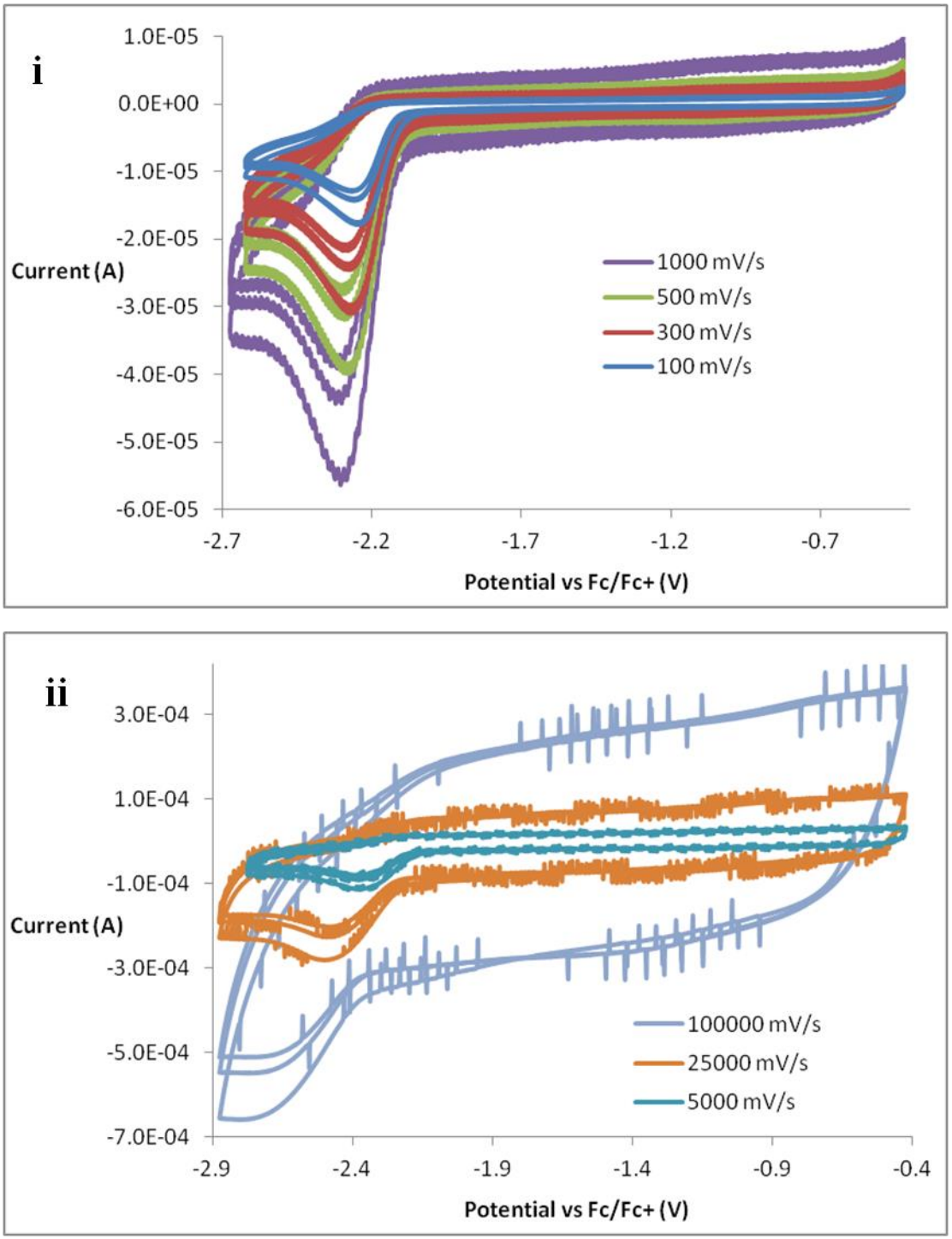

Appendix C.19 Cyclic voltammetry with varied scan rate of **i.** 100, 300, 500 and 1000 and **ii.** 5000, 25000 and 100000 mV s^{-1} on the first reduction of H_2pdSal at glassy carbon in DMF with 0.1 M $TBAPF_6$ and 5% water

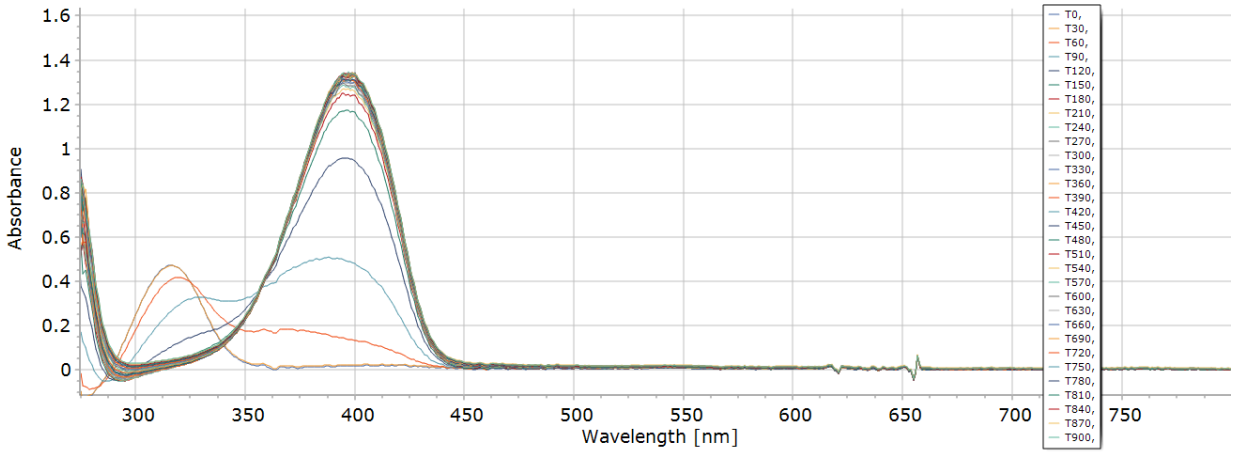

Appendix C.20: As per Figure 4.42. UV-visible spectra acquired from 0 to 900 seconds during the electrolysis of approximately 60 μM H_2pdSal in 15ml DMF/0.1 M $TBAPF_6$ with 15 μl water at -2.71 V vs Fc/Fc^+

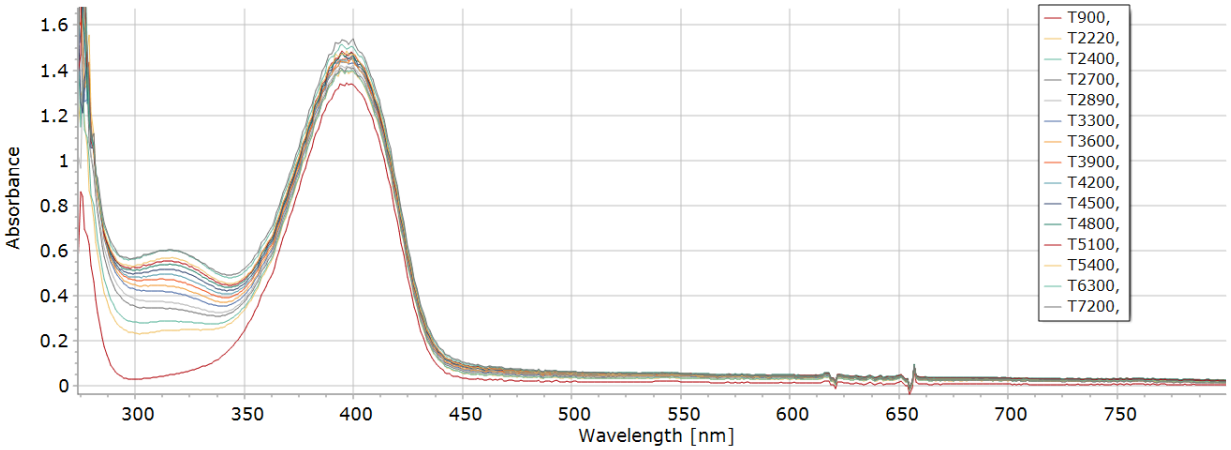

Appendix C.21: As per Figure 4.42. UV-visible spectra acquired from 900 to 7200 seconds during the electrolysis of approximately 60 μM H_2pdSal in 15ml DMF/0.1 M $TBAPF_6$ with 15 μl water at -2.71 V vs Fc/Fc^+

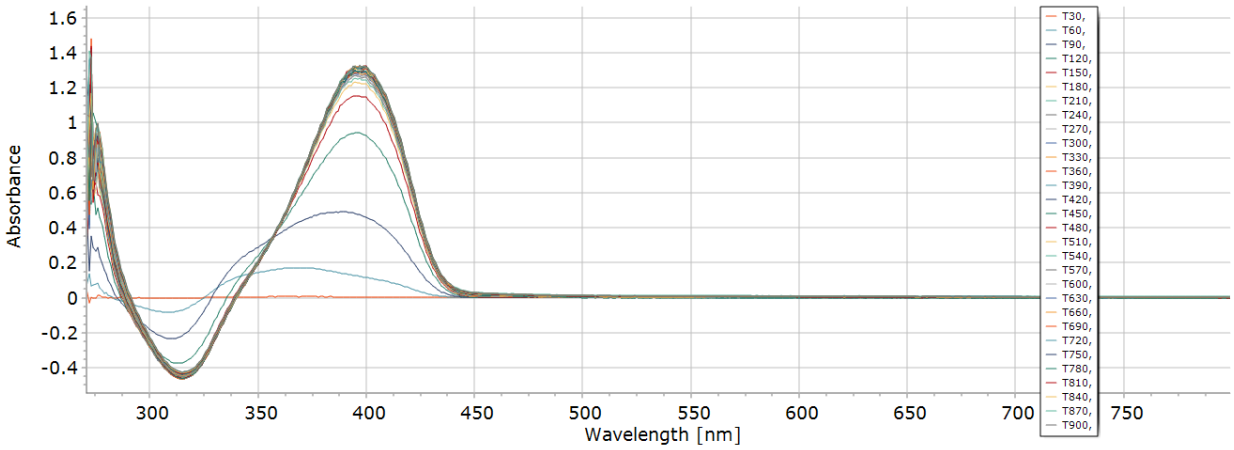

Appendix C.22: As per Figure 4.43. UV-visible difference spectra acquired from 30 to 900 seconds during the electrolysis of approximately 60 μM H_2pdSal in 15ml DMF/0.1 M $TBAPF_6$ with 15 μl water at -2.71 V vs Fc/Fc^+

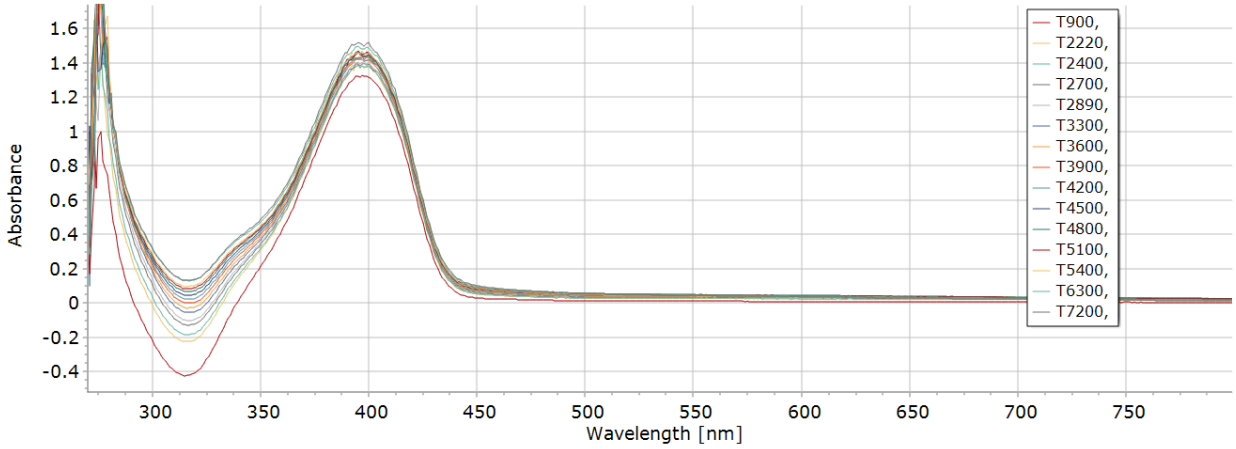

Appendix C.23: As per Figure 4.43. UV-visible difference spectra acquired from 900 to 7200 seconds during the electrolysis of approximately 60 μM H_2pdSal in 15ml DMF/0.1 M $TBAPF_6$ with 15 μl water at -2.71 V vs Fc/Fc^+